

A MOLECULAR SOLUTION TO SOLAR FUELS

Dennis Lee Ashford II

A dissertation submitted to the faculty of The University of North Carolina at Chapel Hill in partial fulfillment of the requirements for the degree of Doctor of Philosophy in the Department of Chemistry.

Chapel Hill
2014

Approved by:

Joseph L. Templeton

Thomas J. Meyer

Maurice S. Brookhart

Cynthia K. Schauer

Wei You

© 2014
Dennis L. Ashford II
ALL RIGHTS RESERVED

ABSTRACT

Dennis Lee Ashford II: A Molecular Solution to Solar Fuels
(Under the direction of Thomas J. Meyer and Joseph L. Templeton)

Increasing demand for energy and the possible environmental impact of burning fossil fuels has resulted in the pursuit to discover a renewable energy source that circumvents these problems. The sun provides sufficient energy every hour to satisfy global energy consumption for an entire year, making it an attractive and probable long-term solution to alternative fuel sources. However, the diurnal cycle of the sun requires that the energy be stored in chemical bonds which can be achieved through water oxidation ($2 \text{H}_2\text{O} + 4 h\nu \rightarrow \text{O}_2 + 4 e^-$) and using the reductive equivalents to reduce water to hydrogen or CO_2 to carbon based fuels.

The absorption of solar energy is the initial step in generating solar fuels from light. Several new series of chromophores were fully characterized both in solution and derivatized on metal oxide electrodes for use in photoanodes. These complexes show that lowering the π^* acceptor orbitals results in the lowering of the excited state reduction potential ($\text{Ru}^{3+/2+*}$) while leaving the ground state oxidation potential ($\text{Ru}^{3+/2+}$) relatively unaffected.

A new strategy to build chromophore-catalyst assemblies based on amide coupling was then devised as a way to systematically change the light harvesting chromophore, water oxidation catalyst, and the intervening spacer between the two metal centers. Photophysical analysis demonstrated that upon photoexcitation, electron injection into the conduction band

of TiO₂ has an efficiency of ~ 95%. Following electron injection, forward electron transfer between the two metal centers is ~ 100% efficient with $\tau = 145$ ps.

While amide coupling to build assemblies is general, it still requires multiply synthetic steps and yields assemblies that are unstable on metal oxides surface at elevated pHs. A new strategy to build spatially controlled, multi-component films on metal oxide electrodes utilizing electropolymerization. These electropolymerized films were found to be significantly more stable compared to the bare surface chromophore under photoelectrochemical conditions. In addition, electropolymerized films on a known water oxidation catalyst demonstrated that the electrocatalytic properties of the catalyst were maintained within the polymer films.

ACKNOWLEDGEMENTS

I would first like to thank my family and in particular my parents, Denise and Dennis Ashford, for all of their support and encouragement in not only my graduate career but throughout my life. Without them, I would not be where I am today. I would also like to thank Stephanie as we have gone through this journey together and have supported each other through the good times and bad of graduate school.

I must also thank my advisors, Professors Joseph L. Templeton and Thomas J. Meyer for all of their help and support during my time at UNC. I came in as a student who did not know how to think on their own to an independent scientist and I owe a lot of that to both of them. They have also taught me valuable life lessons both in my professional and personal life.

I would finally like to thank all of my friends both in the Templeton and Meyer laboratories and outside of these groups. Graduate school has been one of the most enjoyable times of my life and I owe a lot of that to them.

TABLE OF CONTENTS

LIST OF FIGURES	vii
LIST OF TABLES	xxi
LIST OF SCHEMES	xxiii
LIST OF EQUATIONS	xxiv
LIST OF ABBREVIATIONS AND SYMBOLS	xxvii
Chapter 1: USING MOLECULES TO GENERATE SOLAR FUELS	1
1.1 Introduction.....	1
1.2 Current Strategies for Artificial Photosynthesis	3
1.3 Dye-Sensitized Photoelectrosynthesis Cells	10
1.4 Design Principles for Molecular Chromophore-Catalyst Assemblies	13
Chapter 2: CONTROLLING GROUND AND EXCITED STATE PROPERTIES THROUGH LIGAND CHANGES IN RUTHENIUM POLYPYRIDYL COMPLEXES	20
2.1 Introduction.....	20
2.2 Experimental	22
2.3 Results and Discussion.....	32
2.4 Conclusions.....	51
2.5 Acknowledgements	52
2.6 Associated Content.....	52
Chapter 3: VARYING THE ELECTRON STRUCTURE OF SURFACE BOUND RUTHENIUM(II) POLYPYRIDYL COMPLEXES	53

3.1	Introduction	53
3.2	Experimental	54
3.3	Results and Discussion.....	60
3.4	Conclusions	77
3.5	Associated Content.....	78
Chapter 4: AN AMIDE-LINKED CHROMOPHORE-CATALYST ASSEMBLY FOR WATER		
	OXIDATION	79
4.1	Introduction	79
4.2	Experimental	81
4.3	Results and Discussion.....	91
4.4	Associated Content.....	97
Chapter 5: PHOTOINDUCED ELECTRON TRANSFER IN A CHROMOPHORE-CATALYST		
	ASSEMBLY ANCHORED TO TiO ₂	98
5.1	Introduction	98
5.2	Experimental	101
5.3	Results	107
5.4	Discussion	116
5.5	Conclusions	124
5.6	Acknowledgments.....	124
5.7	Associated Content.....	125
Chapter 6: WATCHING PHOTOACTIVATION IN A Ru(II) CHROMOPHORE-CATALYST		
	ASSEMBLY ON TiO ₂ BY ULTRAFAST SPECTROSCOPY	126
6.1	Introduction	126
6.2	Experimental	129
6.3	Results and Discussion.....	131

6.4	Conclusions	148
6.5	Acknowledgments	149
6.6	Associated Content.....	149
Chapter 7: STABILIZATION OF A RUTHENIUM(II) POLYPYRIDYL DYE ON NANOCRYSTALLINE TiO₂ BY AN ELECTROPOLYMERIZED OVERLAYER		
		150
7.1	Introduction	150
7.2	Experimental	152
7.3	Results and Discussion.....	160
7.4	Conclusions	180
7.5	Acknowledgements	181
7.6	Associated Content.....	181
Chapter 8: WATER OXIDATION BY AN ELECTROPOLYMERIZED CATALYST ON DERIVATIZED MESOPOROUS METAL OXIDE ELECTRODES.....		
		182
8.1	Introduction	182
8.2	Experimental	183
8.3	Results and Discussion.....	190
8.4	Associated Content.....	203
8.5	Acknowledgments.....	203
APPENDIX A. CONTROLLING GROUND AND EXCITED STATE PROPERTIES THROUGH LIGAND CHANGES IN RUTHENIUM POLYPYRIDYL COMPLEXES		
		204
APPENDIX B. VARYING THE ELECTRONIC STRUCTURE OF SURFACE BOUND RUTHENIUM(II) POLYPYRIDYL COMPLEXES		
		241
APPENDIX C. AN AMIDE-LINKED CHROMOPHORE-CATALYST ASSEMBLY FOR WATER OXIDATION		
		248
APPENDIX D. PHOTOINDUCED ELECTRON TRANSFER IN A CHROMOPHORE-CATALYST ASSEMBLY ANCHORED TO TiO₂.....		
		255

APPENDIX E. WATCHING PHOTOACTIVATION IN A Ru(II) CHROMOPHORE-CATALYST ASSEMBLY ON TiO ₂ BY ULTRAFAST SPECTROSCOPY	264
APPENDIX F. STABILIZATION OF A RUTHENIUM(II) POLYPYRIDYL DYE ON NANOCRYSTALLINE TiO ₂ BY AN ELECTROPOLYMERIZED OVERLAYER	269
APPENDIX G. WATER OXIDATION BY AN ELECTROPOLYMERIZED CATALYST ON DERIVATIZED MESOPOROUS METAL OXIDE ELECTRODES	279
REFERENCES	307

LIST OF FIGURES

Figure 1.1. (A) World energy consumption (in British thermal units, Btu's) of fossil fuels (black), renewables (red) and nuclear energy (green). (B) World carbon emissions per year. Data obtained from the Energy Information Administration. ¹ All data past 2012 are predictions.	2
Figure 1.2. A) Honda-Fujishima photoelectrochemical cell with TiO ₂ as the photoanode. ⁴³ B) Single semiconductor nanoparticle with WOC (RuO ₂) and RC (Pt) attached. ⁵⁷ C) Photoelectrochemical cell proposed by JCAP with nanowire arrays as the light harvesters. ⁶⁸ Reprinted from ref. 68 with permission from the Royal Society of Chemistry.	7
Figure 1.3. PV-electrolysis photoelectrochemical cell with 3-jn PV as the light harvester wired (A) and wireless (B). ²⁸	8
Figure 1.4. A) Single GaAs p-n junction cell with p-type GaInP ₂ cathode. ⁷⁶ B) Schematic diagram of a Z-scheme with two photocatalyst.	9
Figure 1.5. Ru-oxo single-site water oxidation mechanism. Adapted with permission from ref. 35. Copyright 2013 American Chemical Society. (Alexander J. Miller)	11
Figure 1.6. Dye-sensitized photoelectrosynthesis cell (DSPEC) for water oxidation and CO ₂ reduction to CH ₄ . (James F. Cahoon).....	12
Figure 1.7. Design principles for a photoanode in a DSPEC.	13
Figure 2.1. Structures of the generic complex and ligands in the series [Ru(bpy) ₂ (N-N)] ²⁺	22
Figure 2.2. ORTEP diagram of complex 6 from single crystal X-ray analysis with thermal ellipsoids at the 50% probability level. Hydrogen atoms are omitted for clarity.....	35
Figure 2.3. Cyclic voltammogram of complexes 7 (black), 4 (red), 1 (green), Ru(bpy) ₃ ²⁺ (blue), and 3 (orange) in dry CH ₃ CN at 22°C with a glassy carbon working electrode, Pt-wire counter electrode, and a Ag/AgNO ₃ reference electrode with $E_{1/2}$ (Ru(bpy) ₃ ^{3+/2+}) = 1.29 V vs SCE.	37
Figure 2.4. Cyclic voltammogram for complexes 9 (orange), 3 (blue), 1 (red), and Ru(bpy) ₃ ²⁺ (black), in dry CH ₃ CN at 22°C under a nitrogen atmosphere with a glassy carbon working electrode, Pt-wire counter, and a Ag/AgNO ₃ reference (relative to Ru(bpy) ₃ ²⁺ at 1.29 V vs SCE).	38
Figure 2.5. UV-Visible spectra of Ru(bpy) ₃ ²⁺ , 2 , and 9 in CH ₃ CN at room temperature.....	40
Figure 2.6. UV-Visible spectrum of complex 6 at room temperature in CH ₃ CN (black line) and calculated TD-DFT transitions (vertical red bars with heights illustrating	

oscillator strengths). The calculated transition energies are red-shifted 15 nm for visualization purposes.	42
Figure 2.7. Normalized emission spectra for Ru(bpy) ₃ ²⁺ and 1 - 9 in argon deaerated CH ₃ CN at room temperature.	42
Figure 2.8. Plot of emission energy vs ln τ ⁻¹ for complexes 1 - 9 and Ru(bpy) ₃ ²⁺ in CH ₃ CN at 25°C.	44
Figure 2.9. (Left) Variation of absorption, vabs, red squares, and emission, vem, blue circles, energies on the electrochemical gap ((ΔE _{1/2} = E _{1/2} (Ru ^{3+/2+}) - E _{1/2} (Ru ^{2+/+})) for Ru(bpy) ₃ ²⁺ and 1 - 9 . (Right) Variation of vem with E _{1/2} (Ru ^{2+/+}) in dry CH ₃ CN at 25°C.	45
Figure 2.10. Dependence of the free energy content of the excited state (ΔG _{ES}) on E _{1/2} (Ru ^{3+/2+*}).	48
Figure 2.11. Variation of ground and excited state redox potentials with emission energy in CH ₃ CN (0.1 M TBAPF ₆ for electrochemical measurements) at 25°C.	48
Figure 2.12. Variations in E _{1/2} (Ru ^{3+/2+}), red squares) and E _{1/2} (Ru ^{3+/2+*}), blue circles) with vabs for the lowest energy MLCT λ _{max} in CH ₃ CN at 25°C.	50
Figure 3.1. Structures of RuPOMe , RuPMe , RuP , and RuPBr	54
Figure 3.2. ¹ H NMR spectra of RuPBr (blue), RuP (green), RuPMe (pink), and RuPOMe (red) in D ₂ O.	63
Figure 3.3. Square-wave voltammograms (normalized to peak current value) of RuPOMe (blue), RuPMe (green), RuP (black), and RuPBr (red) immobilized on TiO ₂ as the working electrode, Pt counter, and Ag/AgCl reference (0.197 V vs NHE) electrode in aqueous 0.1 M HClO ₄	65
Figure 3.4. Square-wave voltammogram of RuPMe (1.0 mM in 80:20 CH ₃ CN:H ₂ O, 0.1 M TBAPF ₆ supporting electrolyte, Pt-wire counter, and Ag/AgNO ₃ reference (0.4 V vs NHE).	67
Figure 3.5. UV/Visible absorption spectra for RuPOMe , RuPMe , RuP , and RuPBr in H ₂ O.	68
Figure 3.6. UV-visible spectrum of RuPMe at room temperature in H ₂ O (black line) and calculated TD-DFT transitions (vertical red bars with heights illustrating oscillator strengths, red-shifted by 0.15 eV).	70
Figure 3.7. Normalized emission spectra for RuPBr (black), RuP (green), RuPMe (red), and RuPOMe (blue) loaded onto ZrO ₂ in aqueous 0.1 M HClO ₄ at temperature following excitation at 450 nm.	71

- Figure 3.8.** Dependence of emission energy (vem) on $E_{1/2}(\text{Ru}^{3+/2+})$ in 0.1 M HClO₄ bound to metal oxide surface at 25°C. 72
- Figure 3.9.** Dependence of the free energy content of the excited state (ΔG_{ES} , blue circles) and the 0-0 energy gap (E_0) on the ground state oxidation potential ($E_{1/2}(\text{Ru}^{3+/2+})$) for RuPOMe, RuPMe, RuP, and RuPBr. 74
- Figure 3.10.** Variation of ground and excited state redox potentials with emission energy in H₂O (0.1 M aqueous HClO₄ for electrochemical measurements) at 25°C. 75
- Figure 3.11.** Variation in the excited state reduction potential ($\text{Ru}^{3+/2+*}$) with the ground state oxidation potential ($\text{Ru}^{3+/2+}$). 77
- Figure 4.1.** UV/Visible absorption spectra of **9** (red), **10** (green), **9 + 10** (pink), and **3** (blue) in H₂O at 25°C. 92
- Figure 4.2.** Cyclic voltammogram of **3** at pH = 2.1 (0.05 M NaH₂PO₄, 0.05 M H₃PO₄, 0.5 M KNO₃) at 100 mV/s with a glassy carbon working electrode (0.07 cm², red), and a differential pulse voltammogram of **3** (blue) at 25°C. 93
- Figure 4.3.** $E_{1/2}$ –pH diagram for assembly **3**. $E_{1/2}$ values were obtained as peak current maxima in differential pulse voltammograms. The solid lines are best fits to lines of slope ~ 0 mV/pH for the $-\text{Ru}^{\text{III}}-\text{OH}_2^{3+}/-\text{Ru}^{\text{II}}-\text{OH}_2^{2+}$ and $\text{Ru}^{\text{III/II}}$ - couples, 56 mV/pH for $-\text{Ru}^{\text{III}}-\text{OH}^{2+}/-\text{Ru}^{\text{II}}-\text{OH}_2^{2+}$, 60 mV/pH for $-\text{Ru}^{\text{IV}}=\text{O}^{2+}/-\text{Ru}^{\text{III}}-\text{OH}^{2+}$, 130 mV/pH for $-\text{Ru}^{\text{IV}}=\text{O}^{2+}/-\text{Ru}^{\text{III}}-\text{OH}_2^+$, and 24 mV/pH for the $-\text{Ru}^{\text{IV}}=\text{O}^{2+}/-\text{Ru}^{\text{II}}-\text{OH}^+$ couple. The dashed, vertical lines are pK_a values. The $E_{1/2}$ –pH plots for individual couples are labeled. At 23° C in 0.5 M KNO₃ 0.1 M in total added buffer. The $\text{Ru}^{\text{V}}=\text{O}^{3+}/-\text{Ru}^{\text{IV}}=\text{O}^{2+}$ couple appears at $E_{\text{p,a}} \sim 1.87$ V in 2% water-propylenecarbonate 0.1 M in TBAH. 94
- Figure 4.4.** Comparison cyclic voltammograms in pH = 3.06 (0.1 M phosphate, 0.5 M KNO₃) at 100 mV/s of **3** (blue) and an equal molar solution of **9** and **10** (red). Currents are normalized to the water oxidation catalyst $\text{Ru}^{\text{III/II}}$ redox couple for comparison purposes. 95
- Figure 5.1.** Structures of the assembly $[\text{Ru}(\text{bpy})_2(\text{bpy-NH-CO-trpy})\text{Ru}(\text{bpy})(\text{OH}_2)]^{4+}$ (**1**), chromophore $[\text{Ru}(4,4'-(\text{PO}_3\text{H}_2-\text{CH}_2)_2\text{bpy})_2(\text{dmb})]^{2+}$ (**2**), catalyst $[\text{Ru}(\text{trpy})(4-\text{PO}_3\text{H}_2-\text{CH}_2-\text{bpy})(\text{OH}_2)]^{2+}$ (**3**), and the non-phosphonated assembly $[\text{Ru}(\text{bpy})_2(\text{bpy-ph-NH-CO-trpy})\text{Ru}(\text{bpy})(\text{OH}_2)]^{4+}$ (**4**) previously reported.¹⁸⁹ 101
- Figure 5.2.** (Left) COSY NMR of **7** in d₆-DMSO. (Right) COSY NMR of **8** in CD₃CN. The cross peaks for each of the diastereotopic methylene protons and the NH proton for complexes are highlighted in blue. 109
- Figure 5.3.** (Left) Cyclic voltammogram for **1** at pH = 6.0 (0.1 M phosphate, 0.5 M KNO₃) at 100 mV/s on FTO. (Right) $E_{1/2}$ –pH diagram of **1** on FTO. $E_{1/2}$ values were obtained as peak current maxima in differential pulse voltammograms. The solid lines

are best fits of the variation in $E_{1/2}$ values with pH for the $[-\text{Ru}_b^{\text{III}}-\text{OH}]^{4+}/[-\text{Ru}_b^{\text{II}}-\text{OH}_2]^{4+}$ (green), $[-\text{Ru}_b^{\text{IV}}=\text{O}]^{4+}/[-\text{Ru}_b^{\text{III}}-\text{OH}]^{4+}$ (blue), and $[\text{Ru}_a^{\text{III}}]^{5+}/[\text{Ru}_a^{\text{II}}]^{4+}$ (red) couples. At 23° C in 0.5 M KNO_3 and 0.1 M buffer. 111

Figure 5.4. Absorption spectra for **1** (red), **2** (blue), **3** (pink), and **2 + 3** (green) in H_2O at 25°C. 112

Figure 5.5. (Left) Nanosecond transient absorption difference spectra obtained at 20 ns on TiO_2 (6 μm transparent film) derivatized electrodes at surface coverages- **1** (4.4×10^{-8} mol cm^{-2} , red), **2** (5.8×10^{-8} mol cm^{-2} , orange), and **3** (9.1×10^{-8} mol cm^{-2} , blue) following 532 nm laser flash (5.2 mJ) excitation. Spectra are normalized at the bleach maxima for comparison purposes. (Right) Transient spectrum for **1** ($4. \times 10^{-8}$ mol cm^{-2}) at 20 ns following 532 nm (5.2 mJ, blue) and 437 nm (3 mJ, red) excitation on TiO_2 . In 0.1 M HClO_4 at room temperature. 112

Figure 5.6. Absorption-time traces for **1** on TiO_2 (4.4×10^{-8} mol cm^{-2} , red, 480 nm monitoring), **2** (5.8×10^{-8} mol cm^{-2} , orange, 460 nm monitoring) and **3** (9.1×10^{-8} mol cm^{-2} , blue, 480 nm monitoring) following 532nm laser (5.2 mJ) excitation. 115

Figure 5.7. Absorbance-time traces for **1** on TiO_2 (4.4×10^{-8} mol cm^{-2}) following 532 nm laser flash (5.0 mJ) excitation with monitoring at 480 nm in 0.1 M HClO_4 (red) and at pH = 4.5 (0.18M LiClO_4 with 20mM NaOAc/HOAc buffer, blue). 116

Figure 6.1. (A) Absorption spectra of the chromophore ($[\text{Ru}_a^{\text{II}}]^{2+}$) (blue), catalyst ($[\text{Ru}_b^{\text{II}}-\text{OH}_2]^{2+}$) (red), and chromophore-catalyst assembly ($[\text{Ru}_a^{\text{II}}-\text{Ru}_b^{\text{II}}-\text{OH}_2]^{4+}$) (gray) in water at 298 K. The black dashed line is the calculated absorption of the chromophore-catalyst assembly. Inset: emission from chromophore ($[\text{Ru}_a^{\text{II}}]^{2+}$) (blue), catalyst ($[\text{Ru}_b^{\text{II}}-\text{OH}_2]^{2+}$) (red), and chromophore-catalyst assembly ($[\text{Ru}_a^{\text{II}}-\text{Ru}_b^{\text{II}}-\text{OH}_2]^{4+}$) (black) in water following excitation at 415 nm. The spectra for the catalyst and assembly are scaled by a factor of 15. (B) Absorption spectra of TiO_2 - $[\text{Ru}_a^{\text{II}}-\text{Ru}_b^{\text{II}}-\text{OH}_2]^{4+}$ (black) and TiO_2 - $[\text{Ru}_a^{\text{II}}]^{2+}$ (blue). 132

Figure 6.2. (A) Femtosecond transient absorption of chromophore in pH 1.0 HClO_4 aqueous solution, $[\text{Ru}_a^{\text{II}}]^{2+}$. (B) Transient absorption spectra of chromophore on TiO_2 in pH 1.0 HClO_4 aqueous solution, (TiO_2 - $[\text{Ru}_a^{\text{II}}]^{2+}$). (C) Kinetic traces at 375 nm for $[\text{Ru}_a^{\text{II}}]^{2+}$ in solution (black) and TiO_2 - $[\text{Ru}_a^{\text{II}}]^{2+}$ (blue). (D) Femtosecond transient absorption of assembly $[\text{Ru}_a^{\text{II}}-\text{Ru}_b^{\text{II}}-\text{OH}_2]^{4+}$ in HNO_3 aqueous solution. (E) Transient absorption of assembly on TiO_2 , (TiO_2 - $[\text{Ru}_a^{\text{II}}-\text{Ru}_b^{\text{II}}-\text{OH}_2]^{4+}$) in pH 1.0 HClO_4 aqueous solution. (F) Kinetics at 375 nm for $[\text{Ru}_a^{\text{II}}-\text{Ru}_b^{\text{II}}-\text{OH}_2]^{4+}$ in solution (black) and TiO_2 - $[\text{Ru}_a^{\text{II}}-\text{Ru}_b^{\text{II}}-\text{OH}_2]^{4+}$ (magenta). All femtosecond transient absorption spectra were acquired with $\lambda_{\text{exc}} = 415$ nm at 150 nJ/pulse. 134

Figure 6.3. Electron injection efficiency for TiO_2 - $[\text{Ru}_a^{\text{II}*}]^{2+}$. The transient absorption spectrum of ZrO_2 - $[\text{Ru}_a^{\text{II}*}]^{2+}$ at early delay (dark green) and the UV-vis spectrum of TiO_2 - $[\text{Ru}_a^{\text{II}}]^{2+}$ (light green) provide the 0% and 100% injection limits, respectively. The red curves are transient absorption spectra for TiO_2 - $[\text{Ru}_a^{\text{II}*}]^{2+}$ at 0.5 ps (open circle) and 1.4 ns (filled circle). All curves were normalized to the maximum of the

- bleach signal. At 0.5 ps, ~35% of the complexes have injected, consistent with an ultrafast (<200 fs) injection component that is not observable in our measurements. By 1.4 ns, injection is nearly complete (~95%). 137
- Figure 6.4.** Normalized transient absorption spectra for $\text{TiO}_2\text{-}[\text{Ru}_a^{\text{II}}\text{-Ru}_b^{\text{II}}\text{-OH}_2]^{4+}$. The inset is a plot of the shift in the red edge of the bleach ($\Delta\lambda_{\text{red}}$) with pump-probe delay for $\text{TiO}_2\text{-}[\text{Ru}_a^{\text{II}}\text{-Ru}_b^{\text{II}}\text{-OH}_2]^{4+}$ and $\text{TiO}_2\text{-Ru}_a^{\text{II}}$ 142
- Figure 6.5.** (A) Comparison of global fit (solid lines) to experimental data (points) for four representative spectra at different delay times. (B) Comparison of global fit (solid lines) and experimental data (points) for representative kinetic traces at four different wavelengths. The lower panels show the residuals. 144
- Figure 6.6.** (A) Transient absorption spectra and concentration profiles (B) of the four colored species, chromophore excited state, $[-\text{Ru}_a^{\text{II}*}]^{2+}$, (red), oxidized chromophore, $[-\text{Ru}_a^{\text{III}}]^{3+}$ (purple), catalyst excited state, $[-\text{Ru}_b^{\text{II}*}\text{-OH}_2]^{2+}$ (black), and oxidized catalyst $[-\text{Ru}_b^{\text{III}}\text{-OH}_2]^{3+}$ (green) as determined by the global analysis. 146
- Figure 6.7.** Nanosecond transient absorption-time traces for (A) $\text{TiO}_2\text{-Ru}_a^{\text{II}}$ at $t = 1.0, 5.0, 10, 20, 50, 100,$ and 200 ns (blue) and (B) $\text{TiO}_2\text{-}[\text{Ru}_a^{\text{II}}\text{-Ru}_b^{\text{II}}\text{-OH}_2]^{4+}$ at $t = 1.0, 5.0, 10, 50,$ and 200 ns and 1.0 and 10 μs (red) in pH 1.0 buffer solution with $\lambda_{\text{exc}} = 415$ nm at 150 nJ/pulse. (C) 450 nm kinetics for $\text{TiO}_2\text{-}[\text{Ru}_a^{\text{II}}]^{2+}$ (blue) and 470 nm for $\text{TiO}_2\text{-}[\text{Ru}_a^{\text{II}}\text{-Ru}_b^{\text{II}}\text{-OH}_2]^{4+}$ (red) with the fit to multiexponential decay (solid line). 148
- Figure 7.1.** A) Structures of **RuP**, **RuPdmb**, **RuPdvb** and $[\text{Fe}(\text{v-tpy})_2]^{2+}$. B) Schematic diagram of the surface structure following reductive polymerization of $[\text{Fe}(\text{v-tpy})_2]^{2+}$ on $\text{TiO}_2\text{-RuPdvb}$ 152
- Figure 7.2.** Changes in UV/Visible absorption spectra for TiO_2 (dry slide) as the number of reductive cycles from 0 to -1.8 V (vs. Ag/AgNO_3) is increased (0, 10, 20, 30, 40, 50, 70, 100, 150, 200 and 300; red to black) in an acetonitrile solution of 0.5 mM $[\text{Fe}(\text{v-tpy})_2]^{2+}$ (0.1 M TBAPF_6 electrolyte); Pt counter electrode, and Ag/AgNO_3 reference electrode. Inset: Surface coverage of *poly*- $[\text{Fe}(\text{v-tpy})_2]^{2+}$ versus the number of reductive cycles. 164
- Figure 7.3.** (a) Changes in UV/Visible absorption spectra for $\text{TiO}_2\text{-RuPdvb}$ (dry slide) with an increase in the number of reductive scan cycles from 0 to -1.8V (vs. Ag/AgNO_3) in an acetonitrile solution 0.5 mM in $[\text{Fe}(\text{v-tpy})_2]^{2+}$ (0.1 M TBAPF_6 electrolyte); Pt counter electrode, and Ag/AgNO_3 reference electrode. (b) Surface coverage of *poly*- $[\text{Fe}(\text{v-tpy})_2]^{2+}$ versus the number of scan cycles. 165
- Figure 7.4.** Cyclic voltammograms for $\text{TiO}_2\text{-RuPdvb}$ from 0 to 1.5 V (vs. Ag/AgNO_3) in CH_3CN (0.1 M TBAPF_6) after successive reductive scan cycles (100 mV/s) in CH_3CN solution 0.5 mM in $[\text{Fe}(\text{v-tpy})_2]^{2+}$, 0.1 M in TBAPF_6 ; Pt counter electrode; Ag/AgNO_3 reference electrode. 167

- Figure 7.5.** Cross-sectional (A and B) and surface (C and D) SEM images of the TiO₂-**RuPd**vb**** film following 50 (A and C) and 300 (B and D) reductive cycles in an CH₃CN solution containing 0.5 mM [Fe(v-tpy)]²⁺. 169
- Figure 7.6.** Changes in the absorption spectrum of TiO₂-**RuPd**vb****-*poly*-[Fe(v-tpy)]²⁺ (150 cycles, 1:1.8 Ru:Fe) in aqueous 0.1 M HClO₄ under constant 455 nm irradiation (475 mW/cm²) from 0 (red) to 16 hours (black) recorded every 15 minutes. Inset: Desorption rate constant (*k_{des}*) as a function of the number of reductive cycles..... 171
- Figure 7.7.** Time-resolved absorption difference spectra for TiO₂-**RuPd**vb****-*poly*[Fe(v-tpy)]²⁺ (30 cycles, 1:0.5 Ru:Fe) in Ar deaerated aqueous 0.1 M HClO₄. (Excitation at 425 nm, 5.0 mJ/pulse). 175
- Figure 7.8.** Absorption-time traces for TiO₂-**RuPd**vb****-*poly*-[Fe(v-tpy)]²⁺ with various ratios of Ru to Fe in Ar deaerated 0.1 M HClO₄ aqueous solutions monitored at 580 nm (450 nm excitation, 5.0 mJ/pulse). 178
- Figure 8.1.** (A) Structures of **RuPd**vb****²⁺ and **RuOH₂**²⁺ (B) Schematic diagram of the surface structure following reductive electropolymerization of **RuOH₂**²⁺ on *n*TiO₂-**RuPd**vb****²⁺. 183
- Figure 8.2.** Crystal structure of **Ru-NCCH₃**²⁺ grown by slow diffusion of diethyl ether into a solution of **RuOH₂**²⁺ in CH₃CN. Structural details are listed at the end of the Appendix G. 191
- Figure 8.3.** *polyRuOH₂*²⁺ surface coverage on (A) bare *p*FTO and (B) *p*FTO-**RuPd**vb****²⁺ versus the number of reductive cycles in dry PC solution of **RuOH₂**²⁺ (0.5 mM, 0.1 M TBAPF₆), cycling from 0 to -1.8 V (vs Ag/AgNO₃), Pt counter, and Ag/AgNO₃ reference electrode. 192
- Figure 8.4.** Peak current for the *polyRu*^{III/II}OH₂ redox couple versus the scan rate for *p*FTO-**RuPd**vb****²⁺-*polyRuOH₂*²⁺ with 5 (A) and 20 (B) monolayers of *polyRuOH₂*²⁺ in aqueous 0.1 M HClO₄, Pt-wire counter electrode, and Ag/AgCl reference electrode. 192
- Figure 8.5.** *E*_{1/2} vs. pH diagram for *p*FTO-**RuPd**vb****²⁺-*polyRuOH₂*²⁺. (5 layers). *E*_{1/2} values are cited as potentials at the current maxima in square wave voltammograms. The dashed lines fit the *E*_{1/2}-pH trends for the couples *polyRu*^{III}OH₂³⁺/Ru^{II}OH₂²⁺ (~0 mV/pH unit) and *polyRu*^{III}OH²⁺/Ru^{II}OH₂²⁺ (51 mV/pH unit) with p*K*_a = 2.3 for *polyRu*^{III}OH₂³⁺ at 23 °C in aqueous 0.5 M NaClO₄ with 0.1 M buffer..... 193
- Figure 8.6.** *E*_{1/2} versus pH diagram of *p*FTO-**RuPd**vb****²⁺-*polyRuOH₂*²⁺ with 7 (blue circles), 19 (red squares) and 33 (green triangles) monolayer equivalents of **RuOH₂**²⁺ deposited onto *p*FTO-**RuPd**vb****²⁺. *E*_{1/2} values were obtained at peak current maxima in square wave voltammograms. The solid lines are best fits of the variation in *E*_{1/2} values with pH for the Ru^{III}-OH₂/Ru^{II}-OH₂ and Ru^{III}-OH/Ru^{II}-OH₂ redox couples at 23 °C in aqueous 0.5 M NaClO₄ and 0.1 M buffer. 194

- Figure 8.7.** UV/visible spectral changes for $n\text{TiO}_2\text{-RuPdvb}^{2+}$ with an increasing number of reductive scan cycles (0, 10, 20, 30, 40, 50, 60, 70, 80, 90, 100, 150, 200, 300, 450; light red to dark red) in 0.5 mM RuOH_2^{2+} (0.1 M TBAPF₆/PC). Inset: Surface coverage (Γ) of polyRuOH_2^{2+} versus the number of reductive scan cycles. 195
- Figure 8.8.** UV/visible absorption spectra of $n\text{TiO}_2\text{-RuPdvb}^{2+}$ before (black) and after (red) 10 reductive cycles from 0 to -1.8 V (vs Ag/AgNO₃) in PC solution of 0.5 mM RuOH_2^{2+} , Pt counter, and Ag/AgNO₃ reference electrode..... 195
- Figure 8.9.** Cross-sectional SEM images of the $n\text{TiO}_2\text{-RuPdvb}^{2+}$ films following 60 (A and B), 120 (C and D), and 450 (E and F) reductive cycles in a PC solution containing 0.5 mM RuOH_2^{2+} 196
- Figure 8.10.** Changes in the absorption spectrum of $n\text{TiO}_2\text{-RuP}$ (A) and $n\text{TiO}_2\text{-RuPdvb}^{2+}\text{-polyRuOH}_2^{2+}$ following 70 reductive cycles (B, 1:1 chromophore:catalyst) in aqueous 0.1 M HClO₄ under constant 455 nm irradiation (475 mW/cm²) from 0 h (green) to 16 h (black) recorded every 15 min..... 197
- Figure 8.11.** Variation of surface coverage as a function of irradiation time at 475 mW/cm² at 455 nm over a 16 hr photolysis period in aqueous 0.1 M HClO₄. Loss from the surfaces was monitored by absorbance changes at 453 nm ($\epsilon_{453} = 13,500 \text{ M}^{-1} \text{ cm}^{-1}$) which were also corrected for the TiO₂ scatter. 198
- Figure 8.12.** Changes in the absorption spectrum of $n\text{TiO}_2\text{-RuP}$ (A) and $n\text{TiO}_2\text{-RuPdvb}^{2+}\text{-polyRuOH}_2^{2+}$ following 70 reductive cycles (B, 1:1 chromophore:catalyst) in pH 4.7 aqueous solution (0.1 M HOAc/OAc, 0.5 M NaClO₄) under constant 455 nm irradiation (475 mW/cm²) from 0 h (green) to 16 h (black) recorded every 5 min..... 198
- Figure 8.13.** Cyclic voltammograms at 20 mV/s for $n\text{TiO}_2\text{-RuPdvb}^{2+}\text{-polyRuOH}_2^{2+}$ (red) and $n\text{TiO}_2$ (black) in pH 4.7 aqueous solution (0.1 M NaOAc/HOAc, 0.5 M NaClO₄); Pt-mesh counter electrode and Ag/AgCl reference electrode, 0.197 V vs. NHE. 199
- Figure 8.14.** Plots of i_c/i_p (i_c is the current at 1.7 V vs NHE, i_p is the peak current for the $\text{Ru}^{\text{III}}\text{-OH}_2/\text{Ru}^{\text{II}}\text{-OH}_2$ redox couple) versus $1/\nu$ for (A) $n\text{TiO}_2\text{-RuPdvb}^{2+}\text{-polyRuOH}_2^{2+}$, (B) $n\text{TiO}_2\text{-polyRuOH}_2^{2+}$ and (C) $n\text{TiO}_2\text{-[Ru(Mebimpy)(4,4'-(PO}_3\text{H}_2\text{-CH}_2)_2\text{-bpy)(OH}_2)]^{2+}$ (RuPOH_2^{2+}) in pH 4.7 aqueous solution (0.1 M HOAc/OAc, 0.5 M NaClO₄); Pt-mesh counter electrode and Ag/AgCl reference electrode. Surface coverages for each complex were $\sim 1.1 \times 10^{-8} \text{ mol cm}^{-2}$ at 23 °C. The catalytic rate constant, k_{obs} , for water oxidation was evaluated from the slope of the each plot. ... 200
- Figure 8.15.** Controlled potential electrolysis on 1:1 $n\text{TiO}_2\text{-RuPdvb}^{2+}\text{-polyRuOH}_2^{2+}$ (red) and $n\text{TiO}_2$ (black) at 1.7 V (vs. NHE) in pH 4.7 aqueous solution (0.1 M NaOAc/HOAc, 0.5 M NaClO₄); Pt-mesh counter electrode and Ag/AgCl reference electrode with $\Gamma \sim 1.1 \times 10^{-8} \text{ mol cm}^{-2}$ for both complexes..... 201
- Figure 8.16.** Gas chromatographs of headspace following electrolysis of blank $n\text{TiO}_2$ (black) and $n\text{TiO}_2\text{-RuPdvb}^{2+}\text{-polyRuOH}_2^{2+}$ (red) at 1.7 V (vs NHE) in pH 4.7 ((0.1 M

HOAc/OAc, 0.5 M NaClO₄); Pt-mesh counter electrode and Ag/AgCl reference electrode. Surface coverages for both **RuPdvb**²⁺ and *polyRuOH*₂²⁺ were ~ 1.1 × 10⁻⁸ mol cm⁻² 201

Figure 8.17. Cyclic voltammograms of *n*ITO-**RuPdvb**²⁺-*polyRuOH*₂²⁺ pre (A) and post 2 hr (B) electrolysis at 1.7 V (vs NHE) in pH 4.7 ((0.1 M HOAc/OAc, 0.5 M NaClO₄); Pt-mesh counter electrode and Ag/AgCl reference electrode. Surface coverages for both **RuPdvb**²⁺ and *polyRuOH*₂²⁺ were ~ 1.1 × 10⁻⁸ mol cm⁻² pre electrolysis. As noted in the figure, the new waves below 0.4 V are due to a peroxide intermediate in the overall water oxidation cycle. The surface coverage post electrolysis (Figure S17(B)) for *polyRuOH*₂²⁺ was calculated as the sum of the integrated charge under the Ru^{III}-OH/Ru^{II}-OH₂ and Ru^{III}-OOH/Ru^{II}-OOH waves. The latter is known as a surface-bound intermediate in the water oxidation cycle for the RuPOH₂²⁺ catalyst.^{35,149,360,361} 202

Figure A.1. Corrected (black) and calculated (red) emission spectra from spectral fitting of Ru(bpy)₃²⁺ and **1-9** 204

Figure A.2. Absorption spectrum of Ru(bpy)₃²⁺ in CH₃CN at 25°C..... 205

Figure A.3. Absorption spectrum of **1** in CH₃CN at 25°C. 205

Figure A.4. Absorption spectrum of **2** in CH₃CN at 25°C. 206

Figure A.5. Absorption spectrum of **3** in CH₃CN at 25°C. 206

Figure A.6. Absorption spectrum of **4** in CH₃CN at 25°C. 207

Figure A.7. Absorption spectrum of **5** in CH₃CN at 25°C. 207

Figure A.8. Absorption spectrum of **6** in CH₃CN at 25°C. 208

Figure A.9. Absorption spectrum of **7** in CH₃CN at 25°C. 208

Figure A.10. Absorption spectrum of **8** in CH₃CN at 25°C. 209

Figure A.11. Absorption spectrum of **9** in CH₃CN at 25°C. 209

Figure A.12. Calculated geometry of complex **8**. 210

Figure A.13. Calculated geometry of complex **6**. 210

Figure A.14. Calculated electronic spectra of complexes **1-9**..... 210

Figure A.15. Calculated orbitals for the Ru dπ → π* (N-N) transition in complex **2**. A) The Ru dπ orbital. B) π* orbital on the N-N ligands. Orbitals are plotted with MOLEKEN. 211

Figure A.16. Dependence of emission energy on the ground state oxidation potential (Ru ^{3+/2+}).	211
Figure B.1. Corrected (black) and calculated (red) emission spectra from spectral fitting of RuP (A), RuPBr (B), RuPMe (C), and RuPOMe (D).	241
Figure B.2. Adsorption isotherms of RuPOMe (A), RuPMe (B), and RuPBr (C) on TiO ₂ (~7 μm) loaded from 10, 20, 50, 100, 150, and 200 μM solutions in methanol. The black lines are the best fits to the Langmuir isotherm equation.	242
Figure B.3. Square-wave voltammograms of RuPOMe, RuPMe, RuP, and RuPBr in 80:20 CH ₃ CN:H ₂ O with glassy carbon as the working electrode, Pt counter, and Ag/AgNO ₃ reference electrode.	243
Figure B.4. Reductive square-wave voltammograms of RuPOMe (A), RuPMe (B), RuP (C), and RuPBr (d) in 80:20 CH ₃ CN:H ₂ O under an argon atmosphere with a glassy carbon working electrode, Pt-wire counter, and a Ag/AgNO ₃ reference (-0.09 V vs Fc ^{0/+}).	244
Figure B.5. UV/Visible absorption spectra for RuPBr (A), RuPMe (B), RuPOMe (C), and RuP (D) in H ₂ O.	245
Figure B.6. Calculated electronic spectra of RuP, RuPMe, RuPOMe, and RuPBr.	246
Figure B.7. Orbitals contributing for the MLCT excitations for RuPMe.	246
Figure B.8. Variation of ν _{em} with E _{1/2} (Ru ^{2+/+}) in aqueous 0.1 M HClO ₄ at 25°C.	247
Figure C.1. COSY experiment showing the cross peak (blue boxes) for the CH ₂ and the NH in the amide bridge in 3 in CH ₃ CN.	248
Figure C.2. Differential pulse voltammogram of 3 in propylene carbonate with added water (2%). Tetrabutylammonium hexafluorophosphate (0.1 M) as the supporting electrolyte with a glassy carbon working electrode, platinum counter, and Ag/AgNO ₃ reference (0.56 V vs NHE).	248
Figure C.3. Cyclic voltammogram at 100 mV/s of 3 in PC with added water (2%). The supporting electrolyte was tetrabutylammonium hexafluorophosphate (0.1 M) with a glassy carbon working electrode, platinum counter, and Ag/AgNO ₃ reference.	249
Figure C.4. Absorption spectrum of 3 in water (black) and 0.1 M NaOH (red).	249
Figure C.5. Absorption spectrum of 9 in water (red) and in 0.1 M NaOH (blue).	250
Figure C.6. Absorption spectrum of 10 in water.	250

- Figure C.7.** Scan rate dependence of **3** at pH = 4.97 (0.1 M acetate, 0.5 M KNO₃) of scan rate normalized ($i/v^{1/2}$) cyclic voltammograms at a glassy carbon electrode (0.07 cm²) vs Ag/AgCl..... 251
- Figure C.8.** Differential pulse voltammogram of **9** in 0.1 M HNO₃ with a glassy carbon working electrode, platinum counter electrode, and Ag/AgCl reference..... 251
- Figure C.9.** Comparison CV of **3** (red) and Ru(tpy)(bpy)(OH₂)²⁺ (blue) at pH = 4.97 (0.1 M acetate, 0.5 M KNO₃). The currents are normalized to the Ru^{III/II} couples with a glassy carbon working electrode, platinum counter electrode, and Ag/AgCl reference..... 252
- Figure C.10.** Kinetic spectral scan data for loss of 3.6 mM CAN in 1.0 M HNO₃ in the presence of 0.05 mM **3** assembly at 22°C. Inset: Kinetic trace at 380 nm (red) and fitted curve (green) for the model A→B→C→D..... 252
- Figure C.11.** Calculated spectra and concentration profiles for the multiwavelength fit to the kinetic model A → B → C → D with [CAN]₀ = 3.6 mM, [**3**]₀ = 0.05 mM, T = 22.0°C. The spectral features suggest that CAN is decaying at different rates owing to changes occurring within the catalyst assembly over time. Each colored state (A,B,C,D) represents a combination of the remaining [Ce(IV)] with the dominant form of [**3**] during the corresponding decay time period. 253
- Figure C.12.** Steady-state emission spectrum of **3** in water at room temperature. [**3**] = 31 μM, [KNO₃] = 0.5 M, λ_{ex} = 460 nm..... 254
- Figure C.13.** Time-resolved emission decay of **3** in water at room temperature. [**3**] = 31 μM, [KNO₃] = 0.5 M, λ_{ex} = 444 nm, λ_{det} = 444 nm..... 254
- Figure D.1.** ¹H NMR of 4-([2,2':6',2''-terpyridin]-4'-yl)benzoic acid in D₆-DMSO. 255
- Figure D.2.** ¹H NMR of **4** in d₆-DMSO..... 256
- Figure D.3.** (Top) Zoomed in portion of the aromatic region in the ¹H NMR of **7** in d₆-DMSO. (Bottom) COSY NMR of **7** in d₆-DMSO. 257
- Figure D.4.** (Top) Zoomed in portion of the aromatic region in the ¹H NMR of **8** in CD₃CN. (Bottom) COSY NMR of **8** in CD₃CN..... 258
- Figure D.5.** (Top) Zoomed in portion of the aromatic region in the ¹H NMR of **1** in D₂O. (Bottom) ³¹P of **1** in D₂O..... 259
- Figure D.6.** (Top) ¹H NMR of **2** in D₂O. (Bottom) ³¹P of **2** in D₂O..... 260
- Figure D.7.** Reaction progress in the final step in the synthesis of **1**. Spectra are normalized to the MLCT for comparison purposes. 260

- Figure D.8.** Comparison CV in pH=4.8 (0.1 M phosphate, 0.5M KNO₃, red) and pH=6.0 (buffer, blue) at 100 mV/s of **1**. Currents are normalized to the Ru^{II}-Ru^{III}-OH/ Ru^{II}-Ru^{II}-OH₂ couple for comparison purposes. 261
- Figure D.9.** Transient spectrum for TiO₂-**1** in 0.1 M HClO₄ following 532 nm excitation. 261
- Figure D.10.** Transient spectrum of ZrO₂-**1** in 0.1 M HClO₄ at 10 ms following 532 nm excitation. 262
- Figure D.11.** 650 nm transient decay of ZrO₂-**1** monitored at 650 nm following 532 nm excitation. 262
- Figure D.12.** Nanosecond transient absorption difference spectra obtained at 20 ns on TiO₂ derivatized with **1** following 532 nm laser excitation (5.2 mJ). Spectra are normalized at the bleach maxima for comparison purposes. 263
- Figure D.13.** Spectral changes of complex **1** attached on *nano*-ITO electrode, $\Gamma = 1.3 \times 10^{-8}$ mol cm⁻² in 0.1 M HClO₄. (a) after oxidation of [Ru_a^{II}-Ru_b^{II}-OH₂]⁴⁺ to [Ru_a^{II}-Ru_b^{III}-OH₂]⁵⁺ (catalyst) and (b) after oxidation of [Ru_a^{II}-Ru_b^{IV}=O]⁴⁺ to [Ru_a^{III}-Ru_b^{IV}=O]⁵⁺. 263
- Figure E.1.** The percentage of photons absorbed by the chromophore Ru_a^{II} at different wavelengths. 265
- Figure E.2.** (A) fsTA of catalyst Ru_b^{II}-OH₂ in 0.1 M HNO₃ aqueous solution at different delays with λ_{exc} at 415 nm. (B) The kinetic decay at 475 nm. 266
- Figure E.3.** Time-resolved emission of catalyst, Ru_b^{II}-OH₂ in H₂O solution (black) and the fitting (red) with 5% long-lived component likely from the residue of precursor. ... 266
- Figure E.4.** (A) Time-resolved emission of chromophore, Ru_a^{II}, with λ_{mon} at 630 nm in argon deaerated H₂O solution. (B) Time-resolved emission of assembly, Ru_a^{II}-Ru_b^{II}-OH₂ with λ_{mon} at 630 nm in argon deaerated H₂O solution. 267
- Figure E.5.** Steady-state emission of Ru_a^{II} (blue), Ru_a^{II}-Ru_b^{II}-OH₂ (black), Ru_b^{II}-OH₂ (brown), and the calculated emission of Ru_a^{II}-Ru_b^{II}-OH₂ (brown circles) based on the energy transfer. 267
- Figure E.6.** The first four spectral eigenvectors (V) from Singular value decomposition of the spectral kinetic data matrix Y. (B) The fifth and sixth spectra eigenvectors (V) are random noise. 268
- Figure E.7.** (A) Associated time domain eigenvectors U x S for the first four spectral eigenvectors from Singular value decomposition of the spectral-kinetic data matrix Y. (B) Associated time domain eigenvectors U x S for the fifth and sixth spectral eigenvectors. 268

- Figure F.1.** EDS spectra (middle) and the tabulated results (left) obtained for TiO₂-**RuPdvb**-*poly*[**Fe(v-tpy)**]₂²⁺ (50 cycles) at various depths that are indicated by the pink rectangle (far right)..... 269
- Figure F.2.** EDS spectra (middle) and the tabulated results (left) obtained for TiO₂-**RuPdvb**-*poly*[**Fe(v-tpy)**]₂²⁺ (300 cycles) at various depths that are indicated by the pink rectangle (far right)..... 270
- Figure F.3.** UV/Vis absorption spectra of **RuP**, **RuPdvb**, **RuPdmb** and **Fe(v-tpy)**₂²⁺ in H₂O..... 271
- Figure F.4.** Absorption isotherms for **RuP** (a), **RuPdvb** (b), and **RuPdmb** (c) on TiO₂ (~ 7 μm) loaded from 10, 20, 50, 100, 150, and 200 μM solutions in methanol. The black lines are the best fits to the Langmuir isotherm equation. 272
- Figure F.5.** a,c) Cyclic voltammograms and b,d) square-wave voltammograms of all three chromophores immobilized on TiO₂ as the working electrode, with a Pt counter electrode, and a Ag/AgCl or Ag/AgNO₃ reference electrode in a,b) aqueous 0.1 M HClO₄ and c,d) in MeCN (0.1 M TBAPF₆). 272
- Figure F.6.** Emission spectra for **RuP**, **RuPdvb**, and **RuPdmb** on ZrO₂ in Ar deaerated aqueous 0.1 M HClO₄ at room temperature (Excitation at 450 nm). 272
- Figure F.7.** **Fe(v-tpy)**₂²⁺ surface coverage on planar FTO as a function of (a) scan rate (in 0.5 mM **Fe(v-tpy)**₂²⁺) and (b) **Fe(v-tpy)**₂²⁺ concentration (at 100 mV/s) cycling 10 times from 0 to -1.8 V (vs. Ag/AgNO₃) in in dry acetonitrile with 0.1 M TBAPF₆, Pt counter electrode, and Ag/AgNO₃ reference electrode. 273
- Figure F.8.** UV-Visible absorption spectra of TiO₂-**RuPdvb** before (red) and after (blue) 10 cycles from 0 to -1.8V (vs Ag/AgNO₃) in an acetonitrile solution of 0.5 mM *p*-divinylbenzene (0.1 M TBAPF₆ electrolyte); Pt counter electrode, and Ag/AgNO₃ reference electrode. 273
- Figure F.9.** EDS spectra (middle) and the tabulated results (left) for Fe and Ru obtained for TiO₂-**RuPdvb**-*poly*[**Fe(v-tpy)**]₂²⁺ (50 cycles) at various depths that are indicated by the pink rectangle (far right). This film was formed by soaking a *nano*-TiO₂-**RuPdvb** slide in [**Fe(v-tpy)**]₂²⁺ (0.5 mM in 0.1 M TBAPF₆/CH₃CN) for over 24 hours prior to electropolymerization, then stirring during electropolymerization and resting the film for 60 seconds in between each electropolymerization cycle. 274
- Figure F.10.** Changes in the absorption spectrum of TiO₂-**RuPdvb** in aqueous 0.1 M HClO₄ under constant 455 nm irradiation (475 mW/cm²) after 10 (A), 30 (B), 70 (C) and 150 (D) reductive cycles in an acetonitrile solution containing 0.5 mM **Fe(v-tpy)**₂²⁺. (0 hours (black) to 16 hours (green) every 15 minutes). 275
- Figure F.11.** Changes in the absorption spectrum of TiO₂-**RuPdvb**-*poly***Fe(v-tpy)**₂ (150 cycles, 1:1.8 Ru:Fe) in (A) H₂O, (B) pH 5 HClO₄, (C) pH 7 phosphate buffer and (D)

- MeCN with 0.1 M LiClO₄ under constant 455 nm irradiation (475 mW/cm²). (0 hours (black) to 16 hours (green) every 15 minutes). 276
- Figure F.12.** Absorption-time trace for TiO₂-*poly*-[Fe(*v-tpy*)₂]²⁺ (70 cycles) in Ar deaerated 0.1 M HClO₄ aqueous solution measured at 580 nm. Excitation at 450 nm, 5.0 mJ/pulse. 276
- Figure F.13.** Time-resolved absorption difference spectra from for TiO₂-**RuPdvb** with (a) 10, (b) 30, (c) 70 and (d) 150 cycles of [Fe(*v-tpy*)₂]²⁺ in Ar deaerated aqueous 0.1 M HClO₄. (Excitation at 532 nm, 5.1 mJ/pulse). 277
- Figure F.14.** Spectroelectrochemistry of *poly*-[Fe(*v-tpy*)₂]²⁺ on *nano*-ITO in 0.1 M HClO₄ with a Pt counter electrode and a Ag/AgCl reference. Potential was slowly increased from 0.2 V (vs NHE) to 1.6 V (vs NHE) to oxidize the Fe^{II} center to Fe^{III}. 278
- Figure G.1.** Absorption spectrum of **RuOH₂²⁺** at room temperature in H₂O 279
- Figure G.2.** (A) Changes in UV/visible absorption spectra for *n*TiO₂ with increasing number of reductive cycles from 0 to -1.8 V (vs Ag/AgNO₃) in PC solution (0.1 M TBAPF₆) of **RuOH₂²⁺** (0.5 mM), Pt counter, and Ag/AgNO₃ reference. (B) Surface coverage of *poly***RuOH₂²⁺** versus the number of reductive cycles. 279
- Figure G.3.** EDS spectra (middle) and the tabulated results (left) obtained for *n*TiO₂-**RuPdvb²⁺**-*poly***RuOH₂²⁺** following 450 reductive cycles at various depths that are indicated by the pink rectangle (right). 280
- Figure G.4.** (A) Spectroelectrochemistry of *n*ITO-**RuPdvb²⁺**-*poly***RuOH₂²⁺** in 0.1 M HClO₄ with a Pt-mesh counter electrode and Ag/AgCl reference electrode. The *n*ITO-**RuPdvb²⁺**-*poly***RuOH₂²⁺** slide was stepped 0.02 V and held there for 300 s. Following each potential step, a UV/Visible spectrum of the slide was obtained. (B) Calculated spectra for the multiwavelength fit to the kinetic model A ⇌ B ⇌ C ⇌ D with A = [Ru^{II}-Ru^{II}-OH₂]⁴⁺, B = [Ru^{II}-Ru^{III}-OH₂]⁵⁺, C = [Ru^{II}-Ru^{IV}=O]⁵⁺, and D = [Ru^{III}-Ru^{IV}=O]⁶⁺. (C) Calculated concentration profiles versus the applied potential (V vs Ag/AgCl) for the model A ⇌ B ⇌ C ⇌ D. (D) Changes in absorption versus potential at 476 nm (λ_{max, MLCT} for **RuPdvb²⁺**) in black and calculated fit (red) using the model A ⇌ B ⇌ C ⇌ D. (E) Changes in absorption versus potential at 491 nm (λ_{max, MLCT} for **RuOH₂²⁺**) in black and calculated fit (red) using the model A ⇌ B ⇌ C ⇌ D. The data was fit using SPECFIT/32 by a series of three sequential Nernstian steps (A ⇌ B ⇌ C ⇌ D). 281
- Figure G.5.** Cyclic voltammograms at 10 mV/s of *n*ITO-**RuPdvb²⁺**-*poly***RuOH₂²⁺** (red) and *n*ITO-*poly***RuOH₂²⁺** (black) in pH 4.7 aqueous solution (0.1 M HOAc/OAc, 0.5 M NaClO₄); Pt-mesh counter electrode and Ag/AgCl reference electrode. The voltammograms are normalized to the Ru^{III}-OH/Ru^{II}-OH₂ redox couple for comparison purposes. 282

Figure G.6. Plots of i_c/i_p (i_c is the current at 1.7 V vs NHE, i_p is the peak current for the $\text{Ru}^{\text{III}}\text{-OH}_2/\text{Ru}^{\text{II}}\text{-OH}_2$ redox couple) versus $1/v$ for (A) *p*FTO-*polyRuOH* $_2^{2+}$, and (B) *p*FTO-**RuPdvb** $^{2+}$ -*polyRuOH* $_2^{2+}$ in pH 4.7 aqueous solution (0.1 M HOAc/OAc, 0.5 M NaClO $_4$); Pt-mesh counter electrode and Ag/AgCl reference electrode. Surface coverages for each complex were $\sim 1 \times 10^{-10}$ mol cm $^{-2}$ at 23 °C. The catalytic rate constant, k_{obs} , for water oxidation was evaluated from the slope of the each plot. ... **282**

Figure G.7. Cyclic voltammograms of *n*ITO-**RuPdvb** $^{2+}$ -*polyRuOH* $_2^{2+}$ pre (A) and post 14 hr (B) electrolysis at 1.7 V (vs NHE) in pH 4.7 ((0.1 M HOAc/OAc, 0.5 M NaClO $_4$); Pt-mesh counter electrode and Ag/AgCl reference electrode. Surface coverages for both **RuPdvb** $^{2+}$ and *polyRuOH* $_2^{2+}$ were $\sim 1.1 \times 10^{-8}$ mol cm $^{-2}$ pre electrolysis. Following the 14 hr electrolysis, only $\sim 16\%$ of *polyRuOH* $_2^{2+}$ remained mainly as the peroxide intermediate. **283**

LIST OF TABLES

Table 1.1. Incident Photons per Molecule of a Typical Dye Molecule.....	19
Table 2.1. Spectroscopic properties and redox potentials for the series 1 – 9.....	36
Table 2.2. Comparison of TD-DFT calculated absorption maxima for complexes 2 and 9 in CH ₃ CN	41
Table 2.3 Emission spectral fitting parameters for MLCT emission from Ru(bpy) ₃ ^{2+*} and 1-9 in CH ₃ CN at 25°C	46
Table 3.1. Equilibrium Surface Parameters for RuPOMe, RuPMe, RuP, and RuPBr.	64
Table 3.2. Summary of photophysical, electrochemical, and surface binding properties for RuPOMe, RuPMe, RuP, and RuPBr.	65
Table 3.3. TD-DFT calculated excitation for the series of chromophores.	69
Table 3.4. Emission spectral fitting parameter for MLCT emission from RuPOMe, RuPMe, RuP, and RuPBr loaded on ZrO ₂ in aqueous 0.1 M HClO ₄ at 25°C	73
Table 4.1. Multiexponential fits to decay kinetics of CAN in 1.0 M HNO ₃ as a function of [3].	82
Table 4.2. Summary of Electrochemical Properties	95
Table 5.1. Injection yields and back electron transfer rates	113
Table 5.2. pH dependence of back electron of 1 on TiO ₂	115
Table 6.1. Fitting Results for Back Electron Transfer Following Injection by TiO ₂ -Ru _a ^{II*} and TiO ₂ -[Ru _a ^{II*} -Ru _b ^{II} -OH ₂] ⁴⁺	148
Table 7.1. Photophysical, electrochemical and surface binding parameters for RuP, RuPdvb, RuPdmb and [Fe(v-tpy) ₂] ²⁺ in solution and on metal oxide films.	161
Table 7.2. The atomic % and Ru:Fe ratios at the top, middle and bottom of TiO ₂ -RuPdvb films after 50 and 300 reductive cycles (100 mV/s) in an acetonitrile solution containing 0.5 mM [Fe(v-tpy) ₂] ²⁺ (0.1 M TBAPF ₆ electrolyte).	169
Table 7.3. Summary of desorption rate constants (<i>k</i> _{des}) in aqueous 0.1 M HClO ₄ for RuP, RuPdvb, and RuPdmb on TiO ₂ and TiO ₂ -RuPdvb films after 10, 30, 70 and 150 reductive cycles in [Fe(v-tpy) ₂] ²⁺ solution.	171
Table 7.4. Summary of desorption rate constants (<i>k</i> _{des}) for TiO ₂ -RuP, TiO ₂ -RuP stabilized by ~3.3 Å of Al ₂ O ₃ , and in TiO ₂ -RuPdvb- <i>poly</i> -[Fe(v-tpy) ₂] ²⁺ films (150 cycles, 1:1.8 Ru:Fe) under various conditions.	172

Table 7.5. Net electron injection yields (based on the appearance of Fe ^{III}), average back electron transfer lifetimes, and k_{bet} from transient absorption measurements on TiO ₂ -RuPdvb- <i>poly</i> -[Fe(v-tpy) ₂] ²⁺ as a function of Ru:Fe ratio in 0.1 M HClO ₄ with TiO ₂ -RuP as a reference. ^a	177
Table A.1. Crystal data and structure analysis for x1102017.....	213
Table A.2. Anisotropic Displacement Parameters ($\text{\AA}^2 \times 10^3$) for x1102017. The Anisotropic displacement factor exponent takes the form: $-2\pi^2[h^2a^{*2}U_{11} + \dots + 2hka \times b \times U_{12}]$	219
Table A.3. Bond Lengths for x1102017	222
Table A.4. Bond Angles for x1102017.....	224
Table A.5. Torsion Angles for x1102017.....	227
Table A.6. Hydrogen Atom Coordinates ($\text{\AA} \times 10^4$) and Isotropic Displacement Parameters ($\text{\AA}^2 \times 10^3$) for x1102017.....	238
Table F.1. Emission spectra fitting parameters for the MLCT excited states of RuP, RuPdvb, and RuPdmb on ZrO ₂ in 0.1 M HClO ₄ aqueous solution.....	273
Table G.1. Fractional Atomic Coordinates ($\times 10^4$) and Equivalent Isotropic Displacement Parameters ($\text{\AA}^2 \times 10^3$) for DLA-3-216. U_{eq} is defined as 1/3 of of the trace of the orthogonalised U_{ij} tensor.	286
Table G.2. Anisotropic Displacement Parameters ($\text{\AA}^2 \times 10^3$) for DLA-3-216. The Anisotropic displacement factor exponent takes the form: $-2\pi^2[h^2a^{*2}U_{11} + \dots + 2hka \times b \times U_{12}]$	290
Table G.3. Bond Lengths for DLA-3-216.....	294
Table G.4. Bond Angles for DLA-3-216.	296
Table G.5. Torsion Angles for DLA-3-216.....	299
Table G.6. Hydrogen Atom Coordinates ($\text{\AA} \times 10^4$) and Isotropic Displacement Parameters ($\text{\AA}^2 \times 10^3$) for DLA-3-216.....	302

LIST OF SCHEMES

Scheme 2.1 Synthesis of L1	32
Scheme 2.2 Synthesis of <i>p</i> -quinoxaline pyridine ligands L2 and L4	33
Scheme 2.3 General synthetic route for ligand synthesis via Friedlander condensations	33
Scheme 3.1. Synthesis of 4,4-Br ₂ -2,2-bipyridine	60
Scheme 3.2. Synthesis of Ru(4,4'-R ₂ -bpy) ₂ Cl ₂ and [Ru((4,4'-R ₂ -bpy) ₂ ((PO ₃ H ₂) ₂ -bpy)] ²⁺	61
Scheme 4.1. Amide coupling strategy used to prepare the chromophore-catalyst assembly. 80	
Scheme 5.1. Synthesis of 1	108
Scheme 5.2. Summary of possible electron and energy transfer events following excitation of TiO ₂ -1. ^a	113
Scheme 6.1. Illustration of Water Oxidation Catalytic Cycle for Single-Site Ru ^{II} Catalysts	127
Scheme 6.2. Structure of the Chromophore-Catalyst Assembly (1) and the Chromophore Control (2); Illustration of Dynamical Processes Resulting from Photoexcitation of the Chromophore-Catalyst Assembly on TiO ₂ (Lower Panel).....	128

LIST OF EQUATIONS

Equation 1.1	4
Equation 1.2	4
Equation 2.1	35
Equation 2.2	38
Equation 2.3	39
Equation 2.4	39
Equation 2.5	46
Equation 2.6	47
Equation 2.7	47
Equation 2.8	49
Equation 3.1	55
Equation 3.2	65
Equation 3.3	66
Equation 3.4	66
Equation 3.5	69
Equation 3.6	69
Equation 3.7	73
Equation 3.8	76
Equation 3.9	76
Equation 5.1	113
Equation 5.2	114
Equation 5.3	114
Equation 5.4	119
Equation 5.5	119

Equation 5.6	119
Equation 5.7	120
Equation 5.8	120
Equation 5.9	121
Equation 5.10	121
Equation 5.11	121
Equation 5.12	123
Equation 5.13	123
Equation 6.1	130
Equation 6.2	141
Equation 7.1	158
Equation 7.2	158
Equation 7.3	158
Equation 7.4	159
Equation 7.5	160
Equation 7.6	163
Equation 7.7	174
Equation 7.8	174
Equation 7.9	176
Equation 7.10	176
Equation 7.11	176
Equation 7.12	176
Equation 7.13	176
Equation 8.1	185
Equation 8.2	185

Equation 8.3	187
Equation 8.4	187
Equation 8.5	187

LIST OF SYBMOLS AND ABBREVIATIONS

E_0	0-0 energy gap
A	Absorbance or ampere
α	Activity
AM 1.5 G	Air mass 1.5 global solar irradiation
Å	Angstrom
AQY	Apparent quantum yield
APT	Atom-proton transfer
ALD	Atomic layer deposition
$\Delta\bar{\nu}_{1/2}$	Bandwidth at half height
k_B	Boltzmann constant
Btu	British thermal unit
C	Celsius
cm	Centimeter
Q	Charge
E_{CB}	Conduction band edge
COSY	Correlation spectroscopy
CV	Cyclic voltammogram
°	Degree
DSPEC	Dye-sensitized photoelectrochemical cell
DSSC	Dye-sensitized solar cell
$\Delta E_{1/2}$	Electrochemical gap
e^-	Electron
Φ_{inj}	Electron injection yield
eV	Electron volt

S_M	Electron-vibrational coupling constant
EDS	Energy dispersive X-ray spectroscopy
ΔQ_{eq}	Equilibrium displacement change
eq	Equivalent
ES	Excited state
F	Faraday's constant
fs	Femtosecond
FTO	Fluoride-doped tin oxide
$E^{0'}$	Formal potential
ΔG_{ES}	Free energy content of excited state
FWHM	Full width at half maximum
GC	Glassy carbon
g	Gram
GS	Ground state
$E_{1/2}$	Half wave potential
$t_{1/2}$	Half-life
Hz	Hertz
h^+	Hole
hr	Hour
IR	Infrared
$h\nu$	Irradiation
J	Joule
K	Kelvin
kg	Kilogram
kHz	Kilohertz

τ	Lifetime
L	Liter
λ_L	Low frequency modes energy
$\bar{\nu}_{abs}$	Lowest energy absorption
$\bar{\nu}_{em}$	Lowest energy emission
MHz	Megahertz
MLCT	Metal-to-charge transfer
m	Meter
μA	Microampere
μL	Microliter
μM	Micromolar
μs	Microsecond
mA	Milliampere
mg	Milligram
mJ	Millijoule
mL	Milliliter
mm	Millimeter
mM	Millimolar
mmol	Millimole
mOD	Millioptical density
ms	Millisecond
mV	Millivolt
mW	Milliwatt
M	Molar
ϵ	Molar extinction coefficient

mol	Mole
<i>nano</i> ITO	Nanocrystalline tin-doped indium oxide
<i>nano</i> TiO ₂	Nanocrystalline titanium dioxide
<i>nano</i> ZrO ₂	Nanocrystalline zirconium dioxide
ns	Nanosecond
NHE	Normal hydrogen electrode
Ω	Ohm
OD	Optical density
OEC	Oxygen-evolving complex
ppm	Parts per million
ps	Picosecond
PCM	Polarizable continuum model
PSI	Pounds per square inch
PCET	Proton-coupled electron transfer
SCE	Saturated calomel electrode
ν	Scan rate
SEM	Scanning electron microscopy
s	Second
STH	Solar-to-hydrogen efficiency
λ_o	Solvent reorganization energy
E^0	Standard potential
Γ	Surface coverage
TCSPC	Time-correlated single photon counting
TD-DFT	Time-dependent density functional theory
ITO	Tin-doped indium oxide

TA	Transient absorption spectroscopy
UV	Ultraviolet
$\hbar\omega_M$	Vibrational quantum spacing
Vis	Visible
V	Volt
WOC	Water oxidation catalyst
W	Watt
λ	Wavelength

Chapter 1: USING MOLECULES TO GENERATE SOLAR FUELS

1.1 Introduction

As the world's population continues to grow, the U.S. Department of Energy has estimated that the amount of energy consumed is expected to increase from 5.72×10^{20} J in 2012 to 8.12×10^{20} J in 2040. This increase takes into consideration population growth, average gross domestic product per capita, and globally averaged energy intensity.¹ Currently, there are international organizations dedicated to stimulating economic growth while maintaining good environmental practices, such as the Organization for Economic Cooperation and Development (OECD); however, the majority of this growth in energy consumption will come from emerging economies in Asia, Africa, and South America, where many countries are not participating members of organizations like OECD. Despite renewable energy and nuclear energy being the world's two fastest-growing energy markets, both increasing about 2.5% a year, it is still projected that fossil fuels will make up at least 80% of the global energy supply in 2040 (Figure 1.1).¹

Fossil fuel reserves are predicted to last anywhere from less than 100 years to millennia based on current and expected consumptions.²⁻⁵ While there is a general concern over the uncertainties in fossil fuel reserves, the potential for devastating environmental impacts on burning fossil fuels weighs even greater on the scientific community to find alternative energy sources. In 2012 alone, 3.21×10^{13} kg of carbon dioxide was released into Earth's atmosphere from burning fossil fuels (Figure 1.1).¹ As a result, the atmospheric CO₂ concentration has risen to greater than 380 ppm, a level that has not occurred in past 450,000

- 600,000 years.^{2,6-9} In addition, there are no natural mechanisms for destruction of CO₂ in the atmosphere, and mixing between atmospheric CO₂ and the biosphere takes anywhere from 400 to several thousand years. This means that CO₂ released during the next century will be globally maintained over the next 500-2000 years.^{2,9,10}

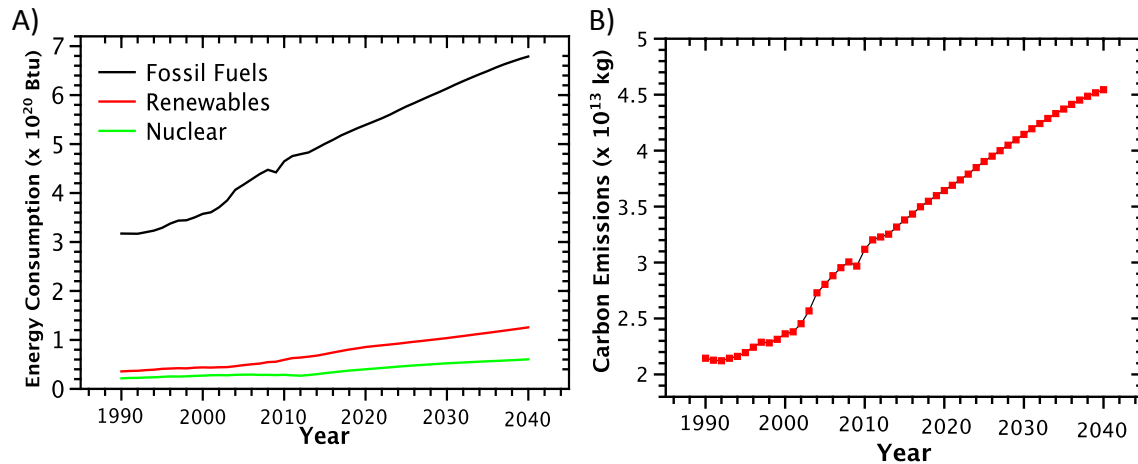


Figure 1.1. (A) World energy consumption (in British thermal units, Btu's) of fossil fuels (black), renewables (red) and nuclear energy (green). (B) World carbon emissions per year. Data obtained from the Energy Information Administration.¹ All data past 2012 are predictions.

It is unclear what type of renewable energy source will emerge as the leader in the near future as a carbon-neutral energy source, be it wind, solar, geothermal, or nuclear. Of the available renewable energy sources, the sun, by far, provides the largest energy resource and is likely the long-term solution for a carbon neutral energy source.^{2,11} By collecting and converting all sunlight striking 2% of the Earth's surface for 8 hr with 12% efficiency, a significant cost:benefit figure of merit, the amount of energy harvested is sufficient to satisfy global energy consumption for an entire month.¹

Although the amount of energy provided by the sun each day is more than enough to completely replace fossil fuels, there are inherent obstacles to overcome before solar energy can become the planet's dominant energy source of choice. The diurnal cycle of the sun

requires that the sun's energy be stored on massive scales for times when the sun's light does not directly hit the Earth's surface, either when it is blocked by water vapor in the atmosphere or during the night. In addition, sunlight is diffuse, mandating maximum efficiency for solar energy conversion devices, which must be made from inexpensive, earth abundant materials.

Today, photovoltaics (PVs) are produced on commercial scales that can directly convert solar energy into electricity with recently reported efficiencies up to 44.7% for a multi-junction solar cell.¹² The solar energy harvested in PVs can be stored in external batteries, typically Li⁺ ion batteries; however, current state-of-the-art Li⁺ ion batteries are currently inapplicable for global energy storage, capable of storing only ~ 1.03 ampere-hrs/g.¹³⁻¹⁹

To overcome these challenges, a strategy has been borrowed from Nature that has evolved over billions of years: photosynthetically generated fuels or solar fuels.²⁰⁻²³ The natural photosynthetic apparatus is extremely complex involving hundreds of thousands of atoms, and is surprisingly inefficient, converting only ~ 1% of sunlight's energy into fuels.²⁴⁻²⁷ Using natural photosynthesis as a model, artificial photosynthesis can simplify the process of converting sunlight to fuels and hence shows great promise as a strategy to produce high-energy fuels from sunlight. Recently, it has been proposed that photoelectrochemical cells, utilizing artificial photosynthesis, have a theoretical maximum efficiency of 10%, high enough to replace fossil fuels as the world's energy source.^{28,29}

1.2 Current Strategies for Artificial Photosynthesis

In the pursuit to reduce water to hydrogen or carbon dioxide to carbon containing fuels (i.e. methanol and methane), the necessary reductive equivalents to carry out these

reactions has to come from an inexhaustible source with little or no release of harmful byproducts. This is where the chemical oxidation of water is key, as it provides the required reductive equivalents to generate hydrogen or carbon containing fuels while only releasing O₂ gas as the byproduct. In addition, the reduction of CO₂ to chemical fuels and the burning of hydrogen gas are closed cycles as both processes regenerate water.

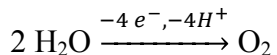
In both natural and artificial photosynthesis, the thermodynamic, mechanistic, and kinetic requirements to achieve chemical oxidation of water with light are extremely challenging. First, the thermodynamic potential for water oxidation at pH 0 is 1.23 V vs NHE exhibiting a Nernstian decrease of 59 mV/pH as described in Equation 1.1 with m the number of protons transferred, n the number of electrons transferred, and a_{H^+} the activity of protons in solution. By pH 14, only 0.40 V vs NHE is needed for water oxidation.³⁰⁻³²

Equation 1.1

$$E = E^{\circ} - \frac{0.059 m}{n} \log_{10} \frac{1}{a_{H^+}} \quad (\text{STP, } 25^{\circ}\text{C})$$

In a net sense, water oxidation involves four electrons, four protons, breaking four bonds, and forming an O–O bond. Despite these daunting mechanistic requirements, numerous water oxidation catalysts (WOCs) have been identified, and studied in detail, culminating in the ability to oxidize water at a single catalytic site (Equation 1.2).³⁰⁻³⁷ To avoid high-energy one-electron oxidations, proton-coupled electron transfer (PCET) events allow for the buildup of the multiple redox equivalents required for water oxidation.³⁸⁻⁴² Following formation of the active state of the catalyst, typically a high oxidation state, high energy intermediate, the O–O bond is formed followed by release of O₂ and regeneration of the ground state catalyst.

Equation 1.2



Significant progress has been made in the development of molecular WOCs. However, incorporation into light-driven systems places more requirements on the catalyst. First, the rate of catalytic water oxidation must be sufficiently fast to avoid inhibitory back reactions, such as charge recombination. This demands that the catalyst be able to keep up with solar flux at the minimum. This will be discussed in greater detail later in this review. The catalyst must be robust where $> 10^6$ turnovers per year are expected to build a commercial device. Also, because these systems will be exposed to solar irradiation, they must be stable to light and avoid self-decomposition pathways.

Several architectures have been proposed to achieve artificial photosynthesis. The first, and a particularly simple design, was first reported by Honda and Fujishima in 1972 where they demonstrated water splitting by TiO_2 nanoparticles on a Pt-electrode connected to a Pt-wire under irradiation (Figure 1.2A).⁴³ Direct band gap excitation of the TiO_2 nanoparticles (3.2 eV, < 390 nm) generates highly oxidizing holes (h^+) capable of oxidizing water to molecular oxygen (Equation 1.2) with the excited electrons used to reduce protons from water oxidation to hydrogen fuel using Pt as the reduction catalyst and an external bias. A bias is applied merely to overcome the thermodynamics of proton reduction not to drive water oxidation at the photoanode.

Although this water splitting strategy is relatively straightforward, it relies on a single material for light absorption, charge transport, and water oxidation catalysis, which can inhibit increasing the efficiency of the individual steps. In addition, TiO_2 only absorbs ultraviolet photons for direct band gap excitation, which constitute only a small portion

(<10%) to the solar spectrum. Substantial progress has been made in improving this multipurpose semiconductor approach with research efforts focused primarily on controlling the band gap and band edges of the semiconductor material to meet the thermodynamic requirements of water splitting while harvesting a greater portion of the solar spectrum.⁴⁴⁻⁵¹ Nevertheless, fast charge recombination and photocorrosion remain as challenges in utilizing semiconducting materials as both the light absorber and catalyst.⁵²⁻⁵⁶

A second architecture that is derived from the Honda/Fujishima design, Figure 1.2B, employs light-absorbing semiconductors derivatized with a WOC and reduction catalyst (RC) to carry out the light-driven catalytic reactions. This strategy separates the tasks of light absorption and charge transport from catalysis, thereby relaxing the demands placed on the semiconductor and leaving headway for improvement by separately modifying either the catalyst or semiconductor. Grätzel and co-workers published some of the earliest work on these systems where they placed RuO₂ (WOC) and Pt (RC) on TiO₂ nanoparticles (Figure 1.2B).⁵⁷ Unfortunately, competing charge recombination and photocorrosion still remain challenges for these systems. Use of semiconductor nanoparticles as light absorbers decorated with catalysts for artificial photosynthesis has been recently reviewed and is outside the scope of this review.⁵⁸⁻⁶⁴

A more sophisticated version of the catalyst-derivatized, light-absorbing nanostructured semiconductor design (Figure 1.2C) has been proposed by the Joint Center for Artificial Photosynthesis (JCAP). Here RC-derivatized, p-type Si nanowires are used as the photocathode and an array of WOC-derivatized metal oxide semiconducting nanowires function as the photoanode.⁶⁵⁻⁶⁹ A recent example demonstrated that p-type silicon nanowires modified with Mo₃S₄ clusters were capable of achieving a 10% solar-to-hydrogen (STH)

conversion efficiency.⁷⁰ STH efficiency describes the overall efficiency of a device under broadband solar irradiation (AM 1.5 G) without an external bias and is measured by the chemical energy of hydrogen produced from protons divided by the solar energy input into the system.⁷¹ Benchmark efficiency measurements are discussed in detail later in this review. Although this result is important in demonstrating the potential for p-type silicon derivatized with a RC to act as a photocathode, the other half reaction, water oxidation, was not achieved in this study.

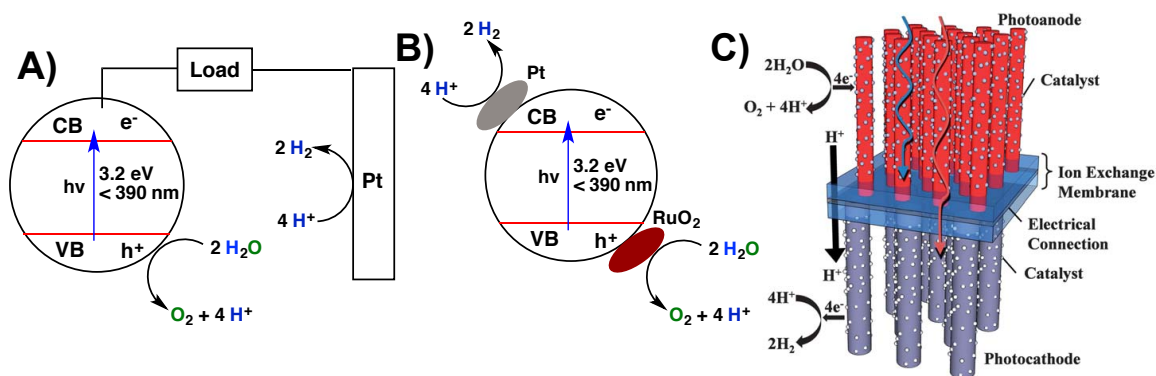


Figure 1.2. A) Honda-Fujishima photoelectrochemical cell with TiO_2 as the photoanode.⁴³ B) Single semiconductor nanoparticle with WOC (RuO_2) and RC (Pt) attached.⁵⁷ C) Photoelectrochemical cell proposed by JCAP with nanowire arrays as the light harvesters.⁶⁸ Reprinted from ref. 68 with permission from the Royal Society of Chemistry.

The combination of PVs and electrolysis is another straightforward architecture utilizing proven technology with long-term device efficiencies. In this architecture, the PV is utilized to apply an electrochemical bias on an anode derivatized with a WOC and a cathode derivatized with a RC. One of the first PV-electrolysis architectures for solar fuel generation was reported by Rocheleau et. al. in 1998 where they modified a triple-junction (3-jn) a-Si PV cell with a $\text{Co}_{0.73}\text{Mo}_{0.27}$ WOC and NiFe_xO_y RC.⁷² In this design, a STH efficiency of 7.8% was reported (for a 0.27 cm^2 device). A more recent example of a PV-electrolysis photoelectrochemical cell was reported by Nocera and co-workers where a 3-jn Si PV was

modified with a Co-borate WOC and a NiMoZn reduction catalyst (Figure 1.3).²⁸ Using a 2 cm² electrode in 1 M K₃BO₃ (pH 9.2) gave a STH efficiency of 4.7%.⁷³⁻⁷⁵ A wireless configuration is also possible utilizing a buried junction. This limits the engineering required for a commercial device (Figure 1.3).

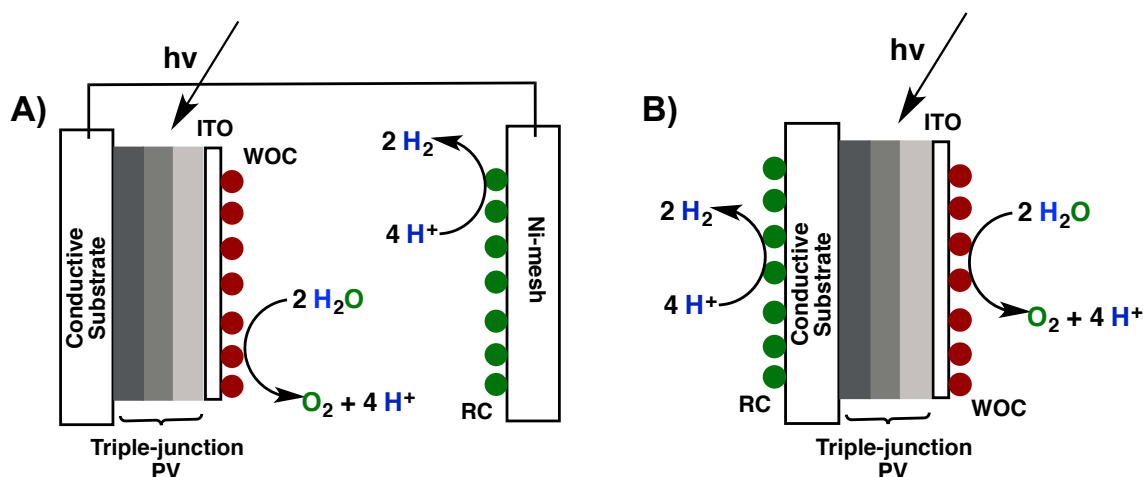


Figure 1.3. PV-electrolysis photoelectrochemical cell with 3-jn PV as the light harvester wired (A) and wireless (B).²⁸

Another example of the PV-electrolysis architecture drives the catalyst-derivatized electrode driven by a single p-n junction PV rather than the triple junction Si PV. One of the earliest examples of this was reported by Turner and Khaselev where a single GaAs p-n junction was used to bias a photocathode that consisted of p-type GaInP₂ (Figure 1.4A).⁷⁶ This system resulted in an impressive 12.4% solar-to-hydrogen efficiency. However, significant photocorrosion and high cost of the devices (~ \$50,000 m⁻²) still remain challenges for systems of this type.⁷⁷

The architecture that most closely resembles the photosynthetic apparatus is the so-called Z-scheme (Figure 1.4B) which was first presented by Bard in 1979.⁷⁸ The Z-scheme is modeled after photosystems I and II which harvest 700 nm and 680 nm, respectively, to carry out their reductive and oxidative reactions. In this approach, two different photocatalysts are

dissolved in solution one WOC and one RC. The system is completed by a redox shuttle comprised of an electron donor, D, and an electron acceptor, A, in solution to carry to redox equivalents between the two photocatalysts (Figure 1.4B). Light can be used more efficiently in a Z-scheme than in a single absorber system because the energy required to drive each photocatalyst is reduced.^{62,79-82} Maeda et. al. demonstrated that a Pt-loaded ZrO_2/TaON (RC) with PtO_x/WO_3 (WOC) and an IO_3^-/I^- redox shuttle yielded an apparent quantum yield (AQY) of 6.3 % for water splitting into H_2 and O_2 under irradiation by 420 nm monochromatic light.⁷⁹ As there is no reliable way to determine the number of absorbed photons for suspended photocatalyst particles, the AQY assumes that all of the incident photons are being absorbed by the particles.⁶² These systems rely on diffusion of the donor (D) or acceptor (A) through solution to interact with the photocatalyst, hence the D and A must be in high concentration, currently limiting the scalability of these systems. In addition, fast charge recombination compared to diffusion kinetics is also a challenge.

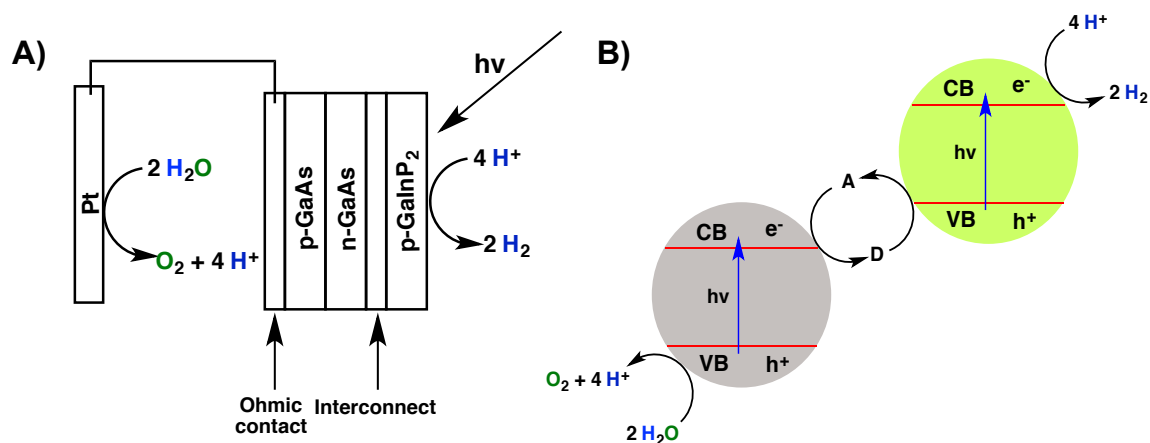


Figure 1.4. A) Single GaAs p-n junction cell with p-type GaInP₂ cathode.⁷⁶ B) Schematic diagram of a Z-scheme with two photocatalyst.

The architectures to achieve artificial photosynthesis discussed above all show great promise and may develop into viable options in the generation of solar fuels on global scales.

These systems rely on two main features for light capture: 1) exciton formation in a semiconductor material and 2) charge transport within a semiconductor material. Although exciton formation upon absorption of photons is typically very efficient in semiconductors, h^+ and e^- charge separation is inefficient due to poor charge transport in these materials, allowing charge recombination to become kinetically competitive with charge separation.⁸³⁻⁸⁷ Fast charge recombination limits efficiency of the device.⁸⁸⁻⁹² As a result, increasing the rate of charge separation is a major driving force to pursue a new architecture. In addition, utilizing chemical synthesis allows for control of light absorption, electron transfer events, redox potentials, and catalytic properties with great precision. An aspect that is difficult to overcome using nanoparticle materials.

1.3 Dye-Sensitized Photoelectrosynthesis Cells

All of the examples listed above utilize metal oxides as the WOC, such as RuO_2 nanoparticles or CoO_x films. While these catalysts have been shown to efficiently oxidize water, the mechanism by which they operate is still unclear.^{93,94} As suggested first by DFT calculations^{95,96} and later confirmed experimentally, single-site Ru-oxo complexes are effective WOCs in the presence of a sacrificial oxidant. Since its co-discovery in 2008 by Concepcion et. al.³⁴ and Tseng et. al.⁹⁷ many single site WOC have been reported that include $Ru^{33,98-103}$, $Ir^{104-109}$, $Co^{110,111}$, Cu^{112} , and $Fe^{113-115}$ and have recently been reviewed elsewhere.¹¹⁶⁻¹¹⁸ The advantages of single site catalysts are the ability to discern the mechanistic details of catalytic water oxidation with great precision while being capable of systematic modifications. Particularly, the mechanism for water oxidation has been described for single site Ru-oxo complexes in great detail (Figure 1.5).^{35,119-121} Mechanistic studies for

other (Ir, Co, Cu, or Fe) single site catalysts have not been as thoroughly studied, but are believed to go through similar high-valent metal-oxo intermediates.^{105,112,113}

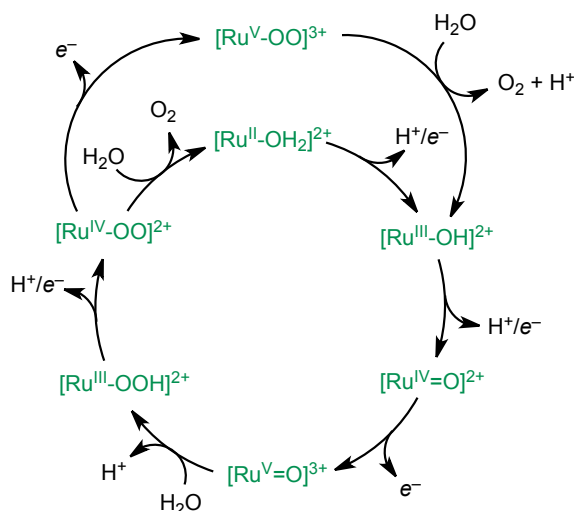


Figure 1.5. Ru-oxo single-site water oxidation mechanism. Adapted with permission from ref. 35. Copyright 2013 American Chemical Society. (Alexander J. Miller)

In the proposed catalytic mechanism for single-site WOCs, four protons and four electrons must be transferred at a single catalytic site. Taking advantage of chemical synthesis allows for strategic manipulation of the catalysts to lower the energetics of the catalytically active state and increase catalytic rates. As a single-site WOC cannot act alone to achieve artificial photosynthesis, an architecture that takes advantage of chemical synthesis by bringing a light absorber and a molecular WOC in close proximity, while retarding charge recombination through efficient charge separation, is the concept of the dye-sensitized photoelectrosynthesis cell or DSPEC.

A DSPEC consist of several key components; 1) a nanostructured semiconductor electrode, 2) a light harvesting chromophore used to sensitize the semiconductor electrode, 3) a WOC, 4) a proton or CO₂ RC, 5) external circuit connecting both the anodic and cathodic portions of the cell, and 6) a membrane separating the anodic and cathodic portions of the cell. (Figure 1.6). The processes at the heart of a functioning DSPEC are 1) efficient excited

state formation of the surface bound chromophore, 2) excited state electron transfer to the semiconductor electrode, 3) electron and proton transfers that are driven by internal free-energy gradients, and 4) oxidation and reduction catalysis.^{42,122-125} In general, light absorption occurs at the anode due to the availability of *n*-type semiconductors, most notably TiO₂. Photocathodic materials, which are outside the scope of this review, have also been developed for use with high valence band semiconductors (i.e. NiO) and although a large amount of progress has recently been made in the implementation of *p*-type DSSCs as well DSPECs,¹²⁶⁻¹³³ this thesis will focus on the well-studied photoanode.

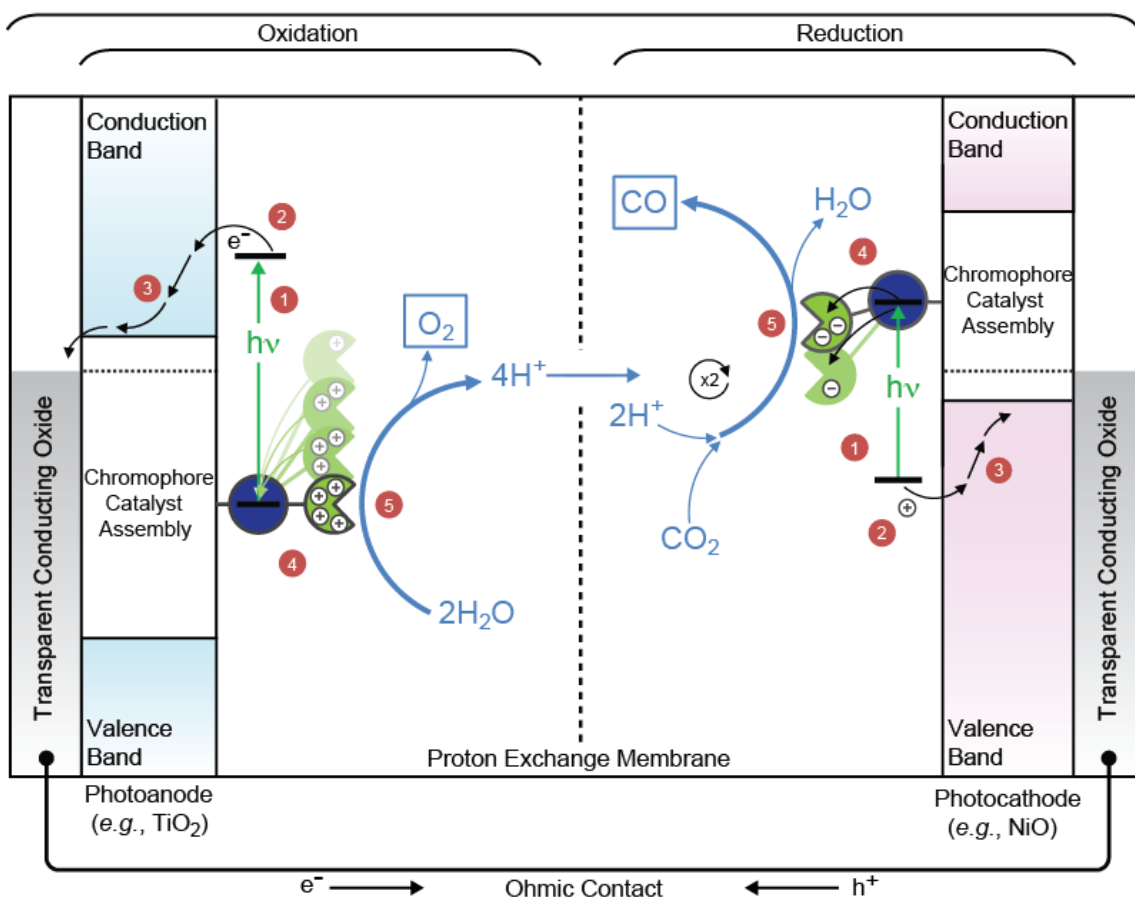


Figure 1.6. Dye-sensitized photoelectrosynthesis cell (DSPEC) for water oxidation and CO₂ reduction to CH₄. (James F. Cahoon)

In a photoanode, photoexcitation of the light absorbing chromophore is followed by excited state electron transfer to the conduction band of a large band gap semiconductor

(typically anatase TiO_2), referred to in this review as electron (e^-) injection. This initial charge separation step is a distinct advantage over semiconductor light-absorbers as it is fundamental in slowing down charge recombination between the e^- and hole (h^+) generated at the chromophore. Following the initial electron injection step, the resulting oxidized chromophore is reduced by a nearby, or chemically attached, WOC, which regenerates the initial ground state of the chromophore along with a singly oxidized WOC. The electron, now in the conduction band of the semiconductor, can be transferred via an external circuit to the cathodic portion of the cell to reduce protons to molecular hydrogen or CO_2 to fuels or fuel precursors. To oxidize water into the components O_2 and 4H^+ , these described photoexcitation and electron transfer events must occur four times to build up the oxidative equivalents required to carry out water oxidation (Equation 1.2).

1.4 Design Principles for Molecular Chromophore-Catalyst Assemblies

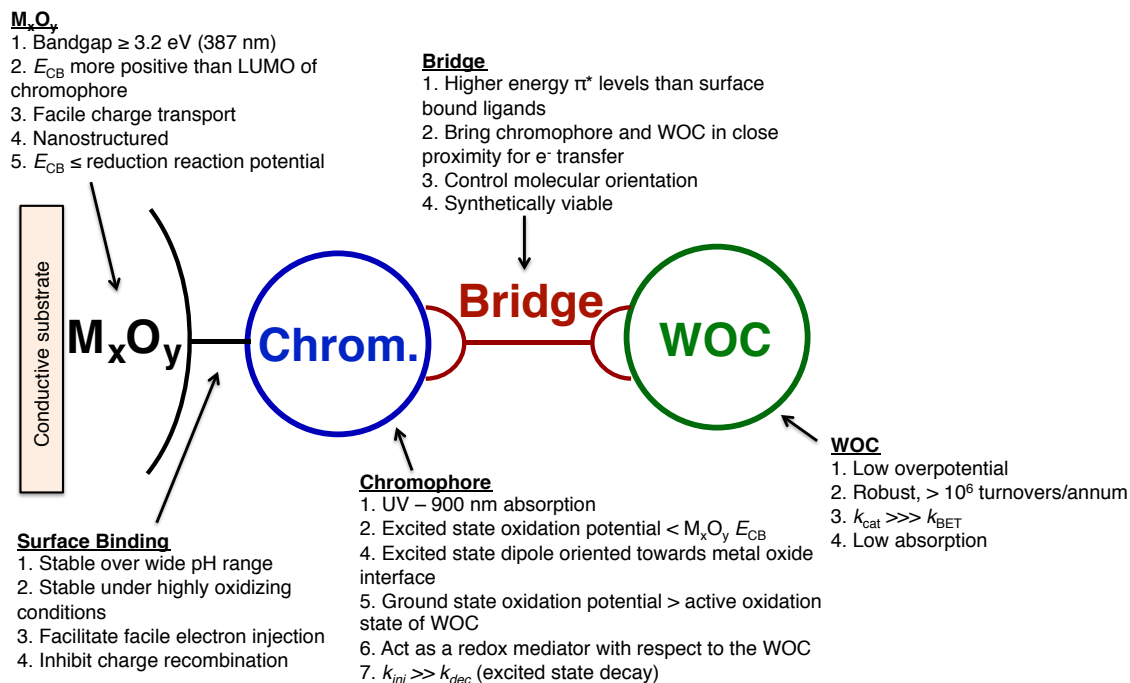


Figure 1.7. Design principles for a photoanode in a DSPEC.

The underlying design principles for a photoanode in a DSPEC are outlined in Figure 1.7. The components of a photoanode include: 1) a light harvesting chromophore that initiates the series of electron transfer events upon photon absorption, 2) a nanostructured metal oxide semiconductor that is able to accept multiple reductive equivalents, 3) a bridging ligand or some other linkage motif that can bring the chromophore and water oxidation catalyst (WOC) in close proximity to each other, 4) a stable and fast WOC, and 5) an underlying conductive substrate to transfer the reductive equivalents to the cathode. Though the design principles are numerous substantial improvement has been achieved for several of the key components shown in Figure 1.7. These are highlighted below and discussed throughout the review.

A functioning photoanode for water oxidation operates through a series of photoinduced reactions (Figure 1.7). First, the light absorbing chromophore undergoes photoexcitation to generate an excited state. A critical design feature of the chromophore is that it absorbs throughout the visible and into the UV and near-IR to maximize efficiency under solar irradiation. To date, the majority of the chromophore-catalyst assemblies bound to metal oxide electrodes utilize a $\text{Ru}(\text{bpy})_3^{2+}$ -like chromophore, which has limited absorption to wavelengths < 500 nm. However, Ru(II) polypyridyl complexes do have significant advantages as chromophores in that they have been extensively studied, undergo photo-induced electron injection into TiO_2 with $\Phi_{\text{inj}} \sim 1$, are able to act as facile redox mediators with respect to the WOC, and have relatively high ground state oxidation potentials.

Upon light absorption, the photo-generated excited state must have the thermodynamic potential to undergo electron injection into the semiconductor. This requires

that the excited state oxidation potential of the chromophore (Chrom.^{GS+/ES*}) be more negative than the energy of the conduction band of the metal oxide semiconductor (E_{CB}). In addition, chromophore excited state formation should be efficient, with the lowest energy excited state oriented towards the metal oxide interface to facilitate fast and efficient electron injection into the semiconductor. It was recently reported that injection efficiencies are significantly lowered by having ancillary ligands (non-surface binding ligands) with lower π^* levels than the metal oxide-bound ligands. This creates a competition within the excited state in which the excited electron spends a significant amount of time away from the metal oxide interface, lowering electron injection (rob brown ref). This was also reported for a chromophore-catalyst assembly, where the bridging ligand π^* levels were lower than the surface-bound ligands.¹³⁴ As a result, it is critical that the excited state dipole of the chromophore be oriented toward the metal oxide interface and not toward the external solution.

Chromophore design requires incorporation of functional groups for surface attachment to the metal oxide. Electronic coupling between the chromophore and the metal oxide has been shown to play a role in the rate and efficiency of electron injection,^{135,136} and the surface attachment must exhibit stability to ensure long life times of the photoanode. Several different metal-oxide binding groups have been studied including alcohols¹³⁷, hydroxamates¹³⁸, silanes¹³⁹, and acetylacetonates¹⁴⁰. However, by far the most widely used surface attachment strategies are carboxylic acids ($-\text{CO}_2\text{H}$) and phosphonic acids ($-\text{PO}_3\text{H}_2$). It has been determined that surface bound chromophores that utilize $-\text{PO}_3\text{H}_2$ groups are more stable under electrocatalytic and photocatalytic conditions than to $-\text{CO}_2\text{H}$ groups.¹⁴¹⁻¹⁴³ The synthesis of phosphonated ligands, in particular 4,4'-(PO_3H_2)₂-bpy ([2,2'-bipyridine]-4,4'-

diylbis(phosphonic acid)), represents a significant challenge in the development of new phosphonate derivatized chromophores. Introduction of a single methylene unit (-CH₂-) between the surface bound functional group and the aromatic ligand decreases the synthetic challenges. Although initial studies indicated that the introduction of a single -CH₂- group lowered injection yields compared to complexes without the methylene group¹⁴⁴, new data suggests that the -CH₂- group may not inhibit electron injection, and slows back electron transfer slightly.¹⁴⁵

Although -PO₃H₂ groups are more stable than -CO₂H groups on metal oxide surfaces, they still suffer from instability in solution where pH > 5.¹⁴⁴ At higher pH values, water oxidation requires less thermodynamic driving force, dropping from 1.23 V (vs NHE) at pH 0 to 0.40 V (vs NHE) at pH 14. This is one of many motivations for performing water oxidation near pH 7, which requires new approaches for stabilizing surface bound chromophores on photoanodes. Significant progress has recently been made in stabilizing light harvesting chromophores and WOCs on metal oxide surfaces in aqueous conditions under electrocatalytic and photocatalytic conditions.¹⁴⁶⁻¹⁵² This is an important step, as most photoelectrochemical experiments are conducted for only short periods of time (< 1 hr) due to chromophore and catalyst desorption from the metal oxide surface during the experiment.

The electron accepting metal oxide also plays an important role in the efficiency of a working photoanode. The semiconductor should be transparent throughout the solar spectrum (bandgap ≥ 3.2 eV) to limit competitive absorption with the chromophore. The metal oxide should also have a high surface area to increase the number of binding sites for chromophore-catalyst assemblies. Adverse processes to device performance, such as back electron transfer from the electron in the semiconductor to the generated hole on the oxidized

chromophore or the WOC (following forward electron transfer), are in competition with forward reactions (such as catalysis) and can limit or completely inhibit device performance. This necessitates facile electron transfer from the semiconductor metal oxide to the external conducting substrate. A breakthrough that has recently been demonstrated is the process of modifying the semiconductor electrode where a semiconductor (shell) is atomically deposited onto a conductive nanocrystalline substrate (core) to generate a “core-shell” mesoporous structure.¹²⁶ Electron injection from the excited chromophore to the semiconductor shell is followed by rapid electron shuttling from the shell to the conductive core, resulting in fast removal of the electron from the system and limited charge recombination. TiO₂ and SnO₂ are the two most commonly used metal oxides for photoanodes due to their low conduction band edge, ease of synthesis, and stability. However, other metal oxides are now being explored including WO₃^{153,154}, ZnO^{155,156}, Nb₂O₅^{157,158}, Zn₂SnO₄¹⁵⁹, and SrTiO₃.^{160,161}

Charge separation at the electrode surface generates an oxidized chromophore, which has to be capable of oxidizing the WOC to a catalytically active state. This requires that the HOMO (or ground state oxidation potential, Chrom.^{GS+/GS}) of the chromophore must be more positive in potential than the active state of the WOC in order for electron transfer from the WOC to the oxidized chromophore to occur. As previously mentioned, water oxidation is a four-electron process, requiring the steps of photoexcitation, electron injection, and electron transfer between the chromophore and WOC, to occur four times, all of which are in competition with back reactions. To increase the likelihood of the generation of multiple redox equivalents on the WOC, the chromophore and WOC must be in close proximity. This can be achieved through a bridging ligand (BL) between the chromophore and catalyst, or by immobilizing the chromophore and WOC in a thin film. Recently, it has been demonstrated

that a BL designed to limit charge recombination, where the two metal centers have limited electronic communication by the introduction of saturated linkers, still maintains high electron injection efficiencies (~95%) as well as electron transfer efficiencies (~95%) on fast time scales ($\tau \sim 145$ ps).¹⁴⁵ It is important to point out that the rate of electron injection and forward electron transfer for the first oxidative equivalent is *five* orders of magnitude greater than that for charge recombination in this system. In some cases, there is not a bridging ligand between the two centers. While synthetically more viable, these strategies can lead to inefficient electron transfer between the chromophore and WOC as well as limit electron injection.^{134,162-164}

The discovery of single site WOCs has initiated a new field of research on its own.^{34,35,97} Utilizing molecular design and control, these catalysts can be systematically altered to determine the best metals and ligand frameworks to carry out water oxidation. While an impressive amount of work has been published in this area, new strategies are still being developed to incorporate these catalysts into chromophore-catalyst assemblies for use as photoanodes. While it is still unclear what molecular WOC is best for use in a photoanode, there are several requirements that must be met for the WOC to build a working device. The WOC must be robust yielding $\geq 10^6$ turnovers per year, a figure of merit for commercialization. The WOC must also be able to withstand several years of operation before it is replaced by new catalyst in a commercial device.

The dependence on solar flux, where photon flux is $\sim 1 - 2 \text{ s}^{-1}$ (Table 1.1), demands that the rate of catalytic water oxidation (k_{cat}) be greater than 1 s^{-1} to keep up with solar flux. It is likely that the rate of water oxidation will have to be significantly higher because it is in competition with back reactions, such as back electron transfer (BET). BET is typically on

the order of $10^3 - 10^6 \text{ s}^{-1}$, requiring k_{cat} to be on the same, or faster, time scale ($k_{\text{cat}} \gg k_{\text{BET}}$).

The WOC must also have a low overpotential for water oxidation as this can waste energy absorbed from photons and puts more strain on the requirements of the chromophore to drive the WOC. Finally, the WOC should absorb little or no light throughout the solar spectrum to limit competitive light absorption with the chromophore.

Table 1.1. Incident Photons per Molecule of a Typical Dye Molecule

Wavelength (nm)	Incident Photons Per Molecule Per Second ^a
280 – 400	0.28
400 – 700	1.98
700 - 1000	1.83

^a Assuming $\Gamma = 1 \times 10^{-7} \text{ mol cm}^{-2}$.

While all of these requirements present a significant challenge when designing molecular chromophore-catalyst assemblies to carry out light-driven water oxidation, the challenges have been identified and several designs have been reported resulting in significant progress in the field. This dissertation focuses on the design and synthesis of light-harvesting chromophores, molecular water oxidation catalyst, molecular chromophore-catalyst assemblies for photoanodes, interfacial dynamics of assemblies bound to TiO_2 , and new strategies to build and stabilize multi-component films on metal oxide electrodes for use as photoanodes.

Chapter 2: CONTROLLING GROUND AND EXCITED STATE PROPERTIES THROUGH LIGAND CHANGES IN RUTHENIUM POLYPYRIDYL COMPLEXES

Reprinted with permission from Ashford, D. L.; Glasson, C. R. K.; Norris, M. R.; Hanson, K.; Concepcion, J. J.; Keinan, S.; Brennaman, M. K.; Templeton, J. L.; Meyer, T. J., Controlling Ground and Excited State Properties through Ligand Changes in Ruthenium Polypyridyl Complexes. *Inorg. Chem.* **2014**, *53* (11), 5637-5646. Copyright American Chemical Society 2014.

2.1 Introduction

Utilization of solar energy to produce fuels requires the integration of UV-visible-near IR light absorption with a sequence of electron and proton transfer events to drive water splitting ($2 \text{H}_2\text{O} \rightarrow 2 \text{H}_2 + \text{O}_2$) or water reduction of CO_2 to carbon-based fuels.^{2,24,42,165,166}

Honda and Fujishima demonstrated light driven water splitting by direct band gap excitation of TiO_2 ($\sim 3.2 \text{ eV}$) where the photogenerated holes (h^+) carry out water oxidation.⁴³

However, the high-energy photons ($< 390 \text{ nm}$) required for direct band gap excitation of TiO_2 make up $< 10\%$ of the available solar spectrum. The energy threshold for water splitting at 1.23 eV/eq requires 4 photons at 1000 nm at zero overpotential, with the energy of the optical transition a good measure of the free energy content of absorbed photons.^{27,167-172}

One approach to solar fuels and artificial photosynthesis is the use of dye-sensitized photoelectrosynthesis cells (DSPECs).^{162,173,174} They utilize chromophore-catalyst assemblies, for light absorption and catalysis, surface-bound to high band gap oxide semiconductors, notably TiO_2 , for photoanode applications. In a DSPEC, excitation and

injection by the chromophore initiates a sequence of events leading to oxidative activation of the catalyst.

For applications in water splitting at a photoanode, desirable properties of the chromophore include absorbing low energy/near-IR light and using electron injection into TiO₂ to create a surface-bound oxidant sufficiently powerful to drive water oxidation.^{29,42,173,175,176} These ligand-influenced properties are counterbalanced by the need for excitation to produce an excited state sufficiently reducing to undergo efficient electron injection into low-lying conduction band states in TiO₂ with a conduction band edge at pH 0 of ~ -0.34 V vs SCE.^{92,125,162} Other metal oxides, such as SnO₂^{177,178} ($E_{CB} \sim -0.04$ V vs SCE in pH 0) and WO₃^{153,154} ($E_{CB} \sim 0.06$ V vs SCE in pH 0), with more positive conduction band edges, resulting in increased driving force for electron injection from an excited state, have also been investigated.

Ruthenium polypyridyl complexes have found extensive use as chromophores in dye-sensitized solar cells (DSSCs) and DSPECs.^{122,124,135,162,165,179,180} The properties of their low-lying metal-to-ligand charge transfer (MLCT) excited states are well understood and they can be surface-bound to oxide surfaces, including TiO₂, as carboxylate or phosphonate derivatives.^{141,144,181} Following MLCT excitation and electron injection, the oxidized forms of the complexes are typically powerful oxidants with redox potentials sufficient to drive water oxidation catalysis. Both excited state energy and redox potentials can be varied systematically by ligand modifications.¹⁸²⁻¹⁸⁸

We have reported the preparation and characterization of a series of ruthenium based chromophore-catalyst assemblies for use in DSPEC devices based on derivatized forms of Ru(bpy)₃²⁺ (bpy = 2,2'-bipyridine) as the light harvesting chromophore.^{126,134,189-194} We

report here the preparation and properties of a series of heteroleptic Ru(II) polypyridyl chromophores having the general structure $[\text{Ru}(\text{bpy})_2(\text{N-N})]^{2+}$ (N-N is a bidentate polypyridyl ligand). The series was designed to explore the manipulation of light absorption from the visible into the near-IR while retaining both the ground-state oxidation potentials necessary for water oxidation and sufficient excited state redox potentials for electron injection into the semiconductor conduction band. The library of complexes synthesized in this work is represented in Figure 2.1.

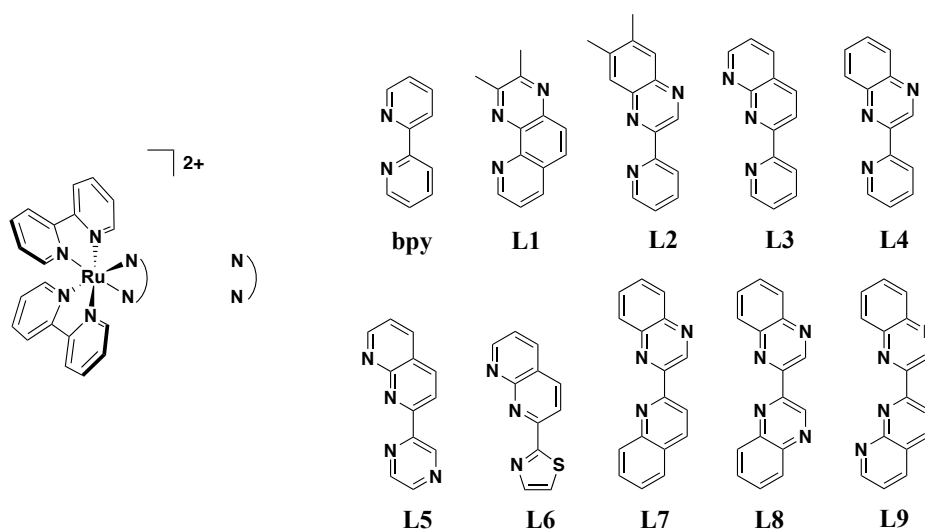


Figure 2.1. Structures of the generic complex and ligands in the series $[\text{Ru}(\text{bpy})_2(\text{N-N})]^{2+}$

2.2 Experimental

Materials

Solvents and reagents were obtained from commercial sources and used as received. Distilled water was further purified using a Milli-Q Ultrapure water purification system. 2-acetylpyridine, o-phenylenediamine, 1,2,3,4-tetrahydroquinoline, 2-acetylthiazole, 2-acetylpyrazine, 4,5-dimethyl-1,2-phenylenediamine and 2,3-butadione were purchased from Sigma Aldrich and used with no further purification. Proton nuclear magnetic resonance

spectra (^1H NMR) were recorded on a Bruker model DRX 400 spectrometer with residual solvent resonances used as the internal standard (^1H NMR: CDCl_3 at 7.26 ppm, CD_3CN at 1.94 ppm). $\text{Ru}(\text{bpy})_2\text{Cl}_2$ was synthesized as reported.¹⁹²

Ligand Synthesis

2,3-Dimethyl-pyrido[2,3-f]quinoxaline (**L1**)

To a stirred solution of 7,8-diaminoquinoline (0.100 g, 0.63 mmol) in ethanol (10 mL) was added 2,3-butadione (66 μL , 0.75 mmol). The reaction was refluxed overnight, cooled to room temperature, and water was added (~ 20 mL). The precipitate was filtered, washed with water, air dried, and collected (0.130 g, 98%). This product was used without further purification. ^1H NMR (400 MHz, CDCl_3): δ 9.19 (d, 1H), 8.26 (d, 1H), 7.99 (d, 1H), 7.93 (d, 1H), 7.62 (dd, 1H), 2.92 (s, 3H), 2.80 (s, 3H).

6,7-Dimethyl-2-(pyridin-2-yl)quinoxaline (**L2**)

4 M hydrochloric acid (2.4 ml) was added to a stirred solution of 4,5-dimethylbenzene-1,2-diamine (1.0 g, 7.34 mmol), 2-acetylpyridine (0.822 ml, 7.34 mmol) and silicon dioxide (0.024 g) in MeOH (30 ml) and refluxed overnight. The reaction mixture was subsequently allowed to cool prior to the addition of 0.1 M potassium hydroxide (100 ml) resulted in the formation of an orange precipitate. The precipitate was isolated by filtration, washed with excess water, dried in a vacuum oven, and collected (0.780 g, 45 %). This product was used without further purification. ^1H NMR (400 MHz, CDCl_3): δ 9.82 (s, 1H), 8.74 (d, 1H), 8.53 (d, 1H), 7.87 (m, 3H), 7.36 (dd, 1H), 2.49 (s, 6H).

2-(pyridin-2-yl)-1,8-naphthyridine (**L3**)

A stirred solution of 2-acetylpyridine (0.606 g, 5 mmol), 2-amino-3-formylpyridine (0.610 g, 5 mmol) and KOH (0.561 g, 10 mmol) in 50% aqueous methanol (10 ml) was

heated to 60°C overnight. The reaction mixture was quenched by the addition of water (20 ml) and the resulting precipitate was isolated by filtration. The crude product was washed with water, dried in a vacuum oven, and collected (0.984 g, 95 %). This product was used without further purification. ¹H NMR (400 MHz, CDCl₃): δ 9.13 (dd, 1H), 8.85 (d, 1H), 8.73 (d, 1H), 8.71 (d, 1H), 8.30 (d, 1H), 8.20 (dd, 1H), 7.86 (ddd, 1H), 7.47 (dd, 1H), 7.36 (dd, 1H).

2-(Pyridin-2-yl)quinoxaline (**L4**)

4 M hydrochloric acid (2.4 ml) was added to a stirred solution of 1,2-phenylenediamine (0.865 g, 8 mmol), 2-acetylpyridine (0.896 ml, 8 mmol) and silicon dioxide (0.024 g) in MeOH (30 ml) and refluxed overnight. The reaction mixture was subsequently allowed to cool prior to the addition of 0.1 M potassium hydroxide (100 ml) resulted in the formation of an orange precipitate. The precipitate was isolated by filtration, washed with excess water, dried in a vacuum oven, and collected (1.410 g, 85 %). This product was used without further purification. ¹H NMR (400 MHz, CDCl₃): δ 9.94 (s, 1H), 8.77 (d, 1H), 8.58 (d, 1H), 8.15 (m, 2H), 7.89 (dd, 1H), 7.76 (m, 2H), 7.39 (dd, 1H).

2-(Pyrazin-2-yl)-1,8-naphthyridine (**L5**)

A stirred solution of 2-acetylpyrazine (0.611 g, 5 mmol), 2-amino-3-formylpyridine (0.610 g, 5 mmol) and KOH (0.561 g, 10 mmol) in 50% aqueous methanol (10 ml) was heated to 60°C overnight. The reaction mixture was quenched by the addition of water (20 ml) and the resulting precipitate was isolated by filtration. The crude product was washed with water, dried in a vacuum oven, and collected (0.947 g, 91 %). This product was used without further purification. ¹H NMR (400 MHz, CDCl₃): δ 10.01 (s, 1H), 9.15 (dd, 1H), 8.64 (s, 2H), 8.63 (d, 1H), 8.33 (d, 1H), 8.22 (dd, 1H), 7.51 (dd, 1H).

2-(1,8-Naphthyridin-2-yl)thiazole (**L6**)

A stirred solution of 2-acetylthiazole (0.636 g, 5 mmol), 2-amino-3-formylpyridine (0.610 g, 5 mmol) and KOH (0.561 g, 10 mmol) in 50% aqueous methanol (10 ml) was heated to 60°C overnight. The reaction mixture was quenched by the addition of water (20 ml) and the resulting precipitate was isolated by filtration. The crude product was washed with water, dried in a vacuum oven, and collected (0.984 g, 98 %). This product was used without further purification. ¹H NMR (400 MHz, CDCl₃): δ 9.13 (dd, 1H), 8.45 (d, 1H), 8.28 (d, 1H), 8.20 (dd, 1H), 7.98 (d, 1H), 7.55 (d, 1H), 7.49, (dd, 1H).

2-(Quinolin-2-yl)quinoxaline (**L7**)

A stirred solution of 2-acetylquinoxaline (0.300 g, 1.74 mmol), 2-aminobenzaldehyde (0.211 g, 1.74 mmol) and KOH (0.195 g, 3.48 mmol) in 50% aqueous methanol (10 ml) was heated to 60°C overnight. The reaction mixture was quenched by the addition of water (20 ml) and the resulting precipitate was isolated by filtration. The crude product was washed with water, dried in a vacuum oven, and collected (0.434 g, 97 %). This product was used without further purification. ¹H NMR (400 MHz, CDCl₃): δ 10.20 (s, 1H), 8.73 (d, 1H), 8.34 (d, 1H), 8.18 (d, 1H), 8.17 (m, 2H), 7.89 (d, 1H), 7.78 (m, 3H), 7.60 (dd, 1H).

2,2'-biquinoxaline (**L8**)

This ligand was synthesized as previously reported.¹⁹⁵ 4 M hydrochloric acid (1.2 ml) was added to a stirred solution of 1,2-phenylenediamine (433 mg, 4 mmol), 2-acetylquinoxaline (689 mg, 4 mmol) and silicon dioxide (12 mg) in MeOH (15 ml) and refluxed overnight. The reaction mixture was subsequently allowed to cool prior to the addition of 0.1 M potassium hydroxide (50 ml) that resulted in the formation of a precipitate. The precipitate was isolated by filtration, washed with excess water and dried in a vacuum

oven. Yield: 310 mg (30 %). $^1\text{H NMR}$ (400 MHz, CDCl_3): δ 10.14 (s, 2H), 8.29 – 8.26 (m, 2H), 8.23 – 8.21 (m, 2H), 7.90 – 7.83 (m, 4H).

2-(1,8-Naphthyridin-2-yl)quinoxaline (**L9**).

A stirred solution of 2-acetylquinoxaline (0.300 g, 1.74 mmol), 2-amino-3-formylpyridine (0.212 g, 1.74 mmol) and KOH (0.195 g, 3.48 mmol) in 50% aqueous methanol (10 ml) was heated at 60°C overnight. The reaction mixture was quenched by the addition of water (20 ml) and the resulting precipitate was isolated by filtration. The crude product was washed with water, dried in a vacuum oven, and collected (0.410 g, 91 %). This product was used without further purification. $^1\text{H NMR}$ (400 MHz, CDCl_3): δ 10.35 (s, 1H), 9.20 (dd, 1H), 8.90 (d, 1H), 8.40 (d, 1H), 8.27 (dd, 1H), 8.20 (m, 2H), 7.81 (m, 2H), 7.56 (dd, 1H).

Complex Synthesis

General Procedure. A stirred solution of $\text{Ru}(\text{bpy})_2\text{Cl}_2^{192}$ and the ligand (**L1-L9**) were dissolved in a 1:1 EtOH:H₂O solution. The solution was refluxed for ~5 hr under an atmosphere of argon, cooled, filtered, and the filtrate was taken to dryness by rotary evaporation. The crude product was then purified by size exclusion chromatography (Sephadex LH-20) with 1:1 MeOH:H₂O as eluent. Similar fractions (based on UV-Visible absorption) were combined, and the solvent was removed by rotary evaporation. The solid was triturated with ether, filtered, washed with ether, and collected. When noted, a salt metathesis was carried out followed by filtration to isolate the final product following purification.

$[\text{Ru}(\text{bpy})_2(\text{L1})](\text{Cl})_2$ (**1**).

The product was isolated as an orange crystalline powder (0.153 g, 92%). ^1H NMR (400 MHz, D_2O): δ 8.63 (d, 1H), 8.56 (m, 4H), 8.38 (d, 1H), 8.21 (d, 1H), 8.09 (dd, 1H), 8.00 (m, 6H), 7.71 (d, 1H), 7.65 (dd, 1H), 7.38 (m, 2H), 7.30 (d, 1H), 7.28 (dd, 1H), 7.15 (dd, 1H), 2.76 (s, 3H), 2.26 (s, 3H). UV-vis in H_2O , λ_{max} , nm (ϵ , $\text{M}^{-1} \text{cm}^{-1}$): 254 (20300), 285 (54000), 337 (9200), 440 (12700); HR-ESI-MS: $m/z = 622.1293$ (calcd for $\text{C}_{33}\text{H}_{26}\text{N}_7\text{Ru}$ ($\text{M} - \text{HCl} - \text{Cl}$) $^+$) 622.1280), 311.5686 (calcd for $\text{C}_{37}\text{H}_{27}\text{N}_7\text{Ru}$ ($\text{M} - 2\text{Cl}$) $^{2+}$) 311.5662). Anal. Found (Calc.) for $\text{C}_{33}\text{H}_{35}\text{Cl}_2\text{N}_7\text{O}_4\text{Ru}$: C 51.77 (51.77), H 4.57 (4.61), N 12.78 (12.81). $[\text{Ru}(\text{bpy})_2(\text{L}2)](\text{ClO}_4)_2$ (**2**).

This complex was isolated as its perchlorate salt by precipitation of the combined chromatographic fractions by the addition of excess NaClO_4 to give a red powder (0.360 g, 85%). ^1H NMR (400 MHz, CD_3CN): δ 9.75 (s, 1H), 8.86 (d, 1H), 8.60 (m, 2H), 8.48 (d, 1H), 8.40 (d, 1H), 8.14 (m, 4H), 7.97 (m, 4H), 7.72 (d, 1H), 7.63 (d, 1H), 7.54 (t, 1H), 7.48 (m, 2H), 7.42 (t, 1H), 7.35 (m, 2H), 7.03 (s, 1H), 2.43 (s, 3H), 1.93 (s, 3H); UV-vis in H_2O , λ_{max} , nm (ϵ , $\text{M}^{-1} \text{cm}^{-1}$): 244 (19600), 250 (20900), 281 (44100), 364 (10800), 383 (11100), 433 (5900), 502 (6300). HR-ESI-MS: $m/z = 794.1156$ (calcd for $\text{C}_{35}\text{H}_{29}\text{F}_6\text{N}_7\text{PRu}$ ($\text{M} - \text{PF}_6$) $^+$) 794.1170), 324.5737 (calcd for $\text{C}_{35}\text{H}_{29}\text{N}_7\text{Ru}$ ($\text{M} - 2\text{PF}_6$) $^{2+}$) 324.5764). Anal. Found (Calc.) for $\text{C}_{35}\text{H}_{31}\text{Cl}_2\text{N}_7\text{O}_9\text{Ru}$: C 48.38 (48.56), H 3.62 (3.61), N 11.36 (11.33).

$[\text{Ru}(\text{bpy})_2(\text{L}3)](\text{ClO}_4)_2$ (**3**).

This complex was isolated as its perchlorate salt by precipitation of the combined chromatographic fractions by the addition of excess NaClO_4 to give a red powder (0.308 g, 75%). ^1H NMR (400 MHz, CD_3CN): δ 8.74 (d, 1H), 8.64 (d, 1H), 8.60 (d, 1H), 8.52 (d, 1H), 8.50 (d, 1H), 8.39 (dd, 1H), 8.34 (dd, 2H), 8.12 (dd, 1H), ; UV-vis in H_2O , λ_{max} , nm (ϵ , $\text{M}^{-1} \text{cm}^{-1}$): 242 (33800), 287 (50900), 316 (30000), 443 (8300), 509 (7700). HR-ESI-MS: $m/z =$

720.0675 (calcd for $C_{33}H_{25}ClN_7O_4Ru (M - ClO_4)^+$) 720.0700), 310.5607 (calcd for $C_{33}H_{25}N_7Ru (M - 2ClO_4)^{2+}$) 310.5577). Anal. Found (Calc.) for $C_{33}H_{25}Cl_2N_7O_8Ru$: C 48.32 (48.36), H 3.17 (3.07), N 12.04 (11.96).

$[Ru(bpy)_2(L4)](PF_6)_2$ (**4**).

This complex was isolated as its hexafluorophosphate salt by precipitation of the combined chromatographic fractions by the addition of excess NH_4PF_6 to give a red powder (0.782 g, 83%). 1H NMR (400 MHz, CD_3CN): δ 9.72 (s, 1H), 8.83 (d, 1H), 8.57 (m, 2H), 8.45 (d, 1H), 8.37 (d, 1H), 8.13 (m, 4H), 7.94 (m, 4H), 7.69 (d, 1H), 7.60 (d, 1H), 7.51 (t, 1H), 7.45 (m, 2H), 7.38 (t, 1H), 7.31 (m, 2H), 6.99 (s, 1H); UV-vis in H_2O , λ_{max} , nm (ϵ , $M^{-1} cm^{-1}$): 254 (30200), 282 (53200), 333 (18800), 431 (8100), 511 (9000). HR-ESI-MS: $m/z = 766.0857$ (calcd for $C_{33}H_{25}F_6N_7PRu (M - PF_6)^+$) 766.0839), 310.5607 (calcd for $C_{37}H_{27}N_7Ru (M - 2PF_6)^{2+}$) 310.5583). Anal. Found (Calc.) for $C_{33}H_{25}F_{12}N_7P_2Ru$: C 43.07 (43.33), H 2.80 (2.77), N 10.79 (10.77).

$[Ru(bpy)_2(L5)](ClO_4)_2$ (**5**).

This complex was isolated as its perchlorate salt by precipitation of the combined chromatographic fractions by the addition of excess $NaClO_4$ to give a red powder (0.275 g, 67%). 1H NMR (400 MHz, CD_3CN): δ 9.82 (s, 1H), 8.74 (d, 1H), 8.67 (d, 1H), 8.52 (m, 3H), 8.44 (d, 1H), 8.37 (t, 2H), 8.07 (m, 4H), 7.95 (t, 1H), 7.89 (d, 1H), 7.77 (d, 1H), 7.65 (d, 2H), 7.62 (d, 1H), 7.55 (dd, 1H), 7.41 (m, 2H), 7.28 (m, 2H); UV-vis in H_2O , λ_{max} , nm (ϵ , $M^{-1} cm^{-1}$): 241 (31900), 284 (47900), 318 (25800), 427 (8100), 518 (7700); HR-ESI-MS: $m/z = 767.0835$ (calcd for $C_{32}H_{24}F_6N_8PRu (M - PF_6)^+$) 767.0809), 311.0567 (calcd for $C_{32}H_{24}F_6N_8PRu (M - 2PF_6)^{2+}$) 311.0584). Anal. Found (Calc.) for $C_{32}H_{34}Cl_2N_8O_{13}Ru$: C 42.30 (42.21), H 2.87 (3.06), N 12.35 (12.31).

[Ru(bpy)₂(L6)](ClO₄)₂ (**6**).

This complex was isolated as its perchlorate salt by precipitation of the combined chromatographic fractions by the addition of excess NaClO₄ to give a red powder (0.175 g, 42%). ¹H NMR (400 MHz, CD₃CN): δ 8.60 (d, 1H), 8.48 (t, 2H), 8.41 (d, 1H), 8.39 (dd, 1H), 8.35 (t, 2H), 8.10 (d, 2H), 8.03 (m, 3H), 7.79 (d, 1H), 7.73 (t, 2H), 7.55 (d, 1H), 7.51 (dd, 1H), 7.36 (m, 4H), 7.26 (dd, 1H), 7.21 (d, 1H); UV-vis in H₂O, λ_{max}, nm (ε, M⁻¹ cm⁻¹): 240 (24100), 284 (45000), 340 (23300), 442 (7200), 521 (8100); HR-ESI-MS: m/z = 726.0223 (calcd for C₃₁H₂₃ClN₇O₄RuS (M – ClO₄)⁺) 726.0264), 313.5383 (calcd for C₃₁H₂₃N₇RuS (M – 2ClO₄)²⁺) 313.5390). Anal. Found (Calc.) for C₃₁H₂₉Cl₂N₇O₁₁RuS: C 42.33 (42.33), H 2.93 (3.32), N 11.18 (11.15).

[Ru(bpy)₂(L7)](ClO₄)₂ (**7**).

This complex was isolated as its perchlorate salt by precipitation of the combined chromatographic fractions by the addition of excess NaClO₄ to give a red powder (0.200 g, 40%). ¹H NMR (400 MHz, CD₃CN): δ 9.90 (s, 1H), 8.77 (d, 1H), 8.64 (d, 1H), 8.55 (d, 2H), 8.33 (t, 2H), 8.24 (d, 1H), 7.95 – 8.15 (m, 6H), 7.75 – 7.90 (m, 4H), 7.55 – 7.70 (m, 2), 7.30 – 7.46 (m, 6H), 7.24 (ddd, 1H), 7.14 (d, 1H), 6.96 (d, 1H); UV-vis in H₂O, λ_{max}, nm (ε, M⁻¹ cm⁻¹): 254 (31000), 272 (43800), 286 (47400), 355 (18400), 368 (18000), 390 (18500), 428 (6400), 544 (8100); HR-ESI-MS: m/z = 770.0857 (calcd for C₃₇H₂₇ClN₇O₄Ru (M – ClO₄)⁺) 770.0835), 335.5665 (calcd for C₃₇H₂₇N₇Ru (M – 2ClO₄)²⁺) 335.5686). Anal. Found (Calc.) for C₃₇H₃₃Cl₂N₇O₁₁Ru: C 48.22 (48.11), H 3.48 (3.60), N 10.77 (10.72).

[Ru(bpy)₂(L8)](ClO₄)₂ (**8**).

This complex was isolated as its perchlorate salt by precipitation of the combined chromatographic fractions by the addition of excess NaClO₄ to give a red powder (0.225 g,

52%). ^1H NMR (400 MHz, MeOD): δ 8.86 (d, 1H), 8.77 (d, 1H), 8.61 (d, 1H), 8.51 (d, 1H), 8.28 (td, 1H), 8.13 (m, 5H), 7.99 (td, 1H), 7.93 (d, 1H), 7.91 (d, 1H), 7.78 (ddd, 1H), 7.61 (ddd, 1H), 7.56 (d, 1H), 7.53 (ddd, 1H), 7.45 (m, 2H), 7.39 (m, 2H), 7.31 (ddd, 1H), 7.02 (t, 1H), 5.68 (d, 1H); UV-vis in H_2O , λ_{max} , nm (ϵ , $\text{M}^{-1} \text{cm}^{-1}$): 253 (32100), 288 (36200), 334 (16400), 398 (14800), 503 (6700). HR-ESI-MS: $m/z = 673.1418$ (calcd for $\text{C}_{36}\text{H}_{27}\text{N}_8\text{Ru} (\text{M} - 2 \text{ClO}_4 + \text{H})^+$) 673.1402), 337.0754 (calcd for $\text{C}_{36}\text{H}_{27}\text{N}_8\text{Ru} (\text{M} - 2\text{ClO}_4)^{2+}$) 337.0667). Anal. Found (Calc.) for $\text{C}_{38}\text{H}_{29}\text{Cl}_2\text{N}_9\text{O}_8\text{Ru}$: C 51.34 (51.06), H 4.02 (3.70), N 13.63 (13.83). $[\text{Ru}(\text{bpy})_2(\text{L9})](\text{ClO}_4)_2$ (**9**).

This complex was isolated as its perchlorate salt by precipitation of the combined chromatographic fractions by the addition of excess NaClO_4 to give a red powder (0.210 g, 48%). ^1H NMR (400 MHz, CD_3CN): δ 9.91 (s, 1H), 8.94 (d, 1H), 8.77 (d, 1H), 8.57 (d, 2H), 8.47 (dd, 1H), 8.29 (d, 1H), 8.23 (d, 1H), 8.19 (d, 1H), 8.10 (dd, 1H), 8.05 (m, 3H), 7.99 (d, 1H), 7.97 (d, 1H), 7.93 (ddd, 1H), 7.85 (m, 1H), 7.53 (m, 3H), 7.37 (m, 3H), 7.27 (m, 3H); UV-vis in H_2O , λ_{max} , nm (ϵ , $\text{M}^{-1} \text{cm}^{-1}$): 253 (37800), 283 (41700), 362 (20900), 377 (18000), 422 (6200), 562 (7400). HR-ESI-MS: $m/z = 707.1030$ (calcd for $\text{C}_{36}\text{H}_{27}\text{N}_8\text{Ru} (\text{M} - 2 \text{ClO}_4 + \text{H}^+)^+$) 673.1402), 336.0677 (calcd for $\text{C}_{36}\text{H}_{27}\text{N}_8\text{Ru} (\text{M} - 2\text{ClO}_4)^{2+}$) 336.0162). HR-ESI-MS: $m/z = 707.1030$ (calcd for $\text{C}_{36}\text{H}_{26}\text{ClN}_8\text{Ru} (\text{M} - 2 \text{ClO}_4 + \text{Cl})^+$) 707.1800), 336.0162 (calcd for $\text{C}_{36}\text{H}_{27}\text{N}_8\text{Ru} (\text{M} - 2\text{ClO}_4)^{2+}$) 336.0162). Anal. Found (Calc.) for $\text{C}_{38}\text{H}_{29}\text{Cl}_2\text{N}_9\text{O}_8\text{Ru}$: C 52.14 (52.06), H 4.20 (3.90), N 13.74 (13.83).

Measurements.

Electrochemical measurements were conducted on a CH Instruments 660D potentiostat with a glassy carbon working electrode, Pt-wire counter electrode, and a Ag/AgNO_3 reference electrode (standardized with $\text{Ru}(\text{bpy})_3^{2+}$ redox couple^{185-187,196} vs SCE,

0.01 M AgNO₃/0.1 M tetra-n-butylammonium hexafluorophosphate (TBAPF₆) in CH₃CN). E_{1/2} values were obtained from the peak currents in square wave voltammograms. Reductive electrochemistry was carried out in CH₃CN with 0.1 M TBAPF₆ as the supporting electrolyte under an atmosphere of argon. Solutions were degassed with argon for 10 minutes prior to reductive electrochemistry.

UV-visible spectra were recorded on an Agilent 8453 UV/Visible photo diode array spectrophotometer. Extinction coefficients for the complexes in CH₃CN were determined from the absorption spectra of solutions having a known concentration of complex.

Steady-state emission spectra were recorded on thoroughly degassed solutions of the complexes in CH₃CN at room temperature with an Edinburgh FLS920 spectrometer with emitted light first passing through a 495 nm long pass color filter, then a single grating (1800 1/mm, 500 nm blaze) Czerny-Turner monochromator (5 nm bandwidth) and finally detected by a peltier-cooled Hamamatsu R2658P photomultiplier tube. The samples were excited with the light output from a housed 450 W Xe lamp/single grating (1800 1/mm, 250 nm blaze) Czerny-Turner monochromator combination with 5 nm bandwidth.

Computation.

All molecular geometries were calculated by density functional theory (DFT) with the B3LYP^{197,198} functional and the LanL2DZ^{199,200} basis set. Solvent environment effects were described by using the polarizable continuum model (PCM) with the integral equation formalism variant for acetonitrile. Tighter convergence criteria and a more accurate numerical integration grid were specified, to ensure finding the exact geometrical minima. Frequencies were calculated and checked to make sure that all frequencies were positive. Electronic spectra were calculated by TD-DFT, based on the procedure previously outlined

by Jacquemin et al.^{201,202} The geometry-optimized structures were used in the TD-DFT calculations, with the PBE0^{203,204} functional and the same basis-set and solvent effects as in the geometry optimization. The adiabatic approximation of time dependent DFT was used to solve for 60 singlet excited states.²⁰⁵ All calculations were done in Gaussian 09, Revision C.01.²⁰⁶

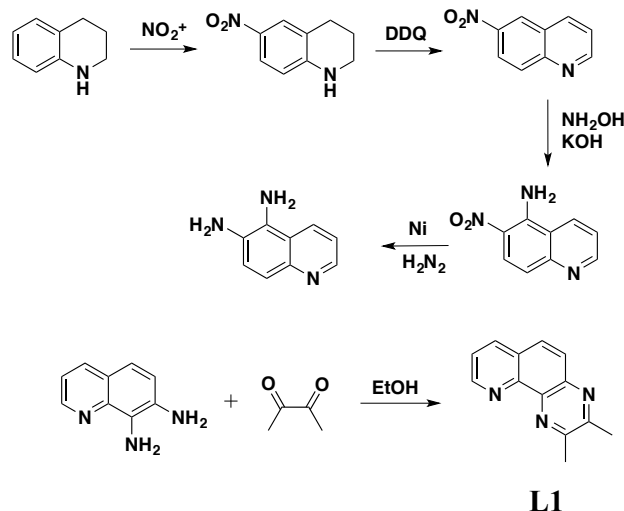
2.3 Results and Discussion

Ligand Synthesis

To tune the redox and photophysical properties of the ruthenium complexes, the π^* acceptor levels of the N-N ligands (**L1** - **L9**) were systematically altered. This was accomplished by using two different ligand designs: 1) incorporation of non-coordinating heteroatoms and 2) introduction of extended conjugation in the ligand backbone through fused aromatic rings. To achieve these structural features, pyrazine, thiazole, quinoxaline, quinoline, and naphthyridine moieties in various combinations were introduced into the diimine ligand (N-N), Figure 2.1.

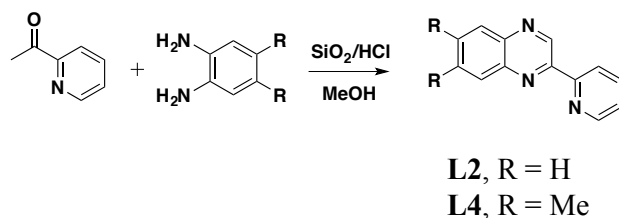
L1 was prepared in high yield by the condensation of 7,8-diaminequinoline and 2,3-butadione in ethanol (Scheme 1). 7,8-diaminequinoline was prepared in four steps starting from 1,2,3,4-tetrahydroquinoline. First, 1,2,3,4-tetrahydroquinoline was converted to 7-nitro-1,2,3,4-tetrahydroquinoline in a mixed acid electrophilic aromatic substitution.²⁰⁷ The nitrated hydroquinoline was then oxidized with 2,3-dichloro-5,6-dicyano-1,4-benzoquinone (DDQ) to give 7-nitroquinoline.²⁰⁸ This latter product was converted into 7-nitroquinoline-8-amine by treatment with hydroxylamine hydrochloride under basic conditions followed by reduction of the nitro group with Raney Nickel to give 7,8-diaminequinoline (Scheme 2.1).²⁰⁹

Scheme 2.1 Synthesis of L1



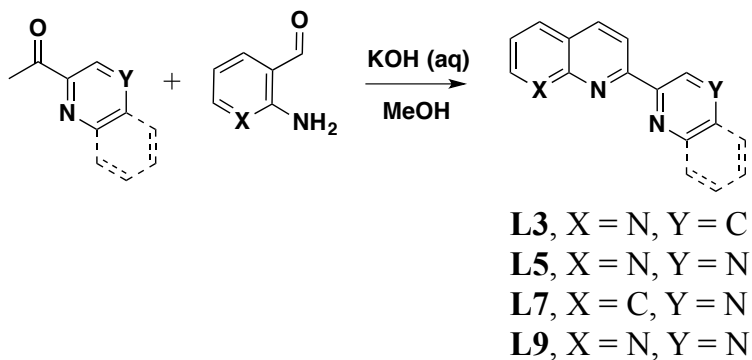
The *p*-quinoxaline pyridine ligands **L2** and **L4** were prepared in 45% and 85% yield, respectively, by a reported acid catalyzed condensation of *o*-phenylenediamine precursors with 2-acetylpyridine (Scheme 2.2).²¹⁰

Scheme 2.2 Synthesis of *p*-quinoxaline pyridine ligands **L2** and **L4**



The Friedländer condensation was used to prepare a series of quinoline (**L7**) and naphthyridine (**L3**, **L5**, **L6**, **L9**) derivatives with heterocyclic substituents in the 2-position (Scheme 2.3). These substituents include pyridine (**L3**), pyrazine (**L5**), thiazole (**L6**), quinoline (**L7**) and quinoxaline (**L9**).²¹¹ This synthetic approach allows for access to a library of subtly varied ligands for systematic studies. **L8** was synthesized by a reported procedure.¹⁹⁵ See Supporting Information for the full experimental procedure for the syntheses of **L1** – **L9**.

Scheme 2.3 General synthetic route for ligand synthesis via Friedlander condensations



Complex Syntheses

The $[\text{Ru}(\text{bpy})_2(\text{N-N})]^{2+}$ complexes were isolated as their chloride salt (or by salt metathesis, to form perchlorate or hexafluorophosphate salts) by the reaction of $\text{Ru}(\text{bpy})_2\text{Cl}_2^{192}$ with each of the bidentate (N-N) ligands **L1** - **L9** in 1:1 EtOH:H₂O (see Appendix A). In general, these reactions can be followed by UV/Visible absorption spectral measurements by monitoring disappearance of the $\text{Ru}(\text{bpy})_2\text{Cl}_2$ MLCT absorptions ($\lambda_{\text{max}} = 363 \text{ nm}$ and 526 nm in CH_3CN)²¹² and the appearance of absorptions due to the complexes **1** – **9** (Table 2.1, Appendix A).

Single crystal X-ray analysis was performed on complex **6** (Figure 2.2) to ensure the sulfur in **L6** did not coordinate competitively with the nitrogen. As shown in Figure 2, the nitrogen is coordinated to the Ru center and has a slightly distorted octahedral geometry around the Ru center ($\text{N1-Ru-N} = 173.7^\circ$, $\text{N14-Ru-N} = 170.0^\circ$). Steric repulsions between N12 and one of the bipyridine ligands distorts the planarity of **L6** upon coordination to the Ru center as indicated by the S-C4-C5-C6 torsion angle of 8.7° . The length of the Ru-N1 bond (2.056 \AA) is similar to that of the Ru-pyridine nitrogen distance, whereas the Ru-N14 (2.122 \AA) is slightly elongated due to the steric repulsion between N12 and the bipyridine

ligand.²¹³ The DFT computed geometry of complex **6** shows the same trends, with distorted octahedral geometry around the Ru center (N1-Ru-N = 175.2°, N14-Ru-N = 170.6°) and the Ru-N1 bond (2.074 Å) shorter than that of Ru-N14 (2.178 Å), Figure A.14.

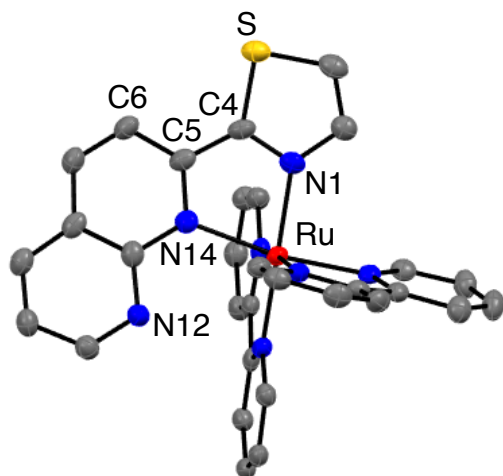
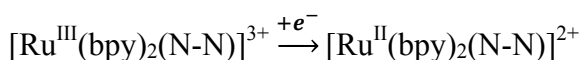


Figure 2.2. ORTEP diagram of complex **6** from single crystal X-ray analysis with thermal ellipsoids at the 50% probability level. Hydrogen atoms are omitted for clarity.

Electrochemistry

The electrochemical properties of complexes **1** - **9** in dry CH₃CN (0.1 M TBAPF₆ supporting electrolyte, TBA = tetrabutylammonium) were examined by cyclic and square-wave voltammetry. $E_{1/2}$ values for the Ru^{3+/2+} couple of each complex, Equation 2.1, are reported in Table 1 with representative cyclic voltammograms shown in Figure 2.3. These complexes exhibit reversible Ru^{3+/2+} redox couples with $E_{1/2}$ values ranging from 1.22 V to 1.47 V (vs SCE).

Equation 2.1



In general, the complexes that incorporate pyrazine units (**2**, **4**, **5**, **7**, **8**, **9**) have Ru^{3+/2+} redox potentials that are more positive than the [Ru(bpy)₃]^{3+/2+} couple (1.29 V vs SCE).^{185-187,196} All of the ligands (**L1** - **L9**) have lower-lying π* orbitals compared to bpy. The decrease in the N-N π* orbital energy increases dπ - π* back bonding from the Ru^{II} center to the N-N ligand, stabilizing the dπ⁶ electronic configuration, resulting in increased redox potentials for the Ru^{3+/2+} couples.^{196,214,215} Complex **8** is a special case in that it has a relatively low Ru^{3+/2+} redox potential (1.28 V vs SCE) considering the electronic nature of **L8** with two pyrazine groups in the ligand framework. Molecular models of **8** indicate that **L8**, when bound to the Ru^{II} center, is significantly distorted from planarity (Figure A.12). This could result in a disruption in the aromaticity in the ligand raising the π* energy levels, causing a lower than expected Ru^{3+/2+} potential. Attempts to grow x-ray quality crystals of **8** were unsuccessful.

Table 2.1. Spectroscopic properties and redox potentials for the series 1 – 9

Complex	Absorbance λ (nm) (ε, x10 ⁴ M ⁻¹ cm ⁻¹) ^a	Emission at RT ^b		ΔG _{ES} ^c eV	$E_{1/2}$ (Ru ^{3+/2+}) V ^d	$E_{1/2}$ (Ru ^{3+/2+*}) V ^e	$E_{1/2}$ (Ru ^{2+*/+}) V ^f	$E_{1/2}$ (Ru ^{2+/+}) V ^d
		λ _{max} (nm)	τ (ns)					
Ru(bpy) ₃ ²⁺	449(1.4)	620	831	2.19	1.29	-0.90	0.89	-1.30
	286 (5.1)							
	243 (2.5)							
1	443 (1.3)	650	26	2.17	1.36	-0.81	1.05	-1.12
	285 (5.4)							
	249 (1.9)							
2	501 (0.63)	755	167	1.81	1.40	-0.41	0.98	-0.83
	283 (4.5)							
	254 (2.1)							
3	507 (0.77)	765	184	1.80	1.22	-0.58	0.84	-0.96
	287 (5.1)							
	244 (3.4)							
4	508 (0.90)	780	105	1.76	1.42	-0.34	1.02	-0.74
	281 (5.4)							
	254 (3.0)							
5	518 (0.77)	790	92	1.73	1.35	-0.38	0.95	-0.78
	284 (4.8)							
	242 (3.2)							
6	520 (0.81)	810	113	1.69	1.24	-0.45	0.80	-0.89

	286 (4.6)							
	249(2.2)							
	544 (0.81)							
7	286 (4.7)	830	93	1.61	1.47	-0.14	1.00	-0.61
	256 (3.1)							
	509 (0.66)							
8	288 (3.6)	850	30	1.61	1.28	-0.33	0.71	-0.57
	253 (3.2)							
	564 (0.75)							
9	285 (4.2)	885	26	1.52	1.39	-0.13	0.96	-0.56
	254 (3.4)							

^a in CH₃CN. ^b in CH₃CN deaerated with Ar for 30 minutes. ^c ΔG_{ES} from a Franck-Condon analysis of emission spectra in CH₃CN, see text. ^d In CH₃CN deaerated with Ar for 10 minutes, 1 mM in complex and 0.1 M TBAPF₆ supporting electrolyte. GC working electrode, Pt-wire counter electrode, and Ag/AgNO₃ (1M) reference (values were adjusted to agree with literature values for [Ru(bpy)₃]^{3+/2+} at 1.29 V vs SCE). ^{37-39,58} $E_{1/2}$ values from differential pulse voltammetry. ^e $Ru^{3+/2+*} = Ru^{3+/2+} - \Delta G_{ES}$. ^f $Ru^{2+*/+} = Ru^{3+/2+} + \Delta G_{ES}$

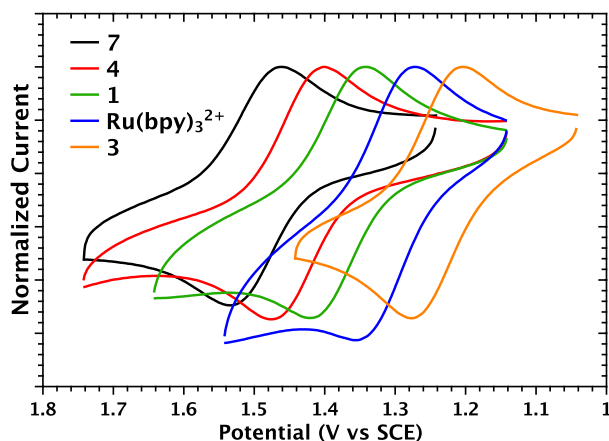


Figure 2.3. Cyclic voltammogram of complexes **7** (black), **4** (red), **1** (green), Ru(bpy)₃²⁺ (blue), and **3** (orange) in dry CH₃CN at 22°C with a glassy carbon working electrode, Pt-wire counter electrode, and a Ag/AgNO₃ reference electrode with $E_{1/2}$ (Ru(bpy)₃^{3+/2+}) = 1.29 V vs SCE.

The first ligand-based reduction potentials (Ru^{2+/*}, Equation 2.2) in dry CH₃CN (0.1 M TBAPF₆ supporting electrolyte) are listed in Table 2.1.¹⁸⁷ The large variations in the first reduction potential (Ru^{2+/*}), -1.12 V to -0.56 V, are significantly larger than variations in the Ru^{3+/2+} potentials, consistent with reduction at **L1** - **L9** as acceptor ligands. The 0.56 V variance in ligand-based reduction potentials reflects the effect of increased conjugation and/or incorporation of heteroatoms on the π^* acceptor levels in the acceptor ligands.¹⁹⁶ As

shown in Figure 2.4 for $\text{Ru}(\text{bpy})_3^{2+}$ and complexes **1**, **3**, and **7**, three reversible ligand-based reduction waves appear from -0.20 V to -2.0 V (vs SCE) with the first ligand-based reduction ranging from -0.56 V to -1.12 V (vs SCE).

Equation 2.2

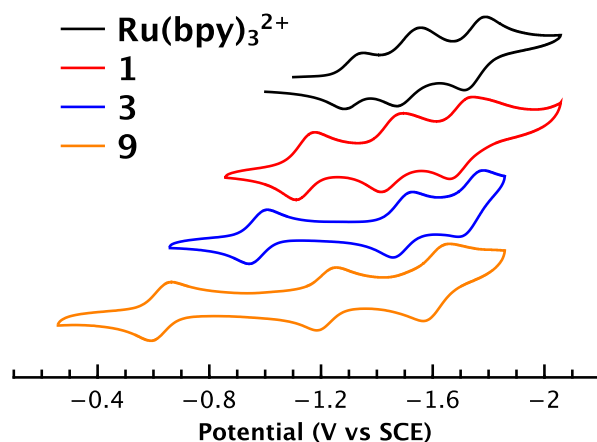
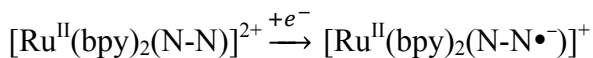


Figure 2.4. Cyclic voltammogram for complexes **9** (orange), **3** (blue), **1** (red), and $\text{Ru}(\text{bpy})_3^{2+}$ (black), in dry CH_3CN at 22°C under a nitrogen atmosphere with a glassy carbon working electrode, Pt-wire counter, and a Ag/AgNO_3 reference (relative to $\text{Ru}(\text{bpy})_3^{2+}$ at 1.29 V vs SCE).

Complex **3** has a lower $\text{Ru}^{3+/2+}$ potential than $\text{Ru}(\text{bpy})_3^{2+}$ by 70 mV (Table 2.1), suggesting that **L3** is a worse π^* -acceptor ligand than bpy even though its first ligand-based reduction (-0.96 V vs SCE) is 340 mV less negative than reduction of $\text{Ru}(\text{bpy})_3^{2+}$ (-1.30 V vs SCE).^{187,216} This is an apparent consequence of decreased orbital mixing with $d\pi(\text{Ru}^{\text{II}})$ highlighting the roles of both ligand π^* acceptor energy and orbital mixing in the design of acceptor ligands.

UV/Visible Absorption

UV/Visible spectra of complexes **1** - **9** in acetonitrile all feature characteristic, intense $\pi \rightarrow \pi^*$ absorptions below 350 nm ($\epsilon \approx 3.5\text{-}5.5 \times 10^4 \text{ M}^{-1}\text{cm}^{-1}$) along with metal-to-ligand

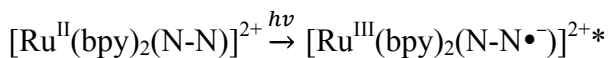
charge transfer (MLCT) absorptions (Table 2.1) in the visible region. The most notable trend in the series is the red shift in the lowest energy MLCT absorption from $\lambda_{\text{max}} = 443 \text{ nm}$ (**1**) to $\lambda_{\text{max}} = 564 \text{ nm}$ (**9**) with molar extinction coefficients that range from $\epsilon = 6.3 \times 10^3 \text{ M}^{-1}\text{cm}^{-1}$ (**2**) to $\epsilon = 1.3 \times 10^4 \text{ M}^{-1}\text{cm}^{-1}$ (**1**). Representative spectra are shown in Figure 2.5, and the remaining spectra are available in Appendix A.

The energies of the lowest energy MLCT absorptions are influenced by both increased conjugation in the N-N ligand and the presence of non-coordinating heteroatoms. The absorption spectra of complexes **2** and **9** illustrate a splitting in the MLCT manifolds. They arise from transitions to both bpy and the N-N ligands and, at higher energies, to higher lying π^* acceptor orbitals on the N-N ligands (Figure 2.5). The lowest energy transitions to bpy and N-N are illustrated in Equation 2.3 and Equation 2.4. The extent of MLCT splitting between bpy and N-N as acceptor ligands increases with the π^* acceptor ability of N-N.^{182,184,217} The use of multiple π^* acceptor ligands and transitions to higher π^* levels was utilized in earlier studies that focused on creating “black” MLCT absorbers.¹⁸²

Equation 2.3



Equation 2.4



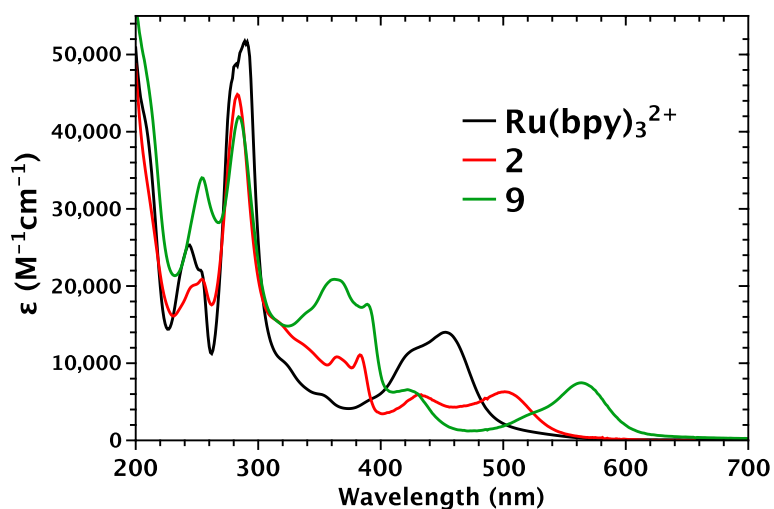


Figure 2.5. UV-Visible spectra of $\text{Ru}(\text{bpy})_3^{2+}$, **2**, and **9** in CH_3CN at room temperature.

Absorption spectra were analyzed by TD-DFT calculations (using the PBE0/LanL2DZ functional/basis-set, Figure A.14) on DFT optimized geometries (using the B3LYP/LanL2DZ functional/basis-set). A continuum model was used for the solvent. The results of the calculations are summarized in Table 2.2 and Figure A.14. They verify the origins of the intense visible absorptions from 400 - 600 nm as MLCT transitions from Ru^{II} either to bpy (Equation 2.3) or to the N-N ligand for **L1** - **L9** (Equation 2.4). The computed spectra correlate well with experimental spectra with strong $\pi \rightarrow \pi^*$ absorptions predicted below 300 nm and MLCT absorptions at longer wavelengths. All computed spectra are blue-shifted relative to the experimental spectra, likely due to solvent effects that are not adequately described by the polarizable continuum model (PCM) model used here.

Table 2.2 compares band assignments from the DFT calculations for complexes **2** and **9**. For complex **2**, the spectra are dominated in the UV by a bpy ligand-based $\pi \rightarrow \pi^*$ transition at 272 nm and high energy MLCT transitions for $d\pi(\text{Ru}^{\text{II}}) \rightarrow \pi_2^*$ (bpy) at 308 nm, and $d\pi(\text{Ru}^{\text{II}}) \rightarrow \pi_2^*$ (N-N) at 475 nm. Calculated orbital compositions are shown in Figure A.15 for the $d\pi(\text{Ru}^{\text{II}}) \rightarrow \pi_2^*$ (N-N) transition. For complex **9**, the calculations point to the

band at 278 nm as an overlap between $\pi \rightarrow \pi^*$ transitions for the bpy and N-N ligands.

Similarly, the band at 327 nm arises from overlapping transitions between $d\pi(\text{Ru}) \rightarrow \pi^*(\text{N-N})$ and $d\pi(\text{Ru}) \rightarrow \pi^*(\text{bpy})$. The calculated spectra also predict a low energy $\pi_1 \rightarrow \pi_2^*$ transition at ~ 750 nm for **9** but with an absorptivity too low to observe experimentally.

Table 2.2. Comparison of TD-DFT calculated absorption maxima for complexes 2 and 9 in CH₃CN

Complex 2			Complex 9		
Calculated	Experimental (ϵ , $\times 10^4 \text{ M}^{-1} \text{ cm}^{-1}$)	Transition	Calculated	Experimental (ϵ , $\times 10^4 \text{ M}^{-1} \text{ cm}^{-1}$)	Transition
272 nm	254 nm (2.1)	$\pi(\text{bpy}) \rightarrow \pi^*(\text{bpy})$	278 nm	254 nm (3.4)	$\pi(\text{bpy}) \rightarrow \pi^*(\text{bpy})$ $\pi(\text{N-N}) \rightarrow \pi^*(\text{bpy})$
308 nm	283 nm (4.5)	$d\pi(\text{Ru}) \rightarrow \pi^*(\text{bpy})$	324 nm	285 nm (4.2)	$d\pi(\text{Ru}) \rightarrow \pi^*(\text{bpy})$ $d\pi(\text{Ru}) \rightarrow \pi^*(\text{N-N})$
475 nm	501 nm (0.63)	$d\pi(\text{Ru}) \rightarrow \pi^*(\text{N-N})$	428 nm	425 nm (0.66)	$\pi(\text{N-N}) \rightarrow \pi^*(\text{N-N})$
			758 nm	564 nm (0.75)	$d\pi(\text{Ru}) + \pi(\text{N-N}) \rightarrow \pi^*(\text{bpy})$

Figure 2.6 shows calculated and experimental spectra for **6** in CH₃CN with the calculated transition energies shown as vertical bars with their heights reflecting relative oscillator strengths. To help in visualization, the calculated transitions are red-shifted by 15 nm. Both the observed and calculated spectra illustrate the ~ 80 nm split in absorption maxima between the MLCT transitions to $\pi^*(\text{bpy})$ and $\pi^*(\text{N-N})$ shown in Equation 2.3 and Equation 2.4.

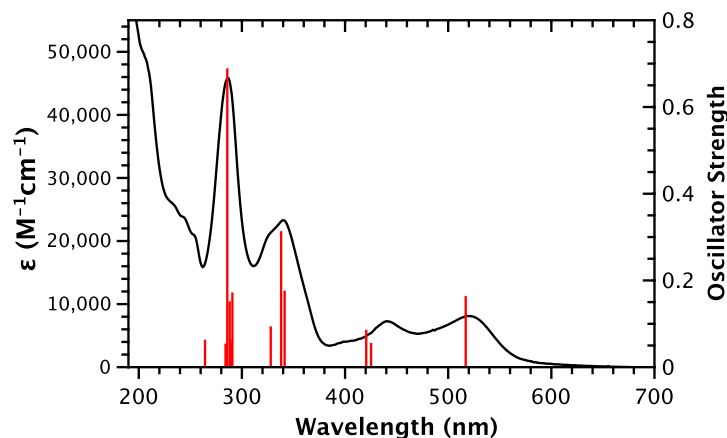


Figure 2.6. UV-Visible spectrum of complex **6** at room temperature in CH₃CN (black line) and calculated TD-DFT transitions (vertical red bars with heights illustrating oscillator strengths). The calculated transition energies are red-shifted 15 nm for visualization purposes.

Emission Spectra

Complexes **1** – **9** exhibit broad emission spectra at room temperature in CH₃CN with emission energies decreasing from **1** ($\lambda_{\text{max}} = 650 \text{ nm}$, $1.54 \times 10^4 \text{ cm}^{-1}$) to **9** ($\lambda_{\text{max}} = 885 \text{ nm}$, $1.12 \times 10^4 \text{ cm}^{-1}$) relative to emission from Ru(bpy)₃²⁺* at $\lambda_{\text{max}} = 620 \text{ nm}$ ($1.61 \times 10^4 \text{ cm}^{-1}$). Emission spectra are compared to Ru(bpy)₃²⁺* in Figure 2.7 with emission energies listed in Table 2.1.

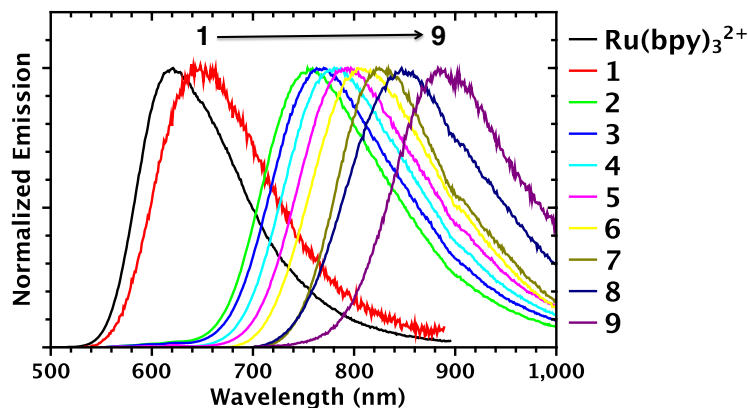


Figure 2.7. Normalized emission spectra for Ru(bpy)₃²⁺ and **1** - **9** in argon deaerated CH₃CN at room temperature.

Trends in emission energies follow those for the lowest energy MLCT absorptions with the highest energy absorption and emission from **1** at $\lambda_{\text{max,abs}} = 443 \text{ nm}$ ($2.26 \times 10^4 \text{ cm}^{-1}$) and

$\lambda_{\text{max,em}} = 650 \text{ nm}$ ($1.54 \times 10^4 \text{ cm}^{-1}$). Variations in acceptor ligand cause red shifts in the lowest MLCT absorption of $> 100 \text{ nm}$ ($4.8 \times 10^3 \text{ cm}^{-1}$) for **9** compared to **1** and of $> 200 \text{ nm}$ ($4.2 \times 10^3 \text{ cm}^{-1}$) for emission from **9** compared to **1**.

Time-resolved emission decay measurements were conducted by time-correlated single photon counting (TCSPC) following 444 nm excitation. Lifetimes (τ , Table 2.1) for this class of chromophores are largely dictated by nonradiative decay with $\eta_{\text{em}} = 6.2\%$ and $k_{\text{nr}} = 4.8 \times 10^5 \text{ s}^{-1}$ for $\text{Ru}(\text{bpy})_3^{2+*}$ under these conditions, with $\tau^{-1} \sim k_{\text{nr}}$.²¹⁸ In addition to MLCT vibrational decay, k_{nr} also includes contributions from thermal population and subsequent rapid deactivation through a low-lying dd excited state pathway.^{183,219-222}

As shown by the energy gap law plot of $\ln \tau^{-1}$ vs. emission energy in Figure 2.8, the decrease in lifetime with changes in acceptor ligand is qualitatively consistent with energy gap law behavior.¹⁸⁸ The existence of the linear correlation in Figure 2.8 suggests that contributions from nonradiative decay from the lowest, emitting MLCT state dominate with dd state participation relatively unimportant. This is expected given the relatively low energies of the diazine-based (N-N) MLCT excited states.^{188,223-225} Complex **1** is the outlier in the correlation, perhaps due to steric crowding. Distortions in the metal-ligand framework induce $d\sigma^*-d\pi$ orbital mixing, decreasing the energy of low-lying dd states and introducing an additional nonradiative decay pathway.^{219,226-228}

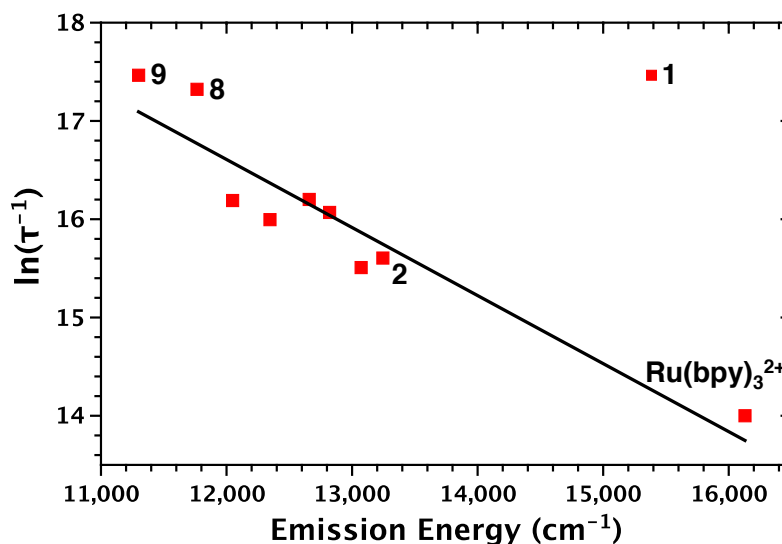


Figure 2.8. Plot of emission energy vs $\ln \tau^{-1}$ for complexes **1 - 9** and $\text{Ru}(\text{bpy})_3^{2+}$ in CH_3CN at 25°C .

Previous studies on related Os^{II} and Ru^{II} diimine complexes of the type $\text{M}^{\text{II}}(\text{bpy})_2\text{L}_2^{2+}$ and $\text{M}^{\text{II}}(\text{bpy})_2(\text{L-L})^{2+}$ ($\text{M} = \text{Os}$ or Ru) have shown that absorption and emission energies increase linearly with the electrochemical gap $\Delta E_{1/2}$, with $\Delta E_{1/2}$ the difference between the ground state $\text{Ru}^{3+/2+}$ potential ($E_{1/2}(\text{Ru}^{3+/2+})$) and the potential for the first ligand-based reduction ($E_{1/2}(\text{Ru}^{2+/+})$).^{185,188,229,230} Figure 2.9 illustrates how the lowest energy absorption ($\bar{\nu}_{abs}$) and emission ($\bar{\nu}_{em}$) maxima vary with $\Delta E_{1/2}$ at room temperature. The linear relationship and slopes of 0.84 for absorption and 0.73 for emission are expected for transitions to and emission from MLCT excited states.^{188,229,231}

Emission energies for complexes **1 - 9** also decrease linearly with $E_{1/2}(\text{Ru}^{2+/+})$, Figure 2.9, showing that variations in excited state energies are mainly a consequence of variations in the energy of the acceptor ligand π^* levels. There is no correlation between emission energy and the ground state metal centered $\text{Ru}^{3+/2+}$ potential ($E_{1/2}(\text{Ru}^{3+/2+})$), Figure A.16.²³¹

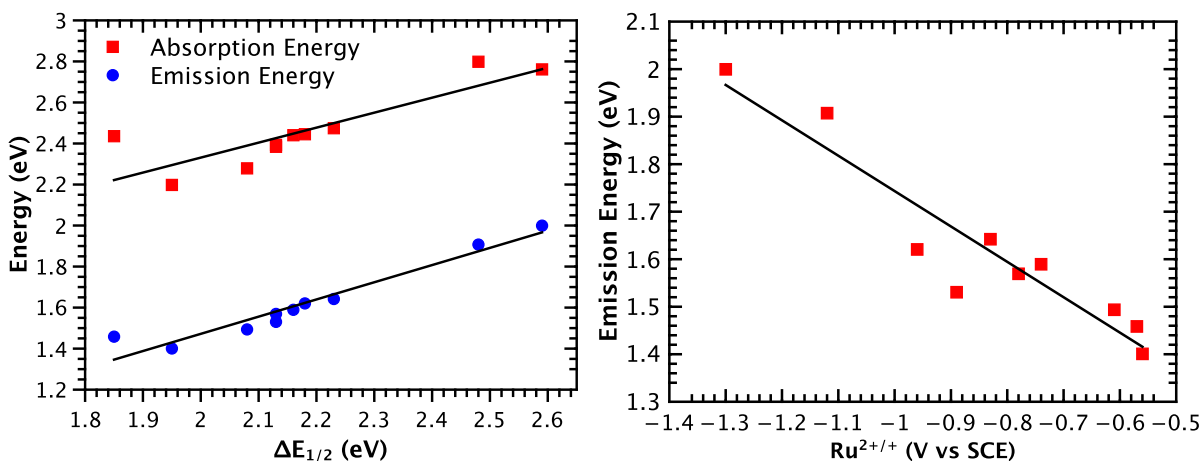


Figure 2.9. (Left) Variation of absorption, $\bar{\nu}_{abs}$, red squares, and emission, $\bar{\nu}_{em}$, blue circles, energies on the electrochemical gap ($\Delta E_{1/2} = E_{1/2}(Ru^{3+/2+}) - E_{1/2}(Ru^{2+/+})$) for $Ru(bpy)_3^{2+}$ and 1 – 9. (Right) Variation of $\bar{\nu}_{em}$ with $E_{1/2}(Ru^{2+/+})$ in dry CH_3CN at 25°C.

Emission Spectral Fitting. Correlation of Excited State Properties

Emission spectra for all 9 complexes were analyzed by use of a one-mode Franck-Condon analysis of room-temperature emission spectra (see Appendix A).^{144,218,232-236} In this analysis contributions from medium frequency $\nu(bpy)$ modes are treated as a single averaged mode with low frequency modes and the solvent being included in the band widths. Spectra were fit to a series of vibronic lines centered on the 0-0 component at energy E_0 and separated by a vibrational quantum spacing of $\hbar\omega_M$. Only transitions from the $\nu' = 0$ level in the excited state to level ν in the ground state are included in the summation. Comparisons between experimental and calculated emission spectra for each complex and for $Ru(bpy)_3^{2+*}$ are shown in Figure A.1.

In the spectral fits, relative intensities of the vibronic lines are determined by the electron-vibrational coupling constant, S_M , which is related to the equilibrium displacement change, ΔQ_{eq} , by $\frac{1}{2}\Delta Q_{eq}^2$. As noted above, additional vibrational contributions from low frequency modes and the solvent are treated classically and included in the bandwidth at half height, $\Delta\bar{\nu}_{1/2}$, with $\Delta\bar{\nu}_{1/2}$ defined in Equation 2.5. In Equation 2.5, $\lambda_{0,L}$ is the sum of the

solvent reorganization energy, λ_0 , and reorganization energy from low frequency modes, λ_L . E_0 in Equation 2.5 is the 0-0 energy gap, the energy of the excited state above the ground state with both states in their $v = 0$ vibrational levels.

Results of the spectral fitting analysis are summarized in Table 2.3. The free energy content of the excited state above the ground state, ΔG_{ES} , was calculated by using Equation 2.5. In Equation 2.5, k_B is the Boltzmann constant and T is the temperature (298 K). As shown by the data in Table 2.1, variations in ΔG_{ES} mirror those in emission energy through the series with ΔG_{ES} decreasing from 2.18 eV for **1** to 1.57 eV for **9**.

Equation 2.5

$$\Delta G_{ES} = E_0 + \lambda_{0,L} = E_0 + \frac{(\Delta \bar{\nu}_{1/2})^2}{16k_B T \ln 2}$$

Table 2.3 Emission spectral fitting parameters for MLCT emission from Ru(bpy)₃^{2+*} and 1-9 in CH₃CN at 25°C

Complex	E_0 (cm ⁻¹)	$\Delta \bar{\nu}_{1/2}$ (cm ⁻¹)	$\hbar\omega_M$ (cm ⁻¹)	S_M	ΔG_{ES} (cm ⁻¹)
Ru(bpy) ₃ ²⁺	16300	1800	1400	1.11	17700
1	15800	1950	1300	1.23	17500
2	13300	1750	1300	0.91	14600
3	13100	1790	1350	0.89	14500
4	12900	1700	1250	0.93	14200
5	12600	1750	1400	0.80	13900
6	12400	1700	1200	0.80	13600
7	12100	1450	1250	0.71	13000
8	11900	1581	1150	0.96	13000
9	11100	1583	1512	0.76	12200

Discerning systematic trends in the data in Table 2.3 is complicated by the fact that excited state properties are dictated largely by the acceptor ligand which varies, bpy vs N-N,

through the series. This can be seen in the relatively large range of $\hbar\omega_M$ values derived from the spectral fits. Nonetheless, one notable trend is the general decrease in electron-vibrational coupling constant (Huang-Rhys factor, S_M) as the energy gap decreases. This is consistent with a decrease in the extent of charge transfer as the energy gap decreases.²³⁷⁻²³⁹ As expected, both the 0-0 energy gap (E_0) and the free energy content of the excited state above the ground state (ΔG_{ES}) decrease with the energy of the π^* acceptor level as measured by $E_{1/2}(\text{Ru}^{2+/+})$, Table 2.1.

Excited State Redox Potentials

Redox potentials for the MLCT excited states were calculated from ΔG_{ES} and the electrochemically measured ground state potentials by Equation 2.6 and Equation 2.7.^{135,183,231} Results for the series from **1** – **9** are summarized in Table 2.1.

Equation 2.6

$$E_{1/2}(\text{Ru}^{2+*/+}) = E_{1/2}(\text{Ru}^{2+/+}) + \Delta G_{ES}$$

Equation 2.7

$$E_{1/2}(\text{Ru}^{3+/2+*}) = E_{1/2}(\text{Ru}^{3+/2+}) - \Delta G_{ES}$$

A plot of ΔG_{ES} vs. $E_{1/2}(\text{Ru}^{3+/2+*})$ is shown in Figure 2.10. Variations in the acceptor ligand decrease the reducing ability of the $[\text{Ru}^{\text{III}}(\text{bpy})_2(\text{N-N}^{\bullet-})]^{2+*}$ excited state from -0.81 V to -0.13 V (vs SCE) across the series from **1** to **9**.²³¹ As shown in Figure 2.11, ground state $\text{Ru}^{2+/+}$ ($d\pi^6/d\pi^6\pi^{*1}$) and excited state $\text{Ru}^{3+/2+*}$ ($d\pi^5/d\pi^5\pi^{*1}$) redox potentials, both ligand based, increase linearly with increasing emission energy. By contrast, ground state $\text{Ru}^{3+/2+}$ ($d\pi^5/d\pi^6$) and excited state $\text{Ru}^{2+*/+}$ ($d\pi^5\pi^{*1}/d\pi^6\pi^{*1}$) redox potentials, with the redox levels localized largely on the metal, remain relatively unchanged as the emission energy increases.

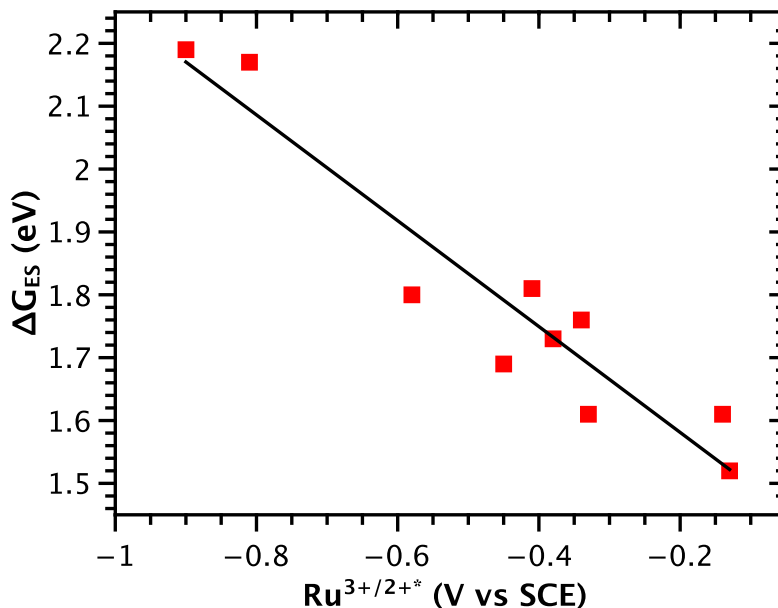


Figure 2.10. Dependence of the free energy content of the excited state (ΔG_{ES}) on $E_{1/2}(\text{Ru}^{3+/2+*})$.

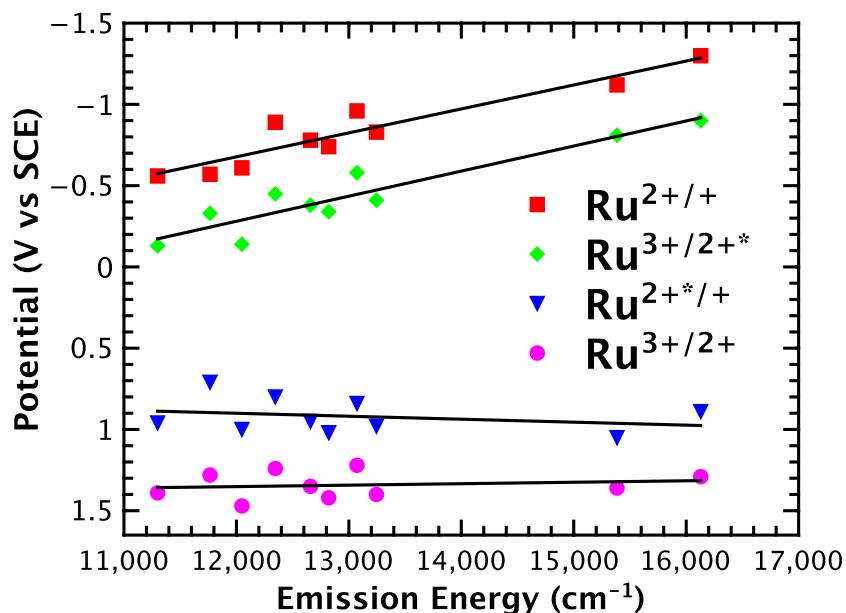
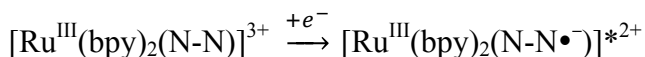


Figure 2.11. Variation of ground and excited state redox potentials with emission energy in CH_3CN (0.1 M TBAPF_6 for electrochemical measurements) at 25°C .

The relationship between the ligand-based $\text{Ru}^{2+/+}$ and $\text{Ru}^{3+/2+*}$ redox couples to the emission energy is an expected result given the ligand-based nature of the redox processes in Equation 2.2 and Equation 2.8. This is in contrast to previously reported correlations based on complexes of the type $[\text{M}(\text{bpy})_2(\text{L})_2]^{2+}$ ($\text{M} = \text{Os}^{\text{II}}, \text{Ru}^{\text{II}}$) where the lowest π^* levels are

based on bpy or phen (1,10-phenanthroline). In these series, the role of variations in L_2 is largely through the $d\pi(M^{II})$ donor levels with $Ru^{3+/2+}$ and $Ru^{2+*/+}$ potentials increasing linearly with emission energy.^{229,231,240-242} In the current series, with the lowest-lying acceptor levels on the N-N ligand, ground state $Ru^{3+/2+}$ and excited state $Ru^{2+*/+}$ potentials are relatively unchanged as the MLCT energy gap varies as shown in Figure 2.11.

Equation 2.8



Controlling Excited State Properties

The motivation for preparing and characterizing the series of complexes $[Ru^{II}(bpy)_2(N-N)]^{2+}$ was to explore the role of the acceptor ligand in modulating key properties for possible DSPEC applications. For photoanode applications the key properties are: 1) broad light absorption in the visible, 2) injection into conduction band states of TiO_2 or other oxides with appropriate acceptor potentials, and 3) sufficient potential as Ru^{3+} to drive water oxidation catalysis. Figure 2.12 addresses these issues by displaying how $E_{1/2}(Ru^{3+/2+*})$ and $E_{1/2}(Ru^{3+/2+})$ vary with the energy of the lowest energy MLCT absorption.

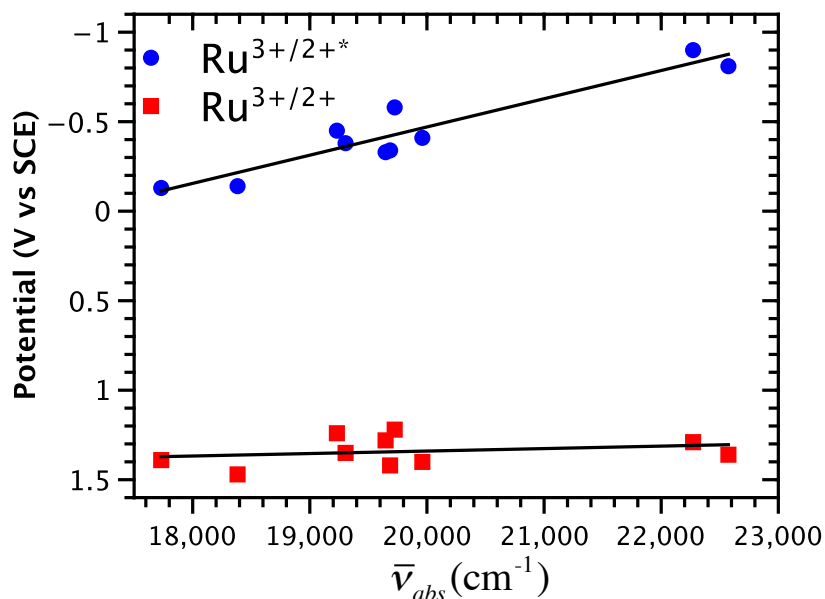


Figure 2.12. Variations in $E_{1/2}(\text{Ru}^{3+/2+})$, red squares) and $E_{1/2}(\text{Ru}^{3+/2+*})$, blue circles) with $\bar{\nu}_{abs}$ for the lowest energy MLCT λ_{max} in CH_3CN at 25°C .

These results point to the interplay between these properties that is caused by variations in the lowest acceptor ligand. In the series $[\text{Ru}^{\text{II}}(\text{bpy})_2(\text{N-N})]^{2+}$, **1** – **9**, replacing bpy by N-N results in only slight increases in $E_{1/2}(\text{Ru}^{3+/2+})$ but with a shift of 121 nm ($4.8 \times 10^3 \text{ cm}^{-1}$) to lower energy for the lowest energy MLCT absorption (Table 2.1). This is a desirable property with ligand variations shifting the low energy absorption edge to the red by lowering the π^* acceptor levels through increased conjugation or incorporation of heteroatoms in the N-N ligand.

Figure 2.12 shows how the two key redox potentials for photoanode applications, $E_{1/2}(\text{Ru}^{3+/2+})$ and $E_{1/2}(\text{Ru}^{3+/2+*})$, vary with $\bar{\nu}_{abs}$. Although the red shifted absorption spectrum has a small effect on $E_{1/2}(\text{Ru}^{3+/2+})$ and water oxidation ability, it comes with a more positive $\text{Ru}^{3+/2+*}$ redox potential, limiting the ability of the excited state to act as a reducing agent. As an example, complex **9** is only slightly more oxidizing than $\text{Ru}(\text{bpy})_3^{3+}$, 1.39 V compared to 1.29 V (vs SCE), and has a considerably red-shifted low energy MLCT absorption, 564 nm ($22,200 \text{ cm}^{-1}$) compared to 449 nm ($17,700 \text{ cm}^{-1}$) for $\text{Ru}(\text{bpy})_3^{2+}$. However, this exchange of

L9 for bpy as the acceptor ligand increases $E_{1/2}(\text{Ru}^{3+/2+*})$ from -0.90 V to -0.13 V vs. SCE, past the potential threshold for injection into TiO_2 with $E_{\text{CB}} \sim -0.34$ V (vs SCE) at pH 0 in water making it unable to undergo electron injection into TiO_2 following photoexcitation.^{92,125,162}

2.4 Conclusions

We have described here the synthesis and characterization of polypyridyl complexes $[\text{Ru}(\text{bpy})_2(\text{N-N})]^{2+}$ (**1** – **9**) with N-N a bidentate polypyridyl ligand with a low-lying π^* acceptor levels. Compared to $\text{Ru}(\text{bpy})_3^{2+}$ as a reference, variations in N-N have a systematic effect on ground state and excited state redox potentials, absorption spectra, emission energies, and excited state lifetimes. The variations originate from the influence of increased delocalization or addition of heteroatoms on the π^* acceptor level(s) of N-N.

From the results of electrochemical measurements, variations in $E_{1/2}(\text{Ru}^{3+/2+})$ with N-N are relatively small and due to stabilization of Ru(II) by $d\pi-\pi^*$ backbonding. By contrast, there are significant variations in $E_{1/2}(\text{Ru}^{2+/+})$ with reduction occurring at the N-N ligand. Through the series, the lowest energy MLCT absorption is red shifted relative to $\text{Ru}(\text{bpy})_3^{2+}$ ($\lambda_{\text{max}} = 449$ nm) reaching $\lambda_{\text{max}} = 564$ nm for complex **9** with the band assignments in agreement with the results of TD-DFT calculations. Emission energies decrease from complex **1** ($\lambda_{\text{max}} = 650$ nm) to complex **9** ($\lambda_{\text{max}} = 885$ nm), relative to $\text{Ru}(\text{bpy})_3^{2+*}$ ($\lambda_{\text{max}} = 620$ nm), with excited state lifetimes varying with emission energy in qualitative agreement with the energy gap law.

The results of Franck-Condon analyses of emission spectral profiles were used to calculate ΔG_{ES} , the free energy of the excited state above the ground state, and from ΔG_{ES} , redox potentials for the excited state couples $\text{Ru}^{3+/2+*}$ and $\text{Ru}^{2+*/+}$ were also calculated. ΔG_{ES}

decreases through the series from **1** to **9** as a result of the decreasing energy of the π^* acceptor level(s) in N-N from **1** to **9**. $E_{1/2}(\text{Ru}^{2+*/+})$ for the metal-centered couple, $[\text{Ru}^{\text{III}}(\text{bpy})_2(\text{N-N}\bullet^-)]^{2+*}/[\text{Ru}^{\text{II}}(\text{bpy})_2(\text{N-N}\bullet^-)]^+$, is relatively unaffected by variations in N-N while $E_{1/2}(\text{Ru}^{3+/2+*})$ for the ligand-centered couple $[\text{Ru}^{\text{III}}(\text{bpy})_2(\text{N-N})]^{3+}/[\text{Ru}^{\text{III}}(\text{bpy})_2(\text{N-N}\bullet^-)]^{2+*}$ varies with $E_{1/2}(\text{Ru}^{2+/*})$. Comparisons in the series show that with variations in the acceptor ligand, red-shifts in light absorption leave the oxidizing strength of Ru(III) relatively unaffected but increase $E_{1/2}(\text{Ru}^{3+/2+*})$ potentials past the threshold for injection into TiO_2 .

2.5 Acknowledgements

This work was primarily supported by the UNC Energy Frontier Research Center “Center for Solar Fuels”, an Energy Frontier Research Center funded by the U.S. Department of Energy, Office of Science, Office of Basic Energy Sciences (DOE BES) under award DE-SC0001011, supporting M.R.N., J.J.C., S.K., and M.K.B. We acknowledge support for D.L.A. from a fellowship from the Department of Energy Office of Science Graduate Fellowship Program (DOE SCGF), made possible by the American Recovery and Reinvestment Act of 2009, administered by ORISE-ORAU under contract number DE-AC05-06OR23100. C.R.G. acknowledges support from the UVA EFRC “Center for Catalytic Hydrocarbon Functionalization”, an EFRC funded by DOE BES under award DE-SC0001298. We also acknowledge Ken Hanson for the photophysical measurements of the compounds.

2.6 Associated Content

Appendix A: Table of emission spectral fitting parameters, UV/visible spectra, crystallographic data, calculation results, and experimental details.

Chapter 3: VARYING THE ELECTRON STRUCTURE OF SURFACE BOUND RUTHENIUM(II) POLYPYRIDYL COMPLEXES

3.1 Introduction

Light absorption throughout the visible and near-IR is required for efficient dye-sensitized solar cells (DSSCs) and dye-sensitized photoelectrosynthesis cells (DSPECs).^{24,42,165,169} In particular, to drive photoelectrochemical water oxidation for use in DSPEC photoanodes, the light-absorbing chromophore requires four distinctive properties; 1) surface binding groups (typically carboxylates or phosphonates), 2) high molar absorptivity throughout the visible and near-IR, 3) sufficient excited state redox potentials to undergo rapid and efficient electron injection into the conduction band of a metal oxide semiconductor (typically anatase TiO₂), and 4) the resulting oxidized chromophore must have the thermodynamic potential sufficient to drive water oxidation at an appropriately arrayed water oxidation catalyst by electron transfer.^{29,124,173,176}

Ruthenium polypyridyl complexes have been extensively studied for use as chromophores in DSSCs and DSPECs.^{122,124,190,243,244} In general, these complexes absorb light in the visible region, have sufficient excited state potentials to inject electrons into the conduction band of TiO₂, and the resulting oxidant can have the thermodynamic potential to drive the water oxidation half-reaction ($2 \text{H}_2\text{O} \rightarrow \text{O}_2 + 4 \text{H}^+ + 4 \text{e}^-$; $E^0 = 1.23 \text{ V}$).

Previously, we have demonstrated that, in aqueous solutions, phosphonate derivatives of Ru(bpy)₃²⁺ form more stable chemical links to metal oxide surfaces compared to carboxylates.^{141,144,189} Despite the advantage of increased stability, relatively few

phosphonated chromophores have been reported, largely because of synthetic difficulties. The dearth of complexes has delayed experiments exploring the role redox potentials play in electron injection and electron transfer in water immobilized on metal oxide surfaces.^{92,135,165,173,245,246} Herein we report a systematic synthetic route to phosphonate-derivatized Ru(bpy)₃²⁺ chromophores having the general structure [Ru(4,4'-R₂-bpy)₂(4,4'-(PO₃H₂)₂-bpy)]²⁺ (4,4'-(PO₃H₂)₂-bpy = [2,2'-bipyridine]-4,4'-diylbis(phosphonic acid); 4,4'-R₂-bpy = 4,4'-R₂-2,2'-bipyridine where R = OCH₃, CH₃, H or Br), Figure 3.1. We also describe their electrochemical, spectroscopic, and excited state properties.

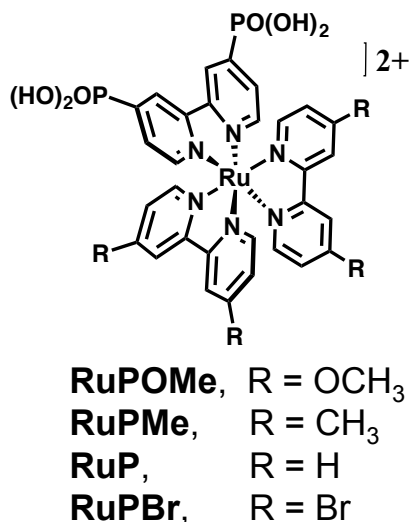


Figure 3.1. Structures of **RuPOMe**, **RuPMe**, **RuP**, and **RuPBr**.

3.2 Experimental

Materials. Tetraethyl-[2,2'-bipyridine]-4,4'-diylbis(phosphonate),¹⁹² *poly*-Ru(1,4-cyclooctadiene)Cl₂,²⁴⁷ **RuP**,¹⁹² were synthesized as previously reported. Distilled water was further purified using a Milli-Q Ultrapure water purification system. All other reagents were ACS grade and used without further purification. Fluoride-doped tin oxide (FTO)-coated glass (Hartford Glass; sheet resistance 15 Ω cm⁻¹) was cut into 10 mm × 40 mm strips and

used as the substrate for ZrO₂ and TiO₂ nanoparticle films. Microwave reactions were carried out using a CEM MARS microwave reactor. A CEM HP-500 Plus Teflon-coated microwave vessel (100 mL) was used at a power setting of 400 W. The vessel was rotated and stirred throughout the microwave procedure. The pressure of the reaction vessel was monitored throughout the reaction, and never exceeded 300 PSI.

Metal oxide films. Nano-TiO₂²⁴⁸ and nano-ZrO₂¹³⁴ films, typically 7 μm thick, with a coating area of roughly 10 mm × 15 mm, were synthesized according to literature procedures. Dye absorption isotherms on TiO₂ (Figure B.2) were obtained by soaking the films in methanol solutions of **RuPOMe**, **RuPMe**, and **RuPBr** at concentrations of 10, 20, 50, 100, 150, and 200 μM. The slides were then removed, rinsed with methanol, and dried over a stream of nitrogen.

Absorption spectra were obtained by placing the dry derivatized films perpendicular to the detection beam path of the spectrophotometer. The expression, $\Gamma = A(\lambda)/\varepsilon(\lambda)/1000$, was used to calculate surface coverage (Γ) on metal oxide electrodes where A is absorption and $\varepsilon(\lambda)$ is the molar absorptivity at wavelength λ .²⁴⁹ Maximum surface coverage (Γ_{\max}) and surface binding constants (K_{ad}) on TiO₂ for **RuPOMe**, **RuPMe**, and **RuPBr** were obtained by use of the Langmuir isotherm (Equation 3.1) with [X] the concentration of the complex in the loading solutions (Figure B.2).²⁵⁰ All subsequent measurements were carried out on films loaded from methanol solution of 100 μM ruthenium complex, which yielded surface coverages $\sim 8 \times 10^{-8}$ mol cm⁻².

Equation 3.1

$$\Gamma = \frac{\Gamma_{\max}K_{\text{ad}}[X]}{1+K_{\text{ad}}[X]}$$

Steady-State and Time-Resolved Emission measurements were carried out by inserting derivatized thin films of ZrO_2 at a 45° angle into a standard 1 mm path length square cuvette containing 0.1 M HClO_4 aqueous solution. Emission spectra were collected at room temperature using an Edinburgh FLS920 spectrometer with luminescence first passing through a 495 nm long-pass color filter, then a single grating (1800 L/mm, 500 nm blaze) Czerny-Turner monochromator (5 nm bandwidth), and finally detected by a peltier-cooled Hamamatsu R2658P photomultiplier tube. For steady-state experiments, samples were excited using light output from a housed 450 W Xe lamp/single grating (1800 l/mm, 250 nm blaze) Czerny-Turner monochromator combination with 5 nm bandwidth. The dynamics of emission decay were monitored using the FLS920s time-correlated single-photon counting capability (1024 channels; 1 ns per channel) with each data set collecting >5000 counts in the maximum channel. Excitation was provided by an Edinburgh EPL-445 ps pulsed diode laser (444.2 nm, 80 ps fwhm) operated at 200 kHz. Kinetics were evaluated using either Edinburgh or Origin software.

Electrochemical measurements were carried out with a CH Instruments 660D potentiostat with a Pt-wire counter electrode, and a Ag/AgNO_3 (0.01 M AgNO_3 /0.1 M tetra-n-butylammonium hexafluorophosphate (TBAPF_6) CH_3CN ; -0.09 V vs $\text{Fc}^{0/+}$) or Ag/AgCl (3 M NaCl ; 0.198 V vs NHE) reference electrode. $E_{1/2}$ values were obtained from the peak currents in square wave voltammograms. Reductive electrochemistry was conducted in 80:20 $\text{CH}_3\text{CN}:\text{H}_2\text{O}$ deaerated with argon for 5 minutes with a glassy carbon working electrode, Pt-wire counter, and a Ag/AgNO_3 reference. Surface electrochemical was completed in 0.1 M HClO_4 with a derivatized TiO_2 film as the working electrode.^{144,192}

Computational Methods. All molecular geometries were calculated by density functional theory (DFT) with the B3LYP^{197,198} functional and the LanL2DZ^{199,200} basis set. Solvent environment effects were described by using the polarizable continuum model (PCM) with the integral equation formalism variant for water. Tighter convergence criteria and a more accurate numerical integration grid were specified, to ensure finding the exact geometrical minima. Frequencies were calculated and checked to make sure that all frequencies were positive. Electronic spectra were calculated using TD-DFT, based on the procedure previously outlined by Jacquemin et al.^{201,202} The geometry-optimized structures were used in the TD-DFT calculations, with the PBE0^{203,204} functional and the same basis-set and solvent effects as in the geometry optimization. The adiabatic approximation of time dependent DFT was used to solve for 100 singlet excited states.²⁰⁵ To prevent spurious effects due to charge localization, the total charge on the molecule was zero by removing two protons from the structure, one from each -PO₃H₂ group. All calculations were conducted in Gaussian 09, Revision C.01.²⁰⁶

Synthesis of Ligands and Complexes

4,4'-dibromo-2,2'-bipyridine

4,4'-dimethoxy-2,2'-bipyridine (2.7 g, 12.5 mmol) was dissolved in PBr₃ (20 mL, 212 mmol) under an atmosphere of argon. The reaction mixture was heated to 180°C with vigorous stirring. The reaction, followed by TLC, was completed in 3 hours. After cooling to room temperature, crushed ice was carefully added to the reaction, followed by the addition of concentrated aqueous ammonia alternating with ice. *Caution:* Addition of ice and ammonia causes the mixture to heat quickly, take great care when adding the two to the PBr₃ solution. Enough ammonia was added to reach pH ~ 10, at which point a significant amount of

precipitate forms. The solution was then transferred to a separatory funnel and extracted with ether (4×70 mL). The organic layers were combined, dried over MgSO_4 , filtered, and the solvent was removed by rotary evaporation. A white solid (1.81 g, 47%) was isolated. The solid appears clean by ^1H NMR but contains a small phosphorus impurity. The impurity can be removed by running the sample through a plug of silica with dichloromethane as the eluent. The characterization matches that of previously reported.²⁵¹ ^1H NMR (400 MHz, CDCl_3): δ (ppm) 8.59 (d, $J=1.6$ Hz, 2H), 8.465 (d, $J=4$ Hz, 2H), 7.49 (dd, $J=5.2$, 2 Hz, 2H).

[2,2'-bipyridine]-4,4'-diylidiphosphonic acid

Tetraethyl [2,2'-bipyridine]-4,4'-diylbis(phosphonate) (1.0 g, 2.33 mmol) was dissolved in anhydrous CH_2Cl_2 (~ 50 mL) under an atmosphere of argon. To the solution was added bromotrimethylsilane (2.15 mL, 12.1 mmol) and the reaction was stirred at room temperature under an atmosphere of argon for 3 days. The solvent was removed under vacuum, and anhydrous methanol (~ 30 mL) was added. The solution was stirred for 30 min at room temperature, the methanol was removed under vacuum, and ether (~ 60 mL) was added to the white solid. The suspension was stirred for 2 hrs and the white solid was collected by suction filtration. This compound was used without further purification (0.74 g, 87%). ^1H NMR (400 MHz, D_6 -DMSO): δ (ppm) 8.85 (t, 2 H), 8.66 (d, 2 H), 7.75 (dd, 2H).

General Procedure for $\text{Ru}(4,4'\text{-R}_2\text{-bpy})_2\text{Cl}_2$

In a typical procedure, *poly*- $\text{Ru}(1,4\text{-cyclooctadiene})_2\text{Cl}_2$ (0.30 g, 0.97 mmol) and 4,4'- R_2 -bipyridine (where $\text{R} = \text{OCH}_3$, CH_3 , or Br) (0.97 mmol) were dissolved in 1,2-dichlorobenzene (~ 35 mL). The solution was thoroughly degassed with argon, and the mixture was heated to 180°C under an atmosphere of argon for 2 hours. The solution was cooled and ether (~ 100 mL) was added and the precipitate was isolated by suction filtration

and collected. These complexes were used without further purification. Yields range from 87%-92%.

General Procedure for [Ru(4,4'-R₂-bpy)₂((PO₃H₂-bpy)](Cl)₂

In a typical procedure, Ru(4,4'-R₂-bpy)₂Cl₂ (0.12 mmol) and [2,2'-bipyridine]-4,4'-diyldiphosphonic acid (0.04 g, 0.12 mmol) were dissolved in 1:1 EtOH:H₂O (~ 35 mL). The solution was then heated to 160°C for 20 minutes in a microwave oven. The solution was cooled, filtered, and taken to dryness by a rotary evaporator. The crude product was purified by size exclusion chromatography (Sephadex LH-20) with 1:1 H₂O:MeOH as the eluent. Similar fractions (based on UV-Vis absorption spectra) were combined and the solvent removed by rotary evaporation. The dark-red solids were triturated with ether and collected.

[Ru(4,4'-dimethoxy-2,2'-bipyridine)₂([2,2'-bipyridine]-4,4'-diyldiphosphonic acid)]Cl₂

(RuPOMe)

Isolated as a red powder (0.104 g, 90%). ¹H NMR (600 MHz, D₂O) δ (ppm) 8.67 (d, 2H), 8.11 (dd, 4H), 7.73 (m, 2H), 7.52 (m, 2H), 7.47 (d, 2H), 7.37 (d, 2H), 6.94 (dd, 2H), 6.89 (dd, 2H), 3.90 (s, 6H), 3.87 (s, 6H). HR-ESI-MS (MeOH; 20% H₂O with 1% HCOOH): *m/z* = 425.0457²⁺ = 850.09, [M - 2Cl]²⁺ = 850.09, *m/z* = 849.0903²⁺ = 1698.1806, [M - 2Cl - H⁺]²⁺ = 1698.16. Anal. Found (Calc.) for C₃₅H₄₀Cl₂N₆O₁₂P₂Ru: C 43.53 (43.31); H 4.31 (4.15); N 8.84 (8.66).

[Ru(4,4'-dimethyl-2,2'-bipyridine)₂([2,2'-bipyridine]-4,4'-diyldiphosphonic acid)]Cl₂

(RuPMe)

Isolated as a red powder (0.099 g, 92%). ¹H NMR (600 MHz, D₂O) δ (ppm) 8.69 (d, 2H), 8.33 (d, 4H), 7.72 (m, 2H), 7.50 (m, 2H), 7.46 (m, 4H), 7.17 (m, 4H), 2.44 (s, 6H), 2.43 (s, 6H). HR-ESI-MS (80:20 NCMe:H₂O, 1% HCOOH): *m/z* = 384.0499²⁺ = 768.0996, [M -

$2\text{Cl}^-]^{2+} = 786.1059$, $m/z = 785.1042^{2+} = 1570.2084$, $[\text{M} - 2\text{Cl}^- - \text{H}^+]_2^{2+} = 1570.196$. Anal.

Found (Calc.) for $\text{C}_{35}\text{H}_{38}\text{Cl}_2\text{N}_6\text{O}_7\text{P}_2\text{Ru}$: C 47.49 (47.31); H 4.50 (4.31); N 9.58 (9.46).

$[\text{Ru}(2,2'\text{-bipyridine})_2([\text{2,2'\text{-bipyridine]-4,4'\text{-diylidiphosphonic acid}})]\text{Cl}_2$ (**RuP**)

Isolated as a red powder (0.086 g, 90%). Characterization matches that of previously reported.¹⁹²

$[\text{Ru}(4,4'\text{-dibromo-2,2'\text{-bipyridine}})_2([\text{2,2'\text{-bipyridine]-4,4'\text{-diylidiphosphonic acid}})]\text{Cl}_2$

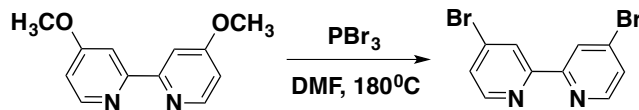
(**RuPBr**)

Isolated as a red powder (0.120 g, 87%). ^1H NMR (600 MHz, D_2O) δ (ppm) 8.94 (d, 4H), 8.73 (d, 2H), 7.71 (m, 2H), 7.62 (m, 8H), 7.52 (d, 2H). HR-ESI-MS (MeOH; 20% H_2O with 1% HCOOH): $m/z = 522.8398^{2+} = 1045.6796$, $[\text{M} - 2\text{Cl}^-]^{2+} = 1045.68$. Anal. Found (Calc.) for $\text{C}_{30}\text{H}_{28}\text{Br}_4\text{Cl}_2\text{N}_6\text{O}_9\text{P}_2\text{Ru}$: C 30.91 (30.79); H 2.52 (2.41); N 7.08 (7.18).

3.3 Results and Discussion

Synthesis. 4,4'-dibromo-bipyridine was synthesized by a modified reported procedure starting from commercially available 4,4'-dimethoxy-bipyridine.²⁵² In previous examples, dimethylformamide (DMF) was used as solvent for the reaction between PBr_3 and 4,4'-dimethoxy-bipyridine. Here 4,4'-dimethoxy-bipyridine was dissolved directly in PBr_3 , heated to 180°C , and the reaction was completed after three hours (as followed by TLC, Scheme 3.1). Following neutralization and extraction, purification is completed by a silica plug, giving a 47% yield (see experimental). The 4,4'-(PO_3H_2)₂-bpy ligand was synthesized by a simple bromotrimethylsilane hydrolysis of the esterified ligand (4,4'-(PO_3Et_2)₂-bpy) which has been previously reported.^{192,253}

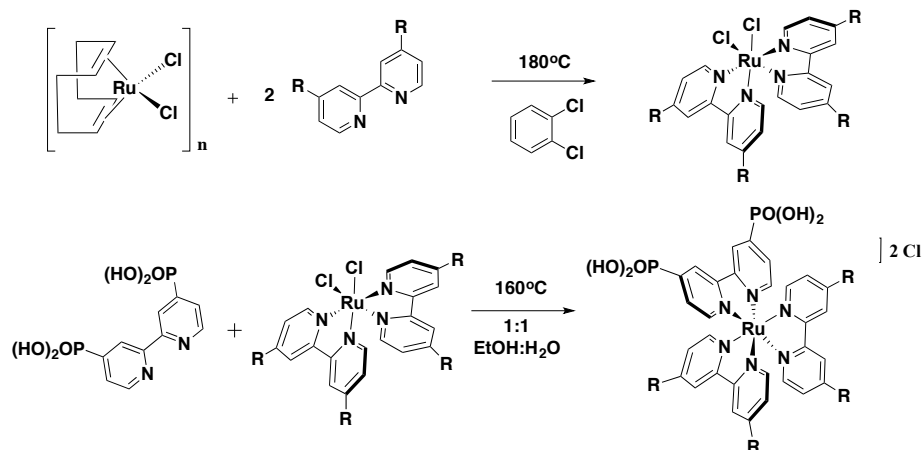
Scheme 3.1. Synthesis of 4,4-Br₂-2,2-bipyridine



All of the complexes reported here have the same general structure $[\text{Ru}(4,4'\text{-R}_2\text{-bpy})_2(4,4'\text{-(PO}_3\text{H}_2)_2\text{-bpy})]^{2+}$ where R = OCH₃, CH₃, H, or Br. The complexes were synthesized in good yields (87%-92%) by a systematic procedure to vary the bidentate 4,4'-R₂-bpy ligand. For the complexes, two equivalents of the 4,4'-R₂-bpy ligand was reacted with *poly*-Ru(1,4-cyclooctadiene)Cl₂²⁴⁷ in *o*-dichlorobenzene at 180°C for two hours under an argon atmosphere (see experimental).¹⁹² Upon the addition of ether, the *cis*-Ru(4,4'-R₂-bpy)₂Cl₂ complexes precipitate from the solution and were used without further purification (Scheme 3.2). Limited solubility makes characterization of the *cis*-Ru(4,4'-R₂-bpy)₂Cl₂ complexes difficult.

The chromophores were isolated as their chloride salts by the reaction of Ru(4,4'-R₂-bpy)₂Cl₂ with one equivalent of 4,4'-(PO₃H₂)₂-bpy in 1:1 EtOH:H₂O in a microwave oven reactor at 160°C for 20 min (Scheme 3.2). These reactions can be followed by UV/Vis absorption spectroscopy by monitoring the disappearance of the Ru(4,4'-R₂-bpy)₂Cl₂²¹² absorption features and the growth of the $[\text{Ru}(4,4'\text{-R}_2\text{-bpy})_2(4,4'\text{-(PO}_3\text{H}_2)_2\text{-bpy})]^{2+}$ absorption features (Figure 3.5, Table 3.2). The crude mixtures were each purified by size exclusion chromatography (Sephadex LH-20), yielding pure complexes.

Scheme 3.2. Synthesis of Ru(4,4'-R₂-bpy)₂Cl₂ and $[\text{Ru}((4,4'\text{-R}_2\text{-bpy})_2((\text{PO}_3\text{H}_2)_2\text{-bpy}))]^{2+}$



The aromatic region of the ¹H NMR of each complex in D₂O is shown in Figure 3.2. The complexes have C₂ symmetry with a single 2-fold axis bisecting the 4,4'-(PO₃H₂)₂-bpy ligand. The C₂ symmetry is apparent in the ¹H NMR spectra of each complex. There are three distinct resonances for the 4,4'-(PO₃H₂)₂-bpy ligands in each complex appearing at ~ 8.70, 7.75, and 7.50 ppm. Their chemical shifts remain relatively unaffected by the variation in the 4,4'-R₂-bpy ligand in the series (Figure 3.2). As expected, the proton resonances of the 4,4'-R₂-bpy ligand vary significantly through the series, with the more electron poor ligand (4,4'-(Br)₂-bpy) having resonances shifted downfield relative to the electron rich ligands (4,4'-(OCH₃)₂-bpy and 4,4'-(CH₃)₂-bpy). In addition, as a result of the C₂ symmetry, the 4,4'-R₂-bpy ligands show 6 unique resonances for the 6 protons on each.

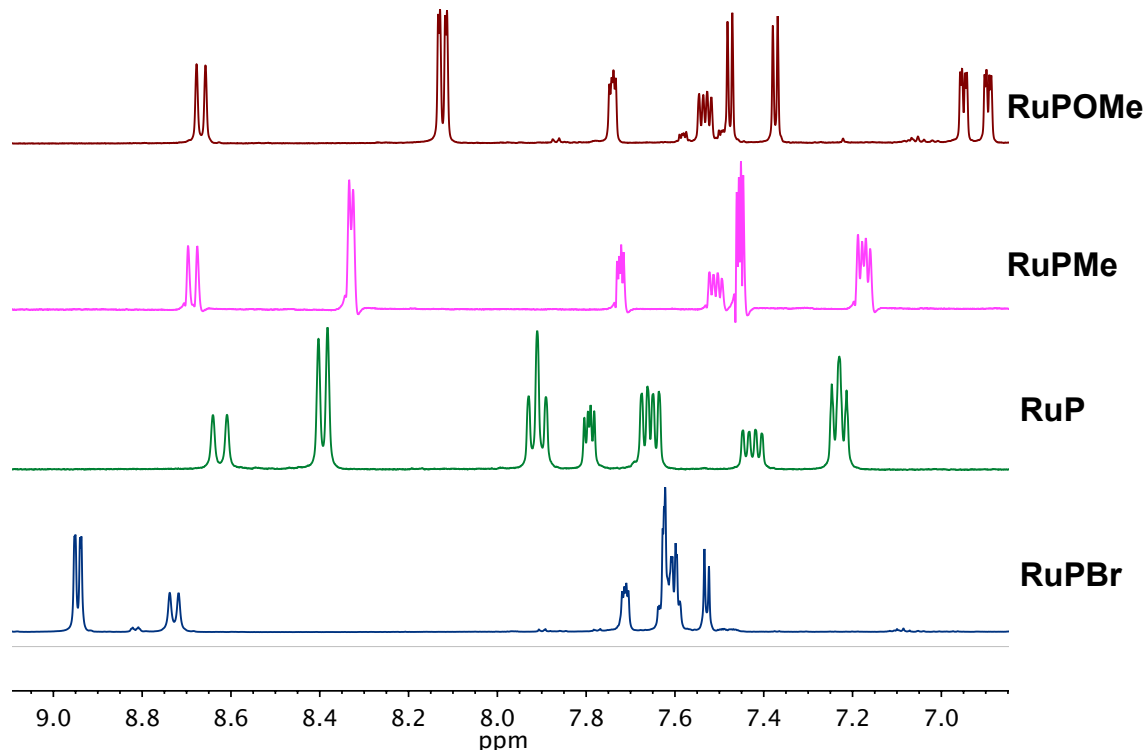


Figure 3.2. ^1H NMR spectra of **RuPBr** (blue), **RuP** (green), **RuPMe** (pink), and **RuPOMe** (red) in D_2O .

Surface Binding. Adsorption isotherms were analyzed by the Langmuir isotherm model by immersing TiO_2 ($4\ \mu\text{m}$)/FTO slides in methanol solutions of 10, 20, 50, 100, 150, and $200\ \mu\text{M}$ of complex (Figure B.2).²⁵⁰ The adsorption constant (K_{ad}) and maximum surface coverage (Γ_{max}) for each complex are listed in Table 3.1. The adsorption constant for **RuPOMe** ($1.8 \times 10^5\ \text{M}^{-1}$), **RuPMe** ($6.7 \times 10^5\ \text{M}^{-1}$), and **RuPBr** ($1.5 \times 10^5\ \text{M}^{-1}$) are all very similar and are roughly an order of magnitude higher than the previously reported value for **RuP** ($3.9 \times 10^4\ \text{M}^{-1}$) under the same conditions.¹⁴⁸ This is likely due to inconsistencies of the TiO_2 /FTO films used in this and previous studies and not a result of stronger binding affinities for **RuPOMe**, **RuPMe**, or **RuPBr**. The maximum surface coverage (Γ_{max}) range from $6.6 \times 10^{-8}\ \text{mol cm}^{-2}$ (**RuPBr**) to $8.5 \times 10^{-8}\ \text{mol cm}^{-2}$ (**RuP**) suggesting similar packing of each complex in the TiO_2 network is similar.

Table 3.1. Equilibrium Surface Parameters for RuPOMe, RuPMe, RuP, and RuPBr.

Complex	Γ_{\max} (mol cm ⁻²) ^a	K_{ad} (M ⁻¹ , $\times 10^5$)
RuPOMe	6.7×10^{-8}	1.8
RuPMe	6.7×10^{-8}	6.7
RuP^b	8.5×10^{-8}	0.39
RuPBr	6.6×10^{-8}	1.5

^a Maximum surface coverages are reported on a per micrometer thickness basis for 4 μm films. ^b Previously reported.¹⁴⁸

Electrochemistry. The electrochemical properties of each complex in solution (80:20 CH₃CN:H₂O with 0.1 M TBAPF₆ supporting electrolyte, TBA = tetra-n-butylammonium) and deposited on TiO₂ in aqueous 0.1 M HClO₄ were investigated by cyclic and square-wave voltammetry. The 80:20 CH₃CN:H₂O solution mixture was used to investigate ligand based reduction potentials (Ru^{2+/+}) under conditions similar to aqueous media without having a significant background H₂O reduction at the electrode. The values for each complex in solution and on TiO₂ are presented in Table 3.2.

All complexes exhibit reversible Ru^{3+/2+} redox couples both in solution and when bound to mesoporous TiO₂. The Ru^{3+/2+} redox potentials are summarized in Table 3.2, as $E_{1/2}$ values vs NHE obtained from square wave measurements. They follow the expected trend with $E_{1/2}$ increasing in the sequence: **RuPOMe** < **RuPMe** < **RuP** < **RuPBr** with values ranging from 1.08 V to 1.45 V (vs NHE) when immobilized on TiO₂, Figure 3.3. The electronic nature of the 4,4'-R₂-bpy ligand influences the π^* acceptor energy levels. In the complexes, the more electron donating groups (R = OCH₃ and CH₃) destabilize the bpy- π^* orbitals, decreasing the amount of $d\pi$ - π^* backbonding from the Ru^{II} center to the 4,4'-R₂-bpy ligand. This destabilizes the $d\pi^6$ electronic configuration resulting in lowered Ru^{3+/2+} redox potentials (Table 3.2). In contrast, the electron withdrawing ligand (4,4'-Br-bpy) stabilize the

bpy- π^* orbitals, increasing $d\pi-\pi^*$ backbonding from the Ru^{II} center. This stabilizes the $d\pi^6$ electronic configuration, resulting in more positive $\text{Ru}^{3+/2+}$ redox couples.^{196,214,215,254}

Equation 3.2

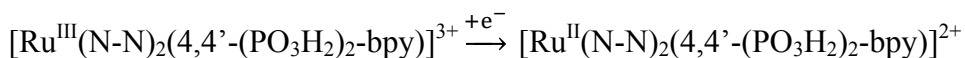


Table 3.2. Summary of photophysical, electrochemical, and surface binding properties for RuPOMe, RuPMe, RuP, and RuPBr.

Complex	Absorbance λ (nm) (ϵ , $\text{M}^{-1}\text{cm}^{-1}$) ^a	Emission λ_{max} ^b	ΔG_{ES} (eV) ^c	$E_{1/2}$ ($\text{Ru}^{3+/2+}$) ^e	$E_{1/2}$ ($\text{Ru}^{3+/2+}$) ^d	$E_{1/2}$ ($\text{Ru}^{2+/+}$) ^d	$E_{1/2}$ ($\text{Ru}^{3+/2+*$) ^g	$E_{1/2}$ ($\text{Ru}^{2+*/+}$) ^h
RuPOMe	477 (11,800)	708	1.97	1.08	1.05	-1.33	-0.89	0.64
RuPMe	461 (12,800)	685	2.01	1.19	1.16	-1.33	-0.82	0.68
RuP	458 (12,700)	667	2.09	1.28	1.27	-1.29	-0.80	0.80
RuPBr	465 (13,400)	644	2.14	1.45	1.40	-1.40 ^f	-0.69	1.05

^a In H_2O . ^b On ZrO_2 in argon deaerated 0.1 M HClO_4 at rt. ^c ΔG_{ES} from a Franck-Condon analysis of emission spectra in CH_3CN , see text. ^d Reported vs NHE in 80:20 $\text{CH}_3\text{CN}:\text{H}_2\text{O}$ deaerated with argon; glassy carbon working, Pt-wire counter, and Ag/AgNO_3 reference electrode (0.40 V vs. NHE). ^e Reported vs NHE in 0.1 M HClO_4 , TiO_2 derivatized with complex working, Pt counter, and Ag/AgCl reference (0.198 V vs NHE). ^g $\text{Ru}^{3+/2+*} = \text{Ru}^{3+/2+} - \Delta G_{\text{ES}}$. ^h $\text{Ru}^{2+*/+} = \text{Ru}^{2+/+} + \Delta G_{\text{ES}}$.

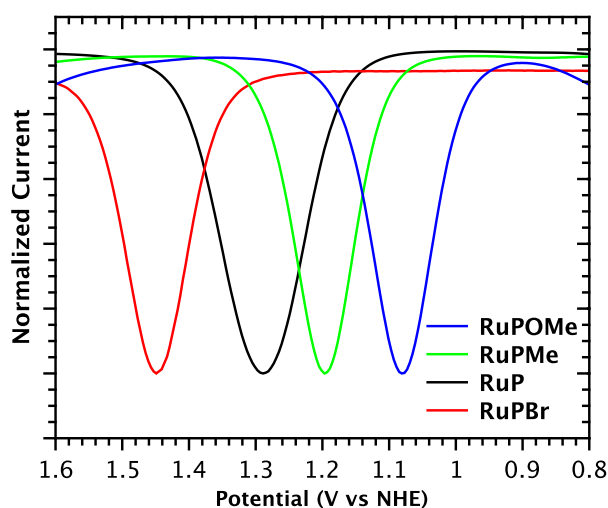
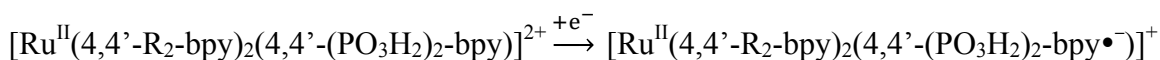


Figure 3.3. Square-wave voltammograms (normalized to peak current value) of **RuPOMe** (blue), **RuPMe** (green), **RuP** (black), and **RuPBr** (red) immobilized on TiO_2 as the working

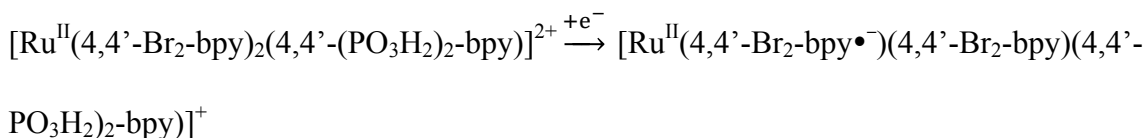
electrode, Pt counter, and Ag/AgCl reference (0.197 V vs NHE) electrode in aqueous 0.1 M HClO₄.

The first ligand-based reduction potential (Ru^{2+/+}) of each complex in solution (in 80:20 CH₃CN:H₂O, 0.1 M TBAPF₆ supporting electrolyte, Pt-wire counter, and Ag/AgNO₃ reference) are listed in Table 3.2. The first reduction of the complexes follows a similar trend to the Ru^{3+/2+} couple where the more electron withdrawing ligand in **RuPBr** (4,4'-Br₂-bpy) results in more positive reduction potentials. The first reduction of **RuPBr** (-1.09 V vs NHE) is significantly more positive than that of **RuP** (-1.29 V vs NHE), **RuPMe** (-1.33 V vs NHE), and **RuPOMe** (-1.33 V vs NHE). The positive shift from -1.33 V (**RuPOMe** and **RuPMe**) to -1.09 V (**RuPBr**) is due to lowering in energy of the π*-acceptor orbitals in 4,4'-Br₂-bpy compared to 4,4'-(OCH₃)₂-bpy or 4,4'-(CH₃)₂-bpy from incorporation of electron withdrawing Br atoms in the bipyridine framework. **RuPOMe**, **RuPMe**, and **RuP** have similar first reduction potentials which suggests that the first reduction is largely 4,4'-(PO₃H₂)₂-bpy based (Equation 3.3). In contrast, the first reduction of **RuPBr** is significantly more positive point to reduction of 4,4'-(Br)₂-bpy (Equation 3.4).

Equation 3.3



Equation 3.4



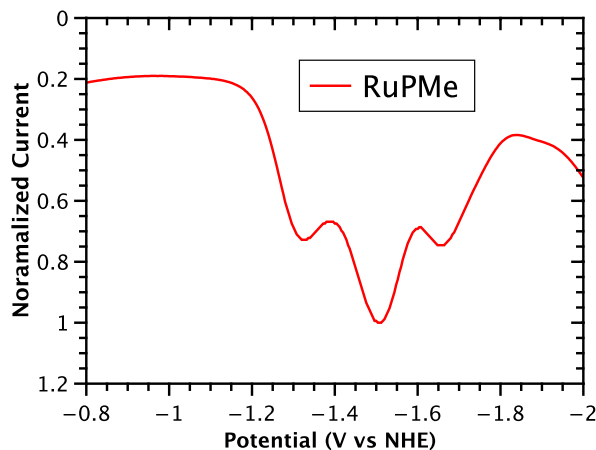


Figure 3.4. Square-wave voltammogram of **RuPMe** (1.0 mM in 80:20 CH₃CN:H₂O, 0.1 M TBAPF₆ supporting electrolyte, Pt-wire counter, and Ag/AgNO₃ reference (0.4 V vs NHE)).

Each complex shows multiple reduction waves within the potential window of the experiments with scans extended to -2.0 V (vs NHE). As an example, three ligand-based reduction waves appear for **RuPMe** between -0.8 V and -2.0 V (vs NHE), Figure 3.4. Although not confirmed spectroscopically, these reductions are tentatively assigned to reduction at 4,4'-(PO₃H₂)₂-bpy followed by reduction of both of the 4,4'-(CH₃)₂-bpy ligands.

UV-Visible Spectra. The absorption spectra of all of the complexes in aqueous solution feature intense $\pi \rightarrow \pi^*$ absorptions below 350 nm ($\epsilon \approx 4.3\text{-}5.7 \times 10^4 \text{ M}^{-1}\text{cm}^{-1}$) and lower energy metal-to-ligand charge transfer (MLCT) absorptions from 400-500 nm (Figure 3.5). Spectral data for the MLCT absorptions are listed in Table 3.2 and absorption spectra in H₂O are shown in Figure 3.5 (single spectra are available in the supporting information). Although there are slight variations in MLCT λ_{max} values in the series, there is no obvious correlation between the electron donating or withdrawing nature of the 4,4'-R₂bpy ligand and these values. The lack of correlation shows that although the $d\pi$ orbitals are stabilized by the electron withdrawing 4,4'-R₂-bpy ligands, resulting in a more positive $E_{1/2}(\text{Ru}^{3+/2+})$, there is a

compensating stabilization in the energies of the π^* -acceptor orbitals that is comparable among the complexes.

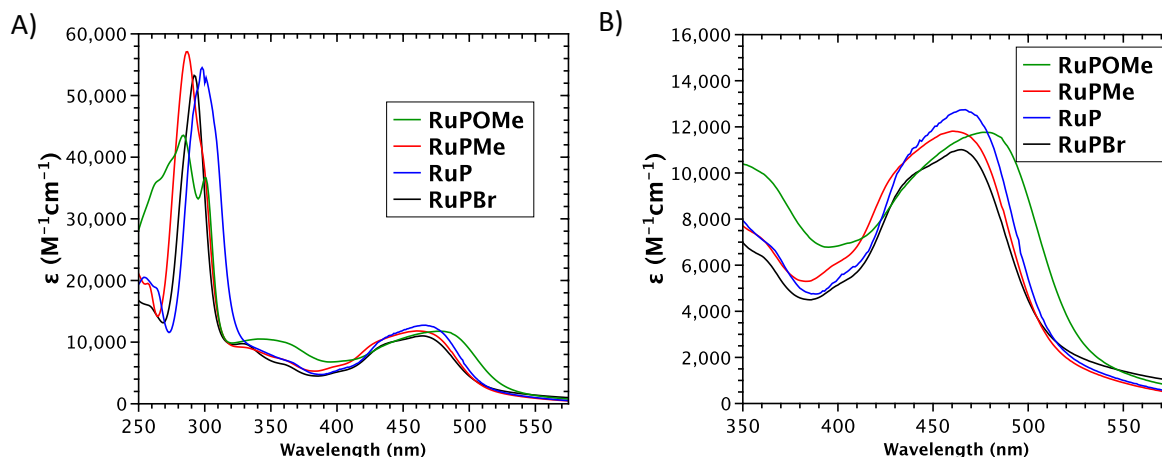


Figure 3.5. UV/Visible absorption spectra for **RuPOMe**, **RuPMe**, **RuP**, and **RuPBr** in H_2O .

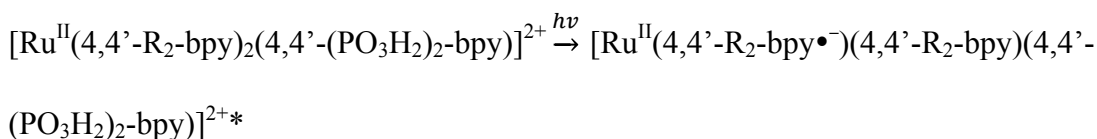
TD-DFT calculations were applied to better understand and quantify the spectral assignments (Figure B.6). Complex geometries were optimized using DFT (B3LYP/LanL2DZ functional/basis-set), and optimized geometries were used in the TD-DFT (PBE0/LanL2DZ functional/basis-set) calculations with a continuum model to account for solvation by H_2O . The results of the calculations are summarized in Figure B.6 and Table 3.3. The computed spectra correlate well with experimental spectra with strong $\pi \rightarrow \pi^*$ absorptions predicted below 300 nm and MLCT absorptions at longer wavelengths (Table 3.3, Figure B.7). The calculations verify the origins of the visible absorptions as excitations arising from $d\pi \rightarrow \pi^*$ transitions to either the 4,4'- R_2 -bpy (Equation 3.5) or the 4,4'- $(\text{PO}_3\text{H}_2)_2$ -bpy (Equation 3.6) ligand. The calculated excitations also show that the excitations to the ancillary 4,4'- R_2 -bpy ligand in **RuP**, **RuPMe**, and **RuPOMe** is higher in energy compared to excitation to the 4,4'- $(\text{PO}_3\text{H}_2)_2$ -bpy ligand (Table 3.3). The computed spectra are blue-shifted relative to the experimental spectra, likely due to the inherent TD-DFT overestimation of

MLCT energies in Ru polypyridyl complexes as well as solvent effects that are not adequately described by polarizable continuum model (PCM) used here.^{255,256}

Table 3.3. TD-DFT calculated excitation for the series of chromophores.

Chromophore	Excitation (nm)	Oscillator Strength	Orbital contribution
RuPOMe	460 nm	0.18	Ru dπ → π* (PO ₃ H ₂) ₂ -bpy
	409 nm	0.1	Ru dπ → π* OMe-bpy
RuPMe	455 nm	0.126	Ru dπ → π* (PO ₃ H ₂) ₂ -bpy
	411 nm	0.155	Ru dπ → π* Me-bpy
RuP	443 nm	0.179	Ru dπ → π* (PO ₃ H ₂) ₂ -bpy
	411 nm	0.153	Ru dπ → π* bpy
RuPBr	431 nm	0.18	Ru dπ → π* Br-bpy + π* (PO ₃ H ₂) ₂ -bpy
	429 nm	0.2	Ru dπ → π* (PO ₃ H ₂) ₂ -bpy + π* Br-bpy

Equation 3.5



Equation 3.6

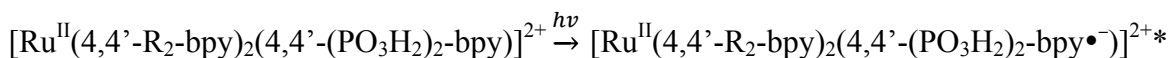


Figure 3.6 shows the calculated and experimental spectra for **RuPMe** in H₂O with the calculated transition energies shown as vertical bars with their heights reflecting relative oscillator strengths. The calculated excitations show the split in the MLCT manifold between the MLCT transitions to π*(4,4'-(CH₃)₂-bpy) and π*(4,4'-(PO₃H₂)₂-bpy) with the higher energy excitation being Ru dπ → π* (4,4'-(CH₃)₂-bpy) (Equation 3.5) and the lower energy excitation being Ru dπ → π* (4,4'-(PO₃H₂)₂-bpy) (Equation 3.6).

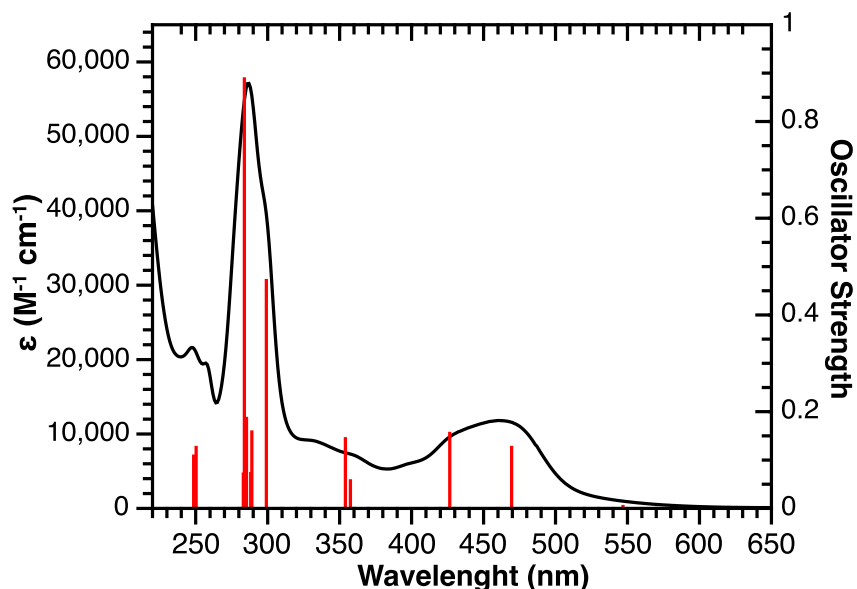


Figure 3.6. UV-visible spectrum of **RuPMe** at room temperature in H₂O (black line) and calculated TD-DFT transitions (vertical red bars with heights illustrating oscillator strengths, red-shifted by 0.15 eV).

Emission Spectra. All complexes exhibit broad emission spectra at room temperature when immobilized onto ZrO₂ in aqueous 0.1 M HClO₄. The emission spectra for each complex is shown in Figure 3.7 with emission energies listed in Table 3.2. Emission energies decrease from **RuPBr** ($\lambda_{\text{max}} = 644 \text{ nm}$, $1.55 \times 10^4 \text{ cm}^{-1}$) to **RuPOMe** ($\lambda_{\text{max}} = 708 \text{ nm}$, $1.41 \times 10^4 \text{ cm}^{-1}$). Emission from these complexes occurs from the lowest lying ³MLCT excited states following intersystem crossing from the initial ¹MLCT excited states that dominate absorption.^{188,196,220,255}

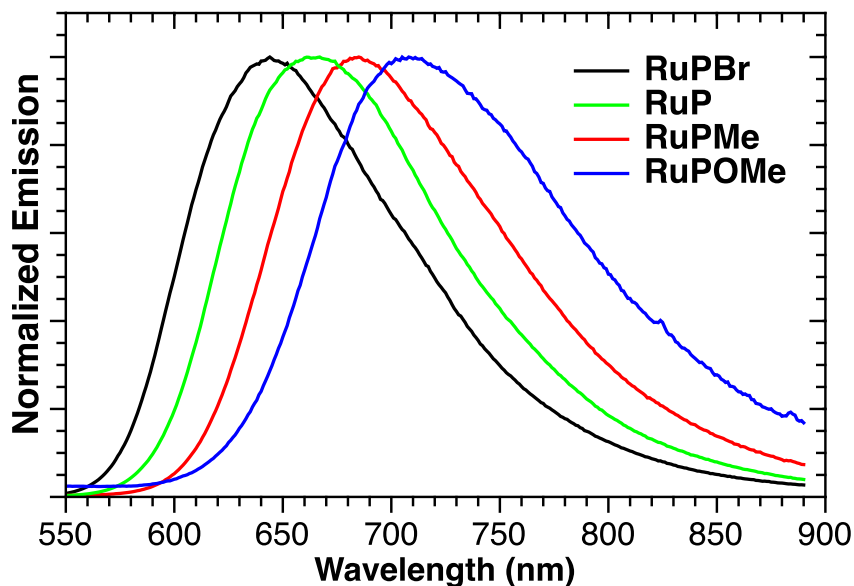


Figure 3.7. Normalized emission spectra for **RuPBr** (black), **RuP** (green), **RuPMe** (red), and **RuPOMe** (blue) loaded onto ZrO_2 in aqueous 0.1 M HClO_4 at temperature following excitation at 450 nm.

Trends in the emission energies ($\bar{\nu}_{em}$) follow those for the $E_{1/2}(\text{Ru}^{3+/2+})$ redox couple where the more positive $\text{Ru}^{3+/2+}$ redox couple yields higher emission energies. This trend is illustrated in Figure 3.8 where there is a linear dependence of the emission energy on $E_{1/2}(\text{Ru}^{3+/2+})$. This relationship suggests that variations in excited state energies with ligand changes are mainly a consequence of variations in the energy of the metal-based $d\pi$ orbitals.^{231,255} There is no correlation between emission energies and the ligand based $E_{1/2}(\text{Ru}^{2+/+})$ values (see Supporting Information Figure B.8).

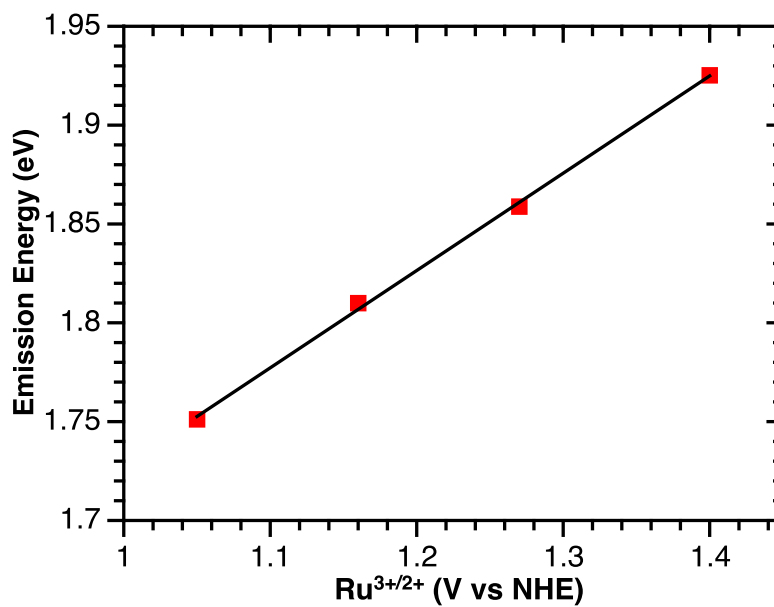


Figure 3.8. Dependence of emission energy ($\bar{\nu}_{em}$) on $E_{1/2}(\text{Ru}^{3+/2+})$ in 0.1 M HClO_4 bound to metal oxide surface at 25°C.

Emission Spectral Fitting. Correlation of Excited State Properties

Emission spectra for all complexes bound to ZrO_2 in aqueous 0.1 M HClO_4 at 25°C were analyzed by use of a one-mode Franck-Condon analysis.^{144,218,233-236,255} In this analysis, contributions from medium frequency $\nu(\text{bpy})$ modes are treated as a single averaged mode with low frequency modes and the solvent being included in the band widths. Emission spectra were fit to a series of vibronic lines centered on the 0-0 component at energy E_0 and separated by a vibrational quantum spacing of $\hbar\omega_M$. Only the transitions from the $\nu'=0$ level in the excited state to level ν in the ground state were included in the summation.

In the spectral fits, relative intensities of the vibronic lines are determined by the electron-vibrational coupling constant, S_M , which is related to the equilibrium displacement change, ΔQ_{eq} , by $\frac{1}{2} \Delta Q_{eq}^2$. As noted above, additional vibrational contributions from low frequency modes and the solvent are treated classically and included in the bandwidth at half height, $\Delta\bar{\nu}_{1/2}$, with $\Delta\bar{\nu}_{1/2}$ defined in Equation 3.7. In Equation 3.7, $\lambda_{0,L}$ is the sum of the solvent reorganization energy, λ_0 , and reorganization energy from low frequency modes, λ_L .

E_0 in Equation 3.7 is the 0-0 energy gap, the energy of the excited state above the ground state with both states in the $\nu = 0$ vibrational levels, k_B is the Boltzmann constant and T is the temperature (298 K).

Equation 3.7

$$\Delta G_{ES} = E_0 + \lambda_{0,L} = E_0 + \frac{(\Delta\nu_{1/2})^2}{16k_B T \ln 2}$$

Results of the spectral fitting analysis are summarized in Table 3.4. The free energy content of the excited states (ΔG_{ES}) were calculated using Equation 3.7. As shown in Table 3.2 and Table 3.4, trends in ΔG_{ES} mirror those for emission energies through the series. The free energy content of the excited state (ΔG_{ES}) and the 0-0 energy gap (E_0) increase as $E_{1/2}(\text{Ru}^{3+/2+})$ increases, Figure 3.9. This trend is expected, given that the emission energy is dependent on the energy of the $d\pi$ levels rather than the π^* levels (see above, Figure 3.8).

Table 3.4. Emission spectral fitting parameter for MLCT emission from RuPOMe, RuPMe, RuP, and RuPBr loaded on ZrO₂ in aqueous 0.1 M HClO₄ at 25°C

Complex	E_0 (cm ⁻¹)	$\Delta\bar{\nu}_{1/2}$	$\hbar\omega_M$	S_M	ΔG_{ES} (cm ⁻¹)
RuPOMe	14300	1920	1350	0.89	15900
RuPMe	14700	1850	1350	0.86	16200
RuP	15200	1930	1350	0.79	16800
RuPBr	15700	1870	1350	0.9	17300

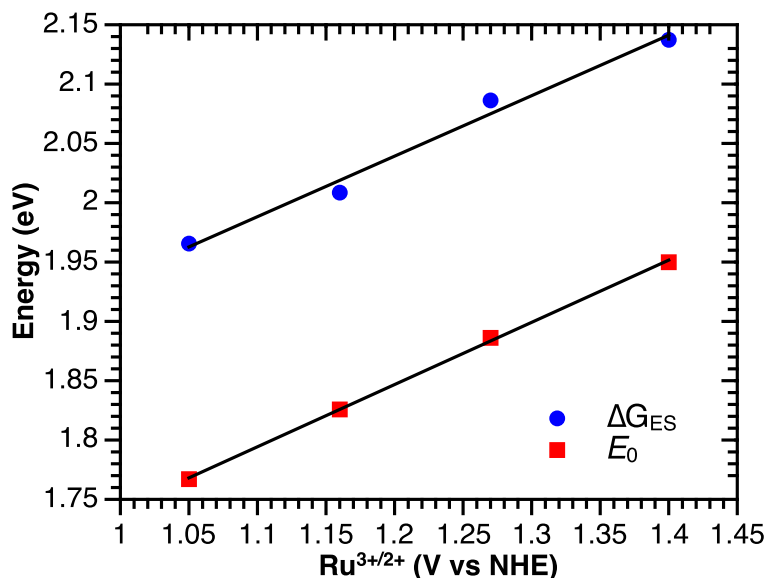


Figure 3.9. Dependence of the free energy content of the excited state (ΔG_{ES} , blue circles) and the 0-0 energy gap (E_0) on the ground state oxidation potential ($E_{1/2}(Ru^{3+/2+})$) for **RuPOMe**, **RuPMe**, **RuP**, and **RuPBr**.

Similarly to previously reported correlations on complexes of the type $[M(bpy)_2(L)]^{2+}$ (where $M = Ru^{II}$, Os^{II} , and L is a neutral, 4 – electron donor), both the ground state $Ru^{3+/2+}$ ($d\pi^5/d\pi^6$) and excited state $Ru^{2+*/+}$ ($d\pi^5\pi^{*1}/d\pi^6\pi^{*1}$), with the redox levels localized largely on the metal center, decrease linearly with emission energy.^{229,241,242} In contrast, the ground state $Ru^{2+*/+}$ ($d\pi^6/d\pi^6\pi^{*1}$) and excited state $Ru^{3+/2+*}$ ($d\pi^5/d\pi^5\pi^{*1}$), both ligand centered, remain relatively unchanged with emission energy. This, again, suggests that the Ru- $d\pi$ levels are influencing the excited state redox potentials instead of the $bpy-\pi^*$ orbital levels.

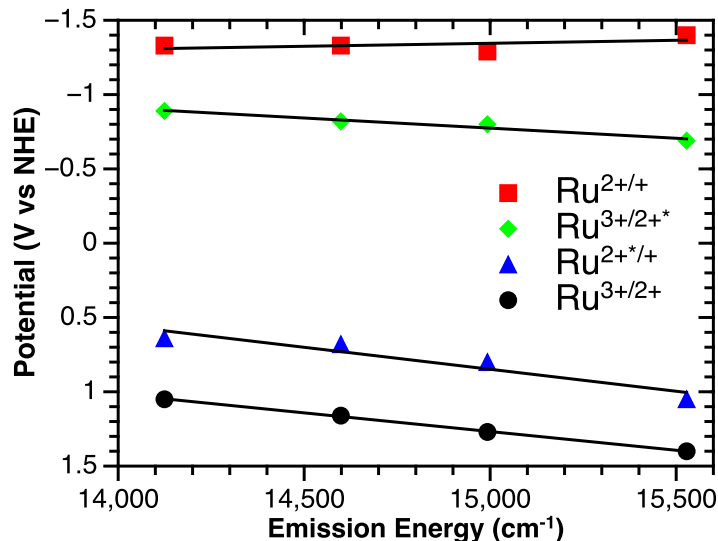


Figure 3.10. Variation of ground and excited state redox potentials with emission energy in H₂O (0.1 M aqueous HClO₄ for electrochemical measurements) at 25°C.

Excited State Redox Potentials

One motivation for synthesizing and characterizing the series of complexes was to explore the role varying the ancillary ligands on the light absorption properties of the surface-bound complexes for possible photoelectrochemical applications. As noted in the Introduction, key properties in this regard include broad light absorption in the visible, excited state electron injection into the conduction band of a high band gap semiconductor, and sufficient potential as Ru³⁺ to drive water oxidation catalysis. In the current series of complexes, the dominating MLCT absorptions in the visible remain relatively constant through the series (Figure 3.5), even with significant variations in $E_{1/2}(\text{Ru}^{3+/2+})$ and $E_{1/2}(\text{Ru}^{2+/+})$ (Table 3.2).

In order to quantitate the impact of ligand variations on excited state redox potentials, $E_{1/2}$ values for the excited state acting as an oxidant, Ru^{2+*/+} (Equation 3.8), and reductant, Ru^{3+/2+*} (Equation 3.9), were calculated from the ground state potentials in Table 3.1 and free energies of the excited state above the ground state, ΔG_{ES} , determined by emission spectral fitting, Table 3.2.^{135,183,231,255}

Equation 3.8

$$E_{1/2}(\text{Ru}^{2+*/+}) = E_{1/2}(\text{Ru}^{2+/+}) + \Delta G_{\text{ES}}$$

Equation 3.9

$$E_{1/2}(\text{Ru}^{3+/2+*}) = E_{1/2}(\text{Ru}^{3+/2+}) - \Delta G_{\text{ES}}$$

Figure 3.11 illustrates $E_{1/2}(\text{Ru}^{3+/2+*})$ varies with the ground state potential ($\text{Ru}^{3+/2+}$) across the series. An important feature in the data is an increase in oxidizing strength of Ru^{3+} across the series with variations in $E_{1/2}(\text{Ru}^{3+/2+})$ induced by varying the 4,4'-R₂-bpy ligand from 1.08 to 1.45 V (vs NHE). Unfortunately, the enhanced oxidative ground state potential for Ru^{3+} is accompanied by a decrease in the excited state oxidation potential with $E_{1/2}(\text{Ru}^{3+/2+*})$ increase in the same series from -0.89 to -0.69 V (vs NHE).

As a particular example, $E_{1/2}(\text{Ru}^{3+/2+})$ for **RuPBr** is 1.45 V (vs NHE) on TiO₂ in aqueous 0.1 M HClO₄ with light absorption properties comparable to **RuP** (Figure 3.5). A $E_{1/2}$ of this magnitude provides the thermodynamic basis for driving water oxidation catalysis. However, the exchange of bpy for 4,4'-Br₂-bpy increases $E_{1/2}(\text{Ru}^{3+/2+*})$ from -0.80 to -0.69 V (vs NHE) lowering the thermodynamic driving force to undergo electron injection into the conduction band of TiO₂ following photoexcitation.^{92,125,162} Analysis of electron injection efficiencies and kinetics is currently under investigation.

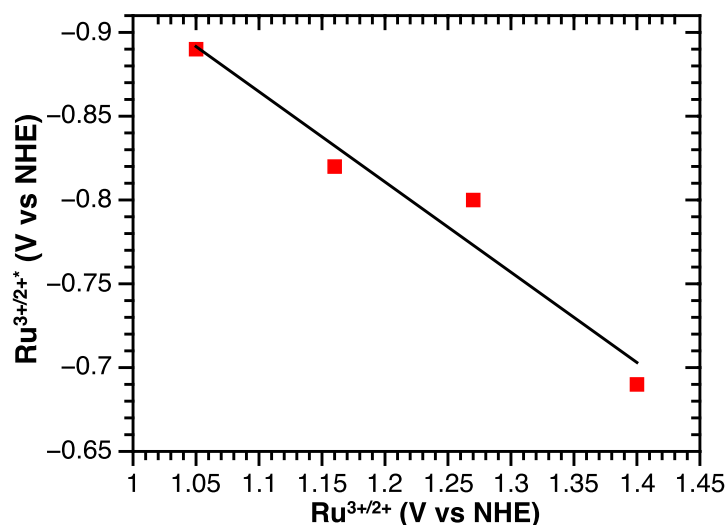


Figure 3.11. Variation in the excited state reduction potential ($\text{Ru}^{3+/2+*}$) with the ground state oxidation potential ($\text{Ru}^{3+/2+}$).

3.4 Conclusions

We have described here a systematic synthetic approach to build complexes of the type $[\text{Ru}(4,4'\text{-R}_2\text{-bpy})_2(4,4'\text{-(PO}_3\text{H}_2)_2\text{-bpy})]^{2+}$ used to modify the ground and excited state redox potentials. The approach taken was to prepare a family of light-harvesting chromophores with the common $4,4'\text{-(PO}_3\text{H}_2)_2\text{-bpy}$ ligand for surface binding with variations in the remaining ligand positions used to modify electronic structure, and with it, light absorption, ground state, and excited state redox potentials

Variations within the series results in chromophores in which the ground state $\text{Ru}^{3+/2+}$ redox potentials vary from 1.08 V to 1.45 V (vs NHE) without significant loss in the visible light absorption properties. Insensitivity of light absorption is attributed to a compensation effect where changes in the π^* levels in the $4,4'\text{-R}_2\text{-bpy}$ ligand are compensated for by changes in the $d\pi$ level, resulting in a nearly constant energy gap.

Results from Frank-Condon analyses of emission spectral profiles were used to calculate the free energy content of the excited state (ΔG_{ES}), and with it, the excited state redox potentials $\text{Ru}^{2+*/+}$ and $\text{Ru}^{3+/2+*}$. Because of the electronic compensation effect,

increasing oxidizing strength in the ground state is paralleled by loss in excited state reducing strength ($\text{Ru}^{3+/2+*}$), resulting in a lower of the driving force for electron injection into the conduction band of a semiconductor.

3.5 Associated Content

Appendix B: Table of emission spectral fitting parameters, Langmuir Isotherms, UV-visible spectra, and calculation results.

Chapter 4: AN AMIDE-LINKED CHROMOPHORE-CATALYST ASSEMBLY FOR WATER OXIDATION

Reprinted with permission from Ashford, D. L.; Stewart, D. J.; Glasson, C. R.; Binstead, R. A.; Harrison, D. P.; Norris, M. R.; Concepcion, J. J.; Fang, Z.; Templeton, J. L.; Meyer, T. J. *Inorg. Chem.* **2012** *51* (12), 6428-6430. Copyright American Chemical Society 2014

4.1 Introduction

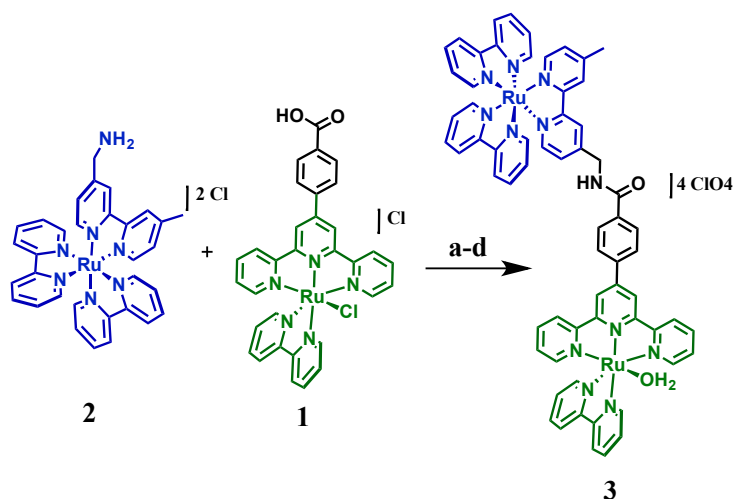
In producing solar fuels from Artificial Photosynthesis, as in natural photosynthesis, integrating visible light absorption with the sequential redox events that drive the coupled half reactions- water oxidation to oxygen and either water/H⁺ reduction to hydrogen or CO₂ reduction to CO, other oxygenates, or hydrocarbons- is an essential element.^{2,34,42,173} The use of “chromophore-catalyst assemblies”, which combine both light absorption and catalysis in linked molecular units bound to large band gap semiconductors is appealing for use in Dye-Sensitized Photoelectrosynthesis Cells (DSPECs, Figure 1.6).^{90,162,169,170,175,180}

Catalytic water oxidation has been demonstrated for [(bpy)₂Ru^{II}(bpm)Ru^{II}(tpy)(OH₂)]⁴⁺ and [(bpy)₂Ru^{II}(bpm) Ru^{II}(Mebimpy)(OH₂)]⁴⁺ (bpy=2,2'-bipyridine)(bpm=2,2'-bipyrimidine)(tpy=2,2':6',2''-terpyridine)(Mebimpy=2,6-bis(1-methyl-benzimidazol-2-yl)pyridine) assemblies.²⁵⁷ Both of these assemblies incorporate a light absorbing chromophore and a water oxidation catalyst. Excitation and injection into TiO₂ was recently reported for the assembly [(dcb)₂Ru(bpy-Mebim₂-py)Ru(bpy)(OH₂)](OTf)₄ (dcb = 4,4'-dicarboxylic acid-2,2'-bipyridine; bpy-Mebim₂py = 2,2'-(4-methyl-[2,2':4',4''-terpyridine]-2'',6''-diyl)bis(1-methyl-1H-benzo[*d*]imidazole),

however, electron injection efficiencies were low due to electron trapping by a lowest lying Metal-to-Ligand Charge Transfer (MLCT) state localized on the π^* system of the bridging ligand.¹³⁴

We report here development of a general synthetic approach to chromophore-catalyst assemblies based on amide coupling that produces chemically linked chromophore-catalyst units free of complications from the photophysical or redox properties of the intervening bridge. In this strategy, the water oxidation catalyst precursor $[\text{Ru}(4-([2,2':6',2''\text{-terpyridin}]-4\text{-yl})\text{benzoic acid})(\text{bpy})(\text{Cl})]^+$ (**1**) and the chromophore $[\text{Ru}(\text{bpy})_2((4'\text{-methyl}-[2,2'\text{-bipyridin}]-4\text{-yl})\text{methanamine})]^{2+}$ (**2**) were used as starting materials for synthesis of the assembly $[(\text{Ru}(\text{bpy})_2(\text{bpy-ph-NH-CO-trpy})\text{Ru}(\text{bpy})(\text{OH}_2))]^{4+}$ (bpy-ph-NH-CO-trpy=4-([2,2':6',2''-terpyridin]-4'-yl)-N-((4'-methyl-[2,2'-bipyridin]-4-yl)methyl) benzamide) (**3**), Scheme 4.1. The flexibility of amide coupling provides a general approach to a family of chromophore-catalyst assemblies that can be configured with different bridge lengths and intervening spacers. The syntheses of both the water oxidation catalyst and the chromophore use straightforward, high yield reactions, without requiring chromatographic separation (see experimental). In the resulting assembly the properties of the constituent units, including water oxidation catalysis, are retained. Initial photophysical studies reveal rapid energy transfer across the amide link but at a rate that is far slower than the known psec time scale for injection into TiO_2 for related complexes. This is an important design feature that ensures efficient injection for related surface-bound integrated assemblies.^{136,145,181,258}

Scheme 4.1. Amide coupling strategy used to prepare the chromophore-catalyst assembly.



a) SOCl_2 b) DMF, DIPEA, 100°C , overnight, LiClO_4 d) AgOTf , MeOH, rt, overnight

4.2 Experimental

Kinetics methods and instrumentation

Materials

Ceric ammonium nitrate (CAN, Aldrich, 99.99+% metals basis) and 70% nitric acid (Aldrich, 99.999%) were used as received and diluted to working concentrations with high-purity deionized water (Millipore Milli-Q Synthesis A10). A 4 mM stock solution Ce(IV) was prepared by dissolving CAN in 1.0 M nitric acid, and protected from room light with aluminum foil. Two solutions (0.5 and 0.05 mM) of the catalyst assembly **3** were also prepared in 1.0 M nitric acid.

Ce(IV) Consumption. The rate of consumption of excess Ce(IV) in the presence of the catalyst assembly **3** was monitored by UV-visible spectroscopy with use of an Agilent 8453 diode array spectrophotometer fitted with an 8 position multicell transport (G1120A), 8×1.00 cm silica cuvettes (NSG) and a 360 nm UV cut-off filter. Sample temperature was maintained at 22.0 ± 0.1 C with a Thermo Haake A28 water bath. Spectra were acquired on a

logarithmic time scale beginning with 30 second intervals after an initial delay time of 3 minutes that was required to initiate the reaction in each of 6 sample cuvettes ($[3] = 0.005, 0.01, 0.02, 0.03, 0.05, 0.10$ mM). The sample solutions were prepared by volumetric dilutions via Eppendorf 1.00 and 5.00 mL pipettes directly into cuvettes containing CAN solutions (3.0 ml total volume). In order to minimize loss of initial kinetic observations the samples were initiated, mixed and loaded into the multicell transport from low to high $[3]$. Owing to the length of the kinetic study (6 days) each set of sample scans was preceded by a new baseline (water) and a CAN-only scan (4 mM). The latter was used to verify that loss of CAN via both thermal and photolytic processes was negligible ($<0.2\%/day$). The excellent stability of CAN under our conditions results in part from the use of high-purity reagents, and notably the avoidance of UV irradiation into the nitric acid band (320 nm, $\epsilon = 7.1 \text{ M}^{-1} \text{ cm}^{-1}$, $\Delta\nu_{1/2} \sim 22$ nm).

Unlike the monomer $[\text{Ru}(\text{tpy})(\text{bpy})(\text{OH}_2)]^{2+}$ (tpy = 2,2',2''-terpyridine, bpy = 2,2'-bipyridine) in 1.0 M HNO_3 ,²⁵⁹ the catalyst assembly **3** exhibited non-exponential decay of sample absorbance in the 380-400 nm region that arises largely from Ce(IV) and a nearly constant offset from the rest state of the catalyst assembly. Factor analysis of the multiwavelength kinetic data during the periods of Ce(IV) loss indicated that there were four colored states and three kinetic processes. The kinetics were well modeled in SPECFIT/32 by a series of three exponential decays ($A \rightarrow B \rightarrow C \rightarrow D$). The resulting fits produced the apparent rate constants shown in Table 4.1.

Table 4.1. Multiexponential fits to decay kinetics of CAN in 1.0 M HNO_3 as a function of $[3]$.

$[3], \text{M}$	$k_1 \text{ s}^{-1}$	$k_2 \text{ s}^{-1}$	$k_3 \text{ s}^{-1}$
1.02×10^{-4}	3.13×10^{-3}	4.93×10^{-4}	7.86×10^{-5}

5.12×10^{-5}	8.07×10^{-4}	1.58×10^{-4}	1.24×10^{-5}
3.07×10^{-5}	3.99×10^{-4}	3.93×10^{-5}	5.83×10^{-6}
2.05×10^{-5}	3.58×10^{-4}	2.82×10^{-5}	4.61×10^{-6}
1.02×10^{-5}	3.41×10^{-4}	2.67×10^{-5}	3.81×10^{-6}
5.12×10^{-6}	3.40×10^{-4}	2.23×10^{-5}	3.97×10^{-6}

The apparent lack of a dependence on catalyst concentration for $[3] < 0.03$ mM suggests that the catalyst is largely deactivated under these conditions, possibly as a result of anation owing to the higher charge (4+) on the catalyst assembly than for the monomer (2+) in the same medium. While there was an increase in the rate of CAN consumption at higher $[3]$, the complexity of the decay kinetics precludes a simple assessment regarding reaction order for the catalyst assembly in 1.0 M HNO₃. In addition to possible anation, the number of species in solution during the catalytic cycle compared to the monomeric catalyst is much larger due to the fast electron transfer between the two metal centers in **3**, which is a result of the redox mediator effect. This has inhibited the ability to determine a correct kinetic model for this system to date.

Electrochemical Analysis

Electrochemical measurements were conducted a CH Instruments 660D potentiostat with a glassy carbon working electrode (0.07 cm²), Pt-wire counter electrode, and a Ag/AgCl reference (saturated NaCl, 0.197 V vs NHE). $E_{1/2}$ values were obtained from the peak currents in differential pulse voltammograms and are reported vs. the normal hydrogen electrode (NHE). UV/Vis spectra were recorded on an Agilent Technologies model 8453 diode-array spectrophotometer.

Transient absorption

Steady-state emission spectra and time-resolved emission decays were obtained with an Edinburgh Instruments FLSP920 spectrometer equipped with an EPL-445 picosecond

pulsed diode laser. Nanosecond transient absorption (TA) data were obtained using the third harmonic output of a Spectra Physics Quanta Ray Nd:YAG laser with a tunable VersaScan OPO as an excitation source (445 nm, 1 Hz, ~5 mJ/pulse). The transient absorption (TA) system was an Edinburgh Instruments LP920, equipped with a Xe900 lamp, LP920-K detector, and Tektronix TDS 3032C Digital Phosphor Oscilloscope. Electronic synchronization was controlled by the provided Edinburgh Instruments software. Kinetic traces obtained from TA were averaged a minimum of 25 times with flashlamp, probe, and luminescence corrections. All photophysical measurements were obtained using Starna GL14 10 mm cells fitted with a rubber septum and argon bubble-degassed for at least 30 minutes. Fits were obtained using SigmaPlot 11.0 software.

Oxygen Measurement

A 1 mM solution of **3** was prepared by dissolution in 1.0 M HNO₃, which had been thoroughly degassed with N₂, taken into a glovebox under a N₂ atmosphere, and allowed to equilibrate in the N₂ atmosphere overnight. The 10 mL round bottom flask containing the solution of **3** was fitted with a silicon septum and sealed with copper wire. Upon injection of CAN (ceric ammonium nitrate, 30 eq.) in 1 M HNO₃ into the red solution of **3**, an immediate color change to green occurred. The completion of the reaction (*i.e.* consumption of CAN) was evident due to the return of the solution color to red, a result of the regeneration of the Ru(bpy)₃²⁺ moiety. At this time, a 1 mL sample from the headspace of the reaction was injected into a gas chromatograph (SRI GC 8610 C in the manufacturer's multiple gas analyzer #3 configuration). Using a two point calibration curve, we calculated a 70% yield of O_{2(g)} evolution.

Synthetic Procedures

Materials

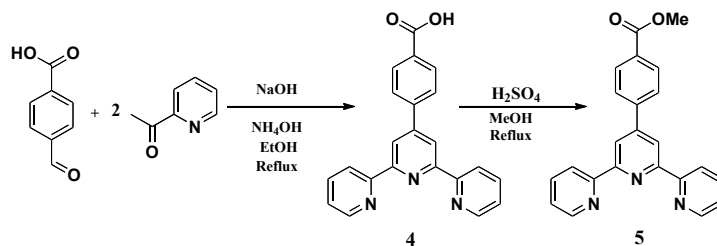
Distilled water was further purified using a Milli-Q Ultrapure water purification system. 4-formylbenzoic acid, 2-acetylpyridine, 2,2'-bipyridine (bpy), 4,4'-dimethyl-2,2'-bipyridine (dmb), and RuCl₃·H₂O, were purchased from Aldrich and used as received. Ru(bpy)₂Cl₂¹⁹², 4'-methyl-[2,2'-bipyridine]-4-carbaldehyde (**6**)²⁶⁰ were prepared as previously reported. All other reagents were ACS grade and used without further purification.

4-([2,2':6',2''-terpyridin]-4'-yl)benzoic acid (**4**)

This ligand was prepared by a reported procedure.²⁶¹ ¹H NMR (600 MHz, DMSO-d₆): δ 8.83 (d, 2H), δ 8.78 (s, 2H), δ 8.70 (d, 2H), δ 8.14 (d, 2H), δ 8.06 (m, 4H), δ 7.56 (dd, 2H). HR-ESI-MS: m/z=354.1234¹⁺, [M + H⁺]¹⁺ = 354.1243.

Methyl 4-([2,2':6',2''-terpyridin]-4'-yl)benzoate (**5**)

4 was esterified before the reaction with RuCl₃ to avoid possible coordination of the carboxylic acid. **4** (2 g, 5.66 mmol) was suspended in anhydrous MeOH (50mL) and concentrated H₂SO₄ (3 mL) was added. The reaction was heated under reflux argon overnight, upon which time all of the solid dissolved. The reaction mixture was cooled and poured into ice water (200 mL). The slurry was stirred approximately 30 min at 0°C, the solid was filtered, air-dried, and collected (1.97 g, 95%). This ligand was used without further purification. ¹H NMR (600 MHz, CD₂Cl₂): δ 8.78 (s, 2H), δ 8.70 (d, 2H), δ 8.68 (d, 2H), δ 8.16 (d, 2H), δ 7.96 (d, 2H), δ 7.9 (t, 2H), δ 7.37 (t, 2H), δ 3.94 (s, 3H). HR-ESI-MS: m/z=390.1212¹⁺, [M + Na⁺]¹⁺ = 390.1221.



$\text{Ru}(\text{methyl } 4\text{-}([2,2':6',2''\text{-terpyridin}]\text{-4'-yl})\text{benzoate})\text{Cl}_3$

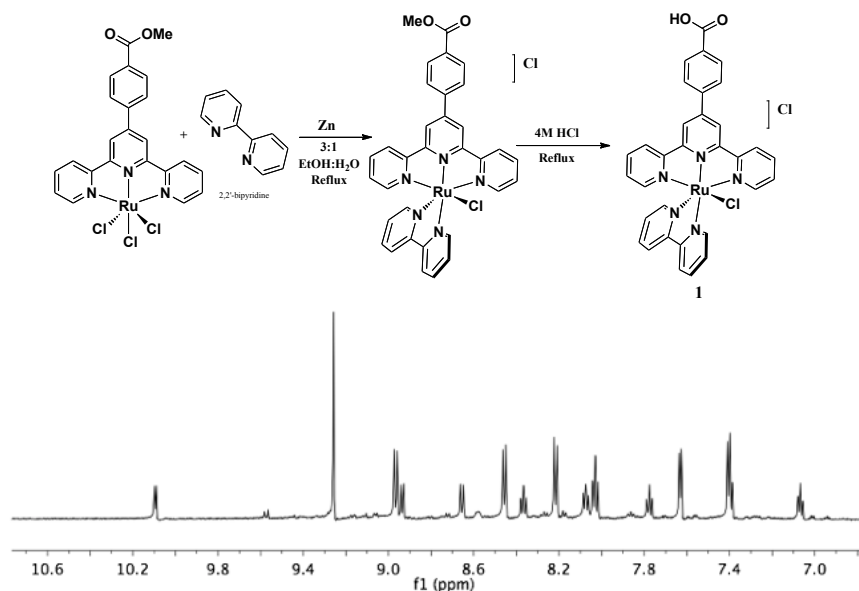
This complex was synthesized as reported for $\text{Ru}(2,2':6',2''\text{-terpyridine})\text{Cl}_3$.²⁶² In a typical procedure, $\text{RuCl}_3 \cdot 3\text{H}_2\text{O}$ (1.06 g, 4.05 mmol) and **5** (1.54 g, 4.19 mmol) were dissolved in EtOH (200 mL). The reaction was heated at reflux for 5 hrs, cooled, and the brownish-black solid was filtered, washed with EtOH and ether, and air-dried (1.77 g, 76%). This compound was used without further purification.

$[\text{Ru}(4\text{-}([2,2':6',2''\text{-terpyridin}]\text{-4'-yl})\text{benzoic acid})(2,2'\text{-bipyridine})(\text{Cl})]\text{Cl}$ (**1**)

$\text{Ru}(\text{methyl } 4\text{-}([2,2':6',2''\text{-terpyridin}]\text{-4'-yl})\text{benzoate})\text{Cl}_3$ (0.7 g, 1.22 mmol), 2,2'-bipyridine (0.2 g, 1.28 mmol), Zn powder (3.1 mmol), and LiCl (0.1 g) were dissolved in 3:1 EtOH:H₂O (140 mL). The solution was degassed with argon, and heated at reflux for 12 hrs under an atmosphere of argon. To the hot reaction was added 20 mL of a concentrated LiCl solution, the reaction was filtered hot, cooled, and the EtOH was removed by rotary evaporation. The suspension was cooled at 0°C for 4 hrs, the solid collected, washed with cold water and ether, and air-dried (0.712 g, 84 %). The methyl ester was then deprotected by refluxing in 4M HCl. $[\text{Ru}(\text{trpy-COOMe})(\text{bpy})(\text{Cl})]$ (0.600 g, 0.864 mmol) was suspended in 4M HCl (90 mL) and the suspension was heated at reflux for 24 hrs. The suspension was taken to dryness by rotary evaporation, the solid was triturated from ether, filtered, washed with cold water and ether, and collected. (0.560 g, 95%). Anal. Found (Calc.) for $\text{C}_{32}\text{H}_{35}\text{Cl}_2\text{N}_5\text{O}_8\text{Ru}$: C, 48.38 (48.67); H, 4.10 (4.47); N, 8.99 (8.87) ¹H NMR (600

MHz, DMSO- d_6): δ 10.1 (d, 1H), δ 9.27 (s, 2H), δ 8.99 (d, 2H), δ 8.95 (d, 1H), δ 8.66 (d, 1H), δ 8.48 (d, 2H), δ 8.39 (t, 1H), δ 8.22 (d, 2H), δ 8.07 (t, 1H), δ 8.02 (t, 2H), δ 7.78 (t, 1H), δ 7.63 (d, 2H), δ 7.41 (m, 3H), δ 7.08 (t, 1H). HR-ESI-MS: $m/z=646.0572^{1+}$, $[M]^{1+} = 646.0584$.

This complex was used without further purification



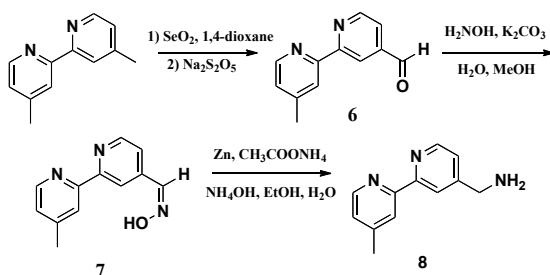
4'-Methyl-[2,2'-bipyridine]-4-carbaldehyde oxime (**7**)

To a solution of **6** (2.5 g, 12.6 mmol) in methanol (30 mL), a mixture containing hydroxylamine hydrochloride (3.0 g, 44 mmol), K₂CO₃ (8.0 g, 60 mmol) and water (30 mL) was added resulting in formation of a white precipitate. The reaction mixture was stirred at 80°C for one hour, and poured into cold water (300 mL). The white solid was collected by filtration and thoroughly washed with copious amounts of water giving a white solid (2.41 g, 90 %), having a ¹H-NMR identical to the literature spectrum.²⁶³

(4'-Methyl-[2,2'-bipyridin]-4-yl)methanamine (**8**)

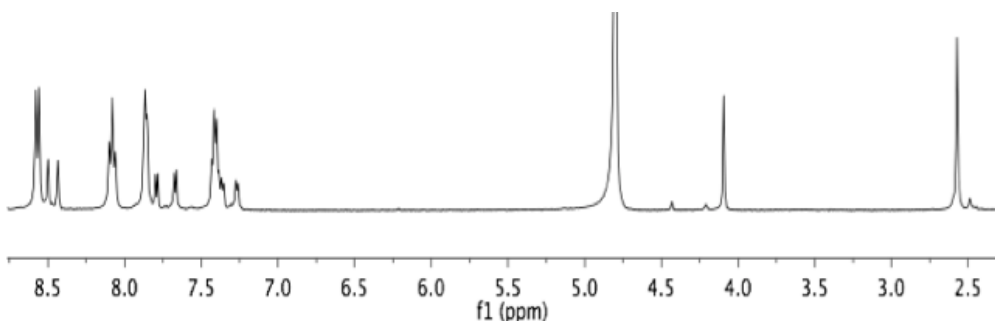
A mixture containing **7** (2.13 g, 10 mmol), ammonium acetate (1.93 g, 25 mmol), ammonia (30 mL, 50 mmol), ethanol (20 mL) and water (20 mL) were heated to reflux. Zinc powder (2.8 g, 50 mmol) was added in small portions over a 30-minute period. After the

reaction mixture was heated at reflux for 3 hours, it was cooled and filtered to remove the zinc residue. The filtrate was concentrated to remove ethanol. NaOH (7 g) was added to form a white precipitate and followed by a slightly turbid solution. The mixture was extracted with methylene chloride (3 x 100 mL), dried over MgSO₄, and the solvent was removed by rotary evaporation to yield a white solid (1.50 g, 75 %). ¹H-NMR (300 MHz, CDCl₃) δ 8.60 (d, 1H), 8.53 (d, 1H), 8.34 (s, 1H), 8.24 (s, 1H), 7.30 (d, 1H), 7.14 (d, 1H), 3.99 (s, 2H), 2.44 (s, 3H); %). ¹³C-NMR (75 MHz, CDCl₃) δ 156.31, 155.79, 153.01, 149.20, 148.85, 148.09, 124.67, 121.94, 121.89, 119.27, 45.54, 21.10. HR-ESI-MS: m/z=119.1002, [M]¹⁺=199.1109.



[Ru(bpy)₂(4'-Methyl-[2,2'-bipyridin]-4-yl)methanamine)]Cl₂ (**2**)

Ru(bpy)₂Cl₂ (0.725 g, 1.49 mmol) and **8** (0.3 g, 1.5 mmol) were dissolved in 1:1 EtOH:H₂O (80 mL). The reaction was heated at reflux under argon for 5 hrs (followed by UV/Vis), filtered hot, and the solvent removed using rotary evaporation. The red solid was triturated from ether, filtered, and air-dried (1.016 g, 96%). This complex was used without further purification. Anal. Found (Calc.) for C₃₂H₄₁Cl₂N₇O₆Ru: C, 48.73 (48.55); H, 5.16 (5.22); N, 12.25 (12.38). ¹H NMR (400 MHz, D₂O): δ 8.56 (bd, 4H), δ 8.49 (s, 1H), δ 8.43 (s, 1H), δ 8.08 (bt, 4H), δ 7.86 (bd, 4H), δ 7.79 (d, 1H), δ 7.66 (d, 2H), δ 7.41 (m, 5H), δ 7.27 (d, 1H) δ 4.09 (s, 2H), δ 2.57 (2, 3H). HR-ESI-MS: m/z=612.1450¹⁺, [M - H⁺]¹⁺=612.1449.



$[(\text{Ru}(\text{bpy})_2(\text{bpy-ph-NH-CO-trpy})\text{Ru}(\text{bpy})(\text{OH}_2))](\text{ClO}_4)_3(\text{OTf})$ (**3**)

1 (0.250 g, 0.366 mmol) was dissolved in SOCl_2 (7 mL) and stirred under an atmosphere of argon at 60°C for 4 hrs. The reaction was cooled to 50°C and the SOCl_2 was removed under reduced pressure to yield a dark red solid. To the same flask was added **2** (0.250 g, 0.366 mmol) and the two solids were purged several times with argon. To the solids was added anhydrous DMF (8 mL) along with anhydrous *N,N*-diisopropylethylamine (DIPEA) (0.5 mL). The reaction was stirred under argon at 100°C for 12 hrs, cooled, and a concentrated LiClO_4 solution (20 mL) along with additional H_2O (30 mL) was added with stirring. The solution was kept at 0°C for 4 hrs, the solid collected, washed with cold water, air-dried, and collected. Due to lack of solubility in water for purification, the coordinated chloride was then removed by dissolving the obtained red solid in MeOH (20 mL) with added AgOTf (0.187 g, 0.727 mmol (2 equivalents assuming a 100% yield of the amide coupling) and stirred under argon in the dark for 12 hrs. The solution was filtered through a bed of celite and a saturated solution of LiClO_4 (20 mL) was added to the filtrate. The MeOH was removed by rotary evaporation, and the solution was cooled to 0°C for 4 hrs. The solid was collected, washed with cold water and ether, air-dried, and collected. The crude product was purified by using size exclusion chromatography (Sephadex LH-20 with 1:1 MeOH: H_2O as eluent). Similar fractions were combined, MeOH removed by rotary evaporation, and dark

red solid collected (0.140 g, 24%). Anal. Found (Calc.) for $C_{65}H_{56}Cl_3F_3N_{12}O_{19}Ru_2S$: C, 45.83 (45.74); H, 3.61 (3.31); N, 9.98 (9.85). UV/Vis λ_{max} , nm (ϵ , $M^{-1}cm^{-1}$): in H₂O, 460 (26085), 334 (sh, 33928), 315 (sh, 49755), 287 (144080), 254 (sh, 47093), 242 (55438) ¹H NMR (600 MHz, CD₃CN): δ 9.61 (d, 1H), δ 8.82 (s, 2H), δ 8.64 (d, 1H), δ 8.57 (d, 2H), δ 8.49 (bd, 5H), δ 8.42 (s, 1H), δ 8.34 (m, 3H), δ 8.24 (d, 2H), δ 8.17 (d, 2H), δ 8.06 (m, 5H), δ 7.96 (t, 1H), δ 7.82 (t, 1H), δ 7.72 (m, 6H), δ 7.63 (d, 1H), δ 7.54 (d, 2H), δ 7.37 (m, 6H), δ 7.34 (d, 1H), δ 7.25 (d, 1H), δ 7.09 (t, 1H), δ 4.79 (d, 2H), δ 2.54 (s, 3H). HR-ESI-MS: $m/z=401.7417^{3+} = 1205.2251$, $[M - H^+]^{3+}=1205.2234$; $m/z=668.1054^{2+}=1336.2108$, $[M + ClO_4 + MeO]^{2+}=1336.1986$; $m/z=1435.144^{1+}$, $[M + 2 ClO_4 + MeO]^{1+}=1435.1471$.

[Ru(trpy-COOH)(2,2'-bipyridine)(OH₂)] (OTf)₂ (**9**)

This complex was prepared for a direct comparison between **3** and the monomer constituents. **1** (0.250 g, 0.367 mmol) was suspended in DCM (80 mL) and triflic acid (4 mL) was slowly added. The reaction was stirred at ambient temperature for 4 hrs with a stream of argon being flowed through the vessel. To the mixture was added ether (200 mL) with stirring. The solid was filtered, washed with ether, and collected (0.313g, 94%). The triflate ligand can be exchanged with water by dissolving the complex in water. UV/Vis λ_{max} , nm (ϵ , $M^{-1}cm^{-1}$): in H₂O, 490 (11499), 333 (19759), 314 (30297), 287 (46809), 233 (24304) ¹H NMR (600 MHz, D₂O/NaOD): δ 9.49 (d, 1H), δ 8.52 (d, 1H), δ 8.45 (d, 2H), δ 8.25 (d, 2H), δ 8.18 (t, 1H), δ 8.15 (d, 1H), δ 7.92 (t, 1H), δ 7.86 (d, 2H), δ 7.72 (m, 4H), δ 7.57 (d, 2H), δ 7.44 (t, 1H), δ 7.15 (t, 2H), δ 6.98 (d, 1H), δ 6.63 (t, 1H). HR-ESI-MS: $m/z= 760.0406^{1+}$, $[M - OH_2 + OTf]^{1+} = 760.0415$

[Ru(bpy)₂(4,4'-dimethyl-2,2'-bipyridine)]Cl₂ (**10**)

This complex was prepared for a direct comparison between **3** and its constituents. Ru(bpy)₂Cl₂ (0.6 g, 1.24 mmol) and 4,4'-dimethyl-2,2'-bipyridine (0.230 g, 1.24 mmol) were heated at reflux in 1:1 EtOH:H₂O for 4 hrs (followed by UV/Vis). The solution was filtered hot and the solvent was removed via rotary evaporation. The red solid was triturated from ether, collected, and air-dried (0.813 g, 96%). This complex was used without further purification. ¹H NMR (300 MHz, D₂O): δ 8.47 (d, 4H), δ 8.29 (s, 2H), δ 7.96 (t, 4H), δ 7.67 (d, 4H), δ 7.55 (d, 2H), δ 7.36 (q, 4H), δ 7.13 (d, 2H), δ 2.45 (s, 6H). HR-ESI-MS: m/z=597.1337¹⁺, [M - H⁺]¹⁺ = 597.134. The molar extinction coefficient at 456 nm (14300 M⁻¹ cm⁻¹) is consistent with previously reported results.

4.3 Results and Discussion

Unlike amide couplings utilizing acid chloride/amine reactions, which are typically carried out at or below room temperature, formation of the amide link between complexes requires elevated temperatures to proceed at reasonable rates due to the decreased nucleophilicity of the coordinated (4'-methyl-[2,2'-bipyridin]-4-yl)methanamine (**8**) ligand.^{264,265} This hypothesis is supported by control experiments: i) the acid chloride derivative of **1** was shown to react with **8** in DMF in the presence of *N,N*-diisopropylethylamine (DIPEA) at room temperature with complete conversion (by NMR) ii) by contrast, **2** does not react with benzoyl chloride or the acid chloride of 4-([2,2':6',2"-terpyridin]-4'-yl)benzoic acid (**4**) in DMF with DIPEA at 40°C, iii) both of these reactions proceed to completion at 100°C.

The methylene-based amide bridge between ligands provides a saturated link between the two metal complexes resulting in retention of the spectral and redox properties of the

constituents. In the UV-Visible absorption spectrum of **3**, a MLCT absorption appears at $\lambda_{\text{max}} \sim 460$ nm arising from overlapping MLCT absorptions of both the chromophore and the catalyst (Figure C.4). The spectrum is the sum of the constituents as shown in Figure 4.1. The high molar absorptivity of the MLCT band for **3** ($26,000 \text{ M}^{-1} \text{ cm}^{-1}$) is near the sum of the component MLCT extinction coefficients, $11,500 \text{ M}^{-1} \text{ cm}^{-1}$ for $[\text{Ru}(4-([2,2':6',2''\text{-terpyridin}]-4'\text{-yl)benzoic acid})(\text{bpy})(\text{OH}_2)^{2+}]^{2+}$ (**9**) and $14,300 \text{ M}^{-1} \text{ cm}^{-1}$ for $[\text{Ru}(\text{bpy})_2(4,4'\text{-dimethyl-2,2'\text{-bipyridine})]^{2+}$ (**10**) (Figure C.5 and Figure C.6).²⁶⁶ Consistent with deprotonation of $-\text{Ru}^{\text{II}}-\text{OH}_2^{2+}$ ($\text{p}K_a = 10.0$) a red shift in the spectrum occurs upon increasing the pH to ~ 13 , Figure C.4.

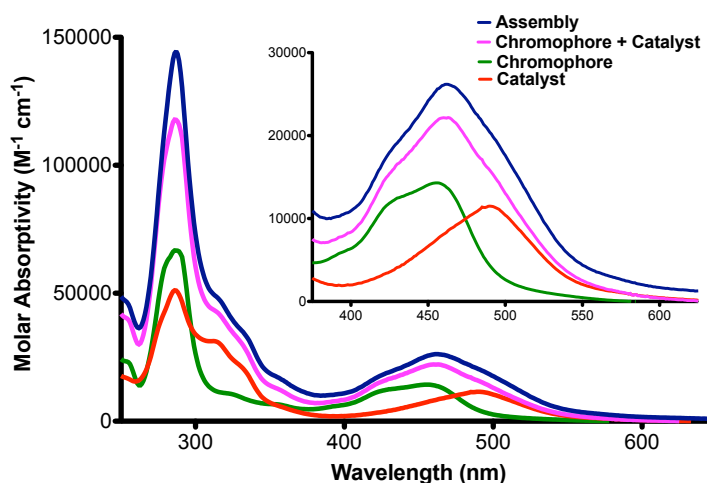


Figure 4.1. UV/Visible absorption spectra of **9** (red), **10** (green), **9 + 10** (pink), and **3** (blue) in H_2O at 25°C .

Cyclic voltammograms of **3** at $\text{pH} = 2.1$ include waves for the expected $\text{Ru}^{\text{II}}-\text{Ru}^{\text{III}}-\text{OH}/\text{Ru}^{\text{II}}-\text{Ru}^{\text{II}}-\text{OH}_2$, $\text{Ru}^{\text{II}}-\text{Ru}^{\text{IV}}=\text{O}/\text{Ru}^{\text{II}}-\text{Ru}^{\text{III}}-\text{OH}$, and $\text{Ru}^{\text{III}}-\text{Ru}^{\text{IV}}=\text{O}/\text{Ru}^{\text{II}}-\text{Ru}^{\text{IV}}=\text{O}$ couples at $E_{1/2} = 1.01 \text{ V}$, 1.11 V , and 1.22 V (vs NHE), respectively (Figure 4.2). As for the related monomer, $\text{Ru}(\text{trpy})(\text{bpy})(\text{OH}_2)^{2+}$, the first two are pH dependent with the results summarized in the $E_{1/2}(\sim E^{\circ})$: E° is the formal potential) vs pH (Pourbaix) diagram in Figure 4.3.^{259,267-269}

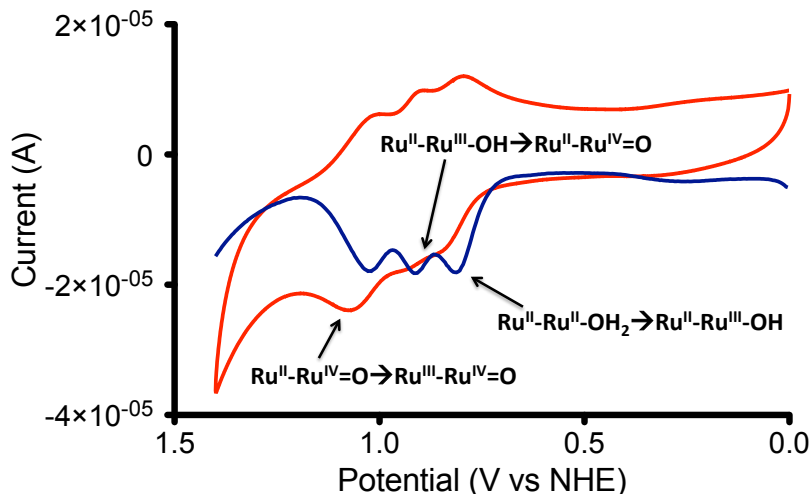


Figure 4.2. Cyclic voltammogram of **3** at pH = 2.1 (0.05 M NaH₂PO₄, 0.05 M H₃PO₄, 0.5 M KNO₃) at 100 mV/s with a glassy carbon working electrode (0.07 cm², red), and a differential pulse voltammogram of **3** (blue) at 25°C.

As a summary of the $E_{1/2}$ -pH results: i) Both $-\text{Ru}^{\text{III/II}}$ and $-\text{Ru}^{\text{IV/III}}$ couples are pH dependent due to acid-base equilibria for $-\text{Ru}^{\text{III}}-\text{OH}_2^{3+}$ ($\text{p}K_{\text{a},1} = 1.0$) and $-\text{Ru}^{\text{II}}-\text{OH}_2^{2+}$ ($\text{p}K_{\text{a},1} = 10.0$). $E_{1/2}$ values are 1.05 V for the $-\text{Ru}^{\text{III}}-\text{OH}_2^{3+}/-\text{Ru}^{\text{II}}-\text{OH}_2^{2+}$ couple and 1.17 V for the $-\text{Ru}^{\text{IV}}=\text{O}^{2+}/-\text{Ru}^{\text{III}}-\text{OH}_2^{3+}$ couple in 0.1 M HNO₃. By comparison, for Ru(tpy)(bpy)(OH₂)²⁺ the corresponding values are 1.04 V for the $\text{Ru}^{\text{III}}-\text{OH}_2^{3+}/\text{Ru}^{\text{II}}-\text{OH}_2^{2+}$ and 1.15 V for the $\text{Ru}^{\text{IV}}=\text{O}^{2+}/\text{Ru}^{\text{III}}-\text{OH}_2^{3+}$.^{17,26-28} Below pH = 1.0, $E_{1/2}$ for the $-\text{Ru}^{\text{IV}}=\text{O}^{2+}/-\text{Ru}^{\text{III}}-\text{OH}_2^{3+}$ couple increases by 120 mV/pH unit consistent with a $1\text{e}^-/2\text{H}^+$ couple. Below pH = 0.5, $E^{\circ}(\text{Ru}^{\text{III/II}}) > E^{\circ}(-\text{Ru}^{\text{IV}}=\text{O}^{2+}/-\text{Ru}^{\text{III}}-\text{OH}_2^{3+})$ and the $\text{Ru}^{\text{III/II}}$ couple at the chromophore is a sufficient oxidant to oxidize the aqua complex from $-\text{Ru}^{\text{III}}-\text{OH}_2^{3+}$ to $-\text{Ru}^{\text{IV}}=\text{O}^{2+}$. iii) At pH = 11.0, the variation in $E_{1/2}$ with pH becomes ~ 30 mV/pH unit consistent with the $2\text{e}^-/1\text{H}^+$ couple $-\text{Ru}^{\text{IV}}=\text{O}^{2+}/-\text{Ru}^{\text{II}}-\text{OH}^+$. As the pH is increased above 11.0, $E^{\circ}(-\text{Ru}^{\text{III}}-\text{OH}^{2+/+}) > E^{\circ}(-\text{Ru}^{\text{IV}}=\text{O}^{2+}/-\text{Ru}^{\text{III}}-\text{OH}^{2+})$, and $-\text{Ru}^{\text{III}}-\text{OH}^{2+}$ is unstable with respect to disproportionation into $-\text{Ru}^{\text{IV}}=\text{O}^{2+}$ and $-\text{Ru}^{\text{II}}-\text{OH}^+$. iv) Oxidation of the chromophore is pH independent and occurs at $E_{1/2}(\text{Ru}^{\text{III/II}}) = 1.23$ V. Notably, within experimental error, the potential for the oxidation of

the chromophore is independent of whether the catalyst is $-\text{Ru}^{\text{III}}-\text{OH}_2^{3+}$ or $-\text{Ru}^{\text{IV}}=\text{O}^{2+}$. This observation is consistent with minimal interactions across the bridge between the complexes. E° values are slightly more positive than for the constituent complexes because of the higher overall charge on the assembly (see Figure 4.4).

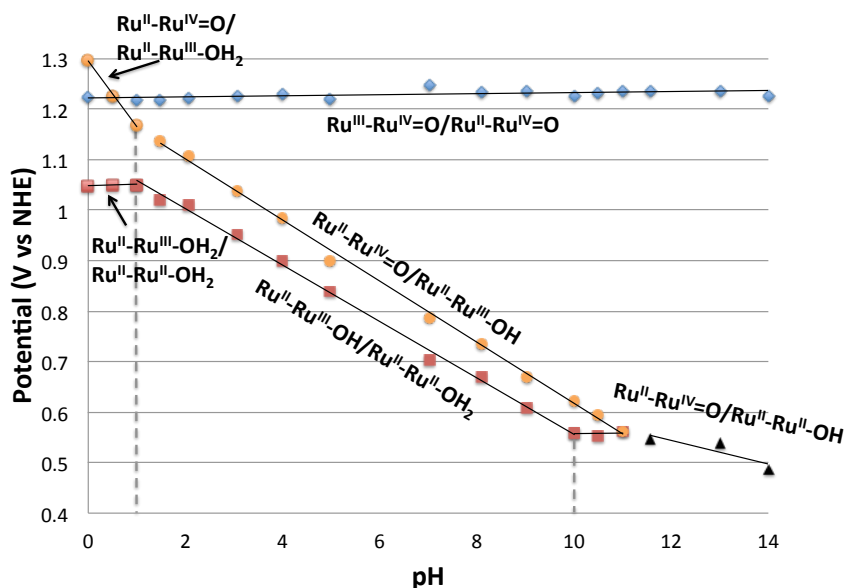


Figure 4.3. $E_{1/2}$ -pH diagram for assembly **3**. $E_{1/2}$ values were obtained as peak current maxima in differential pulse voltammograms. The solid lines are best fits to lines of slope ~ 0 mV/pH for the $-\text{Ru}^{\text{III}}-\text{OH}_2^{3+}/-\text{Ru}^{\text{II}}-\text{OH}_2^{2+}$ and $\text{Ru}^{\text{III/II}}$ couples, 56 mV/pH for $-\text{Ru}^{\text{III}}-\text{OH}_2^{2+}/-\text{Ru}^{\text{II}}-\text{OH}_2^{2+}$, 60 mV/pH for $-\text{Ru}^{\text{IV}}=\text{O}^{2+}/-\text{Ru}^{\text{III}}-\text{OH}_2^{2+}$, 130 mV/pH for $-\text{Ru}^{\text{IV}}=\text{O}^{2+}/-\text{Ru}^{\text{III}}-\text{OH}_2^{2+}$, and 24 mV/pH for the $-\text{Ru}^{\text{IV}}=\text{O}^{2+}/-\text{Ru}^{\text{II}}-\text{OH}^+$ couple. The dashed, vertical lines are pK_a values. The $E_{1/2}$ -pH plots for individual couples are labeled. At 23 $^{\circ}$ C in 0.5 M KNO_3 0.1 M in total added buffer. The $\text{Ru}^{\text{V}}=\text{O}^{3+}/-\text{Ru}^{\text{IV}}=\text{O}^{2+}$ couple appears at $E_{\text{p,a}} \sim 1.87$ V in 2% water-propylenecarbonate 0.1 M in TBAH.

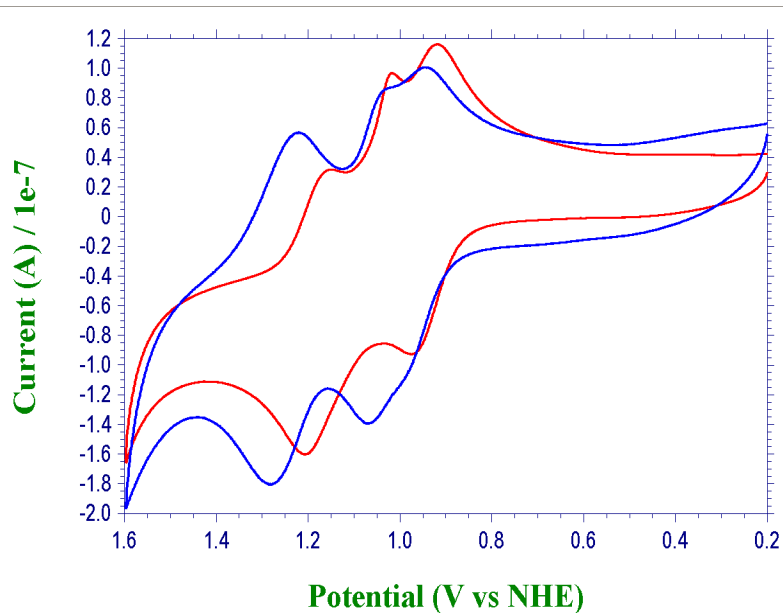


Figure 4.4. Comparison cyclic voltammograms in pH = 3.06 (0.1 M phosphate, 0.5 M KNO₃) at 100 mV/s of **3** (blue) and an equal molar solution of **9** and **10** (red). Currents are normalized to the water oxidation catalyst Ru^{III/II} redox couple for comparison purposes.

In water, the expected Ru^{III}-Ru^V=O³⁺/Ru^{III}-Ru^{IV}=O²⁺ couple was not observable due to the onset of water oxidation at ~1.6 V, Figure 4.2. Oxidation of **3** was investigated by differential pulse voltammetry in 2% water-propylene carbonate (PC; V:V) mixtures to minimize water oxidation.²⁷⁰ These measurements reveal an additional wave for the expected -Ru^V=O³⁺/-Ru^{IV}=O²⁺ couple at E_{p,a} ~1.87 V (E_{p,a} is the anodic peak potential) relative to the (Ru^{III/II})^{3+/2+}-Ru^{IV}=O wave at E_{1/2} = 1.23 V, Figure C.2.

Table 4.2. Summary of Electrochemical Properties

Complex	E _{1/2} (V vs NHE) ^a			pK _a ^c	
	Cat. Ru ^{II/III}	Cat. Ru ^{III/IV}	Cat. Ru ^{IV/V}	Ru ^{II} -OH ₂	Ru ^{III} -OH ₂
3	0.95	1.04	~1.87 ^b	10.0	1.0
9	0.93	1.03	~1.80	10.5 ^d	1.7 ^d
10^e	-	-	-	-	-

a In pH = 3.1 (0.43 M H₂PO₄, 0.07 M H₃PO₄, 0.5M KNO₃) at 23oC from differential pulse voltammetry peak currents at glassy carbon (0.07 cm²) with platinum counter electrode, vs. the Ag/AgCl reference electrode (0.197 vs. NHE). b In 2% water-propylene carbonate, see

text. c From pH-dependent electrochemical measurements (Figure 4.3). d Data for Ru(tpy)(bpy)(OH₂)²⁺.^{259,267-269} e Ru(bpy)₂(4,4'-Me₂bpy)₂⁺.²⁶⁶

As noted in Figure 4.2 and Figure C.7, there is clear evidence for catalytic water oxidation with an onset at ~1.6 V. The ability of **3** to act as a catalyst for net Ce^{IV} oxidation of water, $4 \text{ Ce}^{\text{IV}} + 2 \text{ H}_2\text{O} \rightarrow 4 \text{ Ce}^{\text{III}} + \text{O}_2 + 4 \text{ H}^+$, was investigated by a series of mixing experiments. In these experiments, x30 Ce^{IV} in 1.0 M HNO₃ was added to **3** (Figure C.10). Addition of Ce(IV) resulted in immediate loss of the MLCT absorption of the chromophore with its reappearance upon complete consumption of Ce^{IV}. Evolved oxygen was monitored by gas chromatography giving a yield of ~70% O₂ based on Ce^{IV} added (see Appendix C). Although not studied in detail, as for related single site Ru catalysts^{17,26-28}, water oxidation occurs by oxidative activation by proton coupled electron transfer (PCET) $\text{Ru}^{\text{II}}\text{-Ru}^{\text{II}}\text{-OH}_2^{4+} \xrightarrow{-e^-, -\text{H}^+} \text{Ru}^{\text{II}}\text{-Ru}^{\text{III}}\text{-OH}^{4+}$; $\text{Ru}^{\text{II}}\text{-Ru}^{\text{III}}\text{-OH}^{4+} \xrightarrow{-e^-, -\text{H}^+} \text{Ru}^{\text{II}}\text{-Ru}^{\text{IV}}\text{=O}^{4+}$ followed by two single electron oxidations to $\text{Ru}^{\text{III}}\text{-Ru}^{\text{V}}\text{=O}^{6+}$ and water attack on the electrophilic O-atom by water with proton transfer to a second water molecule by atom-proton transfer (APT) (Figure C.7).^{35,121,271-273}

We have demonstrated here a versatile approach for preparing chromophore-catalyst assemblies based on amide couplings between pre-formed complexes. This route offers synthetic generality and flexibility in the nature of the chromophore, catalyst, and connecting link. The individual properties of the constituents are retained, allowing for optimization of the properties of the separate components before being placed into an assembly by application of the “modular approach”.^{42,134,173,193}

Preliminary transient absorption and emission results in Ar deaerated deionized water at room temperature provide evidence for rapid intra-assembly energy transfer. MLCT

excitation (445 nm) of Ru(trpy)(bpy)(OH₂)²⁺ results in no observable transient on the 15 nsec time scale by absorption monitoring. Emission is observed following excitation of **2** with $\tau = 568$ ns. As monitored by transient absorption and emission measurements, excitation of **3** (445 nm) results in biphasic kinetics with $\tau_1 = 18$, $\tau_2 = 410$ nsec ($k_1 = 5 \times 10^7$ s⁻¹, $k_2 = 2.4 \times 10^6$ s⁻¹), Appendix C. These observations are qualitatively consistent with excitation at the chromophore followed by intra-assembly energy transfer $(\text{Ru}^{\text{II}})\text{-Ru}^{\text{II}}\text{-OH}_2^{2+} \xrightarrow{h\nu} (\text{Ru}^{\text{II}})^*\text{-Ru}^{\text{II}}\text{-OH}_2^{2+} \xrightarrow{\text{rapid}} (\text{Ru}^{\text{II}})\text{-Ru}^{\text{II}}\text{-OH}_2^{2+*}$, and rapid decay of $\text{-Ru}^{\text{II}}\text{-OH}_2$ in competition with emission from the excited state of the chromophore $(\text{Ru}^{\text{II}})^*\text{-Ru}^{\text{II}}\text{-OH}_2^{2+} \longrightarrow (\text{Ru}^{\text{II}})\text{-Ru}^{\text{II}}\text{-OH}_2^{2+}$.²⁷³ The time scale is relatively slow compared to the far faster typical sub-psec rates of injection into TiO₂ for surface-bound analogs. Experiments are currently underway to examine in more detail the photophysical properties of the assembly and its oxidized forms.

4.4 Associated Content

Appendix C: Electrochemical, kinetic, photophysical and oxygen measurement analysis

Chapter 5: PHOTOINDUCED ELECTRON TRANSFER IN A CHROMOPHORE-CATALYST ASSEMBLY ANCHORED TO TiO₂

Reprinted with permission from Ashford, D. L.; Song, W. J.; Concepcion, J. J.; Glasson, C. R. K.; Brennaman, M. K.; Norris, M. R.; Fang, Z.; Templeton, J. L.; Meyer, T. J., *J. Am. Chem. Soc.* **2012**, *134* (46), 19189-19198. Copyright American Chemical Society 2014

5.1 Introduction

In producing solar fuels by artificial photosynthesis, as in natural photosynthesis, a key requirement is the integration of UV-visible-near IR light absorption with a sequence of electron transfer events to drive the component half reactions: water oxidation into protons and oxygen and reduction of CO₂ to CO, other oxygenates, or hydrocarbons.^{2,42,166,176,274}

Water oxidation in photosystem II (PSII) occurs through a series of four sequential single-photon, single-electron transfer events, which activate the multi-electron CaMn₄ catalyst in the oxygen-evolving complex (OEC) towards water oxidation and O₂ release.^{20,21,32,275,276}

Activation and water oxidation are driven by light absorption at an “antenna complex”, followed by sensitization of chlorophyll P₆₈₀ that initiates a series of electron transfer events resulting in oxidative activation of the OEC.^{89,257,277-280} Water oxidation is coupled to reduction of plastoquinone to plastoquinol, ultimately with delivery of reductive equivalents to photosystem I and further to the Calvin cycle for light driven CO₂ reduction.²⁸¹⁻²⁸³

Photosystem II is a highly complex, membrane-bound assembly that has remained unchanged over 2.4 billion years.^{20-22,284} Successful strategies for artificial photosynthesis and large scale solar fuels production will require straightforward approaches and simple

designs. One approach, illustrated in Figure 1.6, is a photoelectrochemical approach based on Dye Sensitized Photoelectrosynthesis Cells (DSPECs, Figure 1.6).^{174,280,285-287} The figure illustrates a photoanode for water oxidation based on a chromophore-catalyst assembly surface-bound to a wide band gap metal oxide semiconductor, typically TiO₂. Chromophore excitation at the surface is followed by excited state electron injection into the conduction band of the semiconductor with the reductive equivalents delivered to a cathode for catalytic water reduction to hydrogen or CO₂ reduction to CH₄, the reaction illustrated in Figure 1.6. The DSPEC approach is closely related to Dye Sensitized Solar Cells (DSSCs), but the target is the production and collection of oxygen and a high energy fuel at spatially separated electrodes rather than a photopotential and photocurrent.^{42,288,289}

Key elements in DSPEC designs include light absorption throughout the solar spectrum ($\lambda < 1000$ nm for water splitting by single photon absorption), excited state electron transfer, utilization of internal free energy gradients to drive long-range electron and proton transfer, and stepwise activation of catalysts for carrying out multiple electron-multiple proton catalysis.^{29,42,175} In a successful photoanode design, the water oxidation catalyst and chromophore must be in sufficiently close proximity for rapid and efficient electron transfer oxidation of the catalyst to occur following chromophore excitation and electron injection into the conduction band of the semiconductor. At the same time, the intramolecular structure should inhibit back electron transfer from the electrode to the oxidatively activated catalyst on a time scale that allows for the initial step in O–O bond formation.^{34,35,42,290}

Exploitation of this strategy requires a versatile synthetic approach for linking chromophores with water oxidation catalysts to control intramolecular electron transfer rates. The strategy must be compatible with the presence of surface binding functional groups, such

as phosphonic acids. These are required for surface stability in aqueous environments and for creating electronic coupling pathways from the excited state of the chromophore to the conduction band or acceptor levels of the metal oxide electrodes.^{141,144,181}

We previously reported on electrocatalytic water oxidation by the assemblies $[(\text{bpy})_2\text{Ru}^{\text{II}}(\text{bpm})\text{Ru}^{\text{II}}(\text{trpy})(\text{OH}_2)]^{4+}$ and $[(\text{bpy})_2\text{Ru}^{\text{II}}(\text{bpm})\text{Ru}^{\text{II}}(\text{Mebimpy})(\text{OH}_2)]^{4+}$ (bpy=2,2'-bipyridine; bpm=2,2'-bipyrimidine; trpy=2,2':6',2''-terpyridine; Mebimpy=2,6-bis(1-methyl-benzimidazol-2-yl)pyridine) both in solution and, as phosphonate derivatives, on metal oxide electrodes.¹⁹³ We have also reported on photoinduced electron injection and back electron transfer rates for the assembly $[(\text{dcb})_2\text{Ru}(\text{bpy-Mebim}_2\text{-py})\text{Ru}(\text{bpy})(\text{OH}_2)](\text{OTf})_4$ (dcb = 4,4'-dicarboxylic acid-2,2'-bipyridine; bpy-Mebim₂py = 2,2'-(4-methyl-[2,2':4',4''-terpyridine]-2'',6''-diyl)bis(1-methyl-1H-benzo[*d*]imidazole) anchored to TiO₂ by carboxylic acid linkers.¹³⁴ For the latter, low electron injection efficiencies were attributed to a lowest metal-to-ligand charge transfer (MLCT) excited state localized on the conjugated bridging ligand leading to competitive, deleterious nonradiative decay.

Recently, we also reported a general approach for the synthesis of chromophore-catalyst assemblies based on an amide-linkage strategy in the assembly $[(\text{Ru}(\text{bpy})_2(\text{bpy-NH-CO-trpy})\text{Ru}(\text{bpy})(\text{OH}_2)]^{4+}$ (bpy-NH-CO-trpy = 4-([2,2':6',2''-terpyridin]-4'-yl)-N-((4'-methyl-[2,2'-bipyridin]-4-yl)methyl) (4)).¹⁸⁹ In this strategy, the bridging benzamide introduces a unit of saturation between the linked chromophore and catalyst where the separate properties of the chromophore and catalyst are retained.¹⁸⁹ Generically, saturated amide links are appealing in providing a basis for controlling the extent of electronic coupling by synthetic modification, and with it, rates of intramolecular electron transfer.

We report here on the photophysical dynamics of the phosphonic acid-derivatized, amide-linked assembly, $[(\text{PO}_3\text{H}_2\text{-CH}_2)_2\text{-bpy})_2\text{Ru}_a(\text{bpy-NH-CO-trpy})\text{Ru}_b(\text{bpy})(\text{OH}_2)]^{4+}$ ($(\text{PO}_3\text{H}_2\text{-CH}_2)_2\text{-bpy} = ([2,2'\text{-bipyridine}]-4,4'\text{-diyl-bis(methylene)})\text{diphosphonic acid}$) (**1**) on TiO_2 ($\text{TiO}_2\text{-1}$; $[\text{TiO}_2\text{-Ru}_a^{\text{II}}\text{-Ru}_b^{\text{II}}\text{-OH}_2]^{4+}$) which is one of a limited number of phosphonate-derivatized chromophore-catalyst assemblies reported with metal oxide attachment.¹⁹³ A general synthetic procedure is described, as are the characterization, and surface binding of the assembly and its spectroscopic, electrochemical, and photophysical characterization. Interfacial dynamics of the assembly on TiO_2 , injection yields, and back electron transfer rates are compared with the constituent monomers $[\text{Ru}((\text{PO}_3\text{H}_2\text{-CH}_2)_2\text{-bpy})_2(\text{dmb})]^{2+}$ (**2**) ($\text{dmb} = 4,4'\text{-dimethyl-2,2'\text{-bipyridine}}$) and $[\text{Ru}(\text{trpy})((\text{PO}_3\text{H}_2\text{-CH}_2)_2\text{-bpy})(\text{OH}_2)]^{2+}$ (**3**) (Figure 5.1).

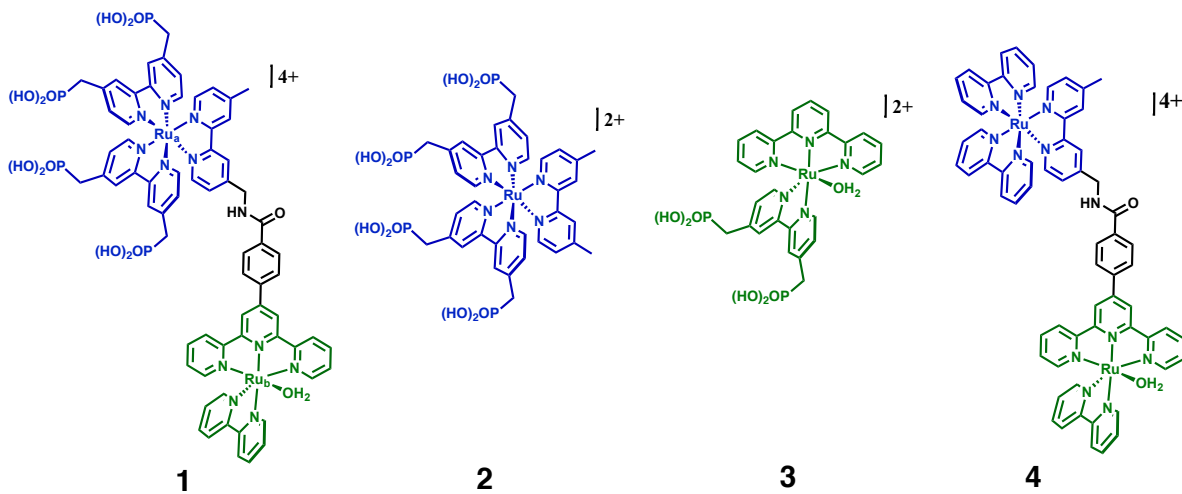


Figure 5.1. Structures of the assembly $[(4,4'\text{-}(\text{PO}_3\text{H}_2\text{-CH}_2)_2\text{-bpy})_2\text{Ru}_a(\text{bpy-NH-CO-trpy})\text{Ru}_b(\text{bpy})(\text{OH}_2)]^{4+}$ (**1**), chromophore $[\text{Ru}(4,4'\text{-}(\text{PO}_3\text{H}_2\text{-CH}_2)_2\text{bpy})_2(\text{dmb})]^{2+}$ (**2**), catalyst $[\text{Ru}(\text{trpy})(4\text{-PO}_3\text{H}_2\text{-CH}_2\text{-bpy})(\text{OH}_2)]^{2+}$ (**3**), and the non-phosphonated assembly $[(\text{Ru}(\text{bpy})_2(\text{bpy-ph-NH-CO-trpy})\text{Ru}(\text{bpy})(\text{OH}_2)]^{4+}$ (**4**) previously reported.¹⁸⁹

5.2 Experimental

Materials

$[\text{Ru}(\eta^6\text{-Bz})(\text{Cl})_2]_2$ ²⁹¹, (4'-methyl-[2,2'-bipyridin]-4-yl)methanamine¹⁸⁹, ([2,2'-bipyridine]-4,4'-diylbis(methylene)) diphosphonic acid²⁹², $\text{Ru}(\text{trpy})\text{Cl}_3$ ²⁶² $[\text{Ru}(\eta^6\text{-Bz})(2,2'\text{-bipyridine})(\text{Cl})](\text{Cl})$ ²⁹², and $[\text{Ru}(\text{trpy})(\text{PO}_3\text{H}_2\text{-CH}_2\text{-bpy})(\text{OH}_2)]^{2+}$ (**3**)^{293,294} were synthesized as reported previously.

4-([2,2':6',2''-terpyridin]-4'-yl)benzoic acid

This ligand was prepared by a modified literature procedure.²⁶¹ 4-formylbenzoic acid (5.57 g, 37.1 mmol) was dissolved in ~120 mL ethanol. To this mixture was added 1-(pyridin-2-yl)ethanone (8.55 g, 70.6 mmol) and 6 mL of concentrated NH_4OH followed by the addition of NaOH (2.5 g) dissolved in ~6 mL H_2O . The reaction was stirred open to the air at 40°C overnight during which time a white precipitate began to form. The reaction was cooled, and the precipitate was collected to give clean 4-([2,2':6',2''-terpyridin]-4'-yl)benzoic acid (5.5 g). Allowing the filtrate to sit for an additional day yielded more precipitate, which yielded additional product (2.5 g). This compound was used without further purification (8.0 g, 61.0%). ¹H NMR (600 MHz, DMSO-d_6): δ (ppm) 8.76 (d, 2H), 8.72 (s, 2H), δ 8.64 (d, 2H), δ 8.07 (d, 2H), δ 8.04 (dt, 2H), δ 7.83 (d, 2H), δ 7.52 (dd, 2H). HR-ESI-MS: $m/z=354.1234^{1+}$, $[\text{M} + \text{H}^+]^{1+} = 354.1243$.

$[\text{Ru}(4\text{-}([2,2':6',2''\text{-terpyridin}]\text{-4'-yl)benzoic acid})(\text{bpy})(\text{Cl})]\text{Cl}$ (**5**)

$[\text{Ru}(\text{bpy})(\eta^6\text{-Bz})(\text{Cl})]\text{Cl}$ (1.75 g, 4.31 mmol) and 4-([2,2':6',2''-terpyridin]-4'-yl)benzoic acid (1.52 g, 4.30 mmol) were heated at reflux for 20 minutes at 160°C in ~40 mL of 1:1 EtOH:H₂O in a microwave oven. The solution was cooled, filtered, and concentrated on a rotary evaporator. The dark red solid was triturated with ether, collected, and air dried (2.89 g, 98%). This complex was used without further purification. ¹H NMR and mass spectrometric analysis match those of the previously reported complex.¹⁸⁹ ¹H NMR

(600 MHz, DMSO- d_6): δ (ppm) 10.1 (d, 1H), 9.27 (s, 2H), 8.99 (d, 2H), 8.95 (d, 1H), 8.66 (d, 1H), 8.48 (d, 2H), 8.39 (t, 1H), 8.22 (d, 2H), 8.07 (t, 1H), 8.02 (t, 2H), 7.78 (t, 1H), 7.63 (d, 2H), 7.41 (m, 3H), 7.08 (t, 1H). HR-ESI-MS: $m/z=646.0572^{1+}$, $[M]^{1+}=646.0584$.

[Ru(bpy-ph-NH-CO-trpy)(bpy)(Cl)]PF₆ (**6**)

[Ru(4-([2,2':6',2''-terpyridin]-4'-yl)benzoic acid)(bpy)(Cl)]Cl (2 g, 2.93 mmol) was dissolved in SOCl₂ (10 mL) and heated at reflux under an atmosphere of argon for 4h. The reaction mixture was cooled to 50°C and SOCl₂ removed under reduced pressure to yield a dark red solid. To the same flask was added (4'-methyl-[2,2'-bipyridin]-4-yl)methanamine (0.584 g, 2.93 mmol). The two solids were purged several times with argon followed by addition of anhydrous DMF (20 mL) and anhydrous *N,N*-diisopropylethylamine (DIPEA) (1 mL). The reaction was stirred under argon at 100°C overnight, the reaction solution cooled to room temperature, and a saturated solution of NH₄PF₆ (5 mL) was added with 50 mL of H₂O. The suspension was stirred for several hours to ensure complete precipitation. The solid was collected, washed with water and ether, and air dried (2.7 g, 97%). This complex was used without further purification. The trpy-bpy protons of the Ru complex are sharp, but the free bipyridine peaks are broad due to the fluxional behavior of the ligand on the NMR time scale. ¹H NMR (600 MHz, DMSO- d_6): δ (ppm) 10.1 (d, 1H), 9.47 (bs, 1H), 9.26 (s, 2H), 8.96 (d, 2H), 8.93 (d, 1H), 8.80 (bs, 2H), 8.65 (bd, 2H), 8.44 (d, 1H), 8.35 (m, 2H), 8.23 (d, 2H), 8.05 (m, 3H), 7.78 (t, 1H), 7.63 (d, 2H), 7.39 (m, 3H), 7.29 (bs, 1H), 7.06 (t, 1H), 7.02 (bs, 1H), 4.70 (bs, 2H), 2.43 (bs, 3H). HR-ESI-MS: $m/z=827.1552^{1+}$, $[M]^{1+}=827.1588$

[Ru(bpy)(Cl)(trpy-bpy)Ru(Bz)(Cl)](Cl)(PF₆) (**7**)

[Ru(bpy)(Cl)(trpy-bpy)]PF₆ (1.49 g, 1.53 mmol) and [Ru(η^6 -Bz)(Cl)₂]₂ (0.38 g, 0.77 mmol) were heated at reflux in anhydrous methanol overnight under an atmosphere of argon.

The reaction was cooled, and the precipitate was collected and washed with methanol and ether. Recrystallization from methanol gave pure product (1.3 g, 70%). This complex was used without further purification. ^1H NMR (600 MHz, d_6 -DMSO): δ (ppm) 10.1 (d, 1H), 9.57 (d, 1H), 9.52 (t, 1H), 9.47 (d, 1H), 9.26 (s, 2H), 8.96 (d, 2H), 8.93 (d, 1H), 8.51 (m, 2H), 8.46 (m, 2H), 8.37 (t, 1H), 8.24 (d, 2H), 8.06 (t, 1H), 8.03 (t, 2H), 7.80 (t, 1H), 7.70 (d, 1H), 7.65 (m, 3H), 7.41 (m, 3H), 7.07 (t, 1H), 6.19 (s, 6H), δ .77 (dd, 2H), 2.58 (s, 3H). HR-ESI-MS: $m/z=521.04346^{2+} = 1042.0869$, $[\text{M}]^{2+} = 1042.0789$, $m/z=1187.03997^{1+}$, $[\text{M} + \text{PF}_6]^{1+} = 1187.0431$.

$[\text{Ru}(\text{bpy})(\text{OTf})(\text{trpy-bpy})\text{Ru}(\text{Bz})(\text{OTf})](\text{OTf})_2$ (**8**)

6 (1.2 g, 0.981 mmol) was suspended in anhydrous dichloromethane (~200 mL) and thoroughly degassed with argon. Under a constant flow of argon, with a vent to release HCl gas, triflic acid (~2 mL) was added. The suspension was stirred at room temperature under a flow of argon for 4 hr. Ether (~200 mL) was added and the precipitate was collected by filtration and washed with ether. This complex was used without further purification (1.52 g, 99%). ^1H NMR (600 MHz, CD_3CN): δ (ppm) 9.65 (d, 1H), 9.35 (d, 1H), 9.23 (d, 1H), 8.91 (s, 2H), 8.77 (bt, 1H), 8.65 (t, 3H), 8.48 (s, 1H), 8.36 (m, 5H), 8.28 (s, 1H), 8.06 (t, 2H), 8.00 (t, 1H), 7.83 (m, 2H), 7.73 (d, 2H), 7.63 (d, 1H), 7.39 (m, 3H), 7.11 (t, 1H), 6.24 (s, 6H), 4.92 (bd, 2H), 2.63 (s, 3H). HR-ESI-MS: $m/z=387.0457^{3+}=1161.1371$, $[\text{M} + \text{NCMe} + \text{OTf}]^{3+}=1161.1210$; $m/z=580.0759^{2+}=1160.1518$, $[\text{M} + \text{NCMe} + \text{OTf} - \text{H}^+]^{2+} = 1160.1131$.

$[\text{((PO}_3\text{H}_2\text{-CH}_2)_2\text{-bpy})_2\text{Ru}(\text{bpy-NH-CO-trpy})\text{Ru}(\text{bpy})(\text{OH}_2)](\text{OTf})_4$ (**1**)

$[\text{Ru}(\text{bpy})(\text{OTf})(\text{trpy-bpy})\text{Ru}(\text{Bz})(\text{OTf})](\text{OTf})_2$ (0.50 g, 0.32 mmol) and ([2,2'-bipyridine]-4,4'-diylbis(methylene)diphosphonic acid (0.22g, 0.64 mmol) were dissolved in anhydrous ethylene glycol. The reaction was heated to 120°C for 5 hrs and followed by

UV/Vis measurements by watching the growth in absorbance at $\lambda_{\text{max}} \approx 470\text{nm}$. At the end of the reaction period, the solution was cooled to room temperature, and acetone was added. The solution was again brought to reflux, cooled, filtered, and washed with acetone to remove unreacted $[\text{Ru}(\text{bpy})(\text{OTf})(\text{trpy-bpy})\text{Ru}(\text{Bz})(\text{OTf})](\text{OTf})_2$. The solid was then suspended in methanol, brought to reflux, cooled, and filtered to remove any insoluble material. The filtrate was taken to dryness by rotary evaporation, and the crude product was purified by size exclusion chromatography (Sephadex LH-20 with H_2O as eluent). Similar fractions (based on UV-Vis) were combined and the solvent was removed by rotary evaporation. The dark red solid was triturated with ether and collected (0.195 g, 28%). ^1H NMR (600 MHz, D_2O): δ (ppm) 9.51 (d, 1H), 9.38 (t, 1H), 8.83 (s, 2H), 8.63 (d, 1H), 8.50 (d, 2H), 8.41 (s, 1H), 8.32 (m, 4H), 8.32 (d, 2H), 8.13 (d, 2H), 8.05 (d, 2H), 7.98 (t, 1H), 7.94 (t, 2H), 7.81 (d, 1H), 7.76 (d, 2H), 7.60 (m, 5H), 7.29 (m, 4H), 7.17 (m, 6H), 6.88 (t, 1H), 3.14 (m, 8H), 2.46 (s, 3.H). ^{31}P NMR δ 16.88. HR-ESI-MS (80:20 $\text{NCMe}:\text{H}_2\text{O}$, 1% HCCOH): $m/z=540.3945^{3+} = 1621.183$, $[\text{M} - 2\text{H}^+ + \text{Na} + \text{H}_2\text{O}]^{3+} = 1621.144$; $m/z=548.0544^{3+}=1644.163$ $[\text{M} - 2\text{H}^+ + \text{Na} + \text{NCMe}]^{3+} = 1644.160$; $m/z=810.0856^{2+} = 1620.1712$, $[\text{M} - 3\text{H}^+ + \text{Na} + \text{H}_2\text{O}]^{2+} = 1620.135$; $m/z=821.57806^{2+}=1643.1561$, $[\text{M} - 3\text{H}^+ + \text{Na} + \text{NCMe}]^{2+}=1643.1525$. Anal. Found (Calc.) for $\text{C}_{70}\text{H}_{80}\text{F}_6\text{N}_{12}\text{O}_{29}\text{P}_4\text{Ru}_2\text{S}_2$: C, 40.38 (40.86); H, 4.16 (3.92); N, 8.32 (8.17).

$[\text{Ru}((\text{PO}_3\text{H}_2\text{-CH}_2)_2\text{-bpy})_2(\text{dmb})](\text{Cl})_2$ (**2**)

This complex was synthesized according to a literature procedure but using 4,4'-dimethyl-2,2'-bipyridine instead of 2,2'-bipyridine.²⁹² ^1H NMR (400 MHz, D_2O): δ (ppm) 8.35 (bd, 4H), 8.26 (s, 2H), 7.70 (dd, 4H), 7.56 (d, 2H), 7.19 (bt, 4H), 7.12 (d, 2H), 3.01 (d, 8H), 2.47 (s, 6H). ^{31}P NMR δ 15.06, 14.93.

Preparation of Modified Electrodes

Titanium isopropoxide, isopropanol, and hydroxypropylcellulose were used as received from Sigma-Aldrich. Fluorine-doped tin oxide (FTO) coated glass (Hartford Glass Co.; sheet resistance $15 \Omega/\text{cm}^2$) was cut into $11 \text{ mm} \times 50 \text{ mm}$ strips and was used as the substrate for TiO_2 nanoparticle films. ITO electrodes (ITO-coated glass, $R_s = 4\text{-}8 \Omega$) were obtained from Delta Technologies, Limited. *NanoITO* powder was obtained from Lihochem. *NanoITO* and TiO_2 were prepared as previously reported.^{248,295,296} Zirconium dioxide was prepared by using a reported literature procedure.¹³⁴

Assembly **1** was loaded onto TiO_2 surfaces by immersing the metal oxide films in methanol solutions of **1** for 12 hours and then thoroughly rinsed with methanol. Surface coverages were calculated by using the expression $\Gamma = A(\lambda)/(\varepsilon(\lambda)*1000)$. Maximum coverage (Γ_0) on $6 \mu\text{m}$ thick TiO_2 films was $\sim 6.7 \times 10^{-8} \text{ mol cm}^{-2}$.

Electrochemical and Spectroscopic Characterization

UV-Visible spectra were recorded on an Agilent-Varian Cary 50 UV/Visible Spectrophotometer. Electrochemical measurements were conducted by using a CH Instruments 660D potentiostat. The working electrode was a planar FTO electrode derivatized with **1**, Pt-wire counter electrode, and a Ag/AgCl reference (3M NaCl, 0.205 V vs NHE). $E_{1/2}$ values were obtained from the peak currents in differential pulse voltammograms and are reported vs. the normal hydrogen electrode (NHE).

Transient Absorption

Transient absorption (TA) measurements were conducted by using nanosecond laser pulses produced by a Spectra-Physics Quanta-Ray Lab-170 Nd:YAG laser combined with a

VersaScan OPO (5-7 ns, operated at 1 Hz) integrated into a commercially available Edinburgh LP920 laser flash photolysis spectrometer system. White light probe pulses generated by a pulsed 450 W Xe lamp passed through a 395 nm long pass filter before reaching the sample to avoid direct band gap excitation of TiO₂. For measurement at timescales > 100 μs, a tungsten/halogen lamp under continuous wave mode was used for the probe beam. The probe light was focused into the monochromator, then detected by a photomultiplier tube (Hamamatsu R928) for 395-800 nm wavelength range, respectively. Detector outputs were processed by using a Tektronix TDS3032C Digital Phosphor Oscilloscope interfaced to a PC loaded with Edinburgh's L900 software. Single wavelength kinetic data were the result of averaging 30-100 laser shots with the data fit by using either Origin or Edinburgh LP900 software. Transient spectra obtained at fixed delay times following laser excitations were obtained by data slicing with averaged absorbance values at a given wavelength obtained during the time interval.

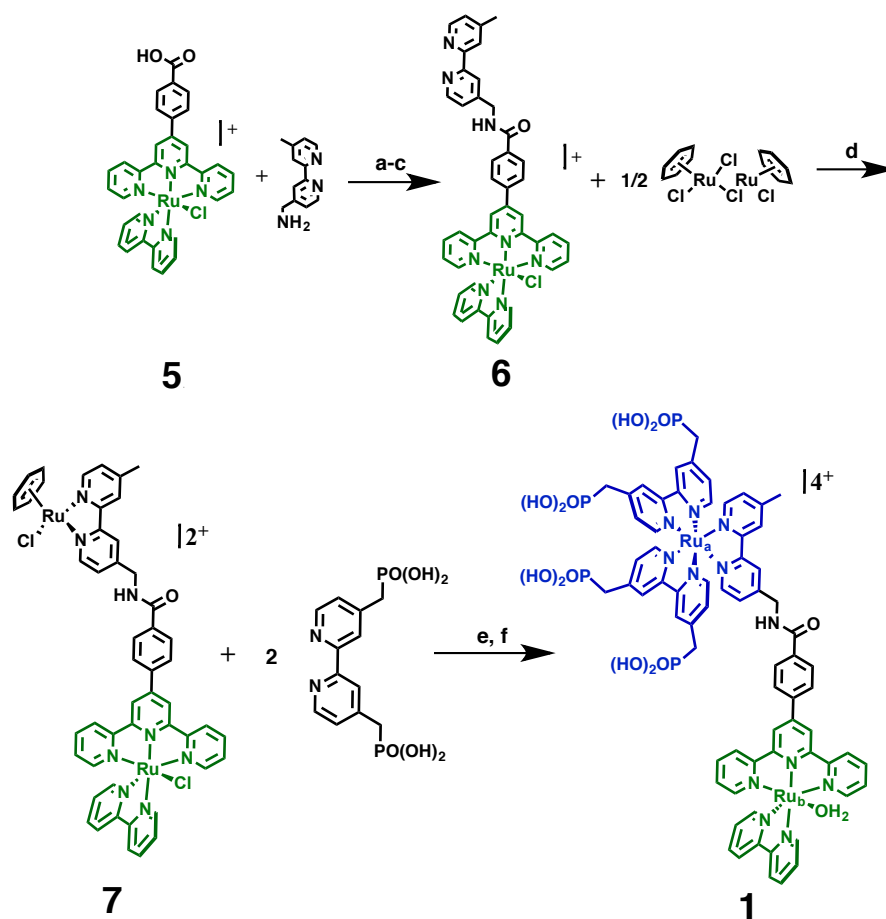
5.3 Results

Synthesis

In a modification of the approach taken in the synthesis of **4**, the phosphonate-derivatized chromophore in **1** was synthesized by use of the [Ru(bpy)(Bz)(Cl)]⁺ analogue, [Ru(bpy)(Cl)(trpy-CO-NH-bpy)Ru(Bz)(Cl)](Cl)(PF₆) (**7**) (Scheme 5.1). This strategy was used because of the limited solubility of the phosphonated chromophore under conditions relevant for amide coupling in dimethylformamide solution.¹⁸⁹ The precursor to **7** is the product of an amide coupling between the water oxidation catalyst precursor [Ru(bpy)(4-([2,2':6',2''-terpyridin]-4'-yl)benzoic acid)(Cl)](Cl) (**5**) and (4'-methyl-[2,2'-bipyridin]-4-

yl)methanamine to give $[\text{Ru}(\text{bpy-ph-NH-CO-trpy})(\text{bpy})(\text{Cl})]^+$ (**6**) in high yields (see experimental). **6** can be used without further purification because **7** precipitates cleanly from the reaction mixture leaving both unreacted **6** and (4'-methyl-[2,2'-bipyridin]-4-yl)methanamine in solution.

Scheme 5.1. Synthesis of **1**



a) SOCl_2 , reflux, 4hr. b) (4'-methyl-[2,2'-bipyridin]-4-yl)methanamine, DMF, DIPEA, 100°C , overnight. c) NH_4PF_6 . d) MeOH, reflux, overnight. e) CH_2Cl_2 , HOTf. f) 2 equiv. $(\text{PO}_3\text{H}_2\text{-CH}_2)_2\text{-bpy}$, ethylene glycol, 120°C , 5 hrs

2-dimensional NMR analysis by COSY was utilized to identify the methylene protons and NH proton in **7** and $[\text{Ru}(\text{bpy})(\text{OTf})(\text{trpy-CO-NH-bpy})\text{Ru}(\text{Bz})(\text{OTf})](\text{OTf})_2$ (**8**) (Figure 3). The shifts for the NH proton, as expected, are dependent on the solvent but were typically

found between δ 8.5 - 9.5 ppm. The methylene protons were between δ 4.8 - 4.9 ppm and the chemical shifts were relatively independent of solvent. The diastereotopic nature of the methylene protons in **7** were resolved in which they appear as an AB pattern giving a pair of doublets (Figure 5.2 and Figure D.3). This analysis was not possible for **1** because of its limited solubility in solvents other than D₂O, in which the methylene protons are masked by the solvent.

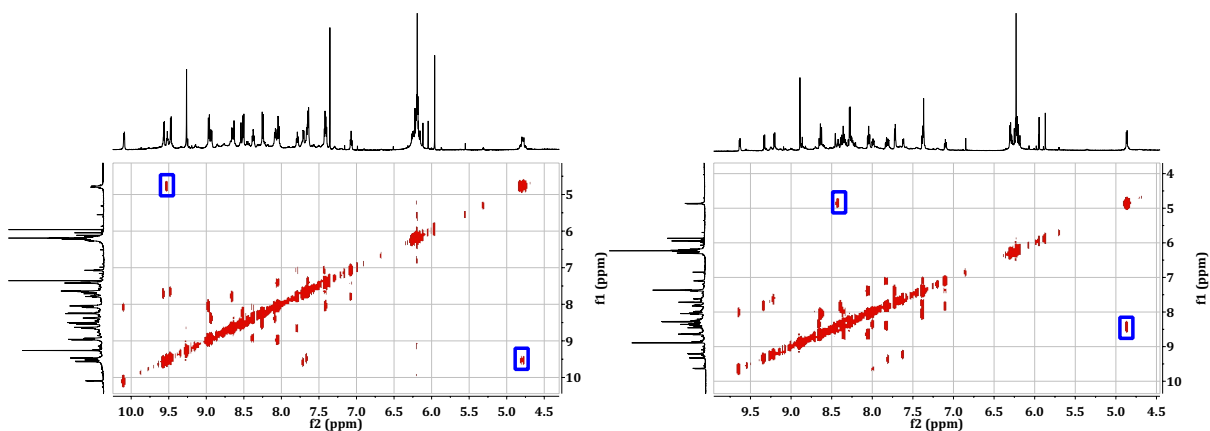


Figure 5.2. (Left) COSY NMR of **7** in d₆-DMSO. (Right) COSY NMR of **8** in CD₃CN. The cross peaks for each of the diastereotopic methylene protons and the NH proton for complexes are highlighted in blue.

The [Ru(Bz)(Cl)(bpy-NH-CO-)] site in **7** is kinetically inert to further substitution and binding. Both the bound chloro ligand and the chloride counterion in **7** can be removed by treatment with triflic acid (HOTf, OTf = trifluoromethanesulfonate anion) to give the triflate derivative, **8**. The triflate derivative undergoes substitution with added 4,4'-(PO₃H₂-CH₂)₂bpy in ethylene glycol, Scheme 5.1. The final substitution step, Scheme 5.1, was followed by UV/Visible measurements where the characteristic [Ru(bpy)₃]²⁺-based absorptions for the [((PO₃H₂-CH₂)₂bpy)₂-Ru_a(bpy-NH-CO-)] fragment grows at $\lambda_{\text{max}} \approx 472$ nm as the reaction proceeds. There were no further spectral changes after 5 hours (Figure D.7).

Electrochemistry

In cyclic voltammograms of **1** immobilized on planar fluoride-doped tin oxide (FTO) at pH = 6.0, pH dependent waves appear for the $[\text{Ru}_a^{\text{II}}-\text{Ru}_b^{\text{III}}-\text{OH}]^{4+}/[\text{Ru}_a^{\text{II}}-\text{Ru}_b^{\text{II}}-\text{OH}_2]^{4+}$, $[\text{Ru}_a^{\text{II}}-\text{Ru}_b^{\text{IV}}=\text{O}]^{4+}/[\text{Ru}_a^{\text{II}}-\text{Ru}_b^{\text{III}}-\text{OH}]^{4+}$, and $[\text{Ru}_a^{\text{III}}-\text{Ru}_b^{\text{IV}}=\text{O}]^{5+}/[\text{Ru}_a^{\text{II}}-\text{Ru}_b^{\text{IV}}=\text{O}]^{4+}$ couples at $E_{1/2}=0.71$ V, 0.83 V, and 1.23 V (vs NHE), respectively (Figure 5.3). In contrast to **4** in solution, the $[\text{Ru}_a^{\text{III}}-]^{5+}/[\text{Ru}_a^{\text{II}}-]^{4+}$ couple is also (weakly) pH dependent (Figure 5.3 and Figure D.8). pK_a values for $[\text{Ru}_a^{\text{II}}-\text{Ru}_b^{\text{II}}-\text{OH}_2]^{4+}$ and $[\text{Ru}_a^{\text{II}}-\text{Ru}_b^{\text{III}}-\text{OH}_2]^{5+}$ were determined previously for **4** in solution (Figure 5.3).^{189,297}

The pH dependent results are summarized in the $E_{1/2}$ ($\sim E^0$: E^0 is the formal potential) vs pH (Pourbaix) diagram in Figure 5.3. As shown in the figure, the slopes of the $E_{1/2}$ -pH plots between pH = 1 and pH = 8 are ~ 74 mV/pH unit, larger than the 59 mV/pH unit predicted by the Nernst equation. The pH dependence for the nominally pH independent $[\text{Ru}_a^{\text{III}}-]^{5+}/[\text{Ru}_a^{\text{II}}-]^{4+}$ couple is ~ 13 mV/pH unit. Spectroelectrochemical results on conductive *nano*-ITO (ITO = tin-doped indium oxide) derivatized with **1** show an oxidation of the catalyst moiety $[\text{Ru}_a^{\text{II}}-\text{Ru}_b^{\text{II}}-\text{OH}_2]^{4+}$ to give $[\text{Ru}_a^{\text{II}}-\text{Ru}_b^{\text{III}}-\text{OH}_2]^{5+}$ followed by a second oxidation of the catalyst that overlaps with the oxidation of the chromophore to give $[\text{Ru}_a^{\text{III}}-\text{Ru}_b^{\text{IV}}=\text{O}]^{5+}$ (Figure 5.3).

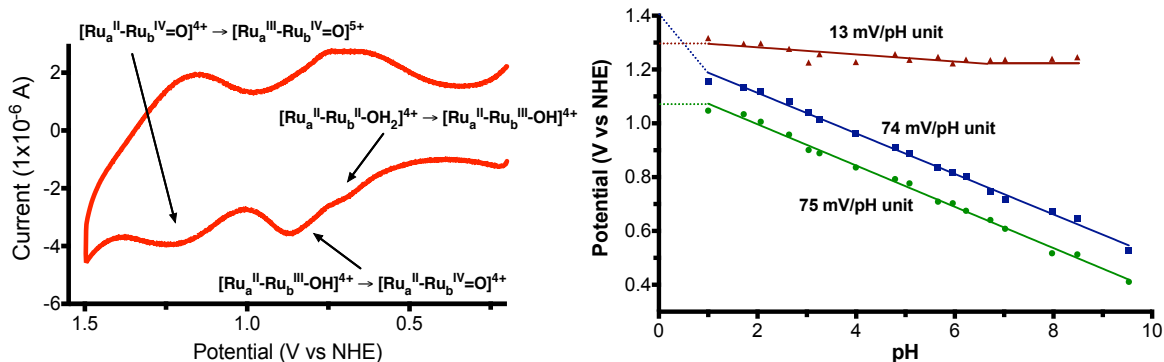


Figure 5.3. (Left) Cyclic voltammogram for **1** at pH = 6.0 (0.1 M phosphate, 0.5 M KNO₃) at 100 mV/s on FTO. (Right) $E_{1/2}$ -pH diagram of **1** on FTO. $E_{1/2}$ values were obtained as peak current maxima in differential pulse voltammograms. The solid lines are best fits of the variation in $E_{1/2}$ values with pH for the $[-\text{Ru}_b^{\text{III}}-\text{OH}]^{4+}/[-\text{Ru}_b^{\text{II}}-\text{OH}_2]^{4+}$ (green), $[-\text{Ru}_b^{\text{IV}}=\text{O}]^{4+}/[-\text{Ru}_b^{\text{III}}-\text{OH}]^{4+}$ (blue), and $[\text{Ru}_a^{\text{III}}-]^{5+}/[\text{Ru}_a^{\text{II}}-]^{4+}$ (red) couples. At 23° C in 0.5 M KNO₃ and 0.1 M buffer.

Transient Absorption

The absorption spectrum of **1** in water at 25°C in the visible is dominated by a MLCT absorption centered at $\lambda_{\text{max}} \sim 472$ nm. This feature results from over-lapping MLCT absorptions at $[\text{Ru}_a^{\text{II}}-]^{4+}$ and $[-\text{Ru}_b^{\text{II}}-\text{OH}_2]^{4+}$ which are unperturbed compared to the constituents due to the weak electronic coupling across the saturated amide link. (Figure 5.4).¹⁸⁹

Interfacial electron transfer dynamics of TiO₂ derivatized with $[\text{Ru}_a^{\text{II}}-\text{Ru}_b^{\text{II}}-\text{OH}_2]^{4+}$ (**1**), $[\text{Ru}^{\text{II}}]^{2+}$ (**2**), and $[\text{Ru}^{\text{II}}-\text{OH}_2]^{2+}$ (**3**) were investigated by nsec transient absorption measurements. Initial electron injection into the TiO₂ conduction band following MLCT excitation was $> 10^8 \text{ s}^{-1}$, too rapid to monitor on the timescale of the experiment (10 ns instrumental time resolution).

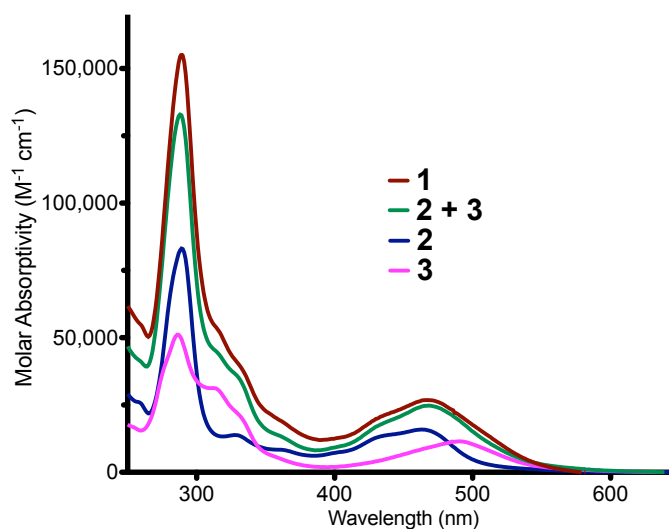


Figure 5.4. Absorption spectra for **1** (red), **2** (blue), **3** (pink), and **2 + 3** (green) in H₂O at 25°C.

Transient absorption difference spectra following 532 nm excitation are shown in Figure 5.5. There is a resemblance in absorption features in the transient spectra of [TiO₂-Ru^{II}_a-Ru^{II}_b-OH₂]⁴⁺ (TiO₂-**1**) and [TiO₂-Ru^{II}-OH₂]²⁺ (TiO₂-**3**) with a maximum bleach at 480 nm. This feature points to the formation of [TiO₂(e⁻)-Ru^{II}_a-Ru^{III}_b-OH₂]⁴⁺ following excitation of TiO₂-**1** at 20 ns. This is consistent with MLCT excitation of [TiO₂-Ru^{II}_a-Ru^{II}_b-OH₂]⁴⁺ followed by rapid injection and sub nsec, intra-assembly oxidation of [TiO₂(e⁻)-Ru^{III}_a-Ru^{II}_b-OH₂]⁴⁺ to [TiO₂(e⁻)-Ru^{II}_a-Ru^{III}_b-OH₂]⁴⁺, Scheme 5.2 and Equation 5.1. Excitation at 437 nm, where light absorption is dominated by [Ru^{II}_a]⁴⁺, gave the same transient response (Figure 5.5). The diminished contribution of the [Ru^{II}_a]⁴⁺ bleach at ~ 445 nm in **1** suggests that > 90% of the photochemically generated injection events results in oxidation of the remote catalyst site. (Equation 5.1). The positive feature at ~650 nm that appears following both 437 and 532 nm excitation is attributable to non-injecting residual excited states (Figure D.10 and Figure D.11).

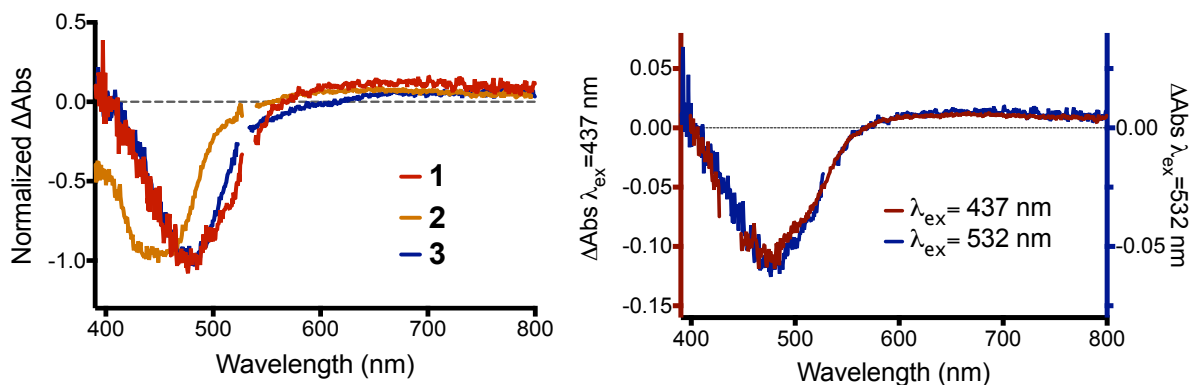
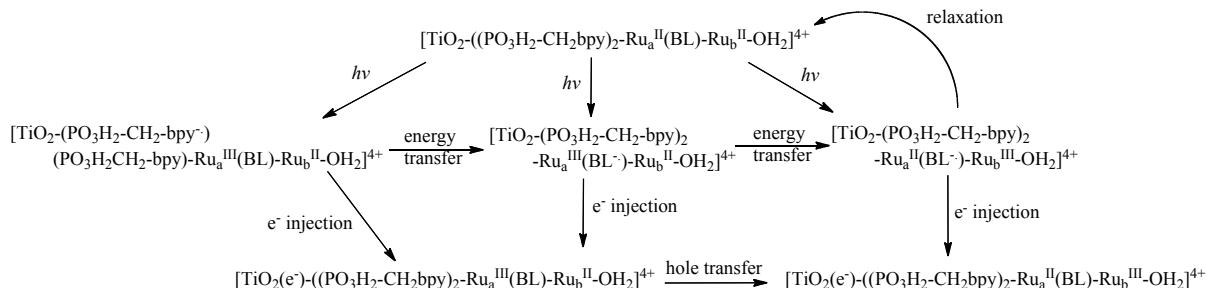


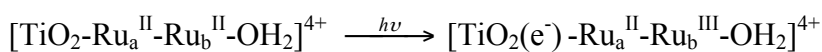
Figure 5.5. (Left) Nanosecond transient absorption difference spectra obtained at 20 ns on TiO₂ (6 μm transparent film) derivatized electrodes at surface coverages- **1** (4.4×10^{-8} mol cm⁻², red), **2** (5.8×10^{-8} mol cm⁻², orange), and **3** (9.1×10^{-8} mol cm⁻², blue) following 532 nm laser flash (5.2 mJ) excitation. Spectra are normalized at the bleach maxima for comparison

purposes. (Right) Transient spectrum for **1** (4×10^{-8} mol cm⁻²) at 20 ns following 532 nm (5.2 mJ, blue) and 437 nm (3 mJ, red) excitation on TiO₂. In 0.1 M HClO₄ at room temperature.

Scheme 5.2. Summary of possible electron and energy transfer events following excitation of TiO₂-1.^a



Equation 5.1



Injection

Injection yields were determined as previously described based on the amplitudes of transient absorption changes.¹⁸¹ Electron injection efficiencies for TiO₂-1 approach ~30% when excited at 440 nm (Table 5.1). At this wavelength, light absorption is dominated by [Ru_a^{II}]⁴⁺. Excitation at 532 nm, with [-Ru_b^{II}-OH₂]⁴⁺ the major light absorber, decreases the injection yield to ~12%. The latter is comparable to the injection yield for TiO₂-3 (~15%, Table 1). 440 nm excitation of [TiO₂-Ru^{II}]²⁺ (TiO₂-2) resulted in an injection yield of ~45%. By comparison, the injection efficiency is ~1 for [Ru(4,4'-(PO₃H₂)₂bpy)₂(bpy)]²⁺ (PO₃H₂-bpy= [2,2'-bipyridine]-4,4'-diylidiphosphonic acid), with the phosphonate groups directly bound to the bpy.¹⁸¹

Table 5.1. Injection yields and back electron transfer rates

Complex	$\Phi_{\text{inj}}^{\text{a}}$		Back Electron Transfer ^b	
	440 nm	532 nm	τ	β

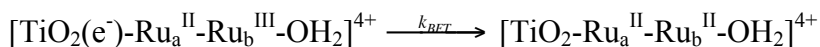
	Excitation	Excitation	(μs)	
1	0.30	0.12	6.7	0.25
2	0.45	0.44	1.8	0.29
3	0.40	0.15	2.2	0.22

a) See text. b) 532 nm excitation with monitoring at 480 nm in 0.1 M HClO₄.

Back Electron Transfer

Back electron transfer between the injected electron in TiO₂ (TiO₂(e⁻)) and the oxidized Ru(III) site, [TiO₂(e⁻)-Ru_a^{II}-Ru_b^{III}-OH₂]⁴⁺ for **1** (Eq. 2), [TiO₂(e⁻)-Ru^{III}]²⁺ for **2**, and [TiO₂(e⁻)-Ru^{III}-OH₂]²⁺ for **3**, was monitored at 480 nm following laser flash excitation at 532 nm. As found in earlier studies, back electron transfer kinetics are complex and non-exponential.^{144,181} Absorbance–time traces (Figure 5.6) could be satisfactorily fit to the stretched exponential function (Equation 5.3), where A is a pre-exponential constant, τ is the characteristic lifetime and β is a parameter that is inversely related to the width of underlying Lévy distribution of lifetimes, 0 < β < 1.^{298,299} Lifetimes and β values are presented in Table 5.1 with τ the inverse of the characteristic rate constant for back electron transfer in the distribution, *k*_{BET}. The lifetime for **1**, **2**, and **3** are 6.7, 1.8, and 2.2 μs respectively. For a 100 μs time window, ~5% of the total ΔA change remained for TiO₂-**2** and ~10% for TiO₂-**1** and TiO₂-**3** although back electron transfer for TiO₂-**1** is slower initially (Table 5.1, Figure 5.6).

Equation 5.2



Equation 5.3

$$\Delta OD = Ae^{(\frac{1}{\tau})^\beta}$$

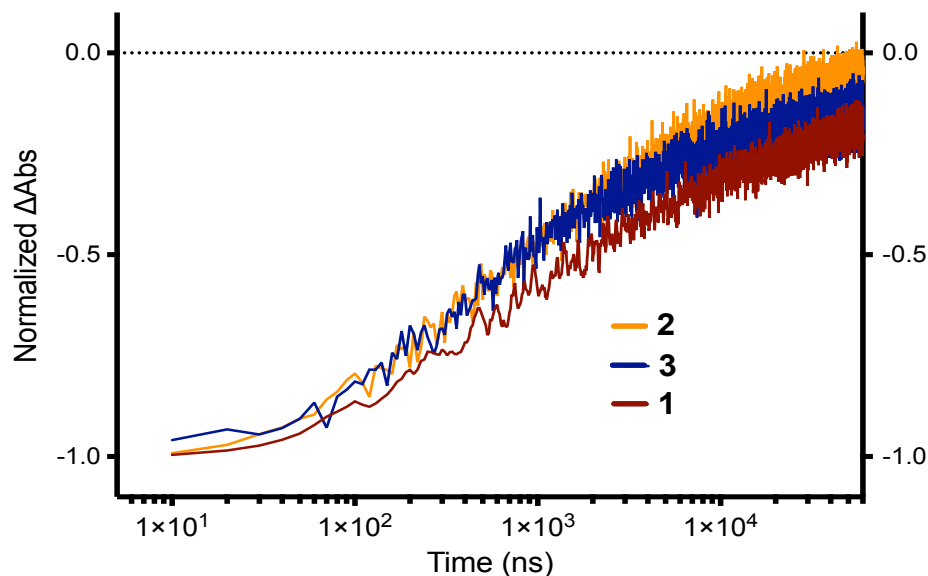


Figure 5.6. Absorption-time traces for **1** on TiO₂ (4.4×10^{-8} mol cm⁻², red, 480 nm monitoring), **2** (5.8×10^{-8} mol cm⁻², orange, 460 nm monitoring) and **3** (9.1×10^{-8} mol cm⁻², blue, 480 nm monitoring) following 532nm laser (5.2 mJ) excitation.

Intra-assembly electron transfer following photochemically generated electron injection of the chromophore in TiO₂-**1** (k_{int} , Equation 5.1 and Equation 5.10) is at least three orders of magnitude more rapid than the rate of back electron transfer in [TiO₂(e⁻)-Ru_a^{II}-Ru_b^{III}-OH₂]⁴⁺ (Equation 5.2) at pH = 1 with $k_{BET} \sim 10^5$ ($k_{BET} = 1/\tau$) and $k_{int} > 10^8$. Back electron transfer rates were also found to be dependent on pH although the data at higher pH could not be satisfactorily fit to Equation 5.3. Rather, the time dependent data are reported as time for half of the total absorbance change to occur ($t_{1/2}$). As can be seen in the data in Table 5.2, $t_{1/2}$ increases from $t_{1/2} = 6 \mu\text{s}$ at pH = 1 to $t_{1/2} = 35 \mu\text{s}$ at pH = 4.5 (Figure 5.7, Table 5.2).

Table 5.2. pH dependence of back electron of 1 on TiO₂

Sample	BET $t_{1/2}$ (μs)	> 2 ms component ^c
1 pH=1 ^a	6	6%
1 pH=4.5 ^b	35	23%

a) 0.1 M HClO₄ at room temperature. b) 0.18M LiClO₄ with 20mM pH 4.5 NaOAc/HOAc buffer. c) % of the ΔA change remaining after 2 ms. Surface coverage: $(6.7 \pm 0.1) \times 10^{-8}$ mol cm⁻²; 532nm (5.0mJ) excitation.

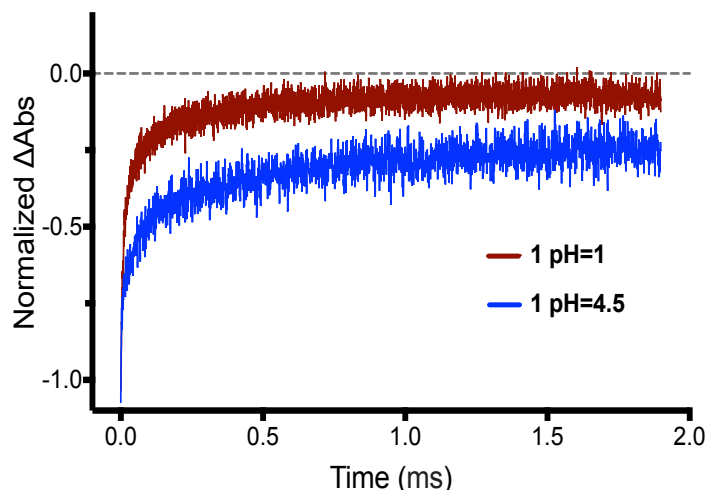


Figure 5.7. Absorbance-time traces for **1** on $\text{TiO}_2(4.4 \times 10^{-8} \text{ mol cm}^{-2})$ following 532 nm laser flash (5.0 mJ) excitation with monitoring at 480 nm in 0.1 M HClO_4 (red) and at pH = 4.5 (0.18M LiClO_4 with 20mM NaOAc/HOAc buffer, blue).

5.4 Discussion

The goal of this research was to develop a systematic approach for the synthesis of metal-oxide bound chromophore-catalyst assemblies used in the fabrication of photoanodes in DSPECs. The current assembly offers the advantage of relative stability of surface binding under aqueous conditions based on the phosphonate-surface links, and a flexible amide link between the chromophore and catalyst. The latter creates a basis for introducing controlled molecular spacers and, with it, a foundation for controlling rates of intra-molecular and interfacial electron transfer.

With these goals in mind, the current results provide the basis for what will be a systematic study of the influence of intra-assembly distance effects on intra-assembly and interfacial electron transfer dynamics in DSPEC photoanode applications. These dynamics ultimately dictate the performance of the DSPEC solar fuel half reactions. Achieving high efficiencies in driving multi-electron, multi-proton solar fuel half reactions, like water oxidation, requires high per photon electron injection efficiencies, stepwise accumulation of

multiple oxidative equivalents, and rates of substrate oxidation that exceed rates of back electron transfer. The demands are greater than for conventional DSSCs where photopotential and photocurrents are generated by single photon, single electron events. Even in these cells, efficiencies are still limited by the recombination of $\text{TiO}_2(e^-)$ with the oxidized form of added redox mediator couples, such as I_3^- .

Synthesis

We report here the development of a general and flexible synthetic strategy for preparing amide linked chromophore-catalyst assemblies with a phosphonate-derivatized chromophore for attachment to oxide surfaces. As previously mentioned, only one other report describes a molecular chromophore-catalyst assembly derivatized with phosphonic acids making the synthetic aspects notable.¹⁹³ Direct amide coupling between the preformed chromophore and catalyst was unsuccessful due to limited solubility of the phosphonate-derivatized chromophore under conditions relevant to amide coupling. This required a strategy that avoided the phosphonated-bipyridine ligands until the final step in the synthesis (Scheme 5.1).

An advantage of this procedure is that the $[\text{Ru}(\text{bpy})(\text{Bz})(\text{Cl})]^+$ -analogue intermediate (**7**) is synthesized in high yields without requiring chromatography (see experimental). In addition, the Cl^- ligands can be replaced with the more labile triflate ligand (OTf^-) to facilitate substitution and for subsequent addition of the phosphonated-bipyridines to build the chromophore. The structure of the triflate-benzene intermediate **8** was evaluated by use of COSY NMR, which identified the $-\text{CH}_2-$ methylene and NH protons, confirming the presence of the amide link after the reaction with HOTf (Scheme 1). Two keys to avoiding hydrolysis of the amide link under the highly acidic conditions used in the synthesis of **8** are

the use of anhydrous solvents and controlled temperature. Avoidance of hydrolysis was also a consideration in the use of anhydrous ethylene glycol in the synthesis of **1** in the reaction with the pre-hydrolyzed ligand ([2,2'-bipyridine]-4,4'-diylbis(methylene)diphosphonic acid). This is an important element since it eliminates the need for hydrolysis of a precursor ester once the ligand has been coordinated.²⁹²

Electrochemistry

All three observable oxidations of **1** on FTO in aqueous solution are pH dependent (Figure 5.3 & Figure D.8). The introduction of a pH dependence for the chromophore oxidation $[\text{Ru}_a^{\text{III}}]^{5+}/[\text{Ru}_a^{\text{II}}]^{4+}$, in contrast to **4**, arises from a combination of deprotonation of acidic protons on the phosphonic acid groups and the influence of the local electric field gradient at the electrode interface.^{193,300-304} The dependence of 13 mV/pH unit for the $[\text{Ru}_a^{\text{III}}]^{5+}/[\text{Ru}_a^{\text{II}}]^{4+}$ couple is in good agreement with earlier observations on surface-bound complexes of the type $[\text{Ru}(\text{bpy})_{3-n}(\text{PO}_3\text{H}_2\text{-CH}_2\text{-bpy})_n]^{2+}$ with $n=1-3$.³⁰⁰ The proton coupled electron transfer (PCET) oxidations, $[\text{Ru}_a^{\text{II}}\text{-Ru}_b^{\text{III}}\text{-OH}]^{4+} / [\text{Ru}_a^{\text{II}}\text{-Ru}_b^{\text{II}}\text{-OH}_2]^{4+}$ and $[\text{Ru}_a^{\text{II}}\text{-Ru}_b^{\text{IV}}\text{=O}]^{4+} / [\text{Ru}_a^{\text{II}}\text{-Ru}_b^{\text{III}}\text{-OH}]^{4+}$, occur with pH dependences of ~ 74 mV/pH unit, which appears to be the sum of the expected Nernstian behavior (59 mV/pH unit) and the pH dependence of the chromophore $[\text{Ru}_a^{\text{III}}]^{5+}/[\text{Ru}_a^{\text{II}}]^{4+}$ couple (13 mV/pH unit).^{193,257,268}

Interfacial Dynamics

Scheme 5.2 provides an overview illustrating the complex sequence of energy and electron transfer events expected to occur following MLCT excitation of $\text{TiO}_2\text{-1}$.¹⁸⁹ The scheme is based on the absorption spectrum and the various, low-lying MLCT excited states that are accessible at the $[\text{Ru}_a^{\text{II}}]^{4+}$ and $[\text{-Ru}_b^{\text{II}}\text{-OH}_2]^{4+}$ sites in **1**.

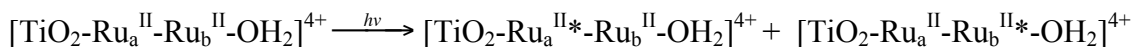
A more detailed, ultrafast photophysical investigation is currently being undertaken, but our experiments on the nsec time scale provide significant insight into the dynamics of the events that occur following MLCT excitation at 440 and 532 nm.

Injection

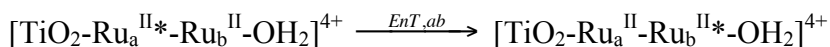
For TiO₂-**1** in 0.1 M HClO₄, the injection yield, following 440 nm excitation, with [Ru^{II}-]⁴⁺ the dominant light absorber, is $\eta_{inj} \sim 0.30$. η_{inj} falls to 0.12 with 532 nm excitation with [-Ru^{II}-OH₂]⁴⁺ as the dominant light absorber. These values, obtained by transient absorbance measurements at the MLCT bleach minimum at 480 nm, are low relative to TiO₂-**2** with $\eta_{inj} \sim 0.45$ under the same conditions.

The lower injection efficiencies relative to TiO₂-**2** are presumably due to competitive light absorption by the remote [-Ru^{II}-OH₂]⁴⁺ site. Injection by the excited state [-Ru^{II*}-OH₂]⁴⁺ is expected to be slower because of weak electronic coupling with TiO₂ acceptor levels and a higher medium reorganization energy, which is also distance dependent. Loss of this excited state is dominated by nonradiative decay, Equation 5.6.¹³⁴ Intra-assembly energy transfer to give the lowest energy, remote MLCT excited state, [Ru^{II}-((H)N(CO)trpy⁻)Ru^{III}-OH₂]⁴⁺, Equation 5.5, was found to be much slower than injection in **4** and is not expected to decrease injection yields.¹⁸⁹

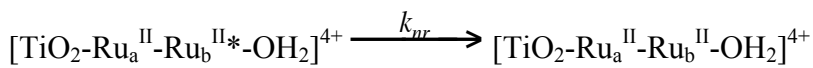
Equation 5.4



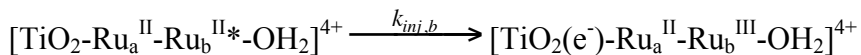
Equation 5.5



Equation 5.6



Equation 5.7



By inference, injection by $[\text{TiO}_2\text{-Ru}_a^{\text{II}*}]^{4+}$ is relatively efficient, Equation 5.8, with some loss to competitive light absorption by $[-\text{Ru}_b^{\text{II}*}\text{-OH}_2]^{4+}$, Equation 5.6. Injection from $\text{TiO}_2\text{-3}$ is also wavelength dependent. A higher injection efficiency is observed for the surface attached $\text{Ru}^{\text{III}}(\pi_{\text{bpy}}^*)^1$ excited state, which dominates absorption at 440 nm compared to 532 nm where light absorption gives dominantly a $\text{Ru}^{\text{III}}(\pi_{\text{trpy}}^*)^1$ excited state oriented away from the interface.

Equation 5.8

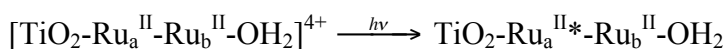


There is an additional loss in injection efficiency for both $\text{TiO}_2\text{-1}$ and $\text{TiO}_2\text{-2}$ due to the $-\text{CH}_2-$ methylene spacers that intervene between the phosphonate groups linked to the TiO_2 surface and the injecting $-\text{CH}_2\text{-(bpy}^-\text{)Ru}^{\text{III}}$ chromophore. Under comparable conditions, $\eta_{inj} \sim \mathbf{1}$ for $\text{TiO}_2\text{-[Ru(4,4'-(PO}_3\text{H}_2)_2\text{bpy)}_2(\text{bpy})]^{2+}}$ with no methylene spacers.¹⁸¹ Related observations have been made for injection by a family of phosphonate-derivatized Ru-bpy complexes on TiO_2 .¹⁴⁴

The origin of this effect is not clear but it has been suggested that there may be contributions from decreased electronic coupling between the MLCT excited state(s) and surface acceptor levels and/or from the substituent effect of the $-\text{CH}_2-$ spacers. By their electron donating effect these spacers direct the lowest MLCT excited state toward the amide-derivatized bridging ligand and away from the interface with TiO_2 .¹⁴⁴

Excitation at 532 nm with $[-\text{Ru}_b^{\text{II}}-\text{OH}_2]^{4+}$ as the dominant light absorber results in the same transient behavior with the intermediate state $[\text{TiO}_2(\text{e}^-)-\text{Ru}_a^{\text{II}}-\text{Ru}_b^{\text{III}}-\text{OH}_2]^{4+}$, appearing in transient spectra but with a considerably diminished electron injection efficiency as described above. The appearance of $[\text{TiO}_2(\text{e}^-)-\text{Ru}_a^{\text{II}}-\text{Ru}_b^{\text{III}}-\text{OH}_2]^{4+}$ at this excitation wavelength may include a contribution from long-range $[\text{TiO}_2-\text{Ru}_a^{\text{II}}-\text{Ru}_b^{\text{II}*}-\text{OH}_2]^{4+}$ injection, but is probably dominated by injection from the minority light absorber, $[\text{TiO}_2-\text{Ru}_a^{\text{II}*}-]^{4+}$ followed by intramolecular electron transfer, Equation 5.9 - Equation 5.11.

Equation 5.9



Equation 5.10



Equation 5.11



Intra-Assembly and Back Electron Transfer

Following 440 nm excitation in 0.1M HClO₄ of TiO₂-**1**, with light absorption dominated by $[\text{Ru}_a^{\text{II}}-]^{4+}$, a MLCT bleach appears at 480 nm (Figure 5.4). The coincidence between this bleach minimum and the bleach minimum for TiO₂-**3** formed by direct injection by **3** into TiO₂, shows that, at the earliest observation times, MLCT excitation and injection have occurred ($k_{inj,a}$) followed by intra-assembly electron transfer (k_{int}) (Equation 5.9 - Equation 5.11). Based on this observation, $k_{int} > 10^8 \text{ s}^{-1}$, making the rate of intra-assembly forward electron transfer at least three orders of magnitude greater than the rate of back electron transfer. Also, these results suggest that > 90% of injection event are followed by

intra-assembly electron transfer oxidation of the water oxidation catalyst site $[-\text{Ru}_b^{\text{II}}-\text{OH}_2]^{4+}$ in **1** (Equation 5.11).

Based on $pK_a = 1.4$ for $[-\text{Ru}_b^{\text{III}}-\text{OH}_2]^{5+}$ the distribution between the aquo, $[\text{Ru}_a^{\text{II}}-\text{Ru}_b^{\text{III}}-\text{OH}_2]^{5+}$, and hydroxo, $[\text{Ru}_a^{\text{II}}-\text{Ru}_b^{\text{III}}-\text{OH}]^{4+}$, forms of the catalyst in 0.1 M HClO_4 is $[\text{Ru}_a^{\text{II}}-\text{Ru}_b^{\text{III}}-\text{OH}_2]^{5+}/[\text{Ru}_a^{\text{II}}-\text{Ru}_b^{\text{III}}-\text{OH}]^{4+} \sim 2.5$.²⁹⁷ Absorptivity differences between the two forms in the visible are too small to distinguish between them (Figure D.12). This is also evident in the fact that the transient spectrum at $\text{pH} = 4.5$, where the aquo ligand should be deprotonated after oxidation to give $[\text{TiO}_2(\text{e}^-)-\text{Ru}_a^{\text{II}}-\text{Ru}_b^{\text{III}}-\text{OH}]^{4+}$ matches the transient spectrum at $\text{pH} = 1$ (Figure D.12).

Back electron transfer from $\text{TiO}_2(\text{e}^-)$ is typically dictated in whole or part by intra-film dynamics with recombination rates dependent on the density of electrons in TiO_2 . In these experiments total absorption changes for **1**, **2**, and **3** at the probe wavelength were -0.030, -0.032, and -0.040, respectively, with the first 100 ns of data omitted to avoid contributions from residual excited states. Based on the molar extinction coefficient changes, the electron concentration ratios for **1**, **2**, and **3** following injection were $\sim 1: 0.8: 1.3$, respectively, with comparable electron densities for the three.

The results of earlier studies revealed that for **2**, and related surface-bound chromophores, back electron transfer rates following injection are dominated by electron diffusion through a distribution of trap states in the TiO_2 nanoparticles in TiO_2 films which can be described by a multiple trapping model.^{181,305,306} This conclusion was reinforced by the results of a recent study on a series of phosphonate-derivatized chromophores on TiO_2 .¹⁴⁴ The increased spatial separation in the assembly between the surface $\text{TiO}_2(\text{e}^-)$ and the remote $[-\text{Ru}_b^{\text{III}}-\text{OH}_2]^{4+}$ increases the through-bond separation distance for back electron transfer and,

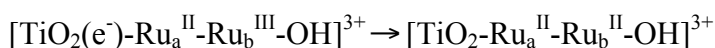
with it, both the extent of electronic coupling and, to a lesser extent, the outer-sphere barrier to electron transfer. The latter is also distance dependent.³⁰⁷⁻³¹⁰

These factors are expected to decrease rates of back electron transfer between $\text{TiO}_2(\text{e}^-)$ and $[-\text{Ru}_b^{\text{III}}-\text{OH}_2]^{4+}$ in the surface-bound assembly. However, the decrease for $[\text{TiO}_2(\text{e}^-)-\text{Ru}_a^{\text{II}}-\text{Ru}_b^{\text{III}}-\text{OH}_2]^{4+} \rightarrow [\text{TiO}_2-\text{Ru}_a^{\text{II}}-\text{Ru}_b^{\text{II}}-\text{OH}_2]^{4+}$ (**1**) compared to $[\text{TiO}_2(\text{e}^-)-\text{Ru}^{\text{III}}-\text{OH}_2]^{2+} \rightarrow [\text{TiO}_2-\text{Ru}^{\text{II}}-\text{OH}_2]^{2+}$ (**3**) is only a factor of ~ 3 less with a decrease from $2\mu\text{s}$ to $6.7\mu\text{s}$ for the characteristic lifetime, Table 5.1. The fact that these rates are comparable suggests that the two rates, intra-film electron transfer and intra-assembly back electron transfer (Equation 5.2) are kinetically coupled.

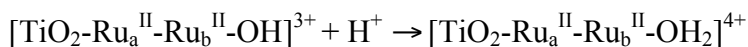
The rate of back electron transfer is also pH dependent as observed in our previous study on $[\text{TiO}_2(\text{e}^-)-\text{Ru}^{\text{III}}]^{2+} \rightarrow [\text{TiO}_2-\text{Ru}^{\text{II}}]^{2+}$ back electron transfer for $[\text{Ru}(4,4'-(\text{PO}_3\text{H}_2)_2\text{bpy}_2)(\text{bpy})]^{2+}$.¹⁸¹ A pH dependence is qualitatively consistent with the multiple state trapping model and the expected influence of pH^{305,306} although the decrease is only a factor of 2 between pH 1 and 5.¹⁸¹ For TiO_2 -**1**, there is a decrease by a factor of ~ 6 in $t_{1/2}$ from 6 to $35\mu\text{s}$ between pH = 1 and 4.5 pointing to an additional effect.

At pH = 4.5, the oxidized assembly undergoes deprotonation to $[\text{TiO}_2(\text{e}^-)-\text{Ru}_a^{\text{II}}-\text{Ru}_b^{\text{III}}-\text{OH}]^{3+}$ with a $\text{pK}_a \sim 1.4$ for $[-\text{Ru}_b^{\text{III}}-\text{OH}_2]^{4+}$.¹⁸⁹ Based on the $E_{1/2}$ values in Figure 5.3, back electron transfer for the hydroxyl form of the assembly, Equation 5.12, is thermodynamically less favorable than reduction of $[-\text{Ru}_b^{\text{III}}-\text{OH}_2]^{4+}$, which also contributes to the decrease in rate, Equation 5.12 and Equation 5.13.

Equation 5.12



Equation 5.13



Another observation of note is the increase in the fraction of ΔOD change that persists to 2 ms from 6% at pH = 1 to 23% at pH = 4.5. Maintaining redox equivalents on the msec and longer timescales is an essential element for building up the multiple redox equivalents required to drive multiple electron solar fuel half reactions.

5.5 Conclusions

We present here a general synthetic strategy for preparing a class of amide-linked, chromophore-water oxidation catalyst assemblies derivatized with phosphonate groups for binding to oxide surfaces. Analysis of interfacial dynamics for TiO₂-1 by nsec transient absorption measurements demonstrates that excitation and injection are followed by rapid oxidation of the remote catalyst site to give $[\text{TiO}_2(\text{e}^-)\text{-Ru}_a^{\text{II}}\text{-Ru}_b^{\text{III}}\text{-OH}_2]^{4+}$. Injection efficiencies are wavelength dependent consistent with inefficient injection by the remote $[\text{-Ru}_b^{\text{II}*}\text{-OH}_2]^{4+}$ excited state. Following injection and intra-assembly electron transfer, back electron transfer from TiO₂(e⁻) to the remote $[\text{-Ru}_b^{\text{III}}\text{-OH}_2]^{4+}$ site is kinetically dictated by an interplay between intra-film and TiO₂(e⁻) → $[\text{-Ru}_b^{\text{III}}\text{-OH}_2]^{4+}$ back electron transfer dynamics. At least 90% of the photochemically generated injection events is followed by rapid intra-assembly electron transfer to generate a remote oxidized catalyst site at $[\text{-Ru}_b^{\text{III}}\text{-OH}_2]^{4+}$. The rate of back electron transfer at pH = 4.5, following deprotonation to give $[\text{-Ru}_b^{\text{III}}\text{-OH}]^{3+}$ is further decreased by a factor of ~ 4 compared to pH = 1.

5.6 Acknowledgments

This work was funded by the UNC Energy Frontier Research Center (EFRC) “Center for Solar Fuels”, an EFRC funded by the U.S. Department of Energy, Office of Science,

Office of Basic Energy Sciences under award DE-SC0001011, supporting D.L.A, M.R.N., and Z.F. (T.J.M., J.L.T., J.J.C., M.K.B.). We acknowledge funding by the Army Research Office through grant W911NF-09-1-0426 supporting C.R.K.G (T.J.M.). Funding for W.S. (T.J.M.) was provided by the CCHF, an EFRC funded by the U.S. Department of Energy, Office of Science, Office of Basic Energy Sciences, under award number DE-SC0001298 at the University of Virginia.

We acknowledge support for the purchase of instrumentation from the UNC EFRC (Center for Solar Fuels, an Energy Frontier Research Center funded by the U.S. Department of Energy, Office of Science, Office of Basic Energy Sciences under award number DE-SC0001011) and UNC SERC (“Solar Energy Research Center Instrumentation Facility” funded by the U.S. Department of Energy,-Office of Energy and Efficiency & Renewable Energy under award number DE-EE0003188).

5.7 Associated Content

Appendix D: 1D and 2D NMR spectra, UV/Vis spectra, electrochemistry, and transient absorption.

Chapter 6: WATCHING PHOTOACTIVATION IN A Ru(II) CHROMOPHORE-CATALYST ASSEMBLY ON TiO₂ BY ULTRAFAST SPECTROSCOPY

Reprinted with permission from Wang, L.; Ashford, D. L.; Thompson, D. W.; Meyer, T. J.; Papanikolas, J. M., Watching Photoactivation in a Ru(II) Chromophore–Catalyst Assembly on TiO₂ by Ultrafast Spectroscopy. *J. Phys. Chem. C* **2013**, *117* (46), 24250-24258. Copyright American Chemical Society 2014

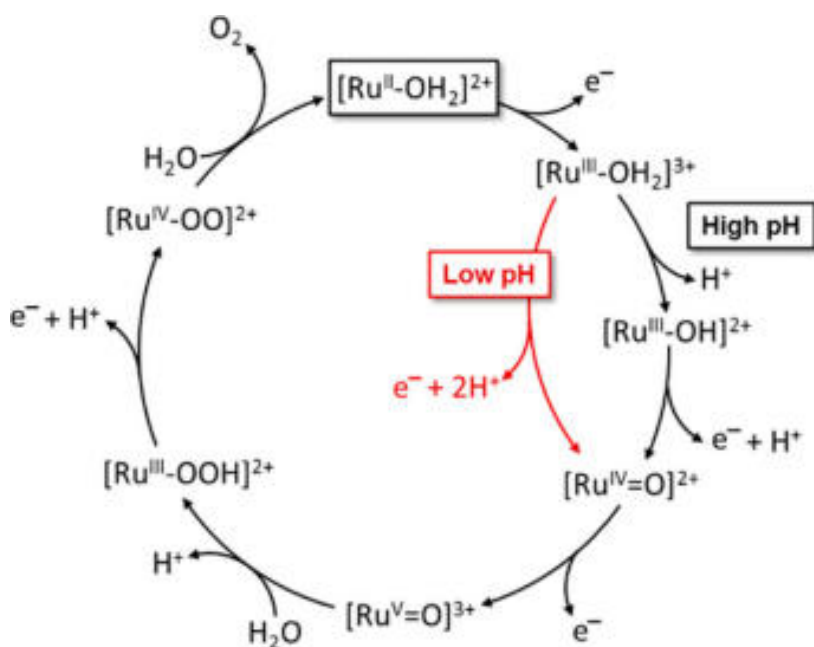
6.1 Introduction

One of the great challenges in the development of light-driven water splitting for solar fuels production is the integration of molecular components that harvest visible light, separate redox equivalents, and use them to drive catalytic water splitting at separate electrodes. Photoelectrochemical cells (PEC) that combine interfacial electron transfer with surface-bound catalysts are one strategy for achieving water splitting, but only a handful of systems are known that incorporate all three components (metal oxide semiconductor, molecular photo-sensitizer, and catalyst) in a complete system (Figure 1.6).^{134,163,164,311,312}

Water oxidation demands sequential transfer of four electrons and four protons in the net reaction $2\text{H}_2\text{O} \rightarrow \text{O}_2 + 4\text{H}^+$. Significant progress has been made in the evolution of polypyridyl-based Ru(II)-aqua catalysts for water oxidation with mechanistic details established both in solution and on oxide surfaces (Scheme 6.1).^{34,35,42} The initial activation step involves the oxidation of $[\text{Ru}^{\text{II}}-\text{OH}_2]^{2+}$ to $[\text{Ru}^{\text{III}}-\text{OH}_2]^{3+}$. This is followed by loss of a proton to give $[\text{Ru}^{\text{III}}-\text{OH}]^{2+}$ above the $\text{p}K_{\text{a}}$ of the coordinated water. Further oxidation results in e^-/H^+ loss to give $[\text{Ru}^{\text{IV}}=\text{O}]^{2+}$. Transfer of the third oxidative equivalent yields $[\text{Ru}^{\text{V}}=\text{O}]^{3+}$. This species is active toward water by O–O bond formation and proton loss to give $[\text{Ru}^{\text{III}}-$

$\text{OOH}]^{2+}$, which is typically the rate-limiting step. Transfer of the fourth oxidative equivalent occurs along with the loss of H^+ to give $[\text{Ru}^{\text{IV}}\text{-OO}]^{2+}$, and finally the O_2 in the active site is replaced with H_2O to regenerate the $[\text{Ru}^{\text{II}}\text{-OH}_2]^{2+}$.

Scheme 6.1. Illustration of Water Oxidation Catalytic Cycle for Single-Site Ru^{II} Catalysts



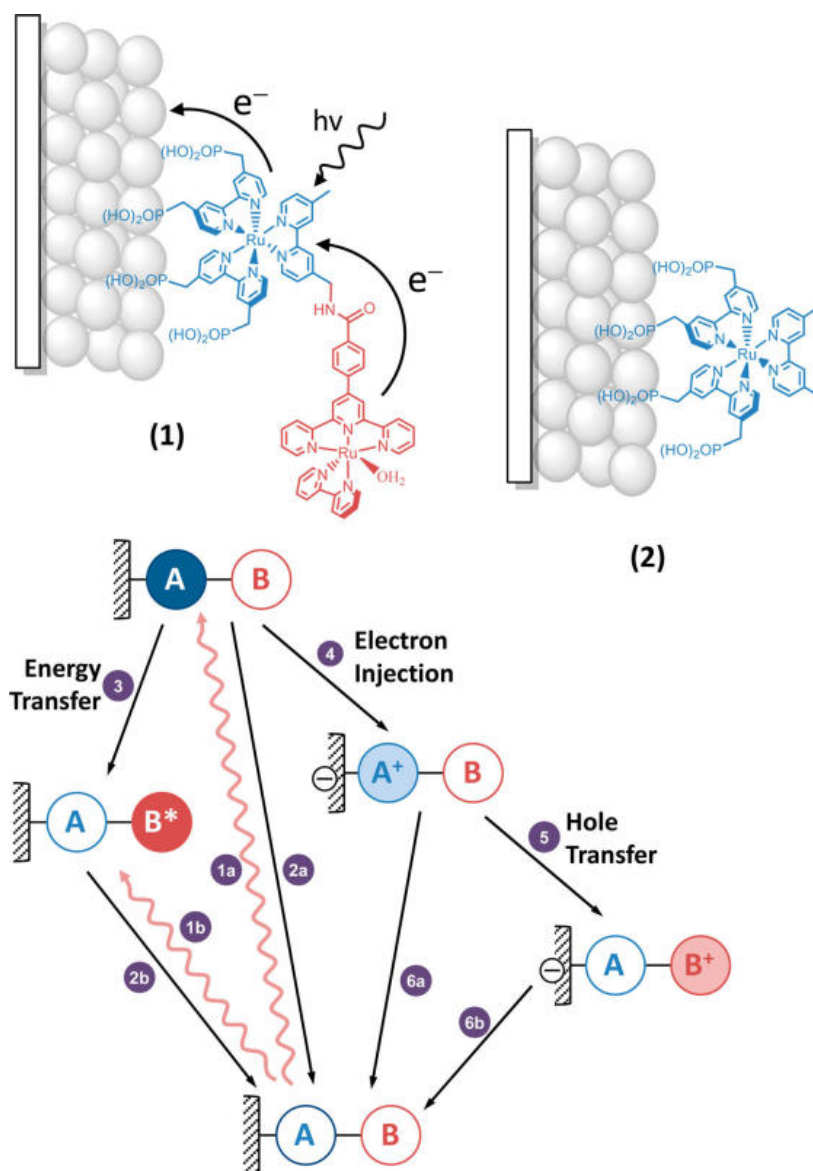
Use of these catalysts in solar fuels production requires coupling to a light-harvesting center and a mechanism, or mechanisms, in which the sequential absorption of four photons results in the transfer of four oxidative equivalents to the catalyst, driving water oxidation.

This chapter describes the use of femtosecond spectroscopy to characterize the initial photoactivation step in the Ru-based chromophore–catalyst assembly anchored to TiO_2 (Scheme 6.2), abbreviated $\text{TiO}_2\text{-}[\text{Ru}_a^{\text{II}}\text{-Ru}_b^{\text{II}}\text{-OH}_2]^{4+}$.¹⁹⁰ In this notation, Ru_a represents the chromophore, $\text{Ru}_a \equiv \text{Ru}^{\text{II}}[(\text{P}_2\text{-bpy})_2(\text{bpy-L})]^{2+}$ ($\text{P}_2\text{-bpy} = ([2,2'\text{-bipyridine}]\text{-}4,4'\text{-diyl-bis-}(\text{methylene}))\text{diphosphonic acid}$; $\text{bpy-L} = 4\text{-}([2,2':6',2''\text{-terpyridin}]\text{-}4'\text{-yl})\text{-N-}((4'\text{-methyl-}$

[2,2'-bipyridin]-4-yl)methyl)), and Ru_b represents the catalyst, $Ru_b \equiv Ru^{II}[(L-trpy)$

$(bpy)OH_2]^{2+}$ ($bpy = 2,2'$ - bipyridine), complexes joined together via benzamide linkage.

Scheme 6.2. Structure of the Chromophore-Catalyst Assembly (1) and the Chromophore Control (2); Illustration of Dynamical Processes Resulting from Photoexcitation of the Chromophore-Catalyst Assembly on TiO_2 (Lower Panel).



Metal-to-ligand charge transfer (MLCT) excitation of the chromophore ($-Ru_a^{II}-$) is followed by electron injection into TiO_2 (Scheme 6.2) on time scales ranging from ~ 100 fs to

several hundred picoseconds, giving rise to the oxidized chromophore $\text{TiO}_2(\text{e}^-)-[\text{Ru}_a^{\text{III}}-\text{Ru}_b^{\text{II}}-\text{OH}_2]^{5+}$. Injection occurs with $\sim 95\%$ efficiency and is followed by electron transfer from the catalyst, $[-\text{Ru}_b^{\text{II}}-\text{OH}_2]^{2+}$, to the chromophore, $[-\text{Ru}_a^{\text{III}}]^{3+}$, resulting in oxidative activation of the catalyst with a transfer time of 145 ps. The photoactivated catalyst, $\text{TiO}_2(\text{e}^-)-[\text{Ru}_a^{\text{II}}-\text{Ru}_b^{\text{III}}-\text{OH}_2]^{5+}$, undergoes back-electron transfer on a microsecond-millisecond time scale.

6.2 Experimental

Materials

The synthesis of the amide-linked chromophore–catalyst assembly with phosphonic acid groups for binding to TiO_2 has been previously reported and characterized by ^1H NMR and high-resolution electrospray ionization mass spectrometry (HR-ESI-MS).¹⁹⁰ The structures of the assembly (**1**) and the chromophore control complex (**2**) are shown in Scheme 6.2.

Preparation of TiO_2 films and loading procedures were reported previously.¹⁹⁰ Surface coverages were calculated by $\Gamma = A(\lambda)/(\varepsilon(\lambda)1000)$ with Γ the surface coverage in moles per square centimeter and $\varepsilon(\lambda)$ the molar absorptivity for the assembly in solution. Maximum coverage (Γ_0) on 6 μm thick TiO_2 films was $\sim 6.7 \times 10^{-8} \text{ mol cm}^{-2}$. Spectroscopic measurements on the loaded TiO_2 films were performed by submerging the slide in water (spectroscopy grade) in 0.1 M HClO_4 with argon sparging for 20 min prior to use.

Steady-State Measurements.

UV–visible spectra were recorded on a diode array spectrometer with 1 nm resolution. Steady-state emission spectra were recorded on a photon-counting spectro-

fluorimeter and were corrected for instrument response and light loss using the correction factors supplied by the manufacturer. Relative emission quantum yields were determined by relative actinometry based on the integrated emission profile (I) and absorbance (A) of an unknown sample relative to a reference compound. The quantum yield of the sample was determined by using Equation 6.1.³¹³

Equation 6.1

$$\Phi_{\text{Sam}} = \Phi_{\text{std}} \left(\frac{A_{\text{std}}}{A_{\text{sam}}} \right) \left(\frac{I_{\text{sam}}}{I_{\text{std}}} \right) \left(\frac{n_{\text{sam}}}{n_{\text{std}}} \right)^2$$

Pump-Probe Transient Absorption Measurement

Transient absorption measurements were conducted by using a Ti:Sapphire chirped pulse amplification (CPA) laser system (Clark-MXR CPA-2001). The 415 nm pump pulse was produced by the sum frequency generation (SFG) from the second harmonic of the idler produced by a near-infrared pumped optical parametric amplifier (OPA) at 900 nm and residual 775 nm pump light. The femtosecond probe pulse was formed by continuum generation in CaF₂. The probe beam was directed through a computer-controlled optical delay stage with 250 mm of travel (~1.5 ns pump-probe delay), passed through the sample, coupled into a spectrometer, and dispersed onto a high-speed 1024 pixel diode-array CMOS detector. Spectra were collected over the range of 300–900 nm on a shot-by-shot (1 kHz) basis, resulting in a high signal-to-noise ratio and an instrument sensitivity of 0.1 mOD. The angle between the pump and probe polarization vectors was set to the magic angle (54.7°) to avoid polarization effects.

The probe pulse for subnanosecond measurements was generated by continuum generation in a diode laser pumped photonic crystal fiber whose timing relative to the

femtosecond pump pulse was controlled electronically. This allowed monitoring of the spectral evolution between 500 ps and 400 μ s. The time resolution of the instrument is \sim 500 ps, dictated by the width of the probe pulse and the timing electronics.

6.3 Results and Discussion

The absorption of a photon by the surface-bound chromophore–catalyst assembly $\text{TiO}_2\text{--}[\text{Ru}_a^{\text{II}}\text{--Ru}_b^{\text{II}}\text{--OH}_2]^{4+}$ can result in either excitation of the chromophore (Scheme 6.2, eq 1a), or the catalyst (Scheme 6.2, eq 1b). Chromophore excitation is followed by electron injection, $\text{TiO}_2\text{--}[\text{Ru}_a^{\text{II}*}\text{--Ru}_b^{\text{II}}\text{--OH}_2]^{4+} \rightarrow \text{TiO}_2(\text{e}^-)\text{--}[\text{Ru}_a^{\text{III}}\text{--Ru}_b^{\text{II}}\text{--OH}_2]^{5+}$ (Scheme 6.2, eq 4). Once formed, transfer of the oxidative equivalent to the catalyst occurs (i.e., intra-assembly electron transfer), $\text{TiO}_2(\text{e}^-)\text{--}[\text{Ru}_a^{\text{III}}\text{--Ru}_b^{\text{II}}\text{--OH}_2]^{5+} \rightarrow \text{TiO}_2(\text{e}^-)\text{--}[\text{Ru}_a^{\text{II}}\text{--Ru}_b^{\text{III}}\text{--OH}_2]^{5+}$ (Scheme 6.2, eq 5), completing the first of four steps in the water oxidation catalytic cycle. Energy transfer from photoexcited chromophore to the catalyst, $\text{TiO}_2\text{--}[\text{Ru}_a^{\text{II}*}\text{--Ru}_b^{\text{II}}\text{--OH}_2]^{4+} \rightarrow \text{TiO}_2\text{--}[\text{Ru}_a^{\text{III}}\text{--Ru}_b^{\text{II}}\text{--OH}_2^*]^{4+}$ (Scheme 6.2, eq 3) is also possible and is a potentially deleterious energy loss pathway. However, the time scale for this process is significantly slower than electron injection, $\text{TiO}_2\text{--}[\text{Ru}_a^{\text{II}*}\text{--Ru}_b^{\text{II}}\text{--OH}_2]^{4+} \rightarrow \text{TiO}_2(\text{e}^-)\text{--}[\text{Ru}_a^{\text{III}}\text{--Ru}_b^{\text{II}}\text{--OH}_2]^{5+}$, limiting its relevance.

Following electron injection, “recombination” by back electron transfer from the semiconductor surface, $\text{TiO}_2(\text{e}^-)\text{--}[\text{Ru}_a^{\text{III}}\text{--Ru}_b^{\text{II}}\text{--OH}_2]^{5+} \rightarrow \text{TiO}_2\text{--}[\text{Ru}_a^{\text{II}}\text{--Ru}_b^{\text{II}}\text{--OH}_2]^{5+}$ (Scheme 6.2, eq 6b) returns the surface assembly to its initial state with the transiently stored oxidative equivalent lost as heat. Successful utilization of these interfacial injection and electron transfer schemes requires long recombination times or rapid removal of injected

electrons from the semiconductor. In the subsections that follow we address each of the dynamical processes for the first photoactivation step.

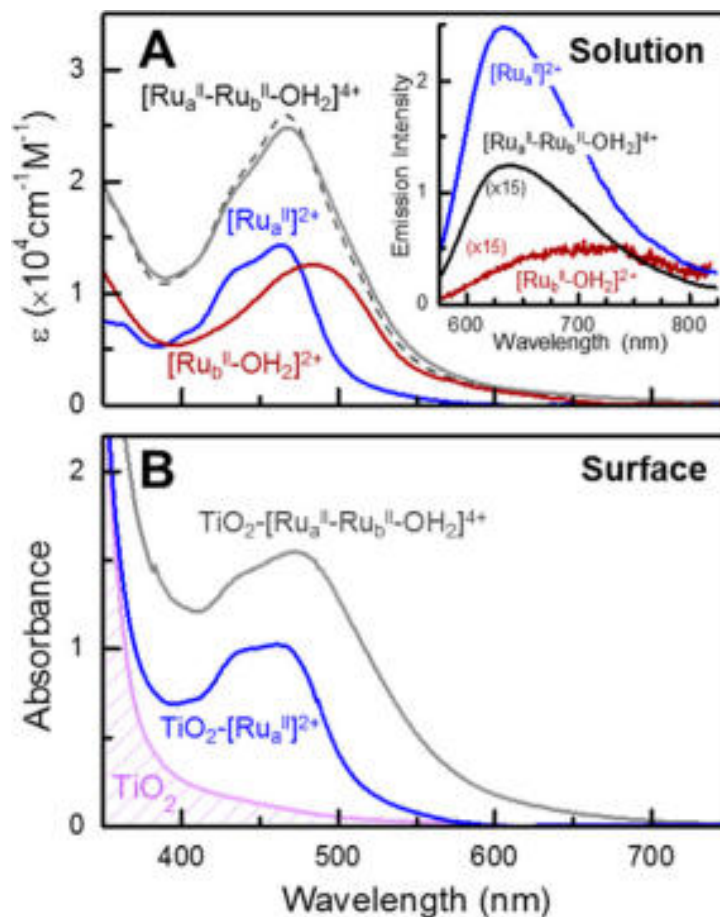


Figure 6.1. (A) Absorption spectra of the chromophore ($[\text{Ru}_a^{\text{II}}]^{2+}$) (blue), catalyst ($[\text{Ru}_b^{\text{II}}-\text{OH}_2]^{2+}$) (red), and chromophore-catalyst assembly ($[\text{Ru}_a^{\text{II}}-\text{Ru}_b^{\text{II}}-\text{OH}_2]^{4+}$) (gray) in water at 298 K. The black dashed line is the calculated absorption of the chromophore-catalyst assembly. Inset: emission from chromophore ($[\text{Ru}_a^{\text{II}}]^{2+}$) (blue), catalyst ($[\text{Ru}_b^{\text{II}}-\text{OH}_2]^{2+}$) (red), and chromophore-catalyst assembly ($[\text{Ru}_a^{\text{II}}-\text{Ru}_b^{\text{II}}-\text{OH}_2]^{4+}$) (black) in water following excitation at 415 nm. The spectra for the catalyst and assembly are scaled by a factor of 15. (B) Absorption spectra of $\text{TiO}_2-[\text{Ru}_a^{\text{II}}-\text{Ru}_b^{\text{II}}-\text{OH}_2]^{4+}$ (black) and $\text{TiO}_2-[\text{Ru}_a^{\text{II}}]^{2+}$ (blue).

Photoexcitation

The ground-state absorption spectrum of the chromophore–catalyst assembly,

$[\text{Ru}_a^{\text{II}}-\text{Ru}_b^{\text{II}}-\text{OH}_2]^{4+}$, is dominated in the visible by a broad MLCT absorption feature at

$\lambda_{\text{max}} = 472 \text{ nm}$ (Figure 6.1A). The spectrum is close to a superposition of spectra for the

chromophore Ru_a^{II} ($\lambda_{\text{max}} = 463 \text{ nm}$) and catalyst $\text{Ru}_b^{\text{II}}\text{-OH}_2^{2+}$ ($\lambda_{\text{max}} = 488 \text{ nm}$), consistent with electronically isolated complexes due to weak electronic coupling across the saturated amide linkage.¹⁸⁹ Attachment to the surface does not significantly alter the absorption bands, and the spectra of $\text{TiO}_2\text{-Ru}_a^{\text{II}}$ and $\text{TiO}_2\text{-[Ru}_a^{\text{II}}\text{-Ru}_b^{\text{II}}\text{-OH}_2]^{4+}$ (Figure 6.1B) are well-described by superimpositions of the absorption spectra of the dye (Ru_a^{II}) or assembly ($[\text{Ru}_a^{\text{II}}\text{-Ru}_b^{\text{II}}\text{-OH}_2]^{4+}$) and the background absorption of TiO_2 .

The large degree of overlap between the MLCT absorptions for the two complexes in the assembly prevents selective excitation of the chromophore. When the assembly is excited at 415 nm, the wavelength used in this work, 75% of the photons are absorbed by the chromophore and 25% by the catalyst (Figure E.1). As a result, the observed dynamics reflects a superposition of dynamical processes resulting from excitation of the catalyst ($[\text{-Ru}_b^{\text{II}}\text{-OH}_2]^{2+}$) as well as the chromophore ($[\text{-Ru}_a^{\text{II}}]^{2+}$).

Electron Injection

The transient absorption spectra following 415 nm excitation of the chromophore in solution ($[\text{Ru}_a^{\text{II}}]^{2+}$) and bound to the surface ($\text{TiO}_2\text{-[Ru}_a^{\text{II}}]^{2+}$) are shown in Figure 6.2. The spectra show a ground-state bleach at 450 nm and excited-state absorptions arising from a $\text{bpy}^{\text{-}} \pi_1^* \rightarrow \pi_2^*$ transition at 375 nm, and overlapped weak ligand-to-metal charge transfer (LMCT) and $\text{bpy}^{\text{-}}$ absorptions that extend to the red past 500 nm.³¹⁴ While the transient spectra for the chromophore in solution ($[\text{Ru}_a^{\text{II}}]^{2+}$) show almost no change during the first nanosecond (Figure 6.2A), when bound to the surface ($\text{TiO}_2\text{-[Ru}_a^{\text{II}}]^{2+}$) the spectra exhibit

simultaneous loss of both the 375 and 525 nm excited-state absorptions, which become a net bleach by 50 ps. The decay of these bands occur with only a slight decrease (<5%) in the bleach amplitude at 450 nm (Figure 6.2B). Although the loss of the excited-state absorptions could, in principle, arise from rapid back electron transfer, the observation of negligible decay of the bleach indicates that the primary contributor is electron injection.

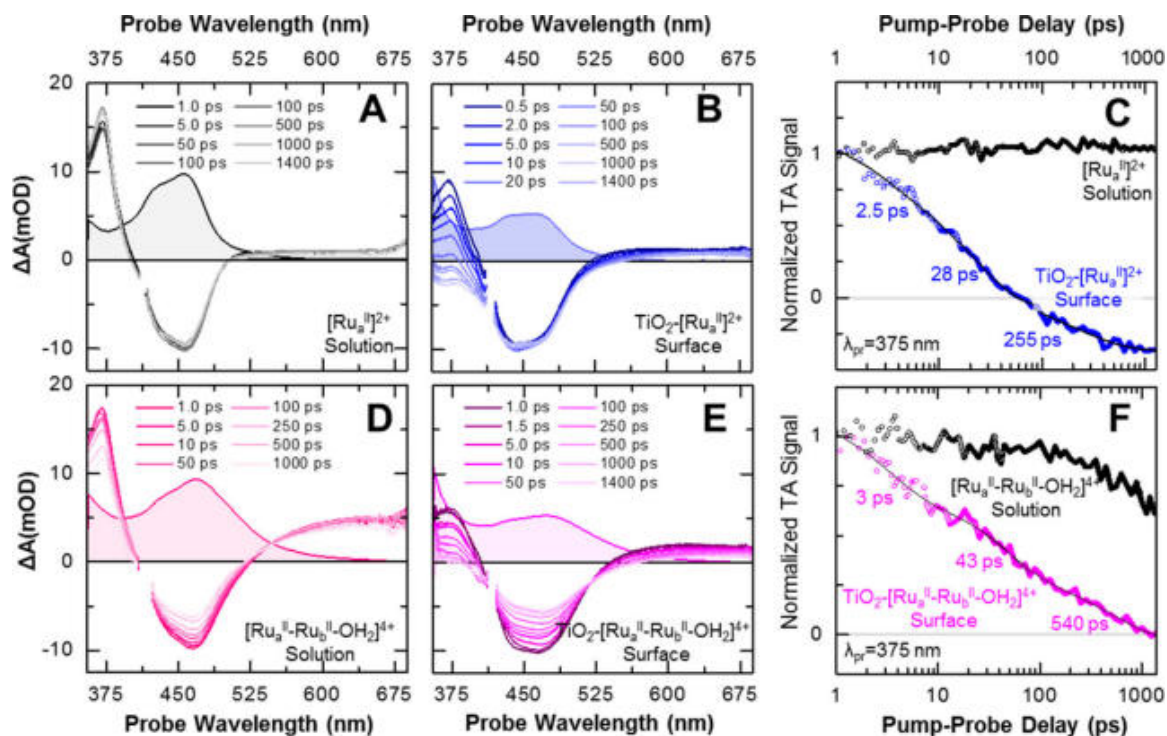


Figure 6.2. (A) Femtosecond transient absorption of chromophore in pH 1.0 HClO₄ aqueous solution, [Ru_a^{II}]²⁺. (B) Transient absorption spectra of chromophore on TiO₂ in pH 1.0 HClO₄ aqueous solution, (TiO₂-[Ru_a^{II}]²⁺). (C) Kinetic traces at 375 nm for [Ru_a^{II}]²⁺ in solution (black) and TiO₂-[Ru_a^{II}]²⁺ (blue). (D) Femtosecond transient absorption of assembly [Ru_a^{II}-Ru_b^{II}-OH₂]⁴⁺ in HNO₃ aqueous solution. (E) Transient absorption of assembly on TiO₂, (TiO₂-[Ru_a^{II}-Ru_b^{II}-OH₂]⁴⁺) in pH 1.0 HClO₄ aqueous solution. (F) Kinetics at 375 nm for [Ru_a^{II}-Ru_b^{II}-OH₂]⁴⁺ in solution (black) and TiO₂-[Ru_a^{II}-Ru_b^{II}-OH₂]⁴⁺ (magenta). All femtosecond transient absorption spectra were acquired with λ_{exc} = 415 nm at 150 nJ/pulse.

The kinetics of the electron injection by TiO₂-Ru_a^{II}* are given by the decay in the amplitude of the 375 nm absorption band as a function of pump-probe delay (Figure 6.2C).

In solution, there is no appreciable decay of this band on the nanosecond time scale, which is consistent with its 360 ns excited-state lifetime.

When bound to the surface, the decay includes multiple kinetic components with time constants of 2.5 ps (30%), 28 ps (40%), and 255 ps (30%). In addition to these picosecond components, the Moran group observed a sub-200 fs component for this chromophore,³¹⁵ underscoring the wide range of time scales associated with injection by $\text{TiO}_2\text{-[Ru}_a^{\text{II}*}]^{2+}$. The presence of multiple kinetic components has been observed for other, related sensitizers.³¹⁶⁻³²⁰

This distribution of injection rates most likely arises from a combination of factors. Following excitation, the initially formed $^1\text{MLCT}$ state or states, or vibrationally hot triplet states, undergo rapid injection. Injection from thermally equilibrated $^3\text{MLCT}$ states occurs on time scales ranging from subpicosecond to tens of picoseconds, as reported for other Ru(II) dyes.^{316,320,321} The heteroleptic nature of the chromophore can also play a role. Partitioning of the photoexcitation among the three ligands results in three distinct excited states corresponding to placement of the charge on each of the three ligands. When excitation is directed toward a nonsurface-bound ligand, injection must occur either remotely^{322,323} or be preceded by interligand excitation transfer.³²⁴ Experiments currently underway on a family of related complexes indicate that the slower components arise (at least in part) from equilibrated $^3\text{MLCT}$ states localized away from the surface-bound ligands.

Assembly Injection Dynamics

The transient absorption spectra of the assembly in solution, $[\text{Ru}_a^{\text{II}}\text{-Ru}_b^{\text{II}}\text{-OH}_2]^{4+}$, and bound to the surface, $\text{TiO}_2\text{-[Ru}_a^{\text{II}}\text{-Ru}_b^{\text{II}}\text{-OH}_2]^{4+}$, are shown in Figure 6.2D and Figure 6.2E,

respectively. Both sets of spectra exhibit characteristic transitions that are the same as the those of the chromophore ($[\text{Ru}_a^{\text{II}}]^{2+}$); however because the catalyst has an energy absorption lower than that of the chromophore, the bleach of the chromophore–catalyst assembly extends further to the red compared to that of $[\text{Ru}_a^{\text{II}}]^{2+}$ or $\text{TiO}_2\text{--}[\text{Ru}_a^{\text{II}}]^{2+}$.

Figure 6.2F compares the decay kinetics at 375 nm (bpy excited-state absorption) for the assembly in solution ($[\text{Ru}_a^{\text{II}}\text{--}\text{Ru}_b^{\text{II}}\text{--OH}_2]^{4+}$) and anchored to the surface ($\text{TiO}_2\text{--}[\text{Ru}_a^{\text{II}}\text{--}\text{Ru}_b^{\text{II}}\text{--OH}_2]^{4+}$). In solution, the assembly's decay is single exponential with $\tau = 4.1 \pm 0.50$ ns. Transient absorption and time-resolved emission measurements of the catalyst ($[\text{Ru}_b^{\text{II}}\text{--OH}_2]^{2+}$) in solution show its lifetime to be 3–4 ns (Figure E.2 and Figure E.3), suggesting that the decay for the assembly is largely dominated by the excited-state decay of the catalyst. As discussed below, this is primarily due to chromophore-to-catalyst energy transfer. While this process is rapid compared to the excited-state lifetime of the chromophore, it is slow compared to injection and ultimately plays little role in the dynamics of the assembly on the surface. On the surface, the decay is multiexponential with time constants of 3.0 ps (35%), 43 ps (35%), and 540 ps (30%). The slowest component is likely convoluted with the excited-state decay of the catalyst; the faster components are comparable to those observed in the chromophore control, $\text{TiO}_2\text{--}[\text{Ru}_a^{\text{II}*}]^{2+}$, suggesting qualitatively similar injection dynamics from the assembly.

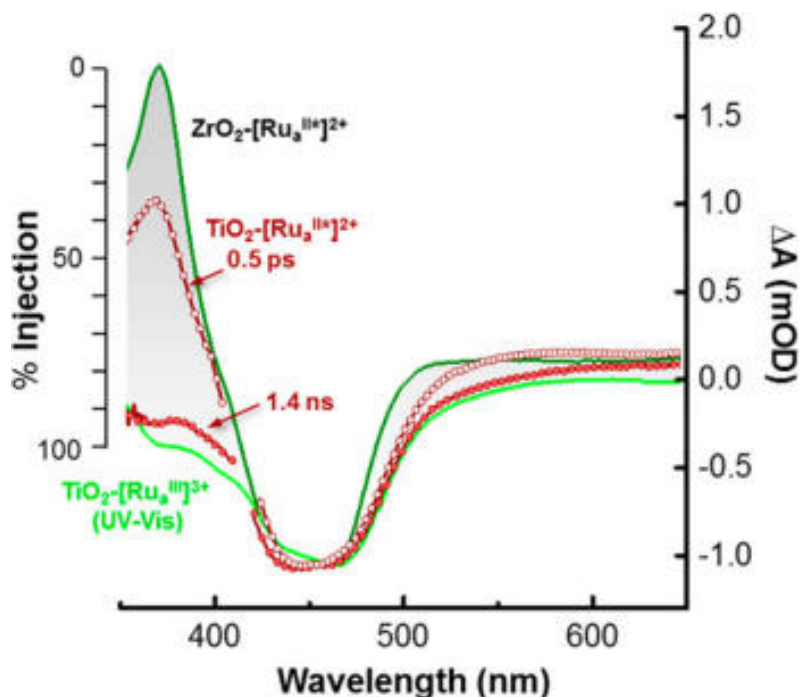


Figure 6.3. Electron injection efficiency for $\text{TiO}_2\text{-}[\text{Ru}_a^{\text{II}*}]^{2+}$. The transient absorption spectrum of $\text{ZrO}_2\text{-}[\text{Ru}_a^{\text{II}*}]^{2+}$ at early delay (dark green) and the UV-vis spectrum of $\text{TiO}_2\text{-}[\text{Ru}_a^{\text{II}*}]^{2+}$ (light green) provide the 0% and 100% injection limits, respectively. The red curves are transient absorption spectra for $\text{TiO}_2\text{-}[\text{Ru}_a^{\text{II}*}]^{2+}$ at 0.5 ps (open circle) and 1.4 ns (filled circle). All curves were normalized to the maximum of the bleach signal. At 0.5 ps, ~35% of the complexes have injected, consistent with an ultrafast (<200 fs) injection component that is not observable in our measurements. By 1.4 ns, injection is nearly complete (~95%).

Injection Yield

Injection efficiencies (Φ_{inj}) are estimated by comparing the intensity of the 375 nm $\text{bpy}^{\bullet-}$ absorption relative to the ground-state bleach. The former provides a measure of the $\text{TiO}_2\text{-}[\text{Ru}_a^{\text{II}*}]^{2+}$ population, while the latter reflects the total number of photoexcitation events giving either $\text{TiO}_2\text{-}[\text{Ru}_a^{\text{II}*}]^{2+}$ or $\text{TiO}_2(\text{e}^-)\text{-}[\text{Ru}_a^{\text{III}}]^{3+}$. The maximum amplitude of the excited-state absorption (relative to the bleach) is observed when $\Phi_{\text{inj}} = 0\%$. This is determined from the transient absorption spectrum of $[\text{Ru}_a^{\text{II}}]^{2+}$ on ZrO_2 , where the conduction band lies at much higher energy compared to TiO_2 and, as a consequence,

injection is not possible (Figure 6.3). As injection proceeds from $\text{TiO}_2\text{-[Ru}_a^{\text{II}*}]^{2+}$, the amplitude of this band decreases, reaching a minimum when $\Phi_{\text{inj}} = 100\%$, at which point the transient spectrum corresponds to $\text{TiO}_2(\text{e}^-)\text{-[Ru}_a^{\text{III}}]^{3+}$. Because the oxidized chromophore is nearly colorless, its primary contribution to the transient spectrum will be the ground-state bleach, which we have approximated as the inverse of the ground-state absorption spectrum.

The transient absorption spectrum for surface-bound $\text{TiO}_2\text{-[Ru}_a^{\text{II}}]^{2+}$ at long delay times lies between the spectra for $\text{TiO}_2\text{-[Ru}_a^{\text{II}*}]^{2+}$ and $\text{TiO}_2\text{-[Ru}_a^{\text{III}}]^{2+}$ with its relative position reflecting the injection efficiency. We estimate that by 1.4 ns $\sim 95\%$ of the chromophores, initially as $\text{TiO}_2\text{-[Ru}_a^{\text{II}*}]^{2+}$, have undergone electron injection. For $\text{TiO}_2\text{-[Ru}_a^{\text{II}}\text{-Ru}_b^{\text{II}}\text{-OH}_2]^{4+}$ this fraction is $\sim 90\%$.

Calculating injection efficiencies in this manner makes two assumptions. The first is that oxidized chromophore, $\text{TiO}_2\text{-[Ru}_a^{\text{III}}]^{3+}$, does not contribute to the signal at 375 nm. This is a reasonable assumption given that $\text{Ru}(\text{bpy})_3^{3+}$ is only weakly absorbing throughout the visible and near-UV. Nevertheless, an excited-state absorption contribution to the transient signal at 375 nm from $\text{TiO}_2\text{-[Ru}_a^{\text{III}}]^{3+}$ would make the efficiency appear smaller relative to its actual value. Second, it is assumed that the amplitude of the bleach signal at 450 nm is a good measure of the population of photoexcited chromophores. This requires that the excited-state absorption of the chromophore does not contribute to the bleach signal at 450 nm and that the bleach does not decay (i.e., no excited-state relaxation) on the time

scale of the measurement. The bleach intensity for $\text{TiO}_2\text{-[Ru}_a^{\text{II}}\text{]}^{2+}$ remains unchanged following injection, suggesting that both assumptions hold.

This measure of the injection efficiency is also consistent with steady-state emission measurements. As a result of electron injection, the chromophore emission is almost completely quenched, with a quantum efficiency of 2.0×10^{-4} for $\text{TiO}_2\text{-[Ru}_a^{\text{II}}\text{]}^{2+}$. This is almost 100 times smaller than the quantum yield in solution ($\Phi([\text{Ru}_a^{\text{II}}]^{2+}) = 0.036$, $\tau = 360$ ns), implying an injection yield greater than 98%. Taken together, the transient absorption and emission measurements suggest an overall injection efficiency that is greater than 95%.

Our estimates of injection efficiency are significantly larger than the 45% and 30% previously reported for $\text{TiO}_2\text{-[Ru}_a^{\text{II}}\text{]}^{2+}$ and $\text{TiO}_2\text{-[Ru}_a^{\text{II}}\text{-Ru}_b^{\text{II}}\text{-OH}_2\text{]}^{4+}$.¹⁹⁰ Those were derived from nanosecond transient absorption measurements and limited to initial observations at 10–20 ns given the time resolution of the instrument used. Transient absorption data collected on the nanosecond time scale discussed below indicate that there is a significant fast back electron transfer component with $k_{\text{ET}}^{-1} \approx 17$ ns, which results in an underestimation of the injection efficiency when measurements are performed on longer time scales.

Ultrafast Injection Yield

Although we cannot directly observe the ultrafast (<200 fs) decay component in our experiment, evidence for such events appears in the transient spectra. In particular, the relative amplitude of the 375 nm absorption to that of the bleach at early times (0.5 ps) is significantly larger for $\text{ZrO}_2\text{-[Ru}_a^{\text{II}}\text{]}^{2+}$ than it is on the surface for $\text{TiO}_2\text{-[Ru}_a^{\text{II}}\text{]}^{2+}$ (Figure 6.3). The reduced amplitude observed on the TiO_2 surface at early pump–probe delays is a

direct consequence of ultrafast electron injection that occurs on a time scale faster than our instrument response. The relative amplitudes of absorption and bleach suggest that ~35% of the injection events occur in the first 500 fs, with the remaining 65% taking place over a few picoseconds to several hundred picoseconds.

Energy Transfer from Chromophore to Catalyst

Energy transfer from the photoexcited chromophore to the catalyst (Scheme 6.2), $[\text{Ru}_a^{\text{II}*}-\text{Ru}_b^{\text{II}}-\text{OH}_2]^{4+} \rightarrow [\text{Ru}_a^{\text{II}}-\text{Ru}_b^{\text{II}*}-\text{OH}_2]^{4+}$, was investigated by time-resolved and steady-state emission measurements in solution free of complications from injection. In the absence of the catalyst, the MLCT emission from $[\text{Ru}_a^{\text{II}*}]^{2+}$ is clearly evident (Figure 6.1A, inset). When incorporated into the assembly, however, the chromophore emission is significantly quenched ($\Phi_{\text{Ru}_a-\text{Ru}_b} = 1.2 \times 10^{-3}$) with the emission broadened toward the red. Both of these observations are suggestive of intra-assembly energy transfer from the chromophore ($[\text{Ru}_a^{\text{II}*}]^{2+}$) to the catalyst ($[\text{Ru}_b^{\text{II}*}]^{2+}$). The energy transfer rate constant (k_{EnT}) estimated from the time-resolved emission quenching data (Figure E.4) is $k_{\text{EnT}} \sim 8.0 \times 10^7 \text{ s}^{-1}$ ($\tau_{\text{EnT}} = k_{\text{EnT}}^{-1} = 12 \text{ ns}$). Alternatively, the energy transfer rate constant (k_{EnT}) can also be determined from emission quantum yields by Equation 6.2 where $\tau_{\text{Ru}_a^{\text{II}}}$ is the emission lifetime of the chromophore in the absence of the catalyst (360 ns) and $\Phi([\text{Ru}_a^{\text{II}*}]^{2+}) = 0.036$. This approach also gives $\tau_{\text{EnT}} = k_{\text{EnT}}^{-1} = (12 \text{ ns})^{-1}$. Although our observations are consistent with energy transfer, we cannot rule out other quenching mechanisms. Regardless of its origin, however, this process is significantly slower than electron injection on TiO_2 . As a

result, it is not competitive with the injection event, and it does not provide an important loss pathway for the assembly on TiO₂.

Equation 6.2

$$k_{EnT} = \left(\frac{1}{\tau_{Ru_a^{II}}} \right) \times \left(\frac{\Phi_{Ru_a^{II}}}{\Phi_{Ru_a^{II}-Ru_b^{II}}} - 1 \right)$$

Transfer of Oxidative Equivalent to the Catalyst

Electron injection is followed by the transfer of the oxidative equivalent to the catalyst (Scheme 6.2). The driving force for this intra-assembly electron transfer based on E^o values for the chromophore (+1.23 eV vs NHE) and catalyst (+0.95 eV vs NHE) is -0.28 eV.¹⁹⁰

This shift of the oxidized site from the chromophore to the catalyst is accompanied by a shift in the bleach from 463 nm in TiO₂(e⁻)-[Ru_a^{III}-Ru_b^{II}-OH₂]⁵⁺ to 488 nm in TiO₂(e⁻)-[Ru_a^{II}-Ru_b^{III}-OH₂]⁵⁺. Figure 6.4 shows transient absorption difference spectra obtained at different pump-probe delays, each normalized to the maximum bleach signal. In this representation, there is a clear broadening of the bleach transition toward the red. This evolution of the spectrum corresponds to a 7–8 nm shift in the red edge of the bleach (measured at the 50% point) that takes place on the 100–1000 ps time scale (Figure 6.4, inset). This broadening is not observed in transient spectra of TiO₂(e⁻)-[Ru_a^{III}]³⁺, which is consistent with its origin in intra-assembly electron transfer.

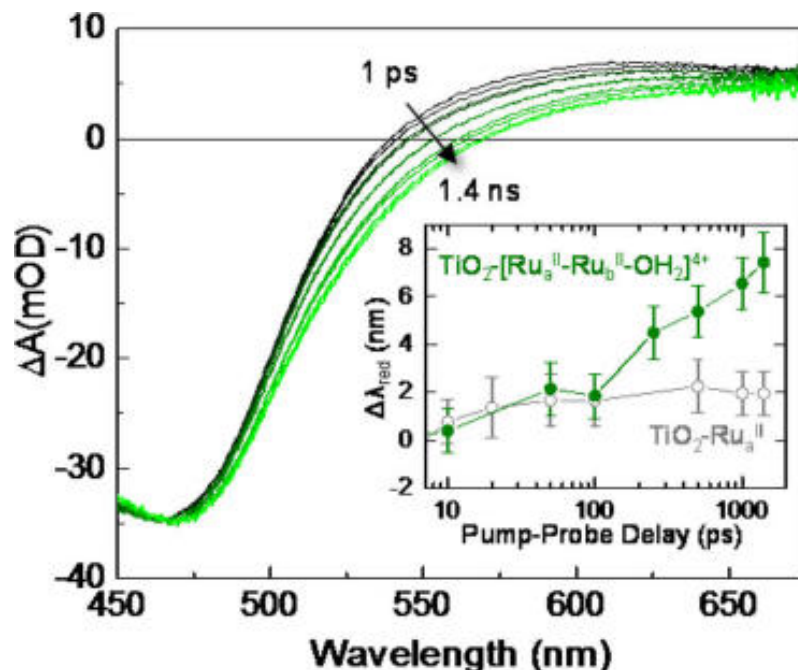


Figure 6.4. Normalized transient absorption spectra for $\text{TiO}_2\text{-}[\text{Ru}_a^{\text{II}}\text{-Ru}_b^{\text{II}}\text{-OH}_2]^{4+}$. The inset is a plot of the shift in the red edge of the bleach ($\Delta\lambda_{\text{red}}$) with pump-probe delay for $\text{TiO}_2\text{-}[\text{Ru}_a^{\text{II}}\text{-Ru}_b^{\text{II}}\text{-OH}_2]^{4+}$ and $\text{TiO}_2\text{-Ru}_a^{\text{II}}$.

Because the bleach spectra for the oxidized chromophore and oxidized catalyst are significantly overlapped, determining the electron transfer rate constant by monitoring the transients at a particular probe wavelength is problematic. A further complication arises from a contribution to the transient spectra from the catalyst excited state, $\text{-}[\text{Ru}_b^{\text{II}*}\text{-OH}_2]^{2+}$, produced by direct excitation. Disentangling the kinetic processes was accomplished by global analysis based on a singular-value decomposition (SVD) algorithm applied to the transient spectra between 250 fs and 1.4 ns. The multivariate data analysis, which was implemented using the global fitting program SPECFIT/32 with a self-defined kinetic model, reveals the presence of four significant spectral components and time domain eigenvectors (Figure E.5 and Figure E.6). They are attributed to the excited states of the chromophore

($[-\text{Ru}_a^{\text{II}*}-]^{2+}$) and catalyst ($[-\text{Ru}_b^{\text{II}*}-\text{OH}_2]^{2+}$) as well as the oxidized chromophore, $[-\text{Ru}_a^{\text{III}}-]^{3+}$, and oxidized catalyst, $[-\text{Ru}_b^{\text{III}}-\text{OH}_2]^{3+}$.

The kinetic model used in the analysis includes photo-excitation of either the chromophore or catalyst (Scheme 6.2), resulting in a mixed initial population of $[-\text{Ru}_a^{\text{II}*}-]^{2+}$ and $[-\text{Ru}_b^{\text{II}*}-\text{OH}_2]^{2+}$. Of the processes included in Scheme 6.2, three are anticipated to contribute during the first 5 ns: electron injection (eq 4, k_{inj}), intra-assembly transfer of the oxidative equivalent (eq 5, k_{ET}), and decay of the catalyst excited state (eq 2b, k_{D}). The other processes excited-state decay of the chromophore (eq 2a), the two back electron transfer reactions (eqs 6a and 6b), and energy transfer from the chromophore to the catalyst (eq 3) all take place on time scales >10 ns, and are excluded from the kinetic analysis of the picosecond data set.

The goodness of fit to the data was assessed by comparing the analysis output with the experimental data. Figure 5 shows representative spectra at different delay times and kinetics at different wavelengths. The small residual values indicate that the fit is a good representation of the spectral-temporal data. Furthermore, analysis of the variance-covariance matrix (**H**) of the parameters indicates that the kinetic processes are uncorrelated, underscoring the uniqueness of the fit.

The global analysis provides the spectra and concentration profiles for each of the four species (Figure 6.6). The spectral changes from loss of catalyst ground state by direct excitation, $\text{TiO}_2-[\text{Ru}_a^{\text{II}}-\text{Ru}_b^{\text{II}*}-\text{OH}_2]^{4+}$, and injection, $\text{TiO}_2(\text{e}^-)-[\text{Ru}_a^{\text{II}}-\text{Ru}_b^{\text{III}}-\text{OH}_2]^{5+}$, are similar to each other but are red-shifted from those arising from the loss of the chromophore ground state, $\text{TiO}_2-[\text{Ru}_a^{\text{II}*}-\text{Ru}_b^{\text{II}}]^{4+}$ and $\text{TiO}_2(\text{e}^-)-[\text{Ru}_a^{\text{III}}-\text{Ru}_b^{\text{II}}]^{5+}$, which is consistent with

the ground-state absorption spectra for the chromophore and the catalyst. The similarity between $\text{TiO}_2\text{-[Ru}_a^{\text{II}}\text{-Ru}_b^{\text{II}*}\text{-OH}_2]^{4+}$ and $\text{TiO}_2(\text{e}^-)\text{-[Ru}_a^{\text{II}}\text{-Ru}_b^{\text{III}}\text{-OH}_2]^{5+}$ spectra as well as spectra for $\text{TiO}_2\text{-[Ru}_a^{\text{II}*}\text{-Ru}_b^{\text{II}}]^{4+}$ and $\text{TiO}_2(\text{e}^-)\text{-[Ru}_a^{\text{III}}\text{-Ru}_b^{\text{II}}]^{5+}$ exists because this spectral region is dominated by ground-state bleaches with little contribution from excited-state absorptions.

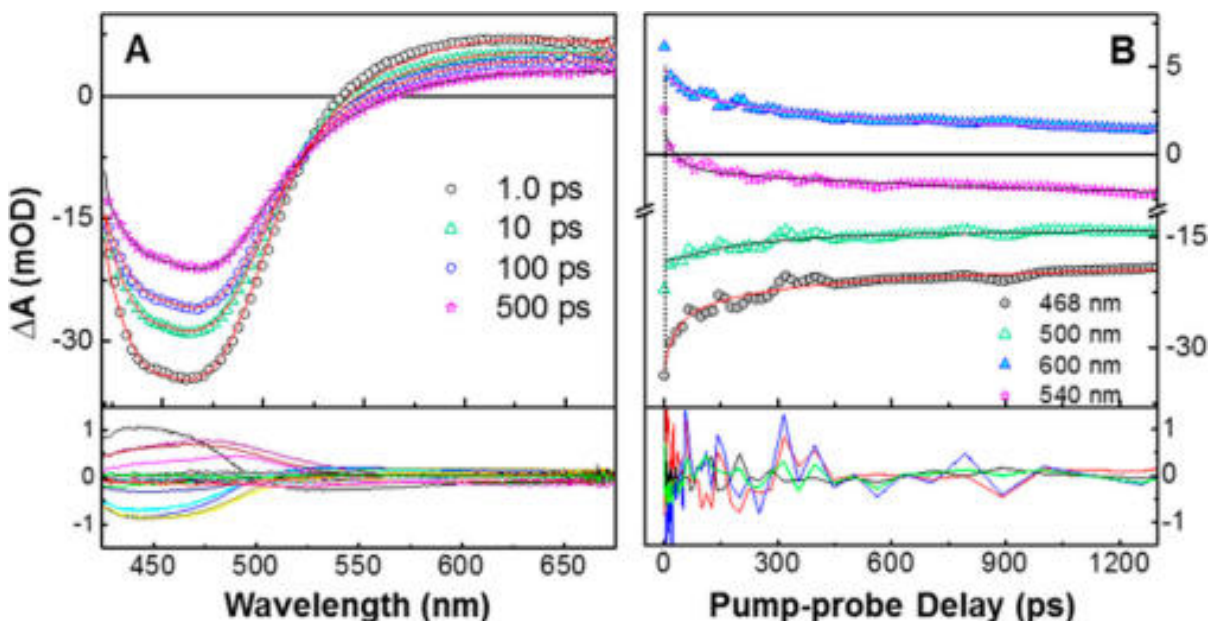


Figure 6.5. (A) Comparison of global fit (solid lines) to experimental data (points) for four representative spectra at different delay times. (B) Comparison of global fit (solid lines) and experimental data (points) for representative kinetic traces at four different wavelengths. The lower panels show the residuals.

The concentration profiles (Figure 6.6B) describe the evolution of each species.

Catalyst excited state formed by direct excitation decays with $k_D^{-1} \approx 4.2$ ns (Scheme 6.2),

consistent with measurements of its excited-state lifetime (Figure 6.2F). The electron

injection process (Scheme 6.2) is evident in the rapid loss of the $[\text{-Ru}_a^{\text{II}*}\text{-}]^{2+}$ excited state in $\text{TiO}_2\text{-[Ru}_a^{\text{II}*}\text{-Ru}_b^{\text{II}}\text{-OH}_2]^{4+}$. Injection occurs simultaneously with a growth in the oxidized

chromophore, $[\text{-Ru}_a^{\text{III}}]^{3+}$. The injection rate constant extracted from the concentration

profiles, $k_{inj}^{-1} \approx 3.6$ ps, is comparable to the 2.5 ps component observed in the decay of the 375 nm absorption feature (Figure 6.2C). At longer times, the oxidative equivalent, initially on the oxidized chromophore, is transferred by intra-assembly electron transfer, $TiO_2(e^-)-[Ru_a^{III}-Ru_b^{II}-OH_2]^{4+} \rightarrow TiO_2(e^-)-[Ru_a^{II}-Ru_b^{III}-OH_2]^{5+}$ (Scheme 6.2), to the catalyst with $\tau_{ET} = k_{ET}^{-1} \approx 145$ ps. The global analysis approximates this process by a single, average rate constant. One should recognize, however, that this is most likely an oversimplification given the heterogeneous nature of the surface as well as the potential for a range of chromophore–catalyst configurations introduced by the flexible linker, both of which would likely lead to a distribution of rate constants.

Because photoexcitation of the assembly is partitioned between the chromophore and the catalyst, the efficiency of creating oxidized catalyst is limited, and an overall yield of 75% is observed. Despite this, the analysis of the transient spectra indicates that nearly 100% of the photons absorbed by the chromophore result in oxidation of the catalyst within several hundred picoseconds after photoexcitation.

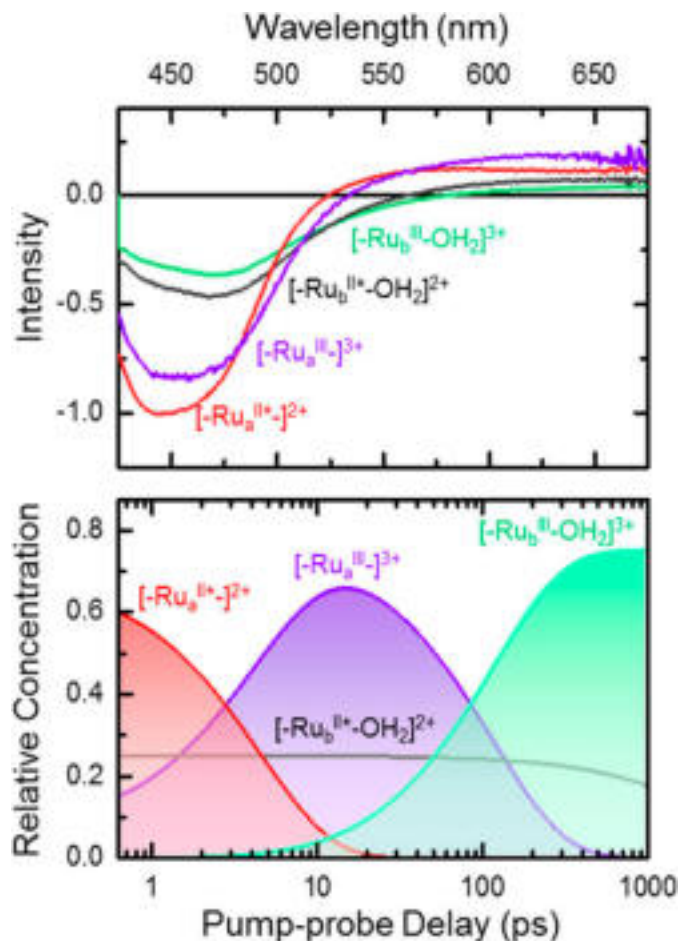


Figure 6.6. (A) Transient absorption spectra and concentration profiles (B) of the four colored species, chromophore excited state, $[-Ru_a^{II*}]^{2+}$ (red), oxidized chromophore, $[-Ru_a^{III}]^{3+}$ (purple), catalyst excited state, $[-Ru_b^{II*}-OH_2]^{2+}$ (black), and oxidized catalyst $[-Ru_b^{III}-OH_2]^{3+}$ (green) as determined by the global analysis.

Back Electron Transfer (BET)

The ground-state bleach decays on the nanosecond/microsecond time scale for both $TiO_2-Ru_a^{II}$ and $TiO_2-[Ru_a^{II}-Ru_b^{II}-OH_2]^{4+}$ (Figure 6.7) which reflects back electron transfer to either the oxidized chromophore or oxidized catalyst. For $TiO_2-[Ru_a^{II}]^{2+}$, back electron transfer occurs from the injected electron to the oxidized chromophore, i.e.,



transfer occurs to the remote catalyst site, i.e., $\text{TiO}_2(\text{e}^-)-[\text{Ru}_a^{\text{II}}-\text{Ru}_b^{\text{III}}-\text{OH}_2]^{5+} \rightarrow \text{TiO}_2-[\text{Ru}_a^{\text{II}}-\text{Ru}_b^{\text{II}}-\text{OH}_2]^{4+}$ (Scheme 6.2).

Decay kinetics at the bleach maximum (450 nm) is multiexponential for both (Figure 6.7), with time components spanning 3 decades, from 10 ns to 10 μs (Table 6.1). In the case of the chromophore, $\text{TiO}_2-[\text{Ru}_a^{\text{II}}]^{2+}$, three distinct time components are observed (τ_1 , τ_2 , and τ_3), which are attributed to recombination of the electron in the TiO_2 with the oxidized chromophore. About 35% of the recombination events occur promptly ($\tau_1 = 17$ ns), with the remaining taking place over hundreds of nanoseconds to microseconds. These slower events have been attributed to charge carrier dynamics within the TiO_2 .¹⁴⁴ In the case of the assembly, we observe a fast component ($\tau_D = 4.5$ ns) that is attributed to excited-state decay of the catalyst. The remaining kinetic components are all 2–3 times slower than those observed for the chromophore. The markedly slower charge recombination in the chromophore–catalyst assembly compared to the chromophore alone is consistent with the expectation that the oxidized site has moved further away from the surface.

In addition to the decay of the bleach, we also observe, on the microsecond time scale, a slight red shift in bleach maximum for the assembly (Figure 6.3B) that is not observed in the chromophore alone (Figure 6.3A). While the origin of this effect is currently under investigation, it appears that it may arise from proton loss from the oxidized assembly, i.e., $\text{TiO}_2(\text{e}^-)-[\text{Ru}_a-\text{Ru}_b-\text{OH}_2] \rightarrow \text{TiO}_2(\text{e}^-)-[\text{Ru}_a-\text{Ru}_b^{\text{III}}-\text{OH}]^{3+} + \text{H}^+$,²⁴ which would constitute the next step in the catalytic cycle.

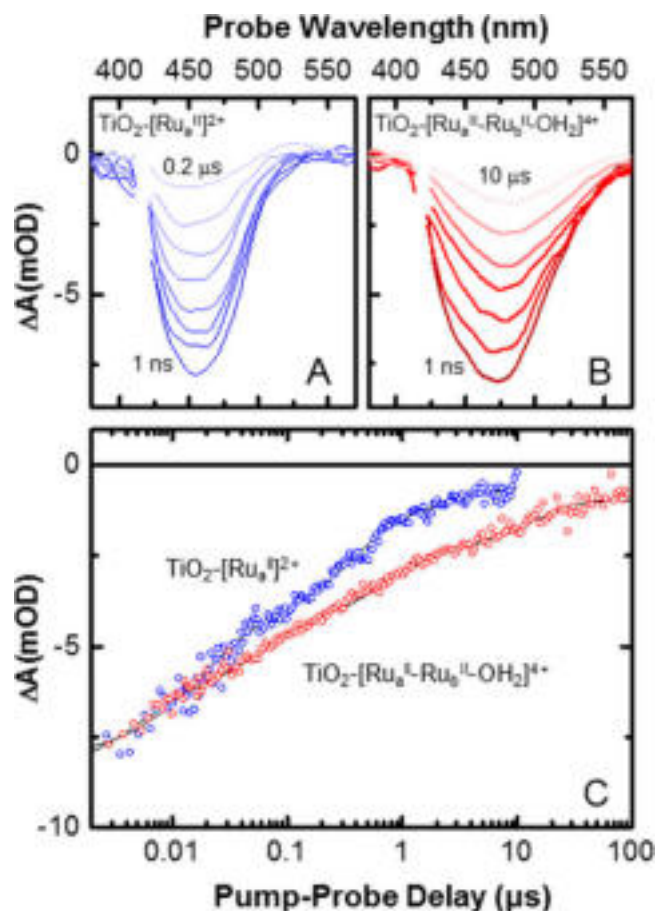


Figure 6.7. Nanosecond transient absorption-time traces for (A) $\text{TiO}_2\text{-Ru}_a^{\text{II}}$ at $t = 1.0, 5.0, 10, 20, 50, 100,$ and 200 ns (blue) and (B) $\text{TiO}_2\text{-}[\text{Ru}_a^{\text{II}}\text{-Ru}_b^{\text{II}}\text{-OH}_2]^{4+}$ at $t = 1.0, 5.0, 10, 50,$ and 200 ns and 1.0 and 10 us (red) in pH 1.0 buffer solution with $\lambda_{\text{exc}} = 415$ nm at 150 nJ/pulse. (C) 450 nm kinetics for $\text{TiO}_2\text{-}[\text{Ru}_a^{\text{II}}]^{2+}$ (blue) and 470 nm for $\text{TiO}_2\text{-}[\text{Ru}_a^{\text{II}}\text{-Ru}_b^{\text{II}}\text{-OH}_2]^{4+}$ (red) with the fit to multiexponential decay (solid line).

Table 6.1. Fitting Results for Back Electron Transfer Following Injection by $\text{TiO}_2\text{-Ru}_a^{\text{II}}$ and $\text{TiO}_2\text{-}[\text{Ru}_a^{\text{II}}\text{-Ru}_b^{\text{II}}\text{-OH}_2]^{4+}$

System	τ_D , ns (%) ^a	τ_1 , ns (%)	τ_2 , ns (%)	τ_3 , ns (%)
$\text{TiO}_2\text{-Ru}_a^{\text{II}}$		17 ± 0.30 (35%)	0.35 ± 0.018 (55%)	3.7 ± 0.50 (10%)
$\text{TiO}_2\text{-}[\text{Ru}_a^{\text{II}}\text{-Ru}_b^{\text{II}}\text{-OH}_2]^{4+}$	4.5 ± 0.28 (22%)	60 ± 3.5 (23%)	0.68 ± 0.045 (45%)	12 ± 0.7 (10%)

^a Assigned to decay of the photoexcited catalyst, i.e., $\text{TiO}_2\text{-}[\text{Ru}_a^{\text{II}}\text{-Ru}_b^{\text{II}}\text{-OH}_2]^{4+}$

6.4 Conclusions

Femtosecond transient absorption spectroscopy is used to characterize the initial photoactivation step in water oxidation by a molecular assembly anchored to TiO_2 . The

assembly, $\text{TiO}_2\text{-}[\text{Ru}_a^{\text{II}}\text{-Ru}_b^{\text{II}}\text{-OH}_2]^{4+}$, consists of a chromophore, $[\text{Ru}_a^{\text{II}}]^{2+}$, and a water-oxidation catalyst, $[\text{Ru}_b^{\text{II}}\text{-OH}_2]^{2+}$. Photoexcitation of the chromophore is followed by rapid electron injection from the Ru(II) metal-to-ligand charge-transfer (MLCT) excited state. Injection is ~95% efficient and exhibits multiple kinetic components with decay times ranging from <250 fs to 250 ps. Electron injection is followed by the transfer of the oxidative equivalent from the chromophore to the catalyst ($\Delta G = -0.28$ eV) with a transfer time of 145 ps and with near unit efficiency. The decrease in overall efficiency of the assembly (~75%) is due to photoexcitation of the catalyst. In the absence of subsequent photoexcitation events, the charge-separated state undergoes charge recombination on the microsecond time scale.

6.5 Acknowledgments

This material is based upon work supported as part of the UNC EFRC: Solar Fuels and Next Generation Photovoltaics, an Energy Frontier Research Center funded by the U.S. Department of Energy, Office of Science, and Office of Basic Energy Sciences under Award DE-SC0001011. D.L.A. acknowledges support from a fellowship from the Department of Energy Office of Science Graduate Fellowship Program (DOE SCGF), made possible in part by the American Recovery and Reinvestment Act of 2009, administered by ORISE-ORAU under contract DE-AC05-06OR23100.

6.6 Associated Content

Appendix E: The details for the global fitting, and justification of the fitting.

Chapter 7: STABILIZATION OF A RUTHENIUM(II) POLYPYRIDYL DYE ON NANOCRYSTALLINE TiO₂ BY AN ELECTROPOLYMERIZED OVERLAYER

Reprinted with permission from Lapides, A. M.; Ashford, D. L.; Hanson, K.; Torelli, D. A.; Templeton, J. L.; Meyer, T. J., Stabilization of a Ruthenium(II) Polypyridyl Dye on Nanocrystalline TiO₂ by an Electropolymerized Overlayer. *J. Am. Chem. Soc.* **2013**, *135* (41), 15450-15458. Copyright American Chemical Society 2014

7.1 Introduction

Stable surface binding of chromophores, catalysts, and chromophore-catalyst assemblies on metal oxide surfaces is an essential element in dye-sensitized photoelectrochemical cells (DSPECs) for solar fuel production, Figure 1.6.^{89,90,165,280,287} In a DSPEC for water oxidation, photo-excitation of a chromophore, or dye, followed by excited state electron injection into the conduction band of a high band gap semiconductor, typically TiO₂, provides the basis for a photoanode.²⁸⁰ Oxidative equivalents produced by electron injection are subsequently transferred to a catalyst for water oxidation. The injected electrons are transferred to a cathode for reduction of either water to H₂ or CO₂ to carbon-containing fuels.^{24,166} The design of water oxidation DSPEC photoanodes is particularly challenging because of the need to integrate both light absorption and catalysis at the oxide interface (Figure 1.6). The resulting interfacial structures must be stable under irradiation while supporting high numbers of turnovers in aqueous environments.^{141,144}

A number of strategies for binding chromophores and catalysts to a metal oxide surface have been reported. They include co-deposition,^{325,326} preformed assemblies,^{190,193} and self-assembled bilayers.¹⁹¹ These strategies are often limited by difficult synthetic procedures.

The stability of the films, critical in all applications, is limited by the nature of the link to the surface. Although often used successfully in non-aqueous solvents, carboxylate-surface binding is unstable in water. Phosphonate-surface binding is far more robust but typically subject to hydrolysis from the surface at pH 5 and above.^{141,144,327}

Oxidative or reductive electropolymerization provides a potentially useful strategy for preparing stable, multiple component films.³²⁸⁻³³¹ Reductive electropolymerization of vinyl-derivatized monomers is especially well developed.³³²⁻³³⁹ In these reactions, electrochemical reduction of the vinyl-group induces radical polymerization and C-C coupling and bond formation.³³³ On planar electrode surfaces, two or more redox carriers have been incorporated into spatially segregated co-polymeric films by sequential reductive cycling in distinct monomer solutions, and into integrated co-polymeric films prepared by cycling in a single solution containing multiple monomers.^{332,334,340}

Despite the impressive background on planar electrodes, few reports have appeared describing electropolymerization on nanocrystalline metal oxide films.^{336,337} In one notable example, Moss et al. demonstrated reductive electropolymerization of an overlayer of $[\text{Ru}(\text{vbpy})_3]^{2+}$ (vbpy = 4-vinyl-4'-methyl-2,2'-bipyridine) on $[\text{Ru}(\text{dcb})(\text{vbpy})_2]^{2+}$ (dcb = 2,2'-bipyridine-4,4'-dicarboxylic acid) that had been pre-bound to nanocrystalline TiO_2 . Significant increases in thermal stability for the surface-bound complex were observed even in basic media with no loss of chromophore over a three week period under conditions where the unprotected surface-bound complex underwent complete desorption in minutes.³³⁶ The photostability and photophysical properties of the resulting overlayer structures were relatively unexplored.¹⁴¹

The electropolymerized overlayer approach to surface assembly stabilization is promising. We report here the synthesis and characterization including photostability and photophysical measurements on multicomponent films on mesoporous TiO_2 prepared by reductive overlayer electropolymerization. The films were prepared by first derivatizing mesoporous TiO_2 films with $[\text{Ru}(5,5'\text{-divinyl-2,2'}\text{-bipyridine})_2(4,4'\text{-(PO}_3\text{H}_2)_2\text{-bpy})]^{2+}$ (**RuPdvb** in Figure 7.1A, $4,4'\text{-(PO}_3\text{H}_2)_2\text{-bpy} = [2,2'\text{-bipyridine}]$ -4,4'-diylbis(phosphonic acid)) followed by reductive electropolymerization of $[\text{Fe}(4'\text{-vinyl-2,2':6':2''-terpyridine})_2]^{2+}$ (**[Fe(v-tpy)] $_2^{2+}$** in Figure 7.1A) to generate an electropolymerized overlayer. A scheme illustrating formation of the resulting $\text{TiO}_2\text{-RuPdvb-poly-[Fe(v-tpy)] $_2^{2+}$$ overlayer structure is shown in Figure 7.1B.

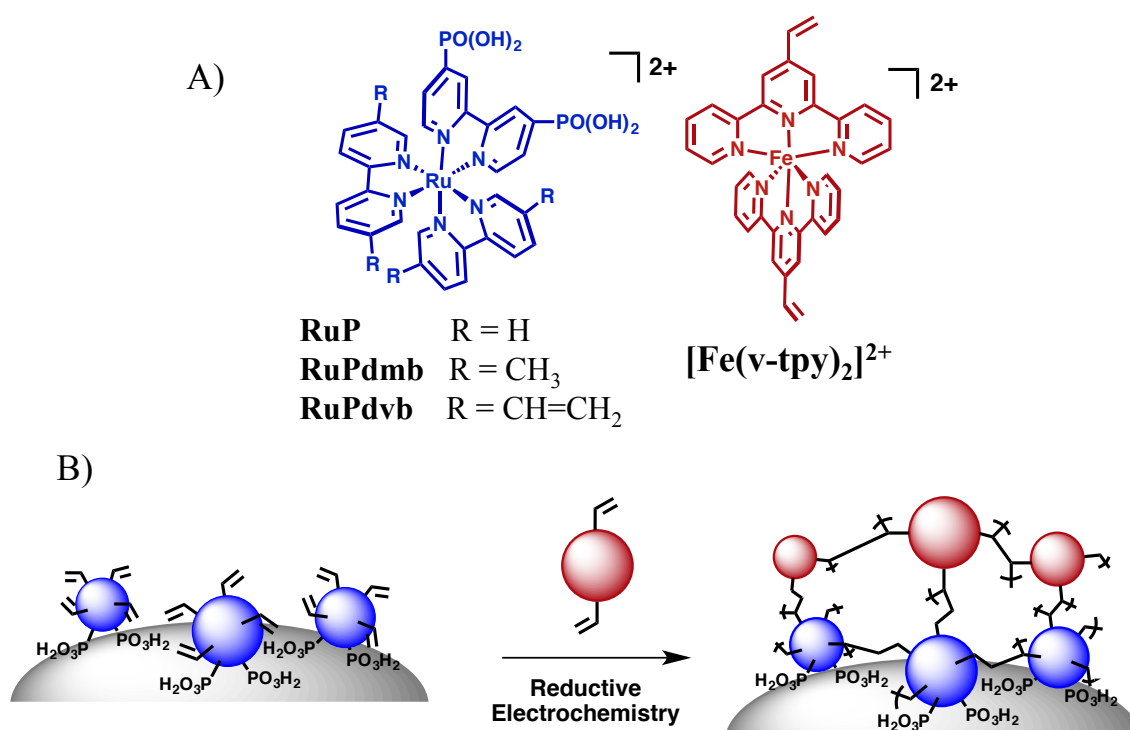


Figure 7.1. A) Structures of **RuP**, **RuPdvb**, **RuPdvb** and **[Fe(v-tpy)] $_2^{2+}$** . B) Schematic diagram of the surface structure following reductive polymerization of **[Fe(v-tpy)] $_2^{2+}$** on $\text{TiO}_2\text{-RuPdvb}$.

7.2 Experimental

Sample Preparation

Materials. $[\text{Ru}(1,4\text{-cyclooctadiene})\text{Cl}_2]_n$,^{192,247} 5,5'-divinyl-2,2'-bipyridine,³⁴¹ $[\text{Ru}(\text{bpy})_2(4,4'\text{-(PO}_3\text{H}_2)_2\text{-bpy})]^{2+}$ (**RuP**, chloride salt),¹⁹² and $[\text{Fe}(\text{v-tpy})_2](\text{PF}_6)_2$ ³³⁵ were synthesized according to previously published procedures. Distilled water was further purified by using a Milli-Q Ultrapure water purification system. All other reagents were ACS grade and used without further purification. Fluoride-doped tin oxide (FTO)-coated glass (Hartford Glass; sheet resistance $15 \Omega \text{ cm}^{-2}$), was cut into $10 \text{ mm} \times 40 \text{ mm}$ strips and used as the substrate for ZrO_2 and TiO_2 nanoparticle films. Microwave reactions were carried out using a CEM MARS microwave reactor. A CEM HP-500 Plus Teflon-coated microwave vessel (100 mL) was used at a power setting of 400 W. The vessel was rotated and stirred throughout the microwave procedure. The pressure of the reaction vessel was monitored throughout the reaction, and never exceeded 300 PSI.

Metal Oxide Films. Nano- TiO_2 ²⁴⁸ films and nano- ZrO_2 ¹³⁴ films, typically $7 \mu\text{m}$ thick ($\sim 20 \text{ nm}$ particle diameter), with a coating area of roughly $10 \text{ mm} \times 15 \text{ mm}$, were synthesized according to literature procedures. Dye adsorption isotherms on TiO_2 were obtained by soaking the films in methanol solutions of **RuPdvb**, $[\text{Ru}(5,5'\text{-dimethyl-bpy})_2(4,4'\text{-(PO}_3\text{H}_2)_2\text{-bpy})]^{2+}$ (**RuPdmb**), and **RuP** at concentrations of 10, 20, 50, 100, 150, and $200 \mu\text{M}$. The slides were then removed, rinsed with methanol, and dried over a stream of nitrogen.

Absorption spectra were obtained by placing the dry derivatized films perpendicular to the detection beam path of the spectrophotometer. The expression, $\Gamma = A(\lambda)/\varepsilon(\lambda)/1000$, was used to calculate surface coverages.²⁴⁹ Molar extinction coefficients (ε) in H_2O were

used; $A(\lambda)$ was the absorbance at the MLCT λ_{\max} . Maximum surface coverages (Γ_{\max}) and surface binding constants (K_{ad}) on TiO_2 for **RuPdvb**, **RuPdmb**, and **RuP** were obtained by use of the Langmuir isotherm with $\Gamma = \Gamma_{\max} \frac{K_{\text{ad}}[\text{X}]}{1+K_{\text{ad}}[\text{X}]}$ with $[\text{X}]$ the concentration of complex in the loading solution.²⁵⁰ All subsequent measurements were carried out on films loaded from methanol solutions of 100 μM in ruthenium complex, which gave complete surface coverage ($\Gamma = 8 \times 10^{-8} \text{ mol cm}^{-2}$).

Synthesis

$\text{Ru}(5,5'\text{-divinyl-2,2'}\text{-bipyridine})_2(\text{Cl})_2$

This compound was synthesized according to a literature procedure with minor modification.¹⁹² $[\text{Ru}(1,4\text{-cyclooctadiene})\text{Cl}_2]_n$ (0.074 g, 0.24 mmol) and 5,5'-divinyl-2,2'-bipyridine (0.1 g, 0.48 mmol) were added to 1,2-dichlorobenzene (20 mL). The suspension was thoroughly degassed, and then heated to 160 °C for 2 hrs under an atmosphere of argon. The reaction was cooled to room temperature and ether (~60 mL) was added. The solid was filtered, washed with ether, dried and collected. This complex was used without further purification (0.134 g, 95%). ¹H NMR (600 MHz, DMSO) δ (ppm) 9.96 (s, 2H), 8.65 (d, 2H), 8.49 (d, 2H), 8.28 (d, 2H), 7.91 (d, 2H), 7.48 (s, 2H), 7.00 (dd, 2H), 6.50 (dd, 2H), 6.23 (d, 2H), 5.78 (d, 2H), 5.64 (d, 2H), 5.34 (d, 2H).

$[\text{Ru}(5,5'\text{-divinyl-2,2'}\text{-bipyridine})_2([2,2'\text{-bipyridine}]\text{-4,4'}\text{-diyl}d\text{iphosphonic acid})](\text{Cl})_2$,

(RuPdvb)

$\text{Ru}(5,5'\text{-divinyl-2,2'}\text{-bipyridine})_2(\text{Cl})_2$ (0.075 g, 0.13mmol) and tetraethyl [2,2'-bipyridine]-4,4'-diylbis(phosphonate) (0.054 g, 0.13 mmol) in ethanol (~20 mL) were heated to 160 °C over 5 min and then heated for 20 min at 160 °C in a microwave reactor. The

reaction was cooled, filtered, and taken to dryness by a rotary evaporator. The solid was triturated with ether, collected, and air-dried and used without further purification. The esterified product (0.054 g, 0.053 mmol) was dissolved in anhydrous acetonitrile (~15 mL). Bromotrimethylsilane (0.07 mL, 0.53 mmol) was added, and the reaction was allowed to stir at 40 °C for 3 days under an argon atmosphere. The acetonitrile was removed under vacuum, anhydrous methanol (~15 mL) was added, and the solution was stirred at 40 °C for 30 min. The methanol was removed under vacuum, and the resulting solid was triturated with acetone, filtered, and washed with acetone. The solid was further purified by size exclusion chromatography (Sephadex LH-20) with 1:1 MeOH:H₂O as eluent. Similar fractions (based on UV/Vis absorption spectroscopy) were combined, and the solvent was removed by rotary evaporation. The dark-red solid was triturated with ether, filtered and dried under vacuum (0.041g, 86%). ¹H NMR (600 MHz, D₂O) δ (ppm) 8.75 (d, 2H), 8.43 (m, 4H), 8.16 (d, 2H), 8.12 (d, 2H), 7.93 (m, 2H), 7.62 (s, 2H), 7.61 (s, 2H), 7.55 (m, 2H), 6.50 (d, 2H), 6.46 (d, 2H), 5.82 (d, 2H), 5.77 (d, 2H), 5.42 (t, 4H). ³¹P NMR (D₂O) δ 6.68. HR-ESI-MS (MeOH; 20% H₂O with 1% HCOOH): m/z = 417.0528²⁺ = 834.1056, [M - 2Cl]²⁺ = 834.1059. Anal. Found (Calc.) C₃₉H₅₂Cl₂N₆O₁₄P₂Ru: C 44.08 (43.99); H 4.93 (4.36); N 7.91 (7.81).

Ru(5,5'-dimethyl-2,2'-bipyridine)₂(Cl)₂

This complex was synthesized with the same procedure as for Ru(5,5'-divinyl-2,2'-bipyridine)₂(Cl)₂ but using 5,5'-dimethyl-2,2'-bipyridine (1.19 g, 6.46 mmol). It was isolated in 93% yield (1.79 g).

[Ru(5,5'-dimethyl-2,2'-bipyridine)₂([2,2'-bipyridine]-4,4'-diyldiphosphonic acid)](Cl)₂,

(RuPdmb)

This complex was synthesized by using the same procedure as for [Ru(5,5'-divinyl-2,2'-bipyridine)₂([2,2'-bipyridine]-4,4'-diylidiphosphonic acid)](Cl)₂ but with Ru(5,5'-dimethyl-2,2'-bipyridine)₂(Cl)₂ (0.104 g, 0.17 mmol) as the starting material. The final product was isolated in 80% yield (0.116 g). ¹H NMR (400 MHz, D₂O) δ (ppm) 8.70 (d, 2H), 8.33 (d, 4H), 7.84 (d, 4H), 7.78 (m, 2H), 7.50 (d, 4H), 2.15 (s, 12H). ³¹P NMR (D₂O) δ 6.39. HR-ESI-MS (MeOH; 20% H₂O with 1% HCOOH): m/z = 785.009⁺, [M - 2Cl⁻ - H⁺]⁺ = 785.103; m/z = 807.0823²⁺ = 1614.1646, [M - 2Cl⁻ - 2H⁺ + Na⁺]²⁺ = 1614.172. Anal. Found (Calc.) for C₃₄H₄₈Cl₂N₆O₁₃P₂Ru: C 41.43 (41.56); H 4.70 (4.92); N 8.53 (8.55).

Electrochemical and Spectroscopic Characterization

Electrochemistry. Electrochemical measurements were conducted on a CH Instruments 660D potentiostat with a Pt-mesh or Pt-wire counter electrode, and a Ag/AgNO₃ (0.01 M AgNO₃/0.1 M tetra-n-butylammonium hexafluorophosphate (TBAPF₆) in CH₃CN; -0.09 V vs. Fc⁺⁰)³⁴² or Ag/AgCl (3 M NaCl; 0.198 V vs. NHE) reference electrode. E_{1/2} values were obtained from the peak currents in square wave voltammograms or from averaging cathodic and anodic potentials at peak current values (E_{p,c} and E_{p,a}) in cyclic voltammograms. Reductive electropolymerization was carried out in anhydrous CH₃CN (dried over 3 Å molecular sieves) with 0.1 M TBAPF₆ as the supporting electrolyte under an atmosphere of argon. Solutions were deaerated with argon for at least 5 minutes prior to reductive electrochemical cycling.

Scanning electron microscopy (SEM) and energy dispersive X-ray spectroscopy (EDS) results were obtained on a FEI Helios 600 Nanolab Dual Beam System equipped with an Oxford instruments, INCA PentaFET-x3 detector. A cross section was taken of mesoporous TiO₂ loaded with **RuPd_{vb}** and then reductively cycled 50 or 300 times in the

presence of $[\text{Fe}(\mathbf{v}\text{-tpy})_2]^{2+}$. Surface images were taken at 20 kV with a 0.69 nA beam current. Three EDS spectra were obtained at the polymer/solution interface (top), in the bulk of TiO_2 nanoparticles (middle), and at the nano- TiO_2/ITO interface (bottom) of the cross section (Figures S1 and S2) unless otherwise noted (Figure S9).

Absorption spectra were recorded on an Agilent 8453 UV/Visible photo diode array spectrophotometer (adsorption isotherms and spectroelectrochemistry), or a Varian Cary 50 UV/Vis spectrophotometer (photostability). Extinction coefficients for the complexes in aqueous H_2O were determined from the absorption spectra of solutions having a known concentration of complex.

Transient absorption (TA) measurements were carried out by inserting derivatized thin films at a 45° angle into a standard 10 mm path length square cuvette containing pH 1 aqueous solutions (0.1 M HClO_4). The top of the cuvette was fit with an o-ring seal with a Kontes valve inlet to allow the contents to be purged with Argon. TA experiments were performed by using nanosecond laser pulses produced by a Spectra-Physics Quanta-Ray Lab-170 Nd:YAG laser combined with a VersaScan OPO (532 nm, 5-7 ns, operated at 1 Hz, beam diameter 0.5 cm, ~ 5 mJ/pulse) integrated into a commercially available Edinburgh LP920 laser flash photolysis spectrometer system. White light probe pulses generated by a pulsed 450 W Xe lamp were passed through the sample, focused into the spectrometer (5 nm bandwidth), then detected by a photomultiplier tube (Hamamatsu R928). Appropriate filters were placed before the detector to reject unwanted scattered light. Detector outputs were processed using a Tektronix TDS3032C Digital Phosphor Oscilloscope interfaced to a PC running Edinburgh's L900 (version 7.0) software package. Single wavelength kinetic data were the result of averaging 50 laser shots and were fit with the Edinburgh software. The

data were fit over the first 10 μs by using the tri-exponential function in Equation 7.1 and the weighted average lifetime ($\langle\tau\rangle$) calculated from Equation 7.2. The results of multiple measurements revealed variations in the kinetic fit parameters of $<5\%$ with general trends reproduced in two separate trials.

Equation 7.1

$$y = A_1 e^{-(1/\tau_1)x} + A_2 e^{-(1/\tau_2)x} + A_3 e^{-(1/\tau_3)x}$$

Equation 7.2

$$\tau_i = 1/k_i ; \langle\tau\rangle = \sum A_i \tau_i^2 / \sum A_i \tau_i$$

Electron injection efficiencies (Φ_{inj}) were calculated by using Equation 7.3 with $\text{TiO}_2\text{-RuP}$ as the reference. $\text{TiO}_2\text{-RuP}$ is known to have an injection yield of 100% in aqueous pH 1 HClO_4 .¹⁴⁴

Equation 7.3

$$\Phi_{inj} = (\Delta A_{sam}(\lambda_p) / \Delta \epsilon_{sam}(\lambda_p) / (1 - 10^{-A_{sam}(\lambda_{ex})})) / (\Delta A_{ref}(\lambda_p) / \Delta \epsilon_{ref}(\lambda_p) / (1 - 10^{-A_{ref}(\lambda_{ex})}))$$

In Equation 7.3, ΔA is transient absorption amplitude, $\Delta \epsilon$ is the molar extinction coefficient difference between ground and excited/oxidized states ($\Delta \epsilon = -6500 \text{ M}^{-1} \text{ cm}^{-1}$ at 400 nm for $\text{TiO}_2\text{-RuP}$ and $\Delta \epsilon = -11,200 \text{ M}^{-1} \text{ cm}^{-1}$ at 580 nm for $\text{TiO}_2\text{-poly-}[\text{Fe}(\text{v-tpy})_2]^{2+}$). At the probe wavelength, λ_p ($=1 - 10^{-A(\lambda_{ex})}$) is the sample absorbance at the excitation wavelength ($\lambda_{ex} = 532 \text{ nm}$).

Steady-State Emission data were collected at room temperature with an Edinburgh FLS920 spectrometer with emitted light first passing through a 495 nm long-pass color filter, then a single grating (1800 l/mm, 500 nm blaze) Czerny-Turner monochromator (5 nm

bandwidth) and finally detected by a Peltier-cooled Hamamatsu R2658P photomultiplier tube. The samples were excited using light output from a housed 450 W Xe lamp / single grating (1800 l/mm, 250 nm blaze) Czerny-Turner monochromator combination with 5 nm bandwidth.

Photostability measurements were performed by a previously reported procedure.¹⁴¹ The light from a Royal Blue (455 nm, FWHM ~30 nm, 475 mW/cm²) Mounted High Power LED (Thorlabs, Inc., M455L2) powered by a T-Cube LED Driver (Thorlabs, Inc., LEDD1B) was focused to a 2.5 mm diameter spot size by a focusing beam probe (Newport Corp. 77646) outfitted with a second lens (Newport, Corp 41230). Light output was directed onto the derivatized thin films placed at 45° in a standard 10 mm path length cuvette containing 3 mL of the solutions of interest. The illumination spot was adjusted to coincide both with the thin films and the perpendicular beam path of a Varian Cary 50 UV/Vis spectrophotometer. The absorption spectrum (360-800 nm) of the film was obtained every 15 minutes during 16 hours of illumination. The incident light intensity was measured with a thermopile detector (Newport Corp 1918-C meter and 818P-020-12 detector). The solution temperature, 22±2°C, was consistent throughout the duration of the experiment.

The absorption-time traces at 480 nm could be satisfactorily fit with the biexponential function in Equation 7.4. For comparative purposes, the results of the multi-exponential analysis were represented by a single rate constant, the disappearance or desorption rate constant, k_{des} , by calculating the weighted average lifetime ($\langle\tau\rangle$) by application of Equation 7.5. In Equation 7.5, A_i and τ_i are the contributions to the absorbance amplitude and lifetime of component i .

Equation 7.4

$$y = A_1 e^{-(1/\tau_1)x} + A_2 e^{-(1/\tau_2)x} + y_0$$

Equation 7.5

$$1/k_{des} = \langle \tau \rangle = \sum A_i \tau_i^2 / \sum A_i \tau$$

7.3 Results and Discussion

Monomer Synthesis and Characterization.

The structures of the complexes investigated in this study are shown in Figure 7.1. They were synthesized as chloride (Ru^{II} complexes) and hexafluorophosphate ($[\text{Fe}(\text{v-tpy})_2]^{2+}$) salts. $[\text{Fe}(\text{v-tpy})_2]^{2+}$ and **RuP** were synthesized by previously reported procedures.^{192,335} **RuPdvb** and **RuPdmb** were synthesized by literature procedures with minor modification.¹⁹² The starting complex, $\text{Ru}(5,5'-(\text{R})_2\text{-bpy})_2\text{Cl}_2$ ($\text{R} = \text{CH}_3$ or $\text{CH}=\text{CH}_2$) was synthesized by heating $[\text{Ru}(1,4\text{-cyclooctadiene})\text{Cl}_2]_n$ and the bipyridine precursors in *o*-dichlorobenzene to 160 °C. The dichloride complexes were subsequently reacted with one equivalent of tetraethyl [2,2'-bipyridine]-4,4'-diylbis(phosphonate) in a microwave reactor. The ethyl esters were then hydrolyzed by using TMSBr in anhydrous acetonitrile to give the unprotected phosphonic acids. **RuPdvb** and **RuPdmb** were isolated as their chloride salts in 86% and 80% yield, respectively.

RuPdvb contains one phosphonated bipyridine ligand for binding to metal oxide surfaces and two bipyridine ligands with vinyl-functional groups in the 5,5' positions for electropolymerization. $[\text{Fe}(\text{v-tpy})_2]^{2+}$ was selected as the monomer precursor for the polymer overlayer because of its readily discernible photophysical and electrochemical properties compared to **RuPdvb**. Following electropolymerization the vinyl groups of **RuPdvb** are converted by C-C coupling into saturated alkyl substituents.³³³ Alkyl-substituted **RuPdmb**

(R= CH₃ in Figure 7.1) was used as a model for the surface bound chromophore following electropolymerization. **RuP** was used as the control chromophore for transient absorption and photostability experiments because its properties are well understood.¹⁴⁴

In aqueous solution, the absorption spectra for **RuP**, **RuPdvb** and **RuPdmb** all feature characteristic, intense π - π^* absorptions below 350 nm and lower energy metal-to-ligand charge-transfer (MLCT) absorptions from 400-500 nm (Table 7.1, Figure F.3, see Appendix F). The slight blue-shift in absorption for **RuPdvb**, and red-shift in absorption for **RuPdmb**, relative to **RuP** is due to stabilization/destabilization effects in the $d\pi^5\pi^*$ MLCT excited states by the electron withdrawing vinyl and donating methyl groups, respectively. [**Fe(v-tpy)**]²⁺ has an MLCT absorption band maximum at 565 nm (ϵ = 15,500 M⁻¹cm⁻¹, Figure F.3).

Table 7.1. Photophysical, electrochemical and surface binding parameters for RuP, RuPdvb, RuPdmb and [Fe(v-tpy)]²⁺ in solution and on metal oxide films.

Complex	MLCT λ_{\max} (nm) (ϵ , M ⁻¹ cm ⁻¹) ^a	Γ_{\max} (mol cm ⁻²)	K_{ad} (M ⁻¹)	$E_{1/2}(\text{Ru}^{\text{III/II}})$ (V vs. Ag/AgNO ₃) ^b	$E_{1/2}(\text{Ru}^{\text{III/II}})$ (V vs. NHE) ^c	ΔG_{ES} (eV) ^d	$E^{o'}(\text{Ru}^{\text{III/II}*})$ (V vs. NHE) ^f
RuP	458 (12,700)	8.5×10^{-8}	3.9×10^4	1.02	1.28	2.04	-0.76
RuPdvb	476 (13,300)	6.7×10^{-8}	2.2×10^4	1.12	1.34	2.02	-0.68
RuPdmb	453 (13,500)	5.2×10^{-8}	5.2×10^5	0.94	1.22	2.06	-0.84
[Fe(v-tpy)] ²⁺	565 (15,500)	-	-	0.79(Fe ^{III/II})	-	- ^e	-

^a In H₂O. ^b In 0.1 M TBAPF₆ CH₃CN; planar FTO working, Pt counter, and Ag/AgNO₃ reference electrode (-0.09 V vs. Fc^{0/+}) ^c In aqueous 0.1 M HClO₄, *nano*-TiO₂ working, Pt counter, and Ag/AgCl reference electrode (0.198 V vs. NHE) ^d ΔG_{ES} from spectral fitting of emission on ZrO₂ in aqueous 0.1 M HClO₄ (Supporting Information). ^e Emission was not observed. ^f $E^{o'}(\text{Ru}^{\text{III/II}*}) = E_{1/2}(\text{Ru}^{\text{III/II}}) - \Delta G_{ES}$.

Surface Loading

Adsorption isotherms were measured by immersing TiO₂ films (~7 μm thickness) in 10 mL solutions of 10, 20, 50, 100, 150 and 200 μM of **RuP**, **RuPdvb**, and **RuPdmb** in

methanol. Adsorption isotherms (Figure F.4) were analysed by the Langmuir isotherm model.²⁵⁰ Adsorption constants (K_{ad}) and maximum surface coverages (Γ_{max}) were similar for all three complexes; the results are summarized in Table 7.1.

Surface Characterization

The electrochemical properties of **RuP**, **RuPdvb**, and **RuPdmb** on TiO₂ were examined by cyclic and square-wave voltammetry in CH₃CN (0.1 M TBAPF₆ electrolyte) and in aqueous 0.1 M HClO₄. The values are reported in Table 7.1. All complexes exhibit reversible Ru^{III/II} couples with $E_{1/2}$ values of 1.28, 1.34, and 1.22 V (vs. NHE in aqueous 0.1 M HClO₄) for **RuP**, **RuPdvb**, and **RuPdmb**, respectively (Figure F.5). Similar to the trends observed in absorption and emission spectra, the positive and negative shifts in $E_{1/2}$ for **RuPdvb** and **RuPdmb**, relative to **RuP**, can be attributed to the electron-withdrawing vinyl and electron-donating methyl groups, respectively.

Emission spectra for **RuP**, **RuPdvb**, and **RuPdmb** on ZrO₂ in aqueous 0.1 M HClO₄ were obtained (Figure F.6). The trends in emission parallel those observed for absorption. The emission spectra were analysed by application of a one-mode Franck-Condon analysis with the procedure described elsewhere.^{144,343,344} The free energy content of the thermally equilibrated ³MLCT excited states (ΔG_{ES}) are given in Table 7.1 with the remaining spectral fitting parameters reported in Table F.1. Excited state reduction potentials for the couples, $Ru^{III} + e^- \rightarrow Ru^{II*}$ ($E^{o'}(Ru^{III/II*})$), were calculated from, $E^{o'}(Ru^{III/II*}) \sim E_{1/2}(Ru^{III/II}) - \Delta G_{ES}$. Based on these values, all three complexes are sufficiently reducing (-0.68 to -0.84 V) to inject into the conduction band of TiO₂ (~ -0.5 V vs. NHE) in aqueous pH 1 HClO₄.³⁴⁵

Polymerization of [Fe(v-tpy)₂]²⁺ on FTO

It has previously been demonstrated that $[\text{Fe}(\text{v-tpy})_2]^{2+}$ will undergo reductive electropolymerization on planar electrodes if the applied potential is more negative than the first v-tpy-based reduction potential (approximately -1.5 V vs. Ag/AgNO₃).^{335,346} As a control experiment, we initially investigated the electropolymerization of $[\text{Fe}(\text{v-tpy})_2]^{2+}$ on a planar fluoride-doped tin oxide slide (FTO). In these experiments FTO was used as the working electrode, platinum as the counter electrode and a Ag/AgNO₃ reference electrode with $[\text{Fe}(\text{v-tpy})_2]^{2+}$ in dry acetonitrile and 0.1 M TBAPF₆ as the electrolyte. The surface coverage (Γ in moles/cm²) of redox active complex was calculated by using Equation 7.6 where Q is the integrated current under the Fe^{III/II} redox couple, F is Faraday's constant (96,485 C), n is the number of electrons transferred ($n = 1$), and A is the area of the electrode ($\sim 1 \text{ cm}^2$).

Equation 7.6

$$\Gamma = Q/nFA$$

The applied potential was cycled from 0 to -1.8 V (vs. Ag/AgNO₃) and FTO surface coverage was monitored as a function of both scan rate (50, 100 and 200 mV s⁻¹) and $[\text{Fe}(\text{v-tpy})_2]^{2+}$ concentration (0.5, 1.0 and 2.0 mM). Surface coverage was found to increase linearly as scan rate decreased or as the $[\text{Fe}(\text{v-tpy})_2]^{2+}$ concentration was increased (Figure F.7).

Polymerization of $[\text{Fe}(\text{v-tpy})_2]^{2+}$ on *nano-TiO*₂

Under sufficiently reducing potentials (more negative than -0.5 V vs. NHE at pH = 1)³⁴⁵ nanocrystalline TiO₂ can readily transport electrons from the FTO electrode, through the metal oxide film, to the TiO₂-electrolyte interface providing a basis for reductive

electropolymerization of $[\text{Fe}(\text{v-tpy})_2]^{2+}$. The high effective surface area of *nano*-TiO₂ allows for monitoring the surface coverage of $\text{poly-}[\text{Fe}(\text{v-tpy})_2]^{2+}$ ($\epsilon_{565\text{ nm}} = 15,500\text{ M}^{-1}\text{ cm}^{-1}$) by UV/Visible absorption measurements. Absorption changes during an electropolymerization on a TiO₂ film cycled from 0 to -1.8 V vs. Ag/AgNO₃ are shown in Figure 7.2.

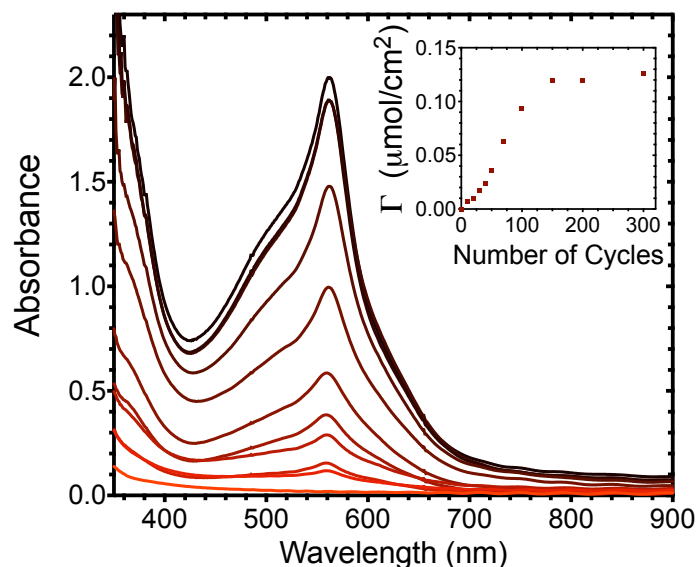


Figure 7.2. Changes in UV/Visible absorption spectra for TiO₂ (dry slide) as the number of reductive cycles from 0 to -1.8 V (vs. Ag/AgNO₃) is increased (0, 10, 20, 30, 40, 50, 70, 100, 150, 200 and 300; red to black) in an acetonitrile solution of 0.5 mM $[\text{Fe}(\text{v-tpy})_2]^{2+}$ (0.1 M TBAPF₆ electrolyte); Pt counter electrode, and Ag/AgNO₃ reference electrode. Inset: Surface coverage of $\text{poly-}[\text{Fe}(\text{v-tpy})_2]^{2+}$ versus the number of reductive cycles.

For the first 70 cycles the surface coverage of $\text{poly-}[\text{Fe}(\text{v-tpy})_2]^{2+}$ increases linearly with the number of cycles (Inset, Figure 7.2) and continues to increase, albeit at a slower rate, from 70 to 150 cycles. Further polymerization was minimal after 150 cycles. At 70 cycles, a single monolayer of $\text{poly-}[\text{Fe}(\text{v-tpy})_2]^{2+}$ was deposited on the TiO₂ surface ($\sim 7 \times 10^{-8}\text{ mol cm}^{-2}$) as determined by UV/Visible absorption measurements. The decreased deposition rate for $[\text{Fe}(\text{v-tpy})_2]^{2+}$ from 70 to 150 cycles may be due to a decrease in the rate of electron transfer from TiO₂ to $[\text{Fe}(\text{v-tpy})_2]^{2+}$ or a decrease in the available internal volume within the

internal voids of the nanostructured films. In any case, electropolymerization is hindered after the deposition of approximately two monolayers (150 cycles), Figure 7.2, inset.

No change in absorption was observed for a TiO₂ electrode cycled in [Fe(v-tpy)]²⁺ solution from 0 V to -1.0 V (vs. Ag/AgNO₃). This potential range is more positive than required for reductive electropolymerization, and this result shows that physical adsorption of [Fe(v-tpy)]²⁺ to TiO₂ prior to electropolymerization does not occur.

Polymerization of [Fe(v-tpy)]²⁺ on nano-TiO₂-RuPdvb

Electropolymerized films of TiO₂-RuPdvb-*poly*-[Fe(v-tpy)]²⁺ were prepared by first derivatizing TiO₂ with a monolayer of RuPdvb (TiO₂-RuPdvb) by loading from methanol. The TiO₂-RuPdvb film was then used as the working electrode during reductive cycling in an acetonitrile solution of 0.5 mM [Fe(v-tpy)]²⁺ (0.1 M TBAPF₆ electrolyte). The changes in the UV/Visible absorption spectra of TiO₂-RuPdvb with increasing number of reductive cycles from 0 to -1.8 V (vs. Ag/AgNO₃) can be seen in Figure 7.3.

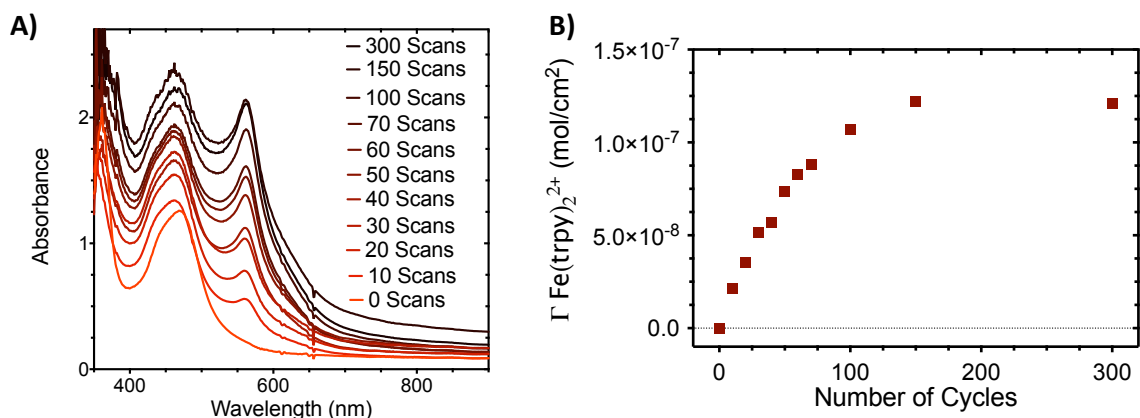


Figure 7.3. (a) Changes in UV/Visible absorption spectra for TiO₂-RuPdvb (dry slide) with an increase in the number of reductive scan cycles from 0 to -1.8V (vs. Ag/AgNO₃) in an acetonitrile solution 0.5 mM in [Fe(v-tpy)]²⁺ (0.1 M TBAPF₆ electrolyte); Pt counter electrode, and Ag/AgNO₃ reference electrode. (b) Surface coverage of *poly*-[Fe(v-tpy)]²⁺ versus the number of scan cycles.

UV/Visible absorption spectra of the polymerized films showed that the MLCT band for **RuPdvb** did not diminish in intensity following reductive polymerization of [**Fe(v-tpy)**]₂²⁺ (Figure 7.3). As with non-derivatized TiO₂ (see above) the surface coverage of *poly*-[**Fe(v-tpy)**]₂²⁺ increases approximately linearly from 0 to 70 cycles, slows from 70-150 cycles, then remains constant above 150 cycles (Figure 7.3). The surface coverage of *poly*-[**Fe(v-tpy)**]₂²⁺ on TiO₂-**RuPdvb** after 70 and 150 cycles corresponds to approximately one and two monolayers, respectively.

A blue-shift (~9 nm) in the MLCT band for **RuPdvb** was observed after the first 10 cycles of electropolymerization (Figure 7.3A). A similar blue-shift (Figure F.8) is also observed for TiO₂-**RuPdvb** after reductive cycling in 0.5 mM *p*-divinylbenzene (absorption <350 nm) showing that the shift in Ru^{II}-based absorption in TiO₂-**RuPdvb**-*poly*-[**Fe(v-tpy)**]₂²⁺ is not due to [**Fe(v-tpy)**]₂²⁺. The absorption spectrum of TiO₂-**RuPdvb** after electropolymerization closely resembles that of TiO₂-**RuPdmb** suggesting that the shift is due to conversion of the electron-withdrawing vinyl groups in **RuPdvb** to saturated alkane groups formed during the polymerization process.³³³

The electrochemical properties of TiO₂-**RuPdvb** were monitored before and after reductive polymerization by cyclic voltammetry. Oxidative scans from 0 to 1.5 V (vs. Ag/AgNO₃) in CH₃CN (0.1 M TBAPF₆) following successive reductive cycles from 0 to -1.8 V (vs. Ag/AgNO₃) are shown in Figure 7.4. TiO₂ is a wide band gap semiconductor with E_{vb} ≈ 2.8 V at pH = 7, and Ru^{II} oxidation to Ru^{III} on the surface is initiated by electron transfer at the FTO interface followed by cross-TiO₂ surface Ru(II) → Ru(III) electron transfer hopping with associated counter ion diffusion.^{345,347}

Before overlayer electrodeposition, $E_{1/2}(\text{Ru}^{\text{III/II}})$ appeared at 1.16 V (vs. Ag/AgNO₃). Upon electropolymerization of the overlayer, the peak current for the Ru^{III/II} couple decreased and the peak-to-peak splitting increased. Past ~50 cycles from 0 to 1.5 V (vs. Ag/AgNO₃) at 50 mV/s, the couple is no longer observed. Nonetheless, after 50 cycles the MLCT absorption band for **RuPdvb** is relatively unchanged in UV/Vis absorption spectra (Figure 7.3) confirming that it is still on the surface. A likely explanation for the decrease and ultimate loss in current for the Ru^{III/II} wave is a blocking effect by the growing *poly*-[**Fe(v-tpy)**]₂²⁺ overlayer film which inhibits diffusion of counter ions to the Ru^{II} sites on the surface to provide charge balance for oxidation of Ru^{II} to Ru^{III} thus inhibiting cross-surface electron transfer.

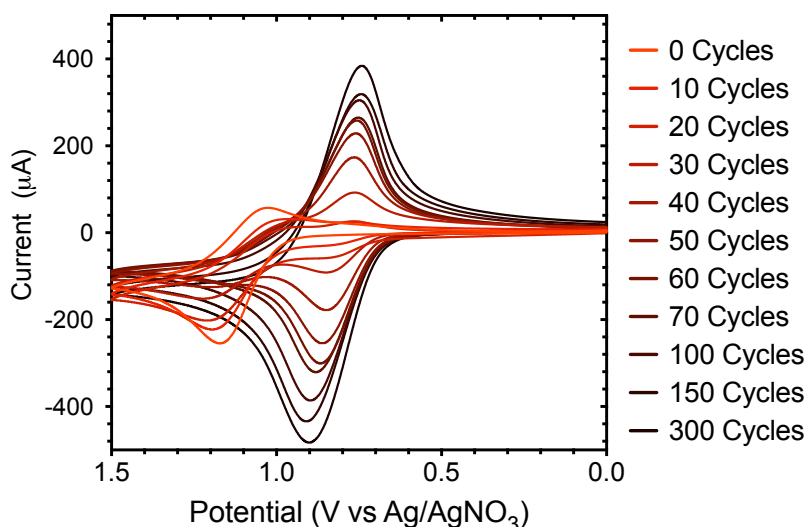


Figure 7.4. Cyclic voltammograms for TiO₂-**RuPdvb** from 0 to 1.5 V (vs. Ag/AgNO₃) in CH₃CN (0.1 M TBAPF₆) after successive reductive scan cycles (100 mV/s) in CH₃CN solution 0.5 mM in [**Fe(v-tpy)**]₂²⁺, 0.1 M in TBAPF₆; Pt counter electrode; Ag/AgNO₃ reference electrode.

After polymerization, a new reversible Fe^{III/II} couple, due to *poly*-[**Fe(v-tpy)**]₂²⁺, is observed at $E_{1/2} = 0.85$ V (vs. Ag/AgNO₃). The integrated current for the Fe^{III/II} wave increases with each successive reductive cycle.

Morphology Characterization.

The morphology and composition of the $\text{TiO}_2\text{-RuPdvb-poly-}[\text{Fe}(\text{v-tpy})_2]^{2+}$ films were examined by scanning electron microscopy (SEM) and energy-dispersive x-ray spectroscopy (EDS). SEM images of $\text{TiO}_2\text{-RuPdvb}$ following 50 and 300 cycles of reductive polymerization can be seen in Figure 7.5. The SEM image of $\text{TiO}_2\text{-RuPdvb-poly-}[\text{Fe}(\text{v-tpy})_2]^{2+}$ after 50 reductive cycles resembles that of $\text{TiO}_2\text{-RuPdvb}$ in that the porosity of the nanocrystalline TiO_2 is retained after polymerization (Figure 7.5A and Figure 7.5C). In contrast, after 300 reductive cycles, the porosity of the film is reduced and a film of $\text{poly-}[\text{Fe}(\text{v-tpy})_2]^{2+}$ has formed on top of the mesoporous TiO_2 film (Figure 7.5B and Figure 7.5D). Presumably, as noted above, the surface film inhibits both substrate and electrolyte diffusion into the film with the latter resulting in the current decreases for the $\text{Ru}^{\text{III/II}}$ couple.

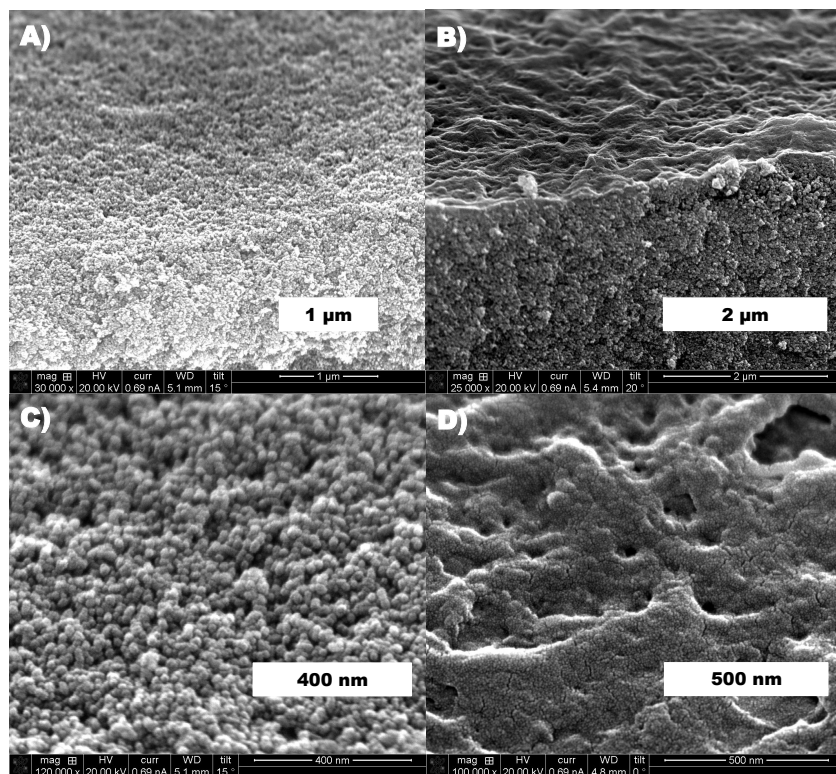


Figure 7.5. Cross-sectional (A and B) and surface (C and D) SEM images of the TiO₂-RuPdvb film following 50 (A and C) and 300 (B and D) reductive cycles in an CH₃CN solution containing 0.5 mM [Fe(v-tpy)₂]²⁺.

EDS was used to determine the concentrations of ruthenium and iron at different depths within the TiO₂ films. The results are summarized in Table 7.2. The EDS data for TiO₂-RuPdvb-*poly*-[Fe(v-tpy)₂]²⁺ films prepared from 50 and 300 reductive cycles both reveal inhomogeneities throughout the mesoporous structure and a gradient in ruthenium complex content as well. The concentration of surface-bound Ru^{II} complex is highest at the TiO₂-solution interface (top, Figure F.1 and Figure F.2) decreasing with depth toward the FTO surface (bottom, Figure F.1 and Figure F.2). This result is consistent with those of O'Regan et al. which demonstrated that standard dye loading procedures on TiO₂ do not uniformly coat the films, but instead result in greater dye loading near the surface.³⁴⁸

Table 7.2. The atomic % and Ru:Fe ratios at the top, middle and bottom of TiO₂-RuPdvb films after 50 and 300 reductive cycles (100 mV/s) in an acetonitrile solution containing 0.5 mM [Fe(v-tpy)₂]²⁺ (0.1 M TBAPF₆ electrolyte).

Sample	Ru Atomic %	Fe Atomic %	Ru:Fe
50 Cycles-Top	1.54	1.05	1:0.7
50 Cycles-Middle	1.31	0.62	1:0.5
50 Cycles-Bottom	0.88	0.43	1:0.5
300 Cycles-Top	0.50	1.20	1:2.4
300 Cycles-Middle	0.51	0.75	1:1.5
300 Cycles-Bottom	0.43	0.60	1:1.4

The EDS results also show that the Fe:Ru ratio is higher at the TiO₂-solution interface (top) compared to the interior of the film. This result suggests that electropolymerization of

$[\text{Fe}(\text{v-tpy})_2]^{2+}$ occurs rapidly at the TiO_2 -solution interface but is limited by diffusion of $[\text{Fe}(\text{v-tpy})_2]^{2+}$ into the mesoporous TiO_2 network. As a result the Fe:Ru ratios determined by UV/Visible absorption measurements represent averages of actual ratios throughout the inhomogeneously loaded films. The Ru:Fe ratios in TiO_2 -**RuPdvb**-*poly*- $[\text{Fe}(\text{v-tpy})_2]^{2+}$ after 50 and 300 cycles, as determined by UV/Visible absorption measurements, were 1:1 and 1:1.7, respectively. A film with a more uniform ratio of Fe:Ru was prepared by soaking a TiO_2 -**RuPdvb** slide in a $[\text{Fe}(\text{v-tpy})_2]^{2+}$ solution (0.5 mM in 0.1 M TBAPF₆/CH₃CN), stirring the solution during the electropolymerization process, and pausing 60 seconds between each electropolymerization cycle (Figure F.9). This suggests that diffusion of $[\text{Fe}(\text{v-tpy})_2]^{2+}$ through the mesoporous TiO_2 is a significant factor when controlling the distribution of the ratio of bound dye to electropolymer overlayer in the formation of these films.

Photostability

The photostabilities of TiO_2 -**RuPdvb**-*poly*- $[\text{Fe}(\text{v-tpy})_2]^{2+}$ relative to **RuP** and **RuPdvb** on TiO_2 were evaluated by a previously published procedure with constant irradiation at 455 nm (FWHM ~ 30 nm, 475 mW/cm², ~ 135 suns at 455 nm).^{141,144} Absorption spectra (360-800 nm) of the films were obtained every 15 minutes during 16 hours of irradiation. Results for TiO_2 -**RuPdvb** with ~ 2 monolayers of *poly*- $[\text{Fe}(\text{v-tpy})_2]^{2+}$ (150 cycles) in aqueous 0.1 M HClO₄ (pH 1) are shown in Figure 7.6. The time-dependent changes in absorption at 480 nm were fit with the biexponential function in Equation 7.4 and are presented as a single average rate constant (k_{des}) calculated as the inverse of the weighted average lifetime ($k_{\text{des}} = \langle \tau \rangle^{-1}$) for the time-dependent absorption changes, Equation 7.5. The results are summarized in Table 7.3 and Table 7.4.

Desorption rate constants for the unprotected surface-bound chromophores increase slightly in the order **RuP** ($4.8 \times 10^{-5} \text{ s}^{-1}$), **RuPdvb** ($5.6 \times 10^{-5} \text{ s}^{-1}$), and **RuPdmb** ($5.8 \times 10^{-5} \text{ s}^{-1}$). All three complexes share a similar surface binding motif based on the 4,4'-(PO_3H_2)₂bpy) ligand and the slight differences in k_{des} are presumably due to the differences in surface packing and morphology/local structure.

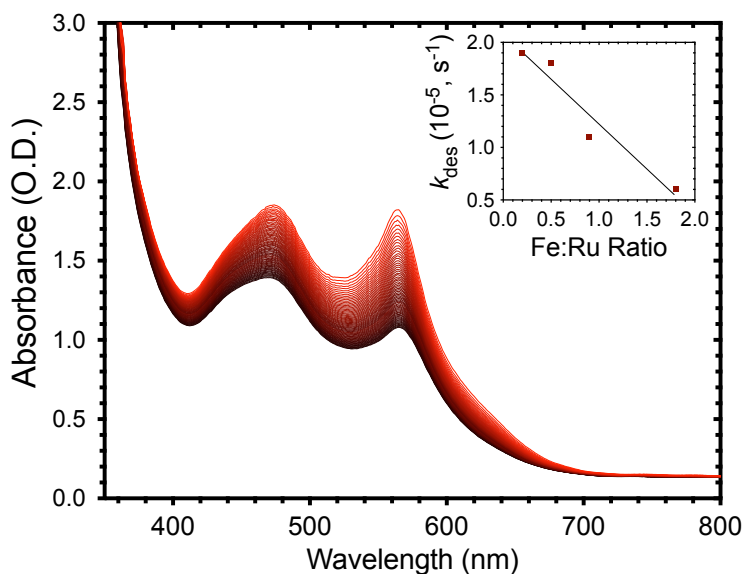


Figure 7.6. Changes in the absorption spectrum of $\text{TiO}_2\text{-RuPdvb-poly-}[\text{Fe}(\text{v-tpy})_2]^{2+}$ (150 cycles, 1:1.8 Ru:Fe) in aqueous 0.1 M HClO_4 under constant 455 nm irradiation (475 mW/cm^2) from 0 (red) to 16 hours (black) recorded every 15 minutes. Inset: Desorption rate constant (k_{des}) as a function of the number of reductive cycles.

Table 7.3. Summary of desorption rate constants (k_{des}) in aqueous 0.1 M HClO_4 for RuP, RuPdvb, and RuPdmb on TiO_2 and $\text{TiO}_2\text{-RuPdvb}$ films after 10, 30, 70 and 150 reductive cycles in $[\text{Fe}(\text{v-tpy})_2]^{2+}$ solution.

Sample	Ru:Fe	$k_{\text{des}} (\times 10^{-5} \text{ s}^{-1})$
RuP	1:0	4.8
RuPdmb	1:0	5.6
RuPdvb	1:0	5.9
RuPdvb + 10 cycles	1:0.2	1.9
RuPdvb + 30 cycles	1:0.5	1.8

RuPdvb + 70 cycles	1:0.9	1.1
RuPdvb + 150 cycles	1:1.8	0.6

The photochemical desorption rate constants for TiO₂-**RuPdvb** in aqueous 0.1 M HClO₄ as a function of Ru:Fe ratios are summarized in Table 7.3 (Figure F.10). With 10 reductive cycles, 1:0.2 (Ru:Fe), k_{des} is three times slower than for unprotected TiO₂-**RuPdm** or **RuPdvb**. From 10 (1:0.2 Ru:Fe) to 150 cycles, 1:1.8 (Ru:Fe), there was an approximately linear decrease in k_{des} from $4.8 \times 10^{-5} \text{ s}^{-1}$ to $0.6 \times 10^{-5} \text{ s}^{-1}$ (Inset Figure 7.6). The desorption rate constant was similar from 400 to 600 nm showing that desorption from the surface, and not photodecomposition of **RuPdvb** or $[\text{Fe}(\text{v-tpy})_2]^{2+}$ is occurring.

Table 7.4. Summary of desorption rate constants (k_{des}) for TiO₂-RuP, TiO₂-RuP stabilized by $\sim 3.3 \text{ \AA}$ of Al₂O₃, and in TiO₂-RuPdvb-*poly*- $[\text{Fe}(\text{v-tpy})_2]^{2+}$ films (150 cycles, 1:1.8 Ru:Fe) under various conditions.

Solvent	$k_{\text{des}} (\times 10^{-5} \text{ s}^{-1})$		
	TiO ₂ - RuP	TiO ₂ - RuP + $\sim 3.3 \text{ \AA}$ of Al ₂ O ₃ ^e	TiO ₂ -RuPdvb- <i>poly</i> - $[\text{Fe}(\text{v-tpy})_2]^{2+}$
pH 1 ^a	4.8	-	0.6
pH 5 ^b	>20	2.3	1.3
H ₂ O	>30	3.2	0.9
pH 7 ^c	-	9.5	5.5
CH ₃ CN ^d	0.8	< 0.01	0.07

^a 0.1 M HClO₄. ^b 10 μM HClO₄. ^c 0.1 M Na₃PO₄ buffer. ^d 0.1 M LiClO₄. ^e From reference ¹⁴⁶.

The mechanism of photo-induced chromophore desorption from the metal oxide surface is not fully understood but mechanisms have been proposed.¹⁴¹ Increased stability after polymerization may arise from a number of factors including: 1) increased steric bulk

provided by the polymer which inhibits hydroxide/water attack at the phosphonate groups on the surface, 2) cross-linking of the film which mechanically prevents desorption of individual chromophores, and 3) the newly formed hydrophobic alkyl linkers reduce the solubility of the film in the external aqueous medium. Similar factors have been suggested for dye-sensitized solar cells that have been stabilized by cross-linking polymerization.³⁴⁹ It is also important to note that under irradiation a photostationary state exists that is dictated by photo-excitation, electron injection, and back electron transfer between the chromophores and the metal oxide surface.

For **RuP**, **RuPdvb**, and **RuPdmb** on TiO₂ under irradiation the surface-bound complex exists as Ru^{III}.³⁵⁰ Conversely for TiO₂-**RuPdvb-poly-[Fe(v-tpy)₂]²⁺** there is a ~300 mV driving force for electron transfer from *poly-[Fe(v-tpy)₂]²⁺* to **Ru^{III}Pdvb** and at the steady state Fe^{III} dominates (see below).

The desorption rate constant for the TiO₂-**RuPdvb-poly-[Fe(v-tpy)₂]²⁺** films (150 cycles, 1:1.8 Ru:Fe) was investigated in a variety of solvents and the results are summarized in Table 7.4 (Figure F.11). In previous experiments, the photostability of TiO₂-**RuP** was maximized in 0.1 M HClO₄ pH 1 ($5.0 \times 10^{-5} \text{ s}^{-1}$) with k_{des} increasing at higher pHs and in buffered solutions.¹⁴¹ It is notable that at pH 5 ($1.3 \times 10^{-5} \text{ s}^{-1}$) and in H₂O ($0.9 \times 10^{-5} \text{ s}^{-1}$) the desorption rate constant for TiO₂-**RuPdvb-poly-[Fe(v-tpy)₂]²⁺** is lower than for TiO₂-**RuP** at pH 1 in water. Even in solutions buffered at pH 7 (0.1 M Na₃PO₄ buffer), the polymerized films have desorption rate constants ($5.5 \times 10^{-5} \text{ s}^{-1}$) comparable to TiO₂-**RuP** in 0.1 M HClO₄. In solutions buffered at pH 7, desorption of **RuP** occurs with $k_{\text{des}} > 30 \times 10^{-5} \text{ s}^{-1}$.

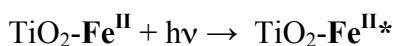
The use of the standard stability measurement protocol allows for comparison between surface stabilization strategies. For example, we recently demonstrated that atomic

layer deposition (ALD) of Al₂O₃ on a TiO₂ surface derivatized with **RuP** significantly increases the stability of the surface-bound complex in water.¹⁴⁷ A comparison of k_{des} for untreated TiO₂-**RuP**, TiO₂-**RuP** stabilized by ~3.3 Å of ALD Al₂O₃, and TiO₂-**RuPdvb**-*poly*[**Fe(v-tpy)**]₂²⁺ films (150 cycles, 1:1.8 Ru:Fe) is shown in Table 7.4. Under aqueous conditions the polymerized films are almost twice as stable as the ALD films and 10 times more stable than the untreated films. This result suggests that reductive electropolymerization is a viable strategy for increasing stability of surface-bound complexes under aqueous conditions.

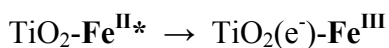
Transient Absorption

Interfacial electron transfer dynamics for TiO₂-**RuP**, TiO₂-*poly*-[**Fe(v-tpy)**]₂²⁺, and TiO₂-**RuPdvb** with 10, 30, 70 and 150 cycles of *poly*-[**Fe(v-tpy)**]₂²⁺ overlayer were investigated by nanosecond transient absorption measurements in aqueous 0.1 M HClO₄. It has previously been demonstrated that photo-excitation of phosphonate-derivatized ruthenium polypyridyl complexes on TiO₂, Equation 7.7, is followed by efficient electron injection into the conduction band of TiO₂, Equation 7.8, with $\Phi_{\text{inj}} = 100\%$ for TiO₂-**RuP** at pH 1.¹⁴⁴ The electron injection process is accompanied by a bleach of the MLCT absorption features from 400 to 520 nm.

Equation 7.7



Equation 7.8



For TiO_2 -*poly*- $[\text{Fe}(\text{v-tpy})_2]^{2+}$ (70 cycles, ~ 1 monolayer), a negligible transient absorption response (< 10 mOD at 580 nm) was observed upon photo-excitation at 450 nm (Figure F.12). The relatively small transient absorption amplitude suggests that the injection yield for excited *poly*- $[\text{Fe}(\text{v-tpy})_2]^{2+}$ on TiO_2 , Equation 7.7, is $< 1\%$ consistent with the known photophysics of related complexes in solution. As shown by McCusker, MLCT excitation is followed by rapid inter-conversion to low-lying dd states and rapid non-radiative decay.³⁵¹

Time-resolved absorption difference spectra for **RuPdvb** with 10, 30, 70 and 150 cycles of *poly*- $[\text{Fe}(\text{v-tpy})_2]^{2+}$ following photo-excitation at 425 nm were constructed from multiple single-wavelength measurements from 440 to 640 nm, acquired every 10 nm. The results are shown in Figure 7.7 and Figure F.13.

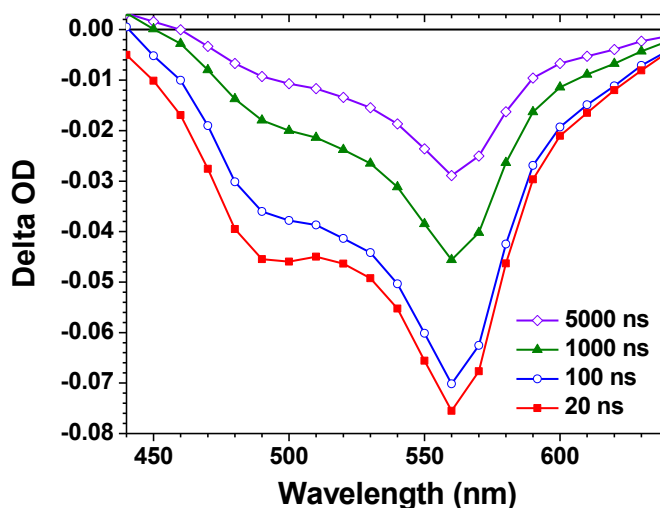


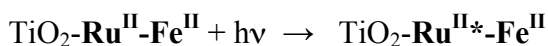
Figure 7.7. Time-resolved absorption difference spectra for TiO_2 -**RuPdvb**-*poly*- $[\text{Fe}(\text{v-tpy})_2]^{2+}$ (30 cycles, 1:0.5 Ru:Fe) in Ar deaerated aqueous 0.1 M HClO_4 . (Excitation at 425 nm, 5.0 mJ/pulse).

In the difference spectra for TiO_2 -**RuPdvb**-*poly*- $[\text{Fe}(\text{v-tpy})_2]^{2+}$ (1:0.5 Ru:Fe) in Figure 7.7, there is evidence for electron injection leading to partial bleaching by the appearance of bleaches arising from loss of MLCT absorbance for Ru^{II} from 450 to 520 nm

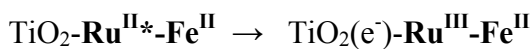
and for loss of absorbance for Fe^{II} from 520 to 640 nm. At the earliest time, ~20 ns, bleaching of both Ru^{II} and Fe^{II} is observed. Following the laser flash, the bleach feature for Ru^{III} decreases more rapidly than the bleach feature for Fe^{II}.

The time-dependent absorption changes appear to arise from competing electron transfer events following photoexcitation (Equation 7.9) and quenching of TiO₂-Ru^{II*} (Equation 7.10). They include back electron transfer from TiO₂(e⁻) to Ru^{III} (Equation 7.11), inter-assembly/inter-layer electron transfer from Fe^{II} to Ru^{III} (Equation 7.12), and back electron transfer from TiO₂(e⁻) to Fe^{III} (Equation 7.13). In these reactions, **RuPdvb** and poly-[Fe(v-tpy)₂]²⁺ are represented by **Ru^{II}** and **Fe^{II}**, respectively, and injection by **Fe^{II*}** is neglected because it is negligible (Figure F.12).

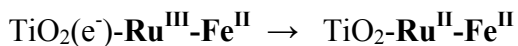
Equation 7.9



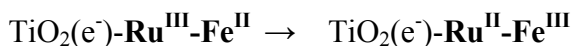
Equation 7.10



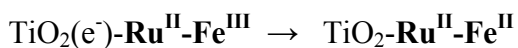
Equation 7.11



Equation 7.12



Equation 7.13



The spectral changes over time suggest that electron transfer from Fe^{II} to Ru^{III} (Equation 7.12) occurs on a timescale of hundreds of nanoseconds. Quantitation is difficult in part because, as noted above, the $\text{TiO}_2\text{-RuPdmb-poly-}[\text{Fe}(\text{v-tpy})_2]^{2+}$ overlayer structures are inhomogeneous in composition with depth in the film. Transient absorption spectral changes include electron transfer events between localized regions with different $\text{Ru}^{\text{II}}:\text{Fe}^{\text{II}}$ ratios. There is also kinetic overlap between intra-assembly $\text{Fe}^{\text{II}} \rightarrow \text{Ru}^{\text{III}}$ electron transfer (Equation 7.12) and back electron transfer from $\text{TiO}_2(e^-)$ to Ru^{III} (Equation 7.11) and Fe^{III} (Equation 7.13). For **RuP** on TiO_2 back electron transfer extends from the nanosecond to millisecond time scales and,¹⁴⁴ as found for other dynamic processes at nanocrystalline metal oxide interfaces, the kinetics are non-exponential and highly complex.^{352,353}

The spectral changes for oxidation/reduction of $\text{poly-}[\text{Fe}(\text{v-tpy})_2]^{2+}$ can be differentiated from those arising from $\text{Ru}^{\text{III/II}}$ by measuring the relative electron injection yield and back electron transfer dynamics at 580 nm. This wavelength is the ground state/oxidized state isosbestic point for **RuPdmb**, the optical model for **RuPdmb** after polymerization. Absorption-time kinetic traces at 580 nm following 450 nm excitation are shown in Figure 7.8. The data were fit over the first ~ 10 μs using the tri-exponential function in Equation 7.1. Weighted average lifetime values, $\langle \tau \rangle$, calculated by use of Equation 7.2, are summarized in Table 7.5.

Table 7.5. Net electron injection yields (based on the appearance of Fe^{III}), average back electron transfer lifetimes, and k_{bet} from transient absorption measurements on $\text{TiO}_2\text{-RuPdmb-poly-}[\text{Fe}(\text{v-tpy})_2]^{2+}$ as a function of Ru:Fe ratio in 0.1 M HClO_4 with $\text{TiO}_2\text{-RuP}$ as a reference.^a

Ru:Fe	^b Φ_{inj}	Lifetime (μs)				$\langle \tau \rangle$	k_{bet} ($\times 10^4 \text{s}^{-1}$)
		τ_1 (A_1)	τ_2 (A_2)	τ_3 (A_3)			

1:0.2	0.15	0.20(1)	1.6(6)	16.5(94)	16.4	6.1
1:0.5	0.35	0.25(1)	1.8(4)	18.5(96)	18.4	5.4
1:0.9	0.30	0.23(1)	1.6(5)	18.2(95)	18.1	5.5
1:1.8	0.20	0.23(1)	1.6(5)	21.3(95)	21.2	4.7
RuP^c	1.00	0.01(2)	0.8(9)	10.7(89)	10.6	9.4

^aexcitation at 450 nm, probed at 580 nm. ^b $\Delta\epsilon$ for **Fe** at 580 nm is -11,200, for **RuP** at 400 nm is -6500. ^cmonitored at 400 nm.

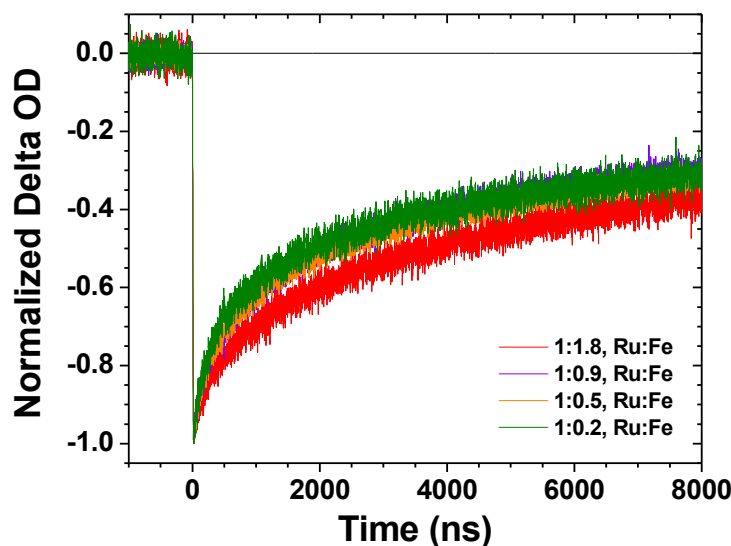


Figure 7.8. Absorption-time traces for $\text{TiO}_2\text{-RuPdvb-poly-}[\text{Fe}(\text{v-tpy})_2]^{2+}$ with various ratios of Ru to Fe in Ar deaerated 0.1 M HClO_4 aqueous solutions monitored at 580 nm (450 nm excitation, 5.0 mJ/pulse).

In Figure 7.8, a bleach feature is present at 580 nm at the earliest observation of ~ 20 ns. Given the lack of direct injection by $\text{Fe}^{\text{II}*}$, this feature is a marker for $\text{Ru}^{\text{II}*}$ injection (Equation 7.10) followed by partial intra-assembly $\text{Fe}^{\text{II}} \rightarrow \text{Ru}^{\text{III}}$ electron transfer (Equation 7.12). Based on these data there is a rapid injection component occurring in less than 20 ns. The bleach feature for Ru^{III} , Figure 7.7, is still present at > 20 ns which shows that another fraction of Ru^{III} sites produced by electron injection undergo relatively slow $\text{Fe}^{\text{II}} \rightarrow \text{Ru}^{\text{III}}$ (Equation 7.12) electron transfer or return to Ru^{II} by back electron transfer from $\text{TiO}_2(\text{e}^-)$, Equation 7.11.

Return of the bleach to the baseline by $\text{TiO}_2(e^-) \rightarrow \text{Fe}^{\text{III}}$ back electron transfer, Equation 7.13, is $\sim 60\%$ complete by $9 \mu\text{s}$. As can be seen in Figure 7.8 and Table 7.5, there is a slight trend toward slower back electron transfer as the Ru:Fe ratio is increased from 1:0.2 ($k_{bet} = 6.1 \times 10^4 \text{ s}^{-1}$) to 1:1.8 ($k_{bet} = 4.7 \times 10^4 \text{ s}^{-1}$).

Relative electron injection efficiencies (Φ_{inj}) for $\text{TiO}_2\text{-RuPd}vb\text{-poly-}[\text{Fe}(\text{v-tpy})_2]^{2+}$ were estimated by using thin film actinometry with $\text{TiO}_2\text{-RuP}$ ($\Phi_{inj} = 1.0$) as the reference.^{144,354} Amplitude changes were evaluated 10 ns following 450 nm laser excitation with injection yields calculated by using Equation 7.3 from the experimental section with $\Delta\epsilon = -6500 \text{ M}^{-1}\text{cm}^{-1}$ at 400 nm for **RuP** and $\Delta\epsilon = -11,200 \text{ M}^{-1}\text{cm}^{-1}$ at 580 nm for $\text{poly-}[\text{Fe}(\text{v-tpy})_2]^{2+}$. The latter were determined by spectroelectrochemical measurements on nano-ITO (Figure F.14). The results are summarized in Table 7.5.

From these data, Φ_{inj} for $\text{TiO}_2\text{-RuPd}vb\text{-poly-}[\text{Fe}(\text{v-tpy})_2]^{2+}$ is significantly lower ($\leq 30\%$) than Φ_{inj} for $\text{TiO}_2\text{-RuP}$ (100%). Since **RuPd}vb** is expected to have a near unity electron injection yield in the polymerized film ($\Phi_{inj(\text{TiO}_2\text{-RuPd}vb)} = 100\%$), there is a significant decrease in Φ_{inj} for $\text{TiO}_2\text{-RuPd}vb\text{-poly-}[\text{Fe}(\text{v-tpy})_2]^{2+}$. It should be noted that the reported net injection yield only accounts for Fe^{III} , and not Ru^{III} , present at 20 ns after the laser flash. Also, photons absorbed by $\text{poly-}[\text{Fe}(\text{v-tpy})_2]^{2+}$ at 450 nm are largely lost since the $\text{poly-}[\text{Fe}(\text{v-tpy})_2]^{2+}$ chromophore acts as a non-productive light absorber/filter. An additional contributing factor may arise from the timescale of the injection measurement. Excitation-injection events followed by back electron transfer on the <20 ns timescale are not included in the experimental Φ_{inj} values.

The transient absorption results demonstrate that electropolymerization can be used to incorporate an electron donor as an overlayer on chromophores pre-attached to a metal oxide surface. The electron donor facilitates directional electron transfer toward the metal oxide surface and slows deleterious back electron transfer. We are currently investigating more elaborate structures with non-absorbing external donors in the outer layer to prepare chromophore-catalyst assembly structures at the interface for possible DSPEC applications.

7.4 Conclusions

We report here a successful, general strategy for synthesizing and characterizing spatially controlled, multi-component films on mesoporous TiO₂. The films were prepared by electropolymerization of [Fe(v-tpy)₂]²⁺ on both TiO₂ and RuPdvb-derivatized mesoporous TiO₂. The Ru:Fe ratio in the overlayer structures can be controlled by the number of reductive electrochemical scan cycles. EDS measurements reveal the films to be inhomogeneous in depth with regard to total concentration and Ru:Fe ratio.

The photostabilities of the TiO₂-RuPdvb-*poly*-[Fe(v-tpy)₂]²⁺ interfacial structures are enhanced by factors of up to 30 compared to the surface-bound complex alone. Notably, surface stabilization is enhanced relative to an ALD overlayer strategy based on Al₂O₃.

Based on the results of transient absorbance measurements on TiO₂-RuPdvb-*poly*-[Fe(v-tpy)₂]²⁺, excitation of surface-bound Ru^{II} is followed by electron injection and both fast and slow outside-to-inside Fe^{II} → Ru^{III} electron transfer. These results show that the electropolymerized overlayer structure facilitates directional electron transfer toward the metal oxide surface and slows back electron transfer from TiO₂(e⁻). The generality of the electropolymerized overlayer approach for synthesis of water stable, multicomponent films is

notable and is currently being exploited to prepare interfacial structures for electrocatalysis and DSPEC applications.

7.5 Acknowledgements

K.H. acknowledges support from the UNC EFRC “Center for Solar Fuels”, an Energy Frontier Research Center funded by the U.S. Department of Energy, Office of Science, Office of Basic Energy Sciences under award DE-SC0001011. A.M.L. acknowledges support from the U.S. Department of Energy, Office of Science, Office of Basic Energy Sciences, under Award No. DE-FG02-06ER15788. D.L.A. acknowledges support from a fellowship from the Department of Energy Office of Science Graduate Fellowship Program (DOE SCGF), made possible in part by the American Recovery and Reinvestment Act of 2009, administered by ORISE-ORAU under contract number DE-AC05-06OR23100.

7.6 Associated Content

Appendix F: EDS analyses, UV/Vis absorption spectra, adsorption isotherms, cyclic voltammograms, emission spectra, time-resolved absorption difference spectra, and photostability measurements is available in Appendix F.

Chapter 8: WATER OXIDATION BY AN ELECTROPOLYMERIZED CATALYST ON DERIVATIZED MESOPOROUS METAL OXIDE ELECTRODES

Reprinted with permission from Ashford, D. L.; Lapides, A. M.; Vannucci, A. K.; Hanson, K.; Torelli, D. A.; Harrison, D. P.; Templeton, J. L.; Meyer, T. J., Water Oxidation by an Electropolymerized Catalyst on Derivatized Mesoporous Metal Oxide Electrodes. *J. Am. Chem. Soc.* **2014**, *136* (18), 6578-6581. Copyright American Chemical Society 2014

8.1 Introduction

Dye-sensitized photoelectrosynthesis cells (DSPECs) offer a potential solution to solar energy storage by using solar energy to generate chemical fuels (Figure 1.6).^{2,92} In a DSPEC for water splitting, configuration of the chromophore and catalyst is important in enabling rapid electron transfer from the catalyst to the oxidized chromophore following the excitation-injection sequence.^{90,162}

Multiple strategies have been described for assembling chromophores and catalysts on metal-oxide surfaces.^{190,191,193,325,326,355-357} They typically suffer from difficult synthetic procedures and/or limited stabilities on oxide surfaces.^{141,180} Recently, we reported reductive electropolymerization/electro-oligomerization of a vinyl-functionalized polypyridyl complex, $[\text{Fe}(4'\text{-vinyl-}2,2':6',2''\text{-terpyridine})_2]^{2+}$, on bare TiO_2 and on TiO_2 surfaces pre-derivatized with the vinyl- and phosphonate-functionalized complex, $[\text{Ru}(\text{dvb})_2((\text{PO}_3\text{H}_2)_2\text{bpy})]^{2+}$ (**RuPdvb**²⁺; dvb = 5,5'-divinyl-2,2'-bipyridine; $(\text{PO}_3\text{H}_2)_2\text{bpy}$ = [2,2'-bipyridine]-4,4'-diylbis(phosphonic acid)).^{148,336} The effect of adding the electropolymerized overlayer is dramatic, leading to a

30-fold enhancement in photostability of the surface-bound chromophore relative to the unprotected film.

Here we describe utilization of this strategy to introduce the vinyl-functionalized water oxidation catalyst, $[\text{Ru}(\text{Mebimpy})(\text{dvb})(\text{OH}_2)]^{2+}$ (RuOH_2^{2+} , Mebimpy = 2,6-bis(1-methyl-1*H*-benzo[*d*]imidazole-2-yl)pyridine), as the electropolymerized overlayer (Figure 8.1). This procedure provides a basis for preparing stable, catalytically active films both with and without the pre-bound RuPdvb^{2+} chromophore on both planar oxide surfaces and in mesoporous, nanoparticle metal oxide films.

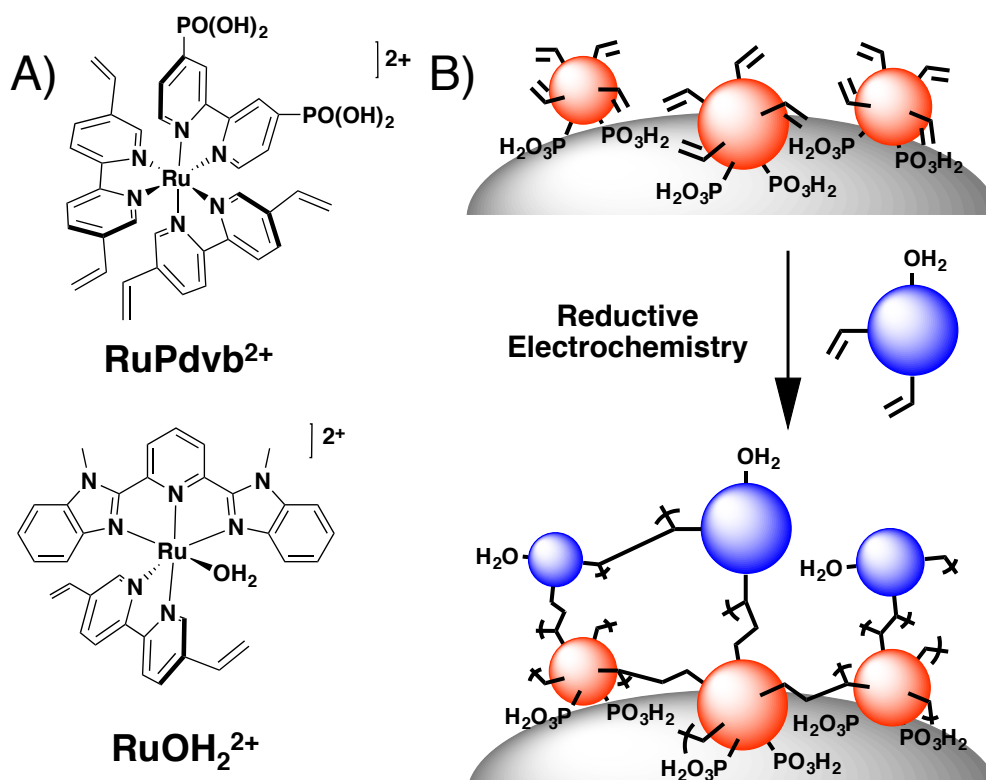


Figure 8.1. (A) Structures of RuPdvb^{2+} and RuOH_2^{2+} (B) Schematic diagram of the surface structure following reductive electropolymerization of RuOH_2^{2+} on $n\text{TiO}_2\text{-RuPdvb}^{2+}$.

8.2 Experimental

Sample Preparation.

Materials. [Ru(η^6 -benzene)(Cl)₂]₂,²⁹¹ 2,6-bis(1-methyl-1H-benzo[d]imidazol-2-yl)pyridine,³³ and 5,5'-divinyl-2,2'-bipyridine³⁴¹ were synthesized as previously reported. Distilled water was further purified by using a Milli-Q Ultrapure water purification system. All other reagents were ACS grade and used without further purification. Fluoride-doped tin oxide (FTO)-coated glass (Hartford Glass; sheet resistance 15 Ω cm⁻²), was cut into 10 mm \times 40 mm strips and used as the substrate for TiO₂ nanoparticle films. Microwave reactions were carried out using a CEM MARS microwave reactor. A CEM HP-500 Plus Teflon-coated microwave vessel (100 mL) was used at a power setting of 400 W. The vessel was rotated and stirred throughout the microwave procedure. The pressure of the reaction vessel was monitored throughout the reaction, and never exceeded 300 PSI.

Metal Oxide Films. nTiO₂ films, typically 4 - 7 μ m thick (\sim 20 nm particle diameter), with a coating area of roughly 10 mm \times 15 mm, were synthesized according to a literature procedure.²⁴⁸

Electrochemical and Photophysical Measurements.

Absorption spectra were obtained by placing the dry derivatized films perpendicular to the detection beam path of the spectrophotometer. The expression, $\Gamma = A(\lambda)/\epsilon(\lambda)/1000$, was used to calculate surface coverages.²⁴⁹ Molar extinction coefficients (ϵ) in H₂O were used; $A(\lambda)$ was the absorbance at the MLCT λ_{max} . All measurements were carried out of films loaded from methanol solutions of 150 μ M in ruthenium complex, which gave complete surface coverage ($\Gamma = 8 \times 10^{-8}$ mol cm⁻²).

Electrochemical measurements were conducted on a CH Instruments 660D potentiostat with a Pt-mesh or Pt-wire counter electrode, and a Ag/AgNO₃ (0.01 M AgNO₃/0.1 M tetra-n-butylammonium hexafluorophosphate (TBAPF₆) in CH₃CN; -0.09 V

vs. $\text{Fc}^{+/0}$ ³⁴² or Ag/AgCl (3 M NaCl; 0.197 V vs. NHE) reference electrode. $E_{1/2}$ values were obtained from the peak currents in square wave voltammograms or from averaging cathodic and anodic potentials at peak current values ($E_{p,c}$ and $E_{p,a}$) in cyclic voltammograms.

Reductive electropolymerization was carried out in anhydrous propylene carbonate (dried over MgSO_4) with 0.1 M tetrabutylammonium hexafluorophosphate (TBAPF_6) as the supporting electrolyte under an atmosphere of argon. Solutions were degassed with argon for at least 5 minutes prior to reductive electrochemical cycling.

Surface coverages on planar FTO electrodes were calculated using Equation 8.1 where Q is the integrated current under the $\text{Ru}^{\text{III/II}}\text{-OH}_2$ redox couple of *polyRuOH*²⁺, F is Faraday's constant (96,485 C), n is the number of electrons transferred ($n = 1$), and A is the area of the electrode ($\sim 1 \text{ cm}^2$).

Equation 8.1

$$\Gamma = Q/nFA$$

Catalytic rate constants for the water oxidation, k_{obs} , were calculated using Equation 8.2 where i_{cat} is the catalytic current taken at 1.7 V (vs NHE), i_{peak} is the current taken for the $\text{Ru}^{\text{III}}\text{-OH/Ru}^{\text{II}}\text{-OH}_2$ redox couple, n_{cat} is the number of electrons involved in the catalytic step (4 for water oxidation), R is the ideal gas constant, T is the temperature, n_p is the number of electrons involved in the $\text{Ru}^{\text{III}}\text{-OH/Ru}^{\text{II}}\text{-OH}_2$ redox couple (1 in this case), F is Faraday's constant, and ν is the scan rate.³⁵⁸

Equation 8.2

$$\frac{i_{\text{cat}}}{i_{\text{peak}}} = \left(\frac{4RTn_{\text{cat}}}{n_p^2 F} \right) k_{\text{obs}} \left(\frac{1}{\nu} \right)$$

Scanning electron microscopy (SEM) and energy dispersive X-ray spectroscopy (EDS) results were obtained on a FEI Helios 600 Nanolab Dual Beam System equipped with an Oxford instruments, INCA PentaFET-x3 detector. A cross section was taken of $n\text{TiO}_2\text{-RuPd}^{\text{vb}^{2+}}$ that had been reductively cycled 60, 120, and 300 times in presence of RuOH_2^{2+} . Surface images were taken at 5 kV with a 86 pA beam current. Three EDS spectra were obtained at the $\text{TiO}_2/\text{solution}$ interface (top), in the bulk of TiO_2 nanoparticles (middle), and at the nano- TiO_2/FTO interface (bottom) of the cross section.

Photostability measurements were performed by a previously reported procedure.¹⁴¹ The light from a Royal Blue (455 nm, FWHM ~ 30 nm, 475 mW/cm^2) Mounted High Power LED (Thorlabs, Inc., M455L2) powered by a T-Cube LED Driver (Thorlabs, Inc., LEDD1B) was focused to a 2.5 mm diameter spot size by a focusing beam probe (Newport Corp. 77646) outfitted with a second lens (Newport, Corp 41230). The light output was directed onto the derivatized thin film placed at 45° in a standard 10 mm path length cuvette containing 3 mL of the solution. The illumination spot was adjusted to coincide both with the thin film and the perpendicular beam path of a Varian Cary 50 UV/Vis spectrophotometer. The absorption spectrum (360 – 800 nm) of the film was taken every 15 minutes over 16 hours of illumination. The incident light intensity was measured with a thermopile detector (Newport Corp 1918-C meter and 818P-020-12 detector). The solution temperature, $22 \pm 2^\circ\text{C}$, was consistent throughout the duration of the experiment.

The absorption-time traces at 400 nm, 450 nm, and 500 nm for the pH 4.6 (0.1 M HOAc/OAc , 0.5 M NaClO_4) could be satisfactorily fit with the biexponential function (Equation 8.3). For comparison purposes, the results of the multi-exponential analysis were represented by a single rate constant by first calculating the weighted average lifetime ($\langle \tau \rangle$)

using Equation 8.4. The three weighted average lifetimes ($\langle \tau \rangle_{400\text{nm}}$, $\langle \tau \rangle_{450\text{nm}}$, $\langle \tau \rangle_{500\text{nm}}$) were then averaged (Equation 8.5) to give a desorption rate constant k_{des} .

Equation 8.3

$$y = A_1 e^{-(1/\tau_1)x} + A_2 e^{-(1/\tau_2)x} + y_0$$

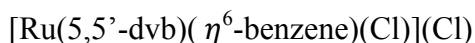
Equation 8.4

$$\langle \tau \rangle = \frac{\sum A_i \tau_i^2}{\sum A_i \tau_i}$$

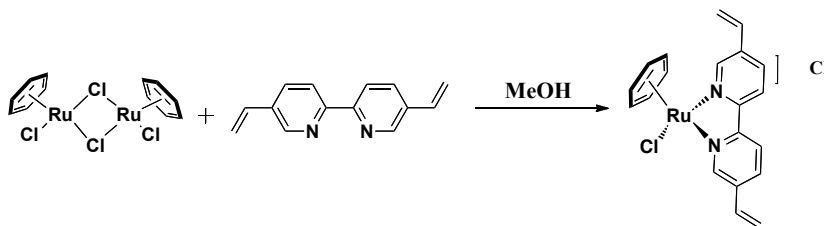
Equation 8.5

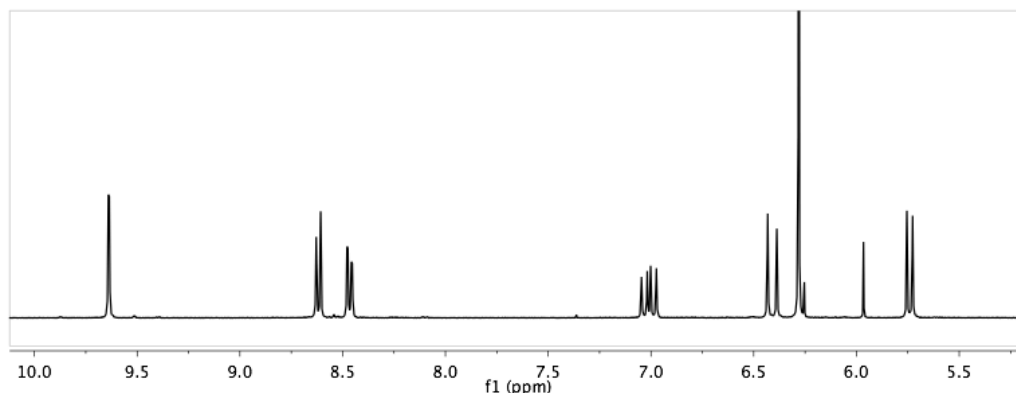
$$1/k_{\text{des}} = (\langle \tau \rangle_{400\text{nm}} + \langle \tau \rangle_{450\text{nm}} + \langle \tau \rangle_{500\text{nm}})/3$$

Synthesis



This complex was synthesized according a modified literature procedure.¹⁹² $[\text{Ru}(\eta^6\text{-benzene})(\text{Cl})_2]_2$ (0.24 g, 0.48 mmol) and 5,5'-divinyl-2,2'-bipyridine (0.2 g, 0.96 mmol) were dissolved in MeOH (~40 mL). The solution was refluxed overnight under an atmosphere of argon. The reaction was cooled, filtered, and the filtrate was taken to dryness by a rotary evaporator. The solid was triturated with ether, collected, and air-dried. This complex was used without further purification (0.42 g, 95%). ¹H NMR (400 MHz, DMSO) δ (ppm) 9.64 (s, 2H), 8.63 (d, 2H), 8.48 (d, 2H), 7.05 (dd, 2H), 6.43 (d, 2H), 6.28 (s, 6H), 5.73 (d, 2H).

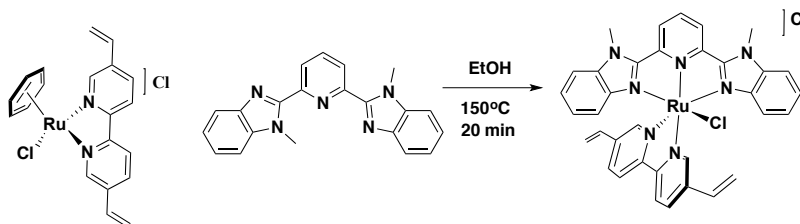


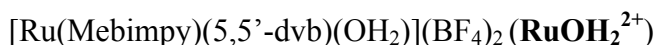
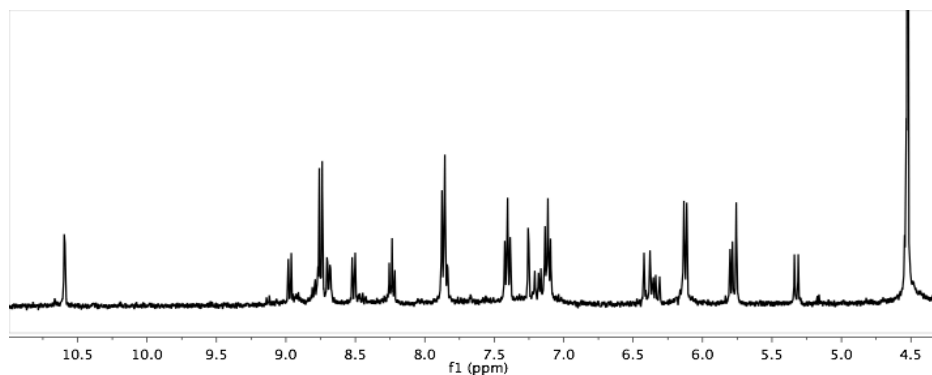


[Ru(Mebimpy)(5,5'-dvb)(Cl)](Cl)

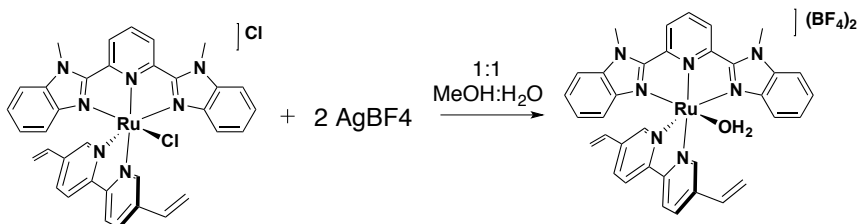
This complex was synthesized according a modified literature procedure.¹⁹⁰ [Ru(5,5'-dvb)(η^6 -benzene)(Cl)]Cl (0.122 g, 0.27 mmol) and 2,6-bis(1-methyl-1H-benzo[d]imidazol-2-yl)pyridine (0.09 g, 0.27 mmol) were heated at reflux for 20 minutes at 150 °C in 40 mL EtOH in a microwave reactor. The solution was cooled, then filtered. A saturated solution of LiCl (~15 mL) was added along with additional H₂O (15 mL), and the EtOH was removed by rotary evaporation. The dark purple precipitate was filtered, washed with water and ether, air dried and collected. This complex was used without further purification (0.169 g, 87%).

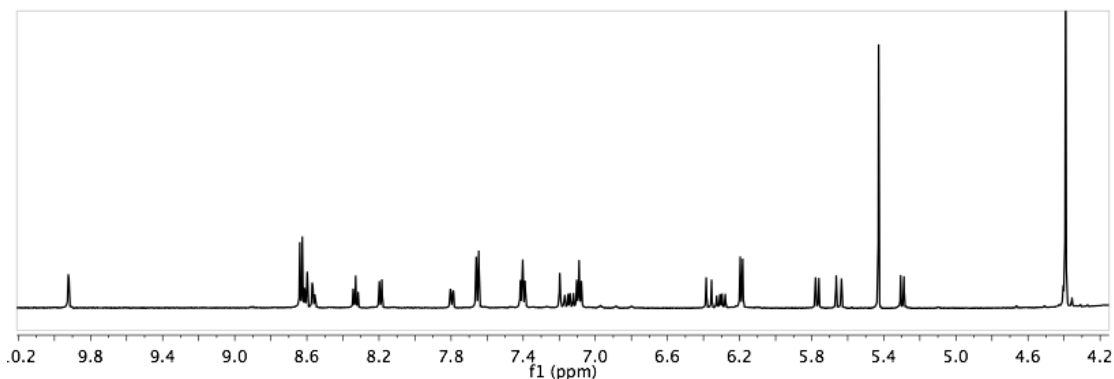
¹H NMR (600 MHz, d₆-DMSO) δ (ppm) 10.6 (s, 1H), 8.98 (d, 1H), 8.76 (m, 2H), 8.70 (d, 1H), 8.50 (d, 1H), 8.24 (t, 1H), 7.87 (m, 3H), 7.40 (t, 2H), 7.26 (s, 1H), 7.11 (m, 3H), 6.42 (d, 1H), 6.32 (d, 1H), 6.11 (d, 2H), 5.79 (m, 2H), 5.32 (d, 1H), 4.53 (s, 6H).





[Ru(Mebimpy)(5,5'-dvb)(Cl)](Cl) (0.344 g, 0.48 mmol) was dissolved in 1:1 MeOH:H₂O (~ 30 mL) under an atmosphere of argon. A solution of AgBF₄ (0.189 g, 0.97 mmol) in H₂O (~10 mL) was added. The solution was refluxed in the dark overnight under an atmosphere of argon. The solution was cooled, filtered through Celite, and the filtrate was taken to dryness using a rotary evaporator. The crude product was then purified by size-exclusion chromatography (Sephadex LH-20) with 1:1 MeOH:H₂O as eluent. Similar fractions (based of UV-Vis spectra) were combined, and the solvent was removed by rotary evaporation. The dark red solid was triturated with ether and collected (0.29 g, 73%). ¹H NMR (600 MHz, CD₃CN) δ (ppm) 9.97 (s, 1H), 8.60 (m, 4H), 8.34 (t, 1H), 8.19 (d, 1H), 7.82 (dd, 1H), 7.67 (d, 2H), 7.44 (t, 2H), 7.22 (d, 1H), 7.18 (dd, 1H), 7.12 (t, 2H), 6.42 (d, 1H), 6.36 (dd, 1H), 6.23 (d, 2H), 5.80 (d, 1H), 5.69 (d, 1H), 5.33 (d, 1H), 4.41 (s, 6H). Anal. Found (Calc.) for C₃₅H₃₇B₂F₈N₇O₄Ru: C 46.83 (47.00), H 3.72 (4.17), N 10.96 (10.96).





8.3 Results and Discussion

The chromophore, **RuPdvb**²⁺, and catalyst, **RuOH**₂²⁺ were synthesized as previously reported (see Experimental).^{148,190} Substitution of coordinated H₂O by CH₃CN was achieved by dissolving **RuOH**₂²⁺ in CH₃CN. Vapor diffusion of diethyl ether resulted in x-ray quality crystals of the CH₃CN-substituted complex (Figure 8.2). In the structure, the geometry around Ru(II) is a slightly distorted octahedron with bond angles of 174.2° for N1-Ru-N3 and 174.4° for N2-Ru-N6. The length of the vinyl C-C bonds (1.30 Å) and the Ru-N bonds (2.037 Å) match those of similar complexes.²¹³

Electropolymerization was conducted in a three-compartment electrochemical cell under an argon atmosphere. All solutions were dried over MgSO₄, filtered and deaerated with argon for 10 minutes before electropolymerization. The working electrodes were planar fluoride-doped tin oxide (*p*FTO), nanocrystalline titanium dioxide (*n*TiO₂), or nanocrystalline indium tin oxide (*n*ITO). Working electrodes were either the bare metal oxide or derivatized with **RuPdvb**²⁺ by soaking overnight in methanol solutions of the complex (150 μM).¹⁴⁸ In a typical electropolymerization experiment, the working electrode was cycled in a solution of **RuOH**₂²⁺ (0.5 mM in complex, 0.1 M TBAPF₆/PC; PC = propylene carbonate) from 0 V to -1.8 V (vs. Ag/AgNO₃) at a scan rate of 100 mV s⁻¹ with a

120 s pause between each cycle. PC was used as the electrochemical solvent rather than CH₃CN to avoid displacing the H₂O ligand of **RuOH₂²⁺**. Solutions were stirred during and between cycles to promote percolation of **RuOH₂²⁺** throughout the mesoporous metal oxides (*n*ITO and *n*TiO₂).¹⁴⁸

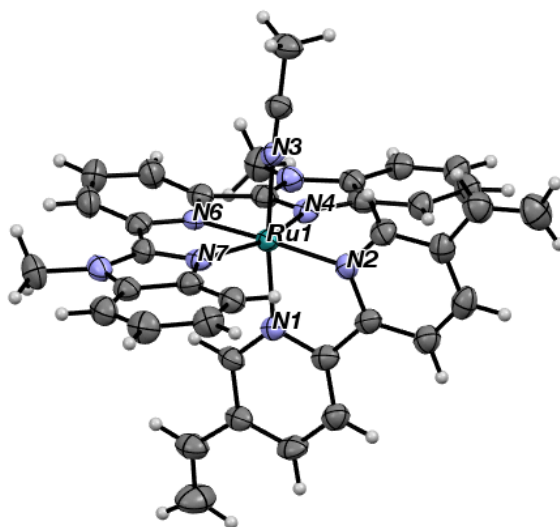


Figure 8.2. Crystal structure of **Ru-NCCH₃²⁺** grown by slow diffusion of diethyl ether into a solution of **RuOH₂²⁺** in CH₃CN. Structural details are listed at the end of the Appendix G.

Initially, electropolymerization was carried out on *p*FTO electrodes and on *p*FTO derivatized with **RuPd**vb**²⁺** (*p*FTO-**RuPd**vb**²⁺**). Surface coverages (Γ) of polymerized **RuOH₂²⁺** on *p*FTO (*polyRuOH₂²⁺*) were determined by cyclic voltammetry (CV). In these measurements, the charge passed under the Ru^{III/II} wave, and the expression in Equation 8.1, were used to establish Γ in mol/cm². Surface coverages on *p*FTO-*polyRuOH₂²⁺* and *p*FTO-**RuPd**vb**²⁺**-*polyRuOH₂²⁺* increased linearly with the number of reductive scan cycles (Figure 8.3). Under the electropolymerization conditions, one monolayer equivalent ($\sim 1 \times 10^{-10}$ mol cm⁻² on planar surfaces) of *polyRuOH₂²⁺* was deposited every ~ 2 cycles on both *p*FTO and *p*FTO-**RuPd**vb**²⁺**. The peak current (i_p) for the *polyRu^{III/II}OH₂^{3+/2+}* couple in aqueous 0.1 M HClO₄ varied linearly with scan rate for *p*FTO-**RuPd**vb**²⁺**-*polyRuOH₂²⁺* with both 5 and 20

layers of $polyRuOH_2^{2+}$ (Figure 8.4), consistent with a non-diffusional surface redox couple.³⁵⁹

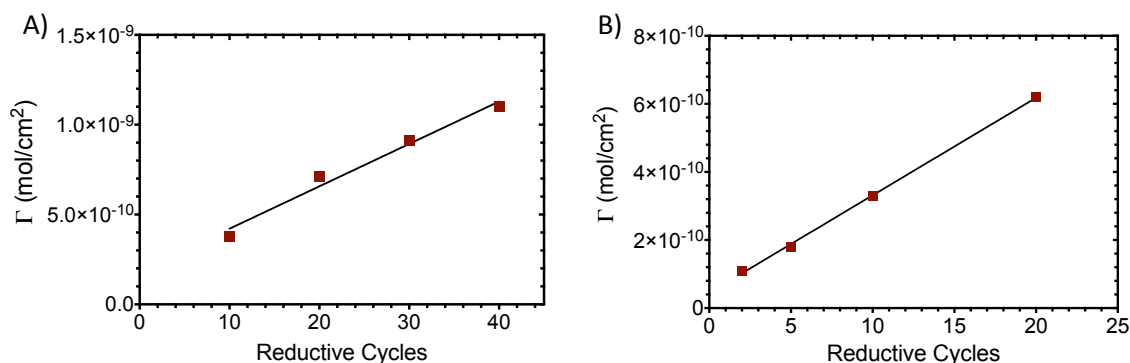


Figure 8.3. $polyRuOH_2^{2+}$ surface coverage on (A) bare pFTO and (B) pFTO-RuPdvb²⁺ versus the number of reductive cycles in dry PC solution of $RuOH_2^{2+}$ (0.5 mM, 0.1 M TBAPF₆), cycling from 0 to -1.8 V (vs Ag/AgNO₃), Pt counter, and Ag/AgNO₃ reference electrode.

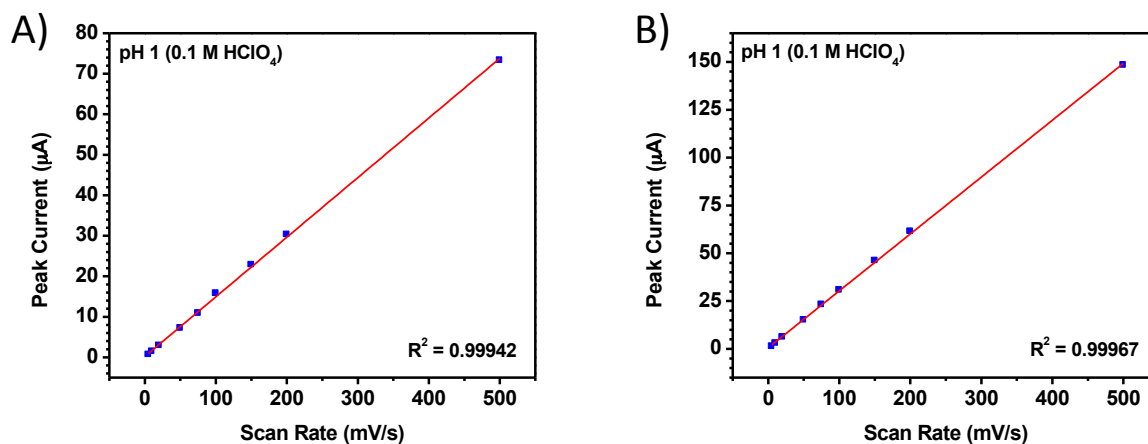
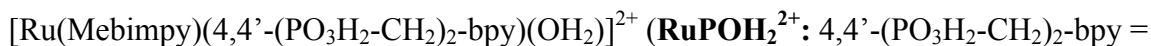


Figure 8.4. Peak current for the $polyRu^{III/II}OH_2$ redox couple versus the scan rate for pFTO-RuPdvb²⁺- $polyRuOH_2^{2+}$ with 5 (A) and 20 (B) monolayers of $polyRuOH_2^{2+}$ in aqueous 0.1 M HClO₄, Pt-wire counter electrode, and Ag/AgCl reference electrode.

The pH-dependence of the $polyRu^{III/II}OH_2^{3+/2+}$ couple on pFTO is illustrated in the $E_{1/2}$ vs. pH (Pourbaix) diagram in Figure 8.5. Below pH 2.3, the couple is pH independent. Above pH 2.3, $E_{1/2}$ decreases by 51 mV/pH unit, suggesting that $pK_a = 2.3$ for $polyRu^{III}OH_2^{3+}$. This value is comparable to that of the surface bound catalyst



([2,2'-bipyridine]-4,4'-diylbis(methylene))bis(phosphonic acid)) on $n\text{TiO}_2$ ($\text{p}K_a = 2.5$).³⁵⁰ The ensuing $\text{polyRu}^{\text{IV}}\text{O}^{2+}/\text{Ru}^{\text{III}}\text{OH}^{2+}$ couple is kinetically inhibited and difficult to observe as documented earlier for related ruthenium complexes.³⁵⁸ The electrochemical response of the couples is independent of film thickness in $p\text{FTO-polyRuOH}_2^{2+}$ in films up to 33 layers (Figure 8.6). These results suggest that the environment at the Ru(II) metal centers in polyRuOH_2^{2+} is open to diffusion of solvent and buffer/electrolyte through the polymer, at least to this level of thickness.

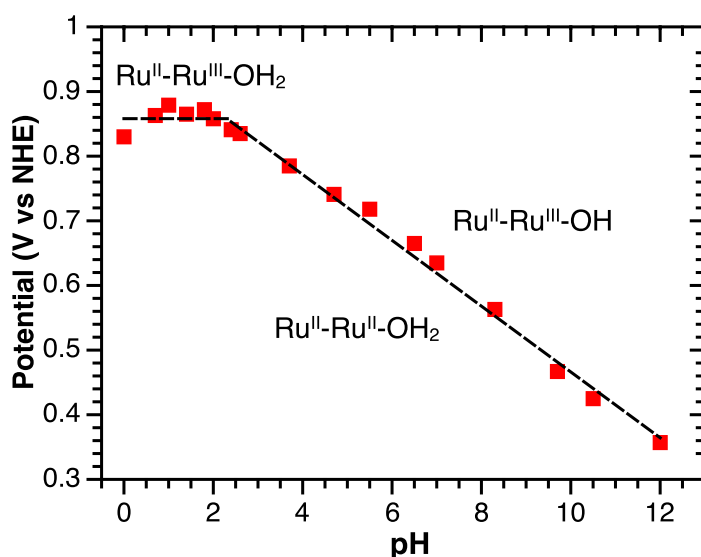


Figure 8.5. $E_{1/2}$ vs. pH diagram for $p\text{FTO-RuPdvb}^{2+}\text{-polyRuOH}_2^{2+}$. (5 layers). $E_{1/2}$ values are cited as potentials at the current maxima in square wave voltammograms. The dashed lines fit the $E_{1/2}$ -pH trends for the couples $\text{polyRu}^{\text{III}}\text{OH}_2^{3+}/\text{Ru}^{\text{II}}\text{OH}_2^{2+}$ (~ 0 mV/pH unit) and $\text{polyRu}^{\text{III}}\text{OH}^{2+}/\text{Ru}^{\text{II}}\text{OH}_2^{2+}$ (51 mV/pH unit) with $\text{p}K_a = 2.3$ for $\text{polyRu}^{\text{III}}\text{OH}_2^{3+}$ at 23 °C in aqueous 0.5 M NaClO_4 with 0.1 M buffer.

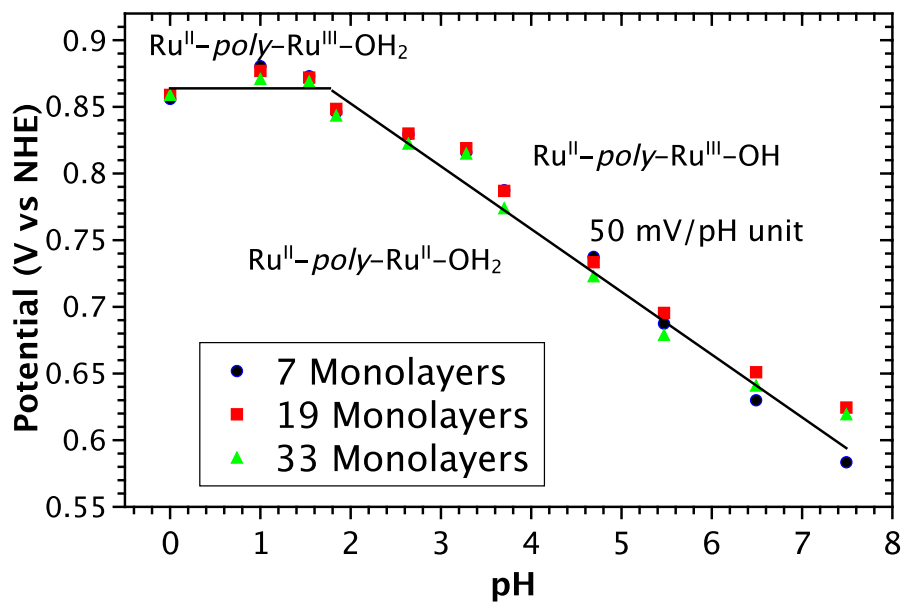


Figure 8.6. $E_{1/2}$ versus pH diagram of $p\text{FTO-RuPdvb}^{2+}$ - polyRuOH_2^{2+} with 7 (blue circles), 19 (red squares) and 33 (green triangles) monolayer equivalents of RuOH_2^{2+} deposited onto $p\text{FTO-RuPdvb}^{2+}$. $E_{1/2}$ values were obtained at peak current maxima in square wave voltammograms. The solid lines are best fits of the variation in $E_{1/2}$ values with pH for the $\text{Ru}^{\text{III}}\text{-OH}_2/\text{Ru}^{\text{II}}\text{-OH}_2$ and $\text{Ru}^{\text{III}}\text{-OH}/\text{Ru}^{\text{II}}\text{-OH}_2$ redox couples at 23 °C in aqueous 0.5 M NaClO_4 and 0.1 M buffer.

Electropolymerization was also investigated on $n\text{TiO}_2$ and $n\text{TiO}_2\text{-RuPdvb}^{2+}$ electrodes (2-4 μm thick). The high surface area electrodes allow for UV/Visible monitoring of surface coverage based on $\lambda_{\text{max}} = 497 \text{ nm}$; $\epsilon_{497 \text{ nm}} = 8200 \text{ M}^{-1} \text{ cm}^{-1}$ for polyRuOH_2^{2+} . On both surfaces, surface coverage of $\text{polyRu}^{\text{II}}\text{OH}_2^{2+}$ increased linearly with the number of scans (Figure 8.7 and Figure G.2) for the first 50 reductive cycles. With additional scans, surface coverage continues to increase, but at a slower rate with a plateau reached after ~ 300 cycles. Surface coverages following 70 and 300 cycles correspond to one ($\Gamma \sim 7 \times 10^{-8} \text{ mol cm}^{-2}$ on $n\text{TiO}_2$) and two layers of $\text{polyRu}^{\text{II}}\text{OH}_2^{2+}$, respectively.

A blue shift in the MLCT absorption maximum from 462 nm to 453 nm is observed for RuPdvb^{2+} in the electropolymerized films (Figure 8.7, Figure 8.8). This shift is consistent with conversion of the π^* acceptor vinyl substituents in RuPdvb^{2+} to saturated,

electron donating alkyl substituents in the electropolymerized polymers.¹⁴⁸ This observation suggests the formation of direct C-C bonds between surface-bound **RuPd**vb**²⁺** and catalyst **RuOH₂²⁺** in the surface assembly.^{148,333} No change in the absorption spectrum of *n*TiO₂-**RuPd**vb**²⁺** was observed following reductive cycling in the absence of **RuOH₂²⁺**.

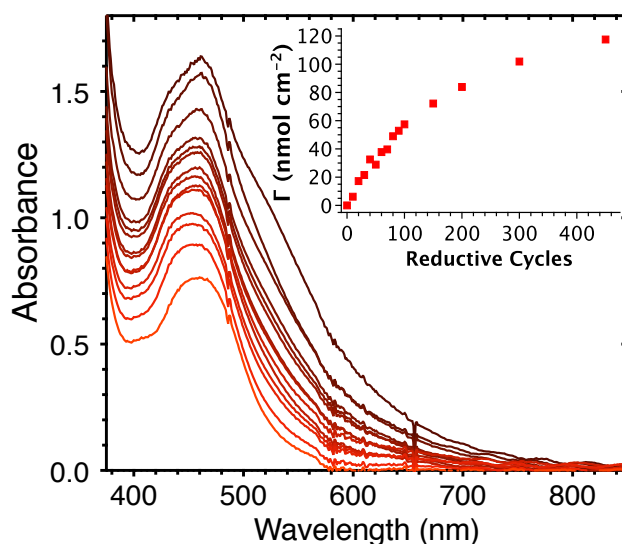


Figure 8.7. UV/visible spectral changes for *n*TiO₂-**RuPd**vb**²⁺** with an increasing number of reductive scan cycles (0, 10, 20, 30, 40, 50, 60, 70, 80, 90, 100, 150, 200, 300, 450; light red to dark red) in 0.5 mM **RuOH₂²⁺** (0.1 M TBAPF₆/PC). Inset: Surface coverage (Γ) of *polyRuOH₂²⁺* versus the number of reductive scan cycles.

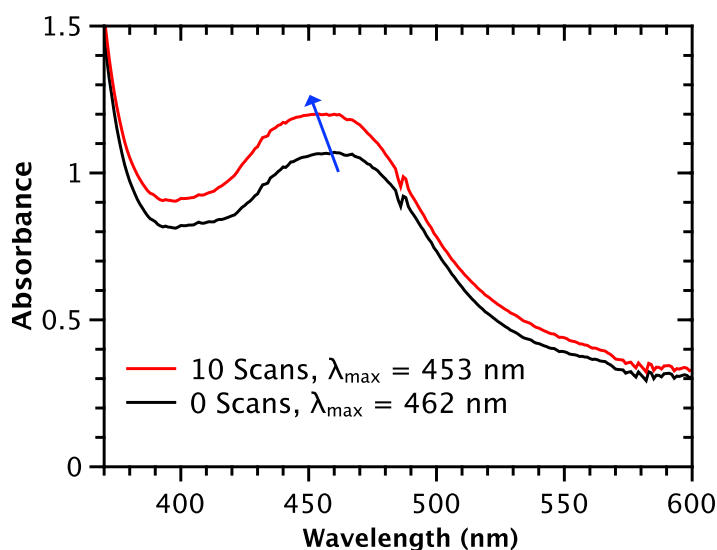


Figure 8.8. UV/visible absorption spectra of *n*TiO₂-**RuPd**vb**²⁺** before (black) and after (red) 10 reductive cycles from 0 to -1.8 V (vs Ag/AgNO₃) in PC solution of 0.5 mM **RuOH₂²⁺**, Pt counter, and Ag/AgNO₃ reference electrode.

Scanning electron microscope (SEM) images of $n\text{TiO}_2\text{-RuPdvb}^{2+}\text{-polyRuOH}_2^{2+}$ films following 60 reductive CVs show that the $n\text{TiO}_2$ films maintain their porosity (Figure 8.9). A decrease in porosity is observed following 120 reductive cycles. Following 450 reductive cycles, a film of polyRuOH_2^{2+} is visible on top of the $n\text{TiO}_2$ substrate. Film formation presumably inhibits electrolyte and complex diffusion into the pores of the mesoporous oxide, inhibiting further internal polymerization (Figure 8.7). Energy-dispersive X-ray spectroscopy (EDS) was used to determine the concentration of Ru at varying depths following 450 reductive scans (Figure G.3). These results suggest a relatively uniform concentration of Ru throughout the $n\text{TiO}_2$ substrate.

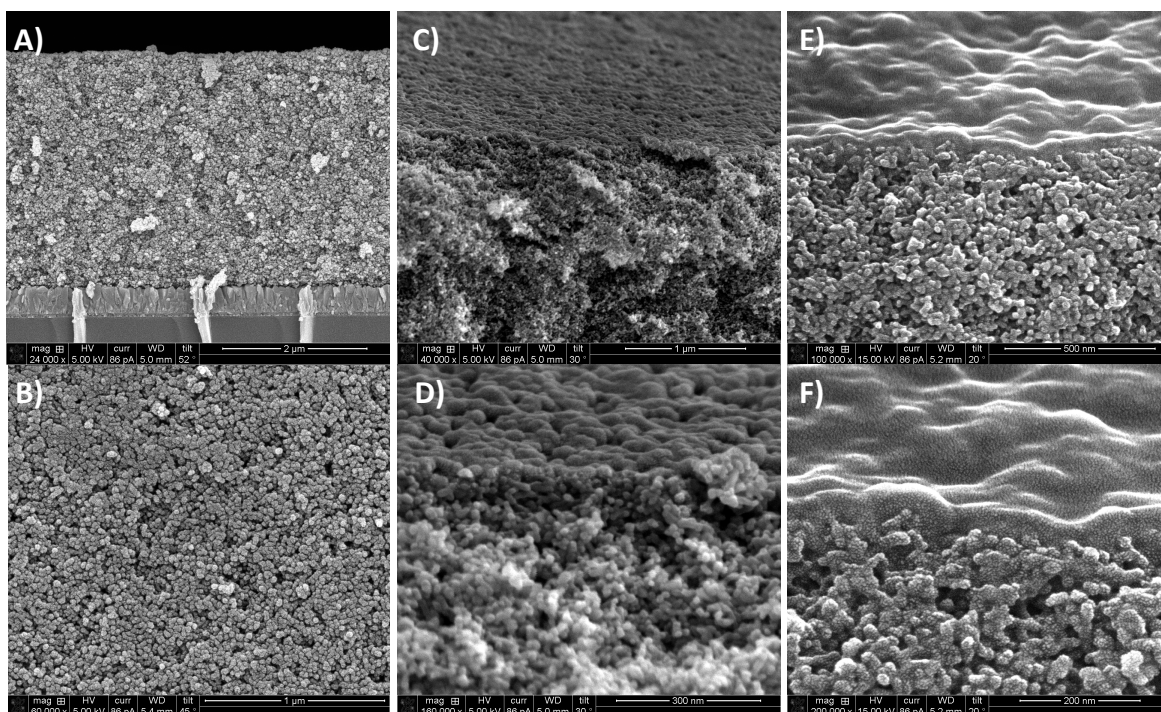


Figure 8.9. Cross-sectional SEM images of the $n\text{TiO}_2\text{-RuPdvb}^{2+}$ films following 60 (A and B), 120 (C and D), and 450 (E and F) reductive cycles in a PC solution containing 0.5 mM RuOH_2^{2+} .

The photostability of the $n\text{TiO}_2\text{-RuPdvb}^{2+}\text{-polyRuOH}_2^{2+}$ films was evaluated by a previously published procedure in which the derivatized electrodes were subjected to

constant irradiation at 455 nm (FWHM ~ 30 nm, 475 mW/cm^2 , ~ 135 suns at 455 nm).¹⁴⁶ Absorption spectra (360 – 800 nm) of the films were obtained every 15 min over 16 h of irradiation. Results for 1:1 $n\text{TiO}_2\text{-RuPdvb}^{2+}\text{-polyRuOH}_2^{2+}$ in aqueous 0.1 M HClO_4 demonstrate significant enhancements in surface stability compared to $n\text{TiO}_2\text{-RuP}^{2+}$ ($\text{RuP}^{2+} = \text{Ru}(\text{bpy})_2((\text{PO}_3\text{H}_2)_2\text{bpy})]^{2+}$, Figure 8.10). Following 16 h of irradiation, the surface coverage of chromophore in $n\text{TiO}_2\text{-RuP}^{2+}$ decreased by $\sim 70\%$ while only $\sim 10\%$ was lost for $n\text{TiO}_2\text{-RuPdvb}^{2+}\text{-polyRuOH}_2^{2+}$ (Figure 8.11). A 15-fold enhancement of stability was observed for $n\text{TiO}_2\text{-RuPdvb}^{2+}\text{-polyRuOH}_2^{2+}$ films ($k_{\text{des}} = 2.8 \times 10^{-5} \text{ s}^{-1}$; k_{des} is the rate constant for loss of the chromophore from the surface) compared to $n\text{TiO}_2\text{-RuP}^{2+}$ ($k_{\text{des}} > 30 \times 10^{-5} \text{ s}^{-1}$) at pH 4.7 (0.1 M NaOAc/HOAc and 0.5 M NaClO_4), Figure 8.12.^{141,146,148}

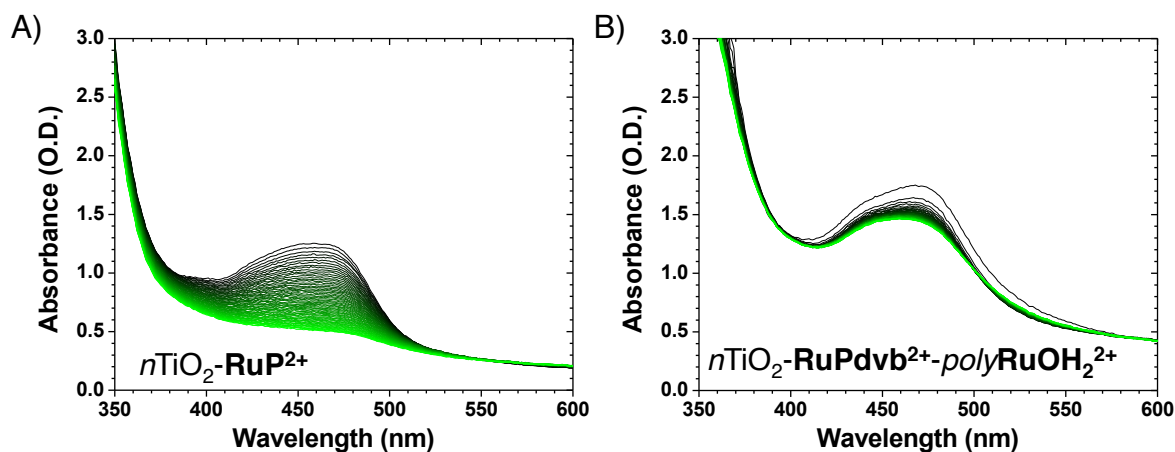


Figure 8.10. Changes in the absorption spectrum of $n\text{TiO}_2\text{-RuP}$ (A) and $n\text{TiO}_2\text{-RuPdvb}^{2+}\text{-polyRuOH}_2^{2+}$ following 70 reductive cycles (B, 1:1 chromophore:catalyst) in aqueous 0.1 M HClO_4 under constant 455 nm irradiation (475 mW/cm^2) from 0 h (green) to 16 h (black) recorded every 15 min.

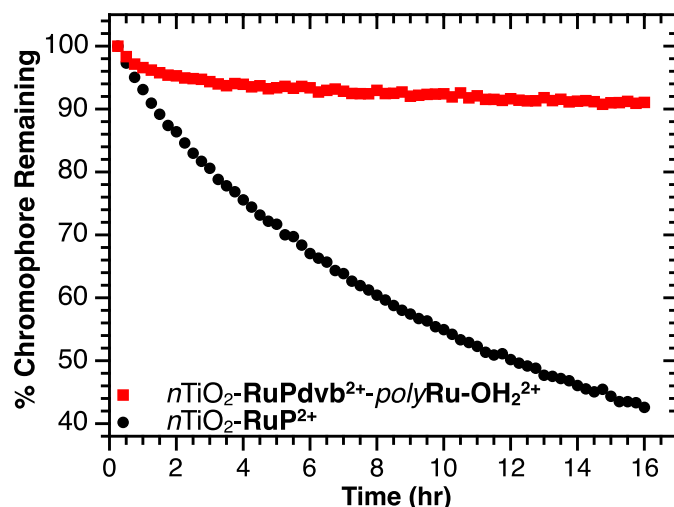


Figure 8.11. Variation of surface coverage as a function of irradiation time at 475 mW/cm^2 at 455 nm over a 16 hr photolysis period in aqueous 0.1 M HClO_4 . Loss from the surfaces was monitored by absorbance changes at 453 nm ($\epsilon_{453} = 13,500 \text{ M}^{-1} \text{ cm}^{-1}$) which were also corrected for the TiO_2 scatter.

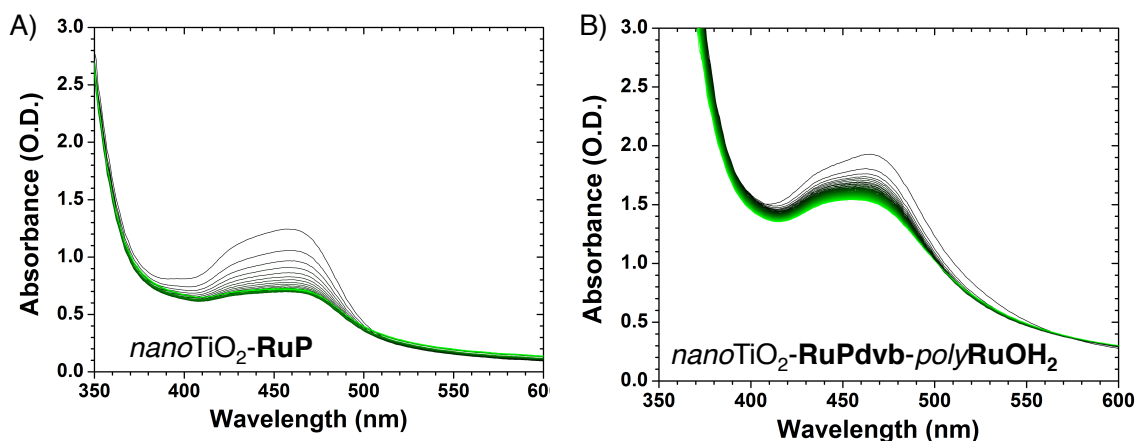


Figure 8.12. Changes in the absorption spectrum of $n\text{TiO}_2\text{-RuP}$ (A) and $n\text{TiO}_2\text{-RuPd vb}^{2+}\text{-polyRuOH}_2^{2+}$ following 70 reductive cycles (B, 1:1 chromophore:catalyst) in pH 4.7 aqueous solution (0.1 M HOAc/OAc , 0.5 M NaClO_4) under constant 455 nm irradiation (475 mW/cm^2) from 0 h (green) to 16 h (black) recorded every 15 min.

Electrocatalytic water oxidation was investigated on $n\text{ITO-RuPd vb}^{2+}\text{-polyRuOH}_2^{2+}$ by CV measurements. At pH 4.7 (0.1 M NaOAc/HOAc , 0.5 M NaClO_4) oxidative waves appear at $E_{1/2} = 0.75 \text{ V}$ and 1.02 V (vs. NHE) for the $-(\text{Ru}^{\text{II}})^{2+}\text{-(Ru}^{\text{III}}\text{-OH)}^{2+}/-(\text{Ru}^{\text{II}})^{2+}\text{-(Ru}^{\text{II}}\text{-OH}_2)^{2+}$ and $-(\text{Ru}^{\text{II}})^{2+}\text{-(Ru}^{\text{IV}}\text{=O)}^{2+}/-(\text{Ru}^{\text{II}})^{2+}\text{-(Ru}^{\text{III}}\text{-OH)}^{2+}$ couples, respectively (Figure 8.13). An additional wave appears at $E_{1/2} = 1.38 \text{ V}$ for the $-(\text{Ru}^{\text{III}})^{3+}\text{-(Ru}^{\text{IV}}\text{=O)}^{2+}/-$

$(\text{Ru}^{\text{II}})^{2+}-\text{(Ru}^{\text{IV}}=\text{O})^{2+}$ redox couple. Spectroelectrochemical measurements on *n*ITO-**RuPdvb**²⁺-*polyRuOH*₂²⁺ in aqueous 0.1 M HClO₄ are consistent with the loss of MLCT absorptions in the visible and with other characteristic spectral changes following oxidation of $-(\text{Ru}^{\text{II}})^{2+}-\text{(Ru}^{\text{II}}-\text{OH}_2)^{2+}$ to $-(\text{Ru}^{\text{II}})^{2+}-\text{(Ru}^{\text{III}}-\text{OH}_2)^{3+}$, $-(\text{Ru}^{\text{II}})^{2+}-\text{(Ru}^{\text{III}}-\text{OH}_2)^{3+}$ to $-(\text{Ru}^{\text{II}})^{2+}-\text{(Ru}^{\text{IV}}=\text{O})^{2+}$, and $-(\text{Ru}^{\text{II}})^{2+}-\text{(Ru}^{\text{IV}}=\text{O})^{2+}$ to $-(\text{Ru}^{\text{III}})^{3+}-\text{(Ru}^{\text{IV}}=\text{O})^{2+}$ (Figure G.4).

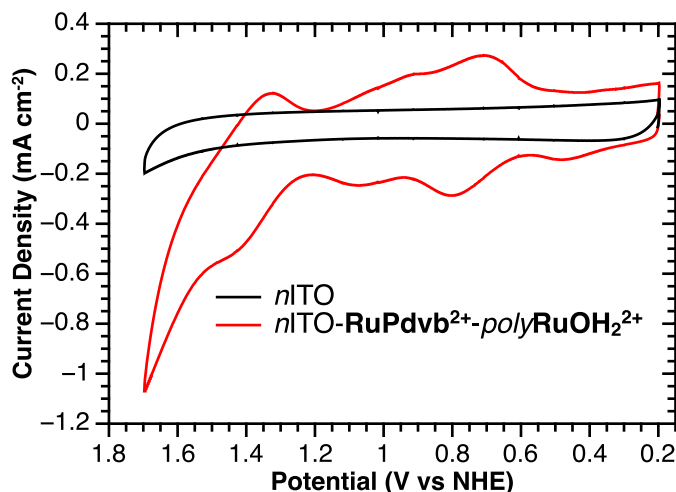


Figure 8.13. Cyclic voltammograms at 20 mV/s for *nano*ITO-**RuPdvb**²⁺-*polyRuOH*₂²⁺ (red) and *n*ITO (black) in pH 4.7 aqueous solution (0.1 M NaOAc/HOAc, 0.5 M NaClO₄); Pt-mesh counter electrode and Ag/AgCl reference electrode, 0.197 V vs. NHE.

Rate constants for water oxidation (k_{obs}) at 1.7 V (vs. NHE) were evaluated at pH 4.7 (0.1 M NaOAc/HOAc, 0.5 M NaClO₄) by CV measurements with application of Equation 8.5 (see Experimental).³⁵⁸ Based on these data, $k_{\text{obs}} = 0.073 \pm 0.030 \text{ s}^{-1}$ for *n*ITO-**RuPdvb**²⁺-*polyRuOH*₂²⁺ with a 1:1 chromophore:catalyst ratio and $k_{\text{obs}} = 0.060 \pm 0.020 \text{ s}^{-1}$ for *n*TiO₂-*polyRuOH*₂²⁺ (Figure 8.14). Under the same conditions, $k_{\text{obs}} = 0.10 \pm 0.010 \text{ s}^{-1}$, for the monomeric catalyst **RuPOH**₂²⁺ on *n*ITO (Figure 8.14). This comparison suggests that the catalytic properties of the catalyst are not significantly altered in the polymer film. Similar k_{obs} were obtained on *p*FTO (Figure G.6).

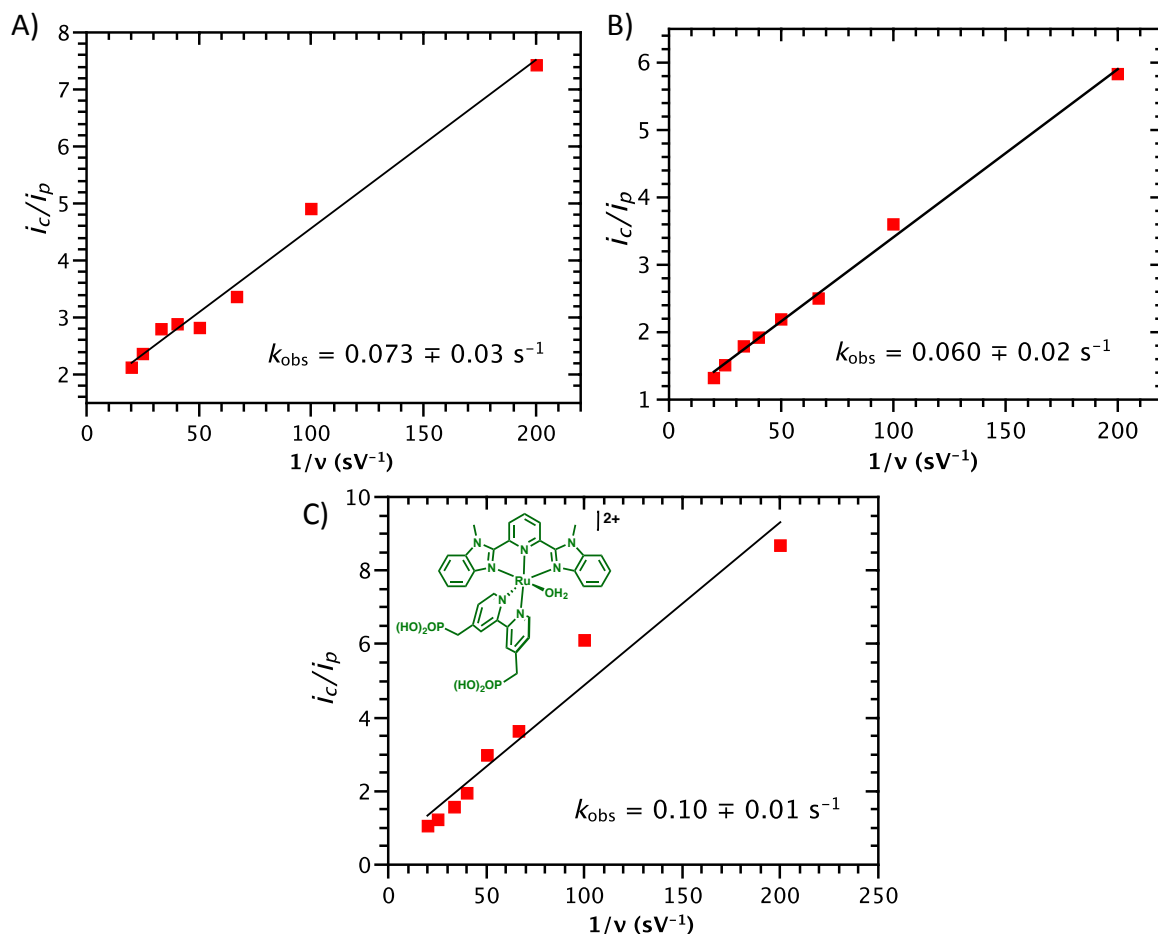


Figure 8.14. Plots of i_c/i_p (i_c is the current at 1.7 V vs NHE, i_p is the peak current for the $\text{Ru}^{\text{III}}\text{-OH}_2/\text{Ru}^{\text{II}}\text{-OH}_2$ redox couple) versus $1/v$ for (A) $n\text{ITO-RuPdvb}^{2+}\text{-polyRuOH}_2^{2+}$, (B) $n\text{ITO-polyRuOH}_2^{2+}$ and (C) $n\text{ITO-[Ru(Mebimpy)(4,4'-(PO}_3\text{H}_2\text{-CH}_2)_2\text{-bpy)(OH}_2)]^{2+}$ (RuPOH_2^{2+}) in pH 4.7 aqueous solution (0.1 M HOAc/OAc, 0.5 M NaClO_4); Pt-mesh counter electrode and Ag/AgCl reference electrode. Surface coverages for each complex were $\sim 1.1 \times 10^{-8} \text{ mol cm}^{-2}$ at 23 °C. The catalytic rate constant, k_{obs} , for water oxidation was evaluated from the slope of the each plot.

Controlled potential electrolysis of 1:1 $n\text{ITO-RuPdvb}^{2+}\text{-polyRuOH}_2^{2+}$ at 1.7 V (vs. NHE) in pH 4.7 (0.1 M NaOAc/HOAc, 0.5 M NaClO_4 , $E^\circ(\text{H}_2\text{O} \rightarrow \frac{1}{2} \text{O}_2 + 2 \text{H}^+ + 2 \text{e}^-) = 0.95 \text{ V vs. NHE}$ at pH 4.7) resulted in sustained catalytic current with no decrease over a 2-hour period (Figure 8.15). Oxygen production was quantified by gas chromatography, giving a Faradaic efficiency of 77% (Figure 8.16). During this experiment, the catalytic sites

underwent 501 turnovers with a turnover frequency of 0.046 s^{-1} (based on oxygen production), comparable to the rate constants obtained by CV measurements.

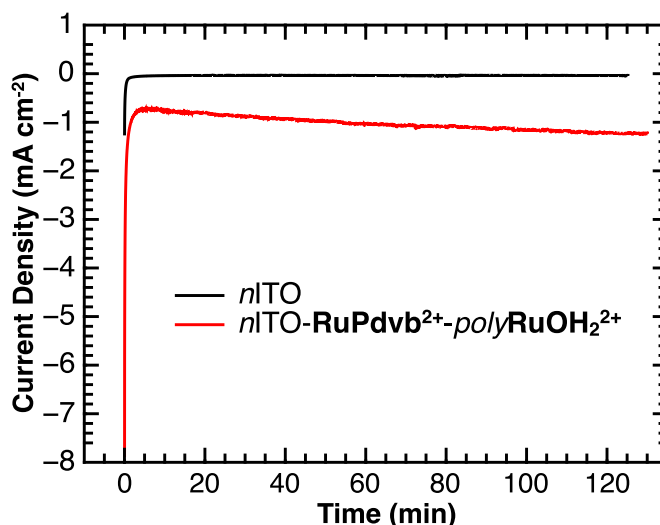


Figure 8.15. Controlled potential electrolysis on 1:1 $n\text{ITO-RuPd vb}^{2+}\text{-polyRuOH}_2^{2+}$ (red) and $n\text{ITO}$ (black) at 1.7 V (vs. NHE) in pH 4.7 aqueous solution (0.1 M NaOAc/HOAc, 0.5 M NaClO₄); Pt-mesh counter electrode and Ag/AgCl reference electrode with $\Gamma \sim 1.1 \times 10^{-8} \text{ mol cm}^{-2}$ for both complexes.

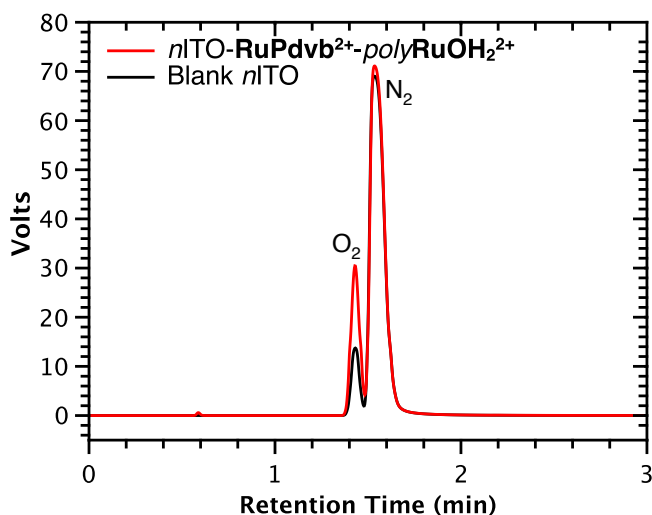


Figure 8.16. Gas chromatographs of headspace following electrolysis of blank $n\text{ITO}$ (black) and $n\text{ITO-RuPd vb}^{2+}\text{-polyRuOH}_2^{2+}$ (red) at 1.7 V (vs NHE) in pH 4.7 ((0.1 M HOAc/OAc, 0.5 M NaClO₄); Pt-mesh counter electrode and Ag/AgCl reference electrode. Surface coverages for both RuPd vb^{2+} and polyRuOH_2^{2+} were $\sim 1.1 \times 10^{-8} \text{ mol cm}^{-2}$.

Following a 2 h electrolysis period, neither catalyst decomposition nor desorption was observed by CV (Figure 8.17). This represents a significant stability enhancement relative to

surface-bound RuPOH_2^{2+} . These measurements reveal a chemical change for surface-bound RuPdvb^{2+} over the electrolysis period with characteristic features appearing in the CVs for a surface-bound analog of $\text{cis-[Ru(bpy)}_2\text{(OH)}_2\text{)]}^{2+}$.³⁵⁰ Its appearance and activity toward water oxidation catalysis may account for the increase in the magnitude of the catalytic current over time observed during electrolysis (Figure 8.16).

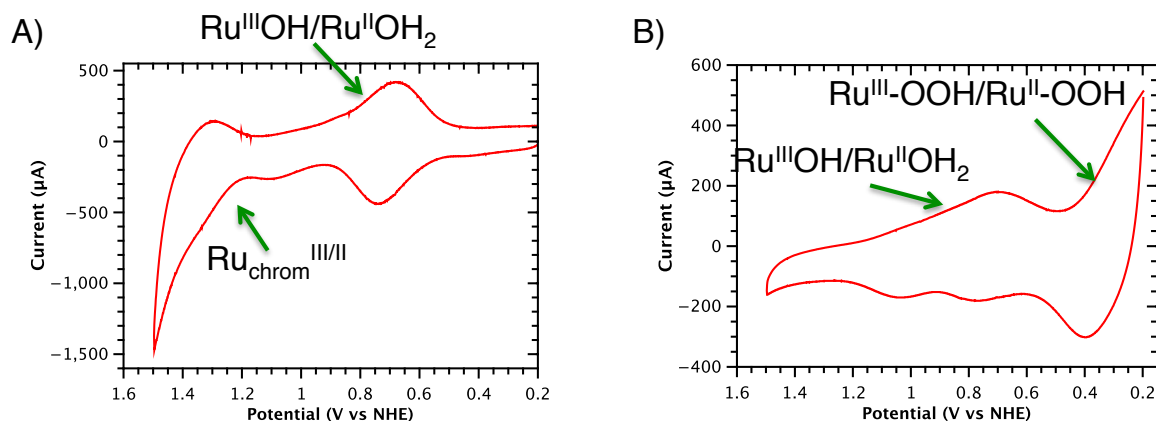


Figure 8.17. Cyclic voltammograms of $n\text{ITO-RuPdvb}^{2+}\text{-polyRuOH}_2^{2+}$ pre (A) and post 2 hr (B) electrolysis at 1.7 V (vs NHE) in pH 4.7 ((0.1 M HOAc/OAc, 0.5 M NaClO₄); Pt-mesh counter electrode and Ag/AgCl reference electrode). Surface coverages for both RuPdvb^{2+} and polyRuOH_2^{2+} were $\sim 1.1 \times 10^{-8} \text{ mol cm}^{-2}$ pre electrolysis. As noted in the figure, the new waves below 0.4 V are due to a peroxide intermediate in the overall water oxidation cycle. The surface coverage post electrolysis (Figure S17(B)) for polyRuOH_2^{2+} was calculated as the sum of the integrated charge under the $\text{Ru}^{\text{III}}\text{-OH}/\text{Ru}^{\text{II}}\text{-OH}_2$ and $\text{Ru}^{\text{III}}\text{-OOH}/\text{Ru}^{\text{II}}\text{-OOH}$ waves. The latter is known as a surface-bound intermediate in the water oxidation cycle for the RuPOH_2^{2+} catalyst.^{35,149,360,361}

Our results are important in describing a general strategy for preparing spatially controlled, multi-component films and bilayers containing both light harvesting chromophores and water oxidation catalysts on planar and mesoporous nanoparticle metal oxide films. The procedure is general with reductive electropolymerization/assembly formation successfully demonstrated on $p\text{FTO}$, $n\text{TiO}_2$, and $n\text{ITO}$ and on these surfaces derivatized with RuPdvb^{2+} . The chromophore:catalyst ratio in the films can be controlled by the number of reductive CVs scan cycles. The PCET character of the RuOH_2^{2+} sites in the

surface structures is maintained and, on *p*FTO, is independent of film thickness up to 33 layers. Importantly, reactivity toward water oxidation is maintained in both *polyRuOH*₂²⁺ films and **RuPd**vb**²⁺-*polyRuOH*₂²⁺ bilayers on *p*FTO and *n*ITO with sustained water oxidation catalysis occurring over a 2-hour electrolysis period with a Faradaic efficiency of 77% with individual catalyst sites undergoing 501 turnovers and a TOF = 0.046 s⁻¹.**

8.4 Associated Content

Appendix G: EDS analysis, UV/Vis absorption spectra, and electrochemical characterization is available in Appendix G.

8.5 Acknowledgments

This research was supported solely by the UNC EFRC Center for Solar Fuels, an Energy Frontier Research Center funded by the U.S. Department of Energy, Office of Science, Office of Basic Energy Sciences, under Award No. DE-SC0001011, supporting A.K.V., K.H., and D.P.H. D.L.A. acknowledges support from the Department of Energy Office of Science Graduate Fellowship Program under Contract No. DE-AC05-06OR23100. A.M.L. acknowledges Government support under FA9550-11-C-0028 and awarded by the DOD, AFOSR, NDSEG Fellowship, 32 CFR 168a.

APPENDIX A. CONTROLLING GROUND AND EXCITED STATE PROPERTIES
THROUGH LIGAND CHANGES IN RUTHENIUM POLYPYRIDYL
COMPLEXES

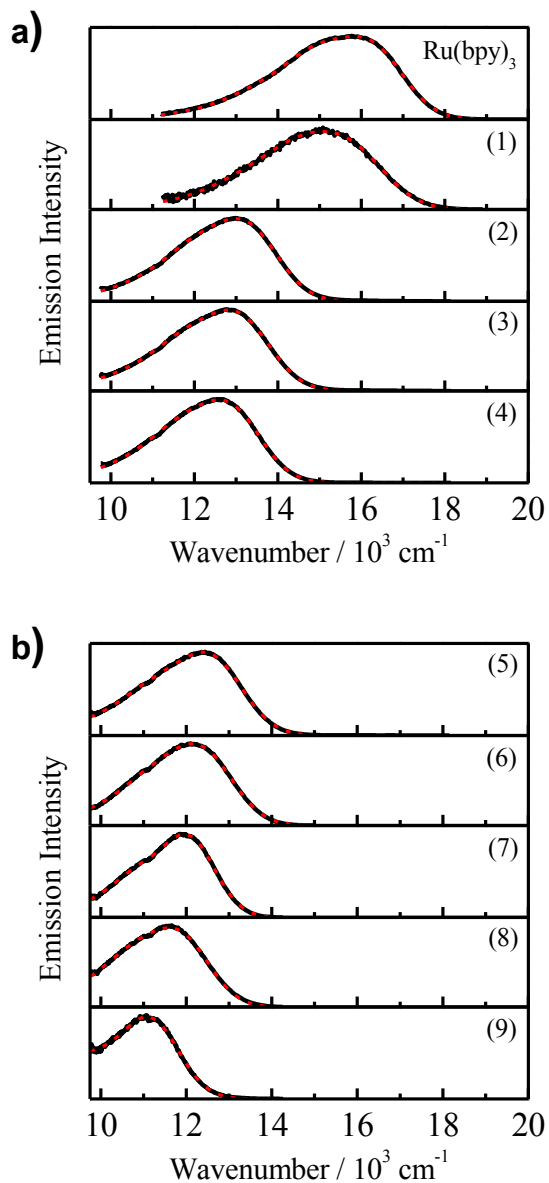


Figure A.1. Corrected (black) and calculated (red) emission spectra from spectral fitting of Ru(bpy)₃²⁺ and 1-9

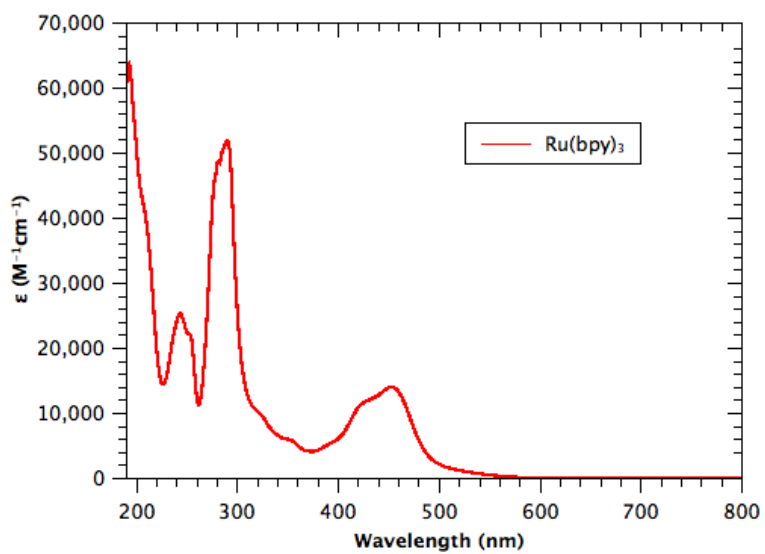


Figure A.2. Absorption spectrum of Ru(bpy)₃²⁺ in CH₃CN at 25°C.

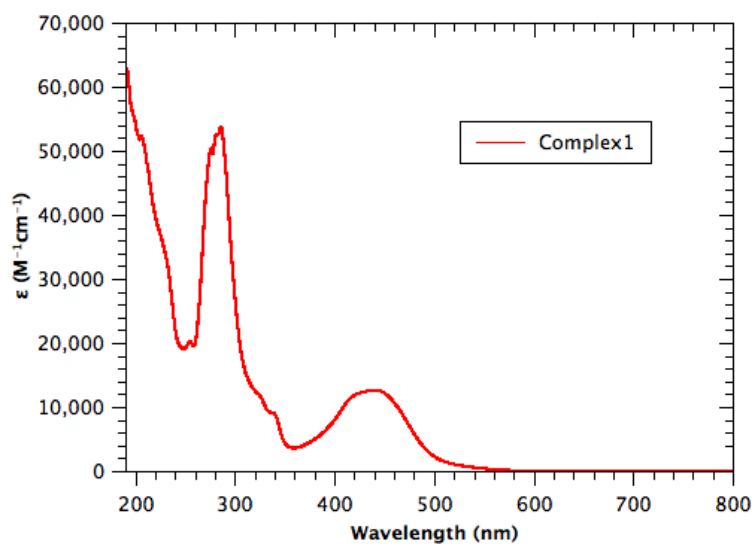


Figure A.3. Absorption spectrum of 1 in CH₃CN at 25°C.

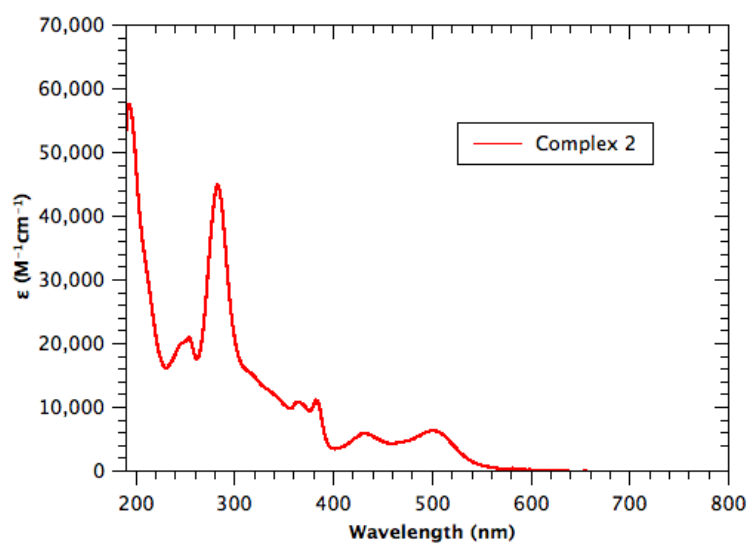


Figure A.4. Absorption spectrum of **2** in CH₃CN at 25°C.

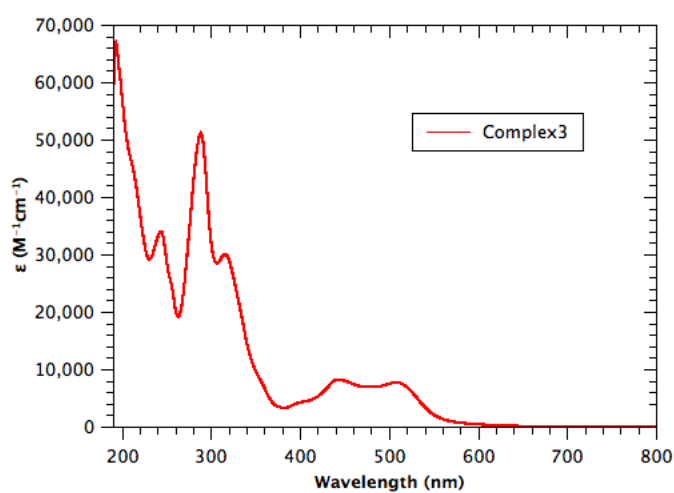


Figure A.5. Absorption spectrum of **3** in CH₃CN at 25°C.

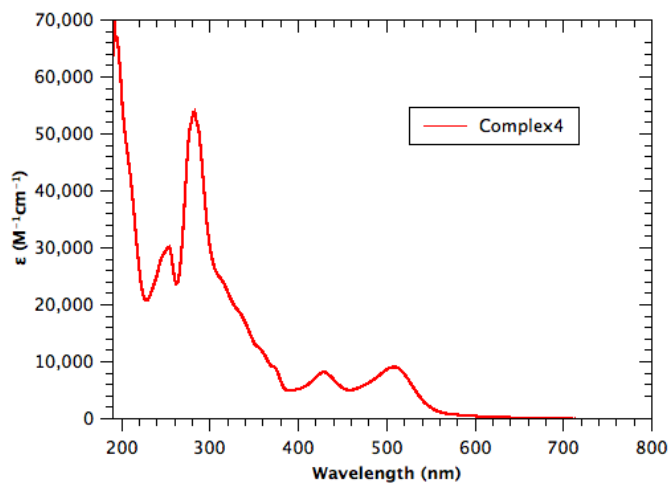


Figure A.6. Absorption spectrum of **4** in CH₃CN at 25°C.

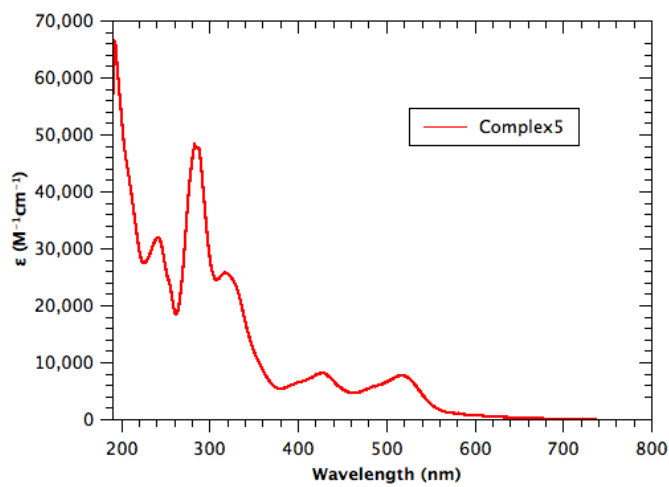


Figure A.7. Absorption spectrum of **5** in CH₃CN at 25°C.

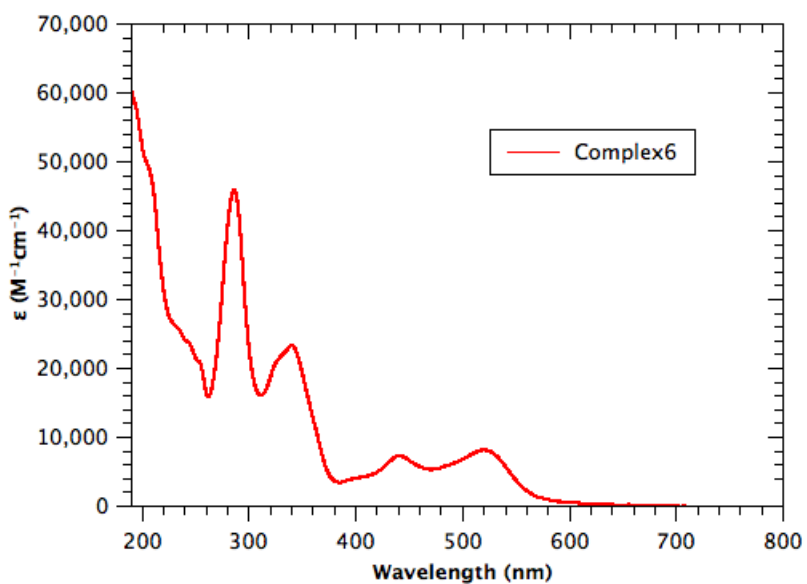


Figure A.8. Absorption spectrum of **6** in CH_3CN at $25^\circ C$.

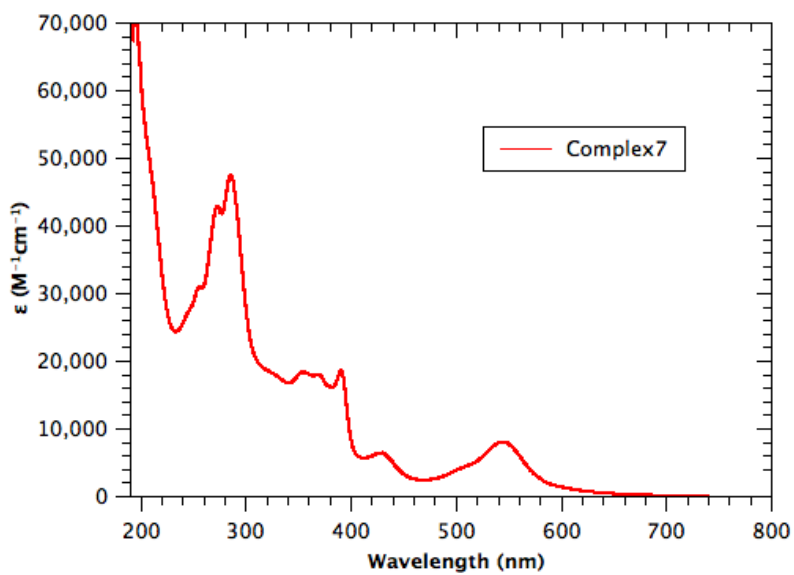
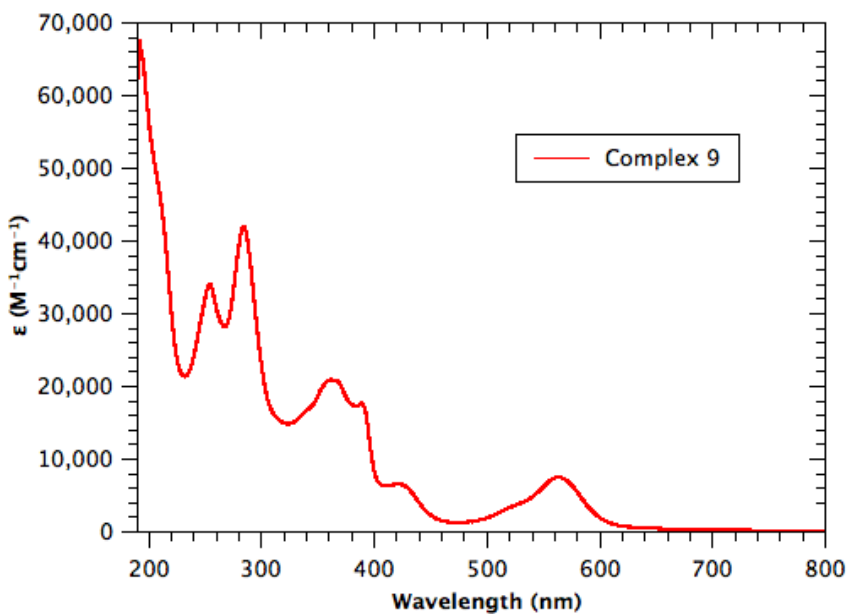
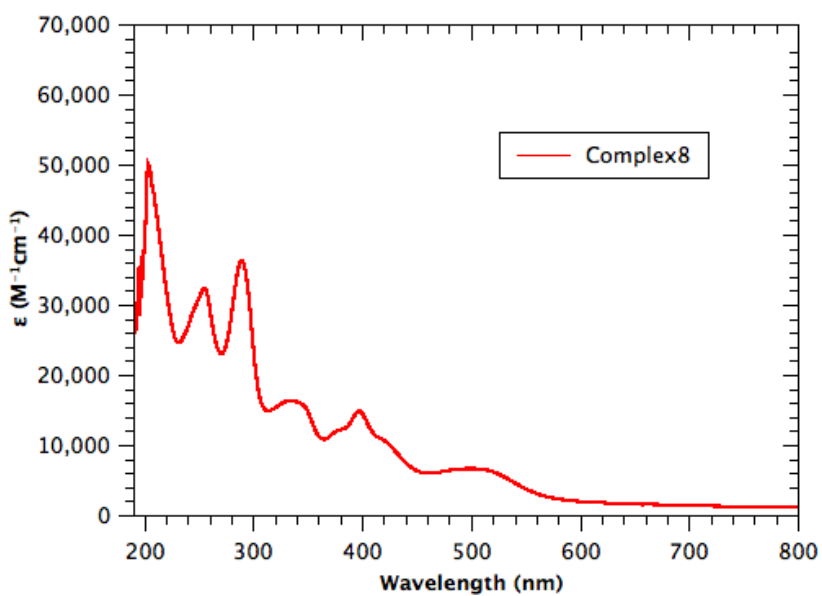


Figure A.9. Absorption spectrum of **7** in CH_3CN at $25^\circ C$.



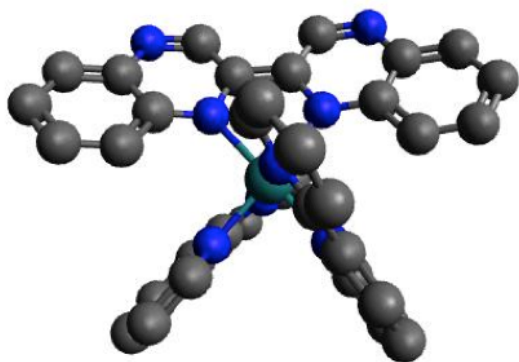


Figure A.12. Calculated geometry of complex 8.

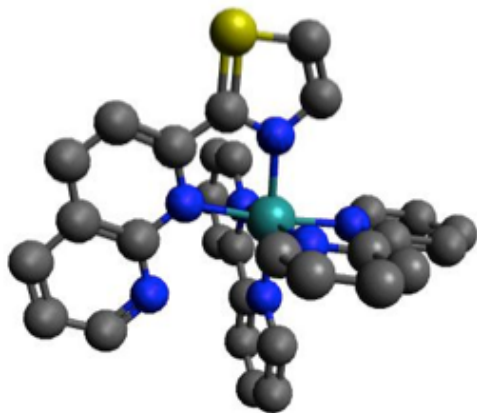


Figure A.13. Calculated geometry of complex 6.

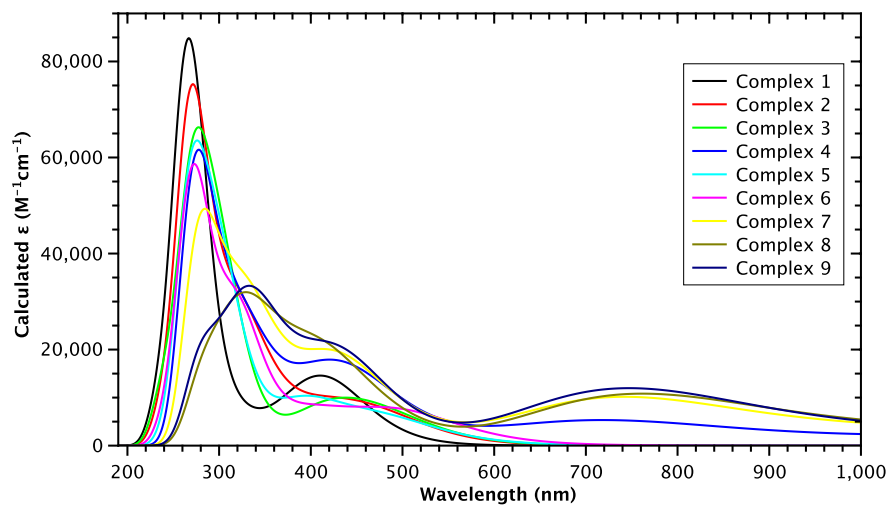


Figure A.14. Calculated electronic spectra of complexes 1-9.

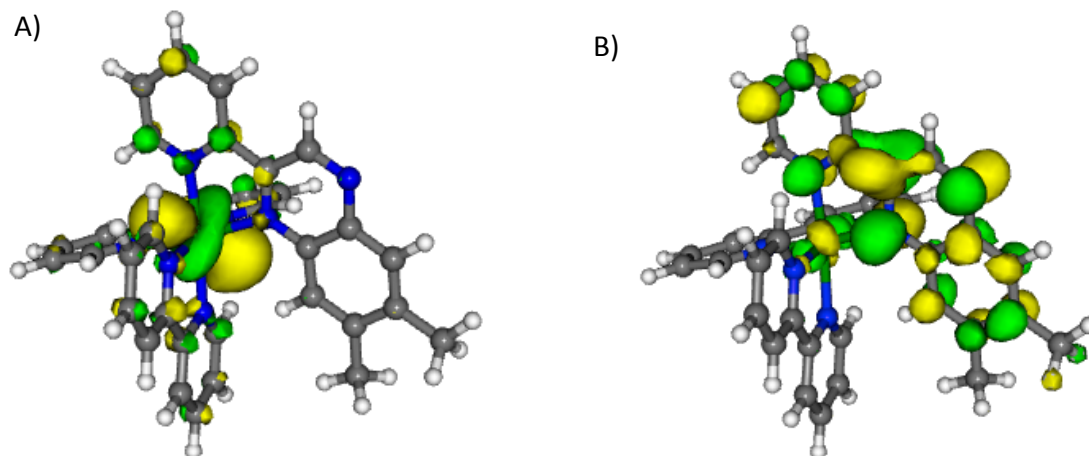


Figure A.15. Calculated orbitals for the Ru $d\pi \rightarrow \pi^*$ (N-N) transition in complex **2**. A) The Ru $d\pi$ orbital. B) π^* orbital on the N-N ligands. Orbitals are plotted with MOLEKEN.

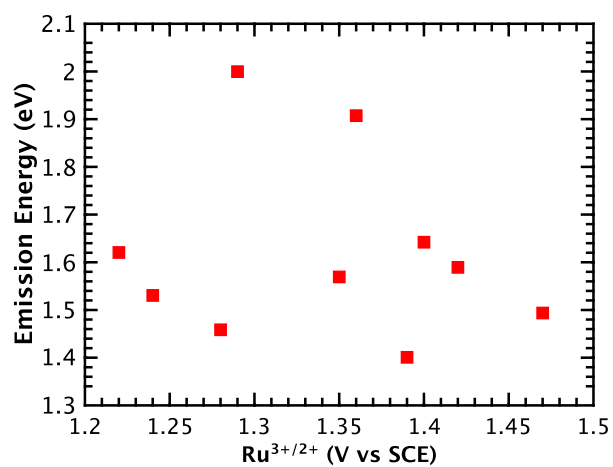


Figure A.16. Dependence of emission energy on the ground state oxidation potential (Ru^{3+/2+}).

Crystal Submitted by:

Dennis Ashford

Crystal Submitted on:

2011-02-18

Data Collected on:

2011-02-21

Structure Solved by:

Peter S White

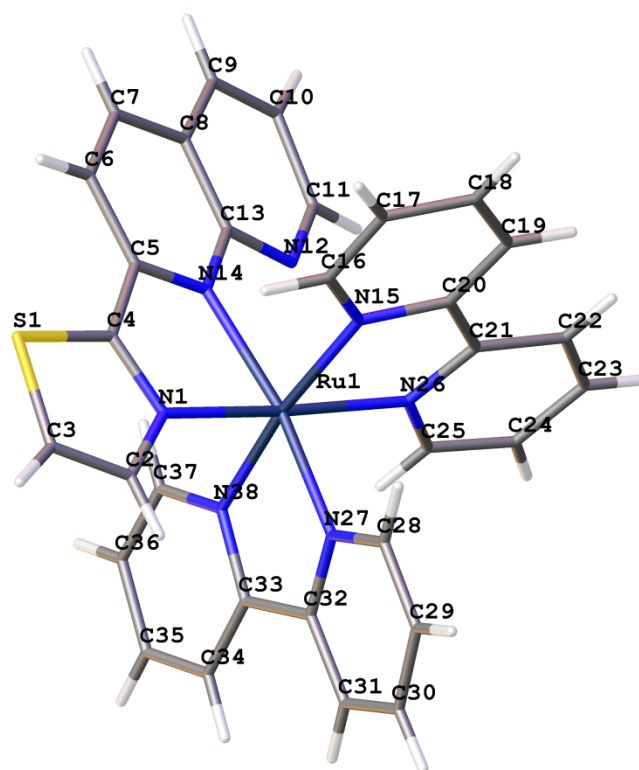


Table A.1. Crystal data and structure analysis for x1102017

Identification code	x1102017
Empirical formula	$C_{33}H_{26}Cl_2N_8O_8RuS$
Formula weight	866.65
Temperature/K	100.0
Crystal system	triclinic
Space group	P-1
a/Å, b/Å, c/Å	9.1095(2), 12.6614(3), 17.4806(4)
$\alpha/^\circ$, $\beta/^\circ$, $\gamma/^\circ$	70.210(2), 79.219(2), 76.201(2)
Volume/Å ³	1829.86(7)
Z	2
$\rho_{\text{calc}}/\text{mg mm}^{-3}$	1.573
m/mm ⁻¹	5.875
F(000)	876
Crystal size/mm ³	0.211 × 0.106 × 0.047
2 Θ range for data collection	5.4 to 132.8°

Index ranges	-10 ≤ h ≤ 10, -13 ≤ k ≤ 15, 0 ≤ l ≤ 20
Reflections collected	14241
Independent reflections	5940[R(int) = 0.0535]
Data/restraints/parameters	5940/0/479
Goodness-of-fit on F ²	1.054
Final R indexes [I > 2σ (I)]	R ₁ = 0.0456, wR ₂ = 0.1089
Final R indexes [all data]	R ₁ = 0.0541, wR ₂ = 0.1122
Largest diff. peak/hole/e Å ⁻³	1.358/-0.501

Fractional Atomic Coordinates ($\times 10^4$) and Equivalent Isotropic Displacement Parameters ($\text{\AA}^2 \times 10^3$) for x1102017. U_{eq} is defined as 1/3 of the trace of the orthogonalised U_{ij} tensor.

Atom	x	y	z	U(eq)
Ru1	4920.3(3)	3080.4(3)	7525.6(2)	20.42(12)
S1	2683.7(13))	5693.4(10)	5420.6(7)	32.9(3)
N1	4051(4)	3928(3)	6428(2)	25.7(8)
C2	3846(5)	3584(4)	5806(3)	28.9(10)
C3	3121(5)	4423(4)	5205(3)	33.6(10)

C4	3513(5)	5023(4)	6316(3)	27.9(9)
C5	3700(5)	5532(4)	6906(3)	26.1(9)
C6	3025(5)	6671(4)	6878(3)	31(1)
C7	3299(5)	7077(4)	7450(3)	31.7(10)
C8	4286(5)	6390(4)	8042(3)	26.8(9)
C9	4663(5)	6753(4)	8632(3)	31.6(10)
C10	5658(5)	6046(4)	9149(3)	31.4(10)
C11	6281(5)	4946(4)	9074(3)	29.9(10)
N12	5919(4)	4543(3)	8548(2)	25.3(8)
C13	4916(5)	5255(4)	8030(3)	26.5(9)
N14	4555(4)	4815(3)	7489(2)	24.8(8)
N15	2823(4)	3010(3)	8230(2)	23.7(7)
C16	1454(5)	3488(4)	7957(3)	26.0(9)
C17	100(5)	3425(4)	8465(3)	28.6(9)
C18	138(5)	2832(4)	9286(3)	29.2(10)
C19	1541(5)	2328(4)	9577(3)	28.3(9)

C20	2864(5)	2443(3)	9042(3)	23.0(9)
C21	4392(5)	1994(3)	9297(3)	24.7(9)
C22	4673(5)	1378(4)	10098(3)	27.1(9)
C23	6168(5)	958(3)	10279(3)	24.6(9)
C24	7334(5)	1167(3)	9648(3)	24.8(9)
C25	6983(5)	1790(4)	8868(3)	25.2(9)
N26	5553(4)	2207(3)	8688(2)	21.2(7)
N27	5242(4)	1526(3)	7346(2)	22.5(7)
C28	4169(5)	876(4)	7526(3)	27.0(9)
C29	4481(6)	-170(4)	7400(3)	32.5(10)
C30	5933(6)	-596(4)	7101(3)	38.1(11)
C31	7035(5)	60(4)	6908(3)	31.9(10)
C32	6648(5)	1133(4)	7018(3)	25.7(9)
C33	7684(5)	1950(4)	6765(3)	23.5(9)
C34	9149(5)	1773(4)	6358(3)	32(1)
C35	10002(5)	2604(4)	6138(3)	30.6(10)

C36	9409(5)	3615(4)	6312(3)	29.7(10)
C37	7955(5)	3767(4)	6717(3)	25.8(9)
N38	7093(4)	2949(3)	6942(2)	21.6(7)
CI41	8707.5(12))	6747.8(9)	6449.6(7)	30.5(2)
O42	7266(5)	6764(4)	6901(4)	75.0(16)
O43	8655(6)	6558(4)	5697(3)	62.9(12)
O44	9766(5)	5807(3)	6902(3)	48(1)
O45	9202(5)	7788(3)	6289(3)	59.3(12)
CI46	364.1(12)	-468.9(9)	8293.4(7)	30.3(2)
O47	1238(4)	-1448(3)	8838(2)	38.9(8)
O48	844(4)	-488(3)	7467(2)	46.7(9)
O49	601(4)	563(3)	8374(3)	56.1(11)
O50	-1219(4)	-528(3)	8490(2)	35.3(7)
N51	1911(5)	5028(4)	9419(3)	44.1(11)
C52	935(6)	5636(5)	9079(3)	39.4(12)
C53	-316(6)	6412(5)	8648(4)	43.8(13)

Table A.2. Anisotropic Displacement Parameters ($\text{\AA}^2 \times 10^3$) for x1102017. The Anisotropic displacement factor exponent takes the form: $2\pi^2 [h^2 a^{*2} U_{11} + \dots + 2hka \times b \times U_{12}]$

Atom	U_{11}	U_{22}	U_{33}	U_{23}	U_{13}	U_{12}
Ru1	18.83(17)	19.76(17)	21.27(19)	-5.43(13)	-2.28(12)	-2.39(11)
S1	31.6(6)	35.7(6)	27.9(6)	-2.1(5)	-10.1(5)	-6.1(5)
N1	17.8(16)	32.3(19)	27(2)	-8.2(17)	-3.5(14)	-5.4(14)
C2	24(2)	34(2)	29(3)	-9(2)	-1.1(18)	-8.3(18)
C3	29(2)	46(3)	25(3)	-9(2)	-1.9(19)	-10(2)
C4	22(2)	28(2)	28(3)	-0.9(19)	-5.7(18)	-2.6(17)
C5	20(2)	24(2)	30(3)	-0.4(19)	-3.4(17)	-6.4(17)
C6	28(2)	22(2)	39(3)	-5(2)	-7(2)	-1.7(18)
C7	32(2)	24(2)	40(3)	-12(2)	-4(2)	-4.4(18)
C8	20(2)	22(2)	33(3)	-5.3(19)	4.8(18)	-6.3(16)
C9	29(2)	26(2)	40(3)	-11(2)	0(2)	-6.3(18)
C10	32(2)	32(2)	35(3)	-17(2)	-2(2)	-7.5(19)
C11	28(2)	33(2)	31(3)	-12(2)	-5.5(19)	-4.3(19)

N12	25.5(18)	24.6(17)	26(2)	-7.7(16)	-5.0(15)	-4.4(15)
C13	24(2)	28(2)	29(3)	-11(2)	2.5(18)	-8.6(18)
N14	24.5(18)	24.3(17)	25(2)	-4.5(16)	-1.3(15)	-9.6(14)
N15	24.6(18)	20.1(16)	28(2)	-10.7(16)	1.7(15)	-5.3(14)
C16	23(2)	28(2)	28(2)	-9.9(19)	-4.8(18)	-2.5(17)
C17	23(2)	31(2)	31(3)	-9(2)	-2.1(18)	-4.7(18)
C18	26(2)	30(2)	33(3)	-11(2)	1.6(19)	-9.7(18)
C19	29(2)	29(2)	30(3)	-13(2)	-4.1(19)	-6.8(18)
C20	26(2)	18.8(19)	27(2)	-10.1(18)	-3.2(17)	-5.1(16)
C21	27(2)	19.1(19)	32(3)	-13.6(19)	-4.4(18)	-3.2(17)
C22	32(2)	26(2)	26(2)	-10.1(19)	-5.9(18)	-6.4(18)
C23	31(2)	19.9(19)	25(2)	-7.1(18)	-9.5(18)	-4.0(17)
C24	26(2)	21(2)	31(2)	-10.1(18)	-7.2(18)	-3.4(17)
C25	26(2)	24(2)	28(2)	-9.6(19)	-4.2(18)	-7.8(17)
N26	21.2(17)	20.0(16)	22.8(19)	-8.0(15)	-3.7(14)	-1.6(13)
N27	26.0(18)	21.6(17)	16.9(19)	-1.9(15)	-2.4(14)	-4.8(14)

C28	29(2)	30(2)	21(2)	-4.3(19)	-1.5(18)	-7.7(18)
C29	38(3)	29(2)	34(3)	-11(2)	1(2)	-15(2)
C30	51(3)	30(2)	35(3)	-15(2)	3(2)	-11(2)
C31	32(2)	33(2)	30(3)	-12(2)	2.9(19)	-7(2)
C32	31(2)	23(2)	21(2)	-5.4(18)	-6.6(18)	-1.1(18)
C33	22(2)	26(2)	20(2)	-4.4(18)	-6.3(17)	-1.0(17)
C34	29(2)	32(2)	34(3)	-14(2)	-8(2)	5.6(19)
C35	17(2)	40(3)	32(3)	-10(2)	-0.8(18)	-4.1(18)
C36	27(2)	36(2)	25(2)	-5(2)	-4.1(18)	-9.3(19)
C37	24(2)	26(2)	25(2)	-6.4(19)	-3.7(17)	-1.4(17)
N38	20.6(17)	21.3(17)	22.1(19)	-5.7(15)	-4.9(14)	-2.2(14)
Cl41	30.5(5)	29.2(5)	29.9(6)	-9.5(5)	-2.4(4)	-2.7(4)
O42	52(3)	50(2)	96(4)	-14(3)	28(3)	-2(2)
O43	84(3)	67(3)	46(3)	-20(2)	-22(2)	-14(2)
O44	59(2)	32.6(18)	49(2)	-13.1(18)	-21.0(19)	8.7(17)
O45	59(3)	40(2)	83(3)	-15(2)	-21(2)	-15.0(19)

Cl46	27.1(5)	31.9(5)	31.7(6)	-12.0(5)	-2.3(4)	-2.5(4)
O47	32.0(17)	48(2)	34(2)	-9.3(17)	-10.6(15)	-3.5(15)
O48	45(2)	51(2)	32(2)	-10.2(18)	-5.7(16)	11.1(17)
O49	41(2)	50(2)	87(3)	-40(2)	17(2)	-19.7(18)
O50	28.1(17)	37.9(18)	40(2)	-13.0(16)	-6.2(14)	-3.0(14)
N51	37(2)	57(3)	41(3)	-14(2)	-2(2)	-18(2)
C52	41(3)	50(3)	35(3)	-20(3)	10(2)	-27(3)
C53	46(3)	48(3)	43(3)	-17(3)	-2(2)	-17(3)

Table A.3. Bond Lengths for x1102017

Atom	Atom	Length/Å	Atom	Atom	Length/Å
Ru1	N1	2.056(4)	C21	C22	1.390(6)
Ru1	N14	2.122(3)	C21	N26	1.358(6)
Ru1	N15	2.074(4)	C22	C23	1.393(6)
Ru1	N26	2.073(4)	C23	C24	1.384(7)
Ru1	N27	2.041(3)	C24	C25	1.378(6)
Ru1	N38	2.047(4)	C25	N26	1.337(6)

S1	C3	1.714(5)	N27	C28	1.352(6)
S1	C4	1.725(5)	N27	C32	1.353(6)
N1	C2	1.358(6)	C28	C29	1.370(6)
N1	C4	1.315(6)	C29	C30	1.380(7)
C2	C3	1.356(7)	C30	C31	1.375(7)
C4	C5	1.442(7)	C31	C32	1.389(6)
C5	C6	1.414(6)	C32	C33	1.469(6)
C5	N14	1.343(6)	C33	C34	1.396(6)
C6	C7	1.353(7)	C33	N38	1.365(5)
C7	C8	1.415(7)	C34	C35	1.365(7)
C8	C9	1.386(7)	C35	C36	1.377(7)
C8	C13	1.420(6)	C36	C37	1.383(6)
C9	C10	1.346(7)	C37	N38	1.357(6)
C10	C11	1.413(6)	Cl41	O42	1.399(5)
C11	N12	1.314(6)	Cl41	O43	1.426(4)
N12	C13	1.354(6)	Cl41	O44	1.440(4)

C13	N14	1.368(6)	Cl41	O45	1.415(4)
N15	C16	1.348(6)	Cl46	O47	1.446(4)
N15	C20	1.360(6)	Cl46	O48	1.436(4)
C16	C17	1.380(6)	Cl46	O49	1.430(4)
C17	C18	1.379(7)	Cl46	O50	1.432(3)
C18	C19	1.391(7)	N51	C52	1.139(7)
C19	C20	1.384(6)	C52	C53	1.456(8)
C20	C21	1.464(6)			

Table A.4. Bond Angles for x1102017

Atom	Atom	Atom	Angle/°	Atom	Atom	Atom	Angle/°
N1	Ru1	N14	77.82(14)	C20	C19	C18	119.6(4)
N1	Ru1	N15	95.49(14)	N15	C20	C19	121.4(4)
N1	Ru1	N26	173.66(14)	N15	C20	C21	115.0(4)
N15	Ru1	N14	86.97(13)	C19	C20	C21	123.6(4)
N26	Ru1	N14	102.58(13)	C22	C21	C20	123.7(4)

N26	Ru1	N15	78.25(14)	N26	C21	C20	115.2(4)
N27	Ru1	N1	92.60(14)	N26	C21	C22	121.1(4)
N27	Ru1	N14	169.98(14)	C21	C22	C23	119.6(4)
N27	Ru1	N15	96.96(13)	C24	C23	C22	118.4(4)
N27	Ru1	N26	87.28(13)	C25	C24	C23	119.2(4)
N27	Ru1	N38	78.76(14)	N26	C25	C24	122.9(4)
N38	Ru1	N1	90.98(14)	C21	N26	Ru1	115.8(3)
N38	Ru1	N14	98.28(13)	C25	N26	Ru1	125.4(3)
N38	Ru1	N15	172.42(14)	C25	N26	C21	118.7(4)
N38	Ru1	N26	95.20(14)	C28	N27	Ru1	125.2(3)
C3	S1	C4	89.5(2)	C28	N27	C32	118.4(4)
C2	N1	Ru1	133.4(3)	C32	N27	Ru1	116.4(3)
C4	N1	Ru1	114.0(3)	N27	C28	C29	121.7(4)
C4	N1	C2	112.6(4)	C28	C29	C30	119.9(4)
C3	C2	N1	114.4(4)	C31	C30	C29	119.1(4)

C2	C3	S1	110.6(4)	C30	C31	C32	118.8(4)
N1	C4	S1	113.0(3)	N27	C32	C31	121.9(4)
N1	C4	C5	119.4(4)	N27	C32	C33	114.3(4)
C5	C4	S1	127.6(3)	C31	C32	C33	123.7(4)
C6	C5	C4	123.0(4)	C34	C33	C32	124.8(4)
N14	C5	C4	113.5(4)	N38	C33	C32	114.5(4)
N14	C5	C6	123.5(4)	N38	C33	C34	120.6(4)
C7	C6	C5	118.4(4)	C35	C34	C33	119.7(4)
C6	C7	C8	120.6(4)	C34	C35	C36	119.9(4)
C7	C8	C13	117.5(4)	C35	C36	C37	119.2(4)
C9	C8	C7	124.1(4)	N38	C37	C36	121.7(4)
C9	C8	C13	118.4(4)	C33	N38	Ru1	115.7(3)
C10	C9	C8	119.5(4)	C37	N38	Ru1	125.4(3)
C9	C10	C11	118.6(4)	C37	N38	C33	118.9(4)
N12	C11	C10	124.5(4)	O42	C141	O43	109.4(3)

C11	N12	C13	116.8(4)	O42	Cl41	O44	108.9(3)
N12	C13	C8	122.2(4)	O42	Cl41	O45	111.0(3)
N12	C13	N14	115.7(4)	O43	Cl41	O44	107.6(3)
N14	C13	C8	122.1(4)	O45	Cl41	O43	109.8(3)
C5	N14	Ru1	113.4(3)	O45	Cl41	O44	110.1(2)
C5	N14	C13	117.5(4)	O48	Cl46	O47	108.8(2)
C13	N14	Ru1	128.6(3)	O49	Cl46	O47	110.1(3)
C16	N15	Ru1	126.0(3)	O49	Cl46	O48	109.7(3)
C16	N15	C20	118.2(4)	O49	Cl46	O50	109.7(2)
C20	N15	Ru1	115.8(3)	O50	Cl46	O47	109.4(2)
N15	C16	C17	122.9(4)	O50	Cl46	O48	109.1(2)
C18	C17	C16	119.0(4)	N51	C52	C53	179.8(8)
C17	C18	C19	118.9(4)				

Table A.5. Torsion Angles for x1102017

A	B	C	D	Angle/°
----------	----------	----------	----------	----------------

Ru1	N1	C2	C3	175.6(3)
Ru1	N1	C4	S1	-176.18(19)
Ru1	N1	C4	C5	5.6(5)
Ru1	N15	C16	C17	-178.7(3)
Ru1	N15	C20	C19	-179.5(3)
Ru1	N15	C20	C21	1.5(4)
Ru1	N27	C28	C29	-178.9(3)
Ru1	N27	C32	C31	176.3(3)
Ru1	N27	C32	C33	-5.9(5)
S1	C4	C5	C6	8.7(7)
S1	C4	C5	N14	-172.3(3)
N1	Ru1	N14	C5	12.8(3)
N1	Ru1	N14	C13	-175.6(4)
N1	Ru1	N15	C16	-4.0(3)
N1	Ru1	N15	C20	177.2(3)

N1	Ru1	N26	C21	-6.8(14)
N1	Ru1	N26	C25	169.0(11)
N1	Ru1	N27	C28	-84.5(3)
N1	Ru1	N27	C32	95.3(3)
N1	Ru1	N38	C33	-95.3(3)
N1	Ru1	N38	C37	84.0(4)
N1	C2	C3	S1	0.2(5)
N1	C4	C5	C6	-173.4(4)
N1	C4	C5	N14	5.6(6)
C2	N1	C4	S1	0.8(5)
C2	N1	C4	C5	-177.4(4)
C3	S1	C4	N1	-0.6(4)
C3	S1	C4	C5	177.4(4)
C4	S1	C3	C2	0.2(4)
C4	N1	C2	C3	-0.7(6)

C4	C5	C6	C7	-178.5(4)
C4	C5	N14	Ru1	-13.6(5)
C4	C5	N14	C13	173.9(4)
C5	C6	C7	C8	2.5(7)
C6	C5	N14	Ru1	165.4(3)
C6	C5	N14	C13	-7.2(6)
C6	C7	C8	C9	177.9(5)
C6	C7	C8	C13	-2.6(7)
C7	C8	C9	C10	-177.6(5)
C7	C8	C13	N12	177.4(4)
C7	C8	C13	N14	-2.2(6)
C8	C9	C10	C11	-0.4(7)
C8	C13	N14	Ru1	-164.4(3)
C8	C13	N14	C5	6.9(6)
C9	C8	C13	N12	-3.1(7)

C9	C8	C13	N14	177.3(4)
C9	C10	C11	N12	-2.3(8)
C10	C11	N12	C13	2.1(7)
C11	N12	C13	C8	0.6(6)
C11	N12	C13	N14	-179.8(4)
N12	C13	N14	Ru1	16.0(6)
N12	C13	N14	C5	-172.7(4)
C13	C8	C9	C10	2.9(7)
N14	Ru1	N1	C2	174.1(4)
N14	Ru1	N1	C4	-9.6(3)
N14	Ru1	N15	C16	73.4(3)
N14	Ru1	N15	C20	-105.4(3)
N14	Ru1	N26	C21	86.0(3)
N14	Ru1	N26	C25	-98.2(3)
N14	Ru1	N27	C28	-101.2(8)

N14	Ru1	N27	C32	78.5(8)
N14	Ru1	N38	C33	-173.1(3)
N14	Ru1	N38	C37	6.2(4)
N14	C5	C6	C7	2.6(7)
N15	Ru1	N1	C2	-100.2(4)
N15	Ru1	N1	C4	76.1(3)
N15	Ru1	N14	C5	-83.5(3)
N15	Ru1	N14	C13	88.1(4)
N15	Ru1	N26	C21	1.9(3)
N15	Ru1	N26	C25	177.7(3)
N15	Ru1	N27	C28	11.4(4)
N15	Ru1	N27	C32	-168.9(3)
N15	Ru1	N38	C33	53.4(11)
N15	Ru1	N38	C37	-127.4(10)
N15	C16	C17	C18	-1.2(6)

N15	C20	C21	C22	-179.2(4)
N15	C20	C21	N26	0.1(5)
C16	N15	C20	C19	1.7(6)
C16	N15	C20	C21	-177.4(3)
C16	C17	C18	C19	0.8(6)
C17	C18	C19	C20	0.8(6)
C18	C19	C20	N15	-2.1(6)
C18	C19	C20	C21	176.8(4)
C19	C20	C21	C22	1.9(6)
C19	C20	C21	N26	-178.9(4)
C20	N15	C16	C17	0.0(6)
C20	C21	C22	C23	178.3(4)
C20	C21	N26	Ru1	-1.6(4)
C20	C21	N26	C25	-177.7(3)
C21	C22	C23	C24	-0.3(6)

C22	C21	N26	Ru1	177.6(3)
C22	C21	N26	C25	1.5(6)
C22	C23	C24	C25	0.8(6)
C23	C24	C25	N26	-0.1(6)
C24	C25	N26	Ru1	-176.7(3)
C24	C25	N26	C21	-1.0(6)
N26	Ru1	N1	C2	-91.6(13)
N26	Ru1	N1	C4	84.6(13)
N26	Ru1	N14	C5	-160.7(3)
N26	Ru1	N14	C13	10.9(4)
N26	Ru1	N15	C16	177.0(3)
N26	Ru1	N15	C20	-1.8(3)
N26	Ru1	N27	C28	89.2(3)
N26	Ru1	N27	C32	-91.0(3)
N26	Ru1	N38	C33	83.4(3)

N26	Ru1	N38	C37	-97.4(3)
N26	C21	C22	C23	-0.8(6)
N27	Ru1	N1	C2	-2.9(4)
N27	Ru1	N1	C4	173.3(3)
N27	Ru1	N14	C5	30.0(9)
N27	Ru1	N14	C13	-158.4(7)
N27	Ru1	N15	C16	-97.3(3)
N27	Ru1	N15	C20	83.9(3)
N27	Ru1	N26	C21	-95.8(3)
N27	Ru1	N26	C25	80.0(3)
N27	Ru1	N38	C33	-2.8(3)
N27	Ru1	N38	C37	176.5(4)
N27	C28	C29	C30	1.6(7)
N27	C32	C33	C34	-175.0(4)
N27	C32	C33	N38	3.4(5)

C28	N27	C32	C31	-3.9(6)
C28	N27	C32	C33	173.9(4)
C28	C29	C30	C31	-2.2(8)
C29	C30	C31	C32	-0.3(8)
C30	C31	C32	N27	3.4(7)
C30	C31	C32	C33	-174.2(4)
C31	C32	C33	C34	2.7(7)
C31	C32	C33	N38	-178.8(4)
C32	N27	C28	C29	1.4(6)
C32	C33	C34	C35	178.7(4)
C32	C33	N38	Ru1	0.6(5)
C32	C33	N38	C37	-178.7(4)
C33	C34	C35	C36	-0.6(7)
C34	C33	N38	Ru1	179.1(3)
C34	C33	N38	C37	-0.2(6)

C34	C35	C36	C37	0.6(7)
C35	C36	C37	N38	-0.5(7)
C36	C37	N38	Ru1	-179.0(3)
C36	C37	N38	C33	0.3(6)
N38	Ru1	N1	C2	75.9(4)
N38	Ru1	N1	C4	-107.9(3)
N38	Ru1	N14	C5	102.0(3)
N38	Ru1	N14	C13	-86.4(4)
N38	Ru1	N15	C16	-152.5(9)
N38	Ru1	N15	C20	28.7(11)
N38	Ru1	N26	C21	-174.3(3)
N38	Ru1	N26	C25	1.5(3)
N38	Ru1	N27	C28	-174.9(4)
N38	Ru1	N27	C32	4.8(3)
N38	C33	C34	C35	0.3(7)

Table A.6. Hydrogen Atom Coordinates ($\text{\AA}\times 10^4$) and Isotropic Displacement Parameters ($\text{\AA}^2\times 10^3$) for x1102017.

Atom	x	y	z	U(eq)
H2	4182	2819	5793	35
H3	2888	4321	4730	40
H6	2394	7140	6466	37
H7	2824	7830	7455	38
H9	4223	7496	8671	38
H10	5935	6281	9555	38
H11	7010	4465	9429	36
H16	1419	3884	7390	31
H17	-843	3785	8252	34
H18	-779	2769	9646	35
H19	1592	1907	10139	34
H22	3850	1244	10519	32
H23	6381	538	10823	29

H24	8366	884	9751	30
H25	7793	1929	8439	30
H28	3172	1151	7745	32
H29	3699	-601	7518	39
H30	6168	-1331	7030	46
H31	8044	-216	6704	38
H34	9551	1077	6234	38
H35	11003	2485	5865	37
H36	9991	4201	6156	36
H37	7549	4463	6841	31
H53A	-55	7172	8389	66
H53B	-1237	6464	9037	66
H53C	-500	6123	8227	66

Experimental

Single crystals of $C_{33}H_{26}Cl_2N_8O_8RuS$ [x1102017] were grown by solution diffusion of diethyl ether into a CH_3CN solution in 6. A suitable crystal was selected and placed on a 'Bruker APEX-II CCD' diffractometer. The crystal was kept at 100.15 K during data

collection. Using Olex2 [1], the structure was solved with the olex2.solve [2] structure solution program using Charge Flipping and refined with the ShelXL [3] refinement package using Least Squares minimisation.

O. V. Dolomanov, L. J. Bourhis, R. J. Gildea, J. A. K. Howard and H. Puschmann, OLEX2: a complete structure solution, refinement and analysis program. *J. Appl. Cryst.* (2009). 42, 339-341.

olex2.solve (L.J. Bourhis, O.V. Dolomanov, R.J. Gildea, J.A.K. Howard, H. Puschmann, in preparation, 2011)

SHELXL, G.M. Sheldrick, *Acta Cryst.* (2008). A64, 112-122

Crystal structure determination of [x1102017]

Crystal Data. $C_{33}H_{26}Cl_2N_8O_8RuS$, $M = 866.65$, triclinic, $a = 9.1095(2)$ Å, $b = 12.6614(3)$ Å, $c = 17.4806(4)$ Å, $\alpha = 70.210(2)^\circ$, $\beta = 79.219(2)^\circ$, $\gamma = 76.201(2)^\circ$, $U = 1829.86(7)$ Å³, $T = 100.0$, space group P-1 (no. 2), $Z = 2$, $\mu(\text{MoK}\alpha) = 5.875$, 14241 reflections measured, 5940 unique ($R_{\text{int}} = 0.0535$) which were used in all calculations. The final $wR(F_2)$ was 0.1122 (all data).

APPENDIX B. VARYING THE ELECTRONIC STRUCTURE OF SURFACE BOUND RUTHENIUM(II) POLYPYRIDYL COMPLEXES

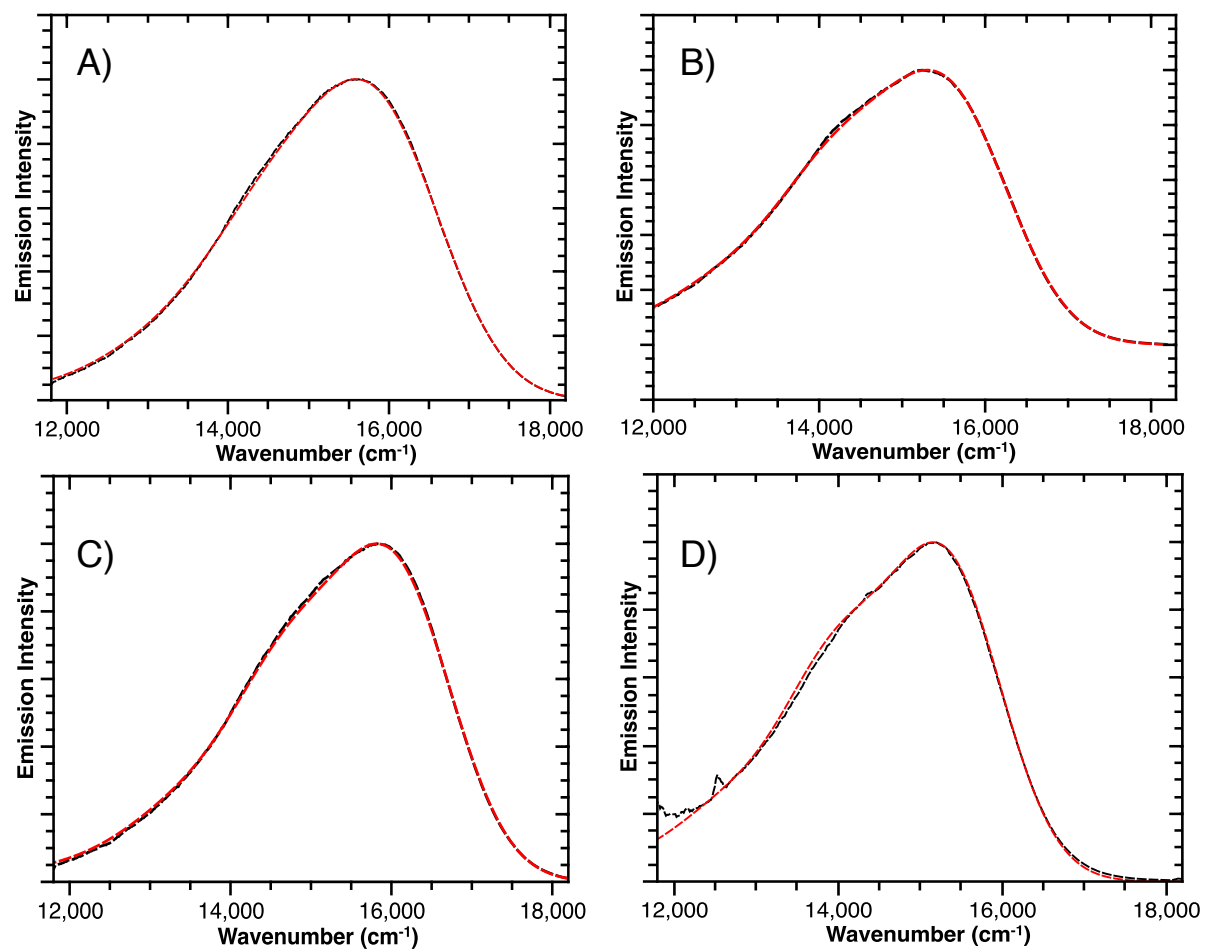


Figure B.1. Corrected (black) and calculated (red) emission spectra from spectral fitting of **RuP** (A), **RuPBr** (B), **RuPMe** (C), and **RuPOMe** (D).

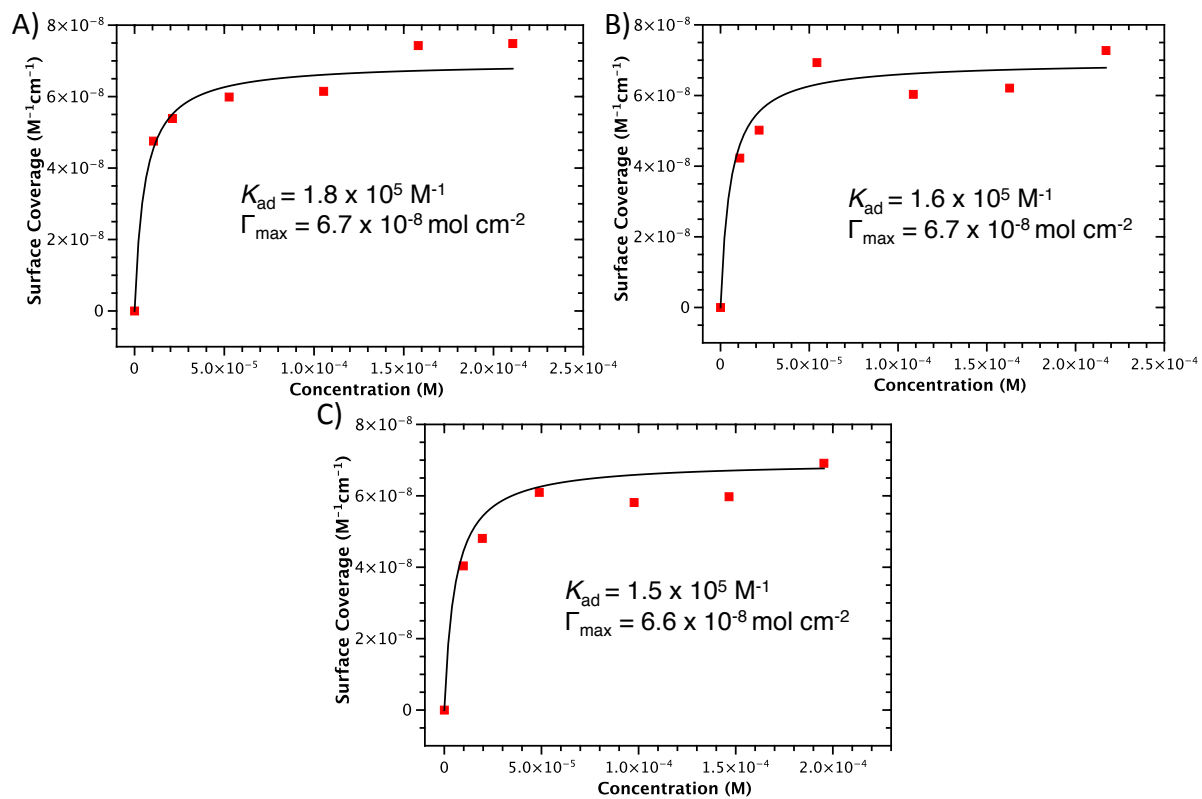


Figure B.2. Adsorption isotherms of **RuPOMe** (A), **RuPMe** (B), and **RuPBr** (C) on TiO_2 ($\sim 7 \mu m$) loaded from 10, 20, 50, 100, 150, and 200 μM solutions in methanol. The black lines are the best fits to the Langmuir isotherm equation.

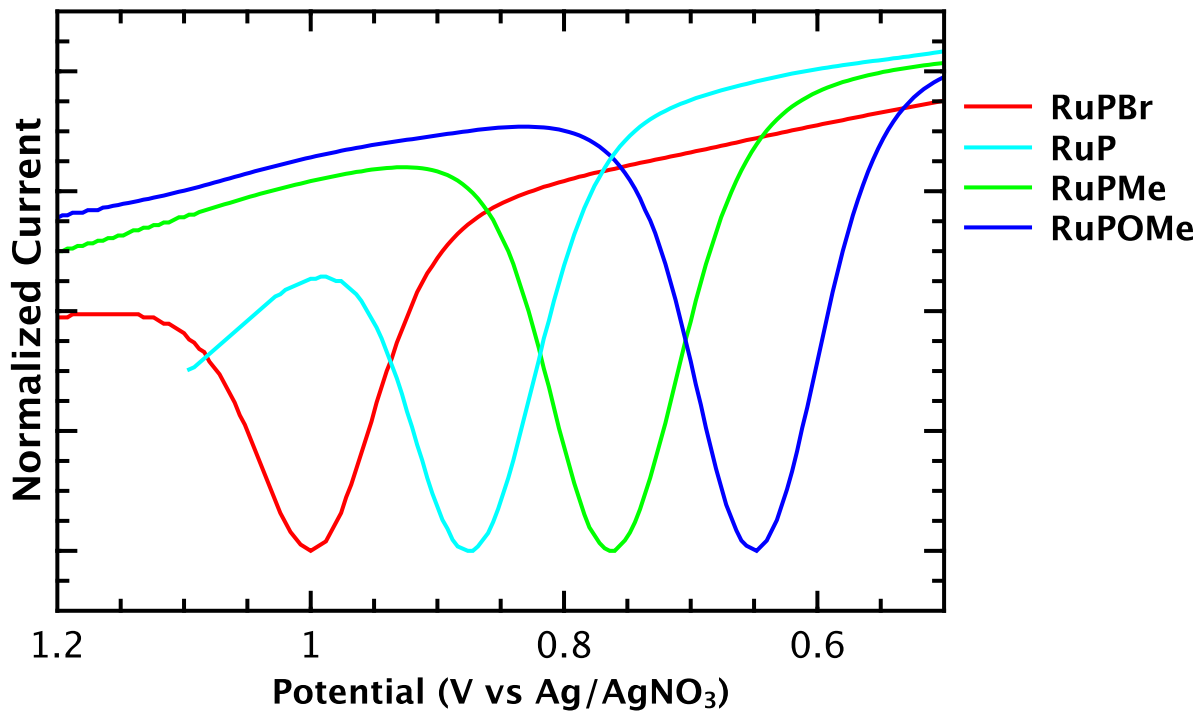


Figure B.3. Square-wave voltammograms of **RuPOMe**, **RuPMe**, **RuP**, and **RuPBr** in 80:20 CH₃CN:H₂O with glassy carbon as the working electrode, Pt counter, and Ag/AgNO₃ reference electrode.

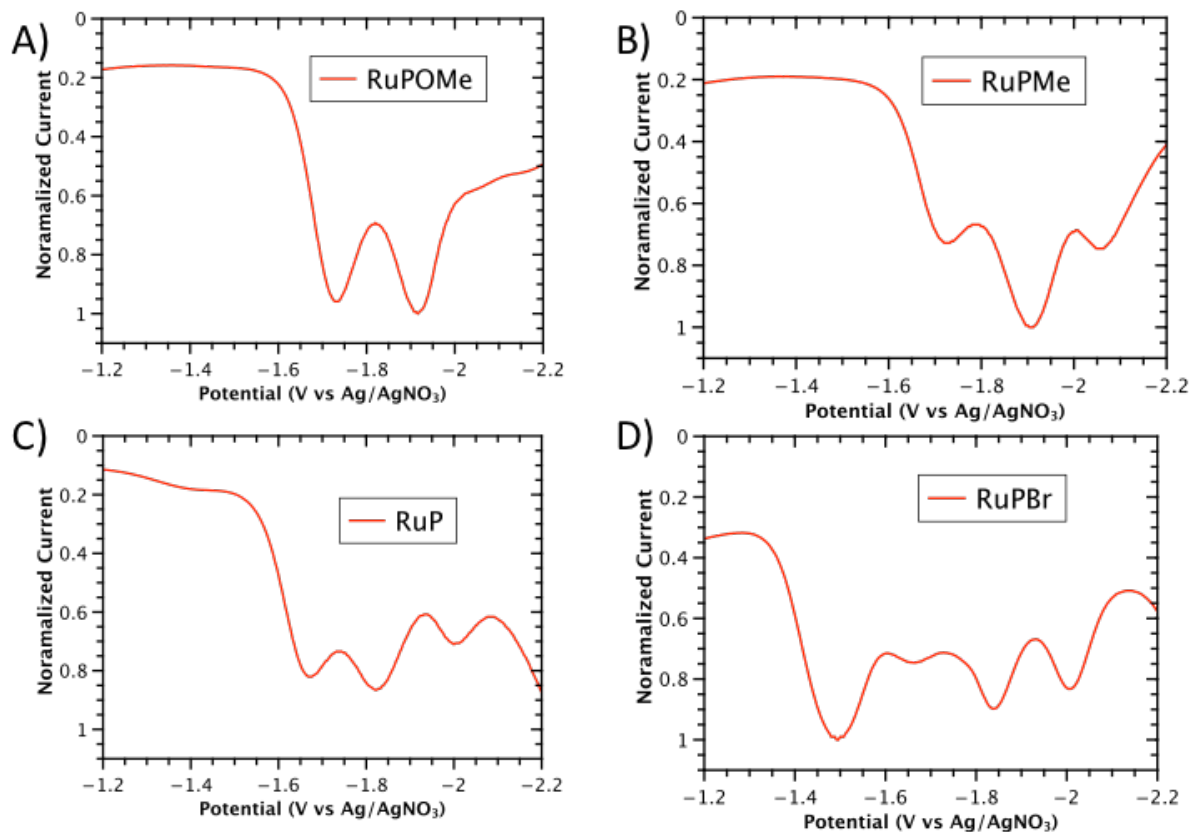


Figure B.4. Reductive square-wave voltammograms of **RuPOMe** (A), **RuPMe** (B), **RuP** (C), and **RuPBr** (d) in 80:20 CH₃CN:H₂O under an argon atmosphere with a glassy carbon working electrode, Pt-wire counter, and a Ag/AgNO₃ reference (-0.09 V vs Fc^{0/+}).

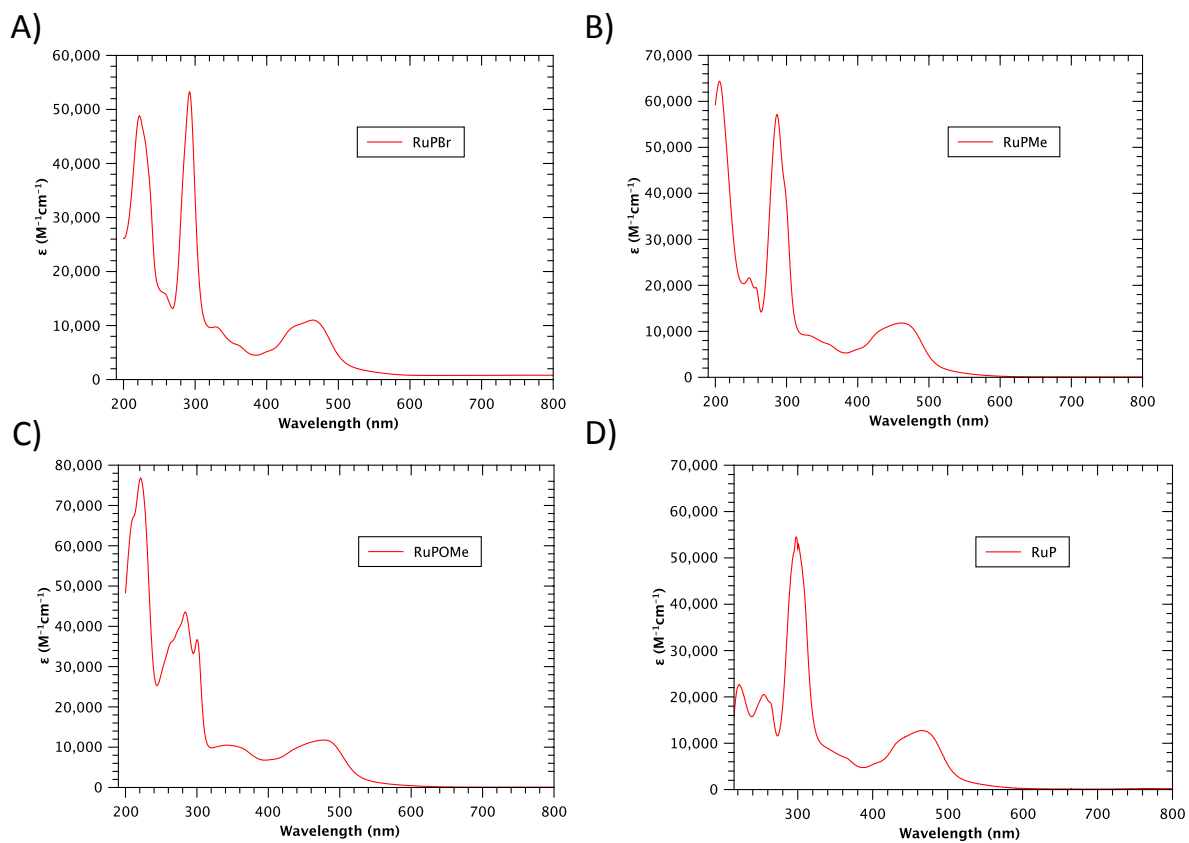


Figure B.5. UV/Visible absorption spectra for **RuPBr** (A), **RuPMe** (B), **RuPOMe** (C), and **RuP** (D) in H₂O.

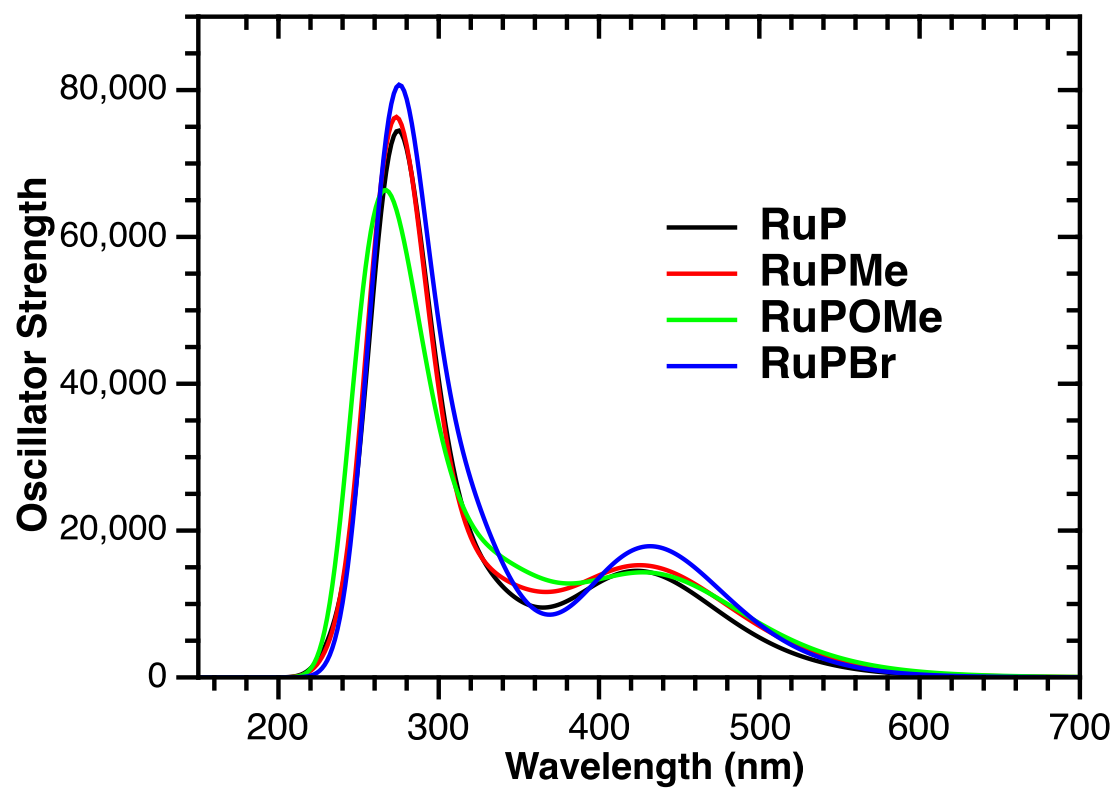


Figure B.6. Calculated electronic spectra of RuP, RuPMe, RuPOMe, and RuPBr.

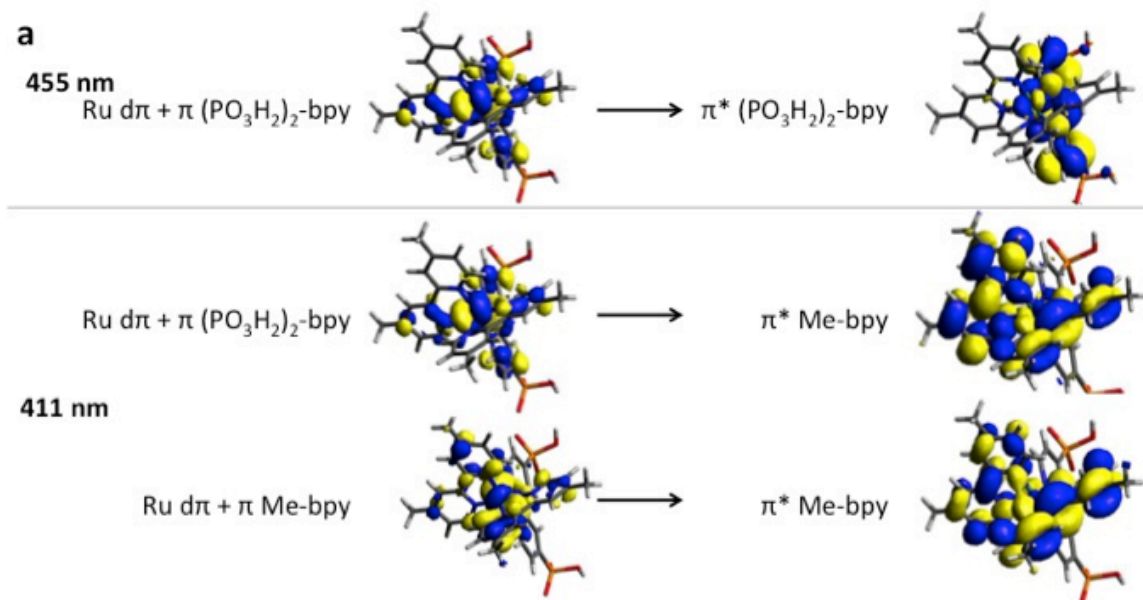


Figure B.7. Orbitals contributing for the MLCT excitations for RuPMe.

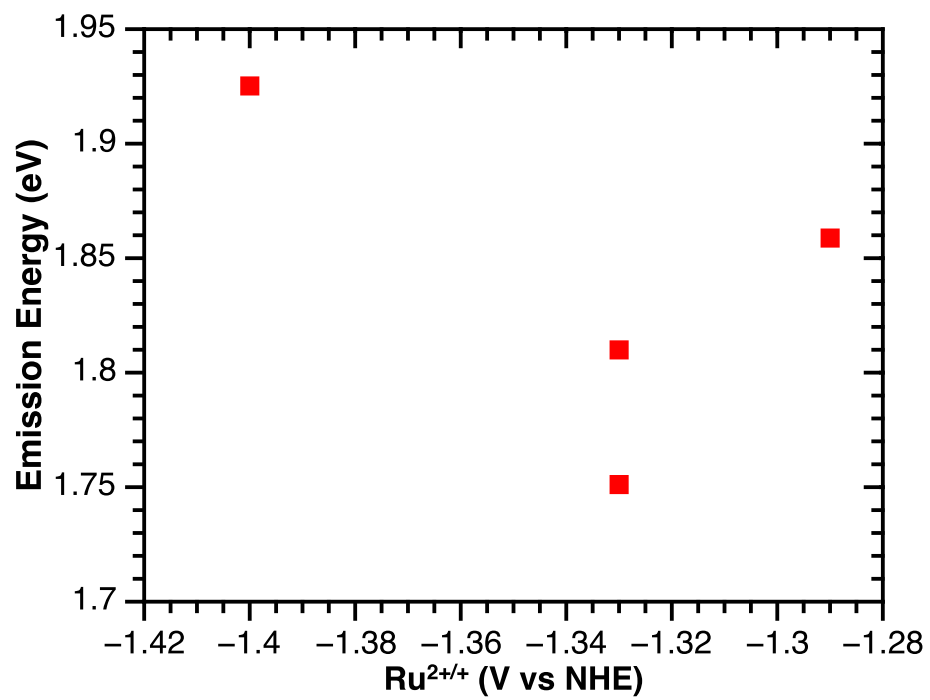


Figure B.8. Variation of $\bar{\nu}_{em}$ with $E_{1/2}(\text{Ru}^{2+/+})$ in aqueous 0.1 M HClO₄ at 25°C.

APPENDIX C. AN AMIDE-LINKED CHROMOPHORE-CATALYST ASSEMBLY FOR WATER OXIDATION

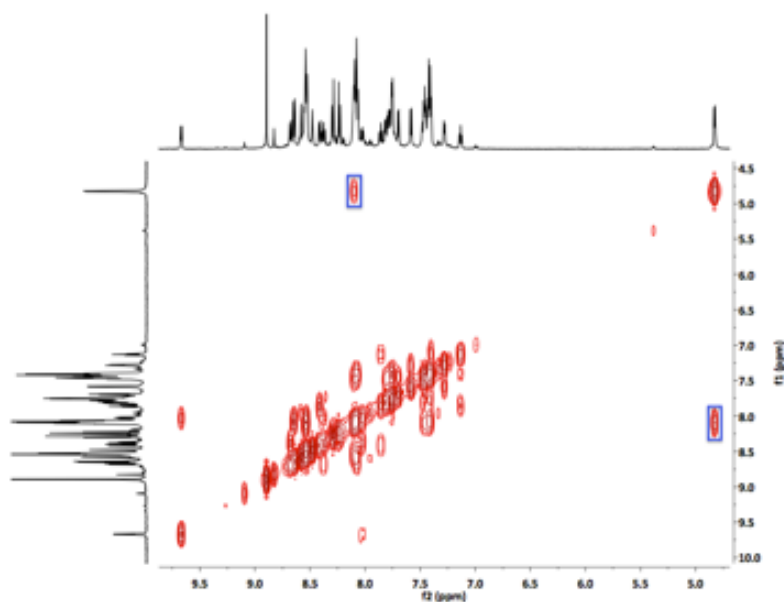


Figure C.1. COSY experiment showing the cross peak (blue boxes) for the CH₂ and the NH in the amide bridge in **3** in CH₃CN.

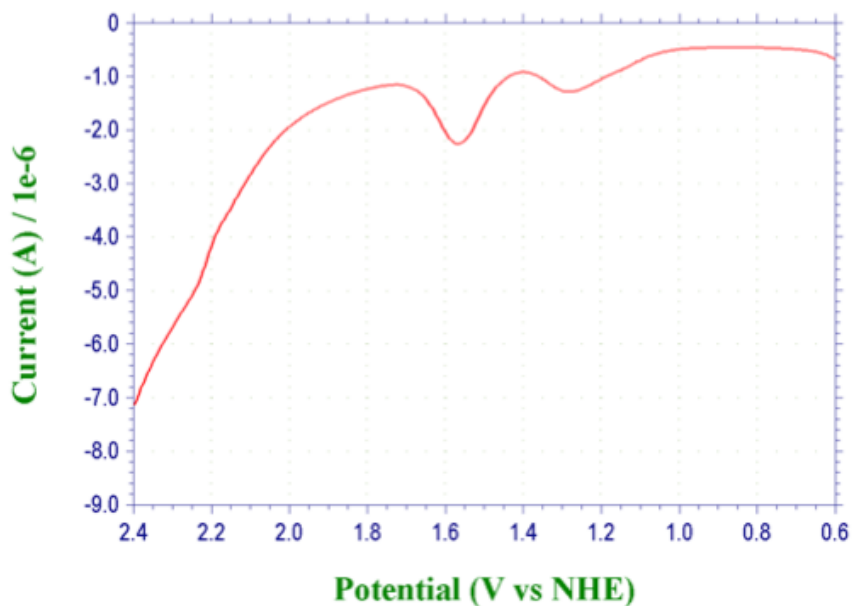


Figure C.2. Differential pulse voltammogram of **3** in propylene carbonate with added water (2%). Tetrabutylammonium hexafluorophosphate (0.1 M) as the supporting electrolyte with a glassy carbon working electrode, platinum counter, and Ag/AgNO₃ reference (0.56 V vs NHE).

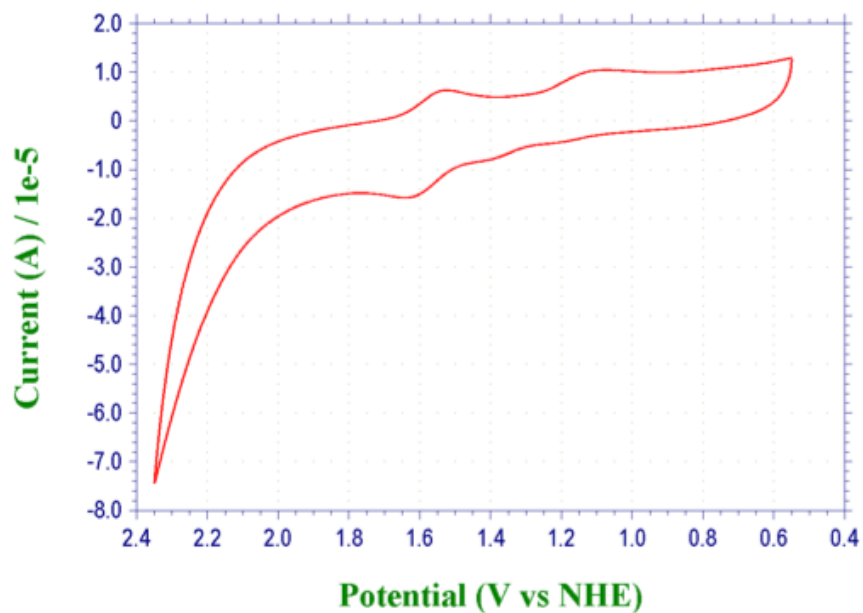


Figure C.3. Cyclic voltammogram at 100 mV/s of **3** in PC with added water (2%). The supporting electrolyte was tetrabutylammonium hexafluorophosphate (0.1 M) with a glassy carbon working electrode, platinum counter, and Ag/AgNO₃ reference.

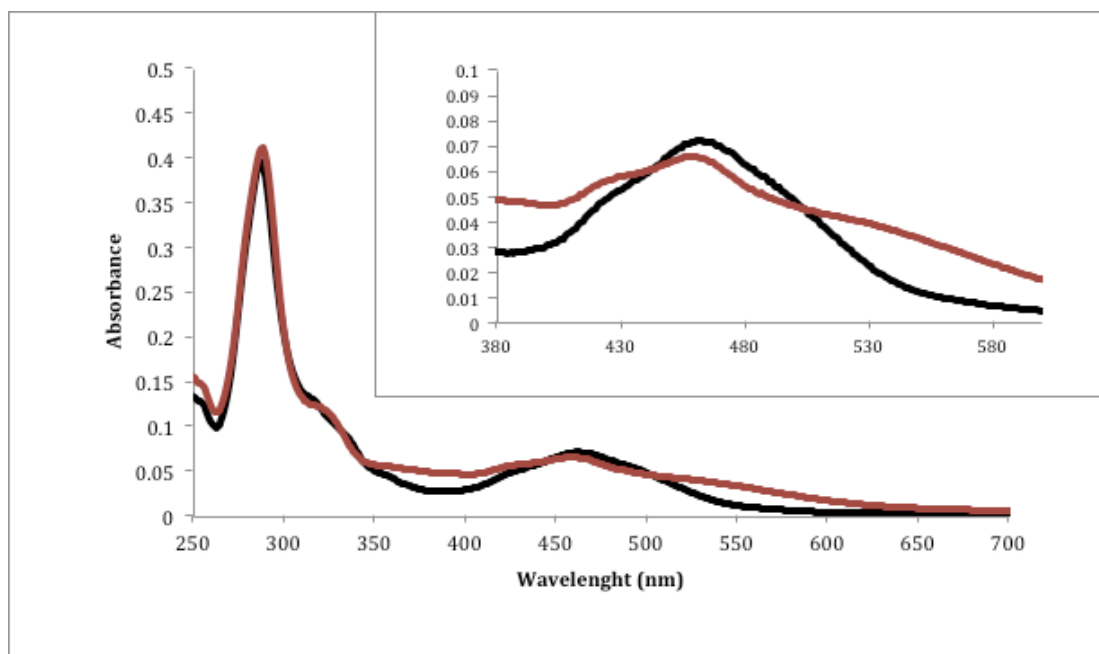


Figure C.4. Absorption spectrum of **3** in water (black) and 0.1 M NaOH (red).

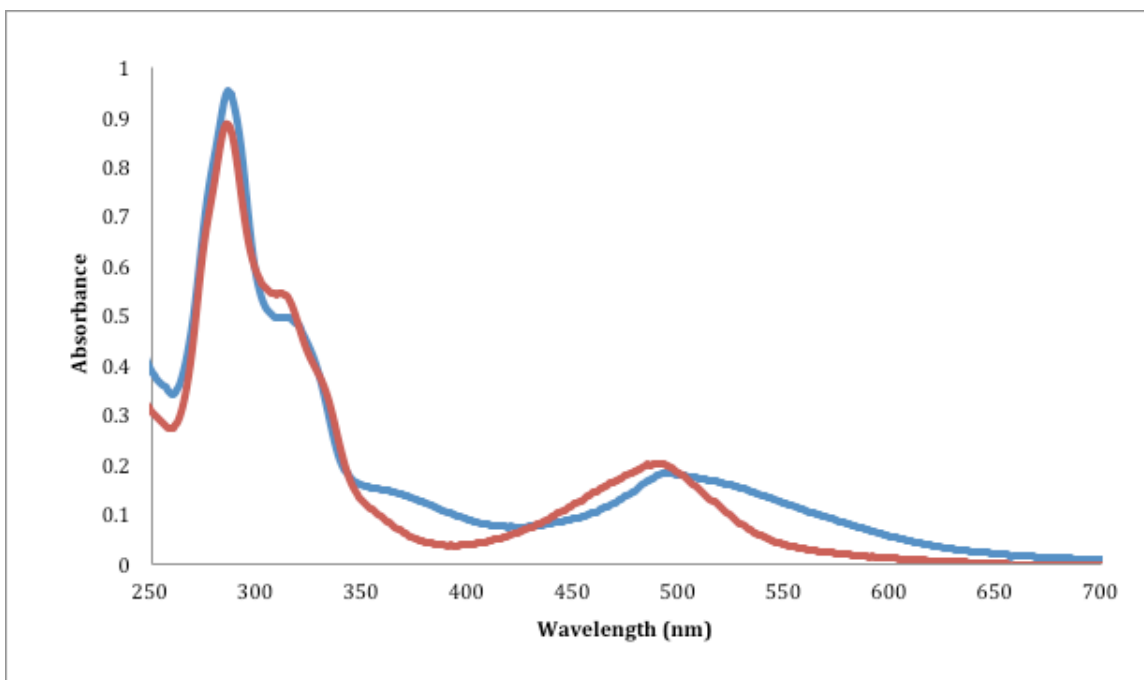


Figure C.5. Absorption spectrum of **9** in water (red) and in 0.1 M NaOH (blue).

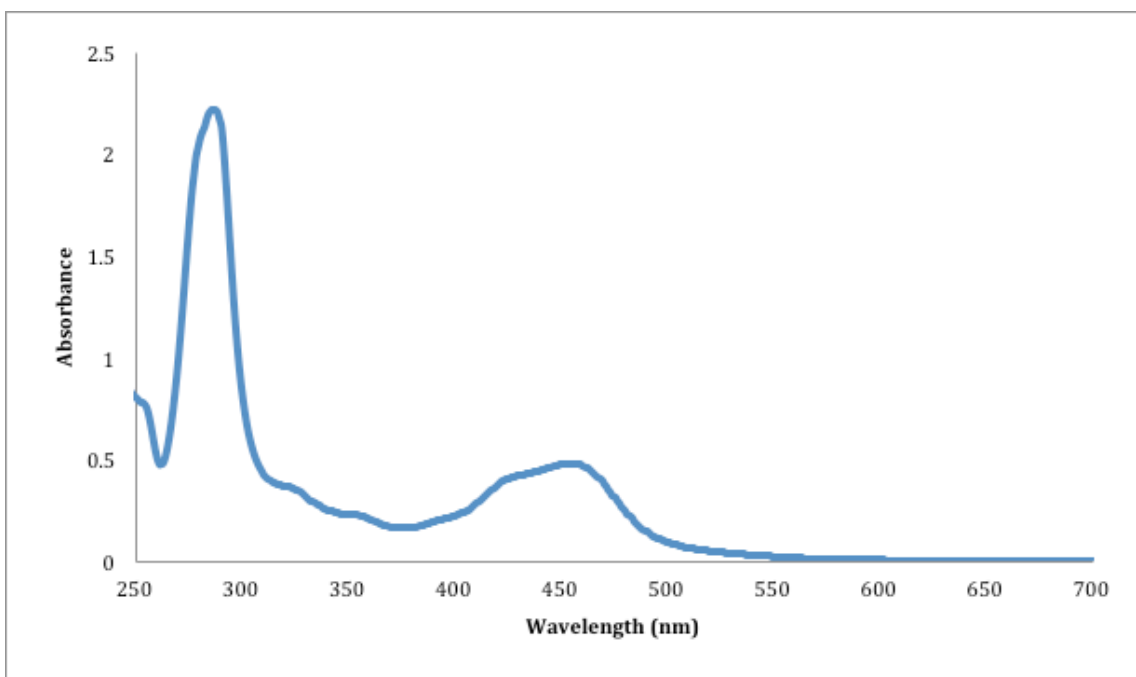


Figure C.6. Absorption spectrum of **10** in water.

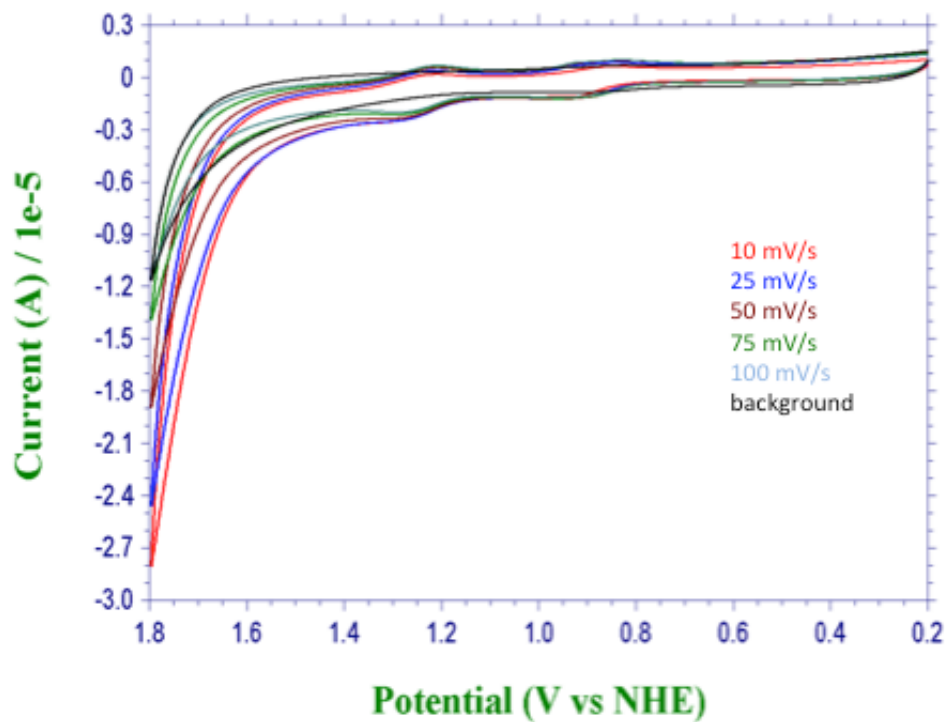


Figure C.7. Scan rate dependence of **3** at pH = 4.97 (0.1 M acetate, 0.5 M KNO₃) of scan rate normalized ($i/v^{1/2}$) cyclic voltammograms at a glassy carbon electrode (0.07 cm²) vs Ag/AgCl.

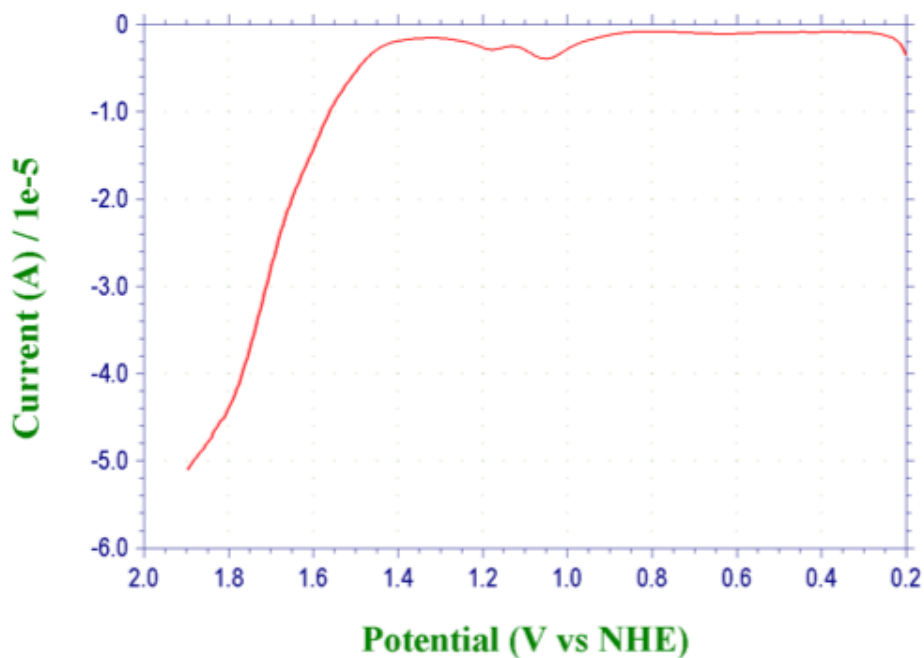


Figure C.8. Differential pulse voltammogram of **9** in 0.1 M HNO₃ with a glassy carbon working electrode, platinum counter electrode, and Ag/AgCl reference.

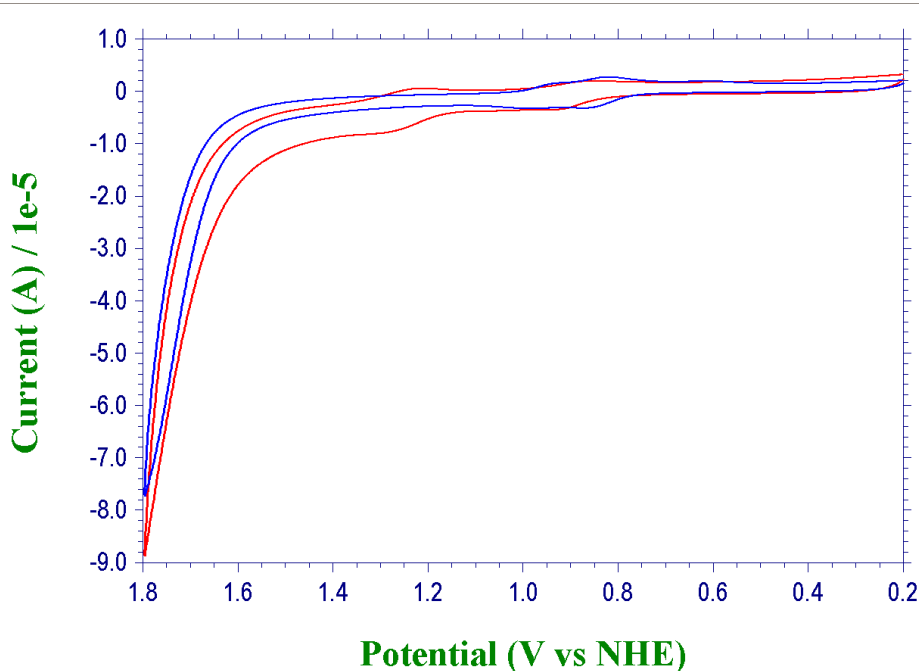


Figure C.9. Comparison CV of **3** (red) and $\text{Ru}(\text{tpy})(\text{bpy})(\text{OH}_2)^{2+}$ (blue) at pH = 4.97 (0.1 M acetate, 0.5 M KNO_3). The currents are normalized to the $\text{Ru}^{\text{III/II}}$ couples with a glassy carbon working electrode, platinum counter electrode, and Ag/AgCl reference.

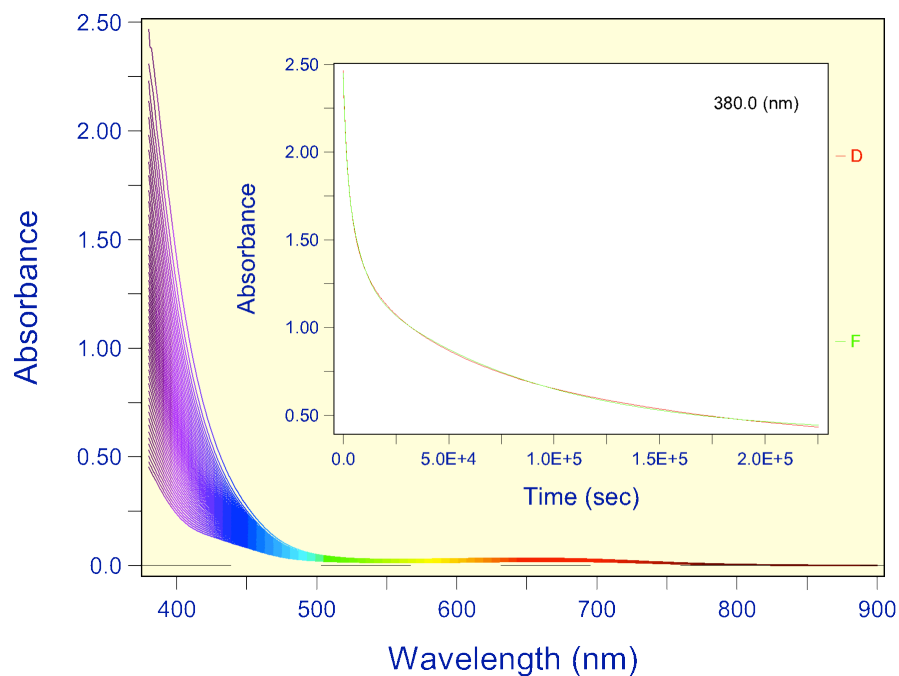


Figure C.10. Kinetic spectral scan data for loss of 3.6 mM CAN in 1.0 M HNO_3 in the presence of 0.05 mM **3** assembly at 22°C. Inset: Kinetic trace at 380 nm (red) and fitted curve (green) for the model $\text{A} \rightarrow \text{B} \rightarrow \text{C} \rightarrow \text{D}$.

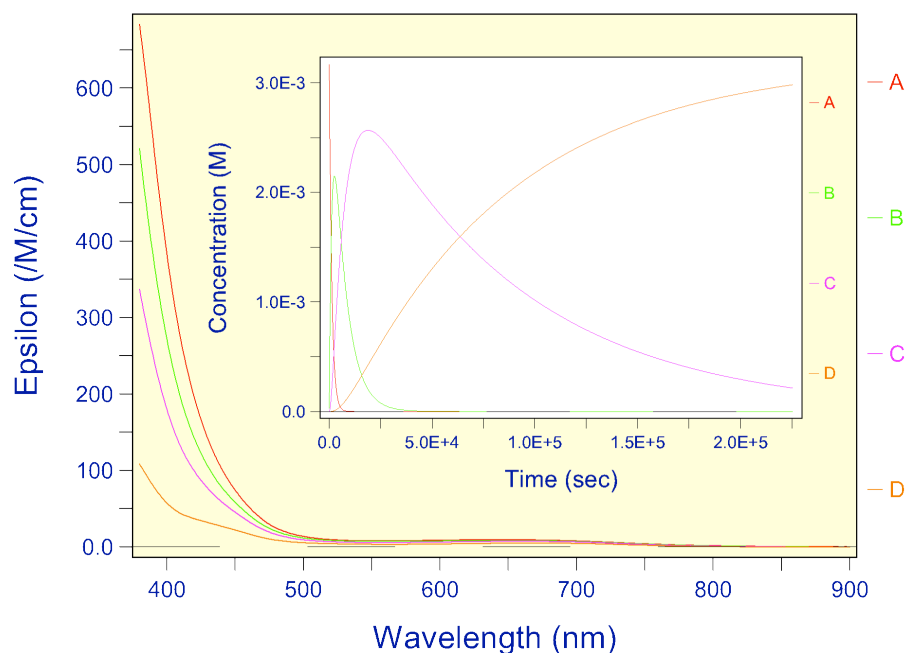


Figure C.11. Calculated spectra and concentration profiles for the multiwavelength fit to the kinetic model $A \rightarrow B \rightarrow C \rightarrow D$ with $[CAN]_0 = 3.6 \text{ mM}$, $[3]_0 = 0.05 \text{ mM}$, $T = 22.0^\circ\text{C}$. The spectral features suggest that CAN is decaying at different rates owing to changes occurring within the catalyst assembly over time. Each colored state (A,B,C,D) represents a combination of the remaining $[Ce(IV)]$ with the dominant form of $[3]$ during the corresponding decay time period.

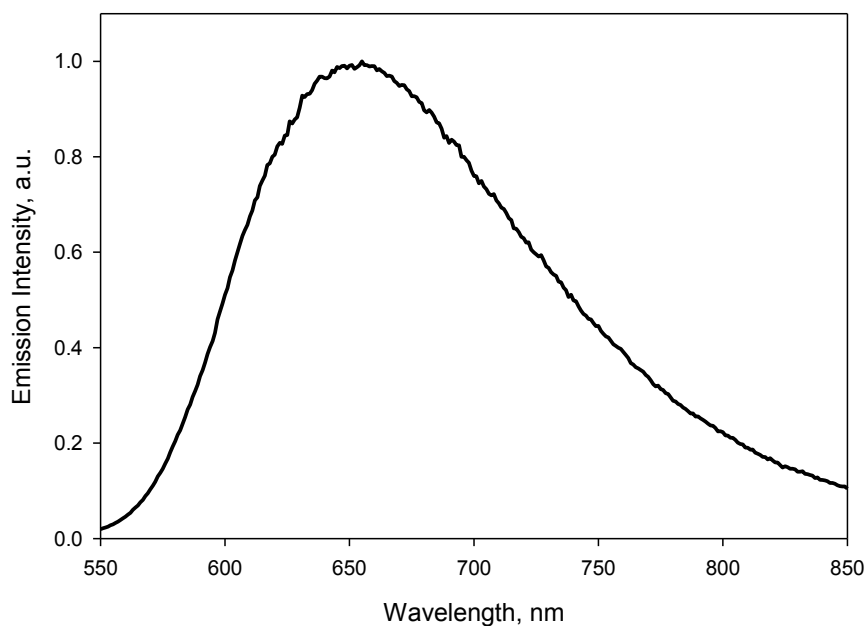


Figure C.12. Steady-state emission spectrum of **3** in water at room temperature. $[\mathbf{3}] = 31 \mu\text{M}$, $[\text{KNO}_3] = 0.5 \text{ M}$, $\lambda_{\text{ex}} = 460 \text{ nm}$.

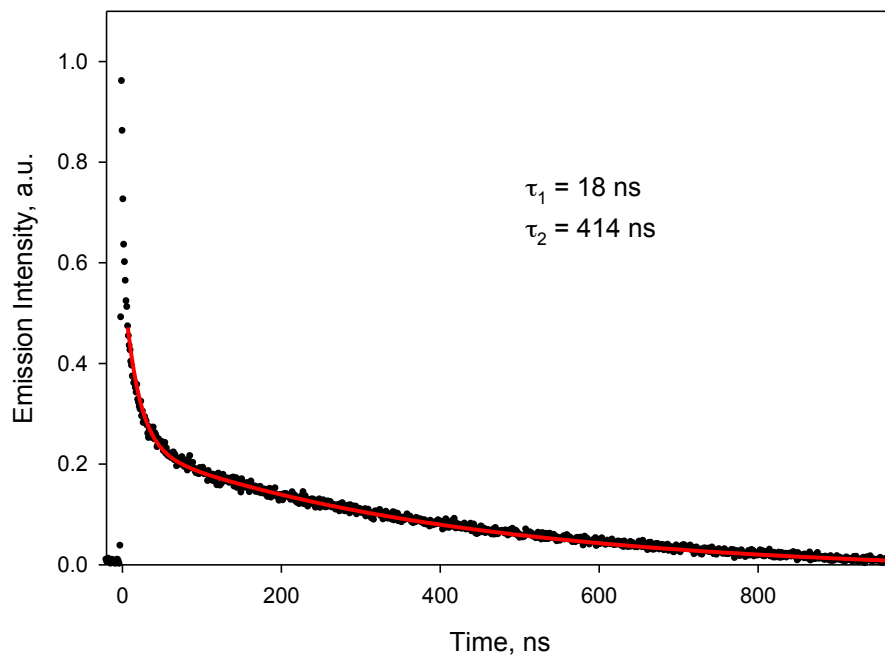


Figure C.13. Time-resolved emission decay of **3** in water at room temperature. $[\mathbf{3}] = 31 \mu\text{M}$, $[\text{KNO}_3] = 0.5 \text{ M}$, $\lambda_{\text{ex}} = 444 \text{ nm}$, $\lambda_{\text{det}} = 444 \text{ nm}$.

APPENDIX D. PHOTOINDUCED ELECTRON TRANSFER IN A CHROMOPHORE-CATALYST ASSEMBLY ANCHORED TO TiO₂

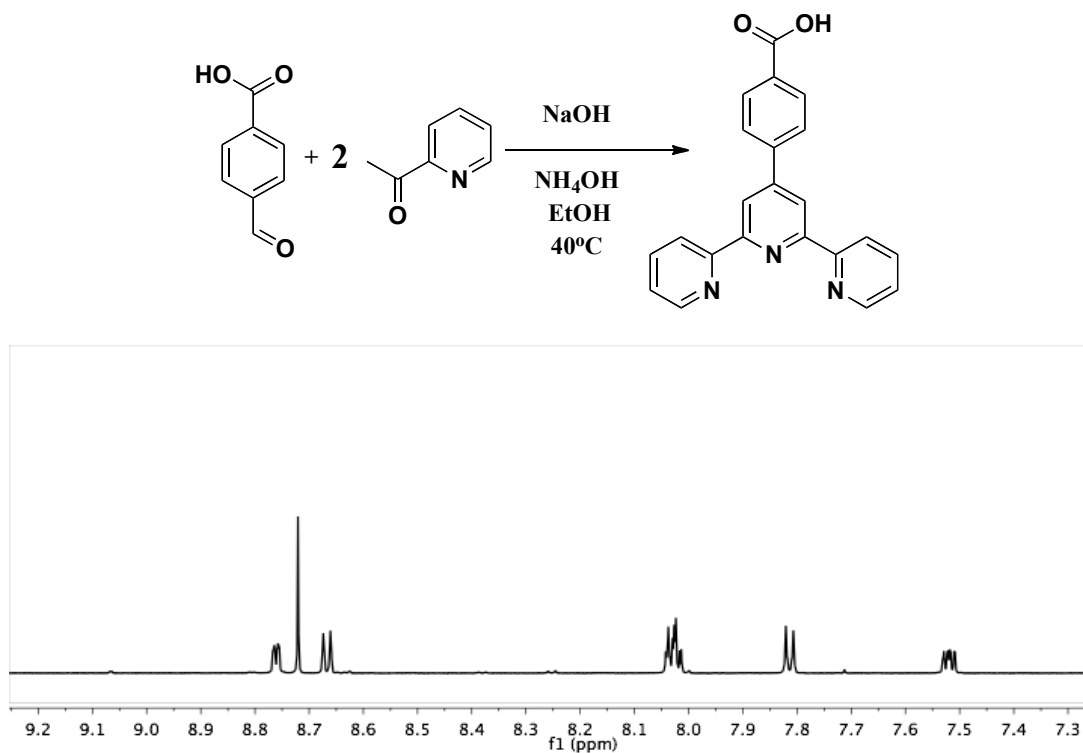
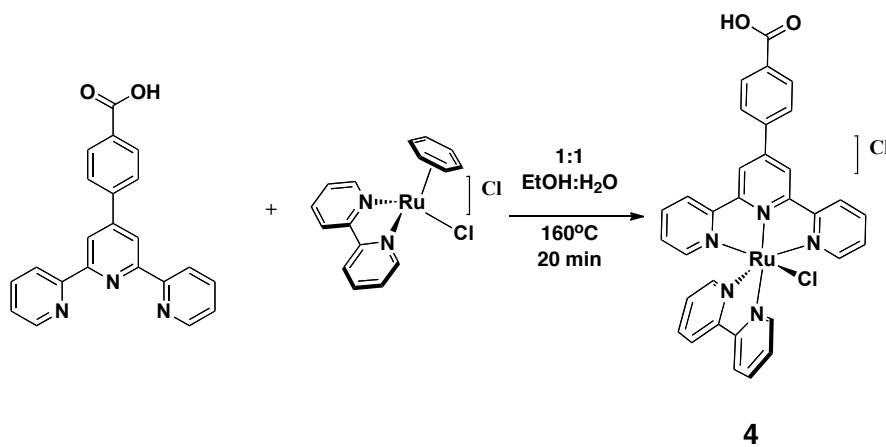


Figure D.1. ¹H NMR of 4-([2,2':6',2''-terpyridin]-4'-yl)benzoic acid in D₆-DMSO.



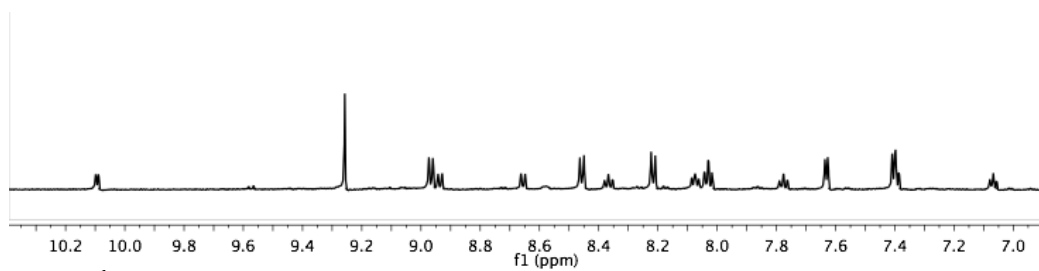
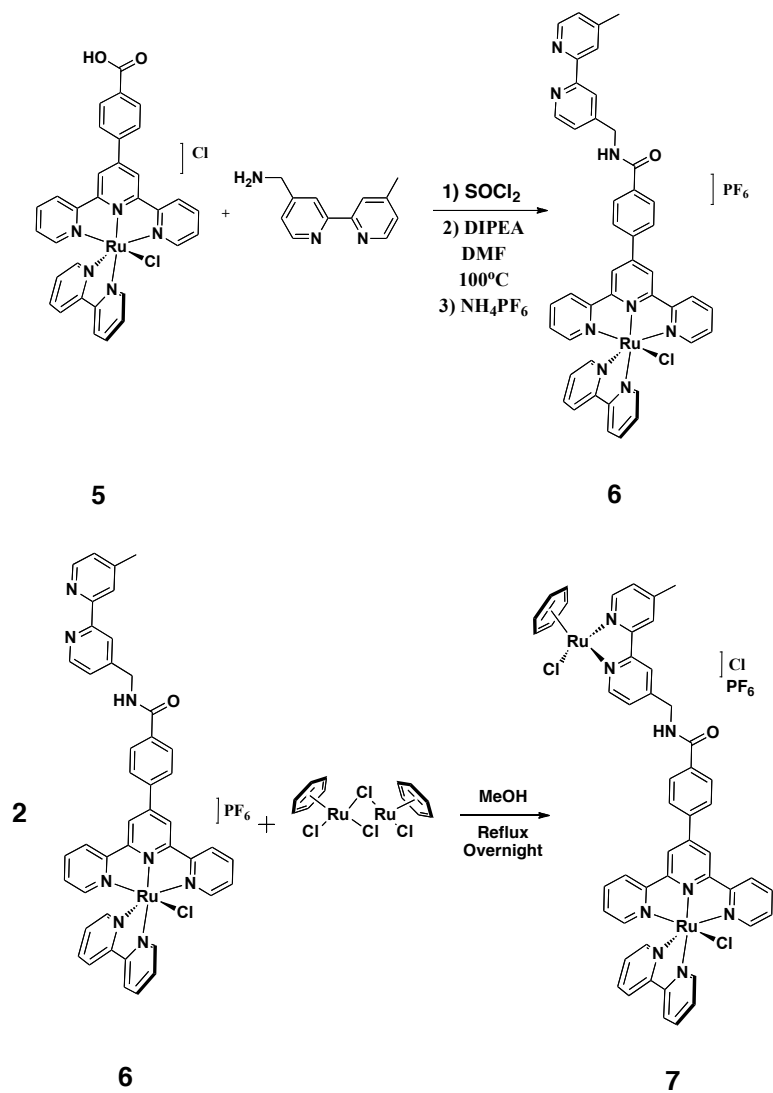


Figure D.2. ^1H NMR of **4** in d_6 -DMSO.



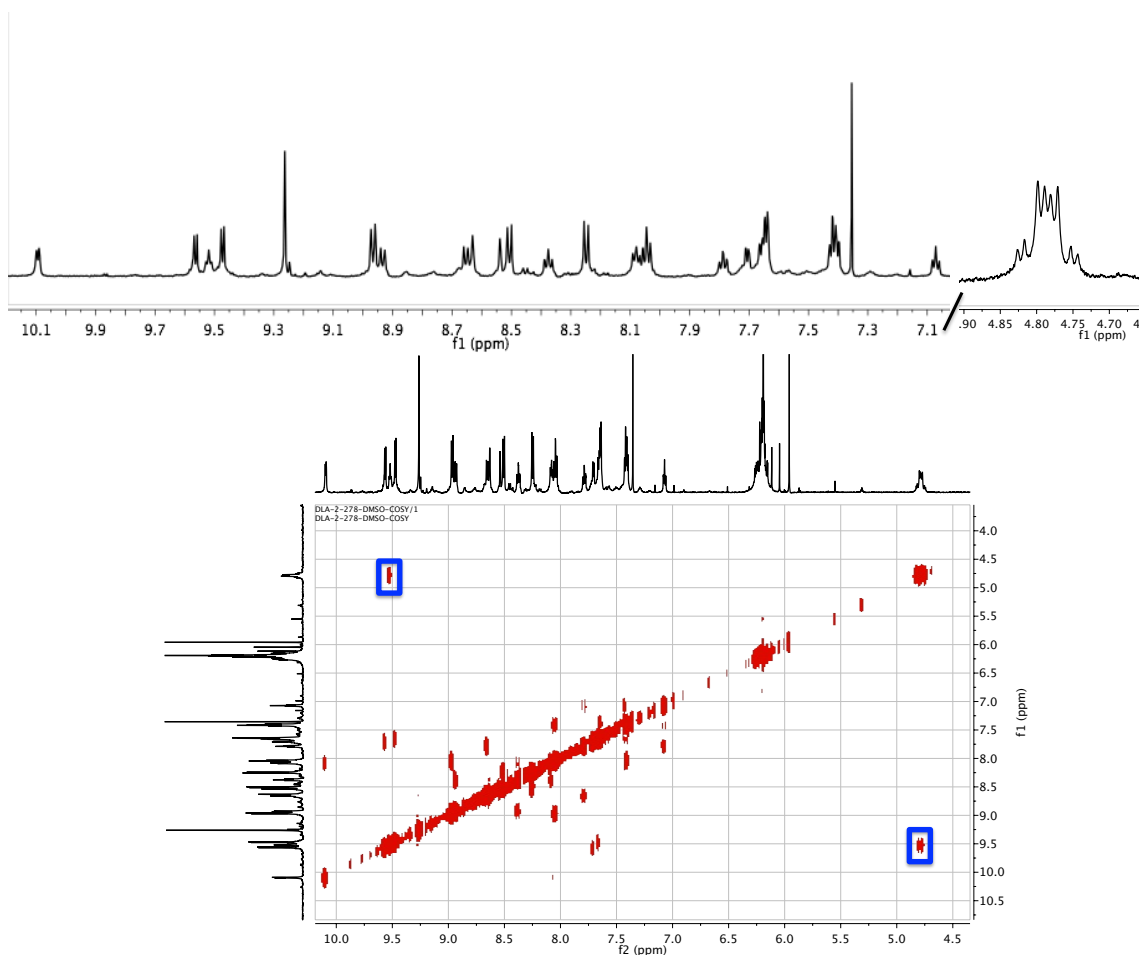
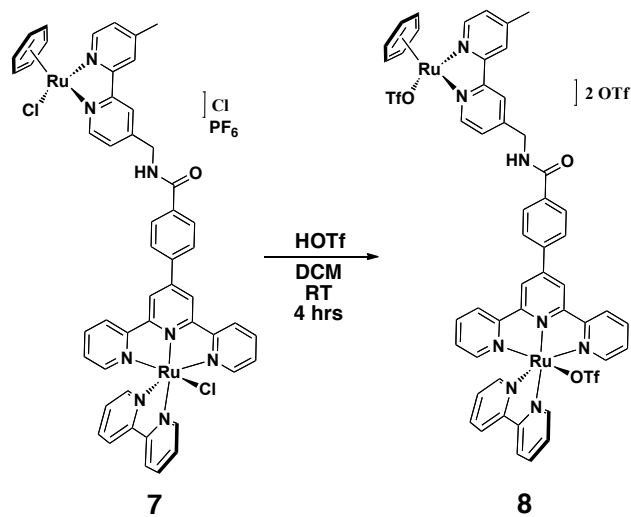


Figure D.3. (Top) Zoomed in portion of the aromatic region in the ^1H NMR of **7** in d_6 -DMSO. (Bottom) COSY NMR of **7** in d_6 -DMSO.



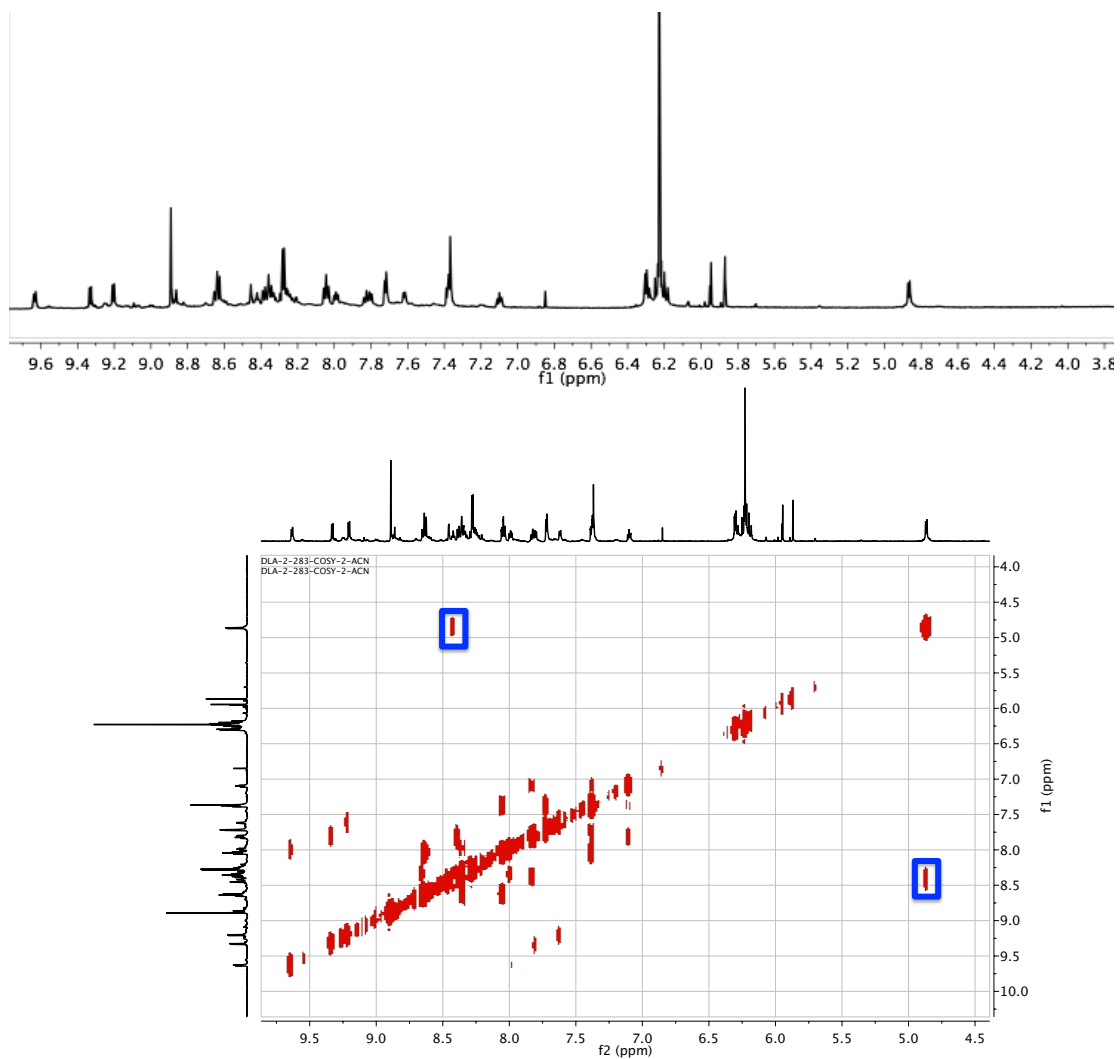


Figure D.4. (Top) Zoomed in portion of the aromatic region in the ^1H NMR of **8** in CD_3CN . (Bottom) COSY NMR of **8** in CD_3CN .

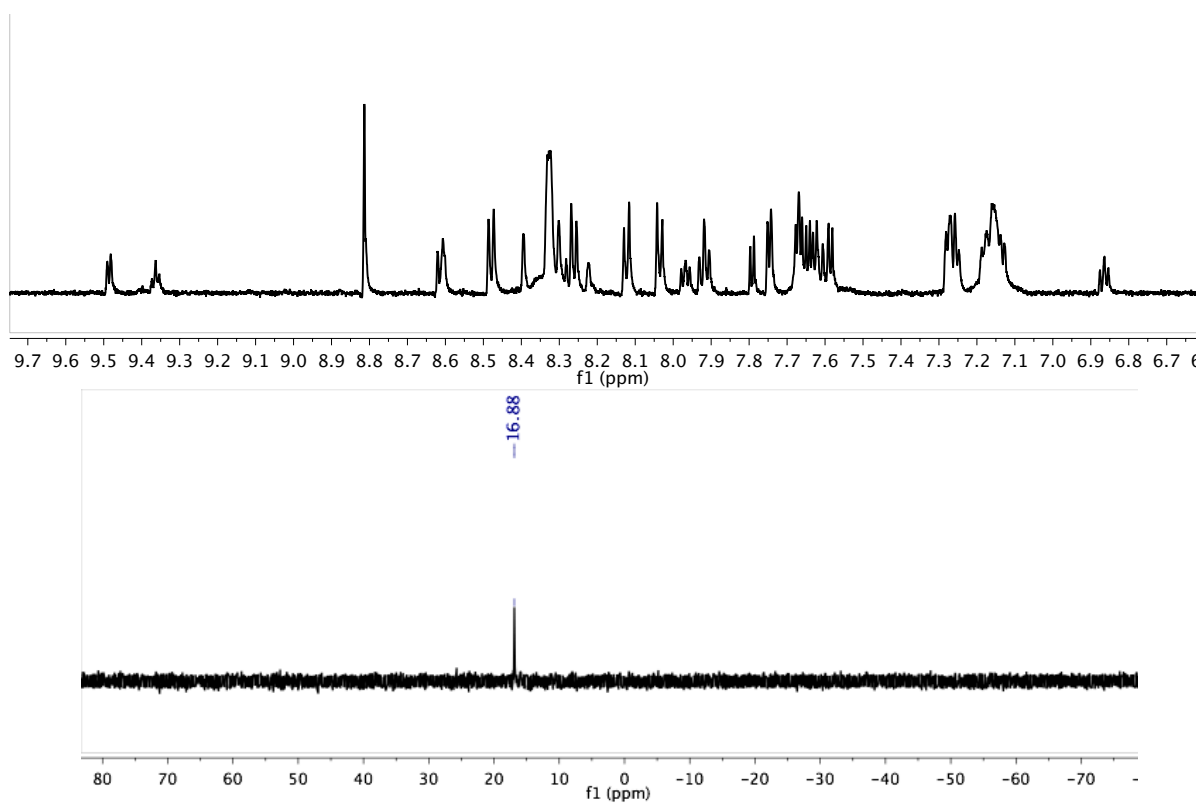
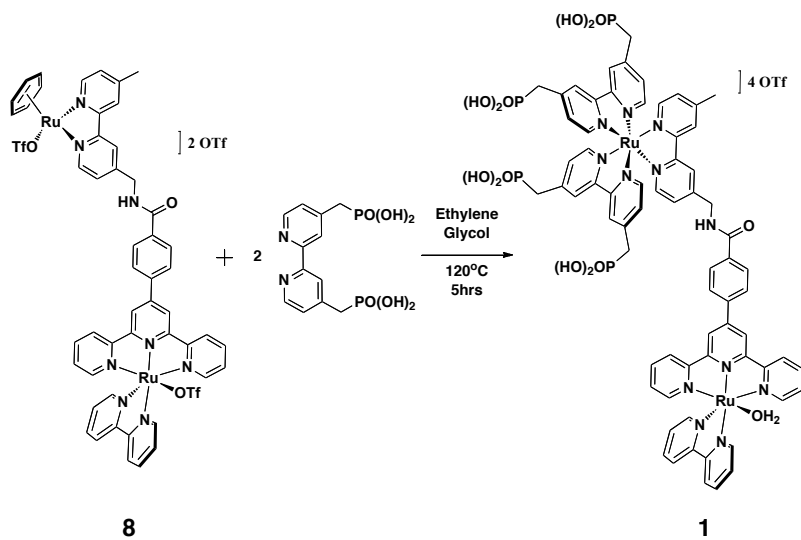


Figure D.5. (Top) Zoomed in portion of the aromatic region in the ^1H NMR of **1** in D_2O . (Bottom) ^{31}P of **1** in D_2O .

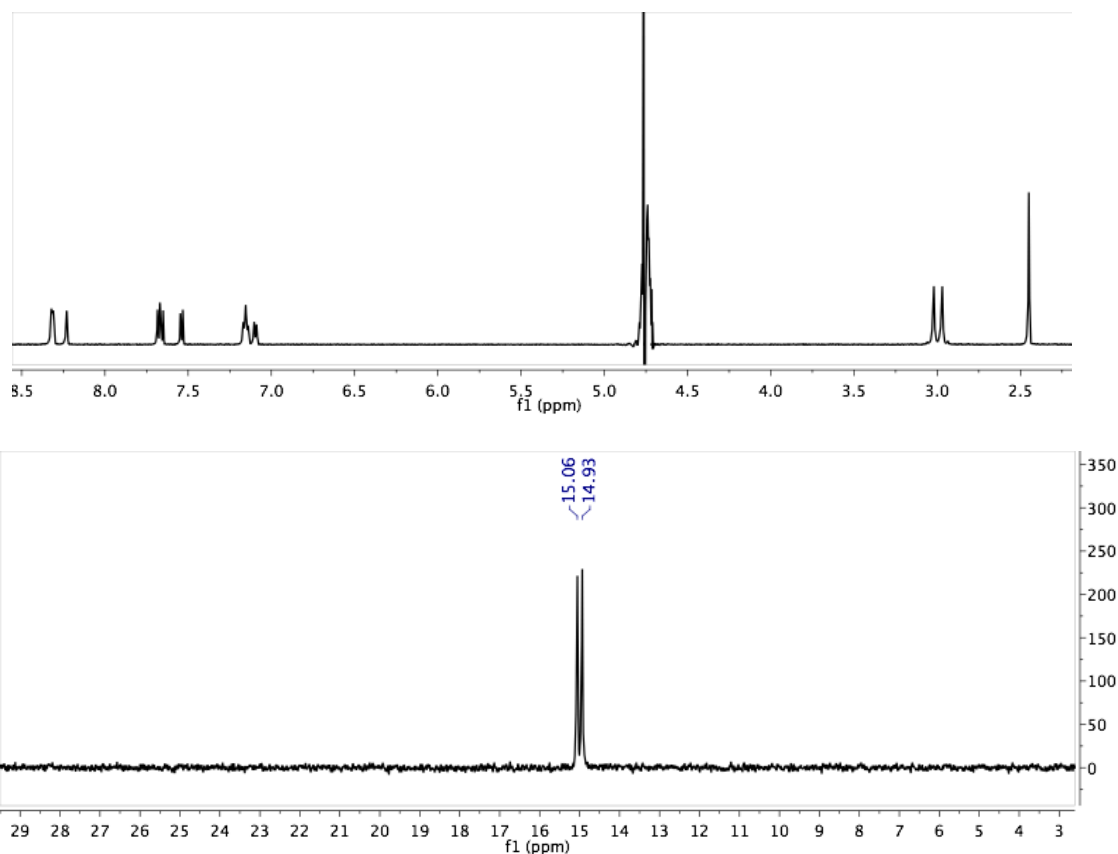


Figure D.6. (Top) ^1H NMR of **2** in D_2O . (Bottom) ^{31}P of **2** in D_2O .

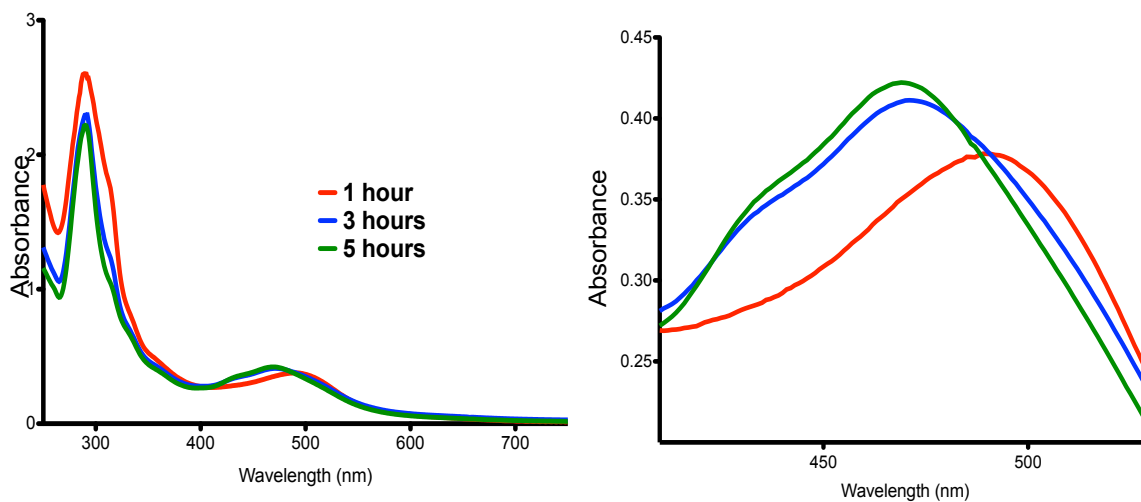


Figure D.7. Reaction progress in the final step in the synthesis of **1**. Spectra are normalized to the MLCT for comparison purposes.

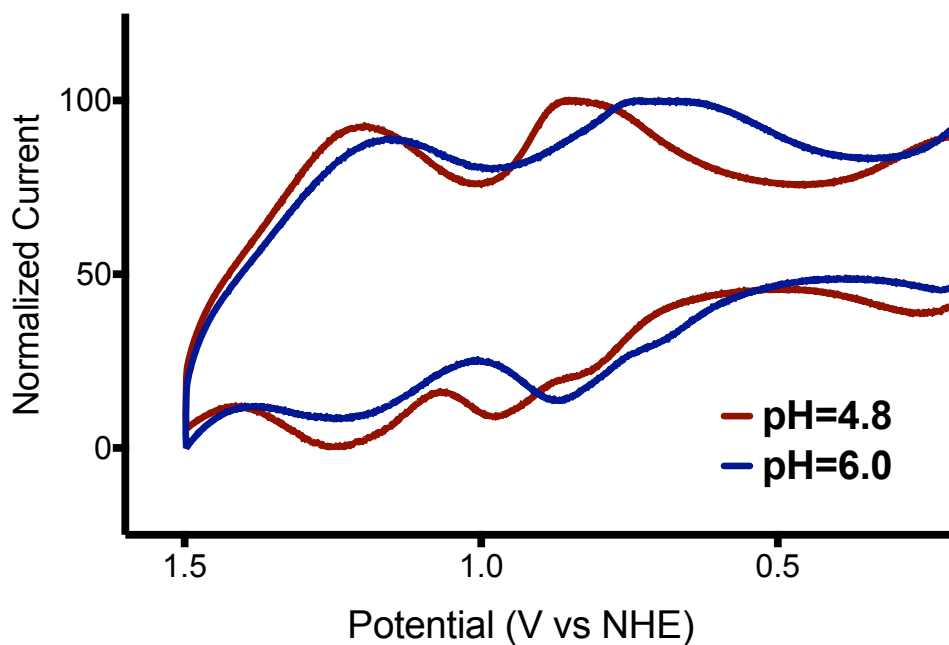


Figure D.8. Comparison CV in pH=4.8 (0.1 M phosphate, 0.5M KNO₃, red) and pH=6.0 (buffer, blue) at 100 mV/s of **1**. Currents are normalized to the Ru^{II}-Ru^{III}-OH/ Ru^{II}-Ru^{II}-OH₂ couple for comparison purposes.

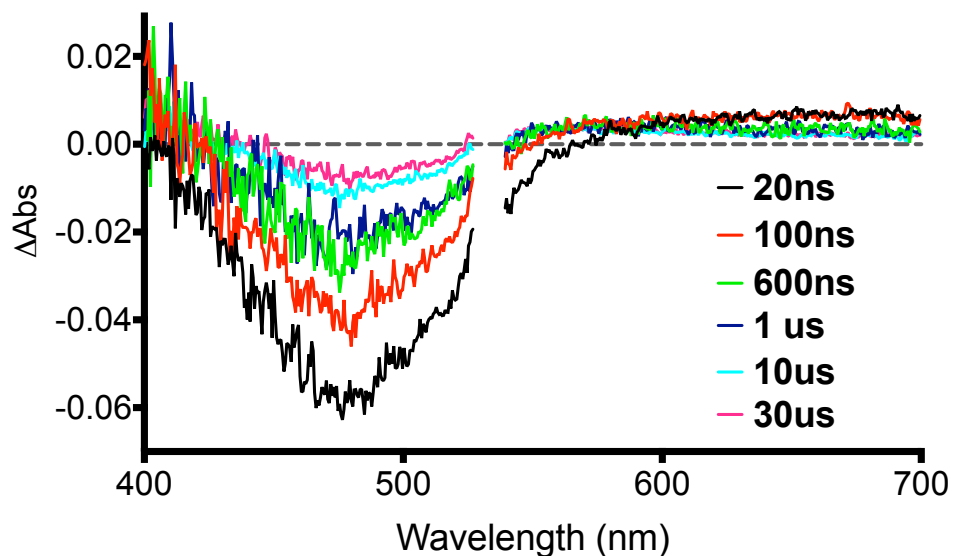


Figure D.9. Transient spectrum for TiO₂-1 in 0.1 M HClO₄ following 532 nm excitation.

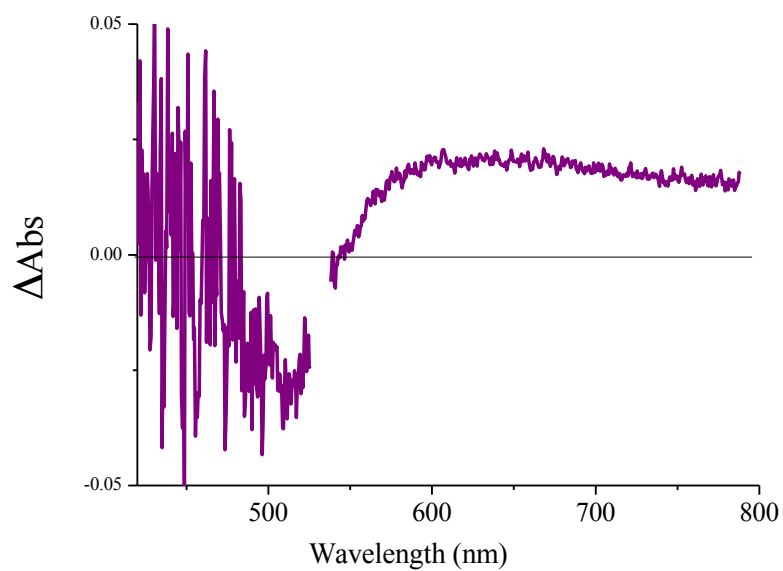


Figure D.10. Transient spectrum of ZrO₂-1 in 0.1 M HClO₄ at 10 ms following 532 nm excitation.

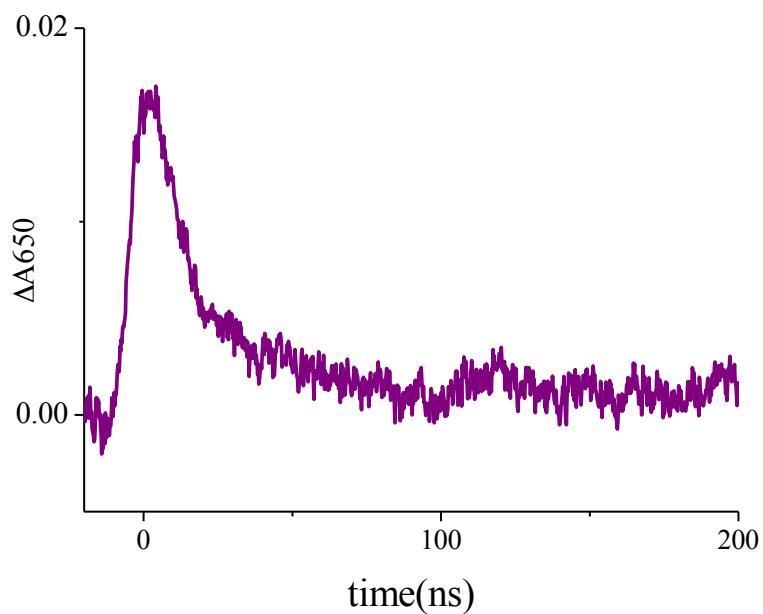


Figure D.11. 650 nm transient decay of ZrO₂-1 monitored at 650 nm following 532 nm excitation.

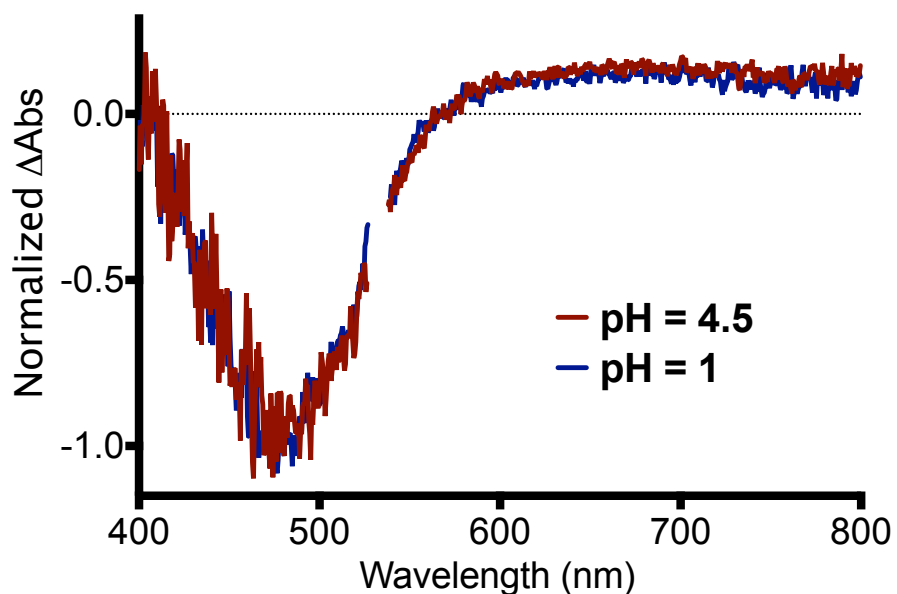


Figure D.12. Nanosecond transient absorption difference spectra obtained at 20 ns on TiO_2 derivatized with **1** following 532 nm laser excitation (5.2 mJ). Spectra are normalized at the bleach maxima for comparison purposes.

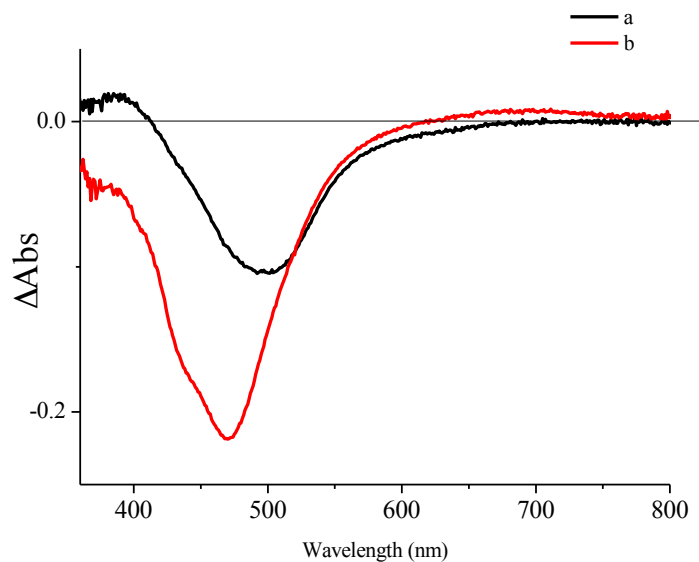


Figure D.13. Spectral changes of complex **1** attached on *nano*-ITO electrode, $\Gamma = 1.3 \times 10^{-8}$ mol cm^{-2} in 0.1 M HClO_4 . (a) after oxidation of $[\text{Ru}_a^{\text{II}}-\text{Ru}_b^{\text{II}}-\text{OH}_2]^{4+}$ to $[\text{Ru}_a^{\text{II}}-\text{Ru}_b^{\text{III}}-\text{OH}_2]^{5+}$ (catalyst) and (b) after oxidation of $[\text{Ru}_a^{\text{II}}-\text{Ru}_b^{\text{IV}}=\text{O}]^{4+}$ to $[\text{Ru}_a^{\text{III}}-\text{Ru}_b^{\text{IV}}=\text{O}]^{5+}$.

APPENDIX E. WATCHING PHOTOACTIVATION IN A RU(II) CHROMOPHORE-CATALYST ASSEMBLY ON TiO₂ BY ULTRAFAST SPECTROSCOPY

Global Fitting by SPECTFIT/32

The spectral-kinetic data of chromophore-catalyst assembly was processed by using the program SPECTFIT/32, which relies on the method of Singular Value Decomposition (SVD) and nonlinear regression by the Levenberg-Marquardt method. Singular Value Decomposition (SVD) reduce the experimental wavelength-time spectral data matrix (Y) into a simpler analytical form, $Y = USV^t$, where U and V are sets of orthogonal (linearly independent) evolutionary and spectral eigenvectors, respectively, and S is a set of singular (weighting) factors. The basic ideas of SVD is to massively reduce the data set by ignoring variation below a particular threshold, and preserve only a small number of significant eigenvectors containing all of the spectral and evolutionary information from the original set. The eigenvectors containing only experimental noise can be eliminated from further consideration without loss of information. Subsequently, the eigenvectors are applied within a global multivariate least-squares regression method (Levenberg-Marquardt) to fit the projection ($Y' = US$) of the multiwavelength kinetic data in the subspace spanned by V to an appropriate model for $Y = CA$, where the matrix C contains the concentration profiles and A represents the molar absorptivity spectra.

As shown in Chapter 6, the SVD revealed the presence of four significant spectral and time domain eigenvectors, which correspond to the three distinct kinetic processes associated with the four colored transient species as in Scheme 6.2, eq. 4, 5 and 2b.

The fifth and sixth spectral eigenvectors are essentially random noise as plotted in Figure 5B. Because the spectra of excited state chromophore, $[-Ru_a^{II*}]^{2+}$ and oxidized

chromophore, $[-\text{Ru}_a^{\text{III}}-]^{3+}$, excited state catalyst $[-\text{Ru}_b^{\text{II}*}-\text{OH}_2]^{2+}$, and oxidized catalyst $[-\text{Ru}_b^{\text{III}}-\text{OH}_2]^{3+}$ are close to each other, the known initial spectrum of $[-\text{Ru}_a^{\text{II}*}-]^{2+}$ is kept fixed to reduce the variable parameters and ensure the fitting results more reliable. The population of non-injected $[-\text{Ru}_a^{\text{II}*}-]^{2+}$ is relatively small (<5%), which could not be distinguished from the noise by the SVD procedure, and this small amount of non-injected $[-\text{Ru}_a^{\text{II}*}-]^{2+}$ was factored as the noise in the analytical data matrix.

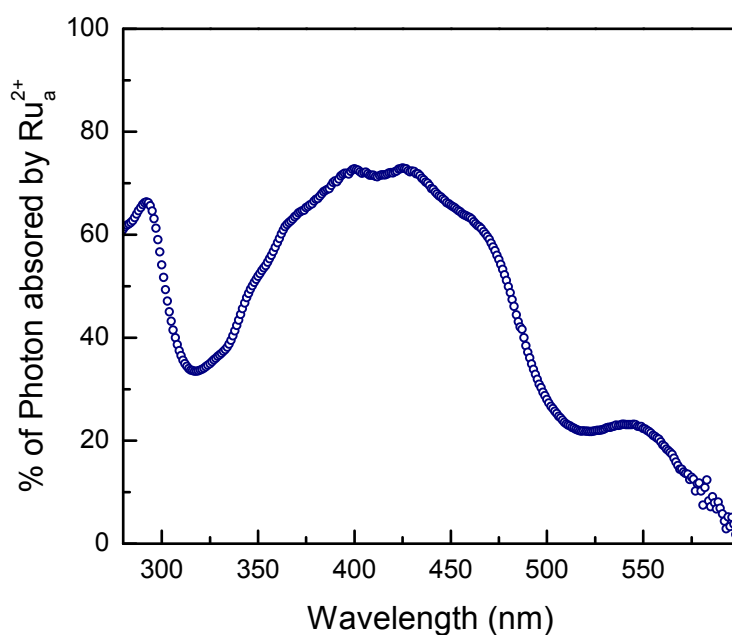


Figure E.1. The percentage of photons absorbed by the chromophore Ru_a^{II} at different wavelengths.

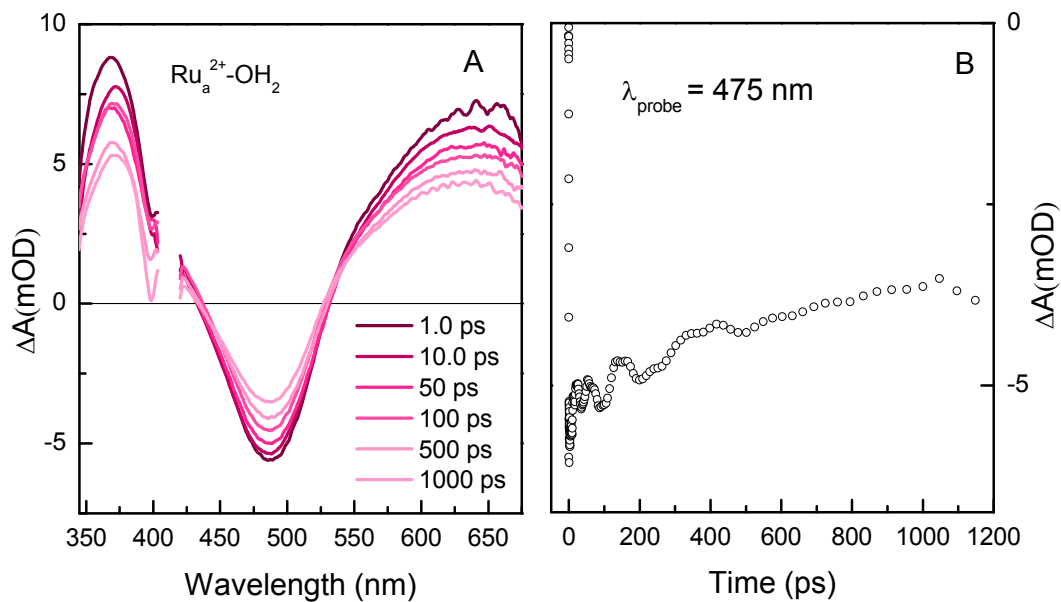


Figure E.2. (A) fsTA of catalyst $\text{Ru}_b^{\text{II}}\text{-OH}_2$ in 0.1 M HNO_3 aqueous solution at different delays with λ_{exc} at 415 nm. (B) The kinetic decay at 475 nm.

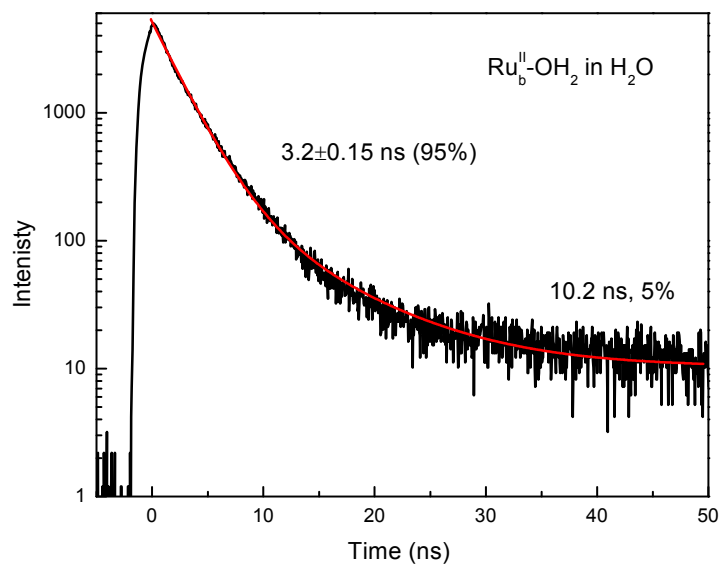


Figure E.3. Time-resolved emission of catalyst, $\text{Ru}_b^{\text{II}}\text{-OH}_2$ in H_2O solution (black) and the fitting (red) with 5% long-lived component likely from the residue of precursor.

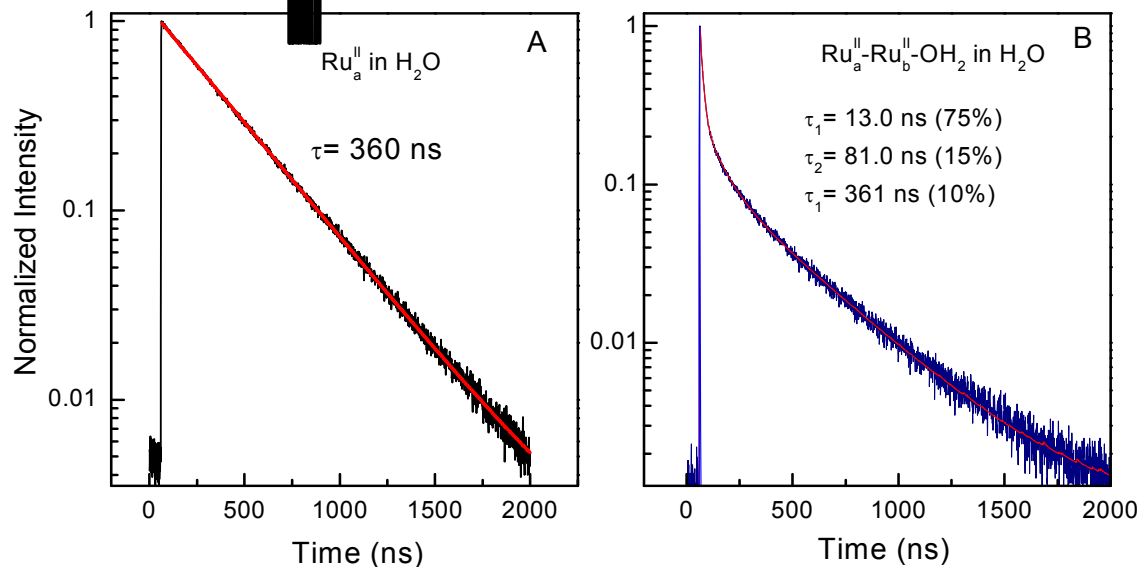


Figure E.4. (A) Time-resolved emission of chromophore, Ru_a^{II}, with λ_{mon} at 630 nm in argon deaerated H₂O solution. (B) Time-resolved emission of assembly, Ru_a^{II}-Ru_b^{II}-OH₂ with λ_{mon} at 630 nm in argon deaerated H₂O solution.

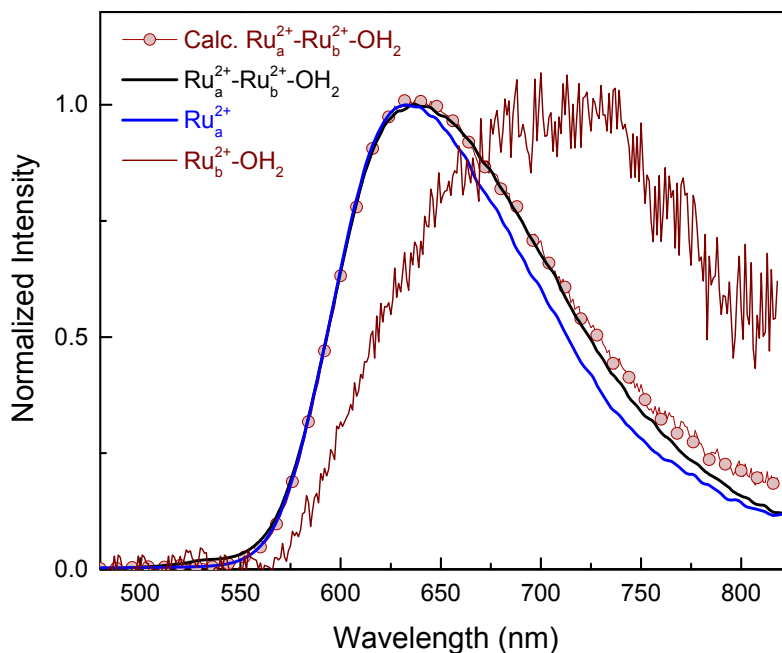


Figure E.5. Steady-state emission of Ru_a^{II} (blue), Ru_a^{II}-Ru_b^{II}-OH₂ (black), Ru_b^{II}-OH₂ (brown), and the calculated emission of Ru_a^{II}-Ru_b^{II}-OH₂ (brown circles) based on the energy transfer

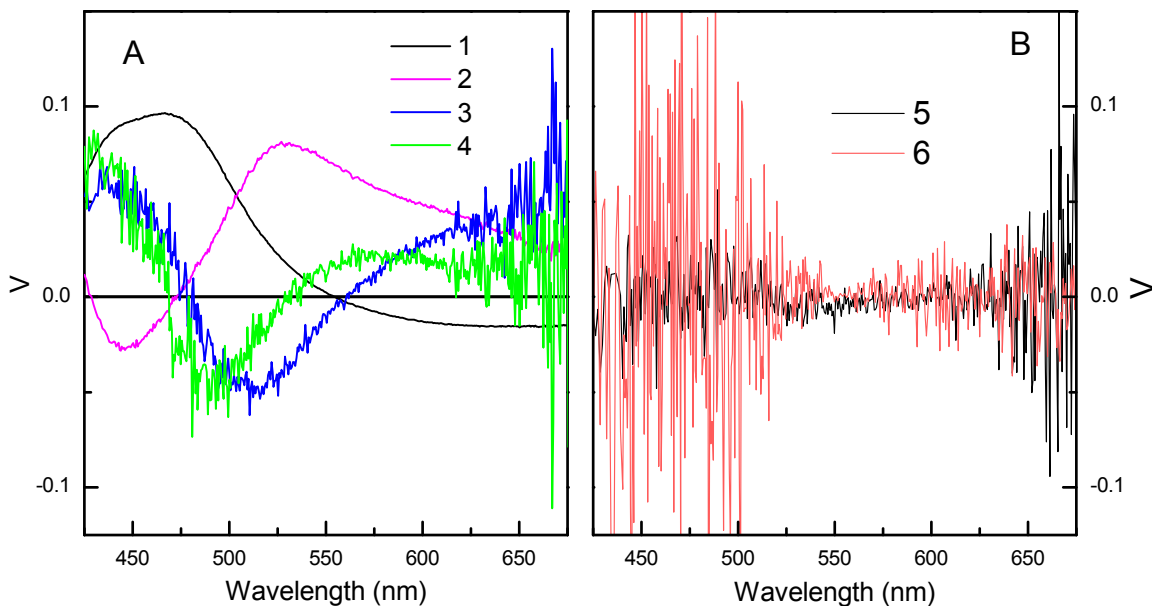


Figure E.6. The first four spectral eigenvectors (V) from Singular value decomposition of the spectral kinetic data matrix Y . (B) The fifth and sixth spectra eigenvectors (V) are random noise.

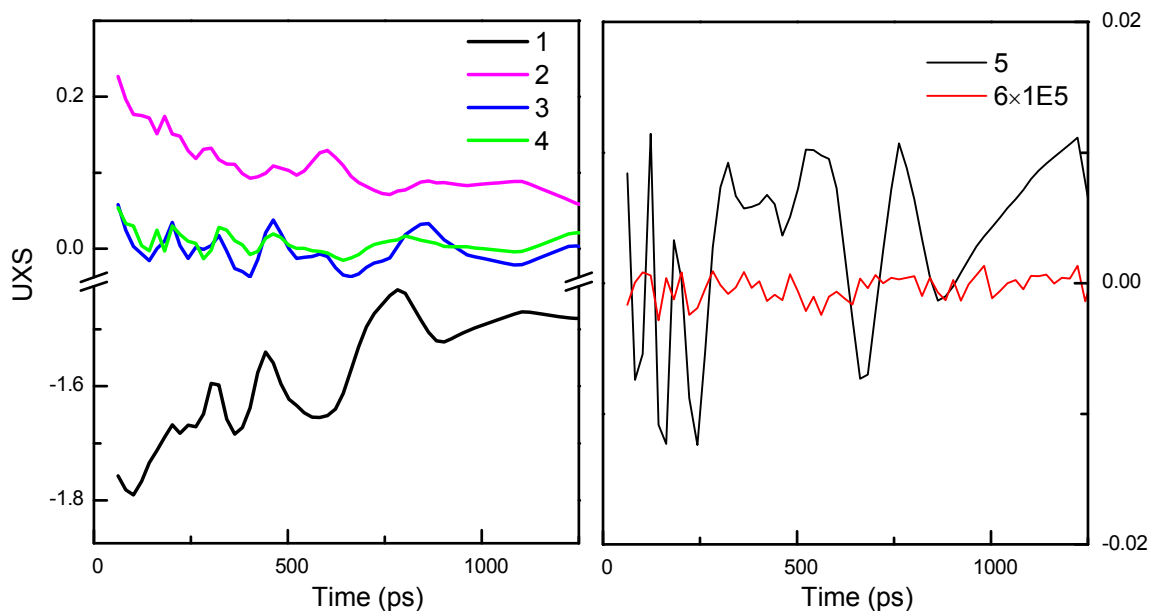


Figure E.7. (A) Associated time domain eigenvectors $U \times S$ for the first four spectral eigenvectors from Singular value decomposition of the spectral-kinetic data matrix Y . (B) Associated time domain eigenvectors $U \times S$ for the fifth and sixth spectral eigenvectors.

APPENDIX F. STABILIZATION OF A RUTHENIUM(II) POLYPYRIDYL DYE ON NANOCRYSTALLINE TiO₂ BY AN ELECTROPOLYMERIZED OVERLAYER

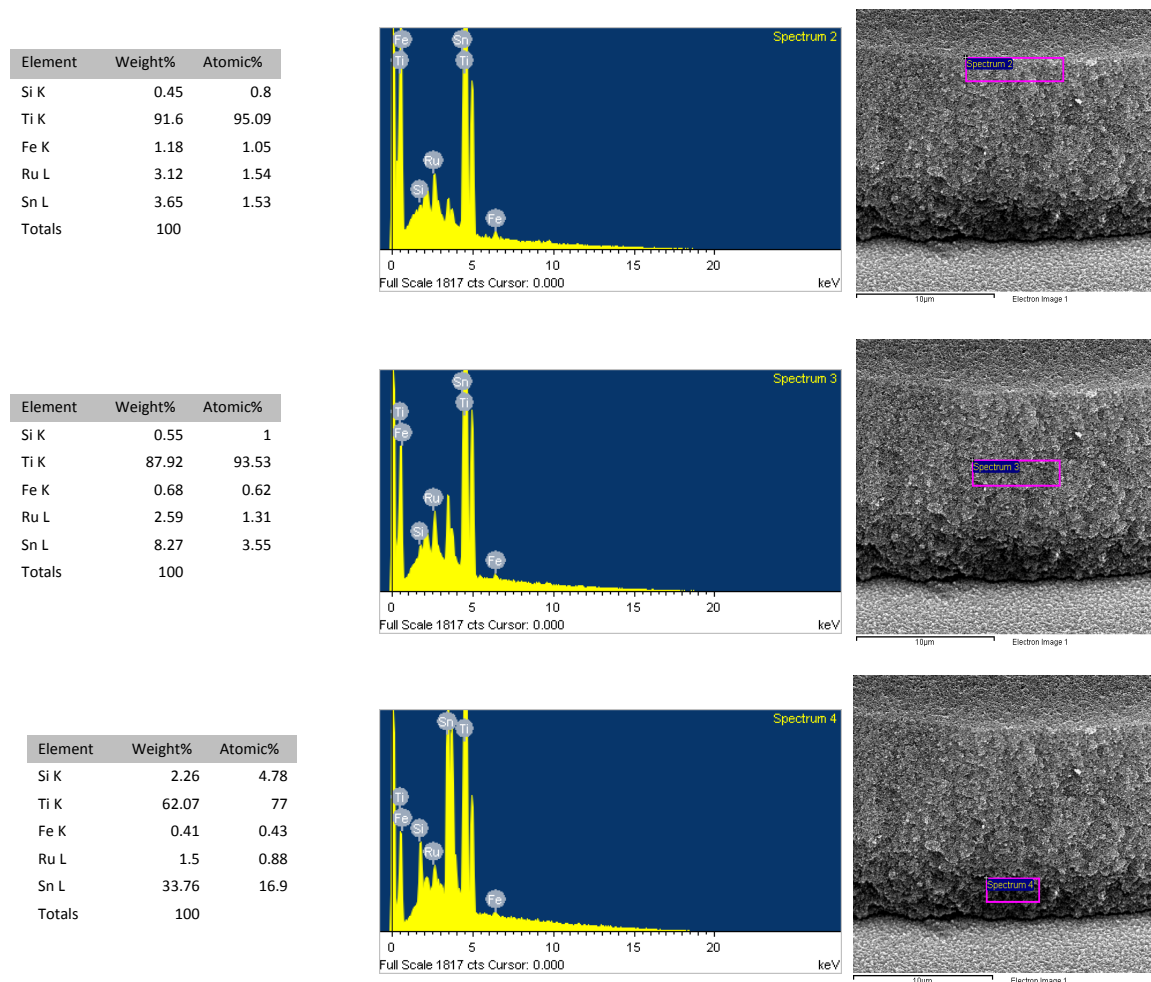


Figure F.1. EDS spectra (middle) and the tabulated results (left) obtained for TiO₂-RuPdvb-*poly*[Fe(v-tpy)₂]²⁺ (50 cycles) at various depths that are indicated by the pink rectangle (far right).

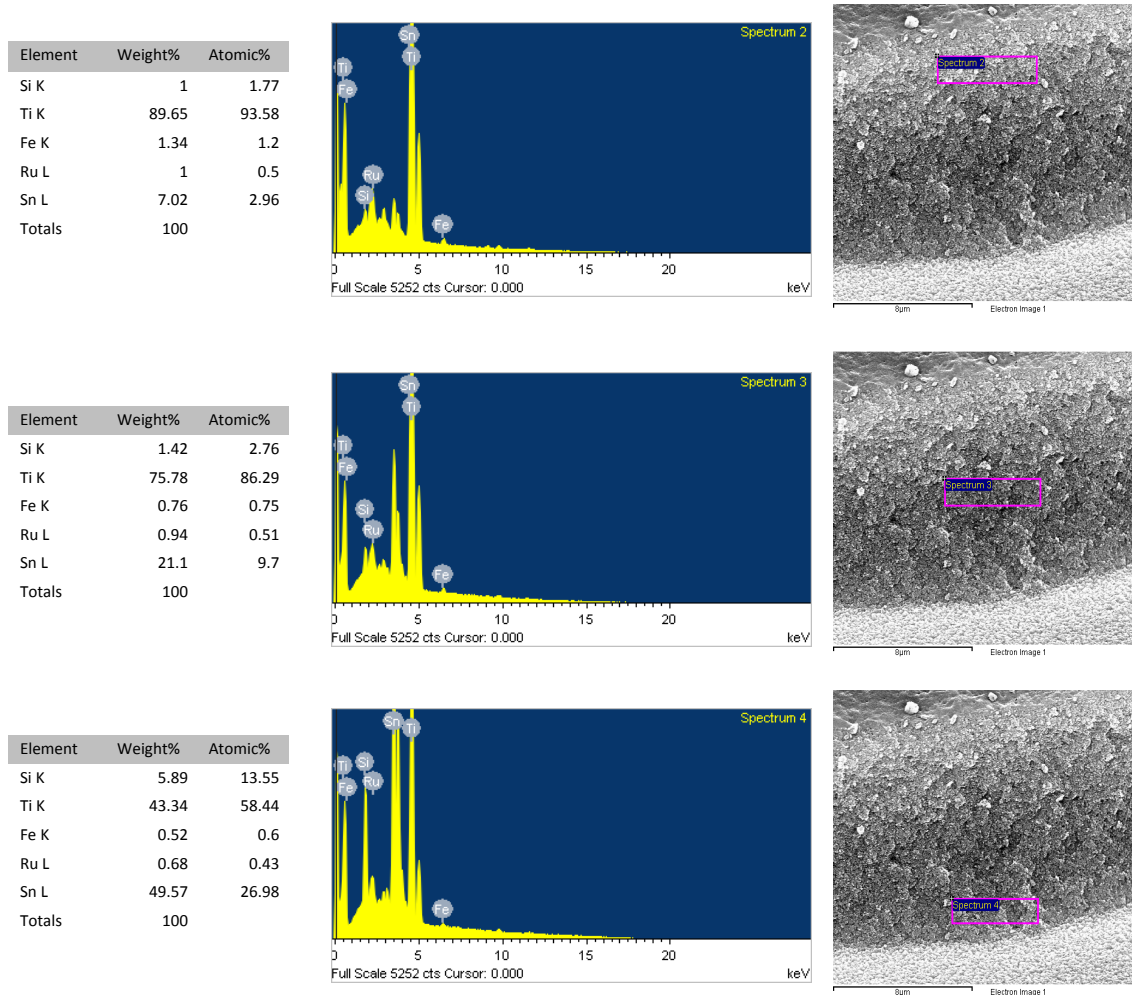


Figure F.2. EDS spectra (middle) and the tabulated results (left) obtained for $\text{TiO}_2\text{-RuPdvb-poly}[\text{Fe}(\text{v-tpy})_2]^{2+}$ (300 cycles) at various depths that are indicated by the pink rectangle (far right).

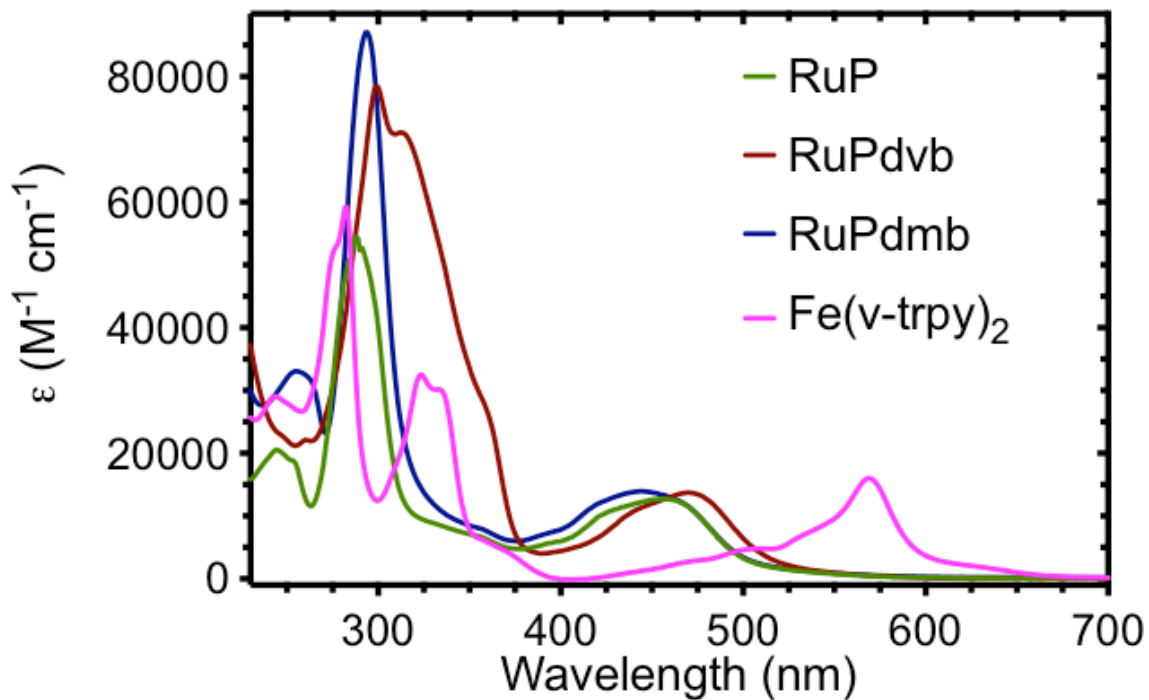


Figure F.3. UV/Vis absorption spectra of **RuP**, **RuPd vb**, **RuPd mb** and **Fe(v-trpy)₂²⁺** in H₂O.

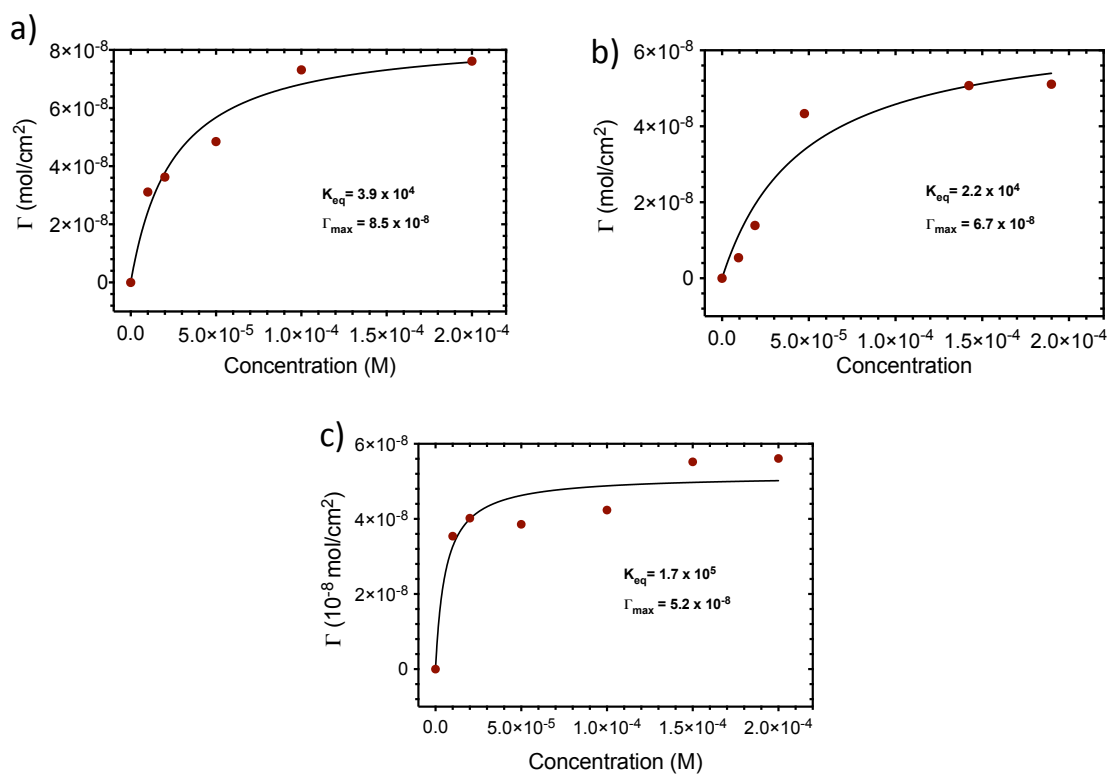


Figure F.4. Absorption isotherms for **RuP** (a), **RuPdvb** (b), and **RuPdmb** (c) on TiO_2 ($\sim 7 \mu\text{m}$) loaded from 10, 20, 50, 100, 150, and 200 μM solutions in methanol. The black lines are the best fits to the Langmuir isotherm equation.

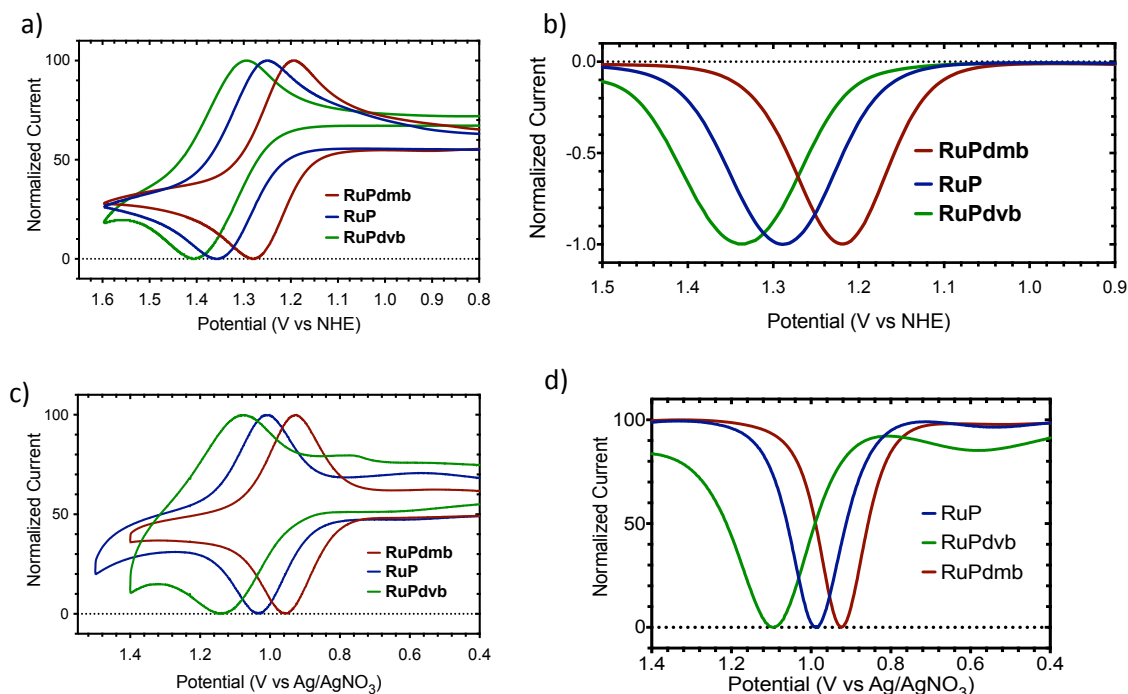


Figure F.5. a,c) Cyclic voltammograms and b,d) square-wave voltammograms of all three chromophores immobilized on TiO_2 as the working electrode, with a Pt counter electrode, and a Ag/AgCl or Ag/AgNO_3 reference electrode in a,b) aqueous 0.1 M HClO_4 and c,d) in MeCN (0.1 M TBAPF_6).

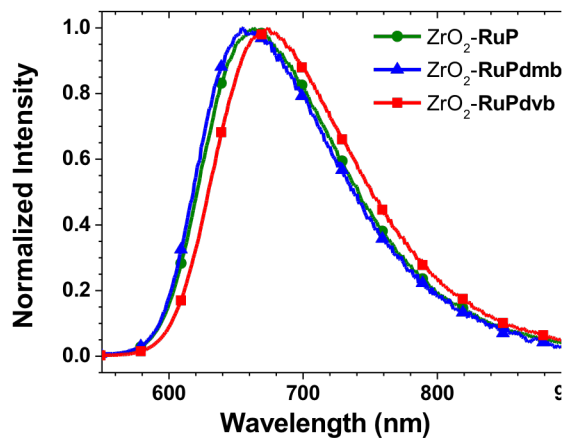


Figure F.6. Emission spectra for **RuP**, **RuPdvb**, and **RuPdmb** on ZrO_2 in Ar deaerated aqueous 0.1 M HClO_4 at room temperature (Excitation at 450 nm).

Table F.1. Emission spectra fitting parameters for the MLCT excited states of RuP, RuPdvb**, and RuPd**mb** on ZrO₂ in 0.1 M HClO₄ aqueous solution.**

Sample	E_0 (cm ⁻¹)	$\Delta v_{1/2}$ (cm ⁻¹)	$\hbar\omega_M$ (cm ⁻¹)	S_M	ΔG_{ES}^a
RuP	15200	1720	1250	1.03	16500
RuPdvb	15100	1650	1250	1.09	16300
RuPdmb	15400	1680	1250	1.08	16600

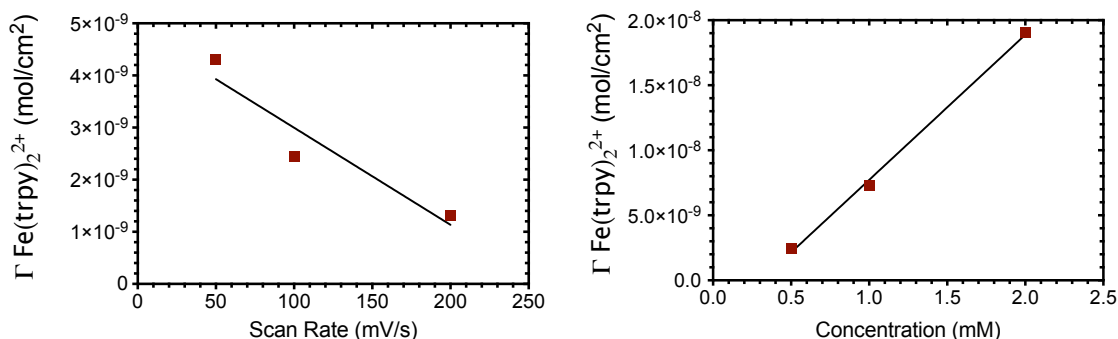


Figure F.7. Fe(v-tpy)₂²⁺ surface coverage on planar FTO as a function of (a) scan rate (in 0.5 mM Fe(v-tpy)₂²⁺) and (b) Fe(v-tpy)₂²⁺ concentration (at 100 mV/s) cycling 10 times from 0 to -1.8 V (vs. Ag/AgNO₃) in in dry acetonitrile with 0.1 M TBAPF₆, Pt counter electrode, and Ag/AgNO₃ reference electrode.

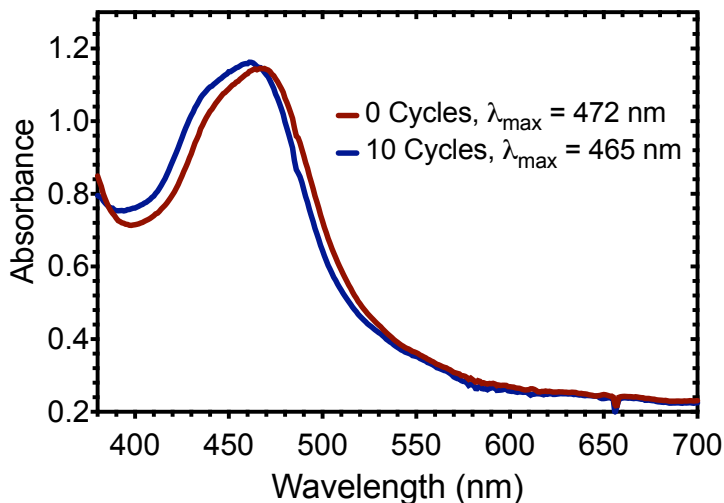


Figure F.8. UV-Visible absorption spectra of TiO₂-RuPdvb** before (red) and after (blue) 10 cycles from 0 to -1.8V (vs Ag/AgNO₃) in an acetonitrile solution of 0.5 mM *p*-divinylbenzene (0.1 M TBAPF₆ electrolyte); Pt counter electrode, and Ag/AgNO₃ reference electrode.**

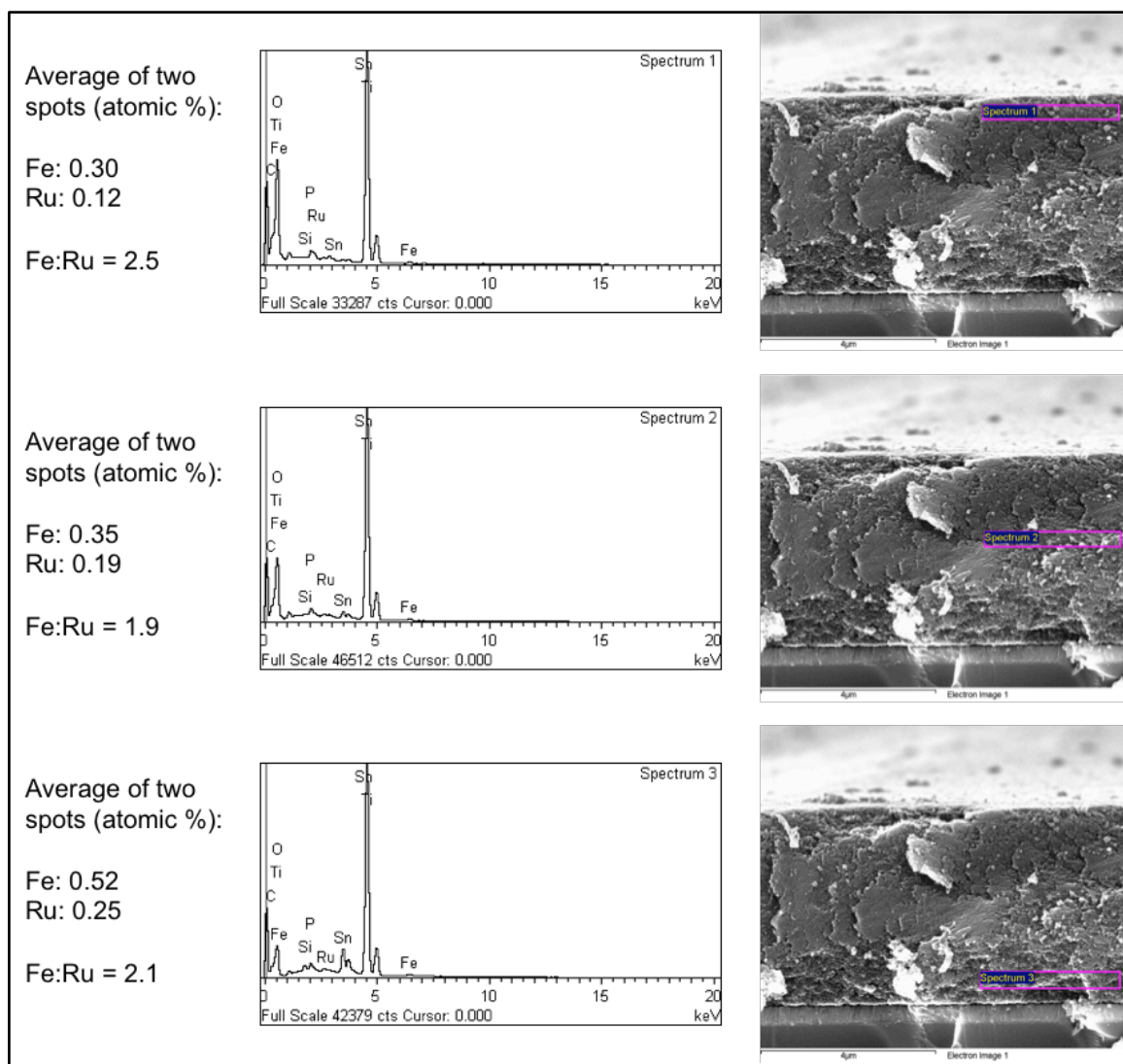


Figure F.9. EDS spectra (middle) and the tabulated results (left) for Fe and Ru obtained for $\text{TiO}_2\text{-RuPdVb-poly}[\text{Fe}(\text{v-tpy})_2]^{2+}$ (50 cycles) at various depths that are indicated by the pink rectangle (far right). This film was formed by soaking a *nano*- $\text{TiO}_2\text{-RuPdVb}$ slide in $[\text{Fe}(\text{v-tpy})_2]^{2+}$ (0.5 mM in 0.1 M TBAPF₆/CH₃CN) for over 24 hours prior to electropolymerization, then stirring during electropolymerization and resting the film for 60 seconds in between each electropolymerization cycle.

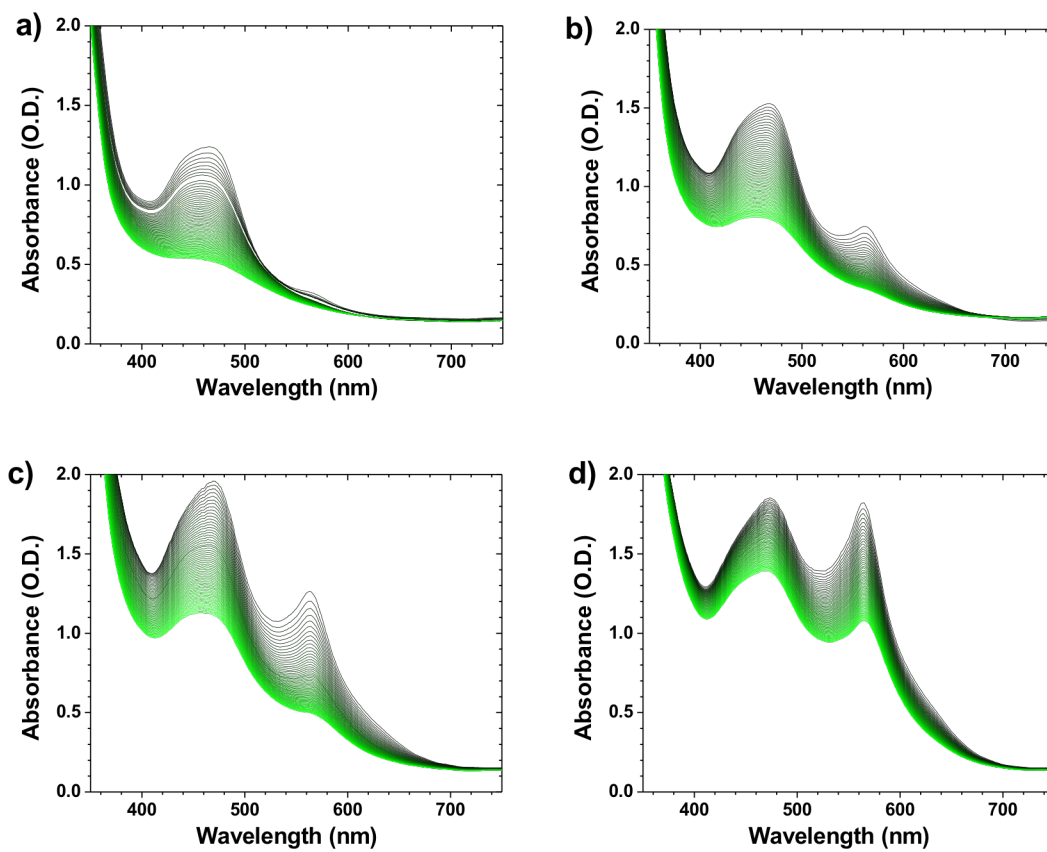


Figure F.10. Changes in the absorption spectrum of $\text{TiO}_2\text{-RuPdvb}$ in aqueous 0.1 M HClO_4 under constant 455 nm irradiation (475 mW/cm^2) after 10 (A), 30 (B), 70 (C) and 150 (D) reductive cycles in an acetonitrile solution containing 0.5 mM $\text{Fe}(\text{v-tpy})_2^{2+}$. (0 hours (black) to 16 hours (green) every 15 minutes).

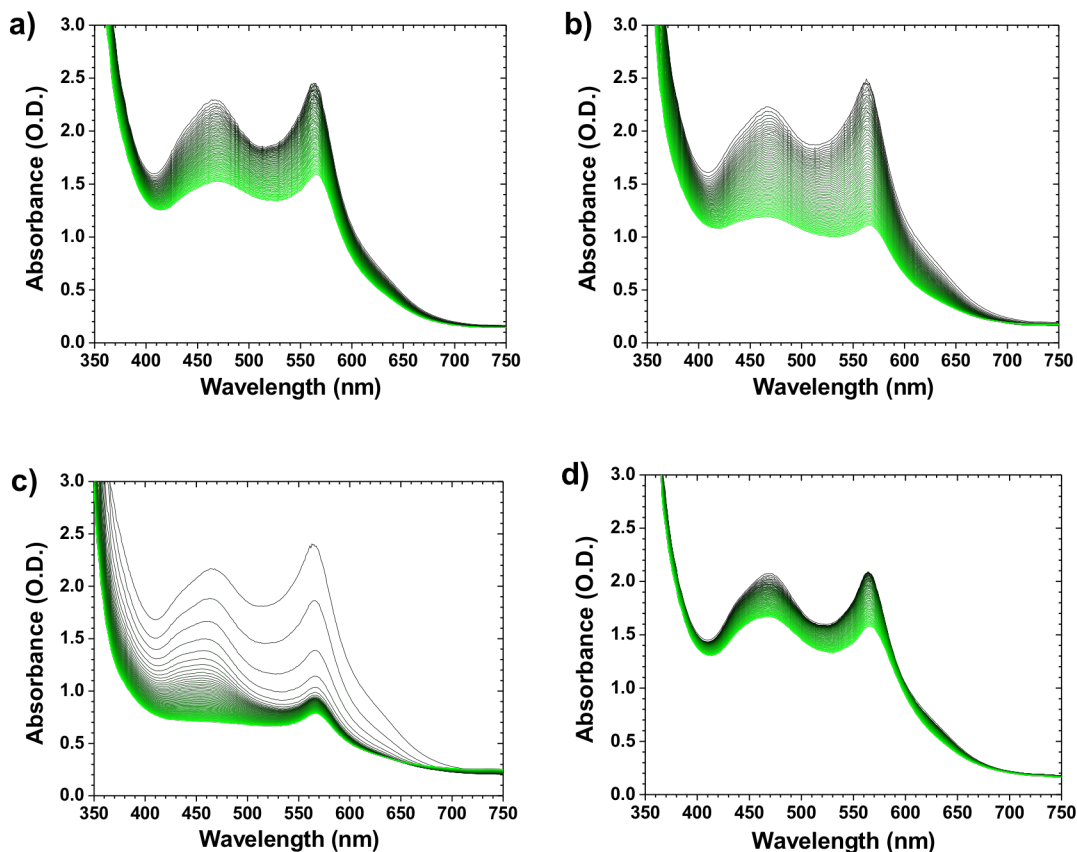


Figure F.11. Changes in the absorption spectrum of $\text{TiO}_2\text{-RuPdvb-polyFe(v-tpy)}_2$ (150 cycles, 1:1.8 Ru:Fe) in (A) H_2O , (B) pH 5 HClO_4 , (C) pH 7 phosphate buffer and (D) MeCN with 0.1 M LiClO_4 under constant 455 nm irradiation (475 mW/cm^2). (0 hours (black) to 16 hours (green) every 15 minutes).

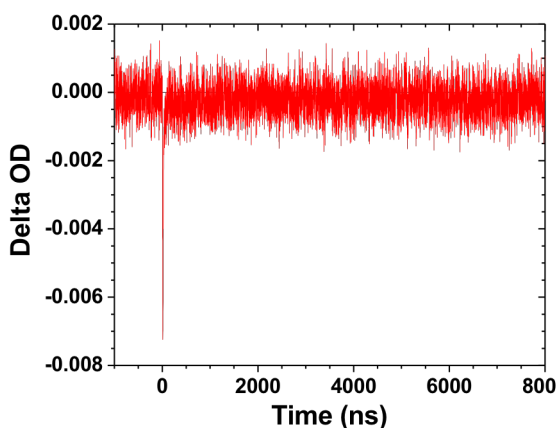


Figure F.12. Absorption-time trace for $\text{TiO}_2\text{-poly-[Fe(v-tpy)}_2\text{]}^{2+}$ (70 cycles) in Ar deaerated 0.1 M HClO_4 aqueous solution measured at 580 nm. Excitation at 450 nm, 5.0 mJ/pulse.

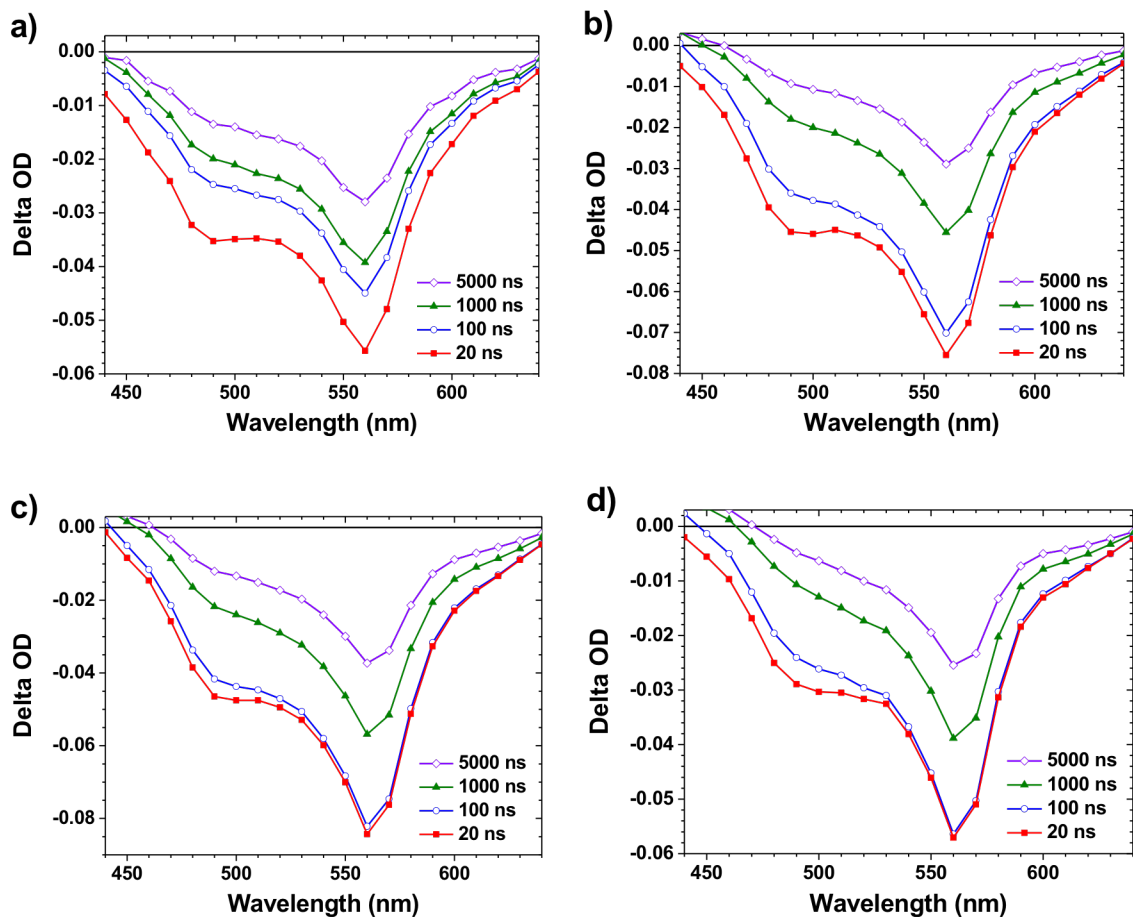


Figure F.13. Time-resolved absorption difference spectra from for $\text{TiO}_2\text{-RuPdvb}$ with (a) 10, (b) 30, (c) 70 and (d) 150 cycles of $[\text{Fe}(\text{v-tpy})_2]^{2+}$ in Ar deaerated aqueous 0.1 M HClO_4 . (Excitation at 532 nm, 5.1 mJ/pulse).

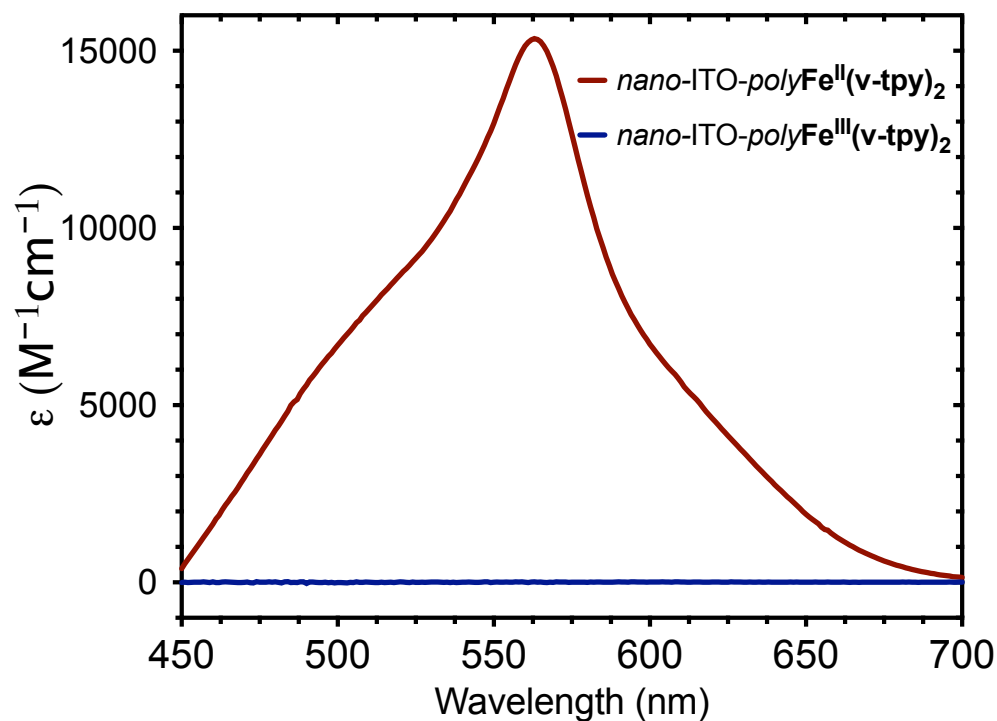


Figure F.14. Spectroelectrochemistry of $\text{poly-}[\text{Fe}(\text{v-tpy})_2]^{2+}$ on *nano*-ITO in 0.1 M HClO_4 with a Pt counter electrode and a Ag/AgCl reference. Potential was slowly increased from 0.2 V (vs NHE) to 1.6 V (vs NHE) to oxidize the Fe^{II} center to Fe^{III} .

APPENDIX G. WATER OXIDATION BY AN ELECTROPOLYMERIZED CATALYST ON DERIVATIZED MESOPOROUS METAL OXIDE ELECTRODES

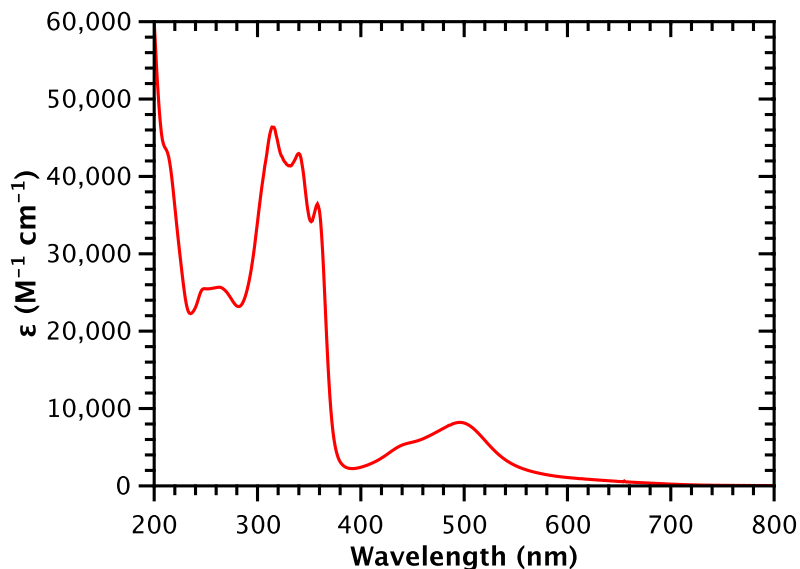


Figure G.1. Absorption spectrum of RuOH_2^{2+} at room temperature in H_2O

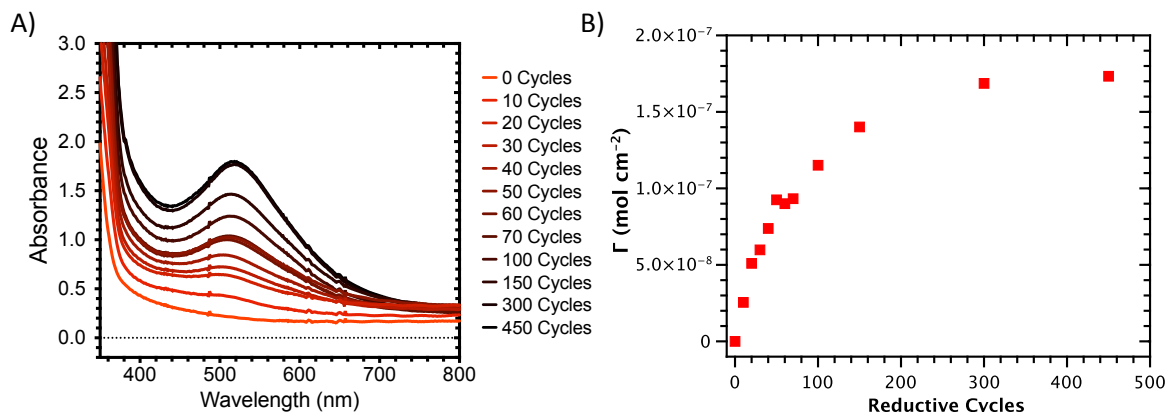


Figure G.2. (A) Changes in UV/visible absorption spectra for $n\text{TiO}_2$ with increasing number of reductive cycles from 0 to -1.8 V (vs Ag/AgNO_3) in PC solution (0.1 M TBAPF_6) of RuOH_2^{2+} (0.5 mM), Pt counter, and Ag/AgNO_3 reference. (B) Surface coverage of polyRuOH_2^{2+} versus the number of reductive cycles.

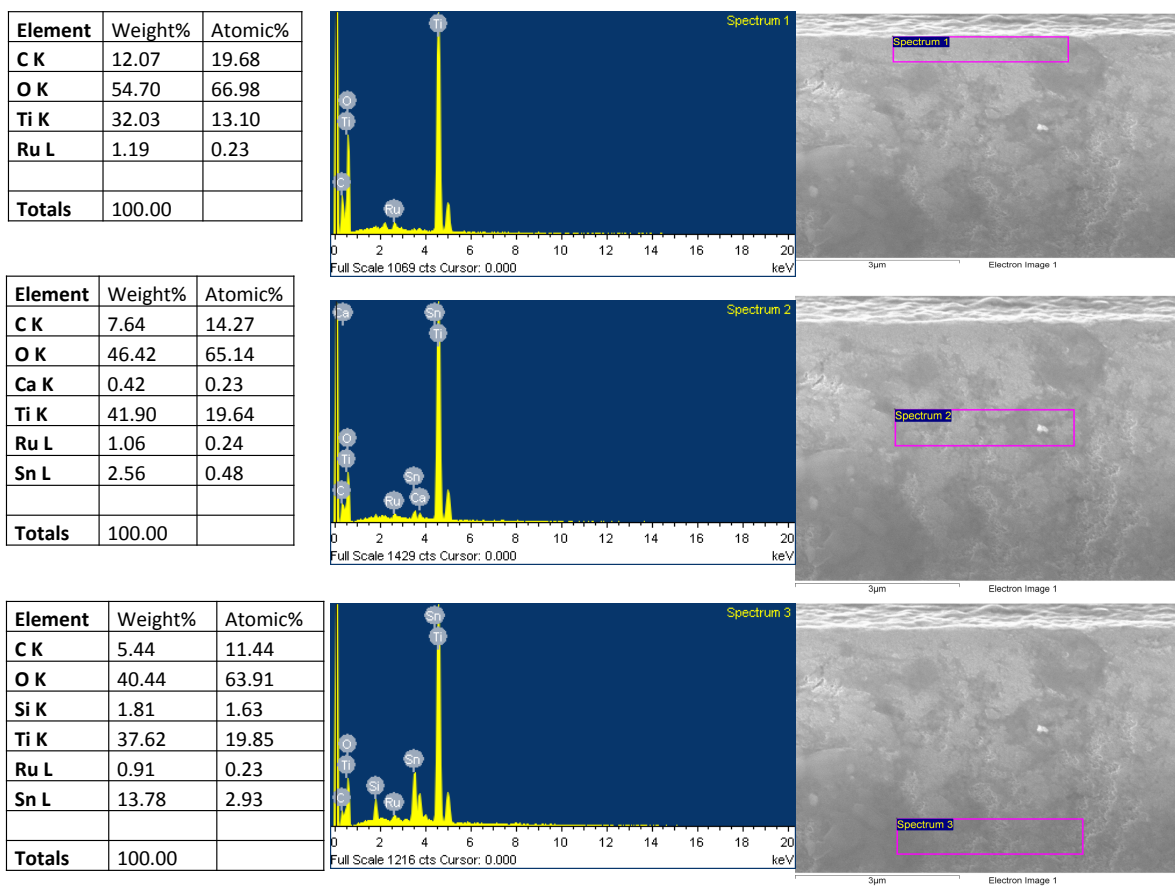


Figure G.3. EDS spectra (middle) and the tabulated results (left) obtained for $n\text{TiO}_2\text{-RuPd}_{\text{vb}}^{2+}\text{-polyRuOH}_2^{2+}$ following 450 reductive cycles at various depths that are indicated by the pink rectangle (right).

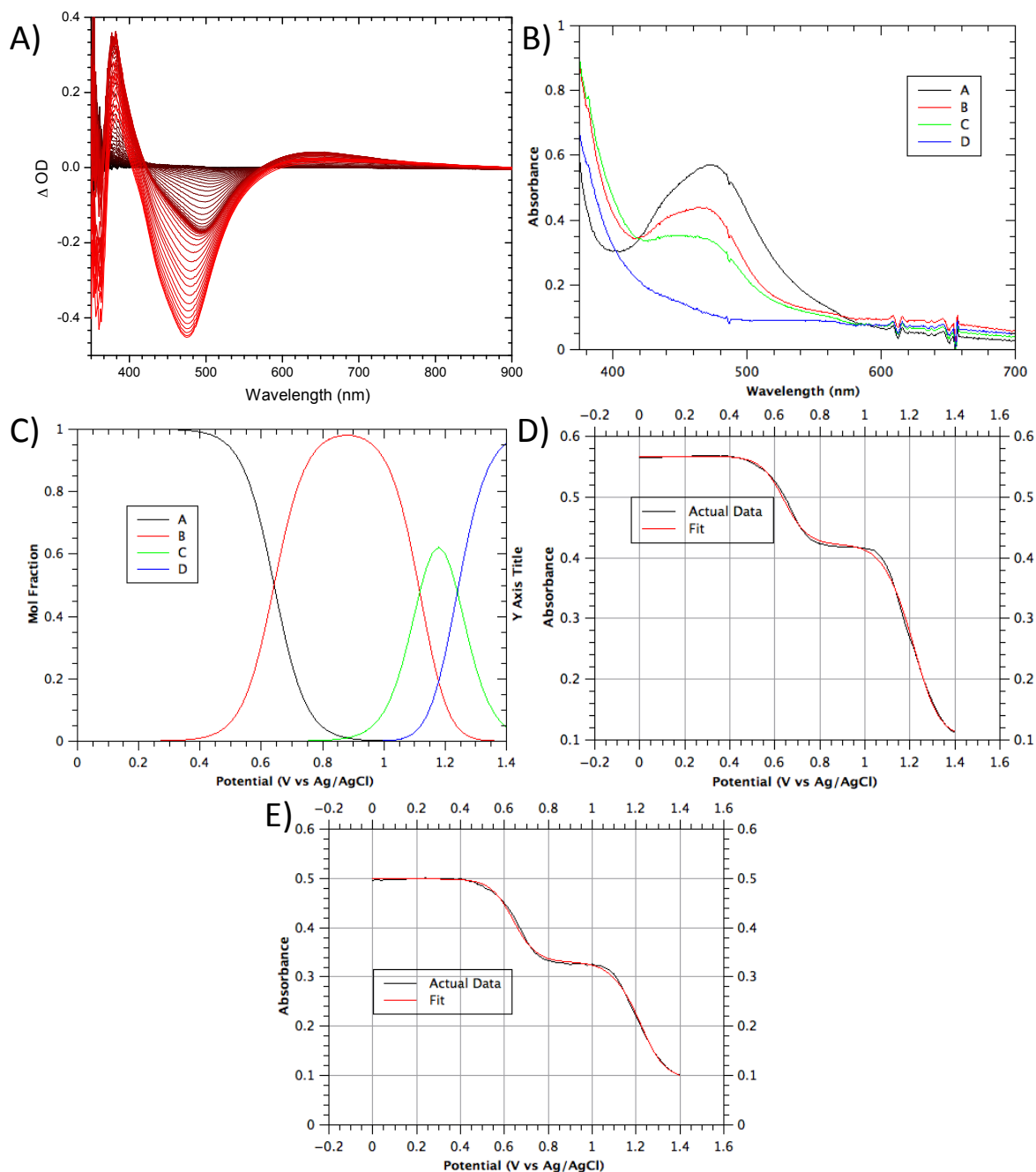


Figure G.4. (A) Spectroelectrochemistry of $n\text{ITO-RuPdvb}^{2+}$ - polyRuOH_2^{2+} in 0.1 M HClO_4 with a Pt-mesh counter electrode and Ag/AgCl reference electrode. The $n\text{ITO-RuPdvb}^{2+}$ - polyRuOH_2^{2+} slide was stepped 0.02 V and held there for 300 s. Following each potential step, a UV/Visible spectrum of the slide was obtained. (B) Calculated spectra for the multiwavelength fit to the kinetic model $A \rightleftharpoons B \rightleftharpoons C \rightleftharpoons D$ with $A = [\text{Ru}^{\text{II}}\text{-Ru}^{\text{II}}\text{-OH}_2]^{4+}$, $B = [\text{Ru}^{\text{II}}\text{-Ru}^{\text{III}}\text{-OH}_2]^{5+}$, $C = [\text{Ru}^{\text{II}}\text{-Ru}^{\text{IV}}\text{=O}]^{5+}$, and $D = [\text{Ru}^{\text{III}}\text{-Ru}^{\text{IV}}\text{=O}]^{6+}$. (C) Calculated concentration profiles versus the applied potential (V vs Ag/AgCl) for the model $A \rightleftharpoons B \rightleftharpoons C \rightleftharpoons D$. (D) Changes in absorption versus potential at 476 nm ($\lambda_{\text{max, MLCT}}$ for RuPdvb^{2+}) in black and calculated fit (red) using the model $A \rightleftharpoons B \rightleftharpoons C \rightleftharpoons D$. (E) Changes in absorption

versus potential at 491 nm ($\lambda_{\text{max, MLCT}}$ for RuOH_2^{2+}) in black and calculated fit (red) using the model $A \rightleftharpoons B \rightleftharpoons C \rightleftharpoons D$. The data was fit using SPECFIT/32 by a series of three sequential Nernstian steps ($A \rightleftharpoons B \rightleftharpoons C \rightleftharpoons D$).

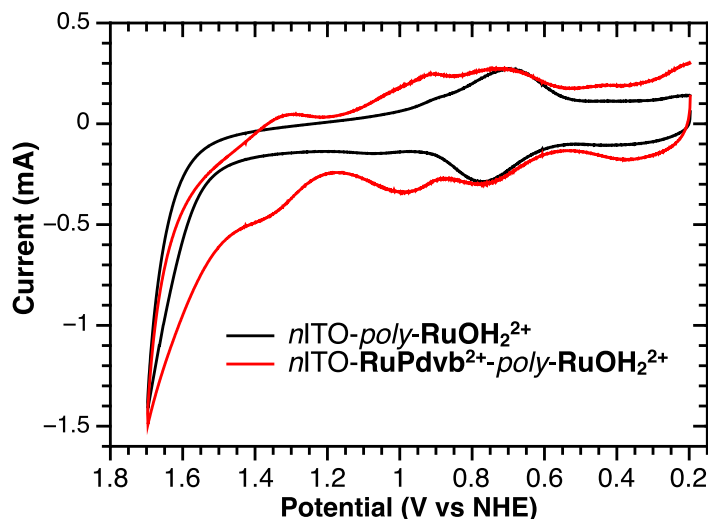


Figure G.5. Cyclic voltammograms at 10 mV/s of $n\text{ITO-RuPdvb}^{2+}\text{-polyRuOH}_2^{2+}$ (red) and $n\text{ITO-polyRuOH}_2^{2+}$ (black) in pH 4.7 aqueous solution (0.1 M HOAc/OAc, 0.5 M NaClO₄); Pt-mesh counter electrode and Ag/AgCl reference electrode. The voltammograms are normalized to the $\text{Ru}^{\text{III}}\text{-OH/Ru}^{\text{II}}\text{-OH}_2$ redox couple for comparison purposes.

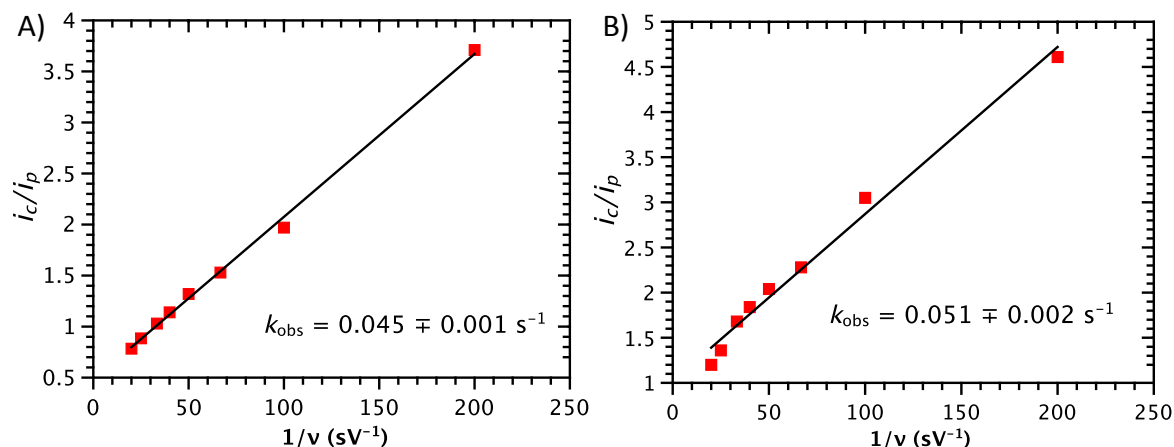


Figure G.6. Plots of i_c/i_p (i_c is the current at 1.7 V vs NHE, i_p is the peak current for the $\text{Ru}^{\text{III}}\text{-OH}_2/\text{Ru}^{\text{II}}\text{-OH}_2$ redox couple) versus $1/v$ for (A) $p\text{FTO-polyRuOH}_2^{2+}$, and (B) $p\text{FTO-RuPdvb}^{2+}\text{-polyRuOH}_2^{2+}$ in pH 4.7 aqueous solution (0.1 M HOAc/OAc, 0.5 M NaClO₄); Pt-mesh counter electrode and Ag/AgCl reference electrode. Surface coverages for each complex were $\sim 1 \times 10^{-10}$ mol cm⁻² at 23 °C. The catalytic rate constant, k_{obs} , for water oxidation was evaluated from the slope of the each plot.

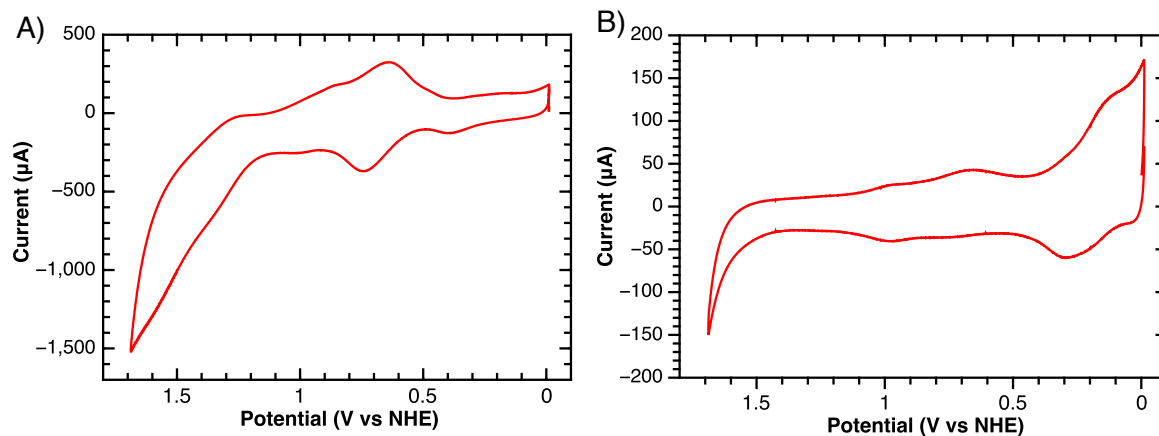


Figure G.7. Cyclic voltammograms of $n\text{ITO-RuPdvb}^{2+}$ - polyRuOH_2^{2+} pre (A) and post 14 hr (B) electrolysis at 1.7 V (vs NHE) in pH 4.7 ((0.1 M HOAc/OAc, 0.5 M NaClO₄); Pt-mesh counter electrode and Ag/AgCl reference electrode. Surface coverages for both RuPdvb^{2+} and polyRuOH_2^{2+} were $\sim 1.1 \times 10^{-8}$ mol cm⁻² pre electrolysis. Following the 14 hr electrolysis, only $\sim 16\%$ of polyRuOH_2^{2+} remained mainly as the peroxide intermediate.

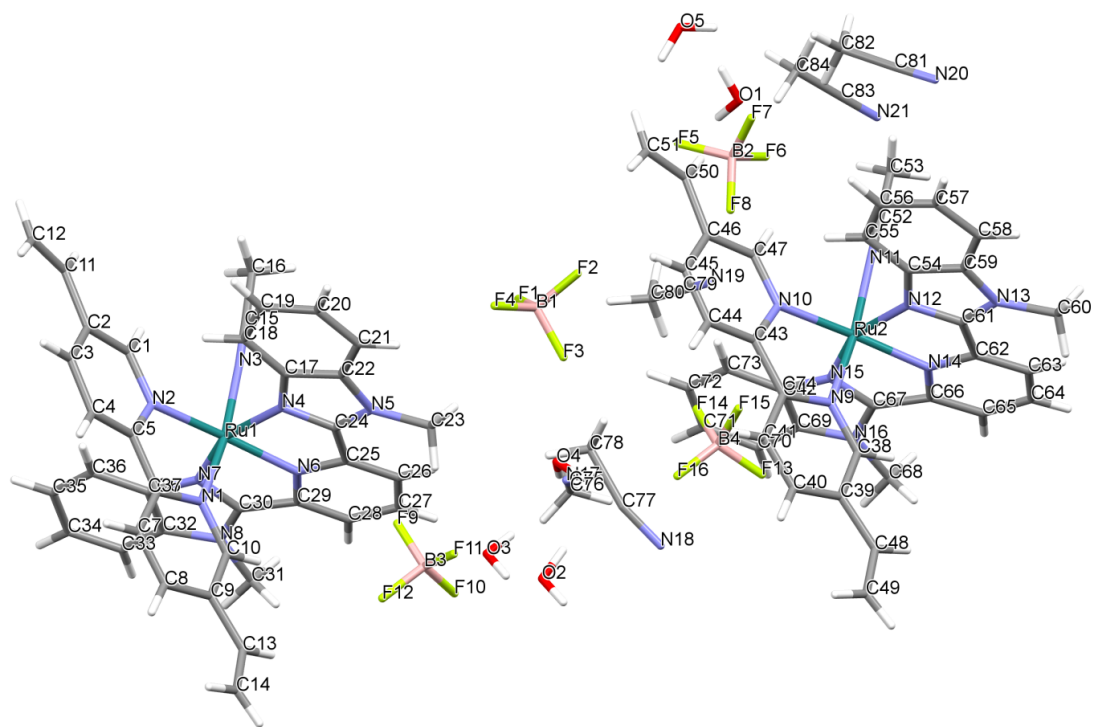


Table S1 Crystal data and structure refinement for DLA-3-216

Identification code	DLA-3-216
Empirical formula	$C_{84}H_{89}B_4F_{16}N_{21}O_5Ru_2$
Formula weight	2022.14
Temperature/K	100.15
Crystal system	monoclinic
Space group	$P2_1/c$
$a/\text{\AA}$	19.0462(4)
$b/\text{\AA}$	25.0845(6)
$c/\text{\AA}$	19.0686(4)
$\alpha/^\circ$	90
$\beta/^\circ$	92.458(2)
$\gamma/^\circ$	90
Volume/ \AA^3	9101.9(3)
Z	4
$\rho_{\text{calc}}/\text{mg}/\text{mm}^3$	1.476
m/mm^{-1}	3.511
F(000)	4128.0
Crystal size/ mm^3	$0.461 \times 0.13 \times 0.042$
2 θ range for data collection	4.644 to 140.488 $^\circ$
Index ranges	$-19 \leq h \leq 23, -29 \leq k \leq 30, -20 \leq l \leq 22$
Reflections collected	66621

Independent reflections 16885[R(int) = 0.0785]
Data/restraints/parameters 16885/18/1197
Goodness-of-fit on F^2 1.014
Final R indexes [$I \geq 2\sigma(I)$] $R_1 = 0.0687$, $wR_2 = 0.1660$
Final R indexes [all data] $R_1 = 0.1148$, $wR_2 = 0.1920$
Largest diff. peak/hole / $e \text{ \AA}^{-3}$ 1.03/-0.69

Table G.1. Fractional Atomic Coordinates ($\times 10^4$) and Equivalent Isotropic Displacement Parameters ($\text{\AA}^2 \times 10^3$) for DLA-3-216. U_{eq} is defined as 1/3 of the trace of the orthogonalised U_{ij} tensor.

Atom	x	y	z	U(eq)
Ru1	9389.8(2)	2275.1(2)	4468.3(2)	30.23(13)
N1	10388(3)	2239(2)	4892(2)	32.1(11)
N2	9470(3)	1473(2)	4712(3)	33.5(11)
N3	8384(3)	2203(2)	4075(3)	32.2(11)
N4	9013(3)	2529(2)	5417(2)	31.6(11)
N5	8751(3)	3226(2)	6092(3)	37.0(12)
N6	9367(2)	3065(2)	4330(3)	30.1(10)
N7	9746(2)	2350(2)	3460(2)	32.0(11)
N8	10076(3)	2896(2)	2611(3)	38.3(12)
C1	8969(3)	1091(3)	4602(3)	38.1(14)
C2	8997(4)	592(3)	4921(4)	40.9(15)
C3	9574(4)	484(3)	5369(3)	44.2(16)
C4	10102(4)	857(3)	5462(3)	40.8(15)
C5	10049(3)	1346(3)	5121(3)	35.3(13)
C6	10586(3)	1764(3)	5181(3)	35.2(13)
C7	11244(3)	1690(3)	5502(3)	40.7(15)
C8	11716(3)	2111(3)	5540(3)	42.5(16)
C9	11526(3)	2609(3)	5255(3)	37.4(14)
C10	10857(3)	2647(3)	4924(3)	35.7(13)
C11	8422(4)	208(3)	4766(4)	51.1(18)
C12	8327(4)	-245(3)	5092(5)	59(2)
C13	11981(3)	3081(3)	5292(4)	47.7(17)
C14	12581(4)	3118(4)	5636(5)	67(2)
C15	7823(3)	2139(3)	3876(3)	36.6(14)
C16	7105(3)	2054(3)	3609(4)	50.2(18)
C17	8783(3)	2334(3)	6047(3)	37.0(14)
C18	8673(3)	1812(3)	6275(3)	39.2(14)
C19	8396(4)	1745(3)	6927(3)	43.7(16)
C20	8253(4)	2189(3)	7357(3)	42.9(16)
C21	8356(3)	2706(3)	7147(3)	37.4(14)
C22	8618(3)	2772(3)	6481(3)	34.4(13)
C23	8692(4)	3773(3)	6353(4)	49.5(17)
C24	8975(3)	3065(3)	5460(3)	34.9(13)
C25	9117(3)	3383(3)	4835(3)	35.1(14)
C26	9008(4)	3919(3)	4727(4)	43.7(16)
C27	9160(4)	4136(3)	4072(4)	47.5(17)
C28	9430(4)	3811(3)	3567(4)	45.3(16)
C29	9535(3)	3275(3)	3704(3)	36.0(14)

C30	9796(3)	2855(3)	3242(3)	36.0(14)
C31	10282(4)	3383(3)	2246(4)	48.5(18)
C32	10210(3)	2389(3)	2386(3)	36.6(14)
C33	10482(4)	2193(3)	1769(4)	45.2(16)
C34	10546(4)	1660(3)	1704(4)	50.3(18)
C35	10329(4)	1297(3)	2239(4)	46.9(17)
C36	10059(3)	1482(3)	2851(3)	40.1(15)
C37	9999(3)	2037(3)	2913(3)	36.3(14)
Ru2	5109.5(2)	7343.9(2)	5400.8(2)	29.41(12)
N9	6128(3)	7325(2)	5793(2)	32.3(11)
N10	5228(3)	6536(2)	5600(3)	31.6(11)
N11	4094(3)	7282.4(19)	5029(2)	29.8(10)
N12	4743(3)	7567(2)	6363(3)	33.7(11)
N13	4433(3)	8232(2)	7066(3)	40.0(13)
N14	5056(3)	8136(2)	5291(3)	33.1(11)
N15	5447(3)	7450(2)	4391(3)	31.3(11)
N16	5775(3)	8011(2)	3557(3)	36.5(12)
C38	6565(3)	7737(3)	5840(3)	37.5(14)
C39	7247(3)	7701(3)	6125(3)	39.6(14)
C40	7474(4)	7212(3)	6373(4)	49.0(18)
C41	7037(4)	6779(3)	6323(4)	47.1(17)
C42	6350(3)	6838(3)	6019(3)	38.2(14)
C43	5855(3)	6396(3)	5942(3)	37.3(14)
C44	5957(4)	5885(3)	6180(4)	45.8(17)
C45	5452(4)	5504(3)	6073(4)	50.6(18)
C46	4829(4)	5634(3)	5702(4)	45.3(16)
C47	4748(3)	6155(3)	5477(3)	36.4(14)
C48	7679(3)	8190(3)	6167(4)	45.8(17)
C49	8321(4)	8232(4)	6439(5)	73(3)
C50	4246(4)	5254(3)	5559(4)	52.3(18)
C51	4212(5)	4774(3)	5819(5)	63(2)
C52	3525(3)	7246(3)	4840(3)	35.5(14)
C53	2804(3)	7206(3)	4576(4)	46.1(17)
C54	4509(3)	7344(3)	6974(3)	36.4(14)
C55	4420(3)	6816(3)	7172(3)	37.5(14)
C56	4141(4)	6723(3)	7825(4)	45.2(16)
C57	3966(3)	7146(3)	8270(3)	48.5(18)
C58	4047(3)	7671(3)	8077(4)	44.2(16)
C59	4320(3)	7762(3)	7421(3)	38.9(15)
C60	4317(4)	8771(3)	7346(4)	47.8(17)
C61	4673(3)	8096(3)	6430(3)	36.8(14)
C62	4806(3)	8434(3)	5821(4)	39.0(15)
C63	4678(4)	8974(3)	5720(4)	47.6(17)

C64	4805(4)	9204(3)	5080(4)	49.4(17)
C65	5081(4)	8902(3)	4549(4)	44.8(16)
C66	5215(3)	8365(3)	4674(3)	35.6(14)
C67	5481(3)	7958(3)	4198(3)	34.1(13)
C68	5949(4)	8519(3)	3204(4)	49.1(18)
C69	5884(3)	7505(3)	3312(3)	35.4(13)
C70	6159(3)	7321(3)	2689(3)	38.6(14)
C71	6187(3)	6779(3)	2600(3)	41.7(15)
C72	5962(3)	6421(3)	3118(3)	38.0(14)
C73	5711(3)	6606(3)	3741(3)	34.7(13)
C74	5680(3)	7152(2)	3836(3)	31.1(13)
F1	5366(5)	4858(3)	1401(4)	145(3)
F2	5060(4)	5121(4)	2481(4)	148(3)
F3	5983(6)	5364(4)	2068(5)	190(5)
F4	5832(7)	4528(4)	2325(5)	219(6)
B1	5556(6)	4944(4)	2061(6)	66(3)
F5	3297(4)	5388(2)	3471(4)	116(3)
F6	2949(3)	6231(2)	3350(3)	70.0(14)
F7	2873(3)	5803(3)	4389(3)	110(3)
F8	3931(3)	6014(3)	3992(3)	97(2)
B2	3260(5)	5862(4)	3816(6)	59(2)
F9	8750(8)	4519(4)	1913(5)	226(7)
F10	9202(4)	5303(2)	1749(3)	111(3)
F11	9056(5)	4987(2)	2827(3)	119(3)
F12	9764(5)	4617(5)	2170(7)	232(7)
B3	9166(6)	4875(4)	2159(5)	58(2)
F13	7913(4)	6646(2)	7888(3)	94(2)
F14	7400(3)	5890(2)	7503(3)	77.9(15)
F15	7496(3)	6080(3)	8664(3)	103(2)
F16	8454(3)	5862(2)	8149(3)	79.6(15)
B4	7837(6)	6131(5)	8005(6)	67(3)
O1	2055(4)	6007(3)	1981(3)	91(2)
O2	9418(8)	5558(8)	4784(8)	294(10)
O3	9770(4)	4787(3)	6002(5)	247(8)
O4	8870(4)	4778(3)	7896(5)	192(6)
O5	3548(4)	4102(3)	9153(5)	109(3)
N17	7953(10)	5525(5)	4077(8)	176(7)
C75	7819(8)	5663(5)	3483(10)	114(6)
C76	7677(7)	5804(6)	2763(9)	145(7)
N18	8802(5)	6266(4)	6208(5)	99(3)
C77	8551(7)	5790(6)	6190(7)	107(4)
C78	8032(12)	5308(8)	6086(12)	246(11)
N19	6443(6)	5234(4)	9575(6)	104(3)

C79	6518(6)	5107(4)	9003(8)	91(4)
C80	6576(7)	4968(5)	8239(7)	126(5)
N20	2979(5)	6447(4)	9831(5)	89(3)
C81	2948(5)	6103(4)	9472(5)	66(2)
C82	2888(6)	5636(4)	8989(6)	88(3)
N21	2687(4)	6640(3)	6156(4)	72(2)
C83	2703(4)	6221(4)	6364(5)	59(2)
C84	2718(6)	5683(4)	6633(8)	122(5)

Table G.2. Anisotropic Displacement Parameters ($\text{\AA}^2 \times 10^3$) for DLA-3-216. The Anisotropic displacement factor exponent takes the form: $2\pi^2[h^2a^{*2}U_{11}+\dots+2hka \times b \times U_{12}]$

Atom	U_{11}	U_{22}	U_{33}	U_{23}	U_{13}	U_{12}
Ru1	26.2(2)	40.2(3)	24.1(2)	3.47(17)	-0.49(16)	-0.24(19)
N1	31(3)	43(3)	22(3)	0.0(19)	1.4(19)	3(2)
N2	34(3)	38(3)	29(3)	6(2)	6(2)	3(2)
N3	32(3)	37(3)	27(3)	2.8(19)	0(2)	4(2)
N4	32(3)	40(3)	23(3)	-2.4(19)	-2.7(19)	-1(2)
N5	35(3)	43(3)	33(3)	-1(2)	5(2)	2(2)
N6	21(2)	36(3)	32(3)	7(2)	-2.4(19)	-2(2)
N7	24(2)	51(3)	21(3)	1(2)	-0.6(18)	0(2)
N8	33(3)	51(3)	31(3)	7(2)	0(2)	-8(2)
C1	40(4)	44(4)	29(3)	2(2)	-5(3)	-3(3)
C2	48(4)	35(3)	41(4)	2(3)	7(3)	0(3)
C3	60(4)	41(4)	32(4)	4(3)	7(3)	7(3)
C4	43(4)	47(4)	33(4)	4(3)	3(3)	4(3)
C5	33(3)	46(4)	27(3)	1(2)	2(2)	7(3)
C6	33(3)	48(4)	25(3)	-2(2)	0(2)	4(3)
C7	40(4)	47(4)	35(4)	3(3)	3(3)	7(3)
C8	33(3)	65(5)	29(4)	2(3)	-8(3)	6(3)
C9	31(3)	59(4)	22(3)	1(3)	0(2)	-2(3)
C10	26(3)	50(4)	31(3)	1(3)	1(2)	-6(3)
C11	51(4)	48(4)	54(5)	0(3)	3(3)	-2(3)
C12	64(5)	45(4)	70(6)	-5(4)	11(4)	-9(4)
C13	33(3)	70(5)	40(4)	-3(3)	-2(3)	-3(3)
C14	48(5)	67(6)	83(7)	-8(4)	-22(4)	-4(4)
C15	31(3)	46(4)	33(3)	1(2)	3(3)	3(3)
C16	31(3)	70(5)	49(5)	0(3)	-3(3)	-2(3)
C17	28(3)	55(4)	28(3)	-2(3)	3(2)	-1(3)
C18	41(4)	46(4)	30(4)	4(3)	1(3)	-2(3)
C19	52(4)	52(4)	28(4)	0(3)	9(3)	-3(3)
C20	50(4)	51(4)	27(3)	2(3)	8(3)	6(3)
C21	38(3)	47(4)	27(3)	-3(3)	-1(2)	2(3)
C22	30(3)	45(4)	28(3)	1(2)	-2(2)	-2(3)
C23	63(5)	49(4)	37(4)	-4(3)	7(3)	2(4)
C24	28(3)	46(4)	31(3)	-1(2)	-1(2)	-2(3)
C25	30(3)	51(4)	24(3)	2(2)	0(2)	2(3)
C26	45(4)	41(4)	46(4)	4(3)	8(3)	-2(3)
C27	60(5)	40(4)	42(4)	9(3)	2(3)	-3(3)

C28	50(4)	47(4)	39(4)	11(3)	2(3)	-9(3)
C29	29(3)	50(4)	29(3)	5(3)	-5(2)	0(3)
C30	33(3)	46(4)	29(3)	9(2)	1(2)	-2(3)
C31	59(5)	49(4)	38(4)	5(3)	12(3)	-12(3)
C32	30(3)	50(4)	30(3)	1(3)	0(2)	-1(3)
C33	43(4)	61(5)	32(4)	5(3)	2(3)	-4(3)
C34	54(4)	66(5)	30(4)	-8(3)	4(3)	1(4)
C35	49(4)	48(4)	43(4)	-4(3)	0(3)	0(3)
C36	37(3)	50(4)	33(4)	3(3)	0(3)	-1(3)
C37	29(3)	49(4)	32(4)	3(3)	0(2)	3(3)
Ru2	29.1(2)	36.0(2)	23.0(2)	1.35(17)	-0.37(16)	-0.63(19)
N9	32(3)	39(3)	25(3)	1.2(19)	0.6(19)	2(2)
N10	34(3)	33(3)	27(3)	2.7(18)	3(2)	1(2)
N11	30(3)	32(3)	27(3)	1.1(18)	3.2(19)	0(2)
N12	29(3)	43(3)	28(3)	-3(2)	-5(2)	-4(2)
N13	40(3)	47(3)	33(3)	-11(2)	-3(2)	2(3)
N14	28(3)	41(3)	31(3)	-5(2)	-1(2)	-3(2)
N15	30(3)	38(3)	26(3)	3.8(19)	0.5(19)	-3(2)
N16	36(3)	41(3)	33(3)	6(2)	1(2)	-8(2)
C38	33(3)	49(4)	31(3)	-3(3)	1(2)	3(3)
C39	39(3)	54(4)	25(3)	-4(3)	1(2)	-1(3)
C40	34(4)	73(5)	40(4)	2(3)	-2(3)	3(3)
C41	44(4)	60(5)	37(4)	5(3)	0(3)	13(3)
C42	37(3)	51(4)	26(3)	4(2)	0(3)	2(3)
C43	41(4)	42(4)	29(3)	3(2)	5(3)	8(3)
C44	40(4)	55(4)	43(4)	13(3)	5(3)	9(3)
C45	57(5)	42(4)	54(5)	9(3)	9(4)	3(3)
C46	54(4)	42(4)	41(4)	4(3)	12(3)	0(3)
C47	40(3)	39(3)	31(3)	0(2)	9(3)	4(3)
C48	35(4)	67(5)	35(4)	-6(3)	-2(3)	-4(3)
C49	53(5)	82(7)	84(7)	-1(5)	-9(5)	-9(5)
C50	60(5)	45(4)	52(5)	-3(3)	8(4)	-3(4)
C51	78(6)	44(5)	66(6)	3(4)	-2(4)	-14(4)
C52	39(4)	44(4)	24(3)	2(2)	3(2)	4(3)
C53	28(3)	69(5)	41(4)	1(3)	-1(3)	-3(3)
C54	27(3)	57(4)	25(3)	-3(3)	-4(2)	4(3)
C55	34(3)	55(4)	24(3)	-5(2)	-3(2)	3(3)
C56	41(4)	61(5)	33(4)	0(3)	1(3)	-3(3)
C57	32(3)	90(6)	24(4)	-3(3)	4(3)	-4(3)
C58	29(3)	67(5)	36(4)	-9(3)	-5(3)	3(3)
C59	32(3)	52(4)	33(4)	-7(3)	-6(2)	-1(3)

C60	48(4)	47(4)	48(4)	-14(3)	-2(3)	3(3)
C61	31(3)	43(4)	36(4)	-5(3)	0(3)	-5(3)
C62	30(3)	43(4)	44(4)	-6(3)	2(3)	-5(3)
C63	48(4)	44(4)	51(5)	-4(3)	8(3)	-2(3)
C64	55(4)	37(4)	57(5)	1(3)	5(3)	-1(3)
C65	48(4)	40(4)	46(4)	1(3)	-5(3)	-8(3)
C66	33(3)	39(3)	35(4)	5(2)	0(3)	-7(3)
C67	27(3)	47(4)	28(3)	8(2)	-7(2)	-1(3)
C68	57(4)	47(4)	44(4)	16(3)	3(3)	-11(3)
C69	34(3)	44(4)	28(3)	5(2)	-1(2)	-2(3)
C70	33(3)	58(4)	25(3)	6(3)	4(2)	-2(3)
C71	40(4)	59(4)	27(3)	3(3)	4(3)	5(3)
C72	36(3)	46(4)	32(4)	-4(3)	1(3)	2(3)
C73	30(3)	47(4)	27(3)	5(2)	2(2)	4(3)
C74	27(3)	42(3)	24(3)	4(2)	-1(2)	0(2)
F1	234(10)	129(7)	68(5)	-27(4)	-28(5)	-55(6)
F2	131(7)	195(9)	122(7)	32(6)	55(5)	53(6)
F3	247(11)	203(10)	124(7)	-90(7)	61(7)	-134(9)
F4	365(16)	134(8)	156(9)	11(6)	1(9)	169(10)
B1	87(8)	52(6)	59(6)	-13(4)	-4(5)	23(5)
F5	121(5)	67(4)	157(7)	-26(4)	-42(5)	12(4)
F6	73(3)	69(3)	69(3)	16(2)	19(3)	7(3)
F7	93(4)	133(6)	106(5)	67(4)	52(4)	37(4)
F8	80(4)	165(6)	45(3)	20(3)	-12(3)	-58(4)
B2	55(5)	47(5)	75(7)	9(4)	21(5)	3(4)
F9	376(17)	190(10)	108(7)	20(6)	-34(9)	-186(11)
F10	248(8)	44(3)	41(3)	4(2)	4(4)	-19(4)
F11	242(9)	66(4)	51(4)	15(3)	35(4)	31(5)
F12	155(9)	297(14)	253(13)	153(11)	105(9)	130(9)
B3	73(7)	47(5)	56(6)	-10(4)	10(5)	6(5)
F13	155(6)	66(4)	59(4)	10(3)	-42(4)	-9(4)
F14	105(4)	74(4)	52(3)	-6(2)	-22(3)	-9(3)
F15	82(4)	155(7)	72(4)	-8(4)	-2(3)	-23(4)
F16	76(4)	77(4)	85(4)	10(3)	-13(3)	-1(3)
B4	53(5)	82(8)	66(7)	-17(5)	-7(5)	-4(5)
O1	120(6)	86(5)	67(5)	-4(4)	13(4)	24(4)
O2	188(14)	510(30)	186(16)	16(17)	6(12)	-103(16)
O3	265(16)	206(14)	262(17)	72(12)	-78(14)	-176(13)
O4	206(12)	88(7)	291(16)	-36(9)	120(11)	-12(8)
O5	62(4)	75(5)	189(9)	-7(5)	-12(5)	-6(4)
N17	300(20)	79(9)	157(14)	-7(8)	84(15)	4(11)

C75	127(11)	56(7)	166(16)	7(8)	73(12)	8(7)
C76	116(11)	134(14)	192(18)	58(12)	67(11)	56(10)
N18	96(6)	92(6)	106(6)	12(5)	-15(5)	9(5)
C77	113(6)	107(6)	102(6)	0(4)	7(4)	-14(4)
C78	249(14)	229(14)	262(14)	-10(9)	51(9)	-23(9)
N19	100(8)	102(8)	110(9)	22(6)	14(7)	31(6)
C79	69(7)	62(7)	144(12)	11(7)	33(8)	2(5)
C80	153(13)	81(9)	148(13)	-36(8)	57(10)	-40(9)
N20	99(7)	83(7)	84(7)	-16(5)	-12(5)	8(5)
C81	64(6)	67(6)	68(6)	1(4)	15(4)	8(5)
C82	119(9)	61(6)	88(8)	-7(5)	45(7)	-5(6)
N21	79(5)	76(6)	62(5)	0(4)	3(4)	7(4)
C83	56(5)	56(5)	67(6)	-2(4)	13(4)	-2(4)
C84	105(9)	57(7)	208(16)	37(8)	53(10)	21(6)

Table G.3. Bond Lengths for DLA-3-216.

Atom	Atom	Length/Å	Atom	Atom	Length/Å
Ru1	N1	2.035(5)	N13	C59	1.382(9)
Ru1	N2	2.069(5)	N13	C60	1.472(8)
Ru1	N3	2.036(5)	N13	C61	1.358(8)
Ru1	N4	2.075(5)	N14	C62	1.358(8)
Ru1	N6	1.998(5)	N14	C66	1.356(8)
Ru1	N7	2.076(5)	N15	C67	1.329(8)
N1	C6	1.359(8)	N15	C74	1.383(7)
N1	C10	1.358(8)	N16	C67	1.374(8)
N2	C1	1.362(8)	N16	C68	1.486(8)
N2	C5	1.360(8)	N16	C69	1.371(8)
N3	C15	1.129(8)	C38	C39	1.389(9)
N4	C17	1.384(7)	C39	C40	1.379(10)
N4	C24	1.350(8)	C39	C48	1.475(10)
N5	C22	1.388(8)	C40	C41	1.369(10)
N5	C23	1.466(8)	C41	C42	1.415(9)
N5	C24	1.357(8)	C42	C43	1.459(9)
N6	C25	1.353(8)	C43	C44	1.371(9)
N6	C29	1.357(8)	C44	C45	1.366(10)
N7	C30	1.338(8)	C45	C46	1.394(10)
N7	C37	1.406(8)	C46	C47	1.382(9)
N8	C30	1.341(8)	C46	C50	1.480(10)
N8	C31	1.468(8)	C48	C49	1.312(10)
N8	C32	1.370(9)	C50	C51	1.305(10)
C1	C2	1.392(9)	C52	C53	1.446(9)
C2	C3	1.390(10)	C54	C55	1.389(9)
C2	C11	1.477(10)	C54	C59	1.407(9)
C3	C4	1.379(10)	C55	C56	1.394(9)
C4	C5	1.391(9)	C56	C57	1.409(10)
C5	C6	1.465(9)	C57	C58	1.378(10)
C6	C7	1.385(9)	C58	C59	1.394(9)
C7	C8	1.386(10)	C61	C62	1.468(9)
C8	C9	1.403(9)	C62	C63	1.390(9)
C9	C10	1.401(8)	C63	C64	1.380(10)
C9	C13	1.467(10)	C64	C65	1.387(10)
C11	C12	1.312(10)	C65	C66	1.390(9)
C13	C14	1.297(10)	C66	C67	1.469(9)
C15	C16	1.456(9)	C69	C70	1.397(8)
C17	C18	1.399(9)	C69	C74	1.402(8)

C17	C22	1.419(9)	C70	C71	1.371(9)
C18	C19	1.381(8)	C71	C72	1.414(9)
C19	C20	1.417(9)	C72	C73	1.381(8)
C20	C21	1.372(9)	C73	C74	1.384(9)
C21	C22	1.394(8)	F1	B1	1.312(12)
C24	C25	1.468(8)	F2	B1	1.339(12)
C25	C26	1.375(9)	F3	B1	1.331(14)
C26	C27	1.405(9)	F4	B1	1.263(12)
C27	C28	1.377(10)	F5	B2	1.362(11)
C28	C29	1.382(9)	F6	B2	1.398(11)
C29	C30	1.472(9)	F7	B2	1.352(10)
C32	C33	1.395(9)	F8	B2	1.362(11)
C32	C37	1.409(9)	F9	B3	1.270(13)
C33	C34	1.349(10)	F10	B3	1.331(11)
C34	C35	1.439(10)	F11	B3	1.330(11)
C35	C36	1.375(9)	F12	B3	1.310(12)
C36	C37	1.402(9)	F13	B4	1.319(13)
Ru2	N9	2.049(5)	F14	B4	1.381(11)
Ru2	N10	2.073(5)	F15	B4	1.446(12)
Ru2	N11	2.038(5)	F16	B4	1.372(12)
Ru2	N12	2.069(5)	N17	C75	1.20(2)
Ru2	N14	2.000(5)	C75	C76	1.43(2)
Ru2	N15	2.074(5)	N18	C77	1.287(15)
N9	C38	1.329(8)	C77	C78	1.57(2)
N9	C42	1.356(8)	N19	C79	1.150(16)
N10	C43	1.381(8)	C79	C80	1.507(17)
N10	C47	1.336(8)	N20	C81	1.100(12)
N11	C52	1.130(8)	C81	C82	1.491(12)
N12	C54	1.383(8)	N21	C83	1.125(11)
N12	C61	1.340(8)	C83	C84	1.443(12)

Table G.4. Bond Angles for DLA-3-216.

Atom	Atom	Atom	Angle/°	Atom	Atom	Atom	Angle/°
N1	Ru1	N2	79.0(2)	C38	N9	Ru2	126.0(4)
N1	Ru1	N3	172.1(2)	C38	N9	C42	119.5(6)
N1	Ru1	N4	91.16(19)	C42	N9	Ru2	114.5(4)
N1	Ru1	N7	91.99(18)	C43	N10	Ru2	114.8(4)
N2	Ru1	N4	97.3(2)	C47	N10	Ru2	126.7(4)
N2	Ru1	N7	105.8(2)	C47	N10	C43	118.3(5)
N3	Ru1	N2	93.2(2)	C52	N11	Ru2	178.2(5)
N3	Ru1	N4	89.61(19)	C54	N12	Ru2	140.4(5)
N3	Ru1	N7	90.36(19)	C61	N12	Ru2	113.0(4)
N4	Ru1	N7	156.9(2)	C61	N12	C54	106.5(5)
N6	Ru1	N1	96.4(2)	C59	N13	C60	125.2(6)
N6	Ru1	N2	173.9(2)	C61	N13	C59	106.8(6)
N6	Ru1	N3	91.43(19)	C61	N13	C60	128.0(6)
N6	Ru1	N4	78.8(2)	C62	N14	Ru2	119.1(4)
N6	Ru1	N7	78.1(2)	C66	N14	Ru2	119.9(4)
C6	N1	Ru1	116.0(4)	C66	N14	C62	120.8(6)
C10	N1	Ru1	125.9(4)	C67	N15	Ru2	113.6(4)
C10	N1	C6	118.1(5)	C67	N15	C74	106.6(5)
C1	N2	Ru1	127.2(4)	C74	N15	Ru2	139.7(4)
C5	N2	Ru1	114.0(4)	C67	N16	C68	126.4(6)
C5	N2	C1	118.0(5)	C69	N16	C67	106.7(5)
C15	N3	Ru1	176.4(5)	C69	N16	C68	126.9(6)
C17	N4	Ru1	141.5(4)	N9	C38	C39	123.3(6)
C24	N4	Ru1	112.3(4)	C38	C39	C48	118.5(6)
C24	N4	C17	106.3(5)	C40	C39	C38	117.7(7)
C22	N5	C23	124.6(6)	C40	C39	C48	123.7(6)
C24	N5	C22	107.6(5)	C41	C40	C39	120.0(7)
C24	N5	C23	127.7(6)	C40	C41	C42	119.7(7)
C25	N6	Ru1	119.8(4)	N9	C42	C41	119.6(6)
C25	N6	C29	120.0(6)	N9	C42	C43	117.4(6)
C29	N6	Ru1	119.8(4)	C41	C42	C43	123.0(6)
C30	N7	Ru1	113.8(4)	N10	C43	C42	113.4(6)
C30	N7	C37	105.6(5)	C44	C43	N10	120.1(6)
C37	N7	Ru1	140.6(5)	C44	C43	C42	126.5(6)
C30	N8	C31	127.9(6)	C45	C44	C43	121.0(7)
C30	N8	C32	107.3(5)	C44	C45	C46	119.4(7)
C32	N8	C31	124.5(6)	C45	C46	C50	123.9(7)
N2	C1	C2	123.5(6)	C47	C46	C45	117.4(7)

C1	C2	C11	119.0(7)	C47	C46	C50	118.7(7)
C3	C2	C1	117.3(6)	N10	C47	C46	123.7(7)
C3	C2	C11	123.7(6)	C49	C48	C39	126.6(8)
C4	C3	C2	119.9(6)	C51	C50	C46	125.1(8)
C3	C4	C5	120.1(6)	N11	C52	C53	178.1(7)
N2	C5	C4	121.0(6)	N12	C54	C55	131.4(6)
N2	C5	C6	115.0(6)	N12	C54	C59	108.0(6)
C4	C5	C6	124.0(6)	C55	C54	C59	120.5(6)
N1	C6	C5	114.5(5)	C54	C55	C56	117.3(6)
N1	C6	C7	121.8(6)	C55	C56	C57	121.4(7)
C7	C6	C5	123.7(6)	C58	C57	C56	121.9(6)
C6	C7	C8	119.6(6)	C57	C58	C59	116.4(6)
C7	C8	C9	120.1(6)	N13	C59	C54	106.8(6)
C8	C9	C13	123.9(6)	N13	C59	C58	130.6(7)
C10	C9	C8	116.7(6)	C58	C59	C54	122.5(7)
C10	C9	C13	119.4(6)	N12	C61	N13	111.9(6)
N1	C10	C9	123.6(6)	N12	C61	C62	118.4(6)
C12	C11	C2	126.0(8)	N13	C61	C62	129.6(6)
C14	C13	C9	126.0(8)	N14	C62	C61	110.4(6)
N3	C15	C16	179.1(7)	N14	C62	C63	119.9(6)
N4	C17	C18	131.1(6)	C63	C62	C61	129.6(6)
N4	C17	C22	108.6(6)	C64	C63	C62	119.5(7)
C18	C17	C22	120.2(6)	C63	C64	C65	120.3(7)
C19	C18	C17	117.5(6)	C64	C65	C66	118.4(7)
C18	C19	C20	121.1(7)	N14	C66	C65	120.9(6)
C21	C20	C19	122.7(6)	N14	C66	C67	109.8(5)
C20	C21	C22	116.1(6)	C65	C66	C67	129.2(6)
N5	C22	C17	105.8(5)	N15	C67	N16	111.4(6)
N5	C22	C21	131.8(6)	N15	C67	C66	118.3(5)
C21	C22	C17	122.4(6)	N16	C67	C66	130.4(6)
N4	C24	N5	111.7(6)	N16	C69	C70	131.5(6)
N4	C24	C25	118.7(6)	N16	C69	C74	107.0(5)
N5	C24	C25	129.4(6)	C70	C69	C74	121.6(6)
N6	C25	C24	109.9(6)	C71	C70	C69	116.8(6)
N6	C25	C26	121.7(6)	C70	C71	C72	121.9(6)
C26	C25	C24	128.4(6)	C73	C72	C71	120.9(6)
C25	C26	C27	118.4(6)	C72	C73	C74	117.6(6)
C28	C27	C26	119.4(7)	N15	C74	C69	108.2(6)
C27	C28	C29	120.0(6)	N15	C74	C73	130.7(5)
N6	C29	C28	120.4(6)	C73	C74	C69	121.1(6)
N6	C29	C30	110.2(6)	F1	B1	F2	117.1(11)

C28	C29	C30	129.3(6)	F1	B1	F3	106.3(10)
N7	C30	N8	112.7(6)	F3	B1	F2	100.3(9)
N7	C30	C29	117.5(5)	F4	B1	F1	109.8(10)
N8	C30	C29	129.7(6)	F4	B1	F2	109.1(11)
N8	C32	C33	132.3(6)	F4	B1	F3	114.0(13)
N8	C32	C37	107.2(6)	F5	B2	F6	107.5(9)
C33	C32	C37	120.5(7)	F7	B2	F5	109.6(8)
C34	C33	C32	117.7(6)	F7	B2	F6	110.8(7)
C33	C34	C35	122.1(7)	F7	B2	F8	111.7(9)
C36	C35	C34	121.1(7)	F8	B2	F5	107.3(8)
C35	C36	C37	116.2(6)	F8	B2	F6	109.8(7)
N7	C37	C32	107.2(6)	F9	B3	F10	113.5(10)
C36	C37	N7	130.5(6)	F9	B3	F11	112.3(10)
C36	C37	C32	122.3(6)	F9	B3	F12	100.7(11)
N9	Ru2	N10	79.4(2)	F11	B3	F10	114.0(8)
N9	Ru2	N12	91.89(19)	F12	B3	F10	109.9(10)
N9	Ru2	N15	90.87(19)	F12	B3	F11	105.2(10)
N10	Ru2	N15	105.06(19)	F13	B4	F14	112.3(10)
N11	Ru2	N9	174.2(2)	F13	B4	F15	106.8(9)
N11	Ru2	N10	94.82(19)	F13	B4	F16	114.6(9)
N11	Ru2	N12	88.75(19)	F14	B4	F15	106.5(8)
N11	Ru2	N15	90.79(18)	F16	B4	F14	114.1(9)
N12	Ru2	N10	98.1(2)	F16	B4	F15	101.3(9)
N12	Ru2	N15	156.8(2)	N17	C75	C76	177.1(16)
N14	Ru2	N9	96.0(2)	N18	C77	C78	162.0(16)
N14	Ru2	N10	174.5(2)	N19	C79	C80	176.0(14)
N14	Ru2	N11	89.7(2)	N20	C81	C82	178.6(12)
N14	Ru2	N12	78.8(2)	N21	C83	C84	179.5(11)
N14	Ru2	N15	78.0(2)				

Table G.5. Torsion Angles for DLA-3-216.

A	B	C	D	Angle/°	A	B	C	D	Angle/°
Ru1	N1	C6	C5	1.8(7)	Ru2	N9	C38	C39	178.6(4)
Ru1	N1	C6	C7	-178.4(5)	Ru2	N9	C42	C41	-177.8(5)
Ru1	N1	C10	C9	176.4(4)	Ru2	N9	C42	C43	1.5(7)
Ru1	N2	C1	C2	-164.6(5)	Ru2	N10	C43	C42	-7.2(6)
Ru1	N2	C5	C4	165.2(5)	Ru2	N10	C43	C44	171.8(5)
Ru1	N2	C5	C6	-13.5(6)	Ru2	N10	C47	C46	-171.6(5)
Ru1	N4	C17	C18	-5.1(12)	Ru2	N12	C54	C55	-1.1(11)
Ru1	N4	C17	C22	178.1(5)	Ru2	N12	C54	C59	-178.4(5)
Ru1	N4	C24	N5	-177.9(4)	Ru2	N12	C61	N13	-180.0(4)
Ru1	N4	C24	C25	6.9(7)	Ru2	N12	C61	C62	4.5(7)
Ru1	N6	C25	C24	6.7(7)	Ru2	N14	C62	C61	5.2(7)
Ru1	N6	C25	C26	-171.6(5)	Ru2	N14	C62	C63	-171.5(5)
Ru1	N6	C29	C28	171.1(5)	Ru2	N14	C66	C65	170.2(5)
Ru1	N6	C29	C30	-6.8(7)	Ru2	N14	C66	C67	-5.9(7)
Ru1	N7	C30	N8	175.3(4)	Ru2	N15	C67	N16	173.7(4)
Ru1	N7	C30	C29	-5.6(7)	Ru2	N15	C67	C66	-6.1(7)
Ru1	N7	C37	C32	-174.2(5)	Ru2	N15	C74	C69	-174.8(5)
Ru1	N7	C37	C36	5.4(11)	Ru2	N15	C74	C73	7.3(11)
N1	C6	C7	C8	0.8(10)	N9	C38	C39	C40	-0.4(9)
N2	C1	C2	C3	-0.5(10)	N9	C38	C39	C48	-178.3(6)
N2	C1	C2	C11	179.8(6)	N9	C42	C43	N10	3.8(8)
N2	C5	C6	N1	7.9(8)	N9	C42	C43	C44	-175.1(6)
N2	C5	C6	C7	-172.0(6)	N10	C43	C44	C45	1.3(10)
N4	C17	C18	C19	-176.0(6)	N12	C54	C55	C56	-177.3(6)
N4	C17	C22	N5	0.3(7)	N12	C54	C59	N13	1.0(7)
N4	C17	C22	C21	178.5(5)	N12	C54	C59	C58	178.6(6)
N4	C24	C25	N6	-8.9(8)	N12	C61	C62	N14	-6.3(8)
N4	C24	C25	C26	169.3(6)	N12	C61	C62	C63	170.0(7)
N5	C24	C25	N6	176.8(6)	N13	C61	C62	N14	179.1(6)
N5	C24	C25	C26	-5.0(11)	N13	C61	C62	C63	-4.5(12)
N6	C25	C26	C27	0.2(10)	N14	C62	C63	C64	0.1(11)
N6	C29	C30	N7	8.0(8)	N14	C66	C67	N15	7.8(8)
N6	C29	C30	N8	-173.2(6)	N14	C66	C67	N16	-172.0(6)
N8	C32	C33	C34	-179.6(7)	N16	C69	C70	C71	-179.0(6)
N8	C32	C37	N7	-0.8(7)	N16	C69	C74	N15	0.3(7)
N8	C32	C37	C36	179.6(6)	N16	C69	C74	C73	178.5(5)
C1	N2	C5	C4	-4.9(9)	C38	N9	C42	C41	2.0(9)
C1	N2	C5	C6	176.4(5)	C38	N9	C42	C43	-178.7(5)
C1	C2	C3	C4	-2.3(10)	C38	C39	C40	C41	1.2(10)
C1	C2	C11	C12	-170.4(8)	C38	C39	C48	C49	177.7(8)

C2 C3 C4 C5 1.5(10)	C39 C40 C41 C42 -0.4(10)
C3 C2 C11 C12 9.8(12)	C40 C39 C48 C49 -0.1(12)
C3 C4 C5 N2 2.3(10)	C40 C41 C42 N9 -1.2(10)
C3 C4 C5 C6 -179.2(6)	C40 C41 C42 C43 179.5(6)
C4 C5 C6 N1 -170.7(6)	C41 C42 C43 N10 -176.9(6)
C4 C5 C6 C7 9.4(10)	C41 C42 C43 C44 4.2(10)
C5 N2 C1 C2 4.1(9)	C42 N9 C38 C39 -1.2(9)
C5 C6 C7 C8 -179.3(6)	C42 C43 C44 C45 -179.8(6)
C6 N1 C10 C9 -1.8(9)	C43 N10 C47 C46 3.2(9)
C6 C7 C8 C9 0.0(10)	C43 C44 C45 C46 1.5(11)
C7 C8 C9 C10 -1.6(9)	C44 C45 C46 C47 -1.9(10)
C7 C8 C9 C13 177.9(6)	C44 C45 C46 C50 -179.7(7)
C8 C9 C10 N1 2.6(9)	C45 C46 C47 N10 -0.5(10)
C8 C9 C13 C14 -6.4(12)	C45 C46 C50 C51 7.4(12)
C10 N1 C6 C5 -179.8(5)	C47 N10 C43 C42 177.4(5)
C10 N1 C6 C7 0.0(9)	C47 N10 C43 C44 -3.6(9)
C10 C9 C13 C14 173.1(8)	C47 C46 C50 C51 -170.4(8)
C11 C2 C3 C4 177.5(6)	C48 C39 C40 C41 179.0(6)
C13 C9 C10 N1 -177.0(5)	C50 C46 C47 N10 177.5(6)
C17 N4 C24 N5 1.6(7)	C54 N12 C61 N13 2.6(7)
C17 N4 C24 C25 -173.7(5)	C54 N12 C61 C62 -172.9(5)
C17 C18 C19 C20 -2.1(10)	C54 C55 C56 C57 -0.9(10)
C18 C17 C22 N5 -176.9(6)	C55 C54 C59 N13 -176.7(5)
C18 C17 C22 C21 1.2(9)	C55 C54 C59 C58 0.9(9)
C18 C19 C20 C21 2.2(11)	C55 C56 C57 C58 1.5(11)
C19 C20 C21 C22 -0.5(10)	C56 C57 C58 C59 -0.9(10)
C20 C21 C22 N5 176.4(7)	C57 C58 C59 N13 176.7(6)
C20 C21 C22 C17 -1.2(9)	C57 C58 C59 C54 -0.3(9)
C22 N5 C24 N4 -1.4(7)	C59 N13 C61 N12 -2.0(7)
C22 N5 C24 C25 173.2(6)	C59 N13 C61 C62 172.9(6)
C22 C17 C18 C19 0.5(9)	C59 C54 C55 C56 -0.2(9)
C23 N5 C22 C17 -176.2(6)	C60 N13 C59 C54 -178.7(6)
C23 N5 C22 C21 5.9(11)	C60 N13 C59 C58 4.0(11)
C23 N5 C24 N4 175.3(6)	C60 N13 C61 N12 177.2(6)
C23 N5 C24 C25 -10.1(11)	C60 N13 C61 C62 -7.9(11)
C24 N4 C17 C18 175.7(7)	C61 N12 C54 C55 175.3(6)
C24 N4 C17 C22 -1.1(7)	C61 N12 C54 C59 -2.1(7)
C24 N5 C22 C17 0.6(7)	C61 N13 C59 C54 0.5(7)
C24 N5 C22 C21 -177.3(6)	C61 N13 C59 C58 -176.8(6)
C24 C25 C26 C27 -177.7(6)	C61 C62 C63 C64 -175.9(7)
C25 N6 C29 C28 -2.2(9)	C62 N14 C66 C65 -4.5(9)
C25 N6 C29 C30 179.9(5)	C62 N14 C66 C67 179.4(5)
C25 C26 C27 C28 -1.7(11)	C62 C63 C64 C65 -2.1(11)

C26 C27 C28 C29 1.3(11)	C63 C64 C65 C66 0.8(11)
C27 C28 C29 N6 0.7(10)	C64 C65 C66 N14 2.5(10)
C27 C28 C29 C30 178.1(7)	C64 C65 C66 C67 177.7(6)
C28 C29 C30 N7 -169.7(6)	C65 C66 C67 N15 -167.9(6)
C28 C29 C30 N8 9.2(12)	C65 C66 C67 N16 12.4(11)
C29 N6 C25 C24 -179.9(5)	C66 N14 C62 C61 179.9(5)
C29 N6 C25 C26 1.8(9)	C66 N14 C62 C63 3.2(9)
C30 N7 C37 C32 1.4(7)	C67 N15 C74 C69 2.4(7)
C30 N7 C37 C36 -179.0(7)	C67 N15 C74 C73 -175.5(6)
C30 N8 C32 C33 178.3(7)	C67 N16 C69 C70 179.1(7)
C30 N8 C32 C37 -0.2(7)	C67 N16 C69 C74 -2.8(7)
C31 N8 C30 N7 -172.6(6)	C68 N16 C67 N15 -174.7(6)
C31 N8 C30 C29 8.5(11)	C68 N16 C67 C66 5.1(10)
C31 N8 C32 C33 -7.6(11)	C68 N16 C69 C70 -1.6(11)
C31 N8 C32 C37 173.9(6)	C68 N16 C69 C74 176.5(6)
C32 N8 C30 N7 1.2(7)	C69 N16 C67 N15 4.6(7)
C32 N8 C30 C29 -177.7(6)	C69 N16 C67 C66 -175.6(6)
C32 C33 C34 C35 1.5(11)	C69 C70 C71 C72 -1.3(10)
C33 C32 C37 N7 -179.5(6)	C70 C69 C74 N15 178.6(6)
C33 C32 C37 C36 0.8(10)	C70 C69 C74 C73 -3.2(9)
C33 C34 C35 C36 -1.5(12)	C70 C71 C72 C73 -0.7(10)
C34 C35 C36 C37 1.0(10)	C71 C72 C73 C74 0.7(9)
C35 C36 C37 N7 179.7(6)	C72 C73 C74 N15 178.9(6)
C35 C36 C37 C32 -0.7(10)	C72 C73 C74 C69 1.2(9)
C37 N7 C30 N8 -1.7(7)	C74 N15 C67 N16 -4.4(7)
C37 N7 C30 C29 177.4(5)	C74 N15 C67 C66 175.8(5)
C37 C32 C33 C34 -1.2(10)	C74 C69 C70 C71 3.2(9)

Table G.6. Hydrogen Atom Coordinates ($\text{\AA}\times 10^4$) and Isotropic Displacement Parameters ($\text{\AA}^2\times 10^3$) for DLA-3-216.

Atom	x	y	z	U(eq)
H1	8579	1170	4292	46
H3	9605	153	5610	53
H4	10501	780	5760	49
H7	11372	1353	5695	49
H8	12169	2062	5760	51
H10	10725	2976	4710	43
H11	8092	298	4398	61
H12A	8644	-352	5464	71
H12B	7940	-467	4955	71
H13	11822	3387	5040	57
H14A	12762	2821	5896	80
H14B	12840	3441	5629	80
H16A	7109	1918	3127	75
H16B	6847	2392	3613	75
H16C	6873	1794	3906	75
H18	8784	1514	5993	47
H19	8300	1396	7090	52
H20	8078	2127	7809	51
H21	8255	3001	7438	45
H23A	8285	3947	6119	74
H23B	9120	3971	6254	74
H23C	8631	3766	6861	74
H26	8833	4137	5087	52
H27	9078	4503	3978	57
H28	9544	3955	3126	54
H31A	10604	3291	1877	73
H31B	10517	3627	2581	73
H31C	9862	3556	2035	73
H33	10617	2426	1407	54
H34	10741	1519	1293	60
H35	10372	924	2168	56
H36	9921	1247	3210	48
H38	6403	8073	5670	45
H40	7935	7175	6580	59
H41	7193	6441	6492	57
H44	6387	5795	6423	55
H45	5524	5153	6249	61
H47	4327	6248	5220	44
H48	7470	8506	5979	55

H49A 8553 7928 6635 88
H49B 8553 8567 6441 88
H50 3868 5368 5254 63
H51A 4579 4645 6126 75
H51B 3819 4554 5701 75
H53A 2779 6979 4158 69
H53B 2626 7563 4454 69
H53C 2516 7051 4938 69
H55 4544 6531 6875 45
H56 4067 6366 7972 54
H57 3788 7068 8716 58
H58 3923 7956 8376 53
H60A 3871 8912 7149 72
H60B 4703 9005 7217 72
H60C 4300 8753 7858 72
H63 4503 9184 6089 57
H64 4704 9571 5004 59
H65 5176 9058 4109 54
H68A 5518 8681 3002 74
H68B 6273 8448 2829 74
H68C 6171 8764 3547 74
H70 6319 7560 2344 46
H71 6362 6640 2178 50
H72 5985 6048 3035 46
H73 5565 6367 4093 42
H1A 2243 5949 1581 136
H1B 1832 5723 2110 136
H2A 9648 5789 5046 441
H2B 8975 5643 4756 441
H3A 9391 4954 5854 371
H4A 9001 5017 8206 288
H4B 8883 4915 7477 288
H3B 10004 4987 6304 288
H5A 3999 4053 9143 164
H5B 3461 4352 9453 164
H76A 8084 5714 2489 218
H76B 7585 6187 2728 218
H76C 7265 5606 2580 218
H78A 7711 5377 5681 369
H78B 7762 5264 6508 369
H78C 8301 4982 6004 369
H80A 6105 4944 8014 189
H80B 6816 4625 8199 189

H80C 6845 5246 8008 189
H82A 3250 5660 8641 132
H82B 2422 5636 8750 132
H82C 2952 5307 9260 132
H84A 2572 5435 6257 183
H84B 2395 5654 7018 183
H84C 3196 5595 6806 183

Experimental

Single crystals of $C_{84}H_{89}B_4F_{16}N_{21}O_5Ru_2$ [DLA-3-216] were grown by solution diffusion of diethyl ether into a $RuOH_2$ solution in CH_3CN resulting in CH_3CN coordination. A suitable crystal was selected and placed on a 'Bruker APEX-II CCD' diffractometer. The crystal was kept at 100.15 K during data collection. Using Olex2 [1], the structure was solved with the olex2.solve [2] structure solution program using Charge Flipping and refined with the ShelXL [3] refinement package using Least Squares minimisation.

O. V. Dolomanov, L. J. Bourhis, R. J. Gildea, J. A. K. Howard and H. Puschmann, OLEX2: a complete structure solution, refinement and analysis program. *J. Appl. Cryst.* (2009). 42, 339-341.

olex2.solve (L.J. Bourhis, O.V. Dolomanov, R.J. Gildea, J.A.K. Howard, H. Puschmann, in preparation, 2011)

SHELXL, G.M. Sheldrick, *Acta Cryst.* (2008). A64, 112-122

Crystal structure determination of **[DLA-3-216]**

Crystal Data for $C_{84}H_{89}B_4F_{16}N_{21}O_5Ru_2$ ($M=2022.14$): monoclinic, space group $P2_1/c$ (no. 14), $a = 19.0462(4) \text{ \AA}$, $b = 25.0845(6) \text{ \AA}$, $c = 19.0686(4) \text{ \AA}$, $\beta = 92.458(2)^\circ$, $V = 9101.9(3) \text{ \AA}^3$, $Z = 4$, $T = 100.15 \text{ K}$, $\mu(\text{CuK}\alpha) = 3.511 \text{ mm}^{-1}$, $D_{\text{calc}} = 1.476 \text{ g/mm}^3$, 66621 reflections measured ($4.644 \leq 2\Theta \leq 140.488$), 16885 unique ($R_{\text{int}} = 0.0785$) which were used in all calculations. The final R_1 was 0.0687 ($I > 2\sigma(I)$) and wR_2 was 0.1920 (all data).

This report has been created with Olex2, compiled on Apr 9 2013 14:10:59. Please let us know if there are any errors or if you would like to have additional features.

REFERENCES

- (1) *Annual Energy Outlook*, US Dept of Energy, Washington, DC, 2013.
- (2) Lewis, N. S.; Nocera, D. G. *Proc.Natl.Acad.Sci.U.S.A.* **2006**, *103*, 15729.
- (3) Shafiee, S.; Topal, E. *Energy Policy* **2009**, *37*, 181.
- (4) Dresselhaus, M. S.; Thomas, I. L. *Nature (London, United Kingdom)* **2001**, *414*, 332.
- (5) Murray, J.; King, D. *Nature (London, United Kingdom)* **2012**, *481*, 433.
- (6) Sigman, D. M.; Hain, M. P.; Haug, G. H. *Nature (London, United Kingdom)* **2010**, *466*, 47.
- (7) Brecker, D. O.; Sharp, Z. D.; McFadden, L. D. *Proc. Natl. Acad. Sci. USA* **2010**, *107*, 576.
- (8) Petit, J. R.; Jouzel, J.; Raynaud, D.; Barkov, N. I.; Barnola, J. M.; Basile, I.; Bender, M.; Chappellaz, J.; Davis, M.; Delaygue, G.; Delmotte, M.; Kotlyakov, V. M.; Legrand, M.; Lipenkov, V. Y.; Lorius, C.; Pepin, L.; Ritz, C.; Saltzman, E.; Stievenard, M. *Nature (London)* **1999**, *399*, 429.
- (9) Siegenthaler, U.; Stocker, T. F.; Monnin, E.; Luethi, D.; Schwander, J.; Stauffer, B.; Raynaud, D.; Barnola, J.-M.; Fischer, H.; Masson-Delmotte, V.; Jouzel, J. *Science* **2005**, *310*, 1313.
- (10) Wigley, T. M. L.; Richels, R.; Edmonds, J. A. *Nature (London)* **1996**, *379*, 240.
- (11) Bak, T.; Nowotny, J.; Rekas, M.; Sorrell, C. C. *Int. J. Hydrogen Energy* **2002**, *27*, 991.
- (12) Valentine, K. ThinkProgress, 2013.
- (13) Christensen, J.; Albertus, P.; Sanchez-Carrera, R. S.; Lohmann, T.; Kozinsky, B.; Liedtke, R.; Ahmed, J.; Kojic, A. *J. Electrochem. Soc.* **2012**, *159*, R1.

- (14) Bruce, P. G.; Freunberger, S. A.; Hardwick, L. J.; Tarascon, J.-M. *Nature Materials* **2012**, *11*, 19.
- (15) Gao, M.-R.; Xu, Y.-F.; Jiang, J.; Yu, S.-H. *Chem. Soc. Rev.* **2013**, *42*, 2986.
- (16) Lu, Y.-C.; Gallant, B. M.; Kwabi, D. G.; Harding, J. R.; Mitchell, R. R.; Whittingham, M. S.; Shao-Horn, Y. *Energy Environ. Sci.* **2013**, *6*, 750.
- (17) Shao, Y.; Park, S.; Xiao, J.; Zhang, J.-G.; Wang, Y.; Liu, J. *ACS Catal.* **2012**, *2*, 844.
- (18) Wang, W.; Luo, Q.; Li, B.; Wei, X.; Li, L.; Yang, Z. *Adv. Funct. Mater.* **2013**, *23*, 970.
- (19) Seh, Z. W.; Li, W.; Cha, J. J.; Zheng, G.; Yang, Y.; McDowell, M. T.; Hsu, P.-C.; Cui, Y. *Nat. Commun.* **2013**, *4*, ncomms2327.
- (20) Renger, G. *Photosynth. Res.* **2007**, *92*, 407.
- (21) Ferreira, K. N.; Iverson, T. M.; Maghlaoui, K.; Barber, J.; Iwata, S. *Science* **2004**, *303*, 1831.
- (22) Barber, J. *Photosynth. Res.* **2004**, *80*, 137.
- (23) Umena, Y.; Kawakami, K.; Shen, J.-R.; Kamiya, N. *Nature (London, United Kingdom)* **2011**, *473*, 55.
- (24) Song, W.; Chen, Z.; Glasson, C. R.; Hanson, K.; Lou, H.; Norris, M. R.; Ashford, D. L.; Concepcion, J. J.; Brennaman, M. K.; Meyer, T. J. *ChemPhysChem* **2012**, *13*, 2882.
- (25) Zhu, X.-G.; Long, S. P.; Ort, D. R. *Annual Review of Plant Biology* **2010**, *61*, 235.
- (26) Wijffels, R. H.; Barbosa, M. J. *Science* **2010**, *329*, 796.
- (27) Blankenship, R. E.; Tiede, D. M.; Barber, J.; Brudvig, G. W.; Fleming, G.; Ghirardi, M.; Gunner, M. R.; Junge, W.; Kramer, D. M.; Melis, A.; Moore, T. A.; Moser, C. C.;

Nocera, D. G.; Nozik, A. J.; Ort, D. R.; Parson, W. W.; Prince, R. C.; Sayre, R. T. *Science* **2011**, *332*, 805.

(28) Reece, S. Y.; Hamel, J. A.; Sung, K.; Jarvi, T. D.; Esswein, A. J.; Pijpers, J. J. H.; Nocera, D. G. *Science* **2011**, *334*, 645.

(29) Gust, D.; Moore, T. A.; Moore, A. L. *Acc.Chem.Res.* **2009**, *42*, 1890.

(30) Gilbert, J. A.; Eggleston, D. S.; Murphy, W. R., Jr.; Geselowitz, D. A.; Gersten, S. W.; Hodgson, D. J.; Meyer, T. J. *J. Am. Chem. Soc.* **1985**, *107*, 3855.

(31) Yagi, M.; Kaneko, M. *Chem. Rev. (Washington, D. C.)* **2001**, *101*, 21.

(32) Meyer, T. J.; Huynh, M. H. V.; Thorp, H. H. *Angew.Chem., Int.Ed.* **2007**, *46*, 5284.

(33) Concepcion, J. J.; Jurss, J. W.; Norris, M. R.; Chen, Z. F.; Templeton, J. L.; Meyer, T. J. *Inorg. Chem.* **2010**, *49*, 1277.

(34) Concepcion, J. J.; Jurss, J. W.; Templeton, J. L.; Meyer, T. J. *J. Am. Chem. Soc.* **2008**, *130*, 16462.

(35) Concepcion, J. J.; Tsai, M. K.; Muckerman, J. T.; Meyer, T. J. *J. Am. Chem. Soc.* **2010**, *132*, 1545.

(36) Hurst, J. K.; Cape, J. L.; Clark, A. E.; Das, S.; Qin, C. *Inorg. Chem.* **2008**, *47*, 1753.

(37) Brimblecombe, R.; Dismukes, G. C.; Swiegers, G. F.; Spiccia, L. *Dalton Transactions* **2009**, 9374.

(38) Weinberg, D. R.; Gagliardi, C. J.; Hull, J. F.; Murphy, C. F.; Kent, C. A.; Westlake, B. C.; Paul, A.; Ess, D. H.; McCafferty, D. G.; Meyer, T. J. *Chem. Rev. (Washington, DC, U. S.)* **2012**, *112*, 4016.

(39) Huynh, M. H. V.; Meyer, T. J. *Chem. Rev.* **2007**, *107*, 5004.

- (40) Cukier, R. I.; Nocera, D. G. *Annu. Rev. Phys. Chem.* **1998**, *49*, 337.
- (41) Mayer, J. M. *Annu. Rev. Phys. Chem.* **2004**, *55*, 363.
- (42) Concepcion, J. J.; Jurss, J. W.; Brennaman, M. K.; Hoertz, P. G.; Patrocínio, A. O. T.; Murakami Iha, N. Y.; Templeton, J. L.; Meyer, T. J. *Acc.Chem.Res.* **2009**, *42*, 1954.
- (43) Fujishima, A.; Honda, K. *Nature (London)* **1972**, *238*, 37.
- (44) Chen, X.; Shen, S.; Guo, L.; Mao, S. S. *Chem. Rev. (Washington, DC, U. S.)* **2010**, *110*, 6503.
- (45) Kudo, A.; Kato, H.; Tsuji, I. *Chem. Lett.* **2004**, *33*, 1534.
- (46) Young, K. M. H.; Klahr, B. M.; Zandi, O.; Hamann, T. W. *Catalysis Science & Technology* **2013**, *3*, 1660.
- (47) Butler, M. A. *J. Appl. Phys.* **1977**, *48*, 1914.
- (48) Hong, S. J.; Lee, S.; Jang, J. S.; Lee, J. S. *Energy Environ. Sci.* **2011**, *4*, 1781.
- (49) Katz, M. J.; Riha, S. C.; Jeong, N. C.; Martinson, A. B. F.; Farha, O. K.; Hupp, J. T. *Coord. Chem. Rev.* **2012**, *256*, 2521.
- (50) Kay, A.; Cesar, I.; Graetzel, M. *J. Am. Chem. Soc.* **2006**, *128*, 15714.
- (51) Ling, Y.; Wang, G.; Wheeler, D. A.; Zhang, J. Z.; Li, Y. *Nano Lett.* **2011**, *11*, 2119.
- (52) Albero, J.; Clifford, J. N.; Palomares, E. *Coord. Chem. Rev.*, Ahead of Print.
- (53) Kochuveedu, S. T.; Jang, Y. H.; Kim, D. H. *Chem. Soc. Rev.* **2013**, *42*, 8467.
- (54) Alexander, B. D.; Kulesza, P. J.; Rutkowska, I.; Solarska, R.; Augustynski, J. *J. Mater. Chem.* **2008**, *18*, 2298.

- (55) Guo, L.; Hung, D.; Wang, W.; Shen, W.; Zhu, L.; Chien, C.-L.; Searson, P. C. *Appl. Phys. Lett.* **2010**, *97*, 063111/1.
- (56) Zhang, Z.; Dua, R.; Zhang, L.; Zhu, H.; Zhang, H.; Wang, P. *ACS Nano* **2013**, *7*, 1709.
- (57) Duonghong, D.; Borgarello, E.; Graetzel, M. *J. Am. Chem. Soc.* **1981**, *103*, 4685.
- (58) Osterloh, F. E. *Chem. Soc. Rev.* **2013**, *42*, 2294.
- (59) Kudo, A.; Miseki, Y. *Chem. Soc. Rev.* **2009**, *38*, 253.
- (60) Osterloh, F. E. *Chem. Mater.* **2008**, *20*, 35.
- (61) Osterloh, F. E.; Parkinson, B. A. *MRS Bulletin* **2011**, *36*, 17.
- (62) Maeda, K. *ACS Catal.* **2013**, *3*, 1486.
- (63) Yang, J.; Wang, D.; Han, H.; Li, C. *Acc. Chem. Res.* **2013**, *46*, 1900.
- (64) Maeda, K.; Lu, D.; Domen, K. *Chemistry - A European Journal* **2013**, *19*, 4986.
- (65) Kelzenberg, M. D.; Boettcher, S. W.; Petykiewicz, J. A.; Turner-Evans, D. B.; Putnam, M. C.; Warren, E. L.; Spurgeon, J. M.; Briggs, R. M.; Lewis, N. S.; Atwater, H. A. *Nature Materials* **2010**, *9*, 239.
- (66) Walter, M. G.; Warren, E. L.; McKone, J. R.; Boettcher, S. W.; Mi, Q.; Santori, E. A.; Lewis, N. S. *Chem. Rev. (Washington, DC, U. S.)* **2010**, *110*, 6446.
- (67) Spurgeon, J. M.; Boettcher, S. W.; Kelzenberg, M. D.; Brunschwig, B. S.; Atwater, H. A.; Lewis, N. S. *Advanced Materials (Weinheim, Germany)* **2010**, *22*, 3277.
- (68) Spurgeon, J. M.; Walter, M. G.; Zhou, J.; Kohl, P. A.; Lewis, N. S. *Energy Environ. Sci.* **2011**, *4*, 1772.
- (69) Lewis, N. S. *Science* **2007**, *315*, 798.

- (70) Hou, Y.; Abrams, B. L.; Vesborg, P. C. K.; Bjoerketun, M. E.; Herbst, K.; Bech, L.; Setti, A. M.; Damsgaard, C. D.; Pedersen, T.; Hansen, O.; Rossmeisl, J.; Dahl, S.; Norskov, J. K.; Chorkendorff, I. *Nature Materials* **2011**, *10*, 434.
- (71) Chen, Z.; Dinh, H. N.; Miller, E. *Photoelectrochemical Water Splitting: Standards, Experimental Methods, and Protocols*; Springer: New York, NY, 2013.
- (72) Rocheleau, R. E.; Miller, E. L.; Misra, A. *Energy Fuels* **1998**, *12*, 3.
- (73) Kanan, M. W.; Nocera, D. G. *Science* **2008**, *321*, 1072.
- (74) Surendranath, Y.; Dinca, M.; Nocera, D. G. *J. Am. Chem. Soc.* **2009**, *131*, 2615.
- (75) Lutterman, D. A.; Surendranath, Y.; Nocera, D. G. *J. Am. Chem. Soc.* **2009**, *131*, 3838.
- (76) Khaselev, O.; Turner, J. A. *Science* **1998**, *280*, 425.
- (77) Joya, K. S.; Joya, Y. F.; Ocakoglu, K.; van de Krol, R. *Angew. Chem. Int. Ed.* **2013**, *52*, 10426.
- (78) Bard, A. J. *Journal of Photochemistry* **1979**, *10*, 59.
- (79) Maeda, K.; Higashi, M.; Lu, D.; Abe, R.; Domen, K. *J. Am. Chem. Soc.* **2010**, *132*, 5858.
- (80) Tada, H.; Mitsui, T.; Kiyonaga, T.; Akita, T.; Tanaka, K. *Nature Materials* **2006**, *5*, 782.
- (81) Iwase, A.; Ng, Y. H.; Ishiguro, Y.; Kudo, A.; Amal, R. *J. Am. Chem. Soc.* **2011**, *133*, 11054.
- (82) Kudo, A. *MRS Bulletin* **2011**, *36*, 32.
- (83) Ingram, D. B.; Linic, S. *J. Am. Chem. Soc.* **2011**, *133*, 5202.

- (84) Mor, G. K.; Shankar, K.; Paulose, M.; Varghese, O. K.; Grimes, C. A. *Nano Lett.* **2005**, *5*, 191.
- (85) Zhu, K.; Neale, N. R.; Miedaner, A.; Frank, A. J. *Nano Lett.* **2007**, *7*, 69.
- (86) Klimov, V. I. *J. Phys. Chem. B* **2006**, *110*, 16827.
- (87) Meyer, B. K.; Alves, H.; Hofmann, D. M.; Kriegseis, W.; Forster, D.; Bertram, F.; Christen, J.; Hoffmann, A.; Strassburg, M.; Dworzak, M.; Habocek, U.; Rodina, A. V. *Phys. Status Solidi B* **2004**, *241*, 231.
- (88) Barnhart, C. J.; Dale, M.; Brandt, A. R.; Benson, S. M. *Energy & Environmental Science* **2013**, *6*, 2804.
- (89) Youngblood, W. J.; Lee, S.-H. A.; Maeda, K.; Mallouk, T. E. *Acc. Chem. Res.* **2009**, *42*, 1966.
- (90) Young, K. J.; Martini, L. A.; Milot, R. L.; Snoeberger, R. C.; Batista, V. S.; Schmuttenmaer, C. A.; Crabtree, R. H.; Brudvig, G. W. *Coord. Chem. Rev.* **2012**, *256*, 2503.
- (91) Concepcion, J. J.; House, R. L.; Papanikolas, J. M.; Meyer, T. J. *Proc. Natl. Acad. Sci. USA* **2012**, *109*, 15560.
- (92) Gratzel, M. *Nature* **2001**, *414*, 338.
- (93) Doyle, R. L.; Godwin, I. J.; Brandon, M. P.; Lyons, M. E. G. *Phys. Chem. Chem. Phys.* **2013**, *15*, 13737.
- (94) Jiao, F.; Frei, H. *Energy Environ. Sci.* **2010**, *3*, 1018.
- (95) Yang, X.; Baik, M.-H. *J. Am. Chem. Soc.* **2004**, *126*, 13222.
- (96) Yang, X.; Baik, M.-H. *J. Am. Chem. Soc.* **2006**, *128*, 7476.

- (97) Tseng, H.-W.; Zong, R.; Muckerman, J. T.; Thummel, R. *Inorg. Chem.* **2008**, *47*, 11763.
- (98) Duan, L.; Bozoglian, F.; Mandal, S.; Stewart, B.; Privalov, T.; Llobet, A.; Sun, L. *Nature Chemistry* **2012**, *4*, 418.
- (99) Duan, L.; Wang, L.; Inge, A. K.; Fischer, A.; Zou, X.; Sun, L. *Inorg. Chem.* **2013**, *52*, 7844.
- (100) Li, F.; Zhang, B.; Li, X.; Jiang, Y.; Chen, L.; Li, Y.; Sun, L. *Angew. Chem. Int. Ed.* **2011**, *50*, 12276.
- (101) Wasylenko, D. J.; Ganesamoorthy, C.; Koivisto, B. D.; Henderson, M. A.; Berlinguette, C. P. *Inorg. Chem. (Washington, DC, U.S.)* **2010**, *49*, 2202.
- (102) Badiei, Y. M.; Polyansky, D. E.; Muckerman, J. T.; Szalda, D. J.; Haberdar, R.; Zong, R.; Thummel, R. P.; Fujita, E. *Inorg. Chem.* **2013**, *52*, 8845.
- (103) Sala, X.; Maji, S.; Bofill, R.; García-Antón, J.; Escriche, L.; Llobet, A. *Acc. Chem. Res.* **2013**.
- (104) Hull, J. F.; Balcells, D.; Blakemore, J. D.; Incarvito, C. D.; Eisenstein, O.; Brudvig, G. W.; Crabtree, R. H. *J. Am. Chem. Soc.* **2009**, *131*, 8730.
- (105) Blakemore, J. D.; Schley, N. D.; Balcells, D.; Hull, J. F.; Olack, G. W.; Incarvito, C. D.; Eisenstein, O.; Brudvig, G. W.; Crabtree, R. H. *J. Am. Chem. Soc.* **2010**, *132*, 16017.
- (106) Schley, N. D.; Blakemore, J. D.; Subbaiyan, N. K.; Incarvito, C. D.; D'Souza, F.; Crabtree, R. H.; Brudvig, G. W. *J. Am. Chem. Soc.* **2011**, *133*, 10473.
- (107) Joya, K. S.; Subbaiyan, N. K.; D'Souza, F.; de Groot, H. J. M. *Angew. Chem. Int. Ed.* **2012**, *51*, 9601.
- (108) McDaniel, N. D.; Coughlin, F. J.; Tinker, L. L.; Bernhard, S. *J. Am. Chem. Soc.* **2008**, *130*, 210.

- (109) Savini, A.; Bellachioma, G.; Ciancaleoni, G.; Zuccaccia, C.; Zuccaccia, D.; Macchioni, A. *Chem. Commun.* **2010**, *46*, 9218.
- (110) Wasylenko, D. J.; Ganesamoorthy, C.; Borau-Garcia, J.; Berlinguette, C. P. *Chem. Commun.* **2011**, *47*, 4249.
- (111) Dogutan, D. K.; McGuire, R.; Nocera, D. G. *J. Am. Chem. Soc.* **2011**, *133*, 9178.
- (112) Barnett, S. M.; Goldberg, K. I.; Mayer, J. M. *Nature Chemistry* **2012**, *4*, 498.
- (113) Codola, Z.; Garcia-Bosch, I.; Acuna-Pares, F.; Prat, I.; Luis, J. M.; Costas, M.; Lloret-Fillol, J. *Chemistry - A European Journal* **2013**, *19*, 8042.
- (114) Ellis, W. C.; McDaniel, N. D.; Bernhard, S.; Collins, T. J. *J. Am. Chem. Soc.* **2010**, *132*, 10990.
- (115) Fillol, J. L.; Codola, Z.; Garcia-Bosch, I.; Gomez, L.; Pla, J. J.; Costas, M. *Nature Chemistry* **2011**, *3*, 807.
- (116) Joya, K. S.; Valles-Pardo, J. L.; Joya, Y. F.; Eisenmayer, T.; Thomas, B.; Buda, F.; de Groot, H. J. M. *ChemPlusChem* **2013**, *78*, 35.
- (117) Wasylenko, D. J.; Palmer, R. D.; Berlinguette, C. P. *Chem. Commun.* **2013**, *49*, 218.
- (118) Cao, R.; Lai, W.; Du, P. *Energy Environ. Sci.* **2012**, *5*, 8134.
- (119) Gagliardi, C. J.; Vannucci, A. K.; Concepcion, J. J.; Chen, Z. F.; Meyer, T. J. *Energy & Environmental Science* **2012**, *5*, 7704.
- (120) Lin, X.; Hu, X.; Concepcion, J. J.; Chen, Z.; Liu, S.; Meyer, T. J.; Yang, W. *Proc. Natl. Acad. Sci. USA* **2012**, *109*, 15669.
- (121) Hughes, T. F.; Friesner, R. A. *J. Phys. Chem. B* **2011**, *115*, 9280.
- (122) Gratzel, M. *Acc. Chem. Res.* **2009**, *42*, 1788.

- (123) Graetzel, M. *Inorg. Chem.* **2005**, *44*, 6841.
- (124) Kay, A.; Graetzel, M. *J. Phys. Chem.* **1993**, *97*, 6272.
- (125) O'Regan, B.; Graetzel, M. *Nature* **1991**, *353*, 737.
- (126) Alibabaei, L.; Brennaman, K. M.; Norris, M. R.; Kalanyan, B.; Song, W.; Losego, M. D.; Concepcion, J. J.; Binstead, R. A.; Parsons, G. N.; Meyer, T. J. *Proc. Natl. Acad. Sci. USA* **2013**, *110*, 20008.
- (127) Morandeira, A.; Fortage, J.; Edvinsson, T.; Le Pleux, L.; Blart, E.; Boschloo, G.; Hagfeldt, A.; Hammarstroem, L.; Odobel, F. *J. Phys. Chem. C* **2008**, *112*, 1721.
- (128) He, J.; Lindstroem, H.; Hagfeldt, A.; Lindquist, S.-E. *J. Phys. Chem. B* **1999**, *103*, 8940.
- (129) Gibson, E. A.; Smeigh, A. L.; Le Pleux, L.; Fortage, J.; Boschloo, G.; Blart, E.; Pellegrin, Y.; Odobel, F.; Hagfeldt, A.; Hammarstrom, L. *Angew. Chem. Int. Ed.* **2009**, *48*, 4402.
- (130) Gibson, E. A.; Smeigh, A. L.; Le Pleux, L.; Hammarstroem, L.; Odobel, F.; Boschloo, G.; Hagfeldt, A. *J. Phys. Chem. C* **2011**, *115*, 9772.
- (131) Le Pleux, L.; Smeigh, A. L.; Gibson, E.; Pellegrin, Y.; Blart, E.; Boschloo, G.; Hagfeldt, A.; Hammarstrom, L.; Odobel, F. *Energy Environ. Sci.* **2011**, *4*, 2075.
- (132) Morandeira, A.; Boschloo, G.; Hagfeldt, A.; Hammarstroem, L. *J. Phys. Chem. B* **2005**, *109*, 19403.
- (133) Li, L.; Duan, L.; Wen, F.; Li, C.; Wang, M.; Hagfeldt, A.; Sun, L. *Chem. Commun.* **2012**, *48*, 988.
- (134) Song, W.; Glasson, C. R. K.; Luo, H.; Hanson, K.; Brennaman, M. K.; Concepcion, J. J.; Meyer, T. J. *J. Phys. Chem. Lett.* **2011**, *2*, 1808.
- (135) Ardo, S.; Meyer, G. J. *Chem. Soc. Rev.* **2009**, *38*, 115.

- (136) Giokas, P. G.; Miller, S. A.; Hanson, K.; Norris, M. R.; Glasson, C. R. K.; Concepcion, J. J.; Bettis, S. E.; Meyer, T. J.; Moran, A. M. *Journal of Physical Chemistry C* **2013**, *117*, 812.
- (137) Zou, C.; Wrighton, M. S. *J. Am. Chem. Soc.* **1990**, *112*, 7578.
- (138) McNamara, W. R.; Milot, R. L.; Song, H.-e.; Snoeberger, R. C., III; Batista, V. S.; Schmuttenmaer, C. A.; Brudvig, G. W.; Crabtree, R. H. *Energy Environ. Sci.* **2010**, *3*, 917.
- (139) Haller, I. *J. Am. Chem. Soc.* **1978**, *100*, 8050.
- (140) McNamara, W. R.; Snoeberger, R. C.; Li, G.; Schleicher, J. M.; Cady, C. W.; Poyatos, M.; Schmuttenmaer, C. A.; Crabtree, R. H.; Brudvig, G. W.; Batista, V. S. *J. Am. Chem. Soc.* **2008**, *130*, 14329.
- (141) Hanson, K.; Brennaman, M. K.; Luo, H.; Glasson, C. R. K.; Concepcion, J. J.; Song, W.; Meyer, T. J. *ACS Appl. Mater. Interfaces* **2012**, *4*, 1462.
- (142) Gillaizeau-Gauthier, I.; Odobel, F.; Alebbi, M.; Argazzi, R.; Costa, E.; Bignozzi, C. A.; Qu, P.; Meyer, G. J. *Inorg. Chem.* **2001**, *40*, 6073.
- (143) Jung, Y. M.; Park, Y.; Sarker, S.; Lee, J.-J.; Dembereldorj, U.; Joo, S.-W. *Sol. Energy Mater. Sol. Cells* **2010**, *95*, 326.
- (144) Hanson, K.; Brennaman, M. K.; Ito, A.; Luo, H.; Song, W.; Parker, K. A.; Ghosh, R.; Norris, M. R.; Glasson, C. R. K.; Concepcion, J. J.; Lopez, R.; Meyer, T. J. *J. Phys. Chem. C* **2012**, *116*, 14837.
- (145) Wang, L.; Ashford, D. L.; Thompson, D. W.; Meyer, T. J.; Papanikolas, J. M. *J. Phys. Chem. C* **2013**, *117*, 24250.
- (146) Hanson, K.; Losego, M. D.; Kalanyan, B.; Ashford, D. L.; Parsons, G. N.; Meyer, T. J. *Chem. Mater.* **2013**, *25*, 3.
- (147) Hanson, K.; Losego, M. D.; Kalanyan, B.; Parsons, G. N.; Meyer, T. J. *Nano Lett.* **2013**, *13*, 4802.

- (148) Lapidés, A. M.; Ashford, D. L.; Hanson, K.; Torelli, D. A.; Templeton, J. L.; Meyer, T. *J. J. Am. Chem. Soc.* **2013**, *135*, 15450.
- (149) Vannucci, A. K.; Alibabaei, L.; Losego, M. D.; Concepcion, J. J.; Kalanyan, B.; Parsons, G. N.; Meyer, T. J. *Proc. Nat. Acad. Sci.* **2013**, *110*, 20918.
- (150) Son, H.-J.; Wang, X.; Prasittichai, C.; Jeong, N. C.; Aaltonen, T.; Gordon, R. G.; Hupp, J. T. *J. Am. Chem. Soc.* **2012**, *134*, 9537.
- (151) Prasittichai, C.; Avila, J. R.; Farha, O. K.; Hupp, J. T. *J. Am. Chem. Soc.* **2013**, *135*, 16328.
- (152) Son, H.-J.; Prasittichai, C.; Mondloch, J. E.; Luo, L.; Wu, J.; Kim, D. W.; Farha, O. K.; Hupp, J. T. *J. Am. Chem. Soc.* **2013**, *135*, 11529.
- (153) Zheng, H.; Tachibana, Y.; Kalantar-zadeh, K. *Langmuir* **2010**, *26*, 19148.
- (154) Sadek, A. Z.; Zheng, H.; Breedon, M.; Bansal, V.; Bhargava, S. K.; Latham, K.; Zhu, J.; Yu, L.; Hu, Z.; Spizzirri, P. G.; Wlodarski, W.; Kalantar-Zadeh, K. *Langmuir* **2009**, *25*, 9545.
- (155) Anta, J. A.; Guillen, E.; Tena-Zaera, R. *J. Phys. Chem. C* **2012**, *116*, 11413.
- (156) Xu, F.; Sun, L. *Energy Environ. Sci.* **2011**, *4*, 818.
- (157) Lenzmann, F.; Krueger, J.; Burnside, S.; Brooks, K.; Graetzel, M.; Gal, D.; Ruehle, S.; Cahen, D. *J. Phys. Chem. B* **2001**, *105*, 6347.
- (158) Luo, H.; Song, W.; Hoertz, P. G.; Hanson, K.; Ghosh, R.; Rangan, S.; Brennaman, M. K.; Concepcion, J. J.; Binstead, R. A.; Bartynski, R. A.; Lopez, R.; Meyer, T. J. *Chem. Mater.* **2013**, *25*, 122.
- (159) Coutts, T. J.; Young, D. L.; Li, X.; Mulligan, W. P.; Wu, X. *J. Vac. Sci. Technol., A* **2000**, *18*, 2646.

- (160) Yang, S.-M.; Kou, H.-Z.; Wang, H.-J.; Cheng, K.; Wang, J.-C. *J. Phys. Chem. C* **2010**, *114*, 815.
- (161) Burnside, S.; Moser, J.-E.; Brooks, K.; Graetzel, M.; Cahen, D. *J. Phys. Chem. B* **1999**, *103*, 9328.
- (162) Swierk, J. R.; Mallouk, T. E. *Chem. Soc. Rev.* **2013**, *42*, 2357.
- (163) Youngblood, W. J.; Lee, S.-H. A.; Kobayashi, Y.; Hernandez-Pagan, E. A.; Hoertz, P. G.; Moore, T. A.; Moore, A. L.; Gust, D.; Mallouk, T. E. *J. Am. Chem. Soc.* **2009**, *131*, 926.
- (164) Li, L.; Duan, L.; Xu, Y.; Gorlov, M.; Hagfeldt, A.; Sun, L. *Chem. Commun.* **2010**, *46*, 7307.
- (165) Hagfeldt, A.; Boschloo, G.; Sun, L.; Kloo, L.; Pettersson, H. *Chem. Rev.* **2010**, *110*, 6595.
- (166) Eisenberg, R.; Gray, H. B. *Inorg.Chem.(Washington, DC, U.S.)* **2008**, *47*, 1697.
- (167) Wasielewski, M. R. *Chem. Rev.* **1992**, *92*, 435.
- (168) Khan, S. U. M.; Al-Shahry, M.; Ingler, W. B., Jr. *Science* **2002**, *297*, 2243.
- (169) Bard, A. J.; Fox, M. A. *Acc. Chem. Res.* **1995**, *28*, 141.
- (170) Meyer, T. J. *Acc. Chem. Res.* **1989**, *22*, 163.
- (171) Hupp, J. T.; Neyhart, G. A.; Meyer, T. J.; Kober, E. M. *J. Phys. Chem.* **1992**, *96*, 10820.
- (172) Hurst, J. K. *Science* **2010**, *328*, 315.
- (173) Alstrum-Acevedo, J. H.; Brennaman, M. K.; Meyer, T. J. *Inorg.Chem.* **2005**, *44*, 6802.
- (174) Treadway, J. A.; Moss, J. A.; Meyer, T. J. *Inorg.Chem.* **1999**, *38*, 4386.

- (175) Balzani, V.; Credi, A.; Venturi, M. *ChemSusChem* **2008**, *1*, 26.
- (176) Wasielewski, M. R. *Acc Chem Res* **2009**, *42*, 1910.
- (177) Green, A. N. M.; Palomares, E.; Haque, S. A.; Kroon, J. M.; Durrant, J. R. *J. Phys. Chem. B* **2005**, *109*, 12525.
- (178) Vinodgopal, K.; Bedja, I.; Kamat, P. V. *Chem. Mater.* **1996**, *8*, 2180.
- (179) Kaerkaes, M. D.; Johnston, E. V.; Verho, O.; Aakermark, B. *Acc. Chem. Res.* **2014**, *47*, 100.
- (180) Frischmann, P. D.; Mahata, K.; Wuerthner, F. *Chem. Soc. Rev.* **2013**, *42*, 1847.
- (181) Brennaman, M. K.; Patrocinio, A. O. T.; Song, W.-J.; Jurss, J. W.; Concepcion, J. J.; Hoertz, P. G.; Traub, M. C.; Murakami Iha, N. Y.; Meyer, T. J. *ChemSusChem* **2011**, *4*, 216.
- (182) Anderson, P. A.; Strouse, G. F.; Treadway, J. A.; Keene, F. R.; Meyer, T. J. *Inorg. Chem.* **1994**, *33*, 3863.
- (183) Thompson, D. W.; Ito, A.; Meyer, T. J. *Pure Appl. Chem.* **2013**, *85*, 1257.
- (184) Anderson, P. A.; Keene, F. R.; Meyer, T. J.; Moss, J. A.; Strouse, G. F.; Treadway, J. A. *J. Chem. Soc., Dalton Trans.* **2002**, 3820.
- (185) Lever, A. B. P. *Inorg. Chem.* **1990**, *29*, 1271.
- (186) Kalyanasundaram, K. *Coord. Chem. Rev.* **1982**, *46*, 159.
- (187) Juris, A.; Balzani, V.; Barigelletti, F.; Campagna, S.; Belser, P.; Von Zelewsky, A. *Coord. Chem. Rev.* **1988**, *84*, 85.
- (188) Caspar, J. V.; Meyer, T. J. *Inorg. Chem.* **1983**, *22*, 2444.

(189) Ashford, D. L.; Stewart, D. J.; Glasson, C. R.; Binstead, R. A.; Harrison, D. P.; Norris, M. R.; Concepcion, J. J.; Fang, Z.; Templeton, J. L.; Meyer, T. J. *Inorg. Chem.* **2012**, *51*, 6428.

(190) Ashford, D. L.; Song, W. J.; Concepcion, J. J.; Glasson, C. R. K.; Brennaman, M. K.; Norris, M. R.; Fang, Z.; Templeton, J. L.; Meyer, T. J. *J. Am. Chem. Soc.* **2012**, *134*, 19189.

(191) Hanson, K.; Torelli, D. A.; Vannucci, A. K.; Brennaman, M. K.; Luo, H.; Alibabaei, L.; Song, W.; Ashford, D. L.; Norris, M. R.; Glasson, C. R. K.; Concepcion, J. J.; Meyer, T. J. *Angew. Chem. Int. Ed.* **2012**, *51*, 12782.

(192) Norris, M. R.; Concepcion, J. J.; Glasson, C. R. K.; Fang, Z.; Lapidés, A. M.; Ashford, D. L.; Templeton, J. L.; Meyer, T. J. *Inorg. Chem.* **2013**, *52*, 12492.

(193) Concepcion, J. J.; Jurss, J. W.; Hoertz, P. G.; Meyer, T. J. *Angew. Chem., Int. Ed.* **2009**, *48*, 9473.

(194) Norris, M. R.; Concepcion, J. J.; Fang, Z.; Templeton, J. L.; Meyer, T. J. *Angew. Chem. Int. Ed.* **2013**, *52*, 13580.

(195) Goswami, S.; Maity, A. C.; Fun, H.-K.; Chantrapromma, S. *Eur. J. Org. Chem.* **2009**, 1417.

(196) Yam, V. W.-W.; Lee, V. W.-M.; Ke, F.; Siu, K.-W. M. *Inorg. Chem.* **1997**, *36*, 2124.

(197) Becke, A. D. *J. Chem. Phys.* **1993**, *98*, 5648.

(198) Lee, C.; Yang, W.; Parr, R. G. *Phys. Rev. B Condens. Matter* **1988**, *37*, 785.

(199) Dunning Jr., T. H.; Hay, P. J. In *Modern Theoretical Chemistry*; Schaefer III, H. F., Ed.; Plenum Press: New York, 1976, p 1.

(200) Wadt, W. R.; Hay, P. J. *J. Chem. Phys.* **1985**, *82*, 284.

(201) Jacquemin, D.; Perpète, E. A.; Scuseria, G. E.; Ciofini, I.; Adamo, C. *Journal of Chemical Theory and Computation* **2008**, *4*, 123.

(202) Jacquemin, D.; Preat, J.; Perpete, E. A.; Adamo, C. *Int. J. Quantum Chem.* **2010**, *110*, 2121.

(203) Perdew, J. P.; Burke, K.; Ernzerhof, M. *Phys. Rev. Lett.* **1996**, *77*, 3865.

(204) Adamo, C.; Barone, V. *J. Chem. Phys.* **1999**, *110*, 6158.

(205) Bauernschmitt, R.; Ahlrichs, R. *Chem. Phys. Lett.* **1996**, *256*, 454.

(206) Frisch, M. J. T., G. W.; Schlegel, H. B.; Scuseria, G. E.; Robb, M. A.; Cheeseman, J. R.; Scalmani, G.; Barone, V.; Mennucci, B.; Petersson, G. A.; Nakatsuji, H.; Caricato, M.; Li, X.; Hratchian, H. P.; Izmaylov, A. F.; Bloino, J.; Zheng, G.; Sonnenberg, J. L.; Hada, M.; Ehara, M.; Toyota, K.; Fukuda, R.; Hasegawa, J.; Ishida, M.; Nakajima, T.; Honda, Y.; Kitao, O.; Nakai, H.; Vreven, T.; Montgomery, Jr., J. A.; Peralta, J. E.; Ogliaro, F.; Bearpark, M.; Heyd, J. J.; Brothers, E.; Kudin, K. N.; Staroverov, V. N.; Kobayashi, R.; Normand, J.; Raghavachari, K.; Rendell, A.; Burant, J. C.; Iyengar, S. S.; Tomasi, J.; Cossi, M.; Rega, N.; Millam, J. M.; Klene, M.; Knox, J. E.; Cross, J. B.; Bakken, V.; Adamo, C.; Jaramillo, J.; Gomperts, R.; Stratmann, R. E.; Yazyev, O.; Austin, A. J.; Cammi, R.; Pomelli, C.; Ochterski, J. W.; Martin, R. L.; Morokuma, K.; Zakrzewski, V. G.; Voth, G. A.; Salvador, P.; Dannenberg, J. J.; Dapprich, S.; Daniels, A. D.; Farkas, Ö.; Foresman, J. B.; Ortiz, J. V.; Cioslowski, J.; Fox, D. J. *Gaussian 09*, Revision C.01; Gaussian, Inc.: Wallingford, CT, 2009

(207) Cordeiro, A.; Shaw, J.; O'Brien, J.; Blanco, F.; Rozas, I. *Eur. J. Org. Chem.* **2011**, 1504.

(208) Norman, M. H.; Zhu, J.; Fotsch, C.; Bo, Y.; Chen, N.; Chakrabarti, P.; Doherty, E. M.; Gavva, N. R.; Nishimura, N.; Nixey, T.; Ognyanov, V. I.; Rzasa, R. M.; Stec, M.; Surapaneni, S.; Tamir, R.; Viswanadhan, V. N.; Treanor, J. J. S. *J. Med. Chem.* **2007**, *50*, 3497.

(209) Sharma, K. S.; Kumari, S.; Singh, R. P. *Synthesis* **1981**, 316.

(210) Jung, D.-i.; Song, J.-h.; Kim, Y.-h.; Lee, D.-h.; Lee, Y.-g.; Park, Y.-m.; Choi, S.-k.; Hahn, J.-t. *Bull. Korean Chem. Soc.* **2007**, *28*, 1877.

(211) Zhao, Q.; Liu, S.; Shi, M.; Wang, C.; Yu, M.; Li, L.; Li, F.; Yi, T.; Huang, C. *Inorg. Chem.* **2006**, *45*, 6152.

- (212) Gu, J.; Chen, J.; Schmehl, R. H. *J. Am. Chem. Soc.* **2010**, *132*, 7338.
- (213) Biner, M.; Buergi, H. B.; Ludi, A.; Roehr, C. *J. Am. Chem. Soc.* **1992**, *114*, 5197.
- (214) Rillema, D. P.; Mack, K. B. *Inorg. Chem.* **1982**, *21*, 3849.
- (215) Ackermann, M. N.; Interrante, L. V. *Inorg. Chem.* **1984**, *23*, 3904.
- (216) Nagle, J. K.; Young, R. C.; Meyer, T. J. *Inorg. Chem.* **1977**, *16*, 3366.
- (217) Wacholtz, W. F.; Auerbach, R. A.; Schmehl, R. H. *Inorg. Chem.* **1986**, *25*, 227.
- (218) Caspar, J. V.; Meyer, T. J. *J. Am. Chem. Soc.* **1983**, *105*, 5583.
- (219) Durham, B.; Caspar, J. V.; Nagle, J. K.; Meyer, T. J. *J. Am. Chem. Soc.* **1982**, *104*, 4803.
- (220) Van Houten, J.; Watts, R. J. *J. Am. Chem. Soc.* **1976**, *98*, 4853.
- (221) Van Houten, J.; Watts, R. J. *Inorg. Chem.* **1978**, *17*, 3381.
- (222) Norrby, T.; Boerje, A.; Aakermark, B.; Hammarstroem, L.; Alsins, J.; Lashgari, K.; Norrestam, R.; Maartensson, J.; Stenhagen, G. *Inorg. Chem.* **1997**, *36*, 5850.
- (223) Allen, G. H.; White, R. P.; Rillema, D. P.; Meyer, T. J. *J. Am. Chem. Soc.* **1984**, *106*, 2613.
- (224) Hammarstroem, L.; Barigelletti, F.; Flamigni, L.; Indelli, M. T.; Armaroli, N.; Calogero, G.; Guardigli, M.; Sour, A.; Collin, J.-P.; Sauvage, J.-P. *J. Phys. Chem. A* **1997**, *101*, 9061.
- (225) Heully, J.-L.; Alary, F.; Boggio-Pasqua, M. *J. Chem. Phys.* **2009**, *131*, 184308/1.
- (226) Sun, Q.; Mosquera-Vazquez, S.; Lawson Daku, L. M.; Guenee, L.; Goodwin, H. A.; Vauthey, E.; Hauser, A. *J. Am. Chem. Soc.* **2013**, *135*, 13660.

- (227) Abrahamsson, M.; Lundqvist, M. J.; Wolpher, H.; Johansson, O.; Eriksson, L.; Bergquist, J.; Rasmussen, T.; Becker, H.-C.; Hammarstroem, L.; Norrby, P.-O.; Akermark, B.; Persson, P. *Inorg. Chem.* **2008**, *47*, 3540.
- (228) Damrauer, N. H.; Boussie, T. R.; Devenney, M.; McCusker, J. K. *J. Am. Chem. Soc.* **1997**, *119*, 8253.
- (229) Li, J.; Djurovich, P. I.; Alleyne, B. D.; Yousufuddin, M.; Ho, N. N.; Thomas, J. C.; Peters, J. C.; Bau, R.; Thompson, M. E. *Inorg. Chem.* **2005**, *44*, 1713.
- (230) Gorelsky, S. I.; Dodsworth, E. S.; Lever, A. B. P.; Vlcek, A. A. *Coord. Chem. Rev.* **1998**, *174*, 469.
- (231) Kober, E. M.; Marshall, J. L.; Dressick, W. J.; Sullivan, B. P.; Caspar, J. V.; Meyer, T. *J. Inorg. Chem.* **1985**, *24*, 2755.
- (232) Kestell, J. D.; Williams, Z. L.; Stultz, L. K.; Claude, J. P. *J. Phys. Chem. A* **2002**, *106*, 5768.
- (233) Knight, T. E.; Goldstein, A. P.; Brennaman, M. K.; Cardolaccia, T.; Pandya, A.; DeSimone, J. M.; Meyer, T. J. *J. Phys. Chem. B* **2011**, *115*, 64.
- (234) Nozaki, K.; Takamori, K.; Nakatsugawa, Y.; Ohno, T. *Inorg. Chem.* **2006**, *45*, 6161.
- (235) Kim, H. B.; Kitamura, N.; Tazuke, S. *J. Phys. Chem.* **1990**, *94*, 7401.
- (236) Ito, A.; Meyer, T. J. *PCCP* **2012**, *14*, 13731.
- (237) Caspar, J. V.; Meyer, T. J. *J. Phys. Chem.* **1983**, *87*, 952.
- (238) Caspar, J. V.; Kober, E. M.; Sullivan, B. P.; Meyer, T. J. *J. Am. Chem. Soc.* **1982**, *104*, 630.
- (239) Dattelbaum, D. M.; Martin, R. L.; Schoonover, J. R.; Meyer, T. J. *J. Phys. Chem. A* **2004**, *108*, 3518.

- (240) Yersin, H. *Top. Curr. Chem.* **2004**, *241*, 1.
- (241) Vogler, L. M.; Jones, S. W.; Jensen, G. E.; Brewer, R. G.; Brewer, K. J. *Inorg. Chim. Acta* **1996**, *250*, 155.
- (242) Dattelbaum, D. M.; Omberg, K. M.; Schoonover, J. R.; Martin, R. L.; Meyer, T. J. *Inorg. Chem.* **2002**, *41*, 6071.
- (243) Argazzi, R.; Bignozzi, C. A.; Heimer, T. A.; Castellano, F. N.; Meyer, G. J. *J. Phys. Chem. B* **1997**, *101*, 2591.
- (244) Anderson, N. A.; Lian, T. *Coord. Chem. Rev.* **2004**, *248*, 1231.
- (245) Gratzel, M. *Journal of Photochemistry and Photobiology, C: Photochemistry Reviews* **2003**, *4*, 145.
- (246) Asbury, J. B.; Hao, E.; Wang, Y.; Ghosh, H. N.; Lian, T. *J. Phys. Chem. B* **2001**, *105*, 4545.
- (247) Doi, T.; Nagamiya, H.; Kokubo, M.; Hirabayashi, K.; Takahashi, T. *Tetrahedron* **2002**, *58*, 2957.
- (248) Lee, S.-H. A.; Abrams, N. M.; Hoertz, P. G.; Barber, G. D.; Halaoui, L. I.; Mallouk, T. E. *J. Phys. Chem. B* **2008**, *112*, 14415.
- (249) Gallagher, L. A.; Serron, S. A.; Wen, X.; Hornstein, B. J.; Dattelbaum, D. M.; Schoonover, J. R.; Meyer, T. J. *Inorg. Chem.* **2005**, *44*, 2089.
- (250) Langmuir, I. *J. Am. Chem. Soc.* **1918**, *40*, 1361.
- (251) Han, W.-S.; Han, J.-K.; Kim, H.-Y.; Choi, M. J.; Kang, Y.-S.; Pac, C.; Kang, S. O. *Inorg. Chem.* **2011**, *50*, 3271.
- (252) Ma, J.; Wu, J.; Liu, W.; Wang, P.; Fan, Z. *Spectrochim. Acta, Part A* **2012**, *94*, 340.

- (253) Hata, T.; Yamada, K.; Futatsugi, T.; Sekine, M. *Synthesis* **1979**, 189.
- (254) Ji, S.; Wu, W.; Wu, W.; Song, P.; Han, K.; Wang, Z.; Liu, S.; Guo, H.; Zhao, J. *J. Mater. Chem.* **2010**, *20*, 1953.
- (255) Ashford, D. L.; Glasson, C. R. K.; Norris, M. R.; Hanson, K.; Concepcion, J. J.; Keinan, S.; Brennaman, M. K.; Templeton, J. L.; Meyer, T. J. *Inorg. Chem.* **2014**, *53*, 5637.
- (256) Kapovsky, M.; Dares, C.; Dodsworth, E. S.; Begum, R. A.; Raco, V.; Lever, A. B. P. *Inorg. Chem.* **2012**, *52*, 169.
- (257) Concepcion, J. J.; Jurss, J. W.; Templeton, J. L.; Meyer, T. J. *Proc.Natl.Acad.Sci.U.S.A.* **2008**, *105*, 17632.
- (258) Galoppini, E.; Guo, W.; Zhang, W.; Hoertz, P. G.; Qu, P.; Meyer, G. J. *J.Am.Chem.Soc.* **2002**, *124*, 7801.
- (259) Wasylenko, D. J.; Ganesamoorthy, C.; Henderson, M. A.; Berlinguette, C. P. *Inorg. Chem.* **2011**, *50*, 3662.
- (260) Peek, B. M.; Ross, G. T.; Edwards, S. W.; Meyer, G. J.; Meyer, T. J.; Erickson, B. W. *Int. J. Pept. Protein Res.* **1991**, *38*, 114.
- (261) Constable, E. C.; Dunphy, E. L.; Housecroft, C. E.; Neuburger, M.; Schaffner, S.; Schaper, F.; Batten, S. R. *Dalton Trans.* **2007**, 4323.
- (262) Sullivan, B. P.; Calvert, J. M.; Meyer, T. J. *Inorg.Chem.* **1980**, *19*, 1404.
- (263) Busche, C.; Comba, P.; Mayboroda, A.; Wadepohl, H. *Eur.J.Inorg.Chem.* **2010**, 1295.
- (264) Ozawa, H.; Sakai, K. *Chem.Lett.* **2007**, *36*, 920.
- (265) Uemura, K.; Kumamoto, Y.; Kitagawa, S. *Chem.--Eur.J.* **2008**, *14*, 9565.

- (266) McClanahan, S. F.; Dallinger, R. F.; Holler, F. J.; Kincaid, J. R. *J. Am. Chem. Soc.* **1985**, *107*, 4853.
- (267) Takeuchi, K. J.; Thompson, M. S.; Pipes, D. W.; Meyer, T. J. *Inorg.Chem.* **1984**, *23*, 1845.
- (268) Wasylenko, D. J.; Ganesamoorthy, C.; Henderson, M. A.; Koivisto, B. D.; Osthoff, H. D.; Berlinguette, C. P. *J.Am.Chem.Soc.* **2010**, *132*, 16094.
- (269) Yoshida, M.; Masaoka, S.; Sakai, K. *Chem.Lett.* **2009**, *38*, 702.
- (270) Chen, Z. F.; Concepcion, J. J.; Luo, H. L.; Hull, J. F.; Paul, A.; Meyer, T. J. *J. Am. Chem. Soc.* **2010**, *132*, 17670.
- (271) Chen, Z. F.; Concepcion, J. J.; Hu, X. Q.; Yang, W. T.; Hoertz, P. G.; Meyer, T. J. *Proc. Nat. Acad. Sci. U.S.A* **2010**, *107*, 7225.
- (272) Young, R. C.; Keene, F. R.; Meyer, T. J. *J.Am.Chem.Soc.* **1977**, *99*, 2468.
- (273) Thompson, D. W.; Fleming, C. N.; Myron, B. D.; Meyer, T. J. *J. Phys. Chem. B* **2007**, *111*, 6930.
- (274) Nocera, D. G. *ChemSusChem* **2009**, *2*, 387.
- (275) Stull, J. A.; Stich, T. A.; Service, R. J.; Debus, R. J.; Mandal, S. K.; Armstrong, W. H.; Britt, R. D. *J.Am.Chem.Soc.* **2010**, *132*, 446.
- (276) Huynh, M. H. V.; Dattelbaum, D. M.; Meyer, T. J. *Coord.Chem.Rev.* **2005**, *249*, 457.
- (277) Sivasankar, N.; Weare, W. W.; Frei, H. *J.Am.Chem.Soc.* **2011**, *133*, 12976.
- (278) Duan, L.-L.; Xu, Y.-H.; Tong, L.-P.; Sun, L.-C. *ChemSusChem* **2011**, *4*, 238.
- (279) Tinker, L. L.; McDaniel, N. D.; Bernhard, S. *J.Mater.Chem.* **2009**, *19*, 3328.

- (280) Song, W.; Chen, Z.; Brennaman, M. K.; Concepcion, J. J.; Patrocinio, A. O. T.; Iha, N. Y. M.; Meyer, T. J. *Pure Appl. Chem.* **2011**, *83*, 749.
- (281) Suzuki, H.; Nagasaka, M.; Sugiura, M.; Noguchi, T. *Biochemistry* **2005**, *44*, 11323.
- (282) Miksovska, J.; Schiffer, M.; Hanson, D. K.; Sebban, P. *Proc. Natl. Acad. Sci. U.S.A* **1999**, *96*, 14348.
- (283) Mueh, F.; Gloeckner, C.; Hellmich, J.; Zouni, A. *Biochimica et Biophysica Acta, Bioenergetics* **2012**, *1817*, 44.
- (284) Olson, J. M.; Pierson, B. K. *Int. Rev. Cyto.* **1987**, *108*, 209.
- (285) Gerischer, H. *Electrochim. Acta* **1993**, *38*, 3.
- (286) Gerischer, H. *Electrochim. Acta* **1995**, *40*, 1277.
- (287) Xu, Y.; Eilers, G.; Borgstroem, M.; Pan, J.; Abrahamsson, M.; Magnuson, A.; Lomoth, R.; Bergquist, J.; Polivka, T.; Sun, L.; Sundstroem, V.; Styring, S.; Hammarstroem, L.; Aakermark, B. *Chem.--Eur. J.* **2005**, *11*, 7305.
- (288) Martinson, A. B. F.; Hamann, T. W.; Pellin, M. J.; Hupp, J. T. *Chem.--Eur. J.* **2008**, *14*, 4458.
- (289) Clifford, J. N.; Martinez-Ferrero, E.; Viterisi, A.; Palomares, E. *Chem. Soc. Rev.* **2011**, *40*, 1635.
- (290) Chen, Z.; Concepcion, J. J.; Hu, X.; Yang, W.; Hoertz, P. G.; Meyer, T. J. *Proc.Natl.Acad.Sci.U.S.A.* **2010**, *107*, 7225.
- (291) Bennett, M. A.; Smith, A. K. *J. Chem. Soc., Dalton Trans.* **1974**, 233.
- (292) Norris, M. R.; Concepcion, J. J.; Glasson, C. R. K.; Ashford, D. L.; Templeton, J. L.; Meyer, T. J. **In Preperation.**

- (293) Kiyota, J.; Yokoyama, J.; Yoshida, M.; Masaoka, S.; Sakai, K. *Chem. Lett.* **2010**, *39*, 1146.
- (294) Gallagher, L. A.; Meyer, T. J. *J. Am. Chem. Soc.* **2001**, *123*, 5308.
- (295) Chen, Z.; Concepcion, J. J.; Hull, J. F.; Hoertz, P. G.; Meyer, T. J. *Dalton Transactions* **2010**, *39*, 6950.
- (296) Hoertz, P. G.; Chen, Z.; Kent, C. A.; Meyer, T. J. *Inorg. Chem.* **2010**, *49*, 8179.
- (297) Trammell, S. A.; Wimbish, J. C.; Odobel, F.; Gallagher, L. A.; Narula, P. M.; Meyer, T. J. *J. Am. Chem. Soc.* **1998**, *120*, 13248.
- (298) Lindsey, C. P.; Patterson, G. D. *J. Chem. Phys.* **1980**, *73*, 3348.
- (299) Williams, G.; Watts, D. C. *Trans. Faraday Soc.* **1970**, *66*, 80.
- (300) Jurss, J. W., ; Binstead, R. A.; Norris, M. R.; Concepcion, J. J.; Templeton, J. L.; Meyer, T. J. **In Preparation.**
- (301) Qu, P.; Meyer, G. J. *Langmuir* **2001**, *17*, 6720.
- (302) Zaban, A.; Ferrere, S.; Gregg, B. A. *J. Phys. Chem. B* **1998**, *102*, 452.
- (303) van der Vegte, E. W.; Hadziioannou, G. *J. Phys. Chem. B* **1997**, *101*, 9563.
- (304) Yan, S. G.; Hupp, J. T. *J. Phys. Chem.* **1996**, *100*, 6867.
- (305) Anta, J. A.; Nelson, J.; Quirke, N. *Phys. Rev. B: Condens. Matter* **2002**, *65*, 125324/1.
- (306) Nelson, J.; Chandler, R. E. *Coord. Chem. Rev.* **2004**, *248*, 1181.
- (307) Bonhote, P.; Moser, J.-E.; Humphry-Baker, R.; Vlachopoulos, N.; Zakeeruddin, S. M.; Walder, L.; Graetzel, M. *J. Am. Chem. Soc.* **1999**, *121*, 1324.

(308) Clifford, J. N.; Palomares, E.; Nazeeruddin, M. K.; Graetzel, M.; Nelson, J.; Li, X.; Long, N. J.; Durrant, J. R. *J. Am. Chem. Soc.* **2004**, *126*, 5225.

(309) Hirata, N.; Lagref, J.-J.; Palomares, E. J.; Durrant, J. R.; Nazeeruddin, M. K.; Gratzel, M.; Di Censo, D. *Chem.--Eur. J.* **2004**, *10*, 595.

(310) Serron, S. A.; Aldridge, W. S., III; Fleming, C. N.; Danell, R. M.; Baik, M.-H.; Sykora, M.; Dattelbaum, D. M.; Meyer, T. J. *J. Am. Chem. Soc.* **2004**, *126*, 14506.

(311) Trammell, S. A.; Moss, J. A.; Yang, J. C.; Nakhle, B. M.; Slate, C. A.; Odobel, F.; Sykora, M.; Erickson, B. W.; Meyer, T. J. *Inorg. Chem.* **1999**, *38*, 3665.

(312) Brimblecombe, R.; Koo, A.; Dismukes, G. C.; Swiegers, G. F.; Spiccia, L. *J. Am. Chem. Soc.* **2010**, *132*, 2892.

(313) Crosby, G. A.; Demas, J. N. *The Journal of Physical Chemistry* **1971**, *75*, 991.

(314) Rack, J. J. *Coord. Chem. Rev.* **2009**, *253*, 78.

(315) Miller, S. A.; West, B. A.; Curtis, A. C.; Papanikolas, J. M.; Moran, A. M. *J. Chem. Phys.* **2011**, *135*, 081101/1.

(316) Benkő, G.; Kallioinen, J.; Korppi-Tommola, J. E. I.; Yartsev, A. P.; Sundström, V. *J. Am. Chem. Soc.* **2001**, *124*, 489.

(317) Juozapavicius, M.; Kaucikas, M.; van Thor, J. J.; O'Regan, B. C. *The Journal of Physical Chemistry C* **2012**, *117*, 116.

(318) Asbury, J. B.; Anderson, N. A.; Hao, E.; Ai, X.; Lian, T. *The Journal of Physical Chemistry B* **2003**, *107*, 7376.

(319) Asbury, J. B.; Ellingson, R. J.; Ghosh, H. N.; Ferrere, S.; Nozik, A. J.; Lian, T. *The Journal of Physical Chemistry B* **1999**, *103*, 3110.

(320) Benkő, G.; Myllyperkiö, P.; Pan, J.; Yartsev, A. P.; Sundström, V. *J. Am. Chem. Soc.* **2003**, *125*, 1118.

- (321) Myahkostupov, M.; Piotrowiak, P.; Wang, D.; Galoppini, E. *The Journal of Physical Chemistry C* **2007**, *111*, 2827.
- (322) Benkő, G.; Kallioinen, J.; Myllyperkiö, P.; Trif, F.; Korppi-Tommola, J. E. I.; Yartsev, A. P.; Sundström, V. *The Journal of Physical Chemistry B* **2004**, *108*, 2862.
- (323) Liu, F.; Meyer, G. J. *Inorg. Chem.* **2005**, *44*, 9305.
- (324) Schoonover, J. R.; Dattelbaum, D. M.; Malko, A.; Klimov, V. I.; Meyer, T. J.; Styers-Barnett, D. J.; Gannon, E. Z.; Granger, J. C.; Aldridge, W. S.; Papanikolas, J. M. *The Journal of Physical Chemistry A* **2005**, *109*, 2472.
- (325) Moore, G. F.; Blakemore, J. D.; Milot, R. L.; Hull, J. F.; Song, H.-e.; Cai, L.; Schmuttenmaer, C. A.; Crabtree, R. H.; Brudvig, G. W. *Energy Environ. Sci.* **2011**, *4*, 2389.
- (326) Gao, Y.; Ding, X.; Liu, J.; Wang, L.; Lu, Z.; Li, L.; Sun, L. *J. Am. Chem. Soc.* **2013**, *135*, 4219.
- (327) Brown, D. G.; Schauer, P. A.; Borau-Garcia, J.; Fancy, B. R.; Berlinguette, C. P. *J. Am. Chem. Soc.* **2013**, *135*, 1692.
- (328) Oyama, N.; Anson, F. C. *J. Am. Chem. Soc.* **1979**, *101*, 3450.
- (329) Murray, R. W. *Acc. Chem. Res.* **1980**, *13*, 135.
- (330) Abruna, H. D. *Coord. Chem. Rev.* **1988**, *86*, 135.
- (331) Aranyos, V.; Hjelm, J.; Hagfeldt, A.; Grennberg, H. *J. Chem. Soc., Dalton Trans.* **2001**, 1319.
- (332) Abruna, H. D.; Denisevich, P.; Umana, M.; Meyer, T. J.; Murray, R. W. *J. Am. Chem. Soc.* **1981**, *103*, 1.
- (333) Calvert, J. M.; Schmehl, R. H.; Sullivan, B. P.; Facci, J. S.; Meyer, T. J.; Murray, R. W. *Inorg. Chem.* **1983**, *22*, 2151.

- (334) Gould, S.; O'Toole, T. R.; Meyer, T. J. *J. Am. Chem. Soc.* **1990**, *112*, 9490.
- (335) Ramos Sende, J. A.; Arana, C. R.; Hernandez, L.; Potts, K. T.; Keshevarz-K, M.; Abruna, H. D. *Inorg. Chem.* **1995**, *34*, 3339.
- (336) Moss, J. A.; Yang, J. C.; Stipkala, J. M.; Wen, X.; Bignozzi, C. A.; Meyer, G. J.; Meyer, T. J. *Inorg. Chem.* **2004**, *43*, 1784.
- (337) Cecchet, F.; Alebbi, M.; Bignozzi, C. A.; Paolucci, F. *Inorg. Chim. Acta* **2006**, *359*, 3871.
- (338) Nie, H.-J.; Shao, J.-Y.; Wu, J.; Yao, J.; Zhong, Y.-W. *Organometallics* **2012**, *31*, 6952.
- (339) Zhong, Y.-W.; Yao, C.-J.; Nie, H.-J. *Coord. Chem. Rev.* **2013**, *257*, 1357.
- (340) Li, X.; Qiu, Y.; Wang, S.; Lu, S.; Gruar Robert, I.; Zhang, X.; Darr Jawwad, A.; He, T. *Physical chemistry chemical physics : PCCP* **2013**, *15*, 14729.
- (341) Liu, Y.; Zhang, S.; Miao, Q.; Zheng, L.; Zong, L.; Cheng, Y. *Macromolecules (Washington, DC, United States)* **2007**, *40*, 4839.
- (342) Connelly, N. G.; Geiger, W. E. *Chem. Rev. (Washington, D. C.)* **1996**, *96*, 877.
- (343) Marcus, R. A. *J. Phys. Chem.* **1989**, *93*, 3078.
- (344) Ito, A.; Stewart, D. J.; Knight, T. E.; Fang, Z.; Brennaman, M. K.; Meyer, T. J. *J. Phys. Chem. B* **2013**, *117*, 3428.
- (345) Katoh, R.; Furube, A.; Yoshihara, T.; Hara, K.; Fujihashi, G.; Takano, S.; Murata, S.; Arakawa, H.; Tachiya, M. *J. Phys. Chem. B* **2004**, *108*, 4818.
- (346) Potts, K. T.; Usifer, D. A.; Guadalupe, A.; Abruna, H. D. *J. Am. Chem. Soc.* **1987**, *109*, 3961.
- (347) Trammell, S. A.; Meyer, T. J. *J. Phys. Chem. B* **1999**, *103*, 104.

- (348) O'Regan, B.; Li, X.; Ghaddar, T. *Energy Environ. Sci.* **2012**, *5*, 7203.
- (349) Park, S.-H.; Lim, J.; Song, I. Y.; Atmakuri, N.; Song, S.; Kwon, Y. S.; Choi, J. M.; Park, T. *Advanced Energy Materials* **2012**, *2*, 219.
- (350) Song, W.; Ito, A.; Binstead, R. A.; Hanson, K.; Luo, H.; Brennaman, M. K.; Concepcion, J. J.; Meyer, T. J. *J. Am. Chem. Soc.* **2013**, *135*, 11587.
- (351) Juban, E. A.; Smeigh, A. L.; Monat, J. E.; McCusker, J. K. *Coord. Chem. Rev.* **2006**, *250*, 1783.
- (352) Durrant, J. R.; Haque, S. A.; Palomares, E. *Coord. Chem. Rev.* **2004**, *248*, 1247.
- (353) Piotrowiak, P.; Galoppini, E.; Wei, Q.; Meyer, G. J.; Wiewior, P. *J. Am. Chem. Soc.* **2003**, *125*, 5278.
- (354) Bergeron, B. V.; Kelly, C. A.; Meyer, G. J. *Langmuir* **2003**, *19*, 8389.
- (355) Glasson, C. R. K.; Song, W.; Ashford, D. L.; Vannucci, A.; Chen, Z.; Concepcion, J. J.; Holland, P. L.; Meyer, T. J. *Inorg. Chem.* **2012**, *51*, 8637.
- (356) Xiang, X.; Fielden, J.; Rodriguez-Cordoba, W.; Huang, Z.; Zhang, N.; Luo, Z.; Musaev, D. G.; Lian, T.; Hill, C. L. *J. Phys. Chem. C* **2013**, *117*, 918.
- (357) Mola, J.; Mas-Marza, E.; Sala, X.; Romero, I.; Rodriguez, M.; Vinas, C.; Parella, T.; Llobet, A. *Angew. Chem. Int. Ed.* **2008**, *47*, 5830.
- (358) Vannucci, A. K.; Hull, J. F.; Chen, Z.; Binstead, R. A.; Concepcion, J. J.; Meyer, T. J. *J. Am. Chem. Soc.* **2012**, *134*, 3972.
- (359) Bard, A. J.; Faulkner, L. R. *Electrochemical Methods: Fundamentals and Applications*; 2nd ed.; Wiley: New York, 2001.
- (360) Chen, Z. F.; Concepcion, J. J.; Hull, J. F.; Hoertz, P. G.; Meyer, T. J. *Dalton Trans.* **2010**, *39*, 6950.

(361) Chen, Z. F.; Vannucci, A. K.; Concepcion, J. J.; Jurss, J. W.; Meyer, T. J. *Proc. Nat. Acad. Sci. U.S.A* **2011**, *108*, E1461.